

This work is protected by copyright and other intellectual property rights and duplication or sale of all or part is not permitted, except that material may be duplicated by you for research, private study, criticism/review or educational purposes. Electronic or print copies are for your own personal, non-commercial use and shall not be passed to any other individual. No quotation may be published without proper acknowledgement. For any other use, or to quote extensively from the work, permission must be obtained from the copyright holder/s.

The geometry and distribution of thrust- fold related fractures in limestone

Mark William Grodner

Ph.D. Geology

June 2024

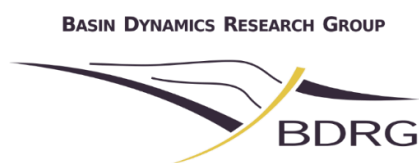


Table of Contents

Chapters.....	i
List of Figures.....	iv
List of Tables.....	xxiii
List of Equations.....	xxiv
Acknowledgements.....	xxv
Abstract.....	xxvi

Chapters

1	Introduction.....	1
1.1	Background	1
1.2	Field area	2
1.3	Aims and Objectives	4
2.	Literature Review	6
2.1	The geology of shelfal marine carbonates.....	7
2.2	Stratigraphy of the field area	13
2.2.1	Saman Suk Formation.....	13
2.2.2	Kawagarh Formation	15
2.2.3	Lockhart Formation	16
2.2.4	Patala Formation	16
2.2.5	Nammal Formation	17
2.2.6	Margalla Hills Formation	17
2.2.7	Chorgali Formation.....	18
2.3	Fold and thrust belts	19
2.3.1	General characteristics of fold and thrust belts.....	19

2.3.2	Types of fold and thrust belts.....	19
2.3.3	The foreland fold and thrust belt of northern Pakistan.....	22
2.4	Folds and fracture characteristics.....	26
2.4.1	Fracture characteristics.....	26
2.4.2	Fold characteristics.....	27
2.5	Fracture mapping methods.....	31
2.5.1	Linear scanline sampling.....	31
2.5.2	Circular scanline sampling.....	32
2.5.3	Topology of fractures.....	33
2.5.4	Fractal analysis of fractures.....	34
2.6	Remote Sensing.....	38
2.6.1	Satellite imagery.....	38
2.6.2	Geospatial data tools.....	39
2.6.3	Electromagnetic data.....	39
2.6.4	Seismic data.....	41
2.6.5	Borehole data.....	42
2.7	Geostatistics of fracture patterns.....	44
2.7.1	Spatial statistics of fracture patterns.....	44
2.8	Summary of literature review.....	47
3.	Methodology.....	49
3.1	Introduction.....	49
3.2	Geographical data capture.....	51
3.3	Geological data capture methods.....	55
3.4	Measurement circles.....	60
3.5	Topology from measurement circles.....	61
3.6	Circle mapping for fractal dimensions.....	68
3.7	Measurement lines.....	72
3.8	Measurement squares.....	75
3.9	Fracture data capture in ArcMap.....	77
3.10	Electronic data.....	85
4.	Field Mapping.....	94
4.1.	Overview of the geology of the field regions.....	94
4.2.	Field regions.....	101
4.2.1.	Losar Baoli region.....	101
4.2.2.	Makhniyal region.....	131
4.2.3.	Najafpur region.....	183

4.2.4.	Talhaar region	214
4.2.5.	Shah Dara region	277
4.2.6	Jabbri region	303
4.2.7.	Changla Gali region	332
5.	Interpretation of fractures.....	346
5.1	Fractures and lithology.....	347
5.2	Fracture characteristics in different geological structures.....	361
5.3	Summary of fracture characteristics	372
6.	Discussion.....	374
6.1	Topology and fractal dimensions of rock types.....	374
6.1.1	Topology and fractal dimensions of rock types in the study area	375
6.1.2	Topology and fractal dimensions of other FAT belt rock types	378
6.2	Topology and fractal dimensions of structures.....	380
6.2.1	Topology and fractal dimensions of structures in the study area.....	381
6.3	Topology and fractal dimensions of different FAT belt types	384
7.	Conclusions.....	386
7.1	Fractal dimensions and topological analysis	386
7.2	Key results	387
7.3	Comparisons with previous studies.....	389
7.4	Further research.....	390
8.	References.....	395

List of Figures

Figure 1.1: Location map of Pakistan, and distribution of field regions	3
Figure 2.1: The classification scheme of Dunham (1962)	8
Figure 2.2: Stratigraphic column of the various formations investigated in this thesis.	14
Figure 2.3: Tectonic plates involved in the development of the Himalayas	23
Figure 2.4: Type, orientation and frequency of fracture sets	27
Figure 2.5: Fracture development models - Transitional Longitudinal and Flexural Flow	28
Figure 2.6: Types of fractures forming around an anticline	30
Figure 2.7: Different topological node types in a measurement circle	34
Figure 2.8: A box-count-fracture example to determine the fractal dimension	36
Figure 2.9: Slope of a log-log graph that represents the fractal dimension	37
Figure 2.10: Magnetotelluric section profile	41
Figure 2.11: Plan view of the seismic image of fracture intensity	42
Figure 2.12: Drill-core	43
Figure 3.1: An example of the Google Earth image of the mapping sites	54
Figure 3.2: Geological map of the Talhaar region	54
Figure 3.3: Google Earth image of all seven mapping sites in the field area.	55
Figure 3.4: Examples of measurement circles chalked on the rock mass	60
Figure 3.5: Node types of intersecting fractures as defined by Mauldon et al. (2001)	61

Figure 3.6: Examples of the 1 m diameter measurement circles.	62
Figure 3.7: Nodes within a 1 m measurement circle.	63
Figure 3.8: Number of different types of nodes present at a s a single measurement.	67
Figure 3.9: Box-counting technique within the 1 m measurement circle.	68
Figure 3.10: Log-log plot of box-count data from a measurement circle.	70
Figure 3.11: Measurement lines.	71
Figure 3.12: Distribution of fracture spacings on the three measurement lines	72
Figure 3.13: The fracture spacing of unmineralised and calcite fractures	72
Figure 3.14: Fracture spacing from measurement circles across a thrust	73
Figure 3.15: Fracture intersection node types within 5 cm grid	74
Figure 3.16: 10 cm squares for analysis of the fracture pattern	75
Figure 3.17: Detailed images of fracture patterns.	76
Figure 3.18: Data-capture methods using ArcMap to define the spatial distribution of fractures	78
Figure 3.19: Variations in fracture length	79
Figure 3.20: Variations in fracture abundance along the exposure.	79
Figure 3.21: Data-capture methods and types produced using ArcMap to define fracture density	80
Figure 3.22: Box-density plot of fractures across the same area as Figure 3.21	81
Figure 3.23: Linear-density plot of fractures across the same area as Figure 3.21	81
Figure 3.24: Fracture lengths across the same area as Figure 3.21	82
Figure 3.25: Digitised fractures in 5 cm measurement circles	83

Figure 3.26: Fracture length distribution within the 5 cm diameter circles digitised in ArcMap.	84
Figure 3.27: Data spreadsheet for the Talhaar field region	85
Figure 3.28: All data from the in each tab (that is circles at each site) in a field area	86
Figure 3.29: Average and standard deviation of the number of nodes and fractal dimensions	87
Figure 3.30: Topological characteristics of various structural domains	88
Figure 3.31: Topological characteristics of various rock types	90
Figure 4.1: Map of Pakistan, and the various field regions	92
Figure 4.2: Stratigraphic column of the field area	95
Figure 4.3: Stratigraphy of the study area	96
Figure 4.4: Mapped stratigraphy of each study site	98
Figure 4.5: Regional structural geology	99
Figure 4.6: Geological map of the Losar Baoli region	100
Figure 4.7: Cross-section through the Losar Baoli region	101
Figure 4.8: View eastward along the Main Boundary Thrust cliffs	101
Figure 4.9: Mapping circle positions at site 1	103
Figure 4.10: One metre measurement circles, site 1	104
Figure 4.11: Node count, site 1	105
Figure 4.12: Fracture characteristics and fractal dimension, site 1	106
Figure 4.13: Fracture characteristics and fractal dimension, site 1	106
Figure 4.14: Photo-mosaic, fracture traces and rock types of site 2	108

Figure 4.15: Site 2 measurement circles	109
Figure 4.16: Node count, site 2	110
Figure 4.17: Fracture characteristics and fractal dimension, site 2	110
Figure 4.18: Fracture characteristics and fractal dimension, site 2	110
Figure 4.19: Positions of measurement circles 1 and 2 at site 3	111
Figure 4.20: Measurement circles, site 3	112
Figure 4.21: Node count, site 3	112
Figure 4.22: Fracture characteristics and fractal dimension, site 3	113
Figure 4.23: Fracture characteristics and fractal dimension, site 3.	113
Figure 4.24: Positions of measurement circles at site 4	114
Figure 4.25: Measurement circles, site 4	115
Figure 4.26: Node count, site 4	115
Figure 4.27: Fracture characteristics and fractal dimension, site 4	116
Figure 4.28: Fracture characteristics and fractal dimension, site	116
Figure 4.29: View eastward along the Kot Jandaan road towards site 5	118
Figure 4.30: Measurement circles, site 5	119
Figure 4.31: Node count, site 5	119
Figure 4.32: Fracture characteristics and fractal dimension, site 5	120
Figure 4.33: Fracture characteristics and fractal dimension, site 5q	120
Figure 4.34: Measurement lines, site 5	121

Figure 4.35: Distribution of fracture spacings on measurement lines	122
Figure 4.36: Author with the local farmer who provided a refreshing tea at site 5	122
Figure 4.37: View towards site 6	123
Figure 4.38: Measurement circles at site 3	125
Figure 4.39: Fault propagation fold located just above Measurement circle	126
Figure 4.40: Block diagram of the components of the fault propagation fold	126
Figure 4.41: Node count, site 6	127
Figure 4.42: Fracture characteristics and fractal dimension	127
Figure 4.43: Fracture characteristics and fractal dimension, site 6	127
Figure 4.44: Position of the sites in the Losar Baoli region, site 6	128
Figure 4.45: Node counts at sites across the Losar Baoli region	129
Figure 4.46: Fracture characteristics and fractal dimensions across the Losar Baoli region.	130
Figure 4.47: Fracture characteristics and fractal dimensions across the Losar Baoli region.	130
Figure 4.48: Road to the hilltop village of Makhniyal	131
Figure.4.49: Geological map of the Makhniyal region	133
Figure 4.50: Google Earth image showing the geology	134
Figure 4.51: Photo-mosaic of site 1	135
Figure 4.52: Line drawing of site	136
Figure 4.53: Diagram s of the Whispering Pines	137
Figure 4.54: Photo-mosaic of the Whispering Pines	138

Figure 4.55: Photo-mosaic of the Whispering Pines Thrust at site 2	138
Figure 4.56: Line drawing of fracture trends of the Whispering Pines Thrust at site 2	138
Figure 4.57: Measurement circles 1 to 6 at site 2	139
Figure 4.58: Measurement circles 7 to 10 at site 2	140
Figure 4.59: Number of nodes at site 2	141
Figure 4.60: MTL, lines, nodes, and branches and fractal dimension at site 2	142
Figure 4.61: Connectivity, fracture intensity, and density and fractal dimension at site 2	142
Figure 4.62: Composite image of the Nammal Formation outcrop at site 3	144
Figure 4.63: Line drawing of the fracture patterns at site 3	144
Figure 4.64: Measurement circles at site 3	145
Figure 4.65: Number of nodes at site 3	146
Figure 4.66: MTL, lines, nodes, and branches and fractal dimension at site 3	146
Figure 4.67: Connectivity, fracture intensity, and density and fractal dimension at site 3	147
Figure 4.68: Image showing the Whispering Pines Thrust, well exposed at site 4	148
Figure 4.69: Node distribution in the different measurement squares	149
Figure 4.70: Average density of x, y, and e fractures in measurement squares	150
Figure 4.71: Site 5 – bedding dips in the direction of view at 30 degrees	152
Figure 4.72: Fracture node measurement circles at site 5	153
Figure 4.73: Number of nodes at site 5	154
Figure 4.74: MTL, lines, nodes, and branches and fractal dimension at site 5.	154

Figure 4.75: Connectivity, fracture intensity, and density and fractal dimension at site 5	155
Figure 4.76: Faulted contact between the Patala and Lockhart formations (site 6)	157
Figure 4.77: 1 m measurement circles in the fractured Lockhart Formation at site 6	158
Figure 4.78: Number of nodes at site 6	160
Figure 4.79: MTL, lines, nodes, and branches and fractal dimension at site 6	161
Figure 4.80: Connectivity, fracture intensity, and density and fractal dimension at site 6	161
Figure 4.81: Steeply south-eastward dipping beds of the Lockhart Formation	162
Figure 4.82: Discontinuities at site 7	163
Figure 4.83: Outcrop at site 7	164
Figure 4.84: Close-up view of fractured rock mass perpendicular to bedding	165
Figure 4.85: Earlier generations of fractures exposed on a late-stage fracture surface	165
Figure 4.86: Fracture lengths of 5 cm wide measurement circles	167
Figure 4.87: Fracture length distribution in the 5 cm wide measurement circles	168
Figure 4.88: Fracture nodes of the measurement circles.	169
Figure 4.89: Site 8 – view northeast along Kohala Bala Road	171
Figure 4.90: Contact between the fine-grained dark grey wackestone and packstone	172
Figure 4.91: Bioclastic foraminiferal packstone	173
Figure 4.92: Younger, dark grey-coloured wackestone	174
Figure 4.93: Measurement circles in distinctly different wackestone and packstone	175
Figure 4.94: Number of nodes at site 8	176

Figure 4.95: MTL, lines, nodes, and branches and fractal dimension at site 8	177
Figure 4.96: Connectivity, fracture intensity, and density and fractal dimension at site 8	178
Figure 4.97: Average number of nodes at the measurement sites in the Makhniyal region	180
Figure 4.98: Fracture characteristics at the various mapping sites in the Makhniyal region	180
Figure 4.99: Fracture characteristics at the various mapping sites in the Makhniyal region	181
Figure 4.100: Contoured plot of nodes versus fractal dimensions in the Makhniyal region	182
Figure 4.101: Total number of nodes vs. fractal dimension at each site in the Makhniyal region	183
Figure 4.102: The number of nodes of vs. fractal dimension in the Makhniyal region	184
Figure 4.103: View southwards from site	185
Figure 4.104: Geological map of the Najafpur region	186
Figure 4.105: Plan-view of light grey wackestone at site 1	188
Figure 4.106: Cross-sectional sketch of the rock types exposed at site 2	189
Figure 4.107: Metre- and decimetre-scale images of the three rock types exposed at site 2	190
Figure 4.108: Node counts for circles at site 2	191
Figure 4.109: Average topological values of site 2	192
Figure 4.110: Eastward looking Google Earth image showing large, overturned anticline	193
Figure 4.111: View eastwards of the outcrop of the Lockhart Formation at site 3	194
Figure 4.112: Fractures characteristics at site 3	196
Figure 4.113: Characteristics of bedding surfaces and fractures contained within a single bed	197
Figure 4.114: Characteristics of cross-cutting fractures of the fold axis	198

Figure 4.115: Length distribution of bedding plane fractures and fractures in bedding planes	198
Figure 4.116: Length distribution of fractures associated with the fold axis at site 3	199
Figure 4.117: Number of fractures and length characteristics.	199
Figure 4.118: Site 3 measurement circles 1 to 4.	201
Figure 4.119: Site 3 measurement circles 5 to 8	202
Figure 4.120: Node counts for circles at site 3	203
Figure 4.121: Fracture characteristics and fractal dimension, site 3	203
Figure 4.122: Fracture characteristics and fractal dimension, site 3	204
Figure 4.123: Steeply dipping strata of the Nammal Formation	205
Figure 4.124: Distribution of measurement circles on the road cutting	205
Figure 4.125: Measurement circles at site 4	206
Figure 4.126: Node counts for circles at site 4	207
Figure 4.127: Bedding and fracture sets defined by the distribution of nodes in circle 1	207
Figure 4.128: Fracture characteristics and fractal dimension, site 4	208
Figure 4.129: Fracture characteristics and fractal dimension, site 4	208
Figure 4.130: View westward at site 5	209
Figure 4.131: Measurement circles at site 5	210
Figure 4.132: Node counts for circles at site 5	211
Figure 4.133: Fracture characteristics and fractal dimension, site 5	211
Figure 4.134: Fracture characteristics and fractal dimension, site 5	212

Figure 4.135: Sketch map of the major geological features	212
Figure 4.136: Node types in the Najafpur region	213
Figure 4.137: Variations in fracture characteristics across the sites in the Najafpur region	214
Figure 4.138: Average number of nodes vs. fractal dimension at all the circles at each site	215
Figure 4.139: Total number of nodes vs. fractal dimension for all the circles at each site	215
Figure 4.140: Geological map of the Talhaar region	216
Figure 4.141: Cross-section through the Talhaar field region,	217
Figure 4.142: View westward along strike from the Talhaar road towards site 1	217
Figure 4.143: View from Margalla Hills Formation to the brown shale of the Nammal Formation	219
Figure 4.144: Fracture sets on a limestone bedding surface of the Margalla Hills Formation	220
Figure 4.145: Thalassinoides trace fossils at site 1	220
Figure 4.146: Number of nodes per circle at site 1	221
Figure 4.147: Fracture characteristics of site 1	221
Figure 4.148: Measurement circles at site 1	222
Figure 4.149: Fracture characteristics of site 1	223
Figure 4.150: Circle and measurement line positions at site 2	224
Figure 4.151: Measurement circles at site 2	225
Figure 4.152: Node counts at site 2	226
Figure 4.153: Fracture characteristics, site 2.	226
Figure 4.154: Fracture characteristics, site 2	227

Figure 4.155: Horizontal Measurement Line 5 at site 2	228
Figure 4.156: Vertical Measurement Line 6 at site	229
Figure 4.157: Fractures at different spacings at Line 5, site 2	229
Figure 4.158: Fractures at different spacings at Line 6, site 2	230
Figure 4.159: Fracture spacing characteristics of measurement lines 5	230
Figure 4.160: View northeast from site 2 along the strike of the thrust fault	232
Figure 4.161: View northeast of the road sidewall at site 3	233
Figure 4.162: Measurement circles at site 3	233
Figure 4.163: Node count, site 3	234
Figure 4.164: Fracture characteristics, site 3	234
Figure 4.165: Fracture characteristics, site 3	234
Figure 4.166: View down road at site 4 showing steep dip of the strata	235
Figure 4.167: Positions of measurement circles at site 4	236
Figure 4.168: Node count, site 4	236
Figure 4.169: Measurement circles, site 4	237
Figure 4.170: Fracture characteristics, site 4	238
Figure 4.171: Fracture characteristics, site 4	238
Figure 4.172: View from site 5, southwards down the hill towards site 4	239
Figure 4.173: Measurement circles, site 5	240
Figure 4.174: Distribution of nodes in circle 2	240

Figure 4.175: Node count of the single measurement circle at site 5	241
Figure 4.176: Fracture characteristics, site 5	241
Figure 4.177: Fracture characteristics, site 5	242
Figure 4.178: Fresh, in-situ, Lockhart Formation exposed within the debris at site 5	243
Figure 4.179: 5 cm * 5 cm detailed images of the fracture patterns at site 5	244
Figure 4.180: 50 cm measurement line at site 5	244
Figure 4.181: 1 m measurement line on a different fragment of Lockhart Formation at site 5	245
Figure 4.182: Fractures at different spacings along the measurement line at site 5	245
Figure 4.183: View northwards from the mountain-top at site 6 into the Najafpur region	246
Figure 4.184: View northwest at site 6, along strike	246
Figure 4.185: Measurement circles, site 6	247
Figure 4.186: Node distribution, in circle 2 at site 6	248
Figure 4.187: Node count, site 6	249
Figure 4.188: Fracture characteristics, site 6	249
Figure 4.189: Fracture characteristics, site 6	249
Figure 4.190: Google earth image showing site 7, 8, and 9 with geological structures	250
Figure 4.191 Composite image of the western sidewall of the road at site 7	252
Figure 4.192: Fracture counts from ArcMap along the sidewall at site 7	254
Figure 4.193: Fracture characteristics at site 7	254
Figure 4.194: Western sidewall at site 7	255

Figure 4.195: Measurement circles 1 to 6, site 7	257
Figure 4.196: Measurement circles 6 to 10, site 7	258
Figure 4.197: Node count, site 7	259
Figure 4.198: Fracture characteristics, site 7	259
Figure 4.199: Fracture characteristics, site 7	259
Figure 4.200: View southwest towards site 7	261
Figure 4.201: Fractured rock mass at site 8	261
Figure 4.202: Location of measurement circles at site 8	262
Figure 4.203: Circles 1 to 6 at site 8	264
Figure 4.204: Node count, site 8	265
Figure 4.205: Fracture characteristics, site 8	265
Figure 4.206: Fracture characteristics, site 8	265
Figure 4.207: View southwards down the valley from site 9 towards site 8 and site 7	266
Figure 4.208: View westward at site 9.	267
Figure 4.209: Photograph and sketch of thrust at site 9	268
Figure 4.210: Eastern side of road with an exposure of the Margalla Hills	269
Figure 4.211: Exposures of fractures in the Margalla Hills Formation in the thrust	270
Figure 4.212: Measurement circles at site 9	270
Figure 4.213: Node count, site 9	270
Figure 4.214: Fracture characteristics, site 9	271

Figure 4.215: Fracture characteristics, site 9	271
Figure 4.216: Sketch-map of location of measurement in the Talhaar region	272
Figure 4.217: Node distribution across the measurement sites in the Talhaar region	272
Figure 4.218: Node distribution across the Talhaar region	273
Figure 4.219: Fracture characteristics in the Talhaar region	274
Figure 4.220: Fracture characteristics in the Talhaar region	274
Figure 4.221: Total number of nodes vs. fractal dimension	275
Figure 4.222: Total number of nodes vs. fractal dimension	276
Figure 4.223: Zoomed in view of the nodes vs. fractal dimensions of the Talhaar region	277
Figure 4.224: Geological map of the Shah Dara site	279
Figure 4.225: Shah Dara picnic site	280
Figure 4.226: Mapping circles at site	281
Figure 4.227: Number of nodes at site 1	282
Figure 4.228: Fracture characteristics at site 1.	283
Figure 4.229: Fracture characteristics at site 1.	283
Figure 4.230: Photographs of site 2	284
Figure 4.231: Line drawing of the thrusts and folds at site 2	285
Figure 4.232: Number of nodes at site 2.	286
Figure 4.233: Fracture characteristics site 2.	287
Figure 4.234: Fracture characteristics site 2	287

Figure 4.235: Measurement circles of at site 2	288
Figure 4.236: Number of nodes at site 3.	289
Figure 4.237: Fracture characteristics, site 3	290
Figure 4.238: Fracture characteristics, site 3	291
Figure 4.239: Composite photograph of site 4	292
Figure 4.240: Line drawing of fracture patterns at site 4	293
Figure 4.241: Fractures and lithological types at site 4	294
Figure 4.242: Measurement circles at site 4	297
Figure 4.243: Number of nodes in the different measurement circles at site 4	298
Figure 4.244: Fracture characteristics, site 4	298
Figure 4.245; Fracture characteristics at site 4	298
Figure 4.246: Schematic cross-section of the Shah Dara region	299
Figure 4.247: Node counts in the circles at	300
Figure 4.248: Fracture characteristics of the various sites of the Shah Dara region	301
Figure 4.249: Average topology and fractal dimension of the of the Shah Dara region	301
Figure 4.250: Average number of nodes and fractal dimensions at Shah Dara	302
Figure 4.251: View downstream (westward) of the river next to site 4	303
Figure 4.252: Geological map of the Jabbri region	304
Figure 4.253: Measurement circle with nodes drawn	306
Figure 4.254: Bed thickness vs. number of fractures.	307

Figure 4.255 Photograph and line-drawing of site 3	.	308
Figure 4.256: Google Earth images of site 3.		309
Figure 4.257: Measurement circles at site 3		310
Figure 4.258: Node count at site 3		311
Figure 4.259: Topological values and fractal dimensions of the circles at site 3		311
Figure 4.260: Photo-mosaic image of site 4	.	313
Figure 4.261: Line-drawing of showing the fractures at site 4	.	313
Figure 4.262: Measurement circles at site 4		314
Figure 4.263: Node count of measurement circles at site 4		315
Figure 4.264: Topology and fractal dimensions of measurement circles at site 4		316
Figure 4.265: Photo-mosaic of the tightly folded Patala Formation at site 5		317
Figure 4.266: Line-diagram of the tightly folded strata of the Patala Formation at site 5		317
Figure 4.267: Annotated photographs of the measurement circles at site 5		318
Figure 4.268: Node count at site 5 - “y” type nodes predominate		319
Figure 4.269: Topological and fractal characteristics of the measurement circles at site 5		320
Figure 4.270: Highly fractured, steeply dipping Lockhart Formation at site 6		321
Figure 4.271: Line sketch of Figure 4.270		321
Figure 4.272: Measurement circle at site 6	.	322
Figure 4.273: Photograph of site 7 showing folded and highly fractured Lockhart Formation		323
Figure 4.274: Line drawing of Figure 4.273		324

Figure 4.275: Circles at site 7	324
Figure 4.276: Node count, circles at site 7	325
Figure 4.277: Topology and fractal dimension, site 7	325
Figure 4.278: 1 m long horizontal measurement strip divided into ten 10 * 10 cm squares	325
Figure 4.279: Node counts of the ten 10 * 10 cm squares at Position 4	326
Figure 4.280: Node count of all sites in the Jabbri region	327
Figure 4.281: Topology and fractal dimension of all sites in the Jabbri region	328
Figure 4.282: Average total number of nodes vs. fractal dimension at each site.	329
Figure 4.283: Total number of nodes vs. fractal dimension for all the circles	330
Figure 4.284: Geological map of the Changla Gali	331
Figure 4.285: Sites and orientation of major geological features at Changla Gali	333
Figure 4.286: Photo-mosaic of site 1, Changla Gali.	334
Figure 4.287: Fractal and topological mapping of site 1, Changla Gali	335
Figure 4.288: Photograph of thrust and anticline at site 2, Changla Gali	337
Figure 4.289: Measurement circles at site 2, Changla Gali	338
Figure 4.290: Node count at site 2, Changla Gali	338
Figure 4.291: Topological and fractal characteristics of the measurement circles at site 2	339
Figure 4.292: Photo-mosaic image and corresponding line drawing of site 3, Changla Gali.	340
Figure 4.293: Measurement circles from site 3, Changla Gali	341
Figure 4.294: Node count at site 3, Changla Gali	342

Figure 4.295: Topological and fractal characteristics of the measurement circles at site 3	342
Figure 4.296: Distribution of the total number of nodes versus fractal	343
Figure 4.297: Tightly clustered data from site 3, Changla Gali.	344
Figure 5.1: Distributions of the closely spaced depositional environments in the study	352
Figure 5.2: Typical ramp limestone sequence within the Patala Formation	353
Figure 5.3: Light-coloured wackestone with TL shale layers deformed by FF	354
Figure 5.4: (a) <i>Thalassinoides</i> and (b) chondrites ichnofossils.	354
Figure 5.5: Discrete burrows within fine grained argillaceous wackestone	355
Figure 5.6: Micrographs illustrating the strong effect of microspar content	356
Figure 5.7: Block diagrams of the idealised fracture patterns in the six rock assemblages	358
Figure 5.8: Number of nodes of each rock assemblage	359
Figure 5.9: Average and standard deviation of the total number of nodes and fractal dimensions	360
Figure 5.10: Topological characteristics of the different rock assemblages	363
Figure 5.11: Shale beds form a decollement surface	364
Figure 5.12: Distribution of geological structures in the field area	366
Figure 5.13: Average , standard deviation of nodes and fractal dimensions of structural features	367
Figure 5.14: Number of nodes of the geological structures and the fractal dimensions	368
Figure 5.15: Schematic cross-section across the study area of the Himalayan Frontal FAT belt	371
Figure 5.16: Pop-up structure	372
Figure 5.17: Anticline	373

Figure 5.18: Normal fault	373
Figure 5.19: Syncline	374
Figure 5.20: Overtured anticline	375
Figure 5.21: Back-thrust	376
Figure 5.22: Fore-thrust	377
Figure 6.1: Preliminary characteristics of different FAT belts	386

List of Tables

Table 2 1: Disaggregated fracture characteristics	46
Table 3.1: Data collection terms and their meaning in this thesis	50
Table 3.2: Geographical locations of mapping sites	52
Table 3.3: Measurement methods per site	57
Table 3.4: Number of nodes considering all fracture sets together	66
Table 4.1: Distribution of stratigraphy and structures across the field areas	97
Table 4.2: Location of mapping sites, Losar Baoli region	102
Table 4.3: Characteristics of the measurement lines at site 5	121
Table 4.4: Location and stratigraphy of study sites	132
Table 4.5: Characteristics of the fractures measured	166
Table 4.6: Node count and topology of circle	170
Table 4.7: Location of mapping sites relative the major structures and their stratigraphy.	187
Table 4.8: Location of mapping sites.	218
Table 4.9: Characteristics of the measurement lines at site 2	227
Table 4.10: Fracture characteristics of Lines 5 and 6.	228
Table 4.11: Ratios of nodes and fracture characteristics	242
Table 12: Location of measurement circles	255
Table 4.13: Compound ranking of different circles at Site 6	258

Table 4.14: Compound ranking of different circles at Site 7	262
Table 4.15: Location of mapping sites and other points of interest.	278
Table 4.16: Box-counting sizes for circles.	290
Table 4.17: Location, stratigraphy and major structure of study sites.	305
Table 4.18: Measurement circle characteristics, site 4.	315
Table 4.19: Topological characteristics of the different measurement scales at site 1.	336
Table 5.1: Typical unit thicknesses and bed thicknesses of the specific rock assemblages	357
Table 5.2: Average topological characteristics of the different combinations of rock types	362
Table 5.3: Summary of average topological characteristics of each of the structural features	369
Table 6.1: Percentage carbonate matrix and compared to the of UCS of various limestone	379
Table 6.2: Preliminary characterisation of FAT belts using fractal dimensions and topology	386

List of Equations

Equation 1: Fractal dimension	36
Equation 2: Number of tips	65
Equation 3: Number of nodes	65
Equation 4: Number of lines	65
Equation 5: Number of branches	65
Equation 6: Fracture intensity	65
Equation 7: Fracture density	65
Equation 8: Mean Trace Length (MTL)	65

Acknowledgements

I suffered a stroke during my Ph.D. I am extremely grateful to my supervisors for aiding me in my physical and mental recovery from this. Stu Clarke, Stuart Burley, and Graham Lesley showed great patience, kindness, and help in assisting me with my thesis. The patience and understanding of the examiners is also gratefully acknowledged. Thank you.

My thesis was partly funded by Orient Petroleum Incorporated (OPI) in Pakistan. I would like to acknowledge the assistance of OPI management, and especially the field geologists Muhammad Saleem and Israr Azfal and our driver Khalid Nazar for their generous assistance in the field.

Abstract

Outcrop study of fracture geometry and topology in limestones of high-level thrust sheets in the Frontal Himalayan Thrust, north of Islamabad, Pakistan has enabled the determination of convergent tectonic spatial geometries and distributions of thrust-fold related fracture networks. Multiple and superimposed stresses generate unique fracture patterns, within this environment and the characteristics had previously been difficult predict and relate to structural domains.

A new type of fracture mapping approach has been developed, combining the topological and fractal characteristics of fractures. Cross-plots of this data created a large amount of fracture information. All fractures are compiled and analysed, enabling complete analysis of the effects of successive tectonic stresses. Rock composition is divided based on percentage of shale and limestone studied, but no distinction is evident in the topological and fractal cross-plots of the various limestones. This consistency is interpreted to be because of their geomechanical similarity, a result of the pervasive abundance of pore-filling micrite and microspar cements in the wackestones which imparts brittle strength.

It is possible to:

- 1. Identify geological characteristics, especially topological and fractal relationships of the rock-mass, allowing discrimination of fracture networks associated with thrusting and folding.*
- 2. Utilise the topological and fractal characteristics to define and compare geological structures at depth and hence determine the fractures and dominant deformation mechanism.*
- 3. Assess the fractal and topological characteristics to enable the evaluation of different fold and thrust belts, both from surface and subsurface to understand potential fracture distributions.*

1 Introduction

1.1 Background

Rock fracturing is a result of the mechanical response of applied stresses on lithologies of varying strengths (Brown, 1984). Rock fractures are ubiquitous in the Earth's upper crustal levels due to brittle deformation where the rock changes shape but cannot reform once it has fractured. There are two types of brittle deformation, tensile, and shear failure (Hobbs, 1964). Tensile failure typically results in joints and veins, and shear failure in faults. These modes of failure can act together to produce complex sets of fractures as the applied stress fields vary in both time and space (Barton *et al.*, 1985).

The distribution of fractures in a rock-mass determines its ability to maintain its structural integrity and hence the excavations or constructions sited within the rock-mass. As mining is becoming deeper, both from excavations underground, and larger open-cast pits, the applied stresses at the mining face are increasing, causing the failure of fractures. This requires a greater understanding of both the intact rock and the existing fractures (i.e., the rock-mass) to prevent accidents when mining.

Fractures play a significant role in discoveries of minerals as fluid movement pathways and storage volumes of valuable metals can be identified (Cox, 2005, Lonergan *et al.*, 1999). The knowledge of fracture patterns has stemmed from the exploitation of metal deposits for many centuries, especially as fractures and faults are not passive conduits but are active in transporting mineral rich fluids during deformation by thrust-fold related pumping and controlling the type of mineralisation (Jolley *et al.*, 1999).

Understanding the variations in the fracture types that causes differences in fluid flow and hence the metal compositions of an ore deposit allow a more efficient identification and environmentally sustainable exploitation of future mines. Fractures are due to the natural applied stresses, the stress per unit area, in a rock of a particular strength. Compressive stresses are the most common at convergent

tectonic plate boundaries causing folds and faults. Tensile stresses cause rocks under tension to lengthen or break apart typically at divergent plate boundaries. Shear stress is the most common stress at transform plate boundaries. Importantly, fractures vary in scales from hundreds of kilometres to abundant fractures of less than one millimetre in size. The fractures at these different scales are all still due to compressive, tensile or shear stresses. Closely spaced fractures can form due to varied strengths of the rock and different magnitudes of the stresses applied to the rock-mass. Highly fractured rocks, such as those adjacent to and associated with thrust structures can form significant fracture networks and they may possess both high permeability and fracture porosity (Aydin, 2000). The porosity, permeability and flow mechanisms in carbonate rocks are primarily due to post-depositional characteristics, such as fractures. Without fractures, carbonates do not typically host viable hydrocarbon fields, and the structural geological history of the carbonates is a significant factor in governing the reservoir potential (Burchette, 2012). Thrust-fold related fracture corridors in limestones can have a permeability order of magnitude greater than the surrounding carbonate rock matrix and have a considerable impact on oil, gas, and water production.

1.2 Field area

The field area is within the Islamabad Capital Territory and Punjab provinces of Pakistan in the vicinity of the capital city of Islamabad (Figure 1.1). Within the field area, the Indian tectonic plate subducts beneath the Eurasian tectonic plate causing the folding and thrusting to form the Himalayas (Chapter 2). Outcrops of folded carbonates and shales ranging from the middle Jurassic Saman Suk Formation to the early Eocene Chorgali Formation occur in these mountainous areas. Chapter 2

(Literature Review) describes the types of these rocks, whilst Chapter 4 (Field Mapping) defines the physical characteristics of the rocks across the sites in the different field regions of the field area.



Figure 1.1: Location map of Pakistan, and its different provinces shown in various shades of grey, including especially Islamabad Capital Territory (ICT) which contains the city of Islamabad. The field area is indicated by the red rectangle.

The northern boundary of the Himalayas foreland fold and thrust belt is marked by allochthonous wedges of pre-Tertiary rocks, which are thrust over the foreland sediments (Alam *et al.*, 2014). These largely Mesozoic and lower Tertiary sediments form the tightly folded decoupled rocks in the field regions above the Main Boundary Thrust, which lies directly on the southern edge of the study area, specifically Field Site 1.

1.3 Aims and Objectives

The principal aim of the research is to identify and quantify the variability of the key characteristics of limestone fractures associated with fold and thrust belts and develop a fundamental understanding of the controls. Most fractures are related to the orientation of local structures, with some sets parallel and some sets perpendicular to local hinge lines, but refolded regional fractures may also be widely distributed (Al-Kindi, 2020). The type and structure of the fold and thrust will be identified, including the tectonic evolution of it (Marshak and Engelder, 1985).

Fractures in rocks are extremely complex and variable and are rarely uniform nor truly random in their spatial distribution. Theoretically, if the strength and stress magnitudes are accurately measured, then the resultant fracture distribution could be quantified. However, this is not the case due to the high degree of uncertainty and variability in the fracture systems of the field area. It is better to determine the combined characteristics of the geometry and distribution of thrust-fold-related fractures in different structures of the limestones. Once these have been quantified, it will be possible to understand the fracture patterns in different areas. Distinctive fracture patterns form in different structural features which allows them to be characterised by the combined sets of data ensuring that all the fractures are considered when evaluating a rock-mass.

The arrangement of the fracture patterns in space will be determined topologically, to provide an improved understanding of the physical properties of intersections of the fractures in the rock-mass (Sanderson and Nixon, 2015). The spatial distribution of the fractures will be evaluated by determining the fractal dimension of the fracture distribution, which indicates the proximity of features.

Three main objectives will be utilised in this thesis:

1. Fieldwork will identify and quantify the geological characteristics, including basic descriptions, geometries, topological and fractal relationships of the rock-mass. This will allow

the discrimination of different fractures and fracture networks associated with the thrusting and folding of the limestones. The most appropriate analytical techniques for defining and grouping of the different data types will be determined.

2. The relationships between the variations of different characteristics including the topological and fractal, in the various different geological environments will be distinguished from the field data. These values will be defined for various rock types and structural features. Different measurement sites will be evaluated, considering all the fracture data within the sites.
3. The ability to evaluate different fracture patterns which represent different structural features and use this to accurately predict the variations will be determined. Fracture groups will be defined by using the different data types, both fractal and topological, increasing the confidence in the set, while at the same time accounting for the variabilities of the grouping.

2. Literature Review

Brittle rock fracture patterns define the characteristics of physical discontinuities within surface and near-surface rocks and have been widely used to determine the economic and safety aspects within the rock-mass (Barton *et al.*, 1974; Bieniawski, 1979; Palmstrom and Stille, 2007). The characteristics of fluid-flow (such as hydrocarbons or water) through the rock are often determined by the distribution of fractures (Cardona *et al.*, 2021). Fractures are rarely uniform nor truly random in their spatial distribution. Because they exhibit some order (Healey *et al.* 2017), several different potential patterns will exist due to specific processes such as different folding and fracturing styles. A non-random arrangement may spontaneously emerge due to interaction among fractures during their propagation, resulting in a self-organised pattern. This is the principal basis of the prediction of the fracture characteristics within the rock-mass in this thesis. The characteristics of the rock-mass and the utilisation of these to define fracture trends are reviewed in this chapter. These are:

- The nature of shelfal marine carbonates, and the effect the alteration of micrite and microspar have on the rock mechanical behaviour of limestones to fracturing.
- The stratigraphy of the field-area.
- The types of fold and thrust (FAT) belts and especially the characteristics of the foreland FAT belt within the study area.
- The characteristics of rocks caused by fracturing and folding.
- Conventional fracture mapping techniques, and especially topological and fractal methods that will be applied in the thesis.
- Geostatistical spatial analysis from remote sensing tools is examined to determine possible links to the outcrop mapping techniques.

2.1 The geology of shelfal marine carbonates

Carbonate rocks display heterogeneity at all scales caused by the combination of a variety of factors (Ham and Pray, 1962; Mogensen and Masalmeh, 2020; Tavakoli, 2020). This heterogeneity can be due to primary sedimentary and biogenic features formed during the deposition limestones ranging from lime mudstone to packstone (Dunham, 1962). However, the porosity, permeability and fluid flow properties in carbonate rocks of the research area are primarily due to post-depositional processes, especially fracturing. Without fractures, these fine-grained lime mudstones and wackestones do not host producing oil and gas fields, and hence the structural characteristics of the fractures and folds of the carbonates in an area such as the field-area is a significant factor in governing the reservoir potential (Burchette, 2012).

The fine-grained sedimentary carbonates and associated clastic rocks (especially siltstone that has been subjected to extensive tectonic stresses such as large-scale thrusts and converted to shale) are the sediments encountered in this research. The types of carbonates present in the field area are reviewed, along with the micritisation and microspar processes which recrystallise the original lime mud matrix. As a result, this modifies and homogenises the rock-mass properties, making the limestones very brittle and thus restricting the variations of the subsequent fracture processes.

Carbonate sediments form by biological, chemical, and detrital processes (Tucker, 2013). More than clastic sediments, carbonates typically continue to undergo major fabric and mineralogical change after deposition – for example, their stratification may be homogenised by burrowing organisms (Ham and Pray, 1962), bioclasts can be altered by diagenesis, recrystallisation and replacement can completely alter fabric and mineralogy (Choquette and Pray, 1970).

Depositional, diagenetic, and biogenic processes create carbonate rock textures and fabrics that are described in connection with carbonate build-ups, or reef growth, and are useful descriptors of physical conditions at the time of formation (Kidwell and Holland, 1991). Allochemical carbonate

grains are transported a distance after their formation and deposited. like the grains of clastic sediments. Orthochemical components form in the site of deposition or are subjected to very limited transport; rocks include carbonate mud, micrite (< 4 μm diameter), and the crystalline calcium carbonate cement, sparry cement, or spar. The most commonly used classification scheme of carbonate rocks is that of Dunham (1962). This scheme includes detrital carbonates (ranging from lime mudstone to grainstone, through biogenic “reef” carbonates to diagenetically altered crystalline carbonates (Figure 2.2). The Dunham classification scheme is used by the majority of geologists working to describe the petrography of carbonate facies (Lokier and Al Junaibi, 2016).

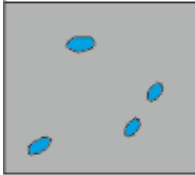
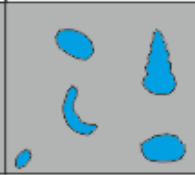
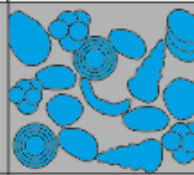
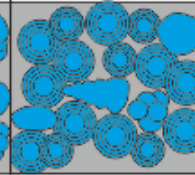
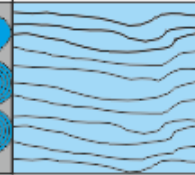
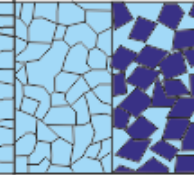




Depositional textures recognisable					Depositional texture not recognisable
Original components not bound together during deposition				Original components bound together shown by intergrown skeletal matter	
Mud-supported		Grain-supported			Subdivided on physical texture or diagenesis
< 10% bioclasts	> 10% grains	< 10% grains	> 10% grains		
Mudstone	Wackestone	Packstone	Grainstone	Boundstone	Crystalline Carbonate
					
 Clastic material	 Calcite cement	 Biological material	 Carbonate crystals		

Figure 2.2: The classification scheme of Dunham (1962).

In the field area, the small-scale mechanical units correspond to entire sequences with no or little rock-property contrasts between beds, due to similar amounts of micritisation and microspar formation (Barbier *et al.*, 2012). Fracture localisation is also influenced on a larger scale by the characteristics of the carbonate rock, even up to sequence stratigraphy levels but this is not present in the rocks that have been investigated (Zahn *et al.* 2010).

2.1.1 Lime mud, micrite and microspar

Most carbonates are extremely susceptible to mineralogical and textural change, cementation and dissolution that affect porosity. These alterations can occur at any time from initial deposition to deep burial. The original primary porosity in limestones containing lime mud may thus be totally destroyed during diagenesis and significant new secondary fracture porosity.

A large volume of most fine-grained limestones usually comprises carbonate mud, which is carbonate material of <2 microns grain size and is typically aragonite or calcite. However, this material is geochemically highly reactive and very quickly changes to micrite, although the actual process remains the subject of debate and research (Lucia, 2017).

Micrite is generally accepted to be derived from the recrystallisation of lime mud, and as a component of carbonate rocks can occur as a matrix, as micrite envelopes around allochems or as peloids (Folk, 1959). The origin of micrites remains poorly understood in carbonate diagenesis due to the non-uniqueness of the processes by which it may be generated. In some marine environments, lime mud that could become micrite can form chemically or biochemically through whitening events, whereas in warm stratified marine waters it might be formed by chemical precipitation. Alternatively, microbial process may lead to micrite formation. Other processes which might produce micrite include the disaggregation of peloids, bioerosion, the mechanical degradation of larger carbonate grains and dissolution-reprecipitation processes. The small size of the grains or crystals in the micrite makes the identification of their origin is difficult to determine (SEPM STRATA, 2022).

Micrite may be precipitated chemically or biochemically from seawater, derived from the abrasion of pre-existing calcium grains. This sediment accumulates in a variety of settings: in the still water of lagoons, below wave base in deeper water, and within and beneath the protection of algal mats. The recrystallisation of pre-existing broken skeletal and non-skeletal grains of micritised grains may be mistaken for fragments of sedimentary micrite (SEPM STRATA, 2022). Limestones with a fine-grained

matrix and carbonate muds (Figure 2.2) are susceptible to the development of micrite and microspar and this forms a dominant constituent of all the limestones in the research area.

During early lime mud diagenesis, calcium carbonate is transferred from metastable carbonate particles to micrite and microspar (calcite) cements which grow in adjacent micropores reducing the pore size (Moshier, 1989). Complete cementation produces a mosaic texture of anhedral micrite- or microspar-size crystals. Micrite crystals are characterised by grains less 4 μm .

Many limestones which contained pervasive micrite are now cemented with calcite microspar, inorganic calcite crystals with grain sizes between 4 and 30 μm , mostly 5-15 μm (Folk, 1959). It is obvious that microspar, typically showing a mosaic-like texture, must be of diagenetic origin (Lasemi and Sandberg, 1984).

Neomorphism is the term used to describe the recrystallisation of micrite to microspar (Longman, 1977). It can be formed by recrystallisation (aggrading neomorphism) of micrite by the removal of Mg^{2+} which forms a gap between the micrite and growing microspar (Folk, 1974). This is triggered by freshwater flow or fresh water from interbedded clays (Carter *et al.*, 2014). Microspar can also be formed in a one-step neomorphic process of cementation of aragonite-dominated precursors without micrite (Munnecke, 1997). Neomorphic growth of microspar from deep surface fluids is proposed to occur due to saturated calcite (Flügel, 2013).

The development of microspar from micrite dramatically changes the porosity and permeability in fine-grained limestones such as wackestones. Micrite is characterised by significant microporosity but microspar becomes much more tightly cemented and typically has very low volumes of microporosity.

In the field area almost all the limestones are cemented by microspar and are investigated to understand the development of fracture patterns in the rock-mass of the Himalayan frontal thrusts.

2.1.2 Diagenetic processes

The major diagenetic environments that were present during the formation of the limestones in the field area were subjected to the vadose, the phreatic, and the mixed meteoric marine zones (Moore, 1989). The vadose diagenetic environment is unique as it is a two-phase system of air and water and is reflected in the unequal distributional patterns and unusual morphology of the cements precipitated in a shoreline environment. For example, chicken-wire-shaped calcite pseudomorphs (after anhydrite) as well as the existence of dolomitised algal mats point towards restricted sedimentary conditions form in the Chorgali Formation of the study-area (Benchilla *et al.*, 2002). The vadose zone is exposed upper ramp surface, where cementation is confined to grain contacts. Most primary intergranular porosity is preserved but permeability can be negatively impacted by precipitation of meniscus cement (Moore and Wade, 2013). Diagenesis is generally slow in the vadose zone and the phreatic zone is characterised by high diagenetic efficiency due to the presence of large volume of water (Moore, 1989). The phreatic meteoric aquifer is open to the atmosphere from the ramp interior to the low-stand shoreline and subsidence of the outer ramp (Moore and Wade, 2013). Carbonate strata show a continuous loss of porosity with depth, and processes acting continuously from the surface to depths in excess of 4 km (Scholle and Halley, 1989).

The structural complexity of FAT belts impacts on the fluid flow and diagenetic processes. Processes including cementation, fracturing or secondary porosity development are impacted (Vandeginste *et al.*, 2012). The control of the cross-cutting relationships between fracture systems in thrusts helps to understand the mutual relationships between different diagenetic phases. This includes the formation of veins and fractures. Bedding parallel fractures form shallower than approximately 600 to 800 m. The early diagenetic processes can exert a significant control on fluid flow pathways later in diagenesis. Tectonic fractures form at steep angles to bedding and re-open especially in folding (Swennen *et al.*, 2003). These tectonic fractures are dominant in folds when only geomechanical processes are considered but if diagenesis is also considered brittle thrusts are expected.

Deeper level diagenesis allows the migration of different types of oils into the fractured limestones. For example, the Eocene Chorgali Formation has different types of oil. The earlier rich light oil have atypical associations of CO₂ and depleted H₂O. The oil could be derived from source rocks in the buried Palaeocene formations, such as the Patala Formation for the first input (Khan *et al.*, 2004). The Patala Formation is exposed in the field area and does not have any oil, indicating how the diagenetic processes have affected the characteristics. A second phase of more mature oil with a large amount of water originated from the deep part of the basin itself and mixed with tectonic and meteoric water along the circulation pathways is also present in the Chorgali Formation. The fluids are mainly driven by tectonics and are expelled from the hinterland farther to the north (Khan *et al.*, 2004). Because of the strong tectonic forces thrusting up the rock, it is possible to form a wide range of diagenetic processes in the field area.

2.2 Stratigraphy of the field area

The carbonate-rich sediments of the formations have a well-defined lithological range dominated by lime mudstones and wackestones with subordinate packstones and grainstones based on the Dunham classification shown Figure 2.1.

The depositional environments of the various formations represent a narrow range of successive transgressive and regressive events resulting in fluctuations between the shallow outer ramp and lagoons of the inner ramp (Khan, 2018; Hussain *et al.*, 2013; Sameeni *et al.*, 2007). A simplified stratigraphic column is shown in Figure 2.3. But the characteristics are especially dependent on the presence of pervasive microspar which increases the strength and brittleness of the rock.

2.2.1 Saman Suk Formation

The lowermost formation encountered in the study area is the Middle Jurassic Samana Suk Formation (Abir *et al.*, 2017). It consists of a sequence of sandy, bioclastic carbonates and interbedded mudstones (Wadood *et al.*, 2021). Bioclastic wackestone containing rugose corals, foraminifera, gastropods, and other species including pelecypods and bryozoans, locally become packstone (Nizami, 2019). The Samana Suk Formation has undergone significant diagenetic alteration, including recrystallisation of the lime mudstone matrix to microspar, precipitation and replacement by dolomite and calcite veins, and developments of stylolites (Ali *et al.*, 2013; Cheema, 2010).

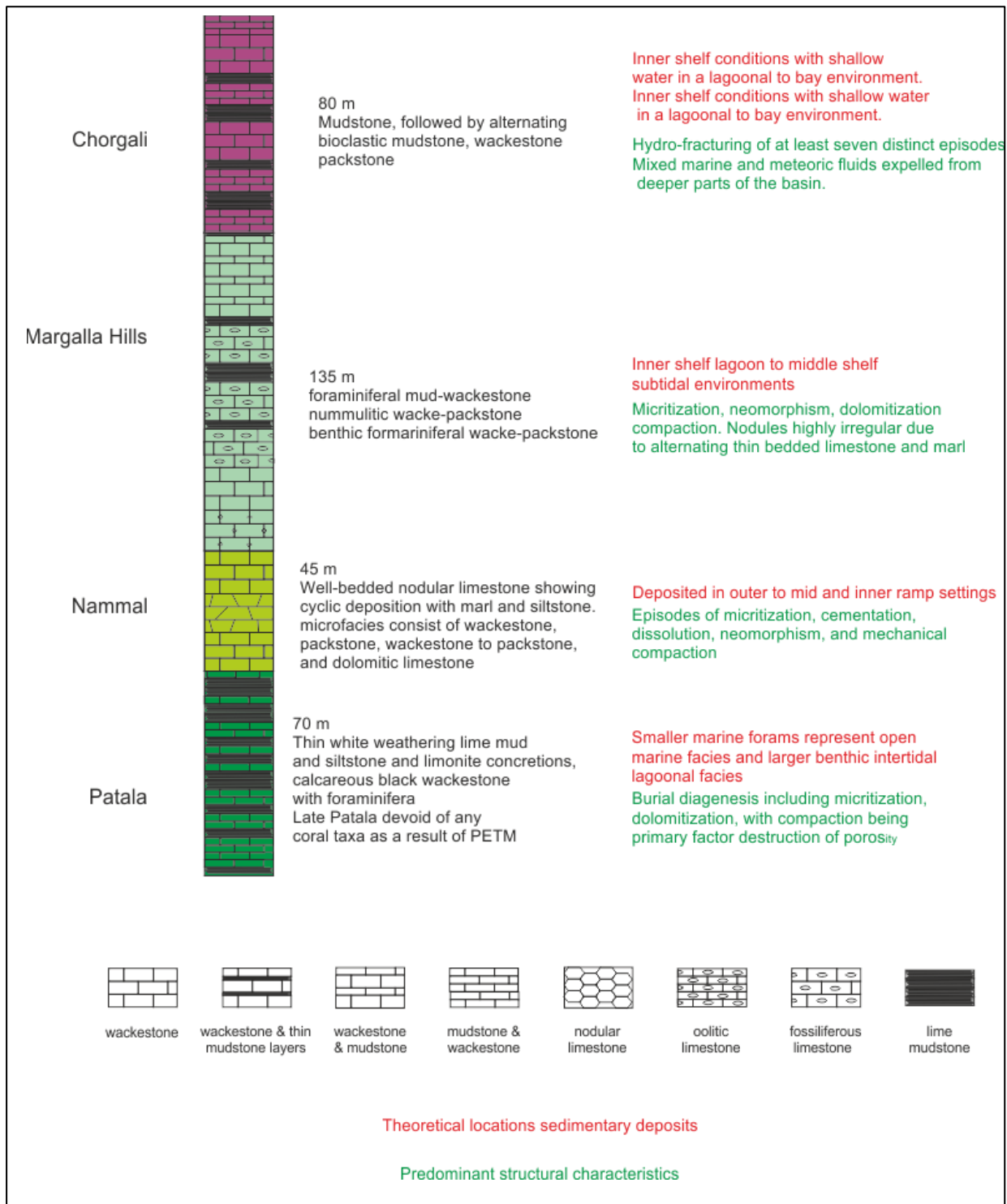


Figure 2.3: Stratigraphic column of the various formations investigated in this thesis. Black coloured text indicates the appropriate formation thickness, and the rock types it contains. Continued below.

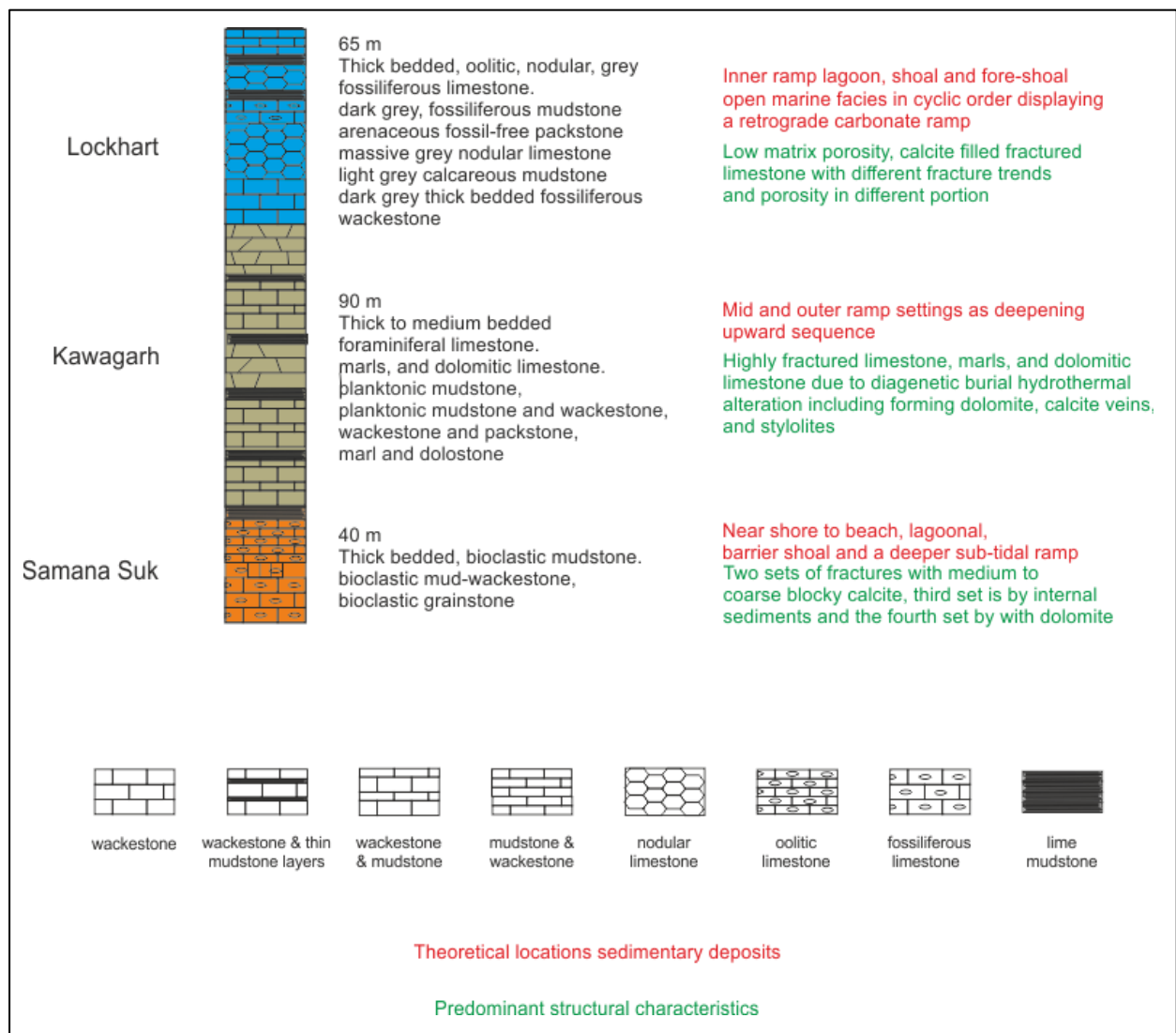


Figure 2.2 continued: Stratigraphic column of the various formations investigated in this thesis. Black coloured text indicates the appropriate formation thickness, and the rock types it contains.

2.2.2 Kawagarh Formation

The Cretaceous Kawagarh Formation is composed of thick to medium bedded foraminiferal wackestones and associated calcareous shales, with some of the wackestones being dolomitised (Rehman *et al.*, 2021). The gradual increase in the frequency of plankton and decrease in detrital content from the underlying calcareous shale microfacies indicates the increase in the water depth that corresponds to the Late Turonian global sea level rise (Rehman, 2021; Ahmed, 2019). The large-

scale occurrences of pervasive dolomite indicate subsurface processes and long-term seawater circulation over platform sediments (Rehman *et al.*, 2021).

2.2.3 Lockhart Formation

The Palaeocene Lockhart Formation was deposited unconformably over the Kawagarh sediments in a marine setting on the northern leading edge of the Indian Plate as the Palaeo-Tethys Ocean closed. It is a thick bedded, sometimes nodular, grey to dark grey fossiliferous limestone. The principal facies associations are lime-mudstone and wackestones (Hanif *et al.*, 2014). The contact of the Lockhart Formation and the younger shallow-marine mudstones and subordinate carbonates of the Patala Formation is transitional (Wandrey *et al.*, 2004).

The Lockhart Formation was extensively examined during the field visits as it forms prominent outcrops that may be folded or thrust forming well developed fractures. Various diagenetic features are apparent in the Lockhart Formation including micritization, development of pervasive microspar cement, pressure dissolution (formation of microstylolites), to tectonically induced fracturing and calcite veining (Khan, 2015). The nodular texture of the Lockhart Formation is at least in part due to pressure dissolution, which reveals a trend from mechanical and chemical compaction, through deep burial pressure dissolution to tectonic fracturing (Khattak *et al.*, 2017). The fracturing of this formation is clearly visible due to the thick lime mudstone and wackestones beds as well as the microspar cement.

2.2.4 Patala Formation

Thinly bedded lime mudstones and foraminiferal wackestones of the Patala Formation are widespread in the study area and are interbedded with shales (Gee and Gee, 1989). The Patala Formation is approximately 70 metres thick and is in sharp contact with the overlying Nammal Formation (Jamil *et al.*, 2014). The limestones in the Patala Formation are dominated by foraminifera including longer ranging smaller types and larger benthic intertidal and lagoonal types (Akhtar and Butt, 1999). The

interbedded lime mudstones and argillaceous shales contain limonite concretions and weather whitish green. The foraminiferal wackestones are finely crystalline and hard due to the presence of micrite and abundant recrystallised calcite microspar (Khan *et al.*, 2018; Malik and Ahmed, 2014). Burial diagenesis, which includes dolomitization, especially of the clastic siltstone, further restricts the intergranular porosity.

2.2.5 Nammal Formation

The sediments of the Eocene Nammal Formation are of Ypresian age (Wandrey *et al.*, 2004) and are dominated by, foraminiferal wackestones with subordinate interbedded lime mudstone and argillaceous siltstone (Gee and Gee, 1989; Wandrey *et al.*, 2004). Based on microfacies assemblages, the Nammal Formation is interpreted to have been deposited in outer to mid ramp settings (Hussain *et al.*, 2021). The formation is modified by diagenesis comprising micritization, microspar cementation, dissolution, neomorphism and mechanical compaction to form stylolites, fractures and veining (Hussain *et al.*, 2021).

2.2.6 Margalla Hills Formation

The early Eocene age Margalla Hills Formation consists of shallow marine shelfal limestones with thin interbeds of shales. It has a diverse faunal and floral assemblage, including foraminifera, echinoderms, molluscs and algae, and varies from wackestone to locally packstone (Swati *et al.*, 2013). The burrowing and bioturbation form irregular nodules.

The nodular fabric is further enhanced by chemical compaction of the alternating sequence of thin bedded limestone and calcareous shale (Azhar *et al.*, 2014). Overall, the depositional environment of the Margalla Hills Formation is interpreted to range from the shallow inner shelf to a middle shelf subtidal setting (Swati *et al.*, 2013).

The diagenetic overprinting of these limestones includes neomorphism of aragonite to calcite transformation, recrystallisation of micrite to microspar, dolomitization and compaction and

disorientation of bioclasts with pressure dissolution fabric (Naeem *et al.*, 2014). The recrystallisation of micrite to microspar and including the dolomitization, forms a much stronger sequence of the interbedded limestone and calcareous shale (Azhar *et al.*, 2014).

2.2.7 Chorgali Formation

The carbonates of the Chorgali Formation range from shales and lime mudstones, followed grey to pale grey wackestones, and by dolomitic limestones, and crystalline dolomites (Wandrey *et al.*, 2004; Khan *et al.*, 2004; Awais *et al.*, 2020). The dolomites are up to 15 m thick creating a strong layer and the near surface sedimentation conditions are also reflected by the presence of dolomite conglomerate pebble and breccia beds in the upper part of the dolomites indicating early diagenetic evaporite collapse breccias (Khan and Ur Rashid, 2022).

2.3 Fold and thrust belts

2.3.1 General characteristics of fold and thrust belts

A fold and thrust belt (FAT belt) is a linear region of the earth's surface, typically on the external edges of orogens that consists of deformed sedimentary rock in which the layers are folded and duplicated by thrust faults. Folds and reverse faults are the dominant structures in unmetamorphosed rocks exposed in a belt that may be tens or hundreds of kilometres wide.

Fold and thrust belts are far from simple structures. Pre-orogenic architecture, basement interactions, sedimentation and mechanical properties of stratigraphy, all play a critical part in the evolution of this convergent tectonic system (Hammerstein *et al.*, 2020). The deformation styles of FAT belts, and hence the fracture patterns are highly sensitive to the mechanical properties of the rock-mass. Less strong rocks form folds with distributed strain so that layer thicknesses become heterogeneous with deformation. In contrast, rock sequences with moderate strength will exhibit flexural slip and therefore form concentric structures with better preservation of layer thickness. With stronger strain weakening properties, the rocks deform with increasing formation of fractures. Pre-existing structures can have an influence on the evolution of a FAT belt, such as the presence of salt, that influences the variability of the Himalayan fold and thrust belt.

2.3.2 Types of fold and thrust belts

FAT belts are remarkably diverse and although they exhibit a number of common characteristics, no single model can provide a global portrayal. The belts are developed in a number of tectonic environments. On a large-scale in map view, fold and thrust belts may be linear, however they show geometrical variations along-strike in the form of salients where the belt bulges. Folds verge usually towards the foreland in the case of foreland FAT belt of the study site, towards the trench in the case of accretionary wedges and towards the basin in the case of toe thrust belts. Although the

dominant orientation of the tectonic transport vector prevails, in detail the sense of motion of each thrust sheet may vary in its orientation spatially and/or through time. The characteristics of different fold and thrust belts are reviewed below, before examining the features of the foreland fold and thrust belt in the field area.

Accretionary prisms are the main locus of deformation in subduction zones, where the rock assemblages are mechanically scraped off the down-going oceanic slab and accreted to the seaward edge of the upper advancing plate forming thrust sheets (Moore, 1989; von Huene and Scholl, 1991). The bulk geometry of the prism and its detailed structure are strongly controlled by the thickness of the sedimentary pile of the subducting oceanic plate. The wedge is underlain by a detachment that ramps up to progressively shallower levels towards the trench and propagates seaward decoupling mass from the down-going slab that accretes to the overriding slab usually in the form of duplex (tectonic underplating).

Toe thrust belts develop in deep water at the leading edge of large-scale gravitationally driven sedimentary prisms. Unlike other FAT belts, they do not require lithospheric shortening, their deformation and transport are achieved entirely by gravity (Poblet and Lisle, 2011). The thrusts are generally detached on salt or over-pressured shales forming sedimentary prisms on continental margins such as those in the Gulf of Mexico and offshore Brazil, or as thick delta complexes such as the Niger delta (Poblet and Lisle, 2011).

The internal portions of a passive-margin fold and thrust sequence are regions that exhibit higher initial-taper angles and thick sections of stronger metasedimentary rocks that detach on weak sedimentary horizons, or brittle-ductile transitions zones, to create hinterland megathrust sheets (Boyer and Elliott, 1982; Boyer, 1995; Mitra, 1997). Megathrust sheets are remarkable for their length, thickness, and lack of internal deformation associated with transport.

Plate subduction FAT boundary belts form by the oceanic crust subducting beneath the adjacent continent before collision such as the Andes that is developed along the western coast of South America by the subduction of the Nazca and Atacama oceanic plates. The denser oceanic crust is forced down beneath and friction between the plates causes them to fracture and deform (Schellart, 2008). With continued subduction oceanic crust is accreted and folded onto the continental plate which increases in thickness. Andesitic magma rise up from the subducted oceanic crust to create large volcanoes prior to collision with the lighter tectonic crust forming accretionary wedges and andesitic lavas (Ort, 1993). Other FAT thrust subduction processes are more evolved and longer existing containing a variety of tectonic sequences including the upper-plate fragmentation, oceanic slab break-off. This is characterised by major shifts in arc magmatism and distributed extension within the upper plate, and progressive migration of deformation that forms for example the complex Zagros fold and thrust belt processes (Agard *et al.*, 2011; Lacombe *et al.*, 2011).

Neighbouring intraplate fold and thrust belt plate convergence requires complex geological movements. The Yinshan Jurassic-Cretaceous FAT belt of China, underwent contractional and normal faulting, folding, and contemporaneous terrestrial sedimentation and magmatism (Poblet and Lisle, 2011) that includes normal faulting, magmatism and thick-skinned deformation.

Inverted rift fold-and-thrust belt are caused by the shallow fold-and-thrust geometry and the shortening of syn-rift strata, due to rift inversion in the cratonic far-foreland setting (Ferreira, 2019) Rift faults control the position of the thrust ramp nucleation, by causing syn-rift strata to overfold and drape fold. Back-thrust and fore-thrust pairs form over elevated horsts. Multiple thrusting and lower relief occur over buried rifts with multiple inverted faults (Izquierdo-Llavall *et al.*, 2018).

The Canadian Rocky Mountains zone is a well-known and extensively studied foreland FAT belt with the influx of immature gold-bearing clastic sediment that accumulates ahead of the thrust sheets, especially in the Klondike Region which has formed due to the tectonic, geometrical and lithostratigraphic complexity of their location (Groves *et al.*, 2016). Significant knowledge of the fold

and thrust belt mountain systems arose from hydrocarbon exploration in the foothills of the Canadian Cordillera and the Rocky Mountains in the USA, both by surface mapping and targeted drilling (Bally *et al.*, 1966; Dahlstrom, 1970). Large-scale structural models have been developed that represented the general geological characteristics. Thin-skinned fold and thrust belts were found to be foreland directed thrust systems. Folds usually verge towards the foreland in the case of foreland FAT belts, towards the trench in the case of accretionary wedges, towards the basin by back thrust belts (Ferrill *et al.*, 2021).

2.3.3 The foreland fold and thrust belt of northern Pakistan

In the field area, crustal collision related to tectonic plate consumption has resulted in the Indian tectonic plate subducting beneath the Eurasian tectonic plate causing the continental crust to thicken by folding and thrusting to form the Himalayas foreland fold and thrust belt due to the low-density contrast between the two plates (Pearson and De Celles, 2005). The fold and thrust belt is the result of the tectonic collision of two continental tectonic plates that was initiated when the tectonic Indo-Australian tectonic plate separated from the African tectonic plate in the Upper Cretaceous Period (84 Ma) and began its very rapid northward drift towards the Eurasia tectonic which continues to this day (Figure 2.4). The northern boundary of the foreland basin is marked by allochthonous wedges of pre-Tertiary rocks, which are thrust over the foreland sediments (Alam *et al.*, 2014). These rocks form the sediments in the field area above the Main Boundary Thrust. With the ongoing tectonism, the southward migrating thrust sheets from the Himalayas shed their erosional products into the Indo-Australian foreland basin (Figure 2.4).

Continual south-directed, décollement-related thrusting of the Indian Plate crust has caused the fold and fault features within northern Pakistan and especially in the study area. There are three main thrust faults in the Himalayas. These are, from north to south, the Main Mantle Thrust (MMT), the Main Central Thrust (MCT) and the Main Boundary Thrust (MBT). Displacement on the MCT is on the

scale of kilometres and is defined by a mylonitic zone separating the High Himalayan Crystalline Terrain from the lower Tertiary sediments in the Lesser Himalayas (Korup *et al.*, 2006). The MBT lies immediately south of the field study area. and thrusts a Tertiary to current molasse of clastic rocks and limestones atop of the Precambrian to Cretaceous lower Indian Plate rocks (Chen and Khan, 2009).

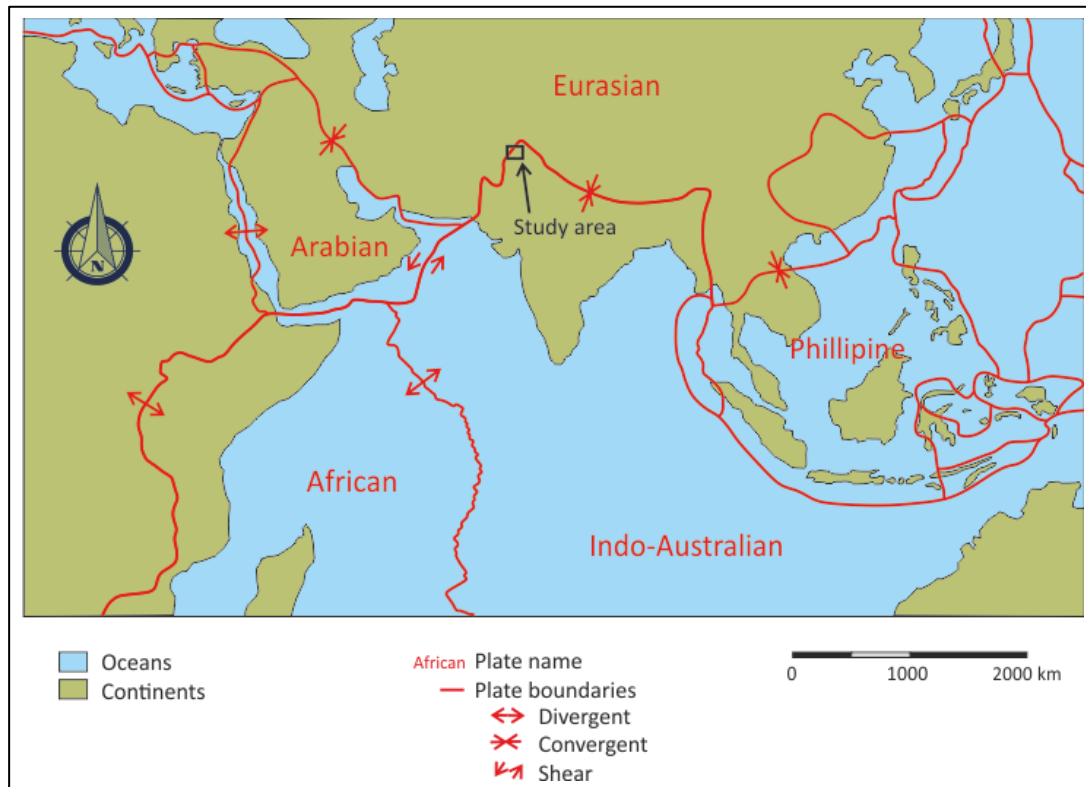


Figure 2 4: Tectonic plates involved in the development of the Himalayas. Location of the study area on the convergent Himalayan plate boundary is shown by black square.

The development of foreland fold and thrust belts consists of many types of folds and thrusts that develop during various periods of tectonism. As the field-area shows, many of these structures are concurrently active. The oldest stage of foreland FAT belts is considered to be the propagation of the basal detachment and formation of foreland-directed fore-thrusts (Yeats and Hussain, 1987). During the subsequent period, corresponding to a subcritical Coulomb wedge stage, back-thrusting accommodates significant shortening (Torres-Carbonell *et al.*, 2011). In addition to folds and thrusts verging and directed respectively towards undeformed regions following a break-forward propagation

sequence, other types of structures (back-thrusts and back-verging folds) occur in many belts behind the deformation front, to the north of the field area (Poblet and Lisle, 2011).

Both fore-thrusts and back-thrusts bound the pop-up structure, which is a deformed zone characterised by thrust-related anticlines (Fabbi and Smeraglia, 2019). Pop-up structures mainly form subnormal to the maximum horizontal stresses and can be the only features which show evidence of an earlier tectonic age or are not significantly affected by the current deformation (Rutty and Cruden, 1993; Grodner *et al.*, 2021).

Towards the hinterland, basement rocks become involved in the thrust sheets (crystalline thrusts). Although these basement rocks may have been transported in a thin-skinned manner on sub-horizontal thrusts over other basement or cover rocks, eventually, the thrusts root down into crystalline basement rocks and lose their thin-skinned character and force the following sub-horizontal thrusts to be confined. This results in the development of strongly deformed back-thrusts.

In thin-skinned tectonics sedimentary strata are detached from their basement along a décollement horizon made up of rocks with low shear strength such as salt or shales. True thin-skinned tectonics requires a detachment layer of sufficient thickness and in most cases, there are several thrusts involved with thin-skinned tectonics. These are typical structures within the field area. In the foreland of the Zagros FAT belt, sedimentary rocks with several décollement horizons have undergone similar in-sequence thrusting thin-skinned region (Sarkarinejad and Goftari, 2019).

In contrast to this, thick-skinned tectonics consists of crustal shortening that involves basement rocks and deep-seated faults (Pfiffner, 2017). In the internal parts of the Zagros fold and thrust belt, the Tutak granite-gneiss dome is associated with sole thrusts and deformation in this part of the orogen was thick-skinned (Sarkarinejad and Goftari, 2019). Thus, FAT belts can exhibit both thin- and thick-skinned tectonics.

The Neoproterozoic Salt Range Formation forms the Salt Range mountains and salt avalanches in front of the range, along the Salt Range Thrust to the south of the field area (Qayyum *et al.*, 2022). This style is laterally transitional toward areas of thinner or lower net salt to up-dip domino fault arrays and down-dip thrust systems such as in the fore-thrusts adjacent to the field area (Stewart, 1999). The structural changes across the Salt Range reflect a systematic variation in the stage of their tectonic development. It has a thick salt sequence, and the distribution of the salt affects thrust, normal, and reverse faults (Ghazi *et al.*, 2014).

2.4 Folds and fracture characteristics

2.4.1 Fracture characteristics

The theoretical characteristics of individual fractures and folds are not investigated in detail in this thesis as the entire fractured rock-mass is considered to represent a specific set of stresses and hence the rock-mass response. A rock-mass consists of all the intact and fractured rock, as the solid fragments may have different strengths and stresses. Various sets of fractures can be defined and used to recognise groups of fractures but within the structural entity, all the fractures interact to a greater or lesser extent. Fractures can be extended or terminated depending on the direction and magnitude of the stresses and strength of the rock-mass. For example, large fractures or a highly fractured rock-mass prevent the stresses cutting across and can reduce the chances of fractures. Therefore, all the fractures are considered when evaluating a structural domain, allowing a greater and more representative sample of the fracture characteristics of a particular fold and thrust type.

It is commonly recognised that the abundance of fractures is different in various rock types and stratigraphic units. A combination of independently variable factors in carbonate rock, including micrite content, sedimentary facies, the position of the bed in the stratigraphic cycle, as well as bed thickness all impact on the fracture pattern (Ortega *et al.* 2010). Identification of mechanical stratigraphy and fracture stratigraphy leads to a clearer understanding of fracture patterns and attributes (Laubach *et al.*, 2009). When considering fluid movement in rocks, fractures are often the most important of geological structures, especially if the unfractured host rock is non-porous as it is the research field area.

Fractures form to accommodate brittle deformation that occurs when the applied stresses exceed the strength of the rock. Figure 2.5 illustrates that the type, orientation, and frequency of fracture sets formed depends on the ratio of δ_1 , δ_2 and δ_3 (Jadoon *et al.*, 2007; Cosgrove 2015).

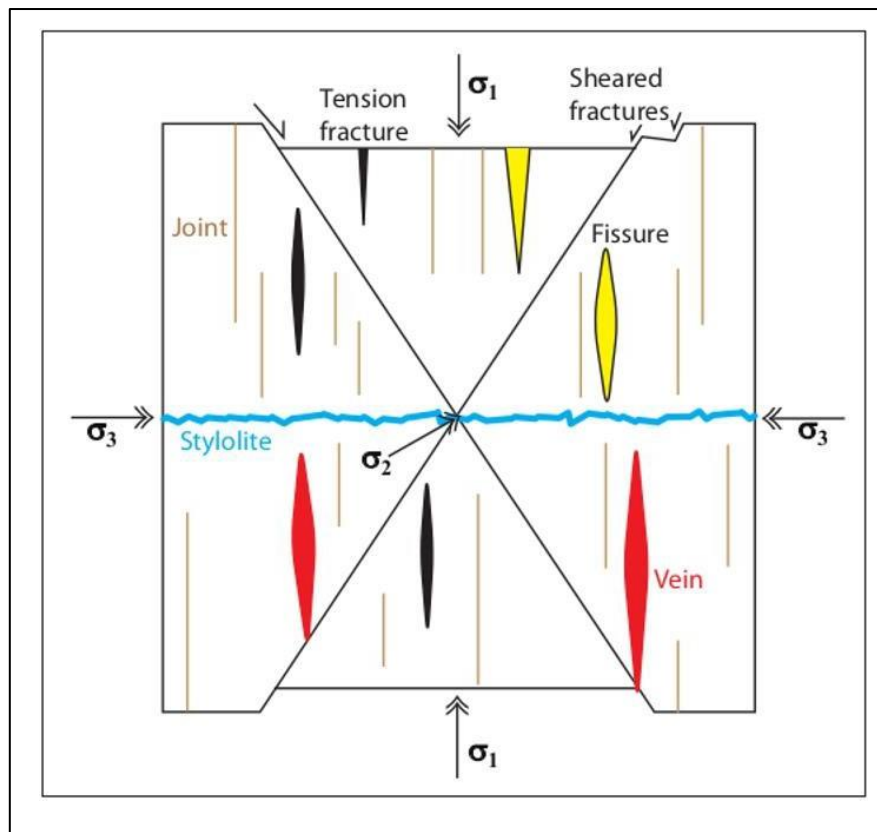


Figure 2.5: Type, orientation, and frequency of fracture sets formed depends on the ratio of δ_1 , δ_2 and δ_3 . From Sorkhabi (2014).

The high level of abundance of fractures in a FAT belt, such as the field area, is because the rocks have experienced numerous different types, phases and degrees of stress until they have reached the current position. This is why it is necessary to quantify all the fractures within a rock mass. Importantly, in this thesis, the different types of fractures, including age, displacement and composition are considered as a single combined entity that defines the overall rock-mass.

2.4.2 Fold characteristics

In the brittle (near-surface) regime the two standard models of strain distribution within a fold are those of the tangential longitudinal (TL) and the flexural flow (FF) (Bonne *et al.* 2001; Cosgrove 2015,). These develop in homogeneous isotropic and anisotropic layers, respectively. In TL folds δ_1 or δ_3 is

always tangential to the layer boundary. In an FF fold, parallel layers such as bedding planes in flexural are planes of zero strain (a neutral surface as shown in Figure 2.6). These two different fold types have the same profile geometries (they are both parallel folds with a uniform orthogonal thickness), but the strain distribution in each is different (Cosgrove, 2015). In the field-area it was noted that Transitional Longitudinal strain was more prevalent in stratigraphic units that were dominated by limestone, such as the Lockhart Formation. In those strata which had a large amount of shale beds between the limestones, such as the Patala Formation, strain deformation was in the form of flexural flow.

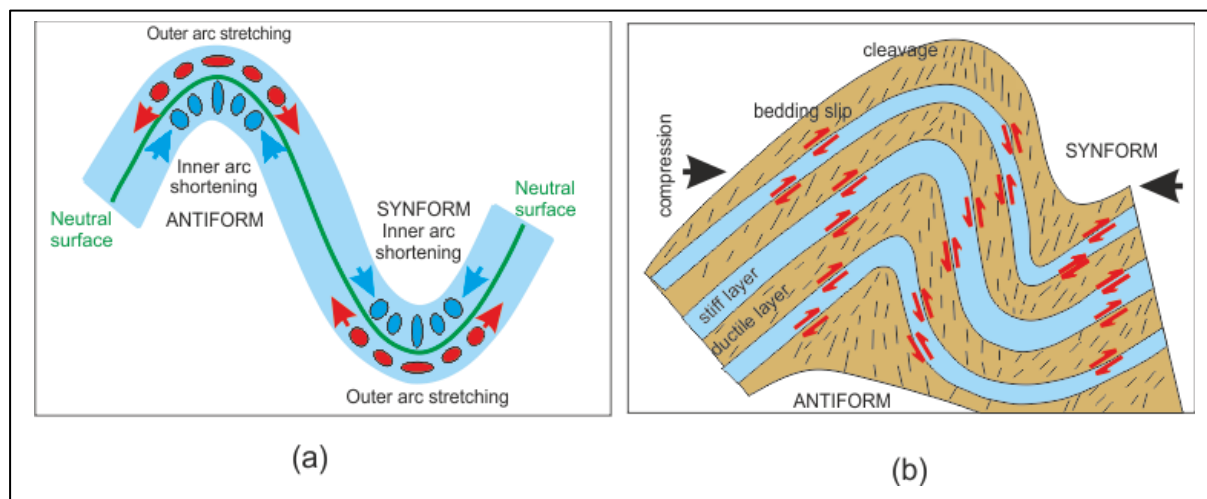


Figure 2.6: The two brittle (near-surface) regime, standard models of strain distribution for the development. (a) Transitional Longitudinal (TL) consisting of isotropic wackestone that have a higher fracture density shown by the changes in the shapes of the ellipses. (b) Flexural Flow (FF) consisting of sheared layers of shale and limestone which form long bedding parallel fractures.

The tensile fracturing above the plane of zero strain (the neutral surface as shown in Figure 2.6a) in a thicker isotropic layer of a TL fold extends along the fold axis (Figure 2.6). The extensional joints may become shear faults as the angle between the fold axis and $\delta 1$ increases. As a result, second-order synthetic and antithetic shears may also develop on the flanks of the fold axis, typically in areas where the dominant mode of deformation has become lateral shear, and the initial tensile fractures are re-

exploited to accommodate the lateral stresses. The utilisation of pre-existing discontinuities (even at a non-perfect orientation) is a typical method of stress relief at all scales (Bladon *et al.* 2015).

In the multilayer sediments being studied, both types of deformation and the associated fractures will develop. The deformation of the more massive brittle limestone is likely to be dominantly by TL fractures, whereas the shales will deform more by flexural flow and bedding-parallel slip (Figure 2.5). During the buckling of the complex multitude of layers of different lithologies and different layer thicknesses, the individual layers will develop their characteristic fracture distribution due to their mechanical properties and thickness (Cosgrove 2015).

The various layers will start fracturing and folding at different times during the shortening with the more competent layers fracturing due to TL strain, before the less competent layers that will accommodate the stresses by shear through FF. It is likely that the flexural flow that results in the shearing of the shales will cause the fracturing of stratigraphic layers and or shearing as the compressive strength of the limestones is significantly higher than this strength. These can become thrusts that break through the hinge regions of the fold (Jadoon *et al.*, 2006). When combined with the fractures generated as a result of TL stresses, this further increases the permeability of the hinge zones. Because of the substantial mechanical anisotropy of the shale and limestone layers, the thrusts typically exploit the weak shale decollement surface for a considerable distance before cutting up through the stratigraphy.

Below the neutral surface, compression parallel to the layer will generate local thrusting or layer parallel buckling and extensional fractures (Figure 2.6). In contrast, fractures that form in FF folds develop as layer parallel shears on the limbs of the folds (the areas of maximum strain). The hinge areas are areas of zero strain and are not fractured as the stresses are accommodated by flexural slip along the layer parallel shears.

Because of the difference in strain distribution, the two types of fold have different fracture patterns. The areas of high strain in TL folds are located in the hinge. In the hinge-zone above the neutral surface

of a TL, in for example a strong limestone, the extension will give rise to either normal faults or extensional fractures (Figure 2.7).

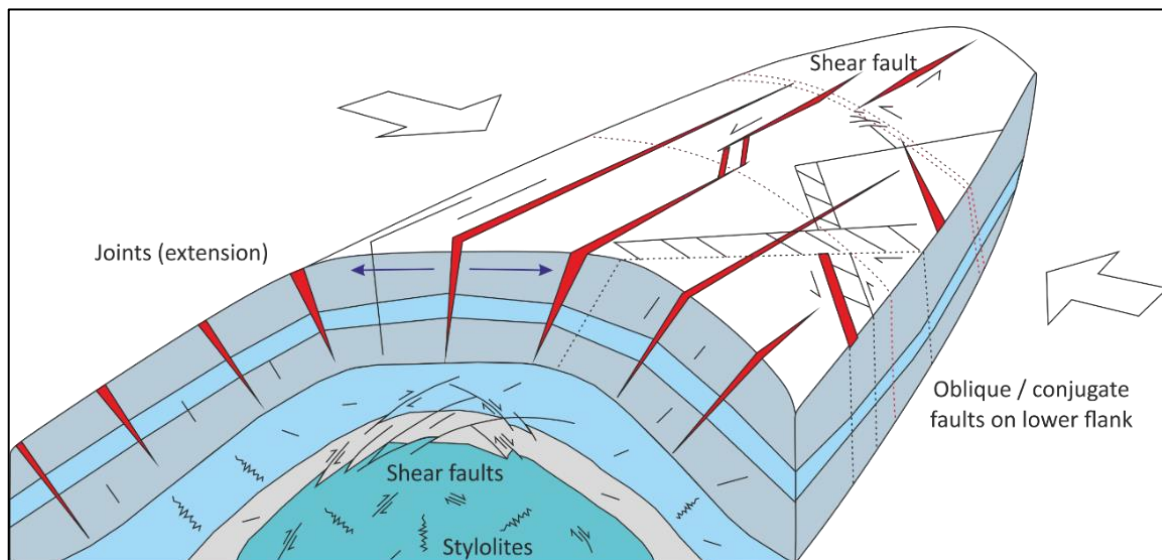


Figure 2.7: Types of fractures forming around an anticline. Modified after Jadoon *et al.*, (2006).

The folds at the end of a thrust can vary along strike from fault-bend to fault-propagation folds (Qayyum *et al.* 2015). As these strata experience different strain histories, different fracture patterns will develop. Where the mechanical anisotropy is higher, upright folds dominate with zones of more intense fracturing in the brittle (in this case limestone) layers (Ferrill *et al.*, 2016). The fractures may not extend through interbedded shales which have deformed by FF.

Fault-bend folds, detachment folds, fault propagation folds, forced folds and roll-over folds are all folds related to a movement on a pre-existing (thrust) fault, and the associated faults and fracture networks are formed as a result of folding. As any of the fault-related folds amplify, they will fracture more. With continued compression, these fracture networks may themselves form faults that cause a variety of folds (Cosgrove, 2015).

2.5 Fracture mapping methods

To allow proper analysis of the fracture systems, the data must be combined into geologically homogenous groups which are characterised, and statistics defined. This is because a single fracture is part of a network of fractures (Laubach, 2003; Hafver *et al.*, 2014; Peacock *et al.*, 2016).

Various types of data may be collected and calculated to characterise a fracture or group of fractures. The relationships between the characteristics of the different data can then be analysed and quantified. The specific kinds of data collected depends on what is being evaluated. Peacock and Sanderson (2018) define seven types of structural analysis:

- Geological descriptions,
- Geometries and topology,
- Age relationships,
- Kinematics,
- Tectonics,
- Mechanics, and
- Fluid flow.

To allow proper analysis of the fracture systems, the data must be combined into geologically homogenous groups which are characterised, and statistics defined. Geospatial and geophysical techniques of relevance also provide information about groups or more correctly networks of features. Common field measurement techniques are described below .

2.5.1 Linear scanline sampling

The simplest method for mapping fractures, apart from simple sketches, are to measure scan-lines of the intersections of fractures or other discontinuity types including sedimentary bedding contacts or

edges of igneous intrusions. Linear scanlines are one-dimensional mapping sections aligned perpendicular to a fracture set likely to be of the same known orientation, timing, mode, or filling (Watkins *et al.*, 2015). The intersection of each fracture with the scanline, as well as attributes such as aperture, throw or mineralisation are recorded. A scanline is subject to orientation bias, as fractures subparallel to the scanline are under-represented. To correct for this bias, several scanlines at different orientations should be measured in the same area. Typically, two scanlines would be set up perpendicular to each other to ensure each fracture set intersects at least one scanline. Due to the limited accessibility of the field area because of steep mountain slopes this would not be suitable.

2.5.2 Circular scanline sampling

Circular scanlines provide an estimate of the fracture characteristics based on the number of fractures intersecting a circular scanline (n) and the number of fracture trace end points (m) within a circular window (Mauldon *et al.*, 2001). The fracture density, intensity, and an estimate of mean trace length for the scanline can then be calculated ensuring the number of fracture ends should exceed 30 (Rohrbaugh *et al.*, 2002). The circular sampling tools and estimators eliminate most sampling biases due to orientation because of its non-directionality. As this method counts fracture intersections with and terminations within each circle, rather than direct measurements of fracture attributes, it is also not affected by length censoring or orientation, unlike the linear scanline. However, the location and the size of the circle can have an impact on the results obtained. Topological measurement circles are better as the characteristics of the nodes (intersections of fractures) allow more information of the fracture characteristics to be determined.

2.5.3 Topology of fractures

Topology is the study of geometrical properties and spatial relations unaffected by the continuous change of shape or size of objects such as lines (fractures). It describes the spatial relationships such as connectivity and continuity of objects and the mapped fracture intersections (nodes) define properties rather than the inherent properties of the individual fractures (Sanderson and Nixon, 2015). This approach provides an improved understanding of the overall behaviour of the physical properties of the rock mass under consideration, particularly in terms of its strength, porosity, and permeability (Sanderson and Nixon, 2015).

Topology emphasises the relationships between structures, e.g., crossing and abutting of faults and joints as nodes and branches. A measurement circle is placed on the outcrop and the number of fracture intersections with the circle edge, and the number of fracture terminations within the circle determined. From these intersections (nodes) the topological characteristics of the outcrop are determined. Fracture topology describes the fracture network as a series of nodes (Sanderson *et al.*, 2018; Procter and Sanderson, 2017; Sanderson and Nixon, 2015). Node are defined as “e” nodes, intersecting the circle edge, “i” nodes, terminating into rock (unconnected terminations), “y” nodes, abutting against another fracture or “x” nodes crossing another branch (Figure 2.8).

The proportions of node types provides a basis for characterising the topology of the network. The relationships between the fractures and, hence, to the network rather than its constitutive elements are evaluated (Sanderson *et al.*, 2018). The main topological descriptions are number of nodes, connectivity(interlinking) of nodes by branches, intensity of nodes, fracture density per unit area and mean trace length.

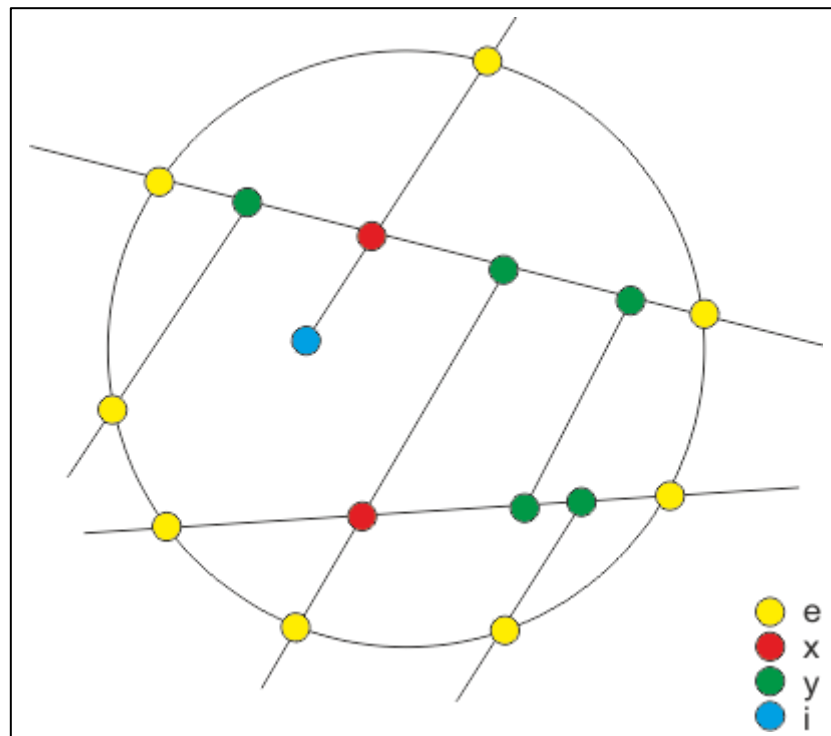


Figure 2.8: Different topological node types in a measurement circle. It is easy to see how the lines within the circle can be equated to fractures and hence the types of nodes determined. Modified after Procter and Sanderson (2017). Node types are: “x” – cross-cutting intersections (red); “y” – abutting against a single branch (green), “i” unconnected terminations in the rock (blue), and “e” intersecting the circle edge (yellow). These colours are used throughout the thesis.

Topology analysis can determine the intensity, frequency, orientation, and length of fractures. The system of branches and nodes can be used to define both geometrical features, such as length and orientation, and the relationship between elements of fracture network – the topology. This can facilitate the prediction of the geotechnical behaviour of the rock.

2.5.4 Fractal analysis of fractures

In Euclidian space, a line is one dimensional, a surface is two dimensional and shape such as a cube is three dimensional. This can also be considered as the number of variables in a system, for example,

each dimension increases the number of different axes. A ratio that determines how detailed the complexity of the variables of the intermediate dimensions determines an irregular geometric object with an infinite nesting of structure at all scales.

The intermediate dimensions are referred to as fractal dimensions and have values between the dimensions of the objects and the dimensions in which the objects are observed. A key property of fractals is that the fractal dimension differs from the conventionally understood dimension (Mandelbrot, 1983). If a fracture was measured with a millimetre-scale ruler, considering all the irregularities, it would show a longer dimension than if it was measured with a single metre-scale ruler. This relative increase in the total measured length is known as the fractal dimension as it increases in fractions from whole spatial dimensions. In this research, fractal dimensions vary from one dimension, a perfectly straight line, to two dimensions when the when the object forms a planar shape. All other fractal dimensions between one and two are greater than a straight line but not a planar shapes which allows the perception of the increase in complexity of the shape. A variety of one-dimensional lines and two-dimensional surfaces associated with fractures were investigated, but it was suggested that these did not exhibit fractal characteristics (Gillespie *et al.*, 1993).

In this study, fractal dimensions are calculated using a scale-independent box-counting method as defined by Mandelbrot (1983) and employed by many authors to characterise fractures (e.g., Cahn, 1989; Kagan, 1991; Odling, 1994; Berntson and Stoll, 1997; Libicki and Ben-Zion, 2005; Zhang, 2020). Other methods for the calculation of fractal dimensions, such as the probability-density (Nykamp, 2020) or pair correlation functions (Sato, 2003), which compare the number of points closer together than a specific distance with the total number of points, may also be employed (Grodner *et al.*, 2021). Importantly, the fractal dimension calculated using the box counting and the pair correlation methods have the same average values (Mou and Wang, 2016). The point analysis methods are typically utilised where there is uncertainty in the validity of the much simpler and more widely recognised box-counting methods.

With the box-counting method, features a square divided overlying the object of interest is divided into a grid of smaller and smaller box sizes (Fernández-Martínez and Sánchez-Granero, 2014). The number of boxes containing the object of interest is then counted for each box size – in this case lines (Figure 2.9).

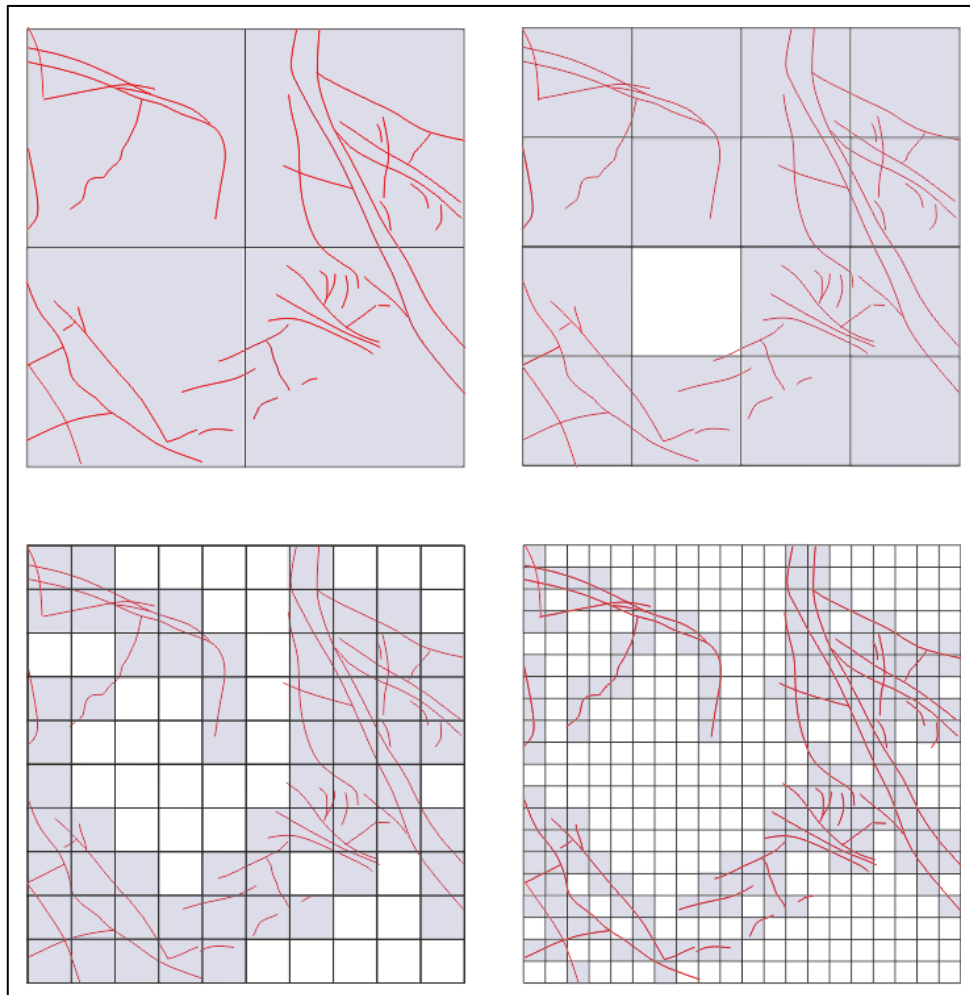


Figure 2.9: A square with red lines sub-divided into a grid of smaller and smaller box sizes. The number of boxes containing fractures (indicated by lilac shading) increases from 4, to 15, to 61, to 165.

The number of boxes containing the object (N) is plotted against the box size (S) to determine the fractal dimension (D), that is shown by $D = \log(N)/\log(1/S)$ (Equation 1.

$$D = \log(N)/\log(1/S) \quad (\text{Equation 1})$$

A number of different box-sizes are measured and a log-log graph of $1/\text{box length}$ vs. number of boxes with the object is plotted. The slope of this graph is the fractal dimension (Figure 2.10).

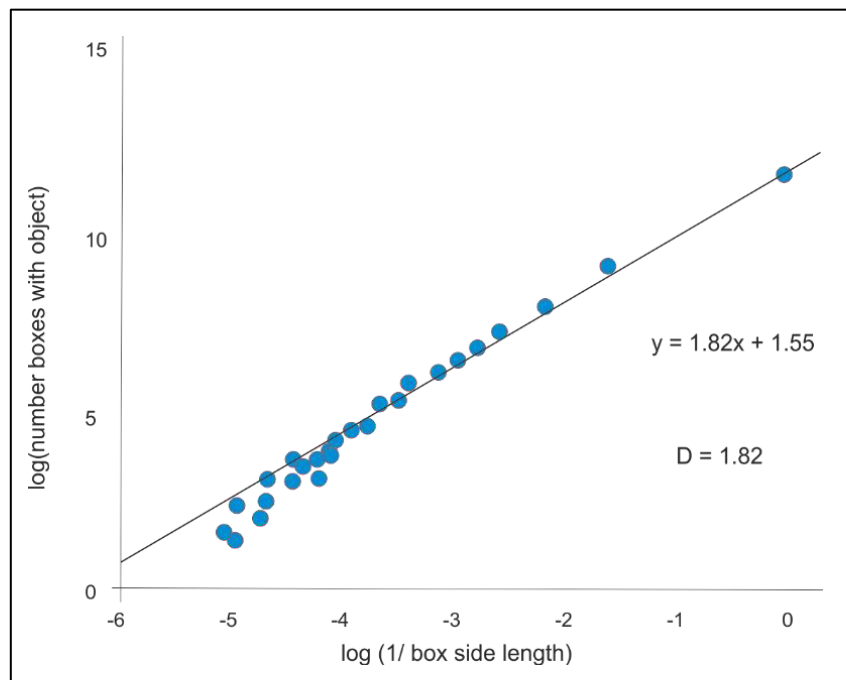


Figure 2.10: Log-log graph of $1/\text{box length}$ vs. number of boxes of different sizes within a dataset. The slope of the best-fit line represents the fractal dimension.

The line of regression defines the trend of the data points on a scatter plot. It is used to predict the behaviour of data using the slope of its line. The lower the correlation between the two axes, the lower the confidence is to predict the accuracy of the trend. In the case of the box-counting curve, especially considering the tightly focused variations in box size and the small number of boxes that do or do not contain fractures in this thesis, it is still possible to derive different fractal dimensions, even though the correlation may not be as high as one would desire.

Determination of the statistical self-similarity of the box-counting dimension is a function of scale, especially at smaller scales (Bouda *et al.*, 2016). Box-counting methods may not be especially accurate in small box scale due to the restriction of pixel sizes in digital images (Wu *et al.*, 2020). Fractals are generally described by the Hurst exponent of a power law. This power law may have implications on fractals as it would require unrealistically large-sized fractures (Baecher, 1983).

Upper and lower restrictions to the box-counting method are clearly important. The greatest spread of box-sizes that do not bias the upper and lower box data are required. Hence, one-metre-wide boxes are utilised to include typical fracture spacings, with a minimum size of five-centimetre boxes to ensure that irregularities at a small scale do not affect the calculation of the fractal dimension. To allow the realistic comparison of topological and fractal data, the circular measurement circles for topological data have all been placed on the fractal grid.

2.6 Remote Sensing

Data pertaining to fracture distribution can be collected remotely, either from satellite, or flight, ground-based surveys, or underground collection. As these techniques are not part of the high-resolution outcrop mapping as described in Section 2.5, they are broadly classified as “remote sensing” techniques. The high-resolution data is used to better understand the characteristics of the remote sensing data.

2.6.1 Satellite imagery

Landsat is a joint NASA / USGS earth observation satellite program that was launched in 1972 – the most recent satellite, Landsat 9 was launched in 2021. It contains optical and thermal sensors, with the OLI optical sensor acquiring data for nine spectral bands with a ground sample distance of 30 m for all bands. Sentinel-2B is a comparable satellite operated by the European Space Agency (ESA) and has a Multispectral Instrument (MSI) that collects data in the visible, near-infrared, and short-wave infrared portions of the electromagnetic spectrum. The ground sample distance is too long for the detection of fractures, stratigraphic contacts, including those caused by faults can only be mapped over a wide scale. Collection and interpretation of this data is expensive, and it was considered inappropriate as the objective of the project was to investigate details fracture patterns.

2.6.2 Geospatial data tools

Google Earth is probably the easiest software that can be used to process satellite images. The visible spectrum images are sourced from a variety of satellite companies and are combined into a mosaic of digital elevation models of images taken over many days, months, and years. The collected imagery is then displayed as one blended image at resolution ranges from 15 metres to 15 centimetres. All the GIS data for this thesis, including spatial positions of mapping sites and stratigraphic and structural information have been captured on Google Earth. Google Earth allows the positioning of the field GPS points and the outcrop mapping can then be rectified by using ridge-lines or linear features (faults).

ArcGIS is geospatial software to analyse geographic data. ArcGIS is built around a geodatabase of spatial data. It links the spatial features with attributes and rules on how features relate to one another. A geodatabase can store multiple feature classes or type of features within one file. Importantly, ArcGIS can be used at a variety of scales to test the geospatial relationship between factors. In this thesis, the spatial relationship of fractures on metre-scale outcrops are analysed using ArcGIS, but on a more detailed scale. The fracture patterns and characteristics are defined using the same spatial and analytical tools. A highly fractured wackestone was also analysed using 5 cm wide circles and it also produced an accurate analysis of the fracture pattern. ArcGIS is however very time-consuming as unless lineaments can be automatically picked up from the image they need to be manually mapped. Unfortunately, the similarity of the colours of the fracture patterns made this impossible.

2.6.3 Electromagnetic data

The variations in the electrical of properties of rocks including conductivity, resistivity, permeability or permittivity are measured by employing electromagnetic fields, including methods that use direct current (electrical or resistivity methods) and induced polarization, especially detection of shallow carbonate landslides (Revil *et al.*, 2020), as well as methods that use microwave frequencies such as

ground-penetrating radar (GPR). GPR provides a high resolution, cross-sectional image of the shallow subsurface as a short pulse of electromagnetic energy is radiated downward. Depth measurements to interfaces are determined from travel time of the reflected pulse and the velocity of the radar signal. GPR is well known to image subsurface geological stratigraphic layers and structures including faults and fracture trends. Other methods that use natural electromagnetic fields known as magnetotelluric methods. As fractures generally have different electrical properties to the host-rock, many of these techniques can be used to identify and map especially large-scale deeper fractures (Figure 2.11).

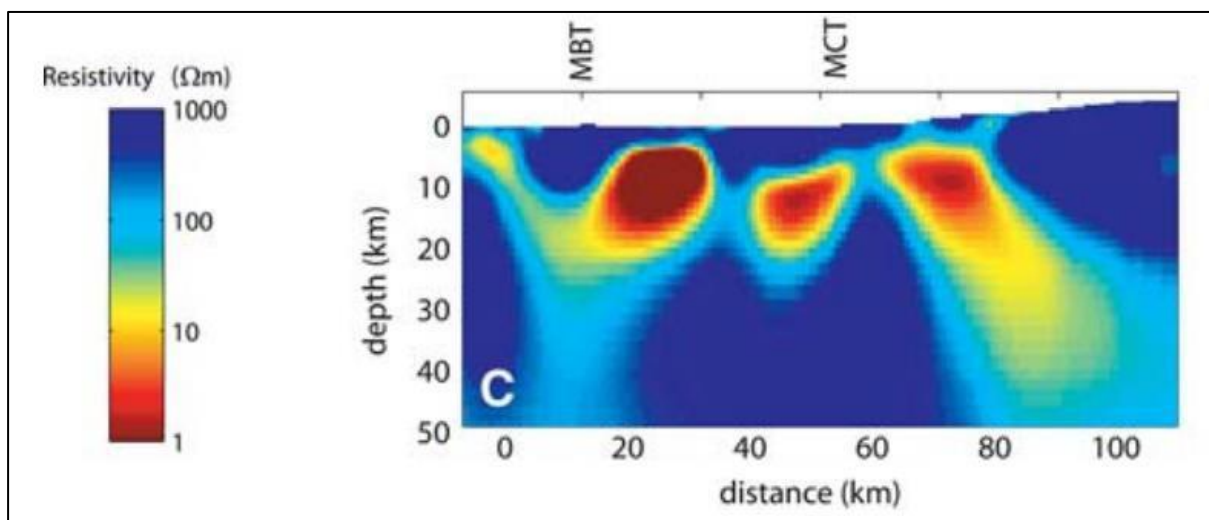


Figure 2.11: Magnetotelluric section profile showing the high resistivity zone ($100 \Omega\text{m}$) zone beneath the Main Boundary Thrust (MBT). From Unsworth (2009).

Electromagnetic techniques can be used on surface and underground in boreholes. The resolution of the target, be it a shear-zone hosted gold deposit or fracture characteristics, ranges from kilometre to millimetre scale utilising satellites to microscopes if there is a strong enough electromagnetic contrast in the target.

Drone mapping of visible spectrum data can acquire high-resolution datasets at altitudes between 10 to a few 100 m (Vollgger and Cruden, 2016).

Photogrammetric modelling of the data in software such as Agisoft or Pix4D generates a georeferenced spatial dataset – a point cloud. Each point within the point cloud is associated with the following nine attributes (Vollgger and Cruden, 2016):

- X, Y, Z coordinates (digital elevation model or DEM);
- Colour channels (red, green, blue); and
- Orientation data of the vertex normal vector (n_x, n_y, n_z) for each point.

Images are mapped on the triangulated DEM surface with sub-centimetre resolution and centimetre accuracy. The DEM creates surfaces from triangulated irregular networks (TINs), the orientation and continuity of which are digitally extracted. This enables automated measurements of planar structures such as fractures, bedding and foliation (Corradetti *et al.* 2017).

Synthetic aperture radar produces its own energy by simulating a synthetic large antenna from a sequence of shorter antenna and recording the amount reflecting back. Radar sensors utilize longer wavelengths at the centimetre to metre scale and can produce high resolution topographic images.

LiDAR uses lasers to produce a high level of accuracy for 3D mapping with a level of a few centimetres. This can be used to map decimetre scale outcrops to detect the fracture pattern. Unfortunately, the Pakistani authorities would not allow me to fly drones in the field area so I could collect these types of data.

2.6.4 Seismic data

This thesis attempts to provide better understanding of how the mapped fracture characteristics can be translated into the subsurface and hence affect the production of hydrocarbons, thereby increasing the understanding from seismic data. Seismic data holds a lot of information. Not only does it identify reserves, but it also provides critical information on fracture density and orientation, which is crucial to accurate drilling and well placement. Fractures in a rock mass influence the velocities and amplitudes of seismic waves that have propagated through them (Boadu and Long, 1996). Detection

of changes in the velocities of seismic waves permits a detection of fractured rock-mass. (Pan *et al.*, 2021). Identification of fracture systems is possible using wide azimuth long offset 3D seismic data together with azimuthal processing techniques such as offset vector tiling, which provides attributes such as fracture intensity, fault likelihood and coherence within the rock-mass (Shoaib *et al.*, 2022). The structures in the oil-bearing sections of a FAT belt are mostly thrust-related anticlines and associated pop-ups, making it important to identify these fracture patterns (Shoaib *et al.*, 2022). Seismic attribute generation associated with the orientations of fractures can be to investigate structural complexities and assign fracture intensities to the rock mass. (Figure 2.12).

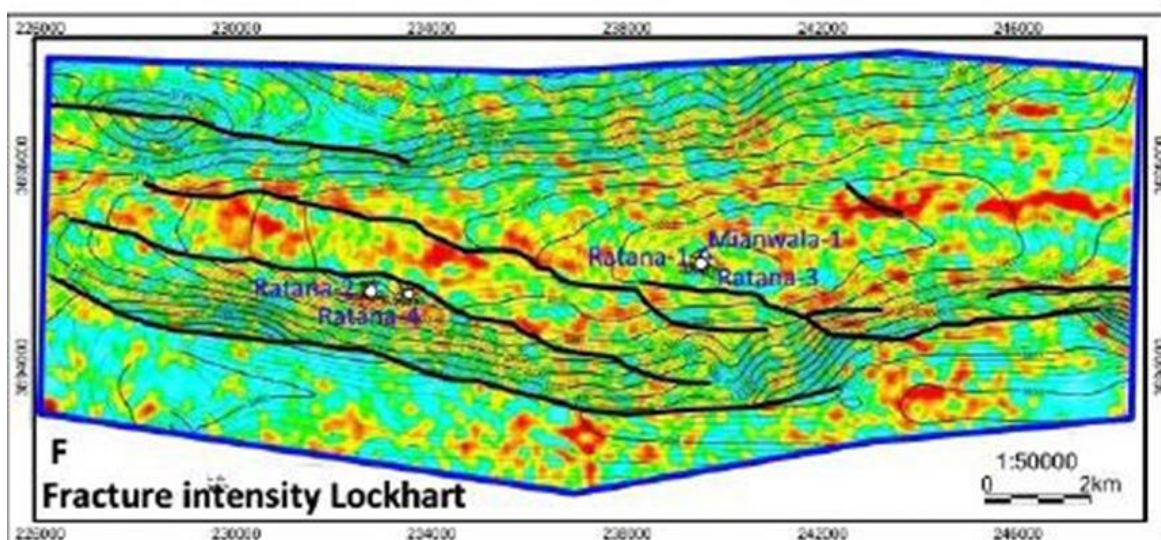


Figure 2.12: Plan view of the fracture intensity of the main carbonate reservoir in Lockhart Formation of the Ratana Field (Shoaib *et al.*, 2022). The study area of this thesis also contains a significant amount of Lockhart Formation.

The investigation of fractures should start early in the exploration stage. Relevant surface outcrops of the reservoir section or reservoir analogues can form the basis of a lithology and structural models (Bratton *et al.*, 2006). Fracture surface maps are likely to be consistent with production data from the field in that areas of high fracture intensity as long as the geological models are correct.

2.6.5 Borehole data

The primary use of boreholes is to generate models of the stratigraphy and structural geology at depth. Boreholes serve to confirm that geophysical projections are accurate. This is acquired by drilling an open drill bit and recovering sections of the core progressively from the hollow core barrel (Figure 2.13a). The extracted core, which is a physical specimen shows clearly what the rock and the fractures are and does not depend on the interpretation of measurements from downhole geophysical tools (Figure 2.13b). The rock-types and stratigraphic succession are logged are directly compared and accurately analysed with the surface exposures of the relevant rocks.

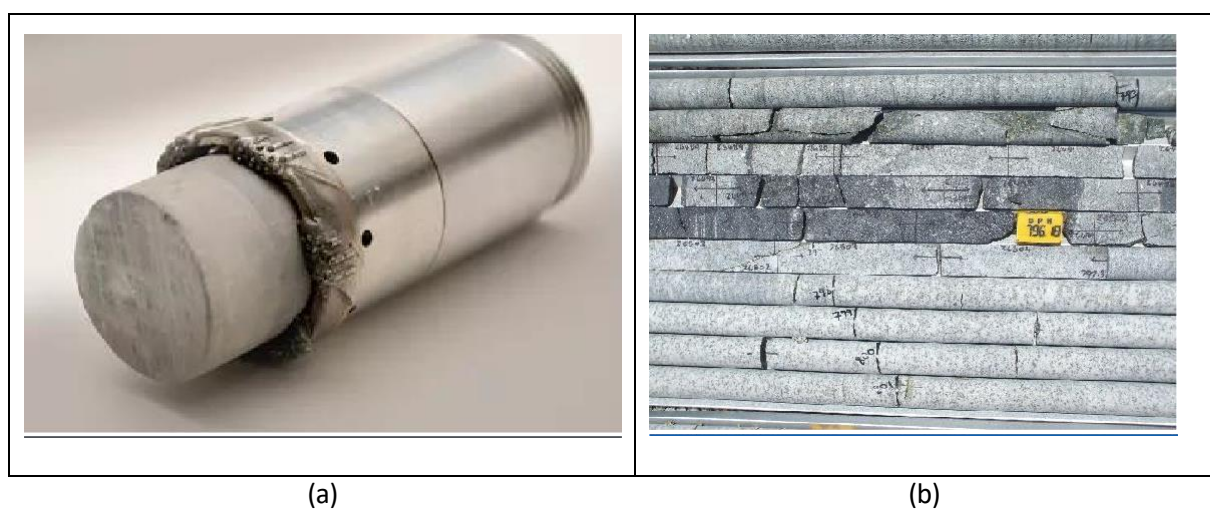


Figure 2.13: (a) Drill-core with a rotary diamond drill bit; (b) Diamond drill-core from the Bushveld Complex, South Africa, showing the physical characteristics of the stratigraphy and fractures and the sampled drill-core (halved core) above the yellow marker.

The structural characteristics of surface exposures can be compared with those mapped in the seismic section and detected in the borehole. Typically, the geological and geophysical characteristics are measured and compared with surface 3D exposure models to permit an understanding of the reservoir shape and size (Raeesi *et al.*, 2012). Downhole tools are utilised in the long boreholes to provide a constant set of data. Two broad groups of measurement are undertaken with downhole tools. Firstly, measurements while drilling (MWD) which are directional drilling measurements mainly to ensuring the smooth operation of the drill (Halliburton, 2019). Logging while drilling (LWD) refers to measurement of the geological characteristics of the rock. LWD tools can measure a suite of geological

features, including density, porosity, resistivity, and formation pressure (Rigzone, 2019). Fracture identification can be done with acoustic logging (Wallace International, 2019). These different datasets provide a high-resolution 3D structural and stratigraphic orientation data that can be utilised to confirm and calibrate seismic interpretations.

2.7 Geostatistics of fracture patterns

Tools to quantify variations in the properties of fractures and fracture sets involve an array of concepts ranging from basic statistical characteristics such as minimum, maximum, mean and variance through fractal analysis, power laws, scaling and resolution, and percolation theory (Guerrieo *et al.*, 2011). If the geostatistical variability between datasets is low or it varies systematically, then it is likely that the fractures are geologically related even with different fracture types showing varying mathematical characteristics (Petford and McCaffrey, 2003). Traditional techniques do not account for the sequence of fracture spacing nor possible coordination between fracture size and position (Bonnet *et al.* 2001).

2.7.1 Spatial statistics of fracture patterns

The stochastic character of fractures is widely recognized; and statistical sampling and evaluation and probabilistic descriptions are in general use. However, in many instances not enough empirical evidence can be obtained to confirm the characteristics of the random variables, and many of the characteristics have thus a significant speculative component. Two potential techniques for describing fracture patterns exist. Firstly, disaggregate characterisation where each fracture characteristic is described separately as shown in Table 2.1 (Dershowitz and Einstein, 1988). The second technique, aggregate characterisation, determines the interdependence of joint characteristics. It allows the regular, uniform, periodic arrangements with some form of clustering or repeating pattern.

Table 2.1: Disaggregated fracture characteristics (after (Dershowitz and Einstein, 1988)).

Parameter	Description
Shape	Fracture boundaries can be polygonal, elliptical or irregular.
Planarity	Fractures can be planar or non-planar and this deviation can occur on a number of scales
Joint size	Generally expressed as trace length on a 2D surface or as the surface area of an individual joint
Persistence	The sum of all the trace lengths or sum of the surface areas
Co-planarity	The number of joints that can be located on the same plane
Location	Position of joint, often it is only the spacing or intensity
Spacing	Distance between points produced by a line perpendicular to the joint surface
Intensity	Number of joints per unit area or unit volume
Orientation	Orientation of the joint plane in space expressed by dip and strike

Fracture surfaces are described to exhibit fractal features, mostly characterised by the Hurst exponent of a power law. This power law may have profound implications on the mathematical modelling of fractures. If this scaling effect exists at all scales the physical properties of fractures must be functions of the fracture sizes in all ranges, which could present problem for the characteristics of the physical properties of large-sized fractures (Baecher, 1983). Proportional length bias in which larger discontinuities are sampled with increased probability, and censoring biases in which larger discontinuities are often only partially observed, complicate the statistical inferences (Baecher, 1983).

The complete description of fractures is difficult because of their three-dimensional nature and their limited exposure in outcrops. An ideal characterisation of fractures would involve the specific description of each fracture in the rock mass, defining its geometric and mechanical properties. Fractures in a rock mass are usually described as an assemblage rather than individually. The fracture

pattern has stochastic character that varies in space. Spatial variability can but does not have to imply random underlying mechanisms. It may just as well be the result of a number of simultaneous or sequential but very specific mechanisms.

The spatial distribution of fractures can be interpreted in the function of the processes responsible for their formation and evolution. The classic example of the analysis of spatial variability of rock fracture orientations or vectorial variables in general is kriging which was created by Danie Krige (hence kriging) in his analysis of the gold reefs of the Witwatersrand Basin in South Africa (Young 1987). With kriging, the variation and hence, the range of influence of object pairs is determined by creating a semi-variogram in different directions. Successively more points are paired up with increasing search radii until the variance no longer increases, reflecting the range of influence of the point. Semi-variograms are determined for various directions, and an ellipsoid is created. Fracture pattern variations can also be determined by kriging. For example, the proximity to a fault strongly influences the magnitude of spatial variability for both fracture intensity and intersection density (Hanke *et al.*, 2018). When there are additional structures, such as a fold, the spatial variability becomes less correlated with trends of the fault. Directional semi-variograms of the fracture intensity and intersection density of the fracture network can become subparallel to the fold axis (Hanke *et al.*, 2018). Prediction of the distribution of fractures requires careful consideration of the sequence-of structural deformation processes (Zahm *et al.*, 2010).

2.8 Summary of literature review

The fieldwork in Pakistan has been undertaken between 5 and 30 km north of the capital city of Islamabad where the geology is dominated by sedimentary deposits and structural features associated with the Himalayan Orogen.

Fold and thrust belts typically form on the external edges of this orogen and consist of deformed sedimentary rock in which the layers are folded and duplicated by thrust faults. This makes it an ideal environment to evaluate folded and fractured rocks. The limestone and shale fractures in the frontal Himalayan fold and thrust belt of the research area, form an evolving stress regimes leading to progressive deformation that is affected by diagenesis and then thrusting up of the slabs of rock. Fractures are rarely uniform nor truly random in their spatial distribution. Specific types of fractures occur that are affected by burial diagenesis with hydrofracturing and then meteoric water modification and especially thrusting in the field area.

Distinctive patterns form in different structural features which allows them to be characterised by the combined sets of data in the fracture. The characteristics of all the different fractures can assist or terminate the growth of the pattern due to the changes of strength and applied stresses within the rock-mass. Therefore, all the fractures should be considered when evaluating a rock-mass. Due to the great exposure of the rock types, it is possible to capture complete data-sets of the fracture patterns of many examples of different structures.

Sedimentary carbonates including wackestones, packstone and lime mud along with associated clastic rocks (especially shale) are encountered in this research area. The depositional environments of the various rock types are considered to represent a narrow range of successive transgressive and regressive events resulting in sedimentary deposits between the shallow outer ramp and lagoons of the inner ramp. Micritisation and microspar processes have however recrystallised the original matrix modifying and homogenising the rock-mass properties of the limestones. The development of

microspar from micrite dramatically changes the porosity and permeability in fine-grained limestones such as wackestones. Micrite is characterised by significant microporosity but microspar becomes much more tightly cemented and typically has very low volumes of microporosity. These brittle and highly strengthened limestone are highly stressed and fracture as larger blocks across the bedding by transitional longitudinal (TL) fracturing (Cosgrove 2015). The shales allow slippage between the numerous closely spaced beds causing parallel shearing due to flexural flow (Cosgrove 2015). Intensely fractured rock causes the termination of different rock-mass responses and hence the shale layers act as barriers between the strong limestones in formations of rocks such as the Patala which contain alternating layers of shale and limestone. This allows the description of the relative proportions of the two rock types, and each mapping site can be described as relative proportion of them.

A different type of fracture mapping approach is suggested, combining the topological and fractal characteristics of fractures. Topology describes the spatial relationships such as connectivity and continuity of objects and the mapped nodes define properties rather than the inherent properties of the individual fractures. Fractal dimensions of fractures on a surface vary from one dimension, a perfectly straight line, to two dimensions when the object forms a planar surface. The fractal dimensions of the mapped fractures are between one and two which allows the determination of the increase in complexity of the fracture.

Both measurement positions are taken in the same location (the topological circle is centred on the measurement grid). This allows a distinctive set of characteristics to be defined for structural features.

3. Methodology

3.1 Introduction

This chapter provides a description of the field techniques and data analysis techniques used and developed for this work. A summary of the most important methods and their implications for a select number of outcrop localities are published in Grodner *et al.*, (2021), whilst full details of all the localities and data are given here. The methods described include geographical data capture to ensure the correct positions of the mapping sites and regional and local geological data. This involved mapping of sites using measurement circles, measurement lines, and interpretation of photographs using ArcMap. Seven field regions have been evaluated in a study area in the Himalayas north of Islamabad, ranging between 5 km west and 45 km northeast from Islamabad (Figure 1.1, Chapter 1). The proximity of the field area to Islamabad allowed access to the mountains of the Himalayas both via tar road, and dirt tracks.

The Himalayan Fold and thrust (FAT) belt is a characteristic structural system (Hammerstein, 2020). FAT belts potentially host large oil and gas fields, but as they are difficult places to explore substantial resources remain thereby promoting research into thrust fold related structures (Graham *et al.*, 2010; Butler *et al.*, 2018; Zuccari *et al.*, 2022). There are many different geological structures in a FAT terrain and the techniques applied here allow the separation and quantification of these features such as thrust fold related structures.

Mapping transects are at right angles to the southwest-northeast main frontal Himalayan structural trends in the field area. These cross-sections are perpendicular to the major structural features including folds and thrusts in the limestones of the hanging-wall of the Main Boundary Thrust. The field-data is analysed using a combination of topological characteristics and fractal dimensions to characterise fracture patterns and relate them to structural domains. When these methods are

considered together for all the fractures within an area, fore-thrusts, pop-ups, synclines, anticlines and back-thrusts can be distinguished (Grodner *et al.*, 2021). Specific nomenclature and descriptive terms are applied to data types and collection methods (Table 3.1).

Table 3.1: Data collection terms and their meaning in this thesis.

Term	Meaning
Fracture	Brittle discontinuity separating the mechanical properties of a rock. It is very narrow in width relative to the other two dimensions. The term includes joints, extension fractures (and veins) as well as shear fractures with displacement sub-parallel to the fracture (Peacock <i>et al.</i> , 2018).
Fracture set and fracture network	A fracture set is a subsection of a fracture system within a rock-mass with similar properties (Peacock <i>et al.</i> , 2018). Properties can include orientation, mineralisation, or genetic origin. The cumulative characteristics of a fracture network are formed by the interactions of different fracture sets that need to be considered to define the rock-mass character.
Rock-mass	A matrix consisting of intact rock and associated fractures. The properties of a rock-mass are a product of the fractures and the intact rock-mass (Bieniawski, 1975; Barton <i>et al.</i> , 1974; Laubsher, 1977).
Measurement line	A tape-measure extended over a fractured rock to permit the spacing of the fractures to be measured. This allows calculations such as fracture density and fracture frequency to be determined.
Measurement circle and box	A 1 m diameter circle drawn on a scaled digital photograph of the rock exposure and used to determine the topological characteristics. A 1 m wide box is centred on the circle and used to collect box-counting data to determine the fractal dimension.

Nodes	Terminations and intersections of fractures in a measurement circle used in the topological analysis of data (Sanderson and Nixon, 2015).
Topology	Quantification of the arrangement fractures and how they are connected (nodes) from which it is possible to derive fracture density, fracture intensity, mean trace length and the number of fracture tips, lines, and branches.
Fractal dimension	A quantification of the self-similarity or scale invariance of a fracture network. There are numerous methods to quantify the fractal dimension. This work employs the box-counting technique (Figure 3.22).
ICE	Microsoft Image Composite Editor (ICE) takes a series of photographs and creates a high-resolution panorama which permits cross-sections of folds and thrust faults to be analysed.
ArcMap	A geospatial processing programme that is used to view, edit, create, and analyse geospatial data. Conventional geospatial evaluation such as analysing geographic maps and satellite images were not applicable. In this research, geospatial data are cross-sections of faults (metre-scale) and closely spaced fractures (centimetre-scale) and was captured using ICE The ArcMap tools for determining the box density, linear density, and length of features are used to characterise different fracture sets.

3.2 Geographical data capture

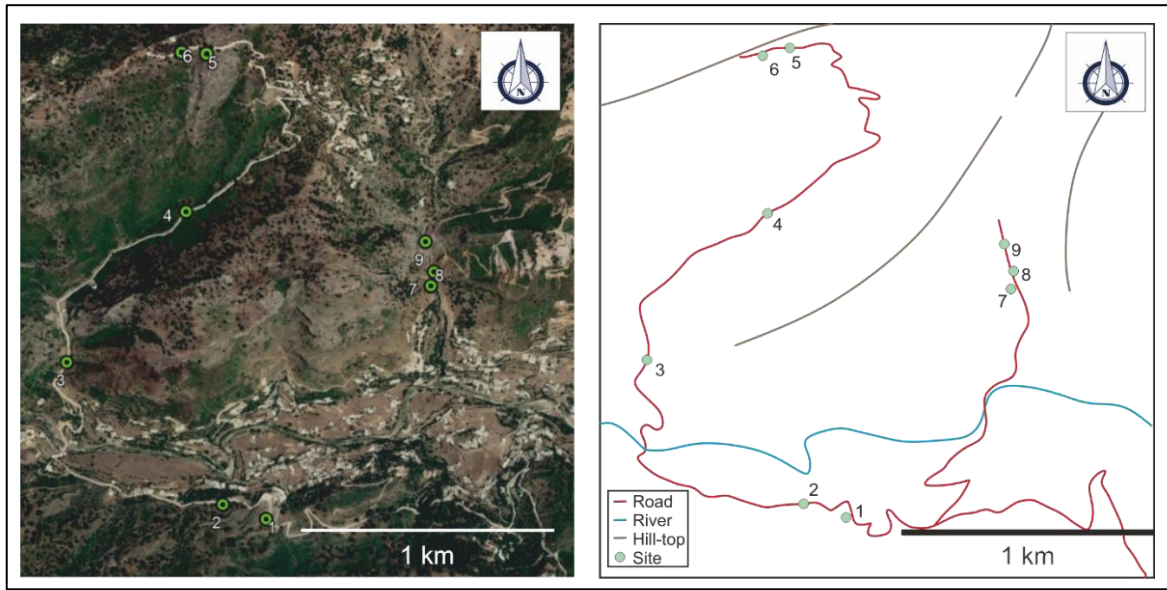
The position of the mapping sites in each of the seven mapping regions was recorded using a hand-held Garmin Map64 GPS navigation device (Table 3.). This data was checked during each evening of the fieldwork to ensure that the positions were correct using known roads, rivers, and topographic features (Figure 3.14). A map was generated in Google Earth to analyse the regional structural setting

of the field area (Figure 3.15). The stratigraphic and structural information was transferred from the maps of the different field sites described in Chapter 4.

Table 3.2: Geographical locations of mapping sites as measured with the Garmin Map64 GPS.

Region	Name	Site	Latitude	Longitude
1	Losar Baoli	1	33.723°	72.916°
		2	33.723°	72.921°
		3	33.725°	72.926°
		4	33.733°	72.922°
		5	33.744°	72.932°
		6	33.746°	72.940°
2	Makhniyal	1	33.807°	73.127°
		2	33.807°	73.126°
		3	33.807°	73.127°
		4	33.807°	73.128°
		5	33.812°	73.134°
		6	33.815°	73.134°
		7	33.820°	73.133°
		8	33.826°	73.129°
3	Talhaar	1	33.766°	73.039°
		2	33.766°	73.037°
		3	33.771°	73.031°
		4	33.776°	73.036°
		5	33.781°	73.037°
		6	33.781°	73.036°

		7	33.773°	73.046°
		8	33.774°	73.046°
		9	33.777°	73.045°
4	Najafpur	1	33.796°	72.998''
		2	33.796°	73.000°
		3	33.792°	73.022°
		4	33.793°	73.035°
		5	33.793°	73.059°
5	Shah Dara	1	33.778°	73.169°
		2	33.779°	73.171°
		3	33.776°	73.170°
		4	33.775°	73.173°
6	Jabbri	1	33.919°	73.203°
		2	33.922°	73.197°
		3	33.922°	73.192°
		4	33.895°	73.171°
		5	33.872°	73.173°
		6	33.867°	73.174°
		7	33.857°	73.161°
7	Changla Gali	1	33.992°	73.392°
		2	33.992°	73.393°
		3	33.993°	73.393°



(a)

(b)

Figure 3.14: (a) An example of the Google Earth image of the mapping sites in the Talhaar region; (b) Locations showing how the mapping sites were confirmed using features such as roads and rivers clearly visible on Google Earth.

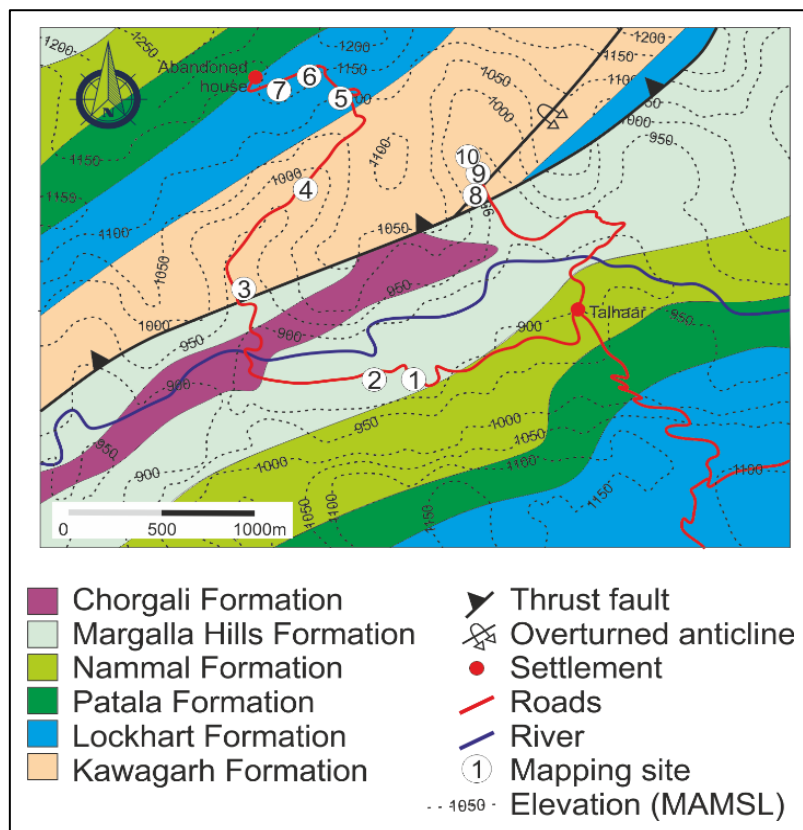


Figure 3.15: Geological map of the Talhaar region.

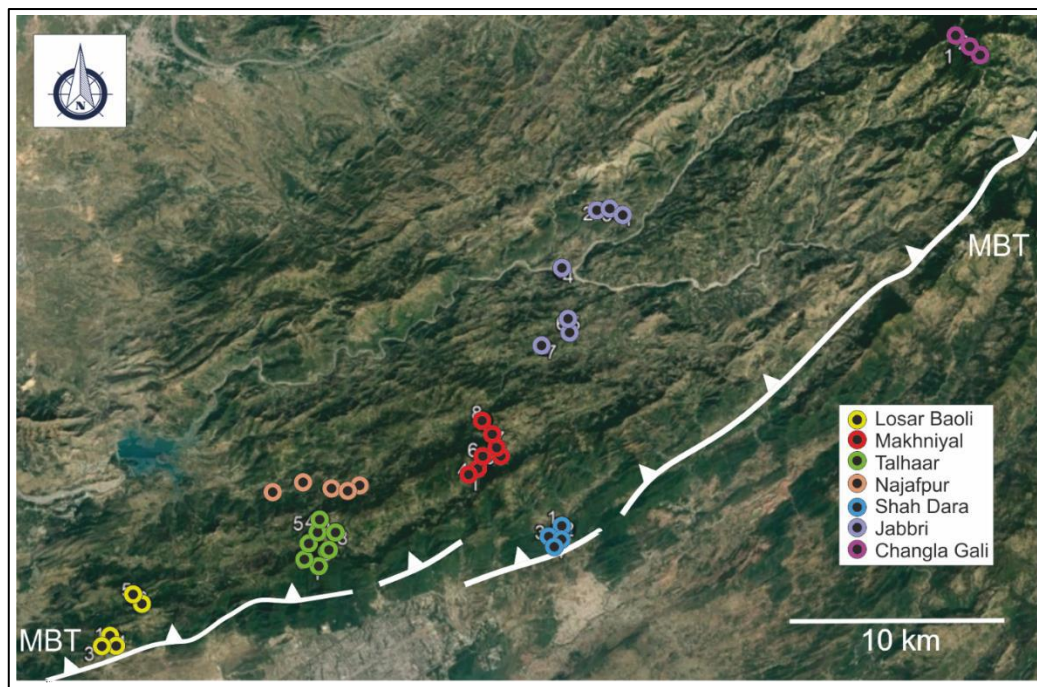


Figure 3.16: Google Earth image of all seven mapping sites in the field area. MBT = Main Boundary Thrust – all the field areas are located in the hanging wall of the MBT. Note the southwest – northeast strike of the geological structures.

3.3 Geological data capture methods

At each mapping site, information on the lithologies and geological structures were collected. The lithological information permitted confirmation of the stratigraphic position of the site and aiding in the understanding of the geomechanical characteristics of the site. Mapping of the structural features is important both to relate the characteristics of each site with large regional structures as well as to determine the appropriate measurement methods.

The individual constituent fracture types within the fracture system are not separated for analysis. In these complexly fractured rocks of the field sites, the concept of fracture sets is problematic. Sets are typically defined as fractures sharing a narrow range of orientations and broadly contemporaneous timing characteristics captured by fracture patterns (abutting and crossing relations) or distinctive mineral deposits (Hancock, 1985). In this thesis, all fractures are considered for analysis to investigate

how the true cumulative effects of successive tectonic stresses can be used to discriminate different characteristics of the strained rock-mass. The fracture patterns investigated during this work reflect progressive deformation resulting in the creation of numerous stresses and fractures associated with each successive deformation event. As such, orientation and other typical aspects of sets are considered to be unreliable markers of relative timing of formation and of set membership. The complexities of the timing of these multiple fracture events, which could potentially be resolved from fracture cement fill sequences and their dating (Laubach *et al.*, 2019), interactions with fracture tip propagation dynamics (Renshaw and Pollard, 1994), and other processes (Long *et al.*, 1996), are impractical to work out without detailed petrographic analysis, which is beyond the scope of this work. The focus of this research is to understand the spatial and connectivity relationships of the whole fracture population in the context of the wider structural scale.

To capture the fracture characteristics, the fracture properties were recorded together at each site. This approach integrates discrete topological and spatial methods for characterising fractures and fracture networks by employing fractal dimension to provide a spatial context of the distribution of the constituent fractures. This data is then combined with analyses of the observed topological relationships and interconnectivity of the fracture networks. The approach provides a more robust assessment and analysis of the fractures observed within the rock-mass and their characteristics than can be achieved from application of either method in isolation (Grodner *et al.*, 2021). As all the topological and fractal data are considered together, all the interactions between fractures, and their effects upon the characteristics of the rock-mass are defined. Moreover, this approach dramatically reduces the time taken for data collection compared to traditional fracture sampling techniques and provides large amounts of unbiased data representative of fracture network characteristics over a wide range of fracture of the rock-mass.

A series of measurement techniques have been employed at each site to quantify the fracture characteristics. The most notable of these techniques is the measurement circle and the associated

topological and fractal data measurements (Grodner *et al.*, 2021). Other field mapping techniques include line mapping, and mapping of fracture characteristics in small (5 and 10 cm wide) squares in highly fractured rock-mass. The fracture density, length, and count has also been determined by digitising images of the rock into ArcMap. The different types of measurements taken at each site are listed in Table 3.3. A total of 151, one metre circles at 42 different sites and 34 additional sets of data were captured including:

- 5 and 20 cm, and 2 m diameter measurement circles (6 in total)
- Measurement lines (12)
- 5 and 10 cm measurement squares (9 in total)
- Digitised ArcMap image analyses (3)

Details of the different data capture methods are described below (Table 3.3).

Table 3.3: Measurement methods per site. “No. circles” refers to the number of measurement circles used to collect topological and fractal data and “Total” is the total number of circles in each region.

	Name	Site	No. circles	Other measurement methods	Other data types
1	Losar Baoli	1	6		
		2	5		
		3	2		
		4	2		
		5	2	Measurement lines * 3	frac spacing and frequency
		6	3		
		Total	20		
2	Makhniyal	1	0	Fracture mapping	
		2	10		
		3	4		

		4	0	10 cm measurement squares * 6	fracture spacing and frequency
		5	6		
		6	5		
		7	0	Fracture digitising in ArcMap of 5 cm diameter measurement circles * 4	fracture density, length, count
		8	6		
		Total	31		
		3	Talhar	1	4
2	4			Measurement lines * 2	frac spacing and frequency
3	3				
4	4				
5	2			Measurement line * 1, detailed 5 cm square * 6	frac spacing and frequency
6	3				
7	10			Fracture digitising in ArcMap	frac density, length, count
8	6				
9	2			Measurement lines * 3	frac spacing and frequency
Total	38				
4	ajafpur	1	0	Measurement lines * 2	frac spacing and frequency
		2	2		
		3	8	Fracture digitising in ArcMap	frac density, length, count
		4	4		

		5	2		
		Total	16		
5	Shah Dara	1	4		
		2	1		
		3	1	2 m and 20 cm diameter circles in same centre	
		4	6		
		Total	12		
6	Jabbri	1	1		
		2	0	Bed thick vs. fracture count	
		3	6		
		4	6		
		5	5		
		6	1		
		7	3	Measurement line * 1	frac spacing and frequency
		Total	22		
7	Changla Gali	1	1	10 cm measurement squares	frac spacing and frequency
		2	5		
		3	6		
		Total	12		

3.4 Measurement circles

Folded and faulted rocks in the study area are characterised by individual fractures that have lateral extents on the scale of centimetres to millimetres and vary in type and orientation within a small area. Characterising each individual fracture is therefore inappropriate at the outcrop scale in these strata. Moreover, the wide range of fracture strikes at any one measurement site means that the one-dimensional scanline technique (Guerriero *et al.*, 2010) has a strong bias as fractures that are sub-parallel to the scanline are less likely to be intersected by it. For such inherently two-dimensional patterns, techniques of rectangular or circular window mapping are preferable (Mauldon *et al.*, 2001; Watkins *et al.*, 2015). Circular window mapping is utilised as topological information can also be derived (Mauldon *et al.*, 2001; Sanderson and Nixon, 2015).

At each sampling location a circle of 1 m in diameter was marked onto the outcrop and photographed with numerous digital photographs covering the 1 m circle (Figure 3.17). Several measurement circles were mapped at each sampling site, on surfaces oriented both parallel to and perpendicular to bedding, and on surfaces created by road-excavations at oblique angles to bedding (Table 3.3). Analyses of the fracture characteristics at each of the sampling sites are based on the combined data of all the circular windows, and the different angles of the circles, thereby reducing orientation bias.



Figure 3.17: Examples of measurement circles chalked on the rock-mass which can be highly fractured. The chalk circle is not clear in the right-hand image due to the high degree of fracturing. To compensate for this, circles of the appropriate size are drawn during the compositing of the photographs of a measurement circle.

3.5 Topology from measurement circles

Topology describes the way in which constituent parts of a system are arranged, interrelated, and connected. The arrangement of components within a geometrical system - in this case, a fracture network - can be defined in terms of topology, and an analysis of that arrangement can provide critical information on network pathways. For example, a high number of cross-cutting fractures suggests interlinked networks with continuous pathways between them. The topological characteristics of a fracture network can be determined at any scale (Sanderson and Nixon, 2015). The types of intersections (termed 'nodes') between fracture traces present within the measurement circles at each of the sites in this study were characterised (Figure 3.18).

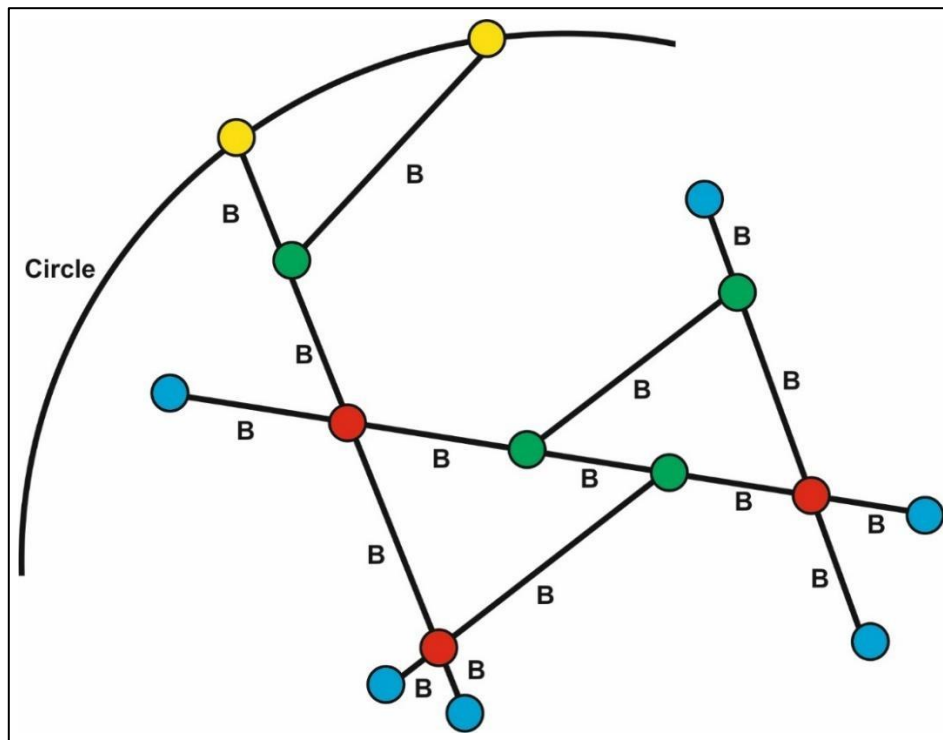


Figure 3.18: Node types of intersecting fractures as defined by Mauldon *et al.* (2001) and Sanderson and Nixon (2015). Fractures branches are labelled “B”. Every “x” (red) node has four branches, every “y” (green) node has three branches and every “i” (blue) node has one branch.

The types of nodes are defined as follows (Mauldon *et al.*, 2001; Sanderson and Nixon, 2015), and are identified in all subsequent diagrams and photographs by the following colours (Figure 3.19):

- “e” nodes (yellow) - intersections of fracture traces with the edge of the circle where the traces continue out with the circle,
- “x” nodes (red) – intersections of fracture traces that cross each other and continue,
- “y” nodes (green) – termination of one fracture trace against another fracture trace,
- “i” nodes (blue) – termination of a fracture trace within the rock-mass contained within in the circle.

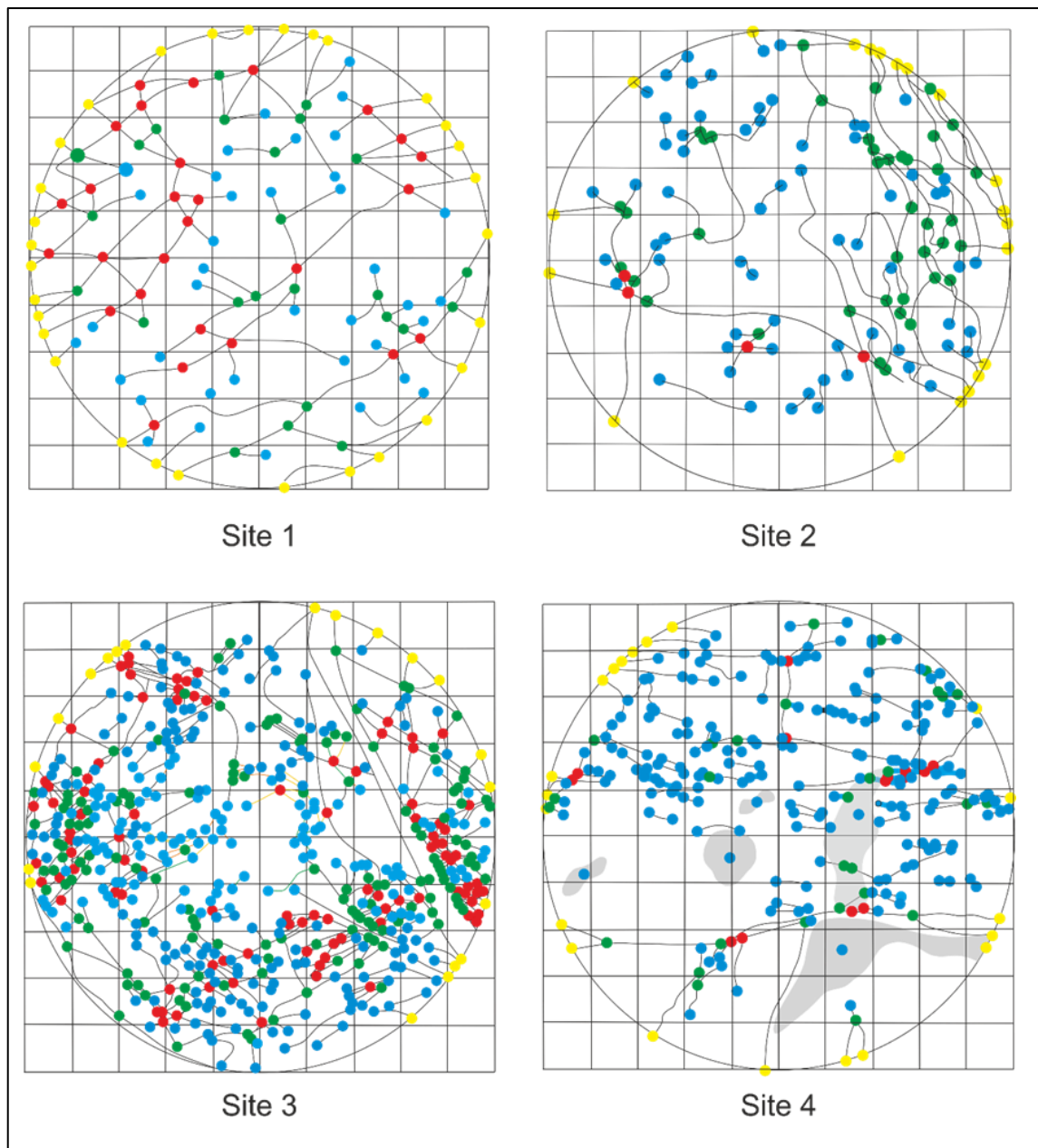


Figure 3.19: Examples of the 1 m diameter measurement circles. Fractures are shown by lines or shaded polygons (for surface-parallel fractures). A 10 cm box grid is overlain on the mapping circles to permit data collection employed in the determination of the fractal dimensions (see Section 3.6 Circle mapping for fractal dimensions). Nodes are coloured as per Figure 3.18.

The node positions were captured on composite digital images as this allowed a more accurate investigation and mapping of the node positions (Figure 3.20). As a result of this methodology, a digital record of all the nodes on all the mapping circles is also available.

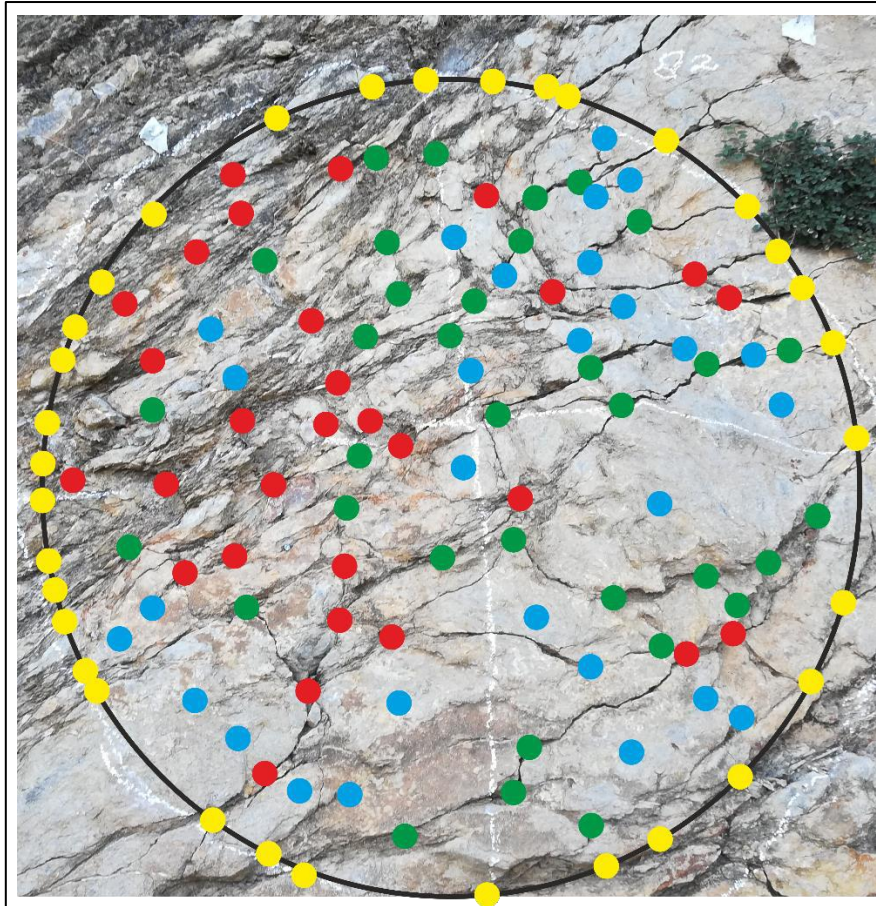


Figure 3.20: Nodes within a 1 m measurement circle. The node colours are defined in Figure 3.18.

The topology of a fracture network is determined by counting the numbers of the different node types and using this to determine specific topological characteristics (Sanderson and Nixon, 2015). As the rockmass is considered as an entity, both the earliest bedding plane fractures in these sedimentary and all the subsequent fractures (that could be of several different generations). This because the rockmass acts a coherent system with stress relief occurring across discontinuities reducing the chance of them from crossing into the adjacent strata or simply rock fragments. Therefore, it was not necessary to discriminate between bedding and fractures (see Table 3.4). Where large voids had been formed by earlier karst development, the symmetrical system of the rockmass does not exist as stresses cannot be applied against the different fragments. In this case, the rockmass can no longer be considered as a system and the discontinuities of different ages are literally not connected.

The number of tips is calculated by summing the number of “i”-(N_I) and “y”-node (N_Y) as each of these is a fracture termination. The number of lines (N_L) is half of this total as each line is terminated by either an “i”-(N_I) or “y”-node (N_Y)

$$N_L = \frac{1}{2}(N_I + N_Y) \quad (\text{Equation 2}):$$

$$N_L = \frac{1}{2}(N_I + N_Y) \quad (\text{Equation 2})$$

As each branch has two nodes, with an “i”-node contributing to one branch, a “y”-node to three branches and an “x”-node (N_X) to four branches, the number of branches (N_B) is calculated as:

$$N_B = \frac{1}{2}(N_I + 3N_Y + 4N_X) \quad (\text{Equation 3})$$

The ratio of the number of branches to lines (N_L) is an important tool for determining the fracture pattern as it indicates how irregular and interconnected the fracture network is (Equation 4).

$$\frac{N_B}{N_L} = (N_I + 3N_Y + 4N_X)/(N_I + N_Y) \quad (\text{Equation 4})$$

The fracture connectivity is dependent on the number of branches (Equation 5).

$$F_C = (N_X + N_Y)/(N_I + N_Y) \quad (\text{Equation 5})$$

Fracture Intensity, (F_I) is a comparative measure of the number of edge-nodes (N_E), within a measurement circle (of radius r) as defined in **Error! Reference source not found..**

$$F_I = \frac{N_E}{4r} \quad (\text{Equation 6})$$

Fracture Density (F_D) represents the number of fractures per unit area (Equation 7) and a fracture is terminated inside a measurement circle of radius r by either a “y” or an “i” node.

$$F_D = (N_Y + N_I)/2\pi r^2 \quad (\text{Equation 7})$$

The Mean Trace Length (MTL) provides an estimate of the average fracture trace length as it considers the number of fractures that are contained within the measurement circle of radius r and the number that transect it. It is derived from multiplying Intensity by area and dividing by number of lines (Equation 8).

$$MTL = \left(\frac{N_E}{N_Y + N_I} * \pi r \right) / 2 \quad (\text{Equation 8})$$

The individual constituent fracture types within the fracture system are not separated for analysis, but rather how the cumulative effects can be used to discriminate the different characteristics of the rock-mass are considered.

Topological analysis of all the fractures was undertaken of each measurement circle and all the nodes, including those formed between different fracture sets, to ensure these were accounted to define the true topological characteristics. Table 3. and Figure 3.21 demonstrate that not considering all the nodes in a single measurement will result in an under-accounting of the intersecting "x" and "y" nodes, an over-accounting of the number of "i" nodes and an under-estimate of the total number of nodes. This will affect the calculation of the topological characteristics.

Table 3.4: Number of nodes considering all fracture sets together in a single measurement compared to summing the number of nodes of individual fracture sets from a site. The number of “e” is the same, “x” and “y” nodes are more common in the former and “i” in the latter. This indicates a greater number of intersections are present when all fractures are considered together which changes the topology.

	Node type	e	x	y	i	all
Single measurement	Unmineralised	19	48	71	97	235
	Mineralised	23	33	58	202	316
	Total	42	81	129	299	551
Fractures cross-cut bedding	Unmineralised	8	0	6	14	28
	Mineralised	7	3	9	36	55
	Total	15	3	15	50	83
Fractures parallel to bedding	Unmineralised	10	2	6	58	76
	Mineralised	4	3	10	51	68
	Total	14	5	16	109	144
Fractures oblique to bedding	Unmineralised	1	17	17	110	145
	Mineralised	12	4	25	97	138
	Total	13	21	42	207	283
Sum of sets	Unmineralised	19	19	29	182	249
	Mineralised	23	10	44	184	261
	Total	42	29	73	366	510

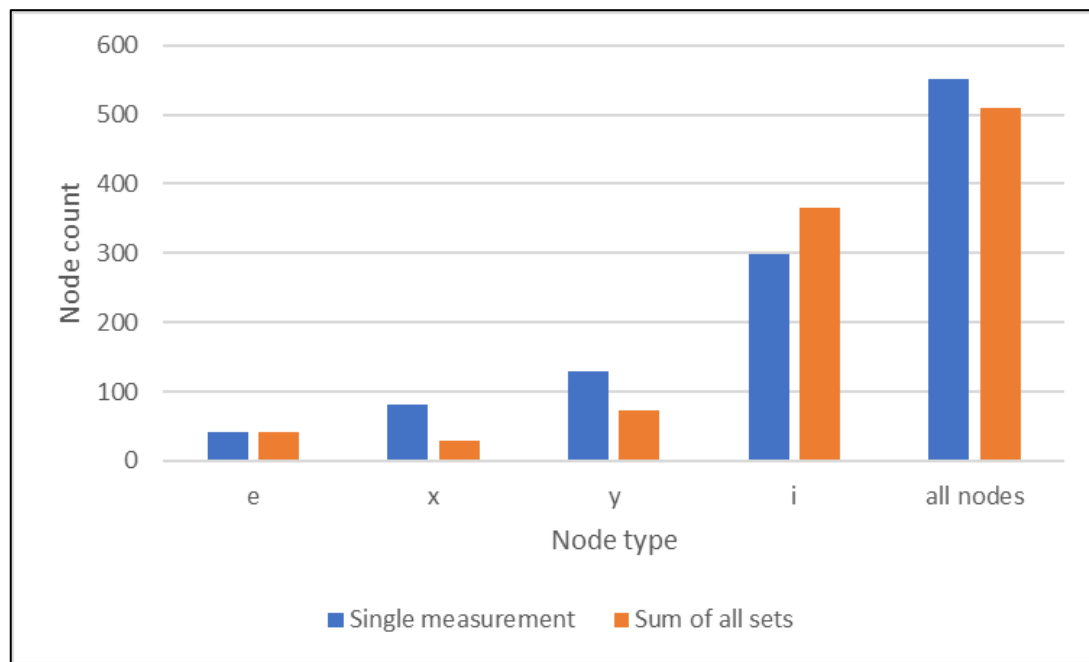


Figure 3.21: Number of different types of nodes present at a site, according to measurement type. The ratios and total number of nodes is different if all fractures are considered in a single measurement.

3.6 Circle mapping for fractal dimensions

Shapes can be quantified relative to the spatial dimension (1D, 2D or 3D) in which they are observed. The intermediate dimensions are referred to as fractal dimensions and have values between the dimensions of the objects and the dimensions in which the objects are observed. In this work, fractal dimensions are between one (the dimension of a fracture line) and two (the dimensions of the measurement surface). The fractal dimensions of each of the entire rock-mass within a measurement circle are calculated utilising a modified scale-independent box-counting method, initially defined by Mandelbrot (1967) and employed by many authors to characterise fractures (including Cahn, 1989; Kagan, 1991; Odling, 1994; Berntson and Stoll, 1997; Libicki and Ben-Zion, 2005). In this thesis, the box-counting only considered the boxes containing fractures within the topological measurement circle (Figure 3.22).

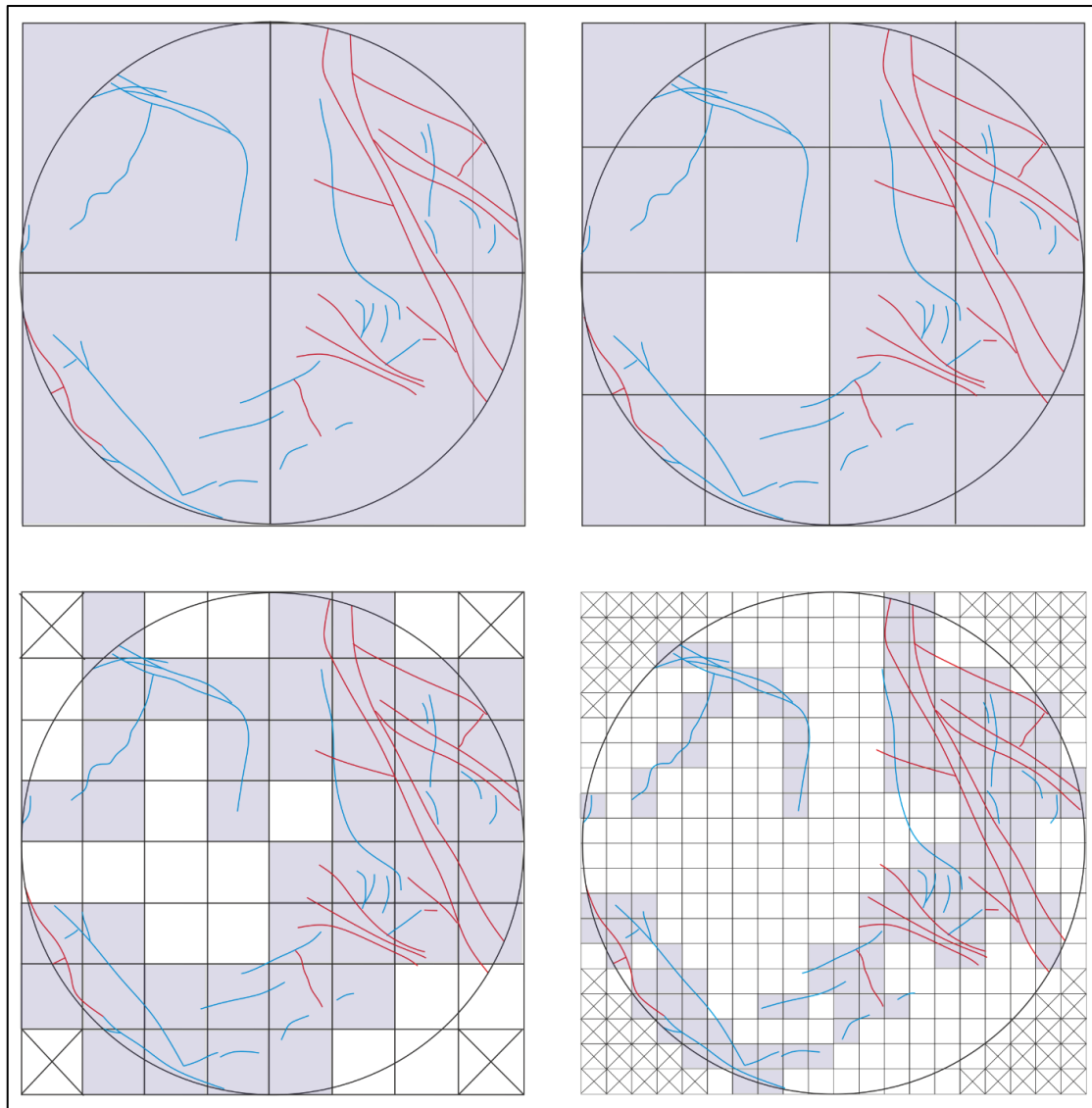


Figure 3.22: Box-counting technique within the 1 m measurement circle with boxes within the circle (shaded). This data are utilised to determine the fractal dimension (D). Crossed out boxes are ignored as these unmapped areas do not contain information about the presence or absence of a fracture because they are outside of the measurement circle. Compare with Figure 2.9 which illustrates the conventional box-counting method.

Boxes of various sizes are laid over the image in a fixed grid pattern. The number of boxes that contain fractures are tallied as a function of box size (Figure 3.7). Box sizes of 100, 50, 25, 20, 10, 7.5 and 5 cm were utilised in this study. Although the area of the 1 m square box used to define the fractal dimension is larger than the area covered by the 1 m measurement circles, these different shapes

were always centred on the same position and hence in each case the relative values of the topological and fractal parameters were compared. The fractal dimension (D) is calculated as:

$$\text{Number of boxes with fractures} = (\text{box size})^{-D} \quad (\text{Equation 9})$$

The fractal dimension can be derived from the slope of the trend-line in a log-log plot of the inverse of the box size against the number of boxes containing fracture traces (Buczowski *et al.*, 1998; Irfan and Stork, 2009). An example of this is shown in Figure 3.23. Although a slightly lower minimum correlation coefficient of 0.95 was decided upon, before the slope of the trend-line was considered to be representative of the fractal dimension, the smaller range of box sizes meant that this value is a correlation coefficient suitable (Roy *et al.*, 2001). The strict methodology of Walsh and Watterson, (1993) was applied to ensure that boxes wholly outside the measurement circle were not included in analyses (Figure 3.22). Care was also taken to ensure that the minimum box size used in any analysis could fully contain the shortest fracture trace, and that the maximum box size used was no larger than the size at which the number of boxes containing fracture traces is equal to the total number of boxes in the analysis (Barton, 1995). The fractal dimension for all fracture traces within the circle is determined from an independent count of boxes containing fracture traces, and not from a summation of the number of boxes containing fractures for each of the different sets, to avoid problems of 'double counting' when boxes contain fractures of more than one set.

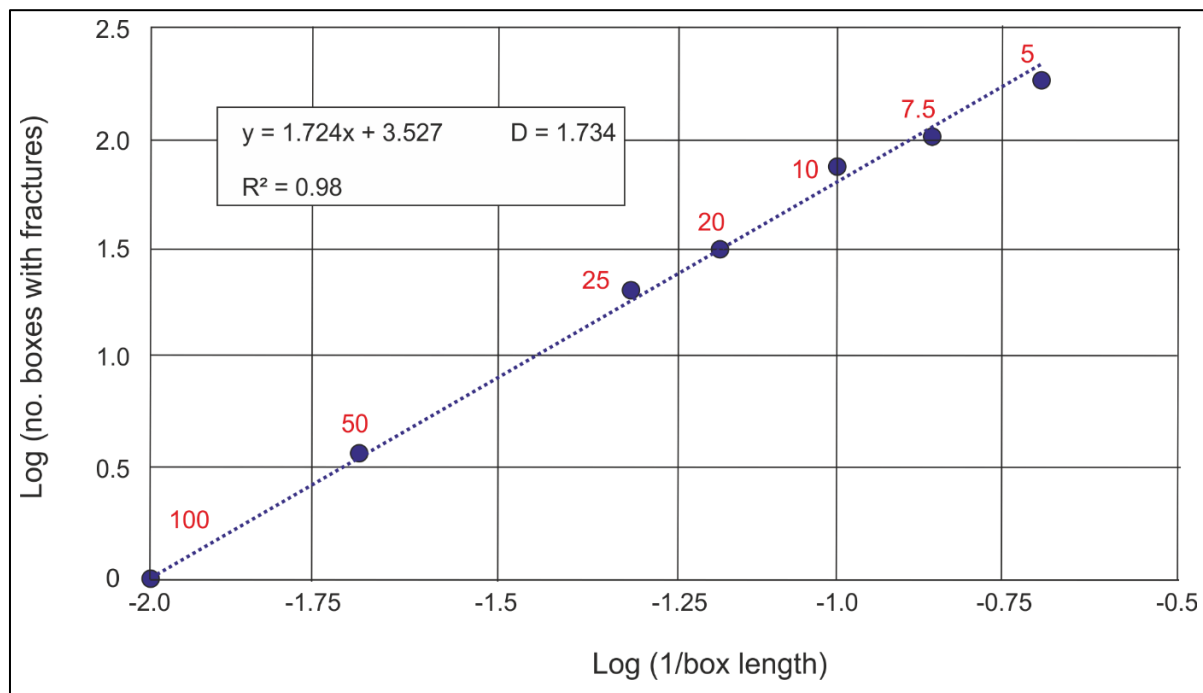


Figure 3.23: Log-log plot of box-count data from a measurement circle. The slope of the best-fit trend-line is the fractal dimension of this data. Red numbers indicate box length in centimetres.

If the box lengths are too large or too small then the gradient of the trend-line may form a plateau at either end of the plot (Walsh and Watterson, 1993). As the minimum (5 cm) and maximum (1 m) box-length of all the fractal data were the same, any relative changes in the gradient of the trend-lines were attributed to changes in the actual fractal dimension and not the mathematical behaviour of the slope. Thus, the box size distribution of between 5 cm and 1 m is considered appropriate for these fractures in this context.

3.7 Measurement lines

To better characterise closely spaced fractures, measurement lines were created parallel to the thrust transport direction to ensure the highest fracture frequency is recorded on the regular planar thrusts common in the field area. An example of these measurement lines is shown in Figure 3.24 where Lines 1 and 2 cross-cut the S1-S2 conjugate shears and Line 3 the J1 fractures. On average, the fractures are 15 mm apart, with Line 3 (J1 fractures) being more closely spaced. It is however noted that the J1 fractures occur in clusters separated by portions of less fractured ground (Figure 3.25).

This simple evaluation of the fracture spacing highlights the distribution of closely spaced fractures. Other characteristics such as the spacing of fractures in different orientations and the spacing of different fracture types can also be compared by employing measurement lines (Figure 3.26).

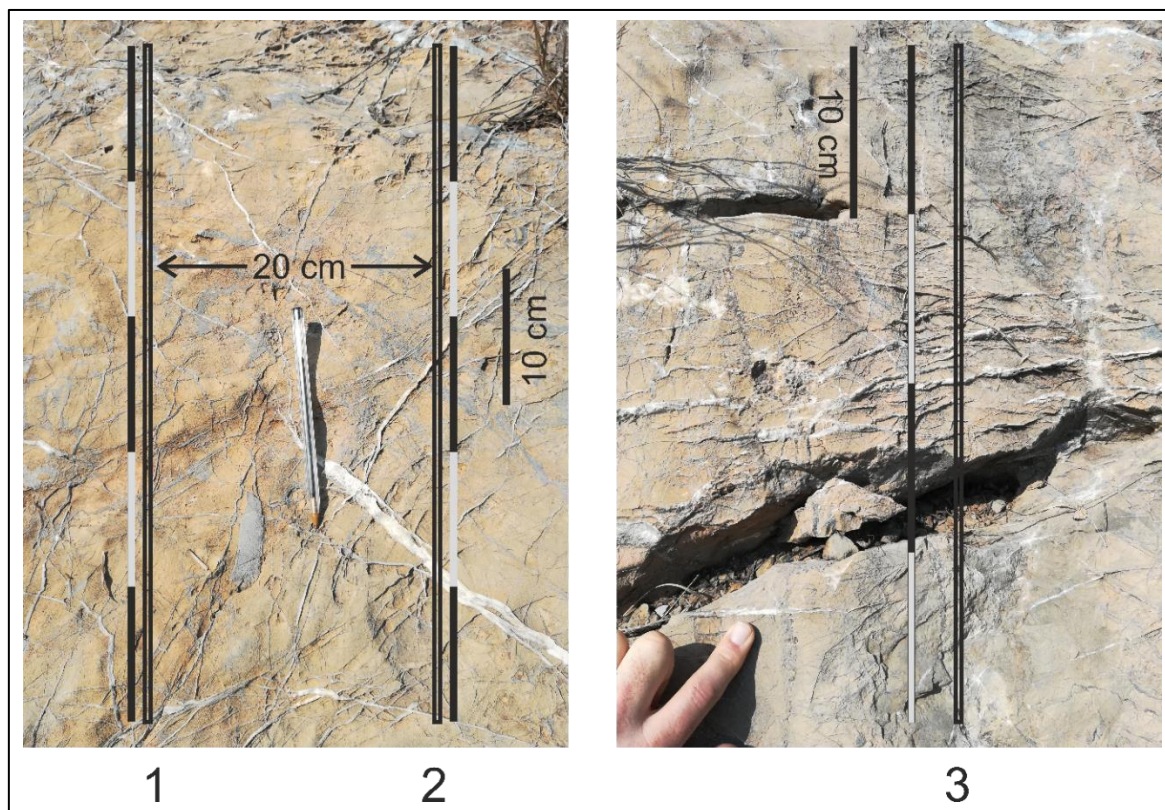


Figure 3.24: Measurement lines. Lines 1 and 2 are 50 cm long and line 3 is 40 cm long. The short lines are sufficient to characterise the spacing of the fractures.

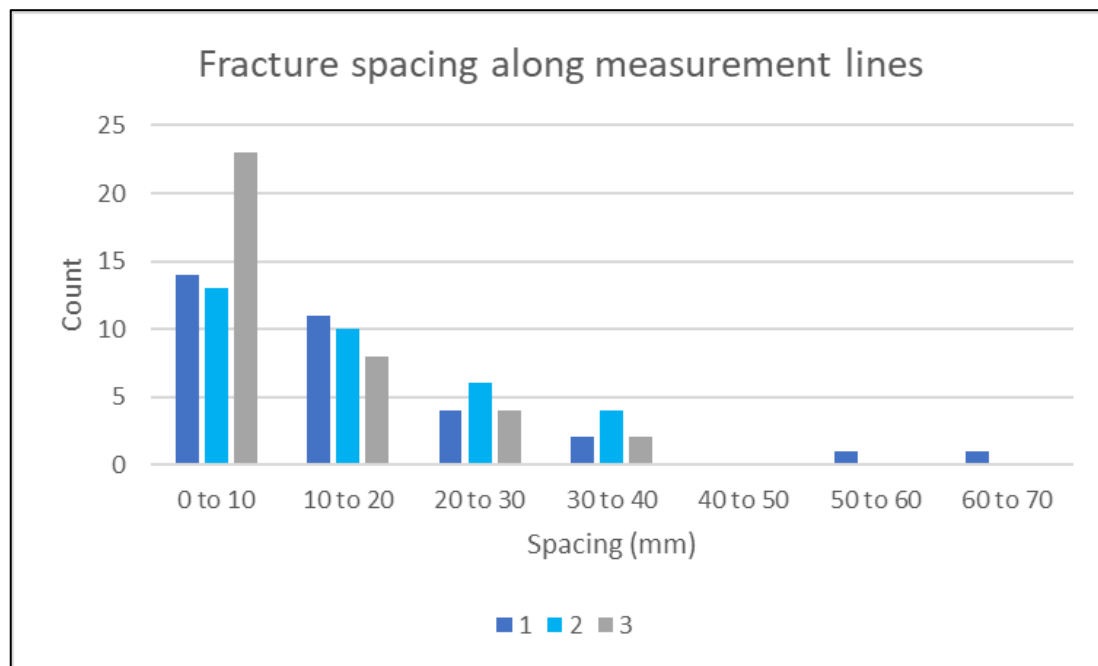


Figure 3.25: Distribution of fracture spacings on the three measurement lines shown in Figure 3.24.

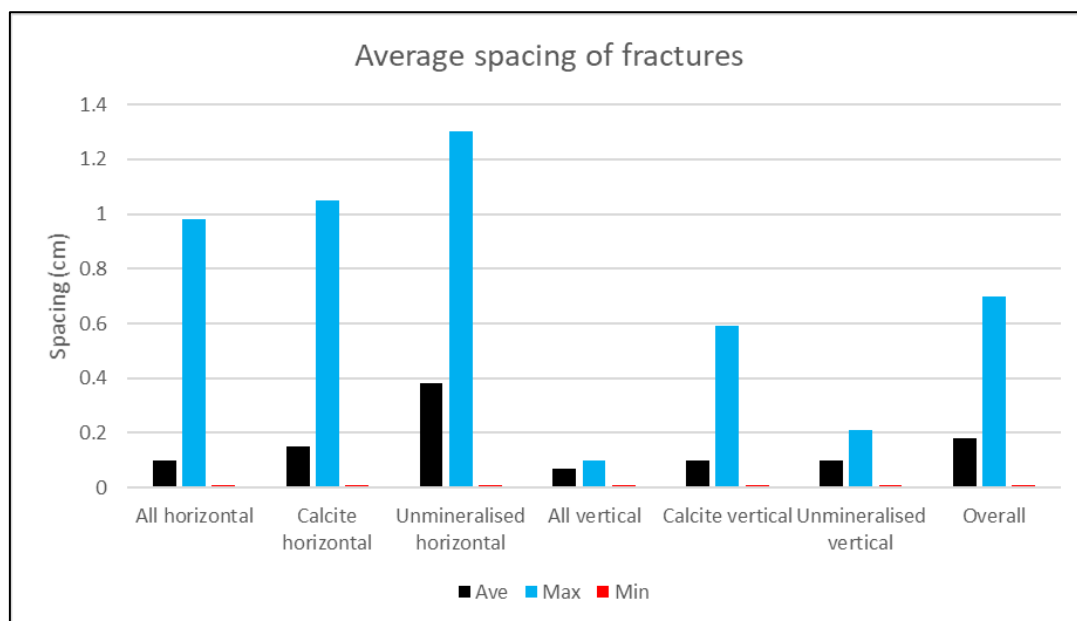


Figure 3.26: The fracture spacing characteristics of unmineralised and calcite mineralised fractures in horizontal and vertical measurement lines as well as the overall spacing of all fractures (Figure 3.24). The graph shows that the calcite fractures in the vertical measurement line (Figure 3.24 (3)) are the dominant type (most closely spaced).

More widely spread measurement lines can be utilised to examine the fracture characteristics of geological structures such as thrusts. For example, abundant fractures are identified from the hanging-wall up to the thrust contact and fewer fractures are present in the foot-wall (Figure 3.27).

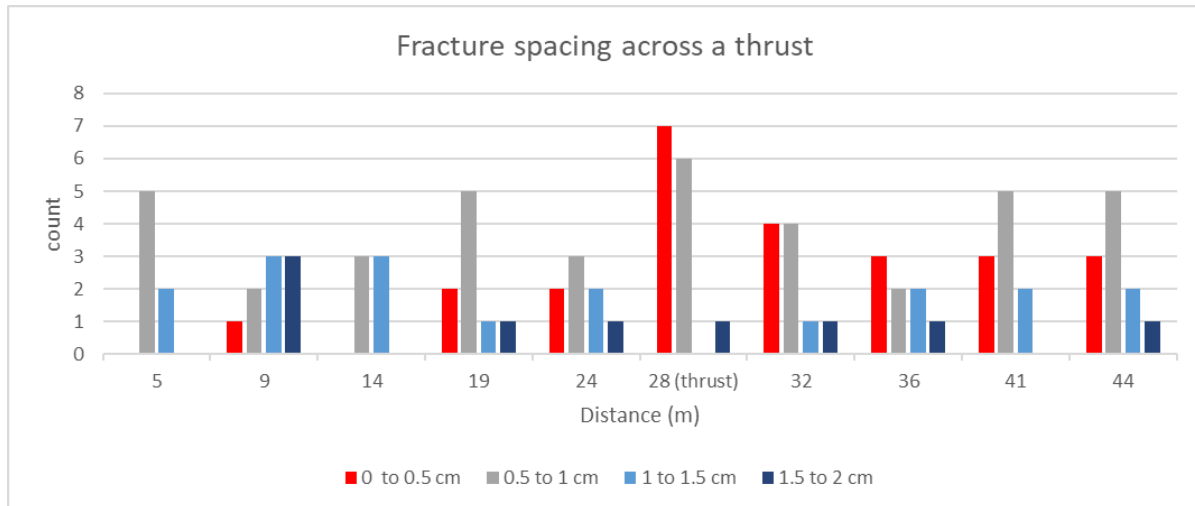


Figure 3.27: Fracture spacing from measurement circles across a thrust. The thrust hanging-wall is to the right with more fractures and the thrust foot-wall to the left with fewer fractures.

Thrust-fracture typically occurs on a shale horizon, due to stresses that result in Flexural Flow (FF). As such the relative abundances of the different topological node types are very different on the thrust bedding plane. The relative abundance of hanging-wall and foot-wall topologies is dependent on if they form closed folds or open structures. For example, in Figure 3.27, more topological nodes in the thrust hanging-wall. The relative abundance of the fractal dimension also increases when the strata become more compressed (in the centre of a synform) or dilated (in an antiform). The behaviour of different portions of a thrust can therefore be identified using the topological and fractal characteristics.

3.8 Measurement squares

At certain sites the fracture intensity was so high, it was decided to examine the fractures in detailed squares (Table 3.3). Two methods were used – firstly a 5 cm grid was placed over the area of interest and the various types of nodes (“e”, “x”, “y”, and “i”) were counted in each square. This data is not valid as the nodes used to determine the topological structures are based on measurements within circles. In addition, even if a relationship could be established between the different nodes, the “e” nodes would be double accounted for on any shared face.

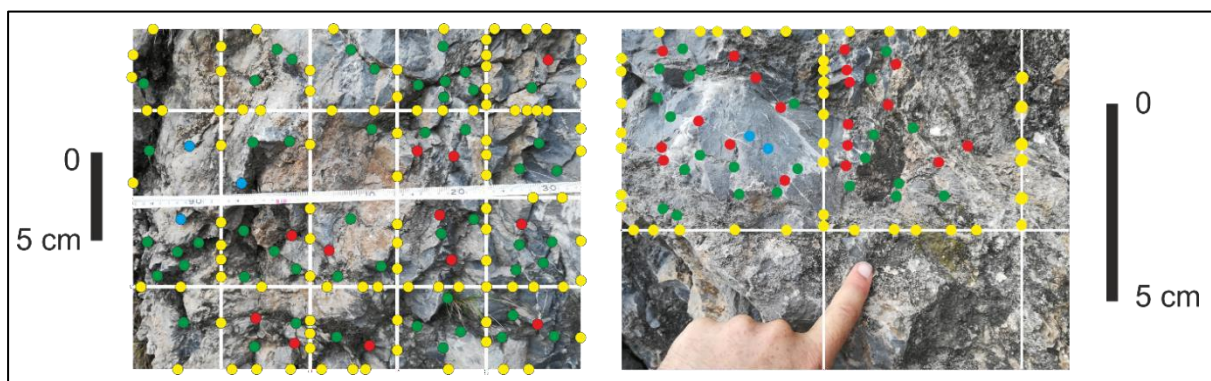


Figure 3. 28: Fracture intersection node types within 5 cm grid. This approach is not valid as topological analysis is based on circular sampling windows.

The second method was the examination of the specific characteristics of the fractures within 10 cm squares at a measurement site (Figure 3.29 and Figure 3.30). The detailed images all show a dominant top-right to bottom-left fracture set. However, the characteristics of the overall fracture pattern vary. Early large-scale tensile fractures Examples of secondary synchronous shear, in some cases clearly dextral are evident. In other areas tensile fractures are developed that are not related to the cross-cutting set are evident. Later fractures are also present. These different fractures suggest that the rock-mass has been subjected to several variations in applied stress. However, a single event, such as dextral shear can produce both the dominant cross-cutting fractures and dextral shears. As measurement circles consider all the different fracture types and ages, the detailed images are useful for understanding the combined effects of the structural events as indicated in Table 3. and Figure 3.21.

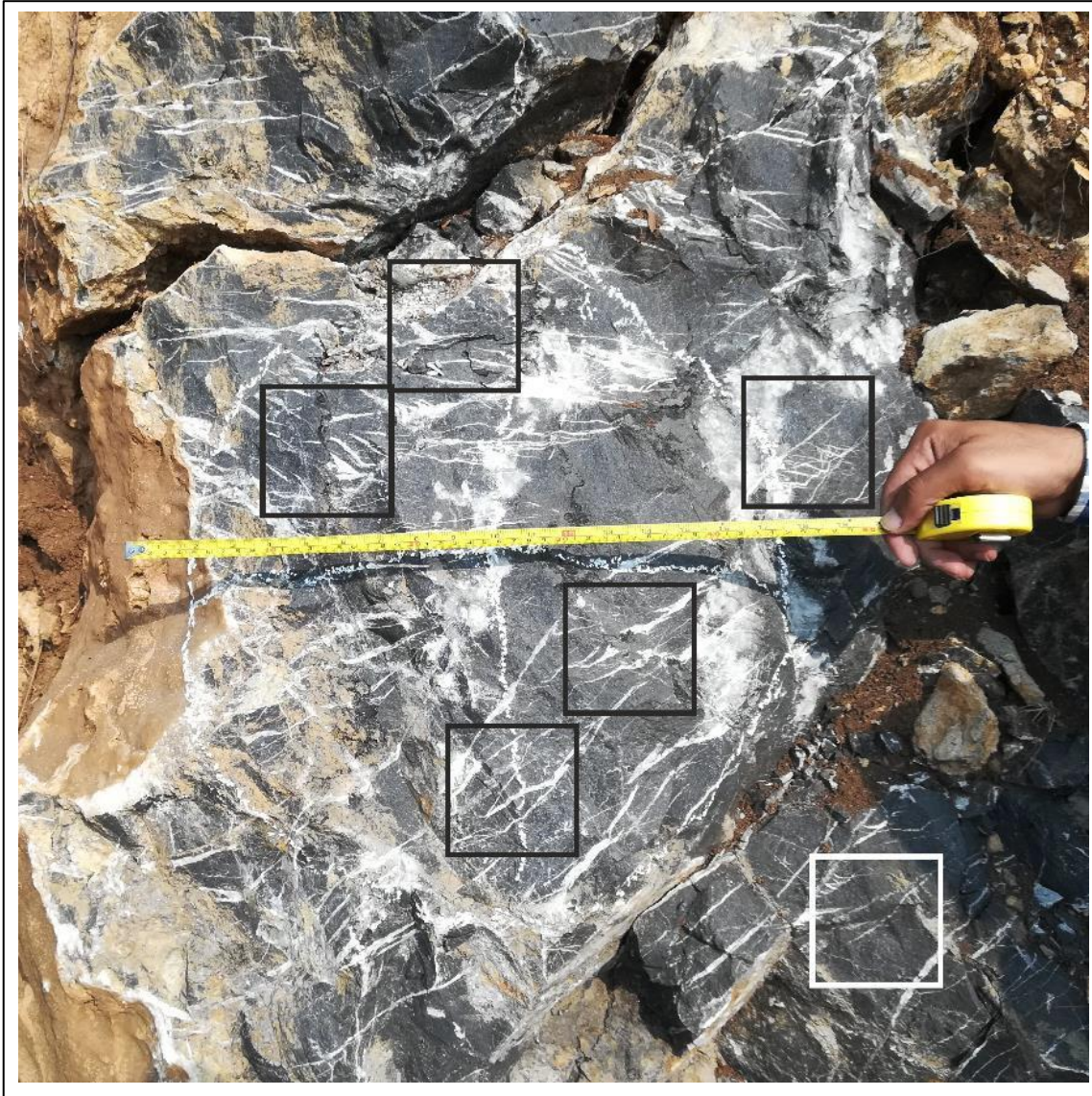


Figure 3.29: 10 cm squares for analysis of the fracture pattern. These are show in Figure 3.30.

The subparallel, closely-spaced en echelon veins are present as sheared calcite filled minor structural features in the limestone (Figure 3.29). These sheared tension fractures are oblique to the overall structural trend caused by the major stress orientation, σ_1 , in the thrust zone. The antithetic second-order fractures generally terminate against the en echelon sets of fractures at approximately 30 degrees.

The sets en echelon veins and the different groups of antithetic have similar relative orientations to each other suggesting that they are related to the thrusting

To what extent do you think the main fractures are all thrust-related (e.g. Fig. 3.29&3.30) – is there any evidence of earlier fracturing?

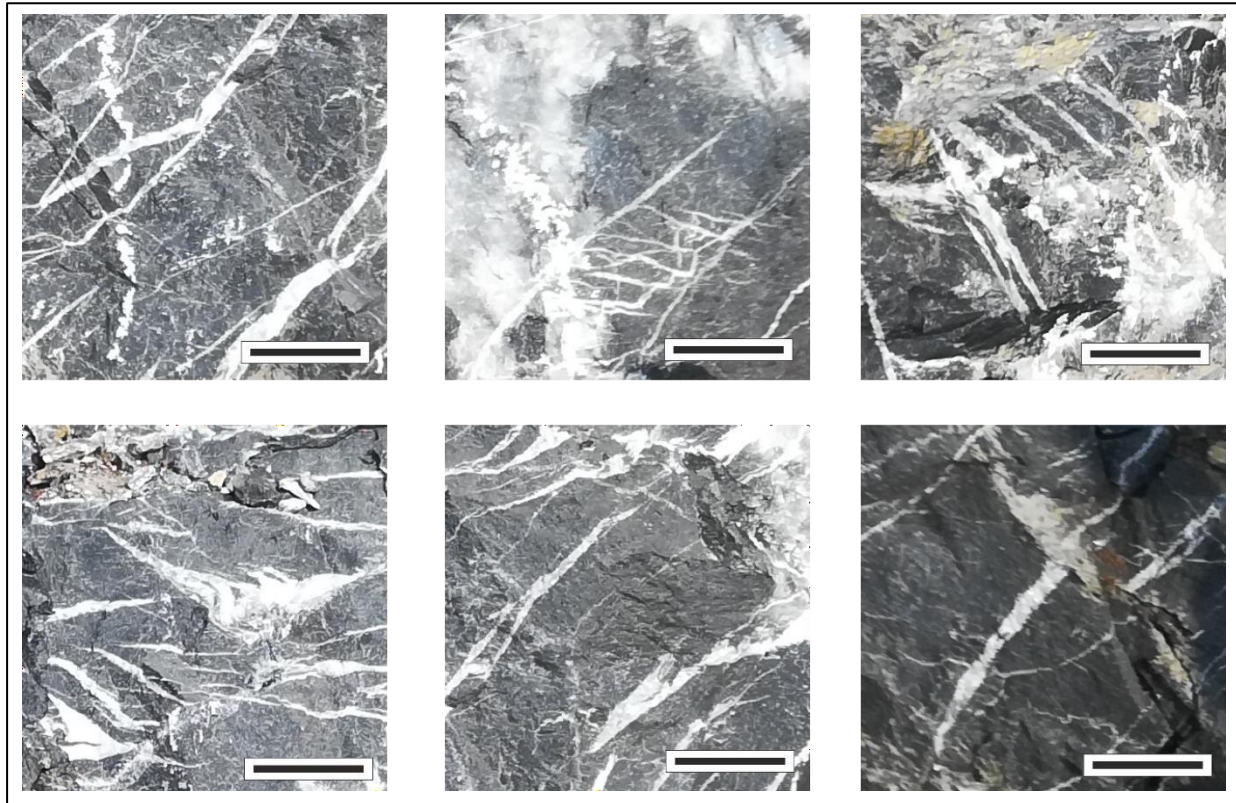


Figure 3.30: Detailed images of fracture patterns from Figure 3.29. Scale bar = 2 cm.

3.9 Fracture data capture in ArcMap

To capture fracture distribution and different types of data from ArcMap, a series of digital photographs of the exposures are combined using Microsoft Image Composite Editor (ICE). This software corrects for distortion and different orientations of the photographs by breaking them down into over 500 individual files and then re-combining them to produce a single uniform JPEG image.

This composited JPEG image is then imported and georeferenced in ArcMap. Standard world geographical co-ordinate systems are not used, both because the images are vertical and because the pictures are far too detailed. The geo-referencing is simply the x and y co-ordinates of the image. For example, the image of a thrust shown in Figure 3.31 is 18 m long and 2 m high, so the minimum and maximum co-ordinates are (0;0 m) and (18;2 m). The geo-referencing is relative to the size of the image, for example the exposure shown in Figure 3.34 is 8 m long and 2 m high and hence the

minimum and maximum co-ordinates are (0;0 m) and (8;2 m). In Figure 3.38, the fracture traces in four 5 cm diameter measurement circles recorded on a geo-spatial grid with the co-ordinates (0; 0 cm) and (15; 11 cm).

The JPEG image is then used to digitise the fractures. ArcMap can then geostatistically represent attributes such as the spatial distribution of features such as the length of fractures or fracture density. This makes it possible to examine facts such the length and density of fractures the in different orientations across a thrust (Figure 3.32). By creating polygons within the co-ordinate system, the fracture data can be sub-divide the into different areas which for example allows the quantification of the fracture characteristics across a thrust (Figure 3.32 and Figure 3.33).

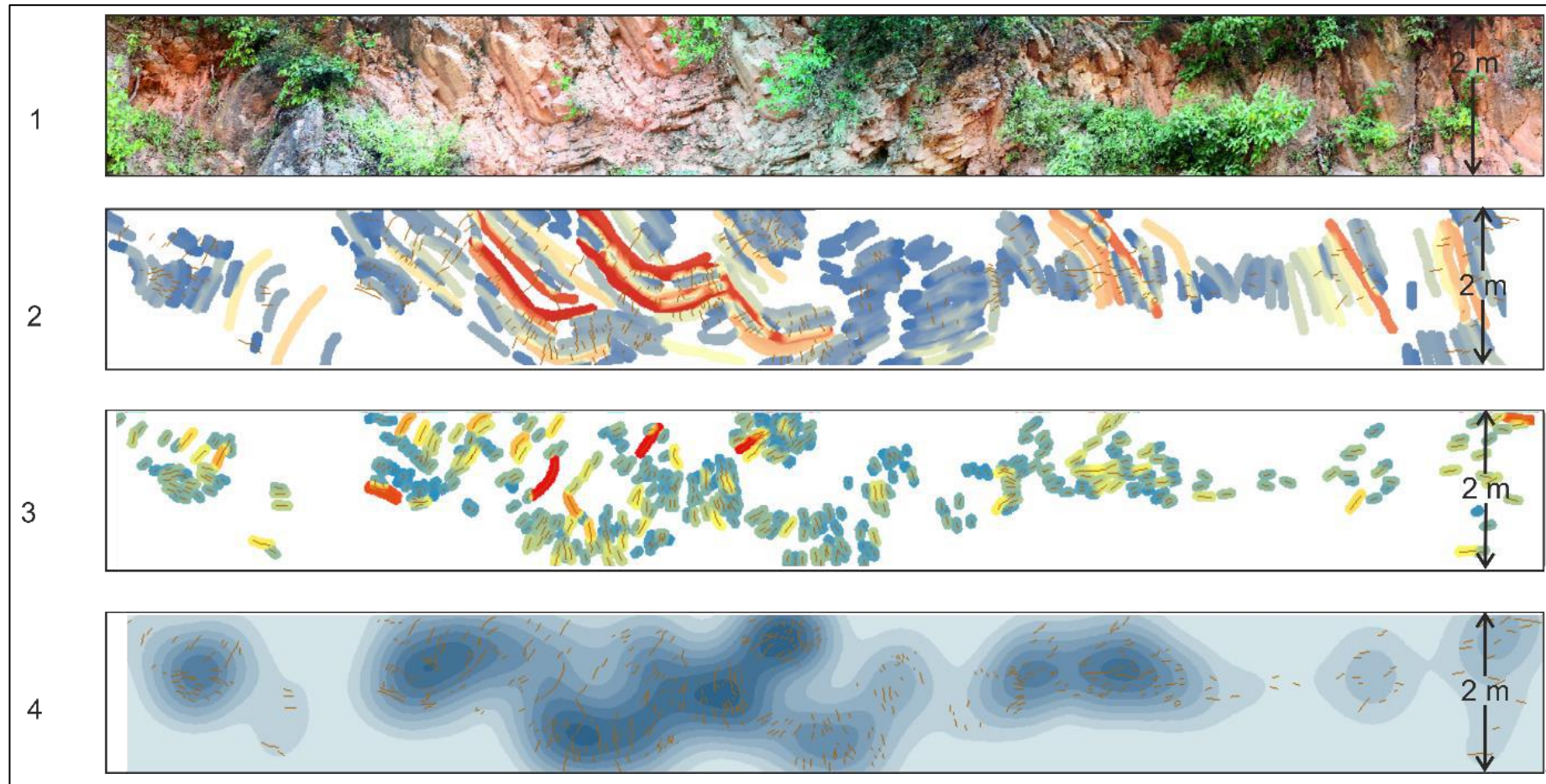


Figure 3.31: Data-capture methods using ArcMap to define the spatial distribution of fractures in an 18 m * 2 m of a thrust in the Talhaar region. The images are based on the geostatistical distribution of the fracture data.

(1) photo-mosaic of 22 images created with ICE, (2) spatial distribution of length of bedding parallel and (3) spatial distribution of lengths of bedding orthogonal fracture (in both cases warmer colours represent longer fractures), (4) fracture density – darker shades represent higher density.

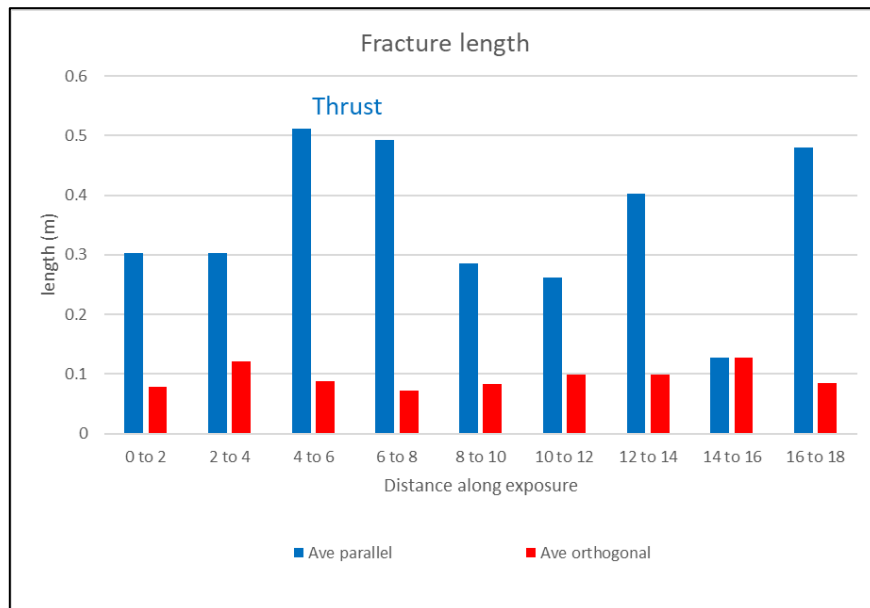


Figure 3.32: Variations in fracture length along the exposure derived from spatial distribution of digitised fractures. The bedding parallel fractures extend towards the thrust and are longer than the orthogonal fractures as is expected in fore-thrusts.

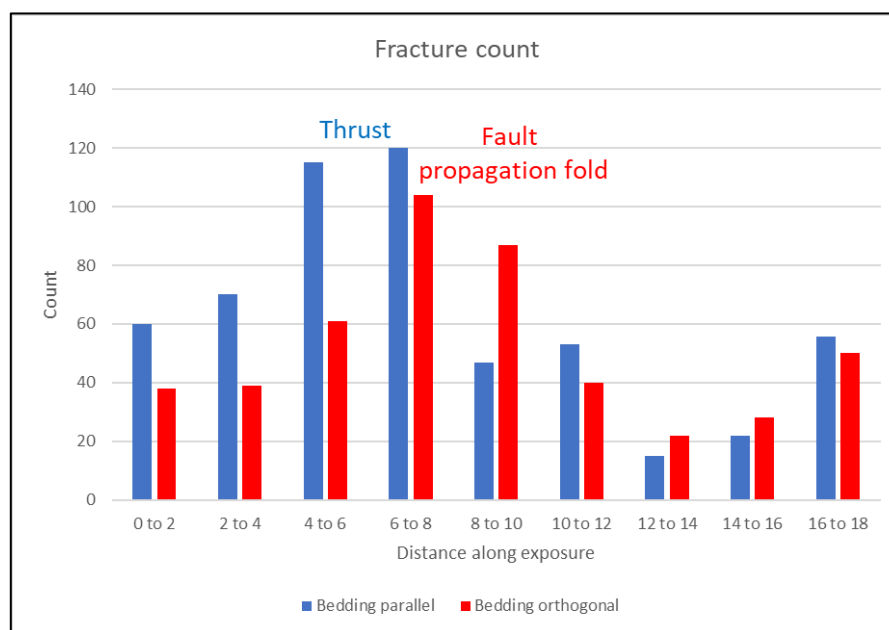


Figure 3.33: Variations in fracture abundance along the exposure. The maximum number of bedding parallel fractures is present in the thrust (4 to 8 m) and the maximum number of bedding orthogonal fractures is in the fault propagation fold (6 to 10 m). See Figure 3.31 for the spatial orientation of the fractures.

The distribution of different fracture groups can also be defined in ArcMap. This based on the box-density function or total length of an object (often roads when examining satellite images, but here fractures) in ArcMap. When all the fractures are considered together at an outcrop, the fracture pattern may be dominated by steeply dipping fractures (Figure 3.34). If different sets are extracted, the specific characteristics become apparent. Figure 3.35 to Figure 3.37 show the cluster of fractures at the core of the overturned anticline and the arcing of the bedding parallel over these fractures.

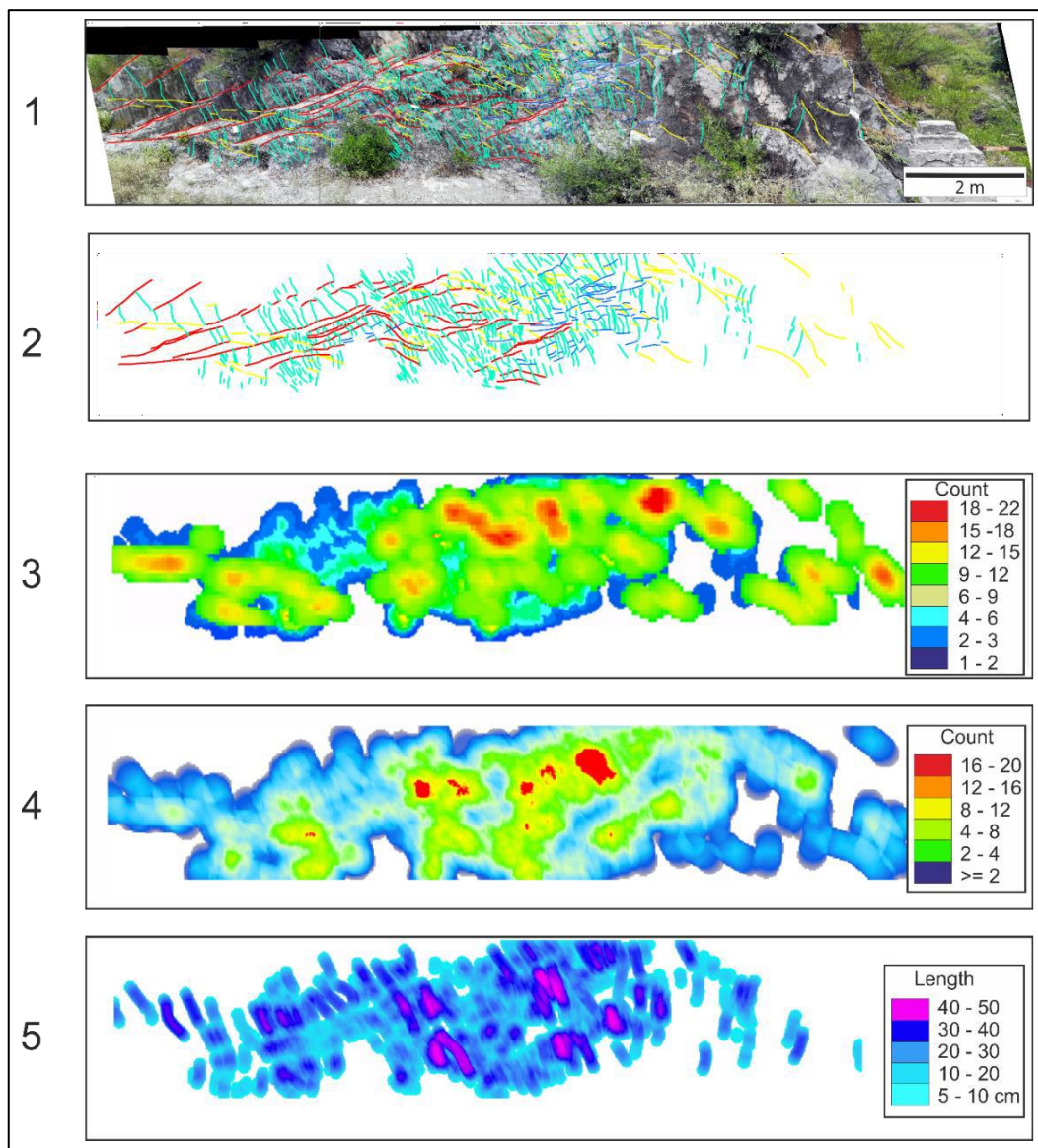


Figure 3.34: Data-capture methods and types produced using ArcMap to define fracture density (linear and box) and fracture length. (1) photo-mosaic created in ICE with fractures traced over it, (2) traced fractures, (3) box-density of all fractures, based on a 50 cm sampling window, (4) linear density of all fractures, based on a 20 cm sampling window, (5) fracture length.

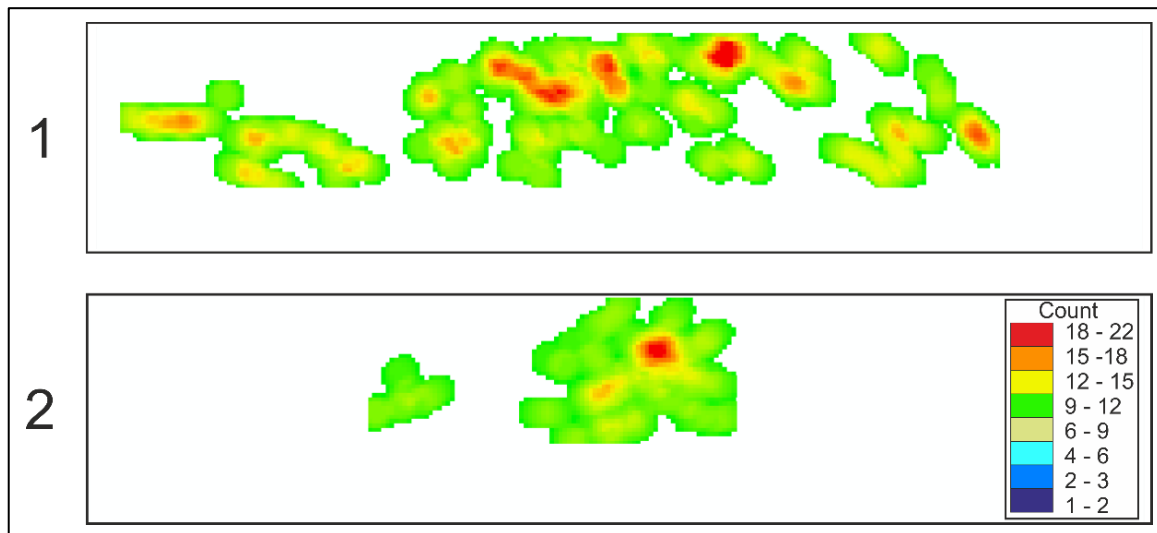


Figure 3.35: Box-density plot of fractures across the same area as Figure 3.34 – (1) bedding parallel fractures across exposure, (2) oblique fractures, principally in fracture zone at the centre of the overturned anticline. The ArcMap data extends to the traced fractures in Figure 3.34 (2).

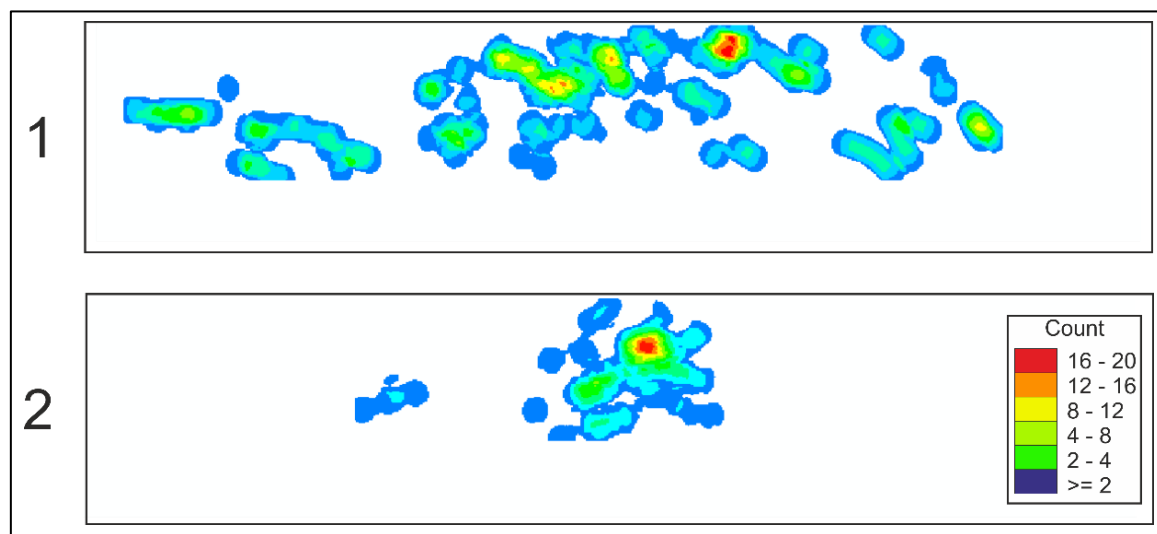


Figure 3.36: Linear-density plot of fractures across the same area as Figure 3.34 – (1) bedding parallel fractures across exposure, (2) oblique fractures, principally in fracture zone at the centre of the overturned anticline. The ArcMap data extends to the traced fractures in Figure 3.34 (2)

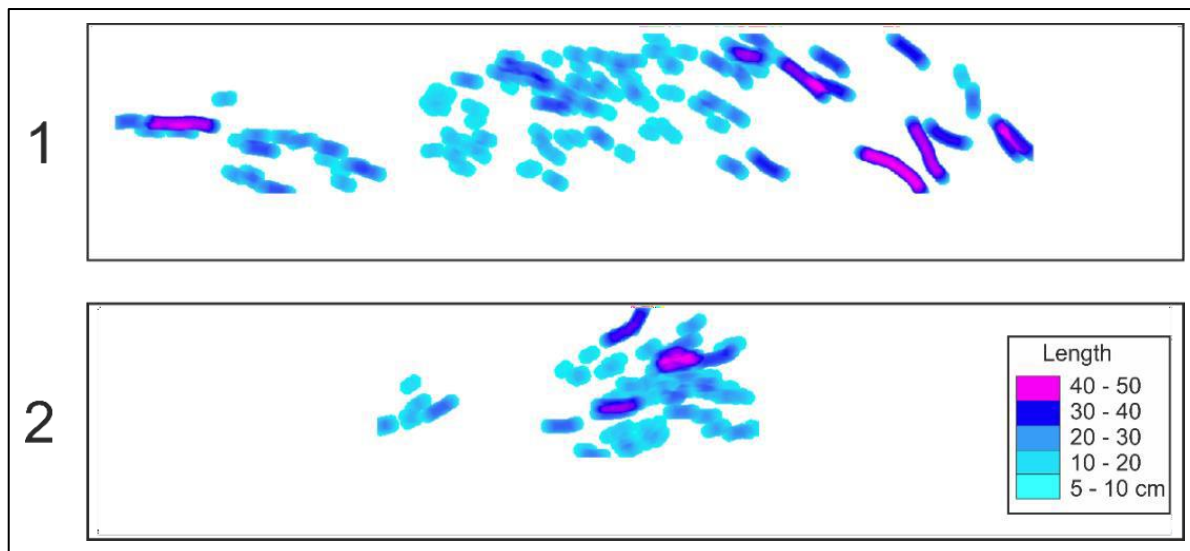


Figure 3.37: Fracture lengths across the same area as Figure 3.34 – (1) bedding parallel fractures across exposure, (2) oblique fractures, principally in fracture zone at the centre of the overturned anticline. The ArcMap data extends to the traced fractures in Figure 3.34 (2).

As it is impractical to measure fracture lengths in highly fractured rock, such as that shown in Figure 3.38, it was decided to digitise the fractures in the four 5 cm wide circles in ArcMap and use the data to define fracture length distribution.

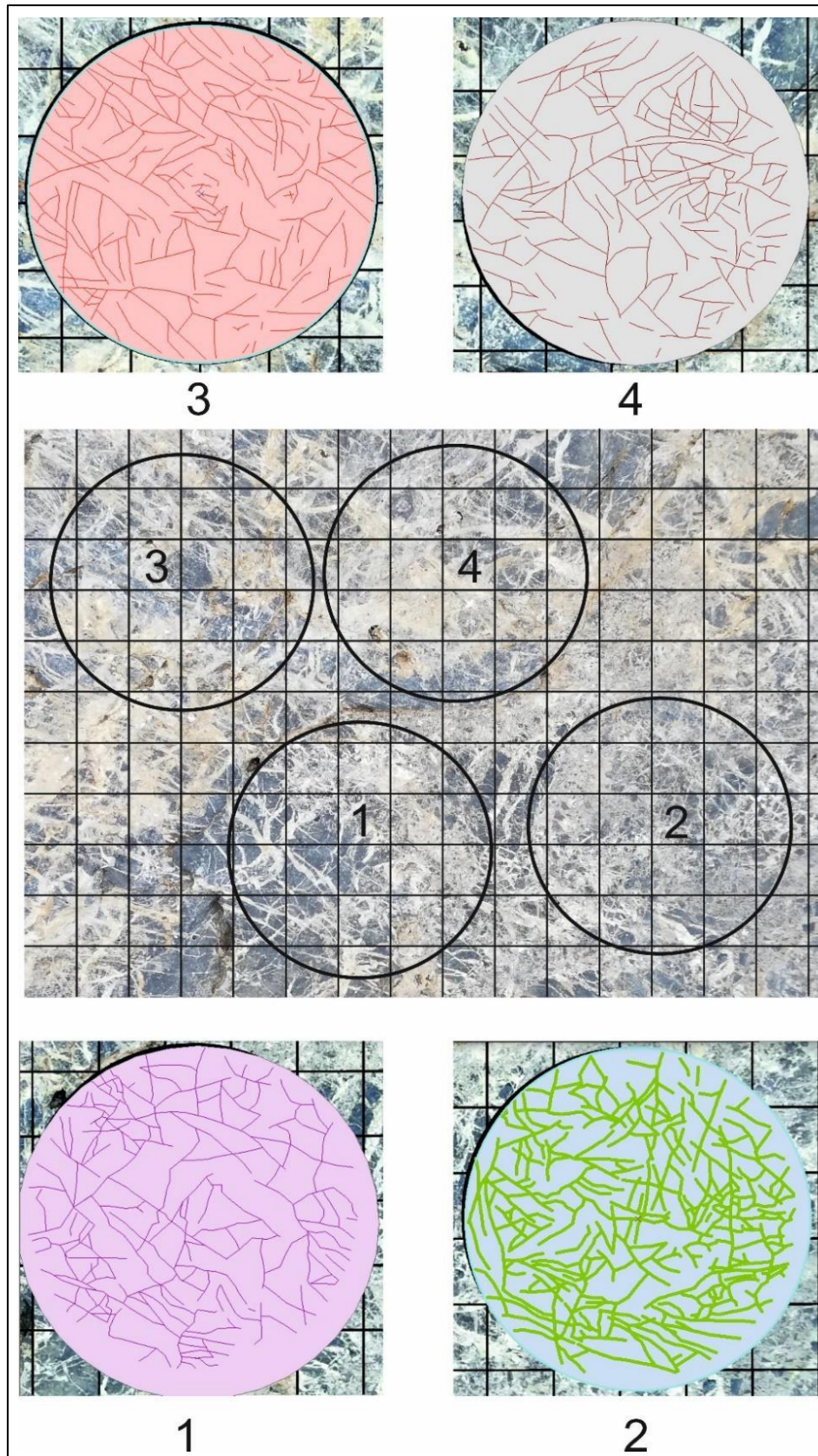


Figure 3.38: Digitised fractures in 5 cm measurement circles. The fracture length distribution in this highly fractured rock has been established by digitising the fractures and calculating their lengths in ArcMap.

The skewed distribution of the fracture lengths derived from the ArcMap data shows that the majority of the fractures are less than 1 cm and that the different measurement circles show similar distribution characteristics (Figure 3.39). This allows a more robust characterisation of the fracture pattern within the rock-mass.

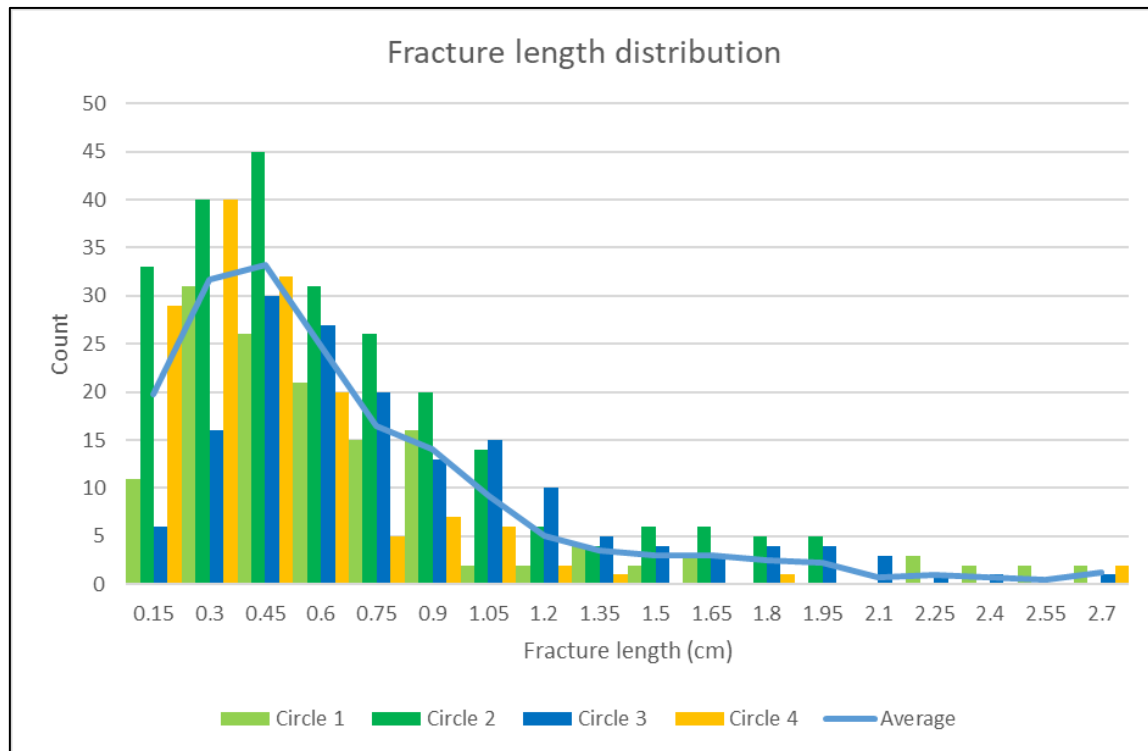


Figure 3.39: Fracture length distribution within the 5 cm diameter circles digitised in ArcMap.

3.10 Electronic data

The number of boxes containing fractures at different grid sizes for fractal dimensions ((Figure 3.40) in each measurement circle are captured in Excel spreadsheets for the various field regions. A standardised table with automatic calculation of all the topological parameters as determined by the number of the different types of nodes and of the fractal dimension from the slope of the log-log plot was developed in Excel (Figure 3.40). Different tabs were created for this data at each measurement

site within the field region, as well as further tabs for different types of data including measurement lines and ArcMap data (Figure 3.40).

	1	2	3	4	
Intersections	e	19	17	19	
	x	0	6	7	
	y	16	25	20	
	i	21	17	15	
	Total	56	63	65	61
Topology	Connectivity	1.73	2.95	3.09	
	Fracture Intensity	10	9	10	
	Fracture density	5.9	7.2	6.7	
	Mean trace length	0.5	0.4	0.5	
	No. lines	19	21	18	
Box size	No. tips	37	42	35	
	No. branches	35	58	52	
	5	265	310	320	
	10	81	80	89	
	20	24	24	25	
Log values	25	16	16	16	
	50	4	4	4	
	100	1	1	1	
	D	1.86	1.83	1.90	1.92
Log values	-0.698970004	2.423245874	-0.698970004	2.389166084	
	-1	1.908485019	-1	1.86923172	
	-1.301029996	1.380211242	-1.301029996	1.361727836	
	-1.397940009	1.204119983	-1.397940009	1.204119983	
	-1.698970004	0.602059991	-1.698970004	0.602059991	
	-2	0	-2	0	

Figure 3.40: Data spreadsheet for the Talhaar field region (see file name at top of image). Tables for the various measurement circles at each site (circles 1 to 4, at Site 1 shown) are created. The topological parameters (blue text) and fractal dimension (green text) are automatically calculated. Tabs for each site were also created (see bottom of image)

The data from all the measurement circles in the various circles in different sites was gathered together for analysis of the characteristics of the sites and the region (the “all” tab in Figure 3.41). The determination of the averages of the numbers of nodes (shown in black Figure 3.41), the different topological characteristics (shown in blue in Figure 3.41) and the average fractal dimension (shown in green in Figure 3.41) are vital for the characterisation of the different characteristics of the rock-mass

utilising the methods applied in this research.

Site	Circle	e	x	y	i	Total	Connectivity	Fracture intensity	Fracture density	Mean trace length	MTL (cm)	No. lines	No. tips	No. branches	Fractal dimension
1	1	19	0	16	21	56	1.73	9.50	5.89	0.51	51.4	19	37	35	1.86
	2	18	4	24	17	63	2.73	9.00	7.16	0.40	40.0	21	41	53	1.83
	3	17	6	25	17	65	2.95	8.50	7.64	0.35	35.4	21	42	58	1.90
	4	19	7	20	15	61	3.09	9.50	6.68	0.45	45.2	18	35	52	1.90
	Ave	18	4	21	18	61	2.62	9.13	6.94	0.43	43.0	19	39	49	1.87
	SD	1	3	4	2	3	0.53	0.41	0.65	0.06	5.9	1	3	9	0.03
2	1	24	28	42	14	108	5.00	12.00	13.37	0.29	28.6	28	56	126	1.95
	2	26	14	48	24	112	3.44	13.00	13.69	0.30	30.2	36	72	112	1.92
	3	26	25	29	14	94	5.02	13.00	10.82	0.38	38.2	22	43	101	1.96
	4	22	27	47	9	105	5.29	11.00	13.21	0.27	26.5	28	56	129	1.98
	Ave	25	24	42	15	105	4.69	12.25	12.77	0.31	30.89	28	57	117	1.95
	SD	2	6	8	5	7	0.73	0.83	1.14	0.04	4.44	5	10	11	0.02
3	1	41	26	77	2	146	5.22	20.50	16.71	0.39	39.0	40	79	169	1.99
	2	36	17	67	3	123	4.80	18.00	13.85	0.41	41.4	35	70	136	1.97
	3	37	27	67	4	135	5.30	18.50	15.60	0.38	37.8	36	71	157	1.96
	Ave	38	23	70	3	135	5.10	19.00	15.38	0.39	39.4	37	73	154	1.97
	SD	2	4	5	1	9	0.22	1.08	1.18	0.01	1.5	2	4	13	0.01
	4	1	42	20	51	0	113	5.57	21.00	11.30	0.59	59.2	26	51	117
2		31	16	52	9	108	4.46	15.50	12.25	0.40	40.3	31	61	115	1.97
3		31	19	46	0	96	5.65	15.50	10.35	0.48	47.7	23	46	107	1.96
4		33	21	39	7	100	5.22	16.50	10.66	0.49	49.3	23	46	104	1.99
Ave		34	19	47	4	104	5.22	17.13	11.14	0.49	49.09	26	51	111	1.98
SD		5	2	5	4	7	0.47	2.27	0.73	0.07	6.73	3	6	5	0.01
5	1	41	61	119	25	246	5.00	20.50	32.63	0.20	20.00	72	144	313	1.99
	2	76	233	282	38	629	6.44	38.00	88.01	0.49	49.25	160	320	908	1.99
	Ave	59	147	201	32	438	5.72	29.25	60.32	0.35	34.63	116	232	611	1.99
	SD	18	86	82	7	192	0.72	8.75	27.69	0.15	14.63	44	88	298	0.00
	1	28	23	66	27	144	3.83	14.00	18.46	0.24	24.14	47	93	159	1.92
	2	33	81	124	80	318	4.02	16.50	45.36	0.12	11.58	102	204	388	1.99
3	30	34	89	68	221	3.13	15.00	30.40	0.16	15.71	79	157	236	1.96	
Ave	30	46	93	58	228	3.66	15.17	31.41	0.17	17.14	76	151	261	1.96	
SD	2	25	24	23	71	0.38	1.03	11.00	0.05	5.23	23	45	95	0.03	
7	1	22	12	65	14	113	3.90	11.00	14.48	0.24	24.2	40	79	129	1.91
	2	22	23	49	4	98	5.43	11.00	12.10	0.29	28.9	27	53	122	1.93
	3	27	19	67	7	120	4.65	13.50	14.80	0.29	29.0	37	74	142	1.90
	4	27	10	54	11	102	3.94	13.50	11.94	0.36	36.0	33	65	107	1.94
	5	29	19	64	16	128	4.15	14.50	15.76	0.29	29.3	40	80	142	1.95
	6	28	14	42	6	90	4.67	14.00	9.87	0.45	45.2	24	48	94	1.92
	7	28	20	54	7	109	4.85	14.00	12.89	0.35	34.6	31	61	125	1.99
	8	28	15	42	17	102	3.86	14.00	11.78	0.38	37.8	30	59	102	1.99
	9	18	0	17	11	46	2.43	9.00	4.46	0.64	64.3	14	28	31	1.95
	10	19	6	35	10	70	3.64	9.50	8.12	0.37	37.3	23	45	70	1.63

Figure 3.41: All data from the various tables in each tab (that is circles at each site) in a field area. Averages and standard deviation for each site are determined as these are used in the analysis of the topological and fractal characteristics as well as variations in the node distributions.

Averages and standard deviations of all the data were determined. All the distributions ranging from circles to sites, to field areas as well as the different rock types and structural features were analysed to determine any trends. Analyses included the relative distribution of nodes (Figure 3.42) and hence the topological characteristics (Figure 3.43).

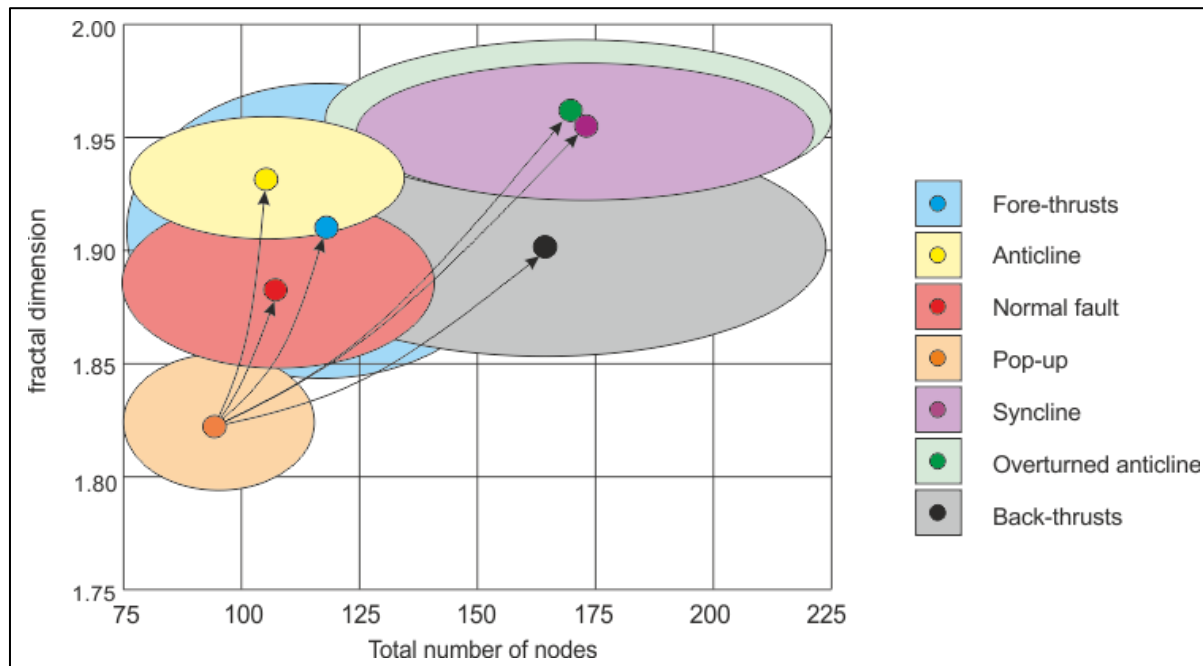


Figure 3.42: Average (solid points) and a single standard deviation (shaded ellipse) of the total number of nodes and fractal dimensions of all circles for each structural feature. The orange point indicates the average value of circles in the pop-up zones. Arrows show the variations from this weakly deformed site relative other structures. The variations in the number of different node types result in different topological characteristics. The figure illustrates the spatial distribution of fractures (fractal dimension) and the fracture intersections (number of nodes) allowing different fracture patterns to be defined (Grodner et al., 2021).

Pop-up features have the lowest total number of nodes and lowest fractal dimension which indicates that they are the least structurally disturbed in the brittle near-surface zone of a thrust-fold belt (Figure 3.42). Normal faults, fore-thrusts and anticlines show an increased fractal dimension, but the total number of nodes remain relatively low, between 80 and 120 (Figure 3.42). The fractal dimensions vary between 1.88 and 1.93 on average but extend from 1.84 to 1.97 (a single standard deviation). This indicates that these structural features contain fewer intersecting fractures, but a greater number of fractures overall. Back-thrusts have a large number of nodes, which is caused by more fracture intersections due to the restricted space in which movement can occur. In contrast to this, both overturned anticlines and synclines have a high number of nodes and high fractal dimension to the

dominant compressive forces crushing the rock mass and increasing the number of fractures.

The analysis of the different structural domains show that pop-up structures have the lowest fractal dimension and also generally the lowest topological value for the fracture density, connectivity, fracture intensity, and mean trace length.

Fracture density represents the number of fractures per unit area. As a fracture is terminated inside a measurement circle which provides the density. The highly compressive stresses within a back-thrust results in the high topological values of this structure. Fracture connectivity is the ratio of the fracture branches formed due to the intersections of the different nodes. Back-thrusts and synclines have the highest fracture connectivity due to the highest compressive stresses. Fracture intensity is a comparative measure of the number of edge-nodes within a measurement circle which indicates how extensive the fractures are. The high values of connectivity and fracture intensity in overturned anticlines and synclines is due to the widespread fracturing of these structures caused by the tight confinement of the folded features. Likewise, the fracture intensity is highest in synclines, back-thrusts, and overturned anticlines. In both of these graphs (Figure 3.43 connectivity and fracture intensity) it is obvious that the overturned anticlines and synclines have the highest fractal dimension, indicating a high number of fractures within the rockmass. Mean trace length represents the average trace length of the fracture and hence the faults and fore-thrusts have longer fracture lengths, as a result of the focus of shear stresses in features such as a fault zone or along shale layers in a fore-thrust.

The characteristics of the rock-mass can be analysed and compared with different structural domains as these have specific features and the deformation exerted deform the rock strongly (Figure 3.43).

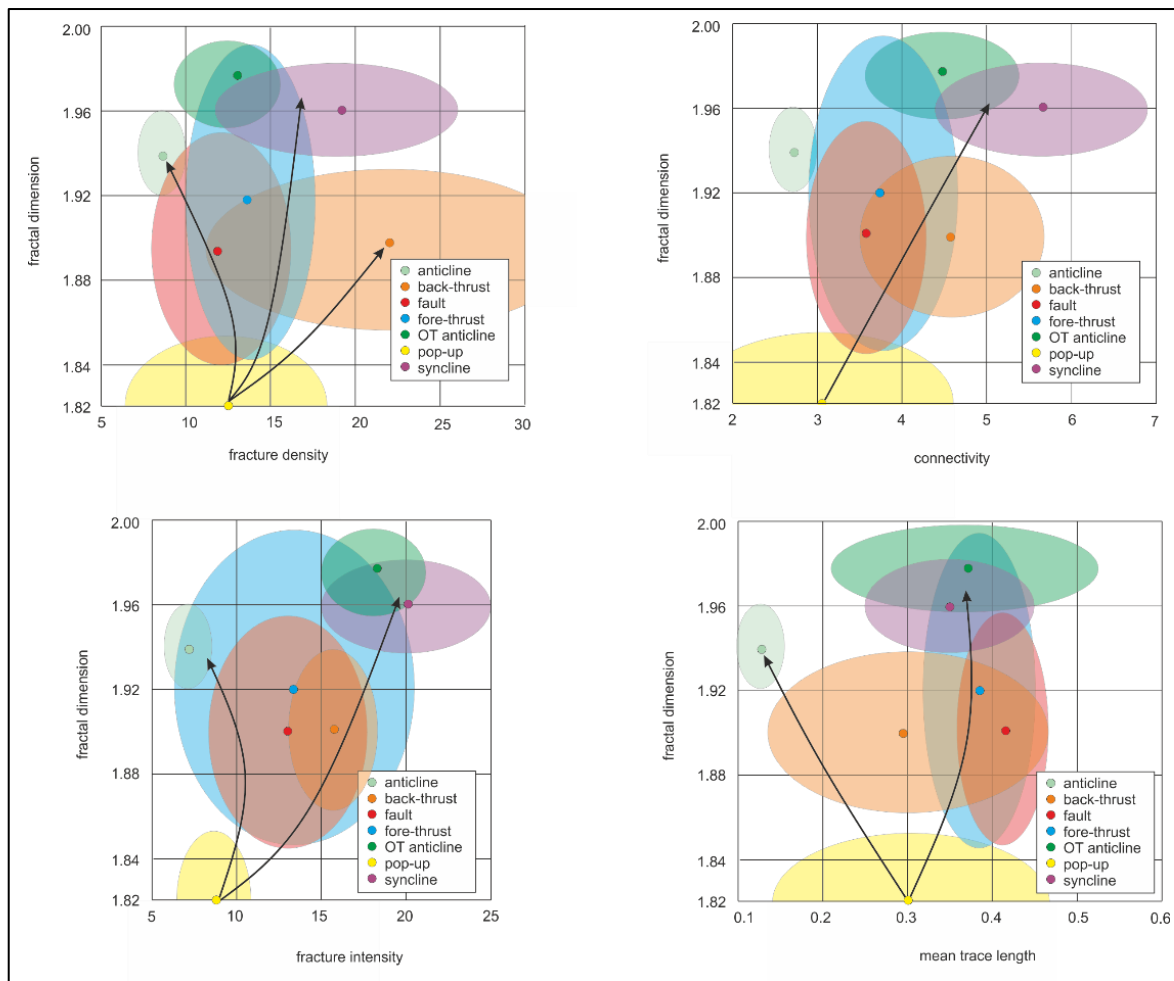


Figure 3.43: Topological characteristics of various structural domains. Solid circles represent the average values of the structures and the shaded ellipse, one standard deviation. The arrows indicate the trend structural features within the fractal dimensions and the different topological features.

The rock compositions are divided into groups based on the relative percent of clastic mudstone (due to the abundance of micrite and microspar). These are:

- Lime mudstone
- Wackestone
- Wackestone and minor shale
- Wackestone and shale
- Interbedded wackestone and shale, and
- Shale

The topological distribution of the rock types is shown in Figure 3.44 which also includes the trends of the fracture patterns of the different structural features (from Figure 3.43) which have less variability than those of the different rock types which show greater range of values. Unlike the structures, there is a consistent low number of nodes, the topological characteristics and fractal dimensions – that is a pop-up structure. In the different topological graphs, the only constant is the high fractal dimension of the lime muds, and the slightly lower fractal dimension of combined mudstone and wackestone. Different fracture mechanics are present here with the high number of fractures in the lime muds being caused by TL stresses being applied and FF stresses being applied in the combined mudstone and wackestone. Therefore, the orientation and strength of the stresses cannot be compared. The other three rock types, wackestone and mudstone, wackestone and minor mudstone, and wackestone do not display consistent trends with regards the topological characteristics of fracture density, connectivity, fracture density, and mean trace length. These can therefore also not be compared (Figure 3.44).

If one considers the various rock types and their topology very few structural features have similar characteristics. Wackestone and mudstone only have similar fracture intensities and mean trace length in back-thrusts, as well as same types of fracture densities and connectivity of overturned anticlines. Lime muds have similar values fracture densities and fracture intensities for synclines. These are the only meaningful correlations between the rock types and structures. There are unfortunately no strong relationships between the rock types and the structural features. Mathematically or statistically it difficult to define trends between the rock types and the structural features.

It indicates that the physical characteristics and processes that form the fracture patterns in the rock types and structures are different. The reasons for this are examined in detail in Chapter 5 (Interpretations) and Chapter 6 (Discussion).

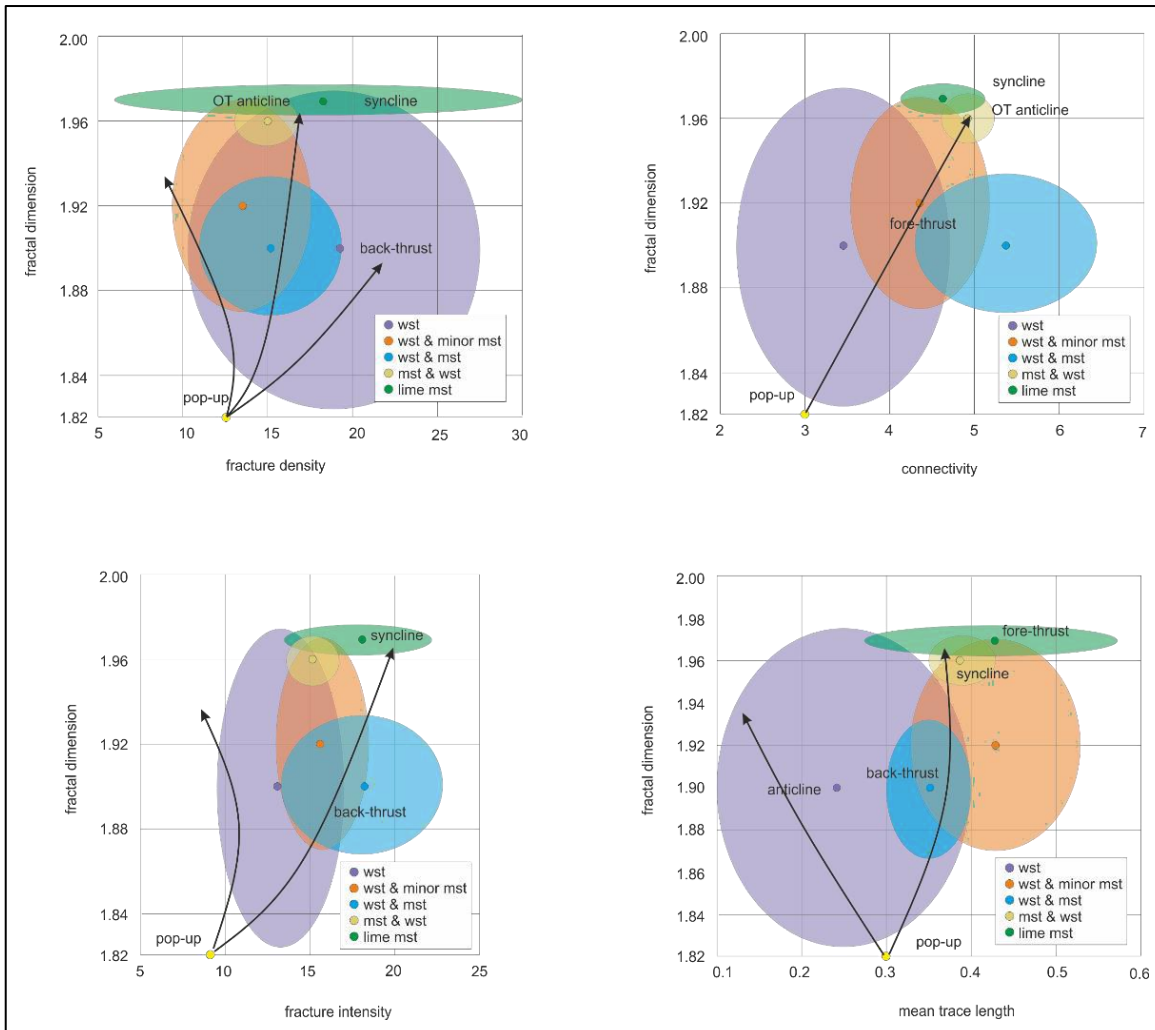


Figure 3.44: Topological characteristics of the various rock types. Solid circles represent the average values of the structures and the shaded ellipse, one standard deviation. The arrows indicate the trend of the structural features within the fractal dimensions and the different topological features. The structures are stronger, more focussed features where-as the standard deviations show a wide variance.

3.11 Summary of methodology

Mapping transects of 42 sites have been measured, approximately perpendicular to the major north-east structural the trends of the folds and thrusts in the limestones of the hanging-wall of the MBT. Topological and fractal data have been collected from all the sites. Topology defines how parts of a system are connected (fractures). Intersections of the fractures are divided into “e” (edge),

“x”(crossing), “y” (intersecting) and “i” (terminating) nodes. The proportions of the various nodes determine the topological characteristics. Importantly, all the nodes and fractures are considered together within a measurement site to ensure the entire structural history is considered. Topological parameters are fracture density, connectivity, fracture density, and mean trace length. Fractals are determined by measuring the number of boxes containing a fracture at various scales. The fractal dimension can be derived from the slope of the trend-line in a log-log plot of the inverse of the box size against the number of boxes containing fracture traces. ArcMap has been used to digitise outcrops and small portions of the rock using photo-mosaics with fractures traced over it. This defines fracture density (linear and box) and fracture length. Other techniques that were used included line mapping, circular mapping, and square mapping. The distribution of nodes and various topological types are cross-plotted against the fractal dimensions of the different structural features. The structural domains have specific abundances of different nodes (and hence topology), as well variations in the fractal dimensions. The pop-up structures have the lowest fractal dimension and generally the lowest topological values. Anticlines have lower topological values and higher fractal dimensions and greater fracture lengths. The rock compositions are divided into groups based on the relative percent of clastic mudstone. There are no clear separations between the cross-plots of topological characteristics and fractal dimensions of the various limestones, due to the abundance of micrite and microspar. Unfortunately, as a result of this, no relationships between the topological characteristics of rock types and structures can be determined.

4. Field Mapping

This chapter presents the field-mapping data, including lithological and structural characteristics. Measurements of the topological and fractal characteristics utilising the methodology described in Chapter 3 are defined for the various sites in the different field regions.

4.1. Overview of the geology of the field regions

A study area consisting of seven field regions has been evaluated in the Himalayas north of Islamabad, Pakistan (Figure 4.1). The regions are between 5 km west and 45 km northeast of the centre of Islamabad.

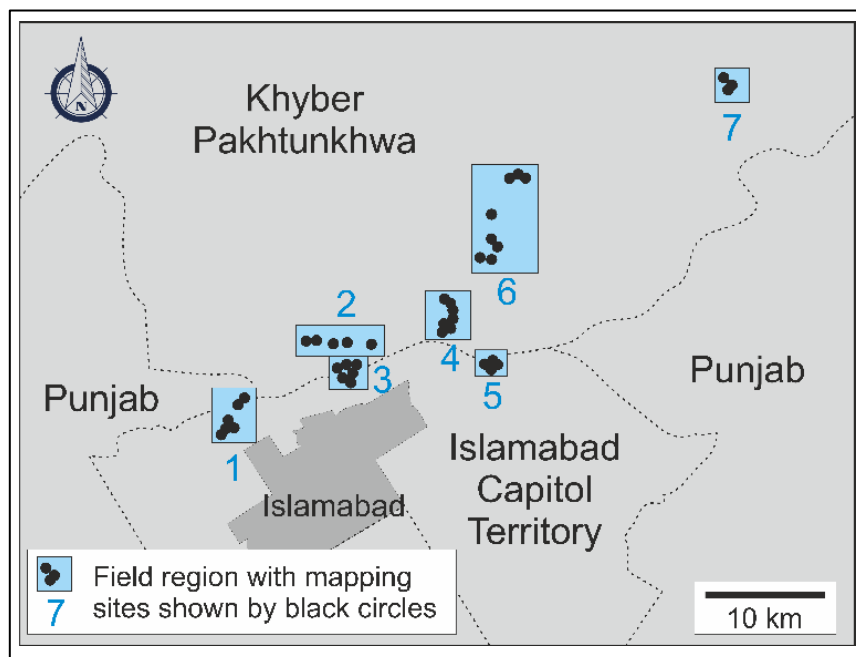


Figure 4.1: The distribution of the field regions are indicated relative to Islamabad as blue rectangles. The names of the various field regions are listed in Table 4..

The field regions and the sites within them were selected based on two criteria:

- Select a site on a major geological structure, especially thrusts.
- Evaluate different types of geological structures in a region.

With these simple, unrestricted guidelines, it was possible to collect data from a wide variety of geological structures in different rock assemblages. The guidelines ensure that different structures across a region and hence across the field area were mapped to allow meaningful comparison of the data from the 42 mapping sites (Table 4.1).

The geology of the study area in the Potwar Basin of northern Pakistan is dominated by sedimentary deposits and structural features associated with the collision of the Indian and Eurasian plates during the ongoing Himalayan Orogeny (Acharyya and Saha, 2018). The oldest mapped rocks in the study area, the Jurassic Samana Suk Formation (Figure 4.2) has a disconformable contact with the underlying Datta Formation. The Samana Suk Formation consists of thick bedded, bioturbated carbonate with shale interbeds. The upper contact with the Chichali Formation is highly sheared. The Lower Cretaceous Chichali Formation consists of glauconitic sandstones and shales. It is overlain by similarly siliciclastic sediments of the Lumshiwai Formation. They consist of freshwater lagoonal or delta front shale and clays, covered by sandstone, micrite and shell fragments with subordinate dolomite (Shah *et al.*, 2013). The overlying Upper Cretaceous Kawagarh Formation consists of marl and marly limestone deposited in mid- and outer-ramp settings.

The Palaeocene Lockhart Formation was then deposited unconformably over these Cretaceous fluvial and marine sediments in a marine setting on the northern leading edge of the Indian Plate as the Palaeo-Tethys Ocean closed. Strata of the Lockhart Formation comprise a series of stacked foraminiferal–algal build-ups intercalated with siltstone and deposited in cycles on a low-energy shelfal carbonate ramp, and the sediments record many shallowing and shoaling events from open marine to inner ramp conditions (Hanif *et al.*, 2014). The limestone units of the formation generally comprise argillaceous wackestones and, more rarely, packstones with little or no primary matrix porosity. The contact between the Lockhart Formation and the younger shallow-marine shales and subordinate carbonates of the Patala Formation is transitional (Wandrey *et al.*, 2004). The late Palaeocene to early Eocene Patala Formation of the Kala Chitta Range represents the latest

Palaeocene foraminiferal dominated unit of the low latitude Tethyan carbonate platform benthic community evolution (Hanif *et al* 2013). The Patala Formation shales are widespread around the study area and varies from green shales with thin limestones (Gee and Gee, 1989) to calcareous black shales. There is a transitional and interfingered contact between the Patala Formation and the overlying Eocene Nammal Formation. The rocks of the Nammal Formation consist of light grey shallow-marine to lagoonal shales with interbedded limestones (Gee and Gee, 1989; Wandrey *et al.*, 2004). The Nammal Formation is overlain by the Margala Hills Formation consisting of marine limestones and shales.

The subsequent carbonates of Chorgali Formation were deposited in shallow environment (Khan *et al.*, 2004) and defines a shallowing upward sequence starting with open marine bioclastic medium-bedded limestones, which grades, into a destructive massive fabric and subsequently fine-crystalline dolomites (Benchilla *et al.*, 2002). The near surface sedimentation conditions are also reflected by the presence of flat channel conglomerate and breccia beds in the upper part of the dolomites. Eocene strata are overlain unconformably by Miocene fluvial sediments of the Murree Formation (Wandrey *et al.*, 2004) that record deposition of post-initial collision Himalayan molasse. Pleistocene and Holocene superficial deposits complete the record of the post- collisional deposition and consist of windblown silt and sand, along with alluvial gravel adjacent to the active thrust scarps (Robert *et al.*, 1997). Figure 4.3 is a regional stratigraphic map. There is a complex inter-relationship between the stratigraphy and the structural geology mapped at each site in the various field areas. This is outlined in Table 4.1. The geographical positions of the mapped stratigraphy relative to the regional stratigraphy is shown in Figure 4.4 and the geographical positions of the mapped structural geology of each site relative to the regional structural trends is shown in Figure 4.5.

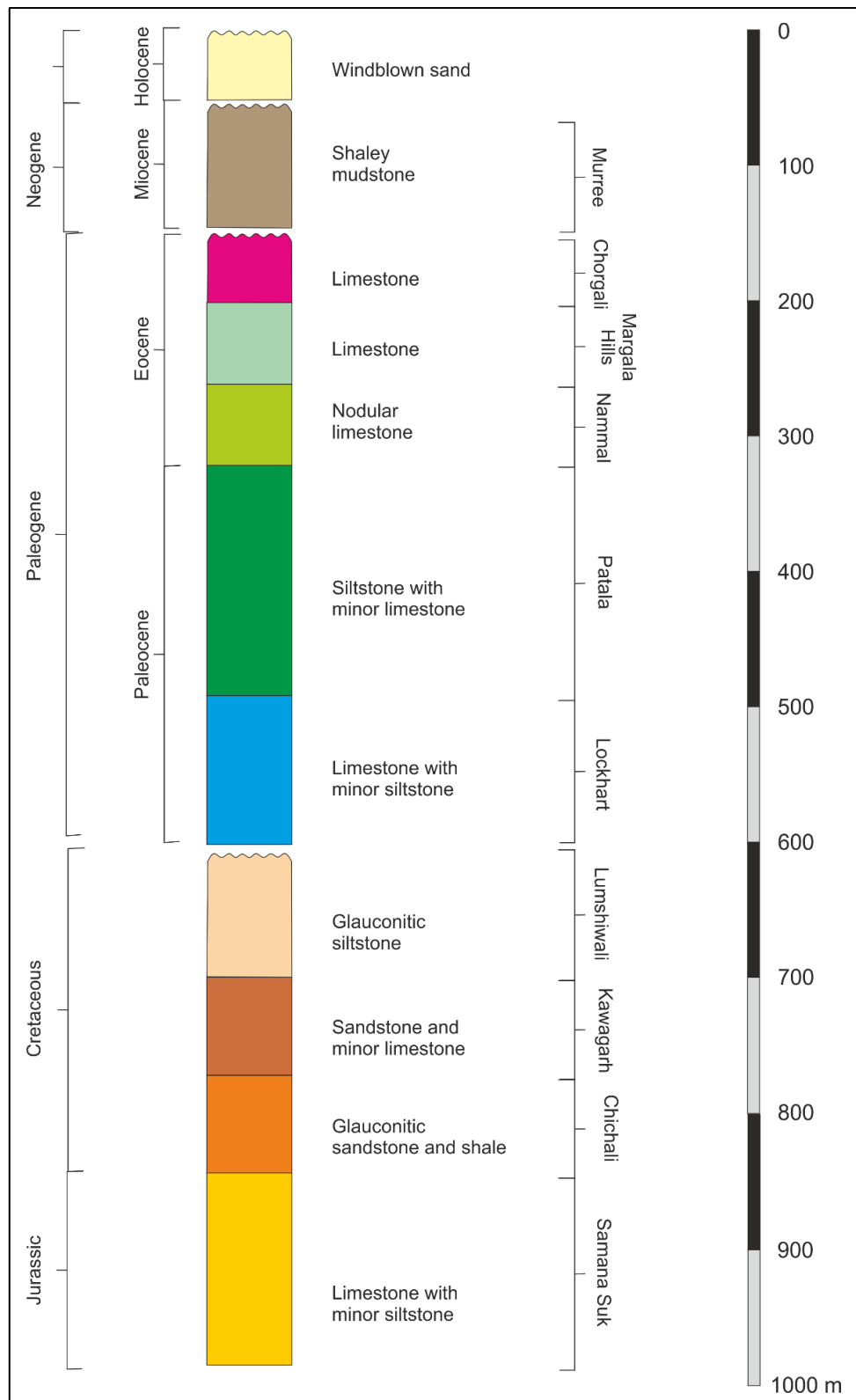


Figure 4.2: Stratigraphic column indicating the age, composition, and thickness (undeformed) of the various formations in the field area.

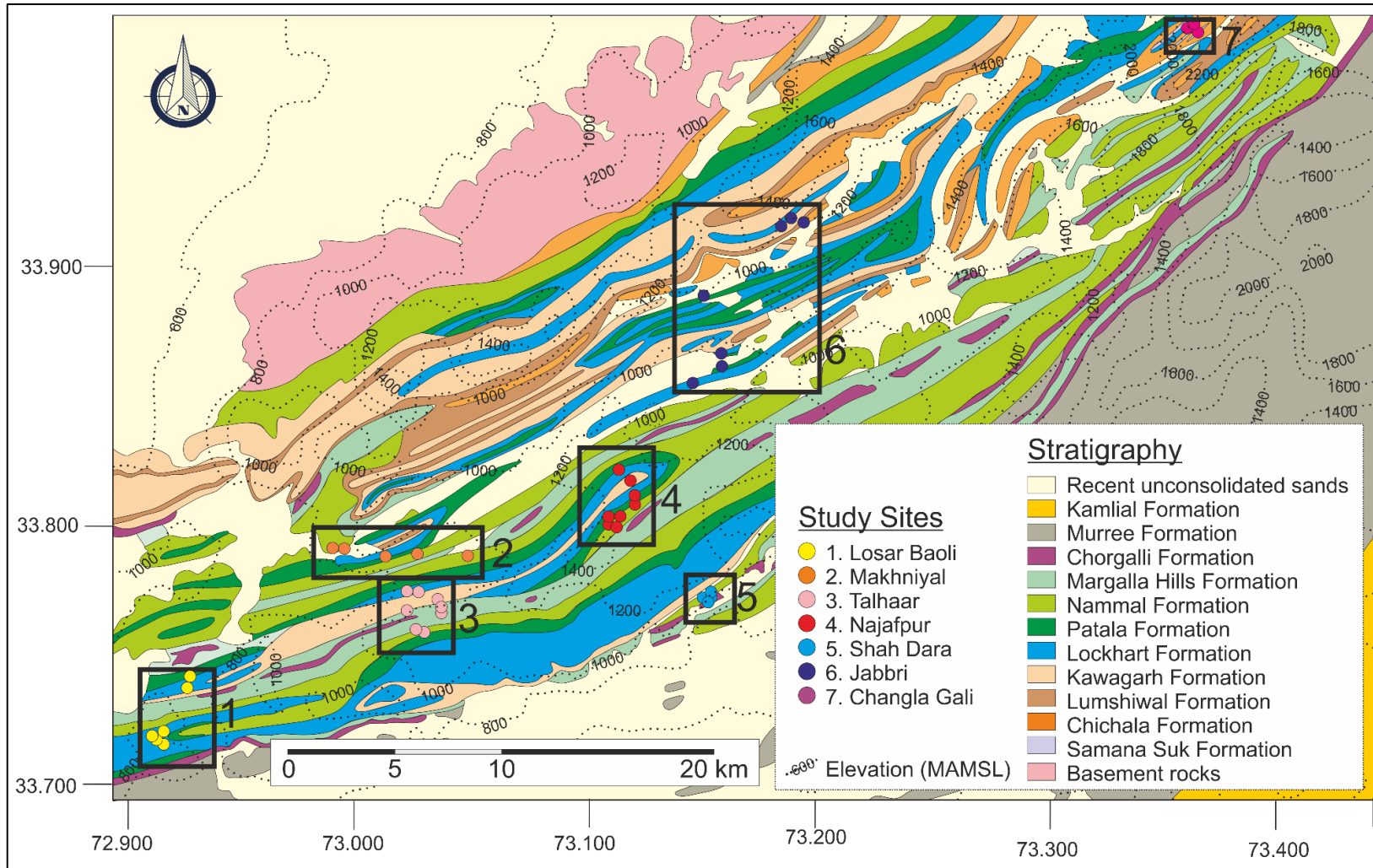


Figure 4.3: Stratigraphic map of the study area with field regions and sites indicated. Names of field regions corresponding to numbers are listed in Table 4. . Modified after Ali (2014). It is noted that the geological maps of the different areas are based on Ali (2014) as well.

Table 4.1: Distribution of stratigraphy and structures across the field areas based on the mapping undertaken by Ali (2014).. Numbers refer to individual sites within the field areas. Figure 4.4 and Figure 4.5 are maps showing the geographical location of these features across the various field areas and sites.

Field area		Formation	Fore-thrust	Back-thrust	Thrust footwall	Anticline	Overturned anticline	Syncline	Shear fault	Normal fault
1	Losar Baoli	Lockhart	1, 2	5, 6		3		4		
2	Makhniyal	Nammal					1,2,5			
		Patala					4			
		Lockhart					3			
3	Talhaar	Margala Hills						1, 2		
		Nammal					3			
		Lockhart				8				
		Kawagarh	5,6		4, 7					
4	Najafpur	Nammal	1		3, 4					5
		Patala								
		Lockhart	2							
		Kawagarh								
5	Shah Dara	Chorgali	3							
		Nammal								
6	Jabbri	Nammal								
		Patala							4	
		Lockhart						5, 6		
		Kawagarh	2, 3							
		Chichali	1							
7	Changla Gali	Lockhart		1						3
		Lumshiwal							2	

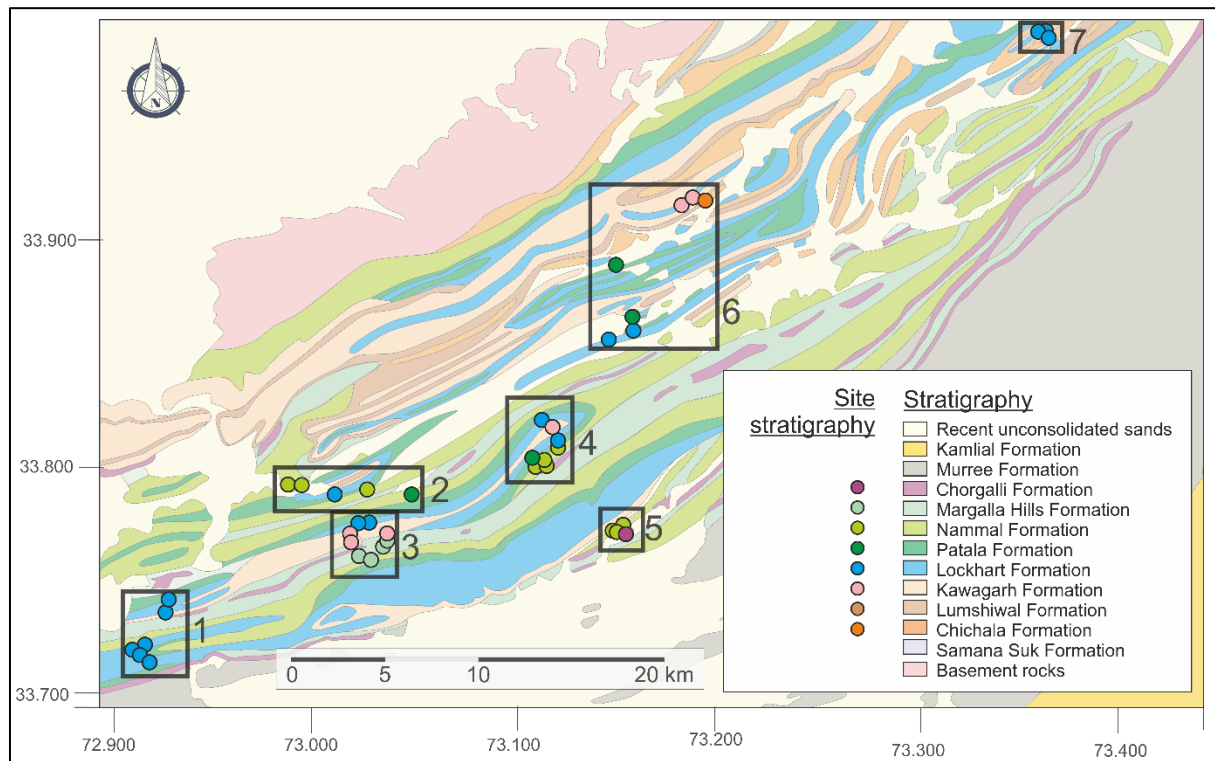


Figure 4.4: Stratigraphy of the field area (see also Figure 4.3) with the mapped stratigraphy of each study site indicated. Names of field regions corresponding to numbers are listed in this chapter. Modified after Ali (2014).

The west-northwest – east-southeast striking structural features of the field area are a product of the on-going collision between the Indian and Eurasian tectonic plates and are typical of fold and thrust (FAT) belts. Although FAT belts are recognized as the most common mechanism to accommodate crustal shortening, there is an enormous heterogeneity in deformation styles. The various folds and thrusts develop between major bounding thrusts - in this study these are the Main Boundary Thrust immediately to the south of the study area and the Main Central Thrust to the north. The Main Boundary Thrust outcrops on the southern edge of the study area, in the Losar Baoli field region. Successive fore-thrusts developed past the Main Boundary Thrust are interpreted as low angle, flat décollement thrusts, of down to 10 km deep accompanied by shallow (< 3 km) back-thrusts (McDougal et al, 1993). This work has found that the fore-thrusts are generally not at a low angle, and this is described in detail in the following sub-sections. The folds initially form by buckling and are then subjected to progressive deformation towards the foreland. Thrusts are developed roughly

perpendicular to the maximum tectonic compression and thrust-related folds develop, especially fault-bend folds and fault tip folds. The distribution and characteristics of fore-thrusts, back-thrusts, and their thrust footwalls are mapped (Figure 4.5). Thrust-related anticlines, synclines and overturned anticline folds are investigated in the various field regions of the FAT-belt (Figure 4.5).

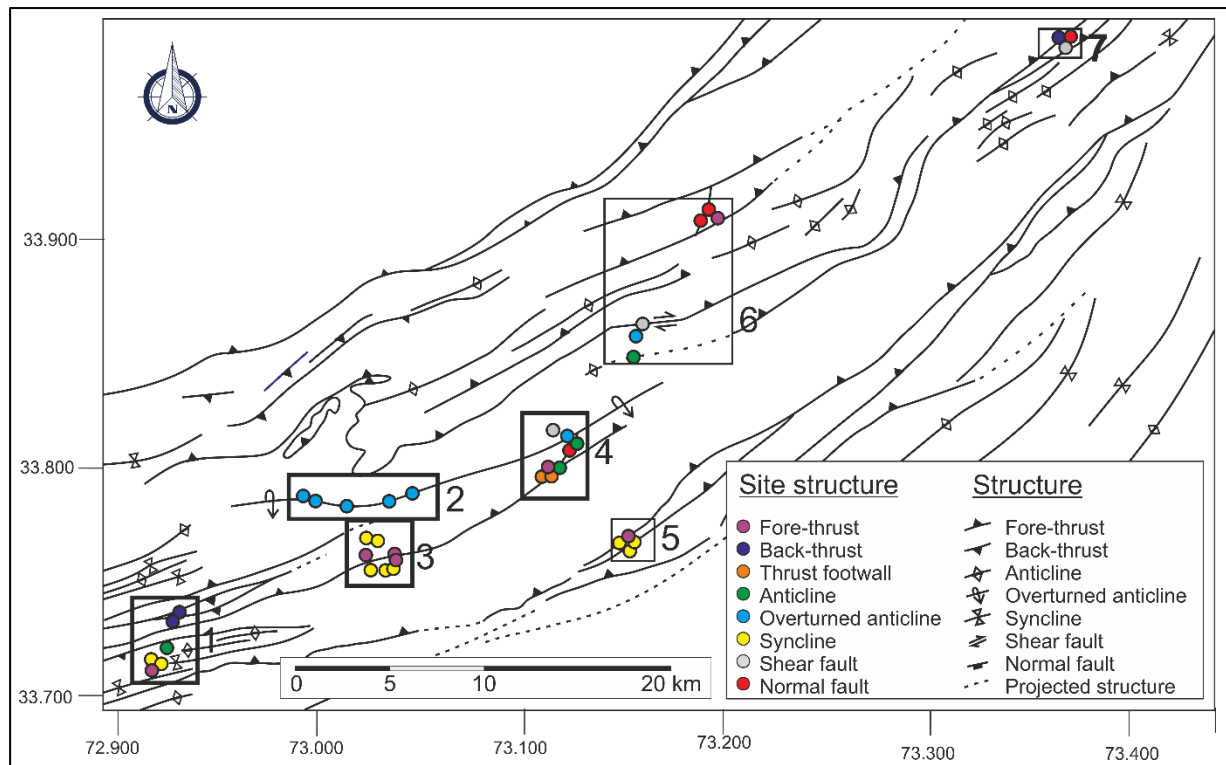


Figure 4.5: Regional structural geology with the mapped structural features of each study site indicated. Broadly based on the map of Ali (2014).

Data from several mapping circles were captured at each site utilising the methodology described in Chapter 3. From this node and fractal data, the topological characteristics of the different measurement circles at the various sites were determined. The graphical results of these measurements are presented together with the descriptions of the lithological and structural characteristics of each site to allow comparison of the various datatypes.

The variations in the different fractal and topological datasets across the sites is compared with the differences in the stratigraphy (including details of the lithologies) and structural features to create an integrated description for the field region.

4.2. Field regions

4.2.1. Losar Baoli region

The Losar Baoli region forms the southwestern edge of the study area. It is located five kilometres northeast of Islamabad along the Margalla Hills road and 5 km southwest of the Talhaar region (Section 5.2.4). A stepwell (Losar Baoli) is present in the centre of the region within the anticline of the pop-up structure. The strata are aligned approximately east-west in a series of folds and thrusts associated with the ongoing Himalayan mountain-building (Figure 4.6 and Figure 4.7). A south-north transect of six sites were measured in the structural domains of this tectonism (Table 4.2).

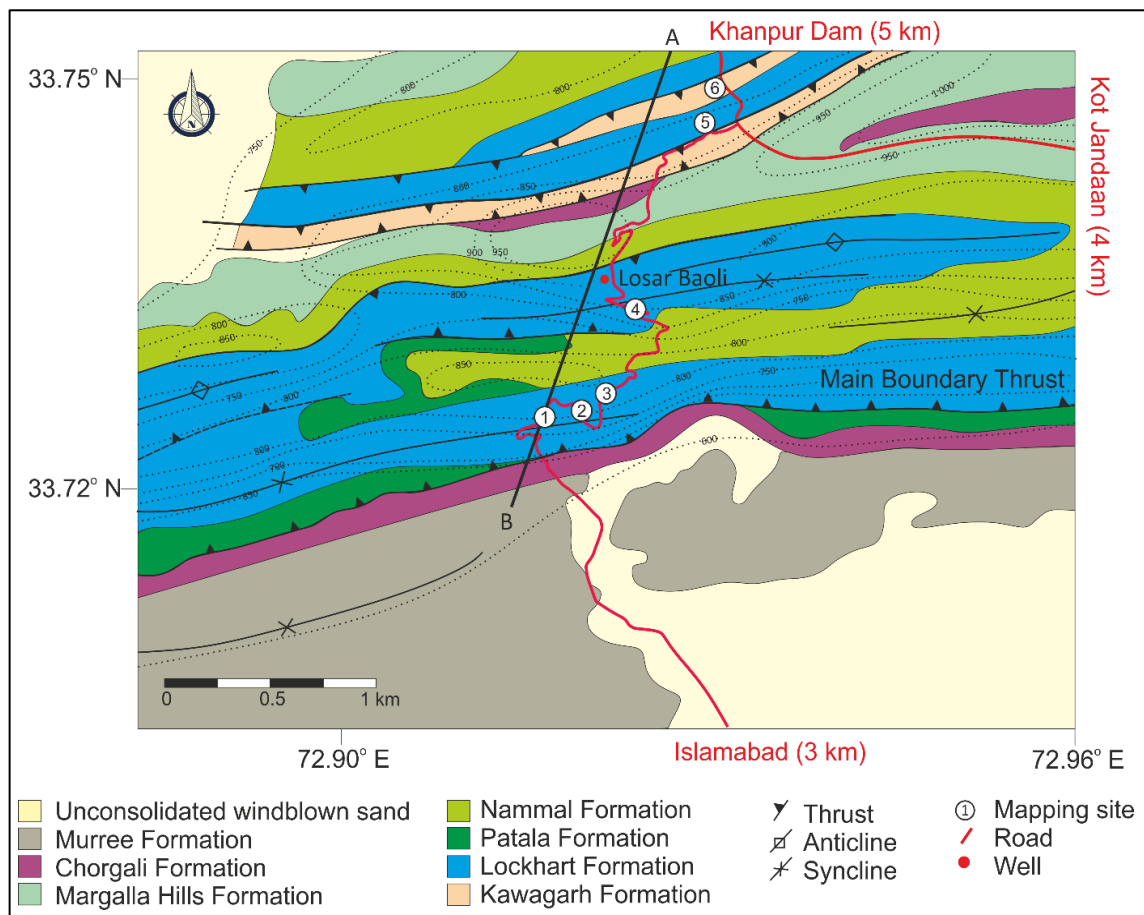


Figure 4.6: Geological map of the Losar Baoli region. It is the most south-westerly region, approximately 5 km southwest of the Talhaar region. All larger scale maps in this chapter are modified after Ali (2014) but include additional unmapped stratigraphic and structural features as well as mapping sites and roads travelled.

Table 4.2: Location of mapping sites, Losar Baoli region.

Site	Latitude (N)	Longitude (E)	Stratigraphy	Structure
1	33.723°	72.916°	Lockhart	Fore-thrust
2	33.723°	72.921°	Lockhart	Fore-thrust
3	33.725°	72.926°	Lockhart	Fore-thrust
4	33.733°	72.922°	Lockhart	Anticline
5	33.744°	72.932°	Lockhart	Back-thrust
6	33.746°	72.940°	Lockhart	Back-thrust

The most significant of these tectonic features in the region is the Main Boundary Thrust (MBT), which forms a steep barrier between Islamabad and the mountains to the north (Figure 4.8). The elevation increases by at least 100 m when crossing from Islamabad.

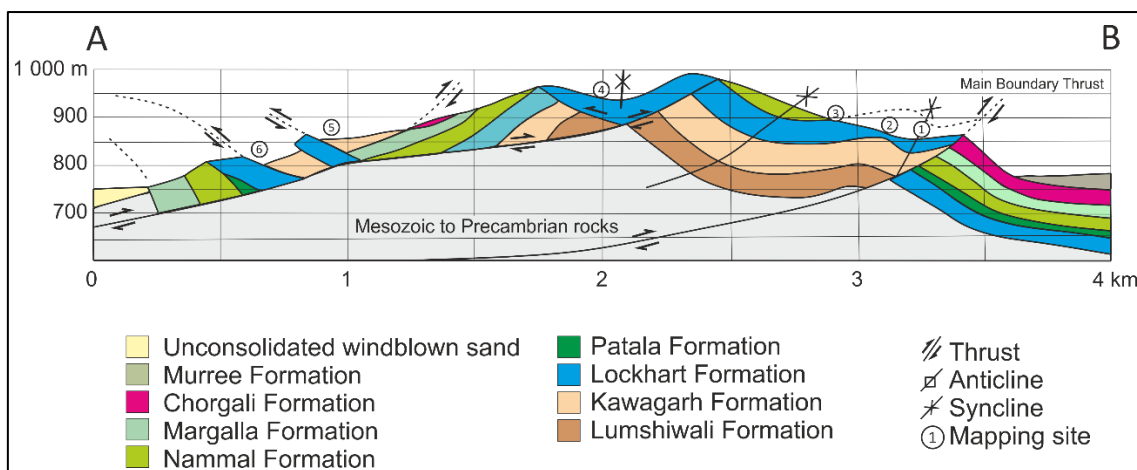


Figure 4.7: Cross-section through the Losar Baoli region. See Figure 4.6 for position of cross-section. based on interpretation of map from Ali (2014) but including updated mapping from this work. All cross-sections have been generated by the author.



Figure 4.8: View eastward along the Main Boundary Thrust cliffs formed in the Lockhart Formation. Islamabad lies directly to the south (right hand side) of this image.

4.2.1.1 Site 1

Site 1 is situated on a sheared silty mudstone layer in between the lighter coloured wackestone of the Lockhart Formation (Figure 4.9). The data from six 1-metre-wide measurement circles at site 1, was captured and analysed. Circles 1 and 2 are in the northern hanging-wall of the thrust, whilst circles 3 to 6 are in the footwall (Figure 4.9). The mudstone layer that forms the décollement surface of the thrust is too highly fractured and weathered to be measured. A strong linear character is evident in all the circles (Figure 4.10). This fabric is likely to have formed early during the deformation process as it is bedding parallel, irrespective of the orientation of the bedding. Later fractures cross-cut these fractures affecting the number and type of nodes present (Figure 4.11).

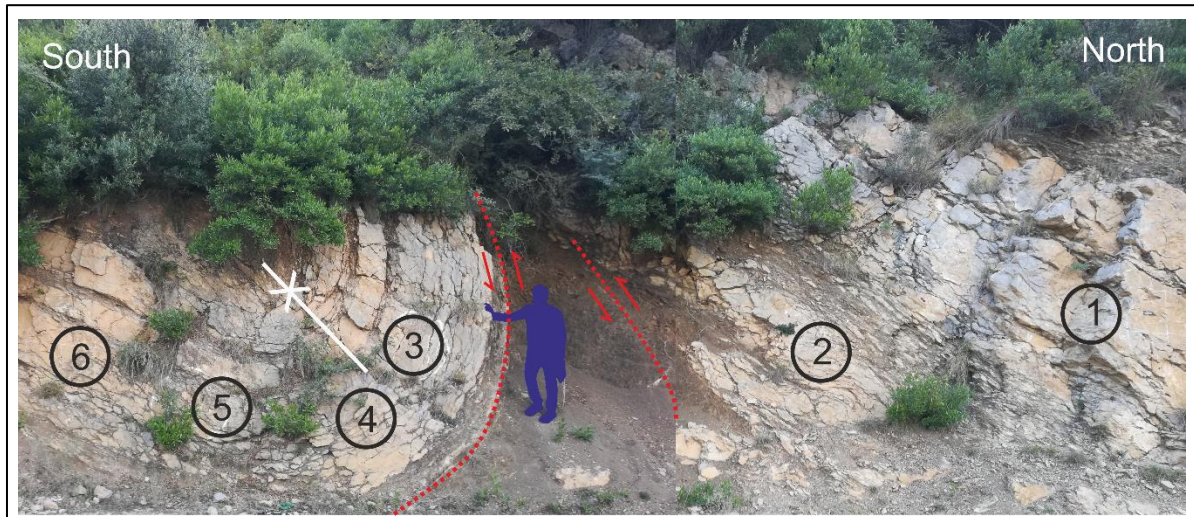


Figure 4.9: Fore-thrust of lime-mud developed over a shale band. Mapping circle positions at site 1. Blue geologist for scale. Detailed mapping of the fracture nodes is shown in Figure 4.10.

Although the total number of nodes measured in the six circles does not vary significantly, the type of node does. In circle 1, high in the hanging-wall of the thrust there are very few cross-cutting “x” nodes (Figure 4.11). Circle 2 in the immediate hanging-wall of the thrust, has fewer nodes. there is a higher number of “e”, “x” and “y” nodes, but only one “i” node. The nodes in circles 3 to 6 in the footwall of the thrust decrease in abundance away from the thrust (Figure 4.11). Circles 3 and 4 either side of the syncline axis in the immediate footwall of the thrust (Figure 4.11) have the greatest number of nodes (Figure 4.11).

Due to their high number of nodes, circles 3 and 4 have the highest number of branches and tips (Figure 4.12). Site 4 has the highest fractal dimension. The average mean trace length (MTL) of the measurement circles is 39 cm, and shortest in circle 3 (19 cm), but doesn’t have a clear trend away from the thrust, apart from circle 6 being nearly twice the average (76 cm). Connectivity is high in circle 6 (Figure 4.13) due to this long MTL.

Connectivity is high in circle 6 due to long MTL. The long MTL has also has highest fracture intensity but lowest fracture density in circle 6, as the fracture pattern is dominated by longer fractures that intersect the edges of the measurement circle (Figure 4.13).

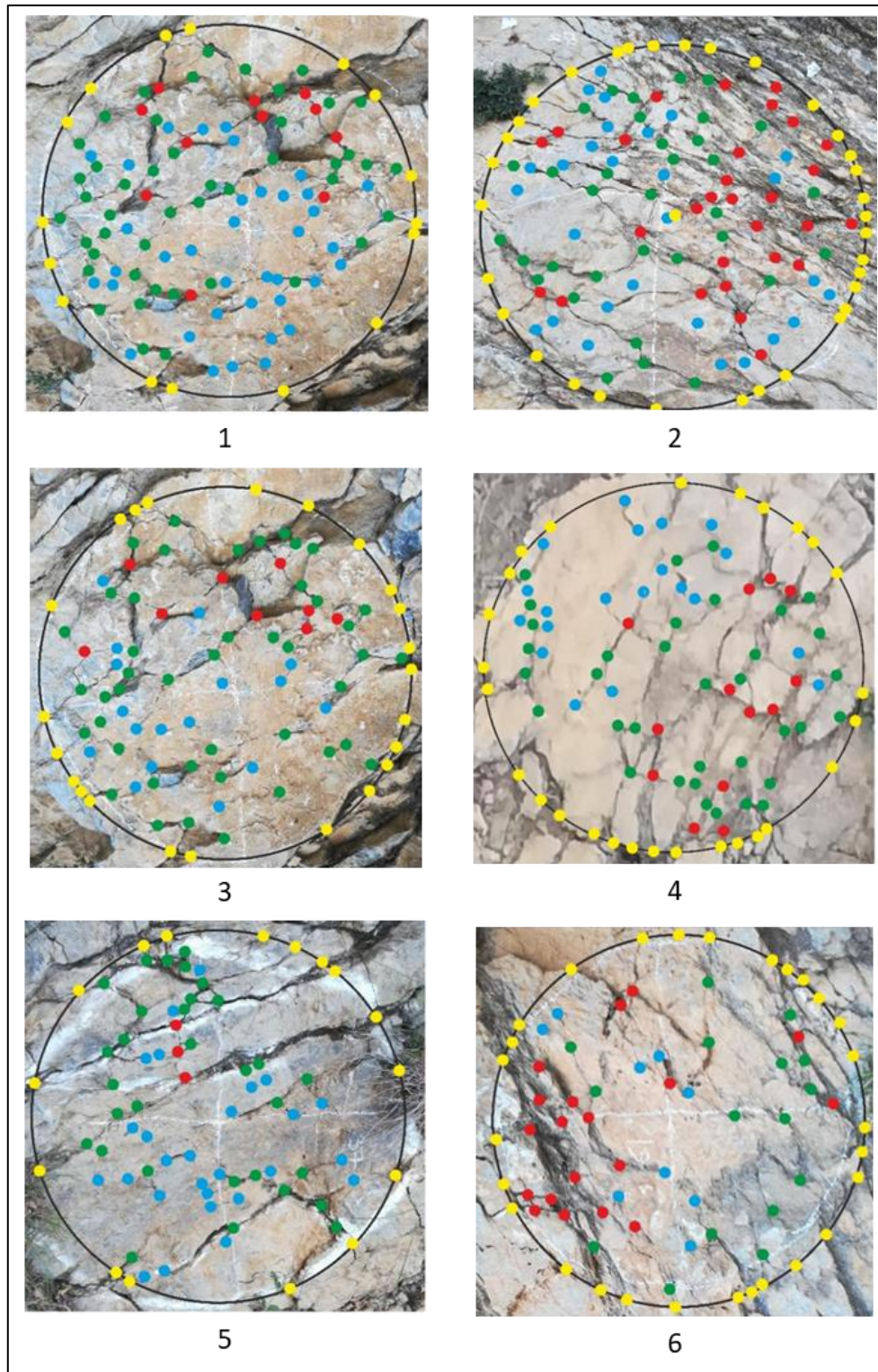


Figure 4.10: One metre measurement circles, site 1. See Figure 4.9 for positions. “e” nodes are shown in yellow, “x” in red, “y” in green and “i” in blue. This colour scheme is used throughout the thesis.

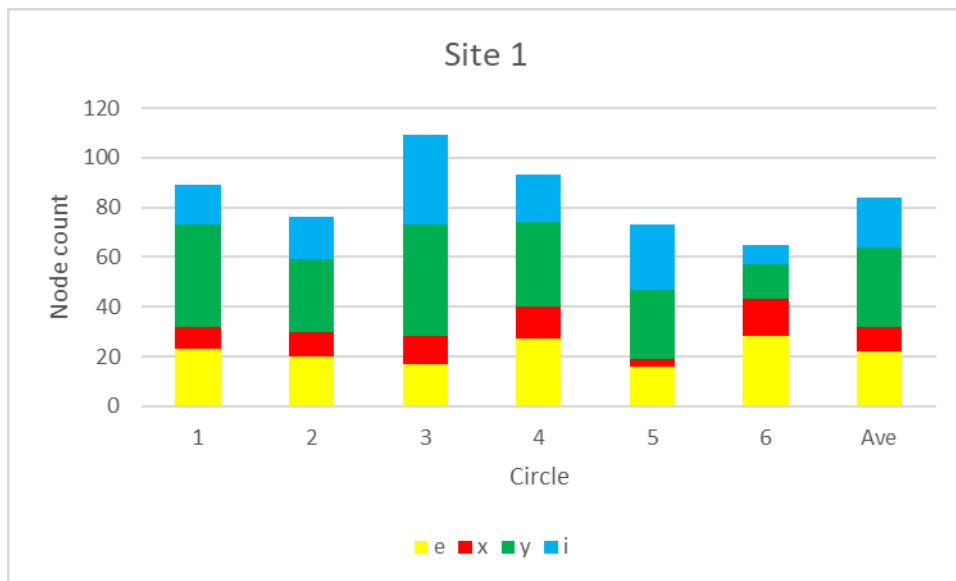


Figure 4.11: Node count, site 1.

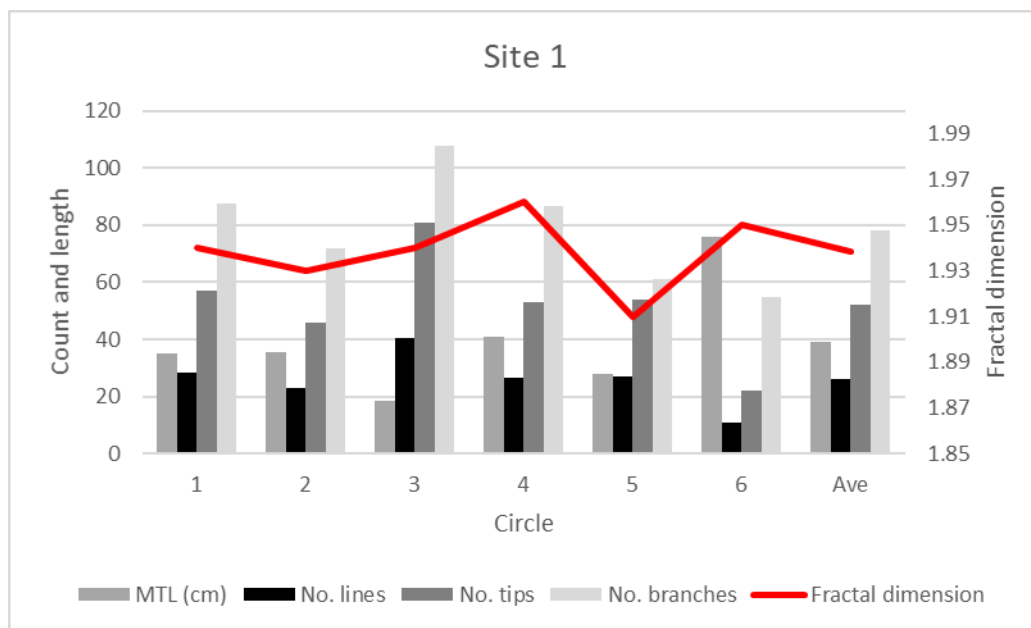


Figure 4.12: Fracture characteristics and fractal dimension, site 1.

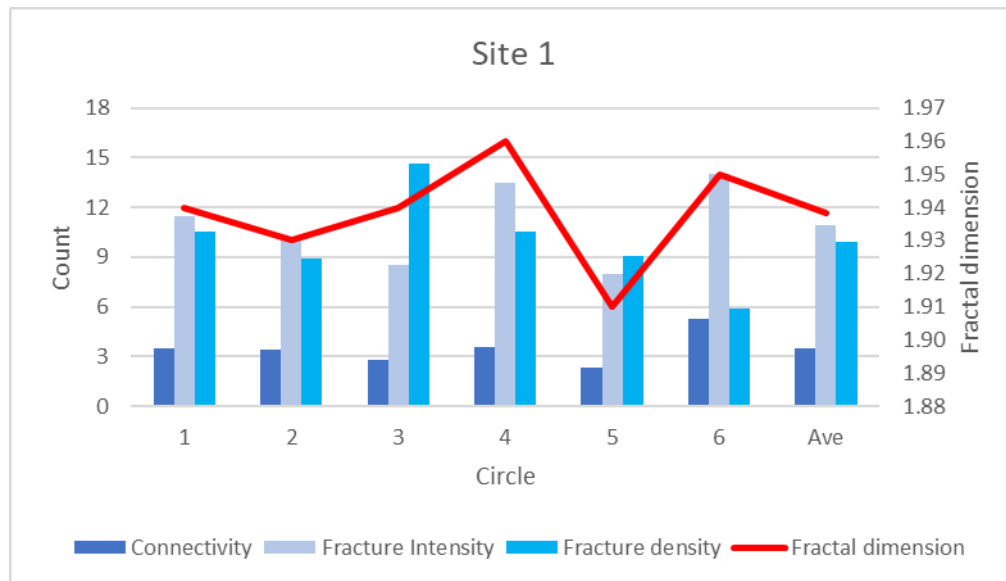


Figure 4.13: Fracture characteristics and fractal dimension, site 1.

4.2.1.2 Site 2

At site 2 the sedimentary sequence consists of the following units:

- Strongly laminated, dark grey, finely bedded shale with twisted and folded vertically oriented fragmented limestone beds.
- Grey-brown, finely bedded marl that is laminated due to deformation.
- Alternating grey (orange-brown weathering) limestones and dark grey siltstone. The siltstone displays an intense tectonic fabric forming fragments of rock approximately 1 cm wide by 10 cm long parallel to the bedding planes whilst the limestone is generally fractured at a steep angle to bedding.
- Grey limestone with minor millimetre thick silty partings.

The distribution of these rock-types is shown in Figure 4.14, where five measurement circles were placed across this exposure

The greatest number of nodes is developed in circle 3, which is sited across the dark grey, finely bedded shale and limestone ((Figure 4.15). This juxtaposition of two rock types with different failure modes (flexural flow for the shale and tangential longitudinal failure for the limestone) increased the

number of nodes. Circle 4 consists predominantly of the strongly laminated, dark grey, finely bedded shale with fewer “e” and “x” nodes and hence has the second highest number of nodes (Figure 4.16). Circle 1 has the lowest fractal dimension (Figure 4.17) because it is on a bedding plane. The number of nodes, the number of lines, tips, and branches is highest in circles 3 and 4 (Figure 4.17). The fracture density and fracture intensity are also greatest in these two circles (Figure 4.18).

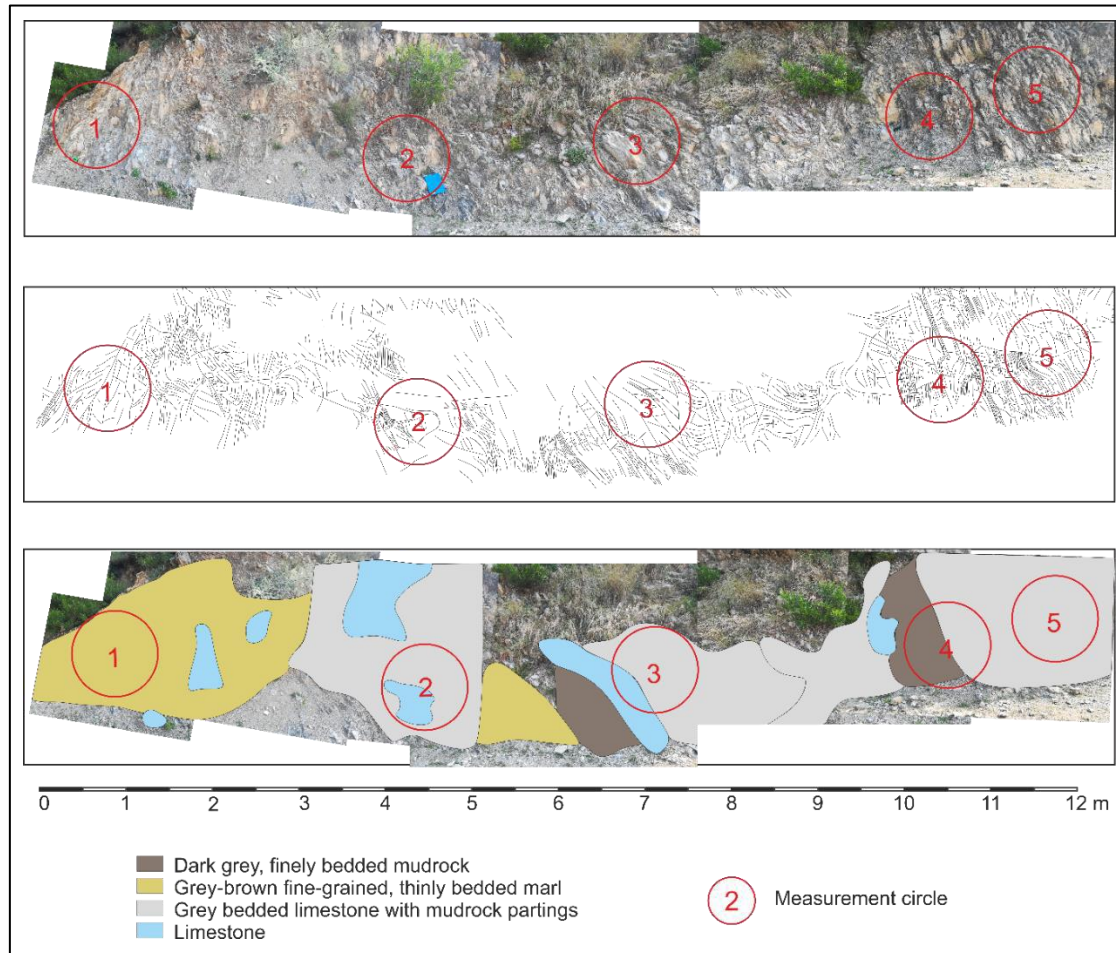


Figure 4.14: Photo-mosaic, fracture traces and rock types of site 2. Positions of the measurement circles are also indicated.

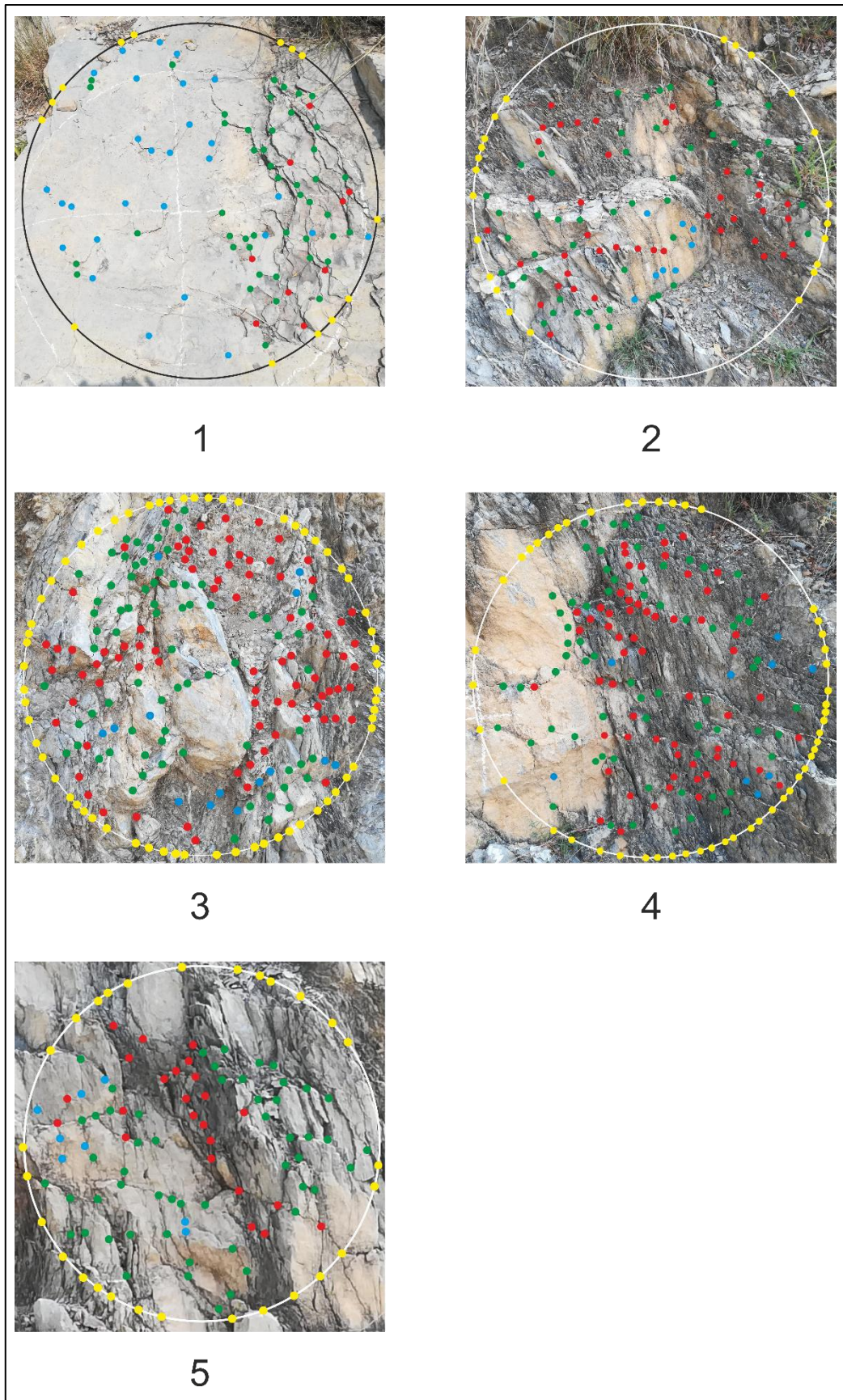


Figure 4.15: Site 2 measurement circles. See Figure 4.14 for positions of circles at site 2.

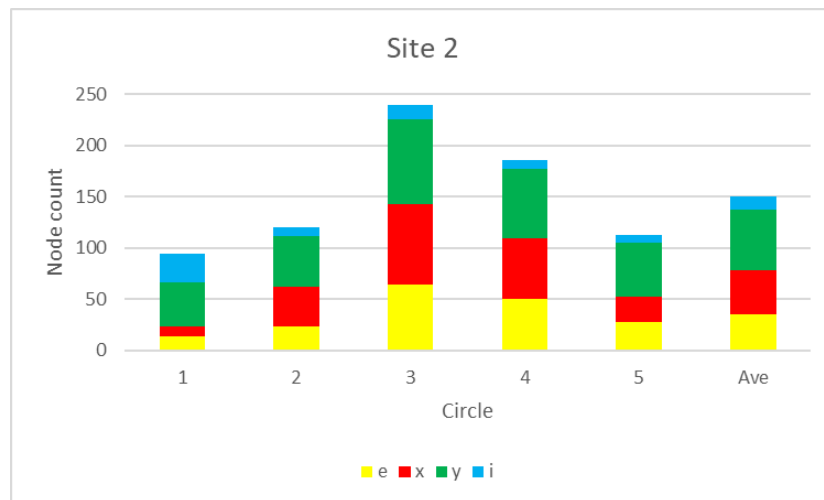


Figure 4.16: Node count, site 2.



Figure 4.17: Fracture characteristics and fractal dimension, site 2.

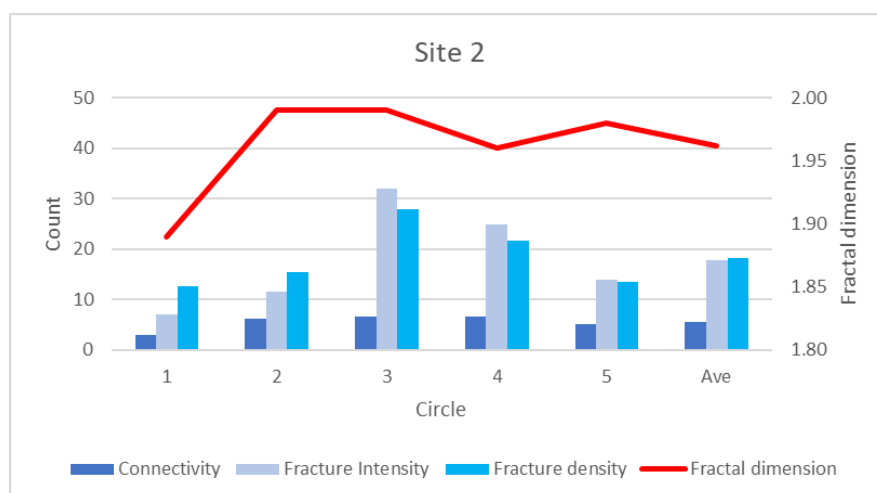


Figure 4.18: Fracture characteristics and fractal dimension, site 2.

4.2.1.3 Site 3

The rocks at site 3 consist of metre thick beds Lockhart Formation that weathers light creamy grey but is light grey on fresh surfaces (Figure 4.19). Circle 1 is smoothly weathered exposing many hairline calcite fractures (Figure 4.20). Circle 1 has the highest number of nodes of all the circles in the region and has resulted in site 3, when considered with the large number of nodes in circle 2, to have the greatest average number of nodes of the region. The hairline calcite fractures terminate within the rock mass of circle 2 creating a large number of "i" nodes (166). The large number of nodes in circle 1 has resulted in high values for all the fracture characteristics (Figure 4.22 and Figure 4.23). The highly fractured nature of both circles has resulted in a fractal dimension of 1.99 (almost 2 dimensional).



Figure 4.19: Positions of measurement circles 1 and 2 at site 3. Resting geologist (in blue) for scale.

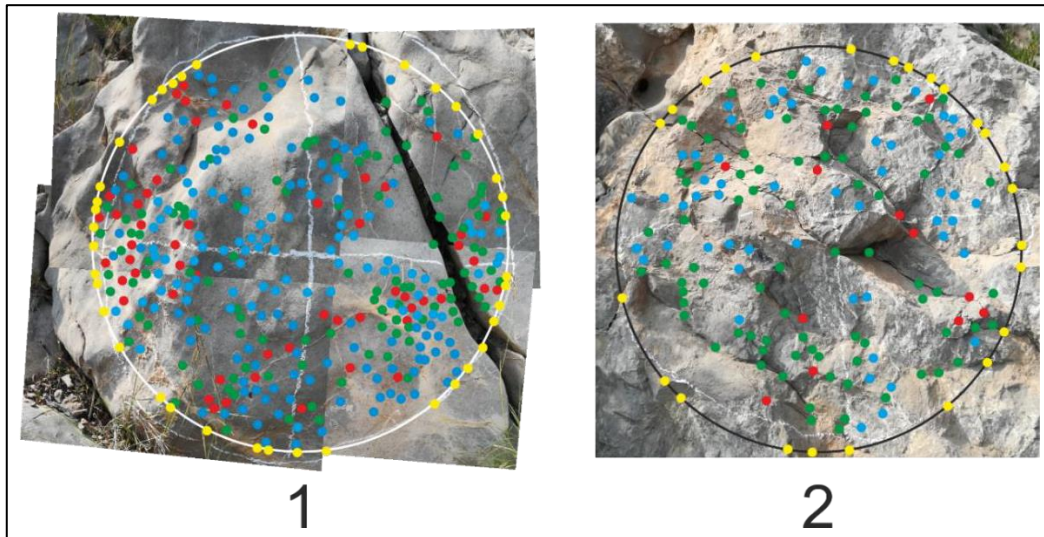


Figure 4.20: Measurement circles, site 3.

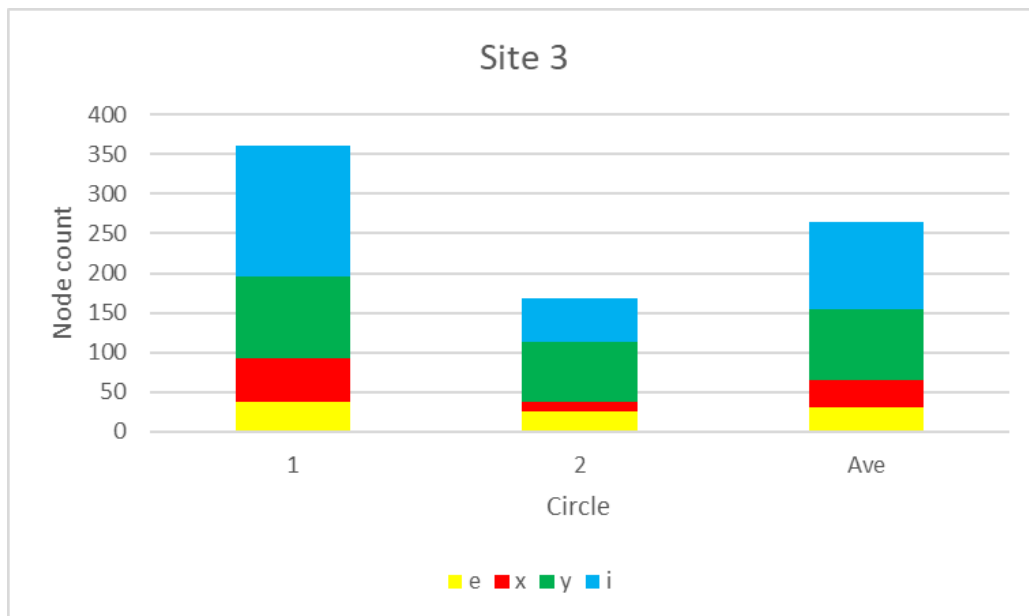


Figure 4.21: Node count, site 3.

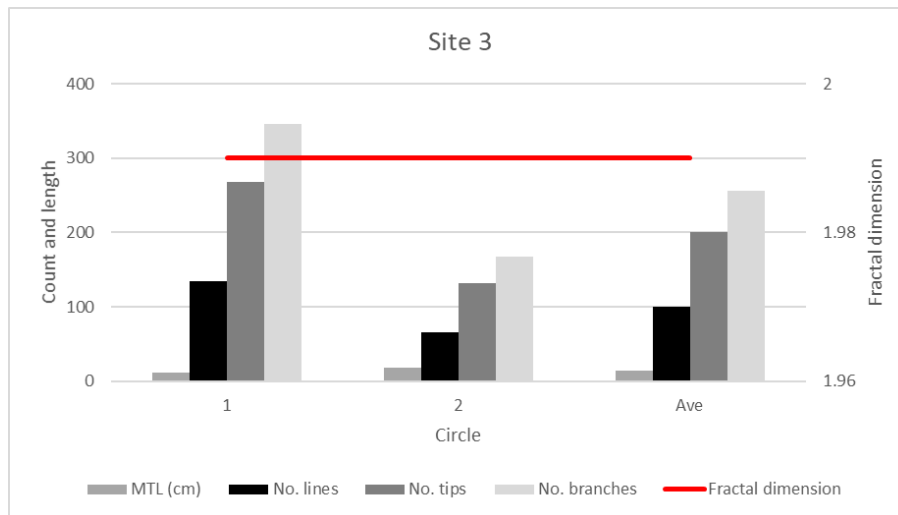


Figure 4.22: Fracture characteristics and fractal dimension, site 3.

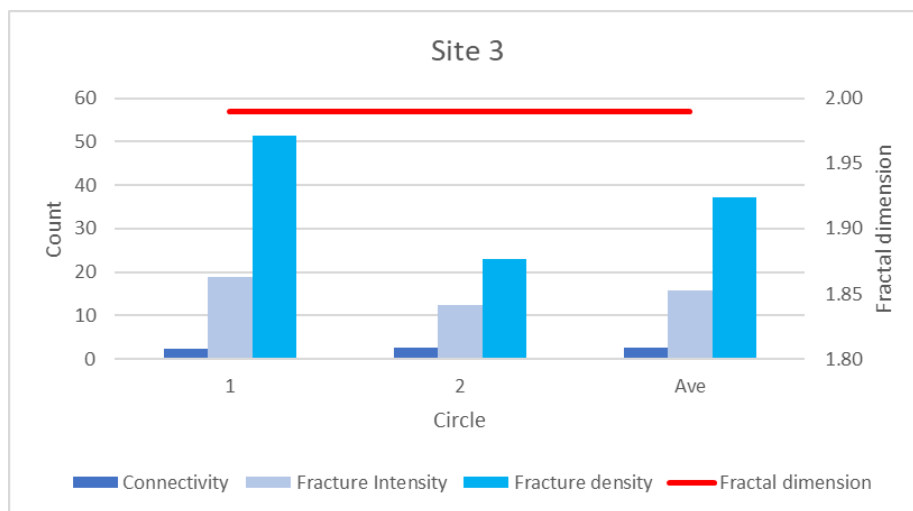


Figure 4.23: Fracture characteristics and fractal dimension, site 3.

4.2.1.4 Site 4

At site 4 the Lockhart Formation has a gentle dip of 14 degrees as it is located in a pop-up structure rather than the surrounding thrusts and folds. Two measurement circles were characterised at the site – circle 1 on the bedding plane and circle 2 across bedding (Figure 4.24). Fine hairline fractures, both filled with calcite and unmineralised are present on the exposed bedding surface (circle 1). The thin mineralised fractures do not penetrate into the limestone bed (circle 2). The mineralised fractures

do not intersect with each other on the bedding surface, resulting in a large number of “i” nodes (Figure 4.26).

There are no mineralised fractures that terminate in the rock mass forming “i” nodes in circle 2 but the total number of nodes is similar (Figure 4.26). As a result of the different abundances of the “y” and “i” nodes in the two circles, the number of tips is greatest in circle 1 and the number of branches is greatest in circle 2 (Figure 4.27). Despite the greater number of intersections (“y” nodes), the mean trace length (MTL) is longer in circle 2 (16 cm) vs. 8 cm in circle 1 (Figure 4.27). The connectivity and fracture intensity is higher in circle 2, where-as the fracture density is highest in circle 1 (Figure 4.28). The average fractal dimension (1.93) at site 4 is the lowest in the region.

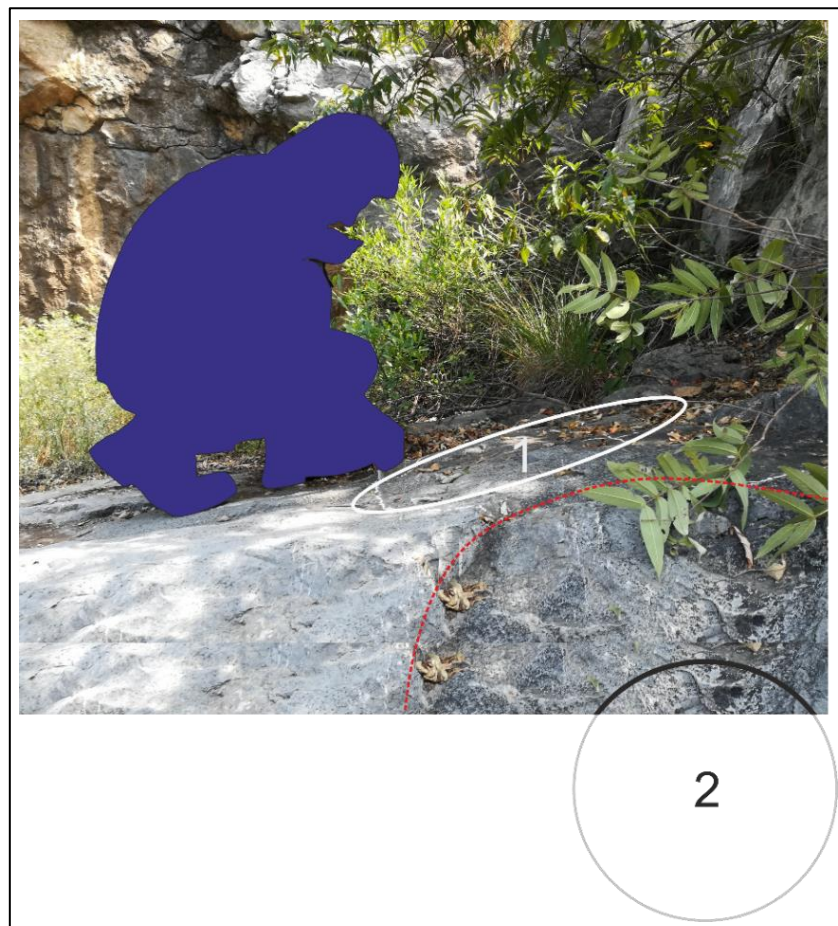


Figure 4.24: Positions of measurement circles at site 4. Circle 1 is located on a bedding plane and circle 2 across the bed. Dotted red line indicates edge of bed. Blue geologist for scale.

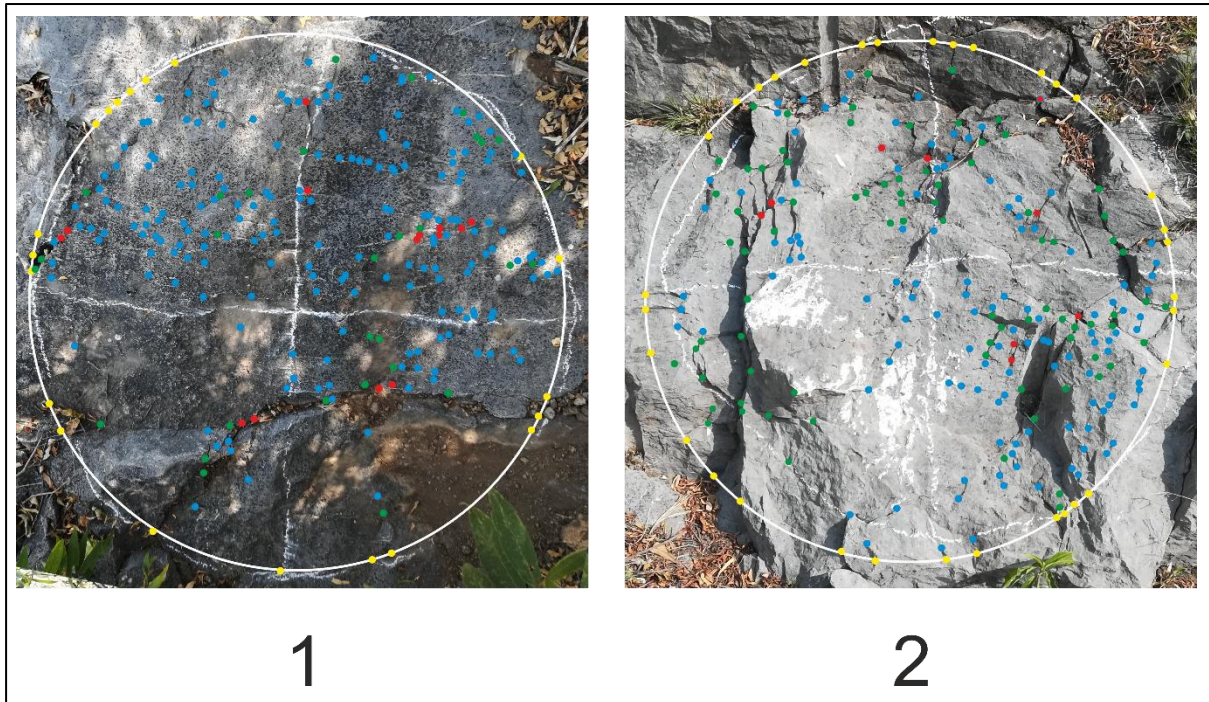


Figure 4.25: Measurement circles, site 4.

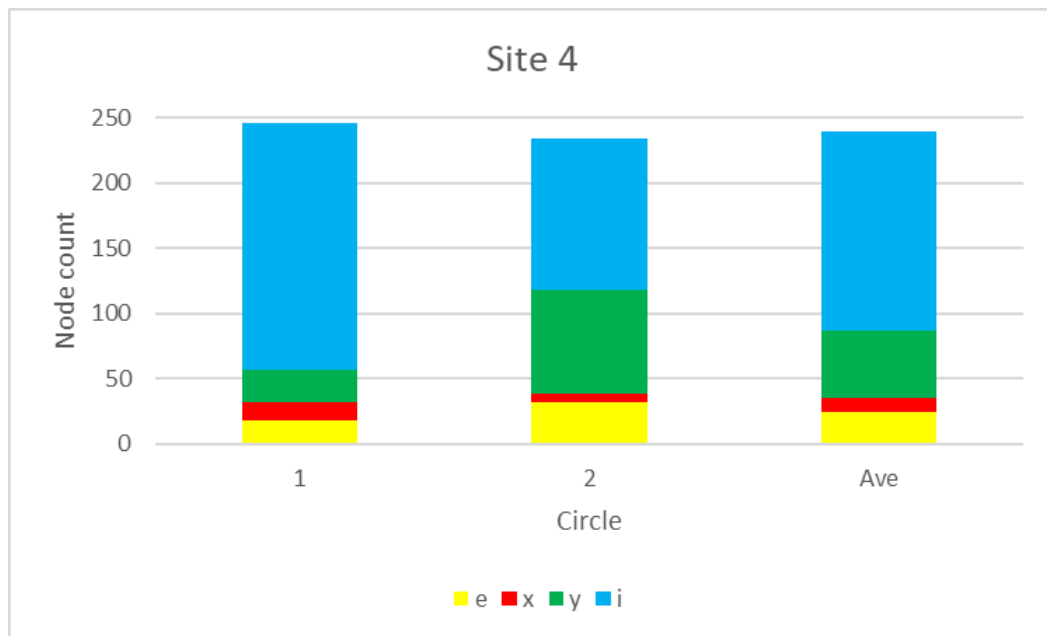


Figure 4.26: Node count, site 4.

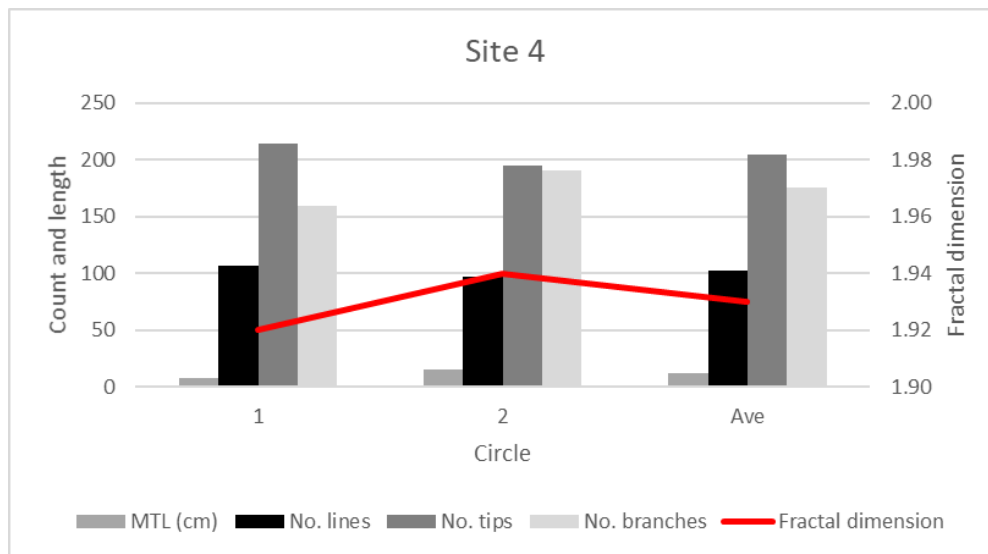


Figure 4.27: Fracture characteristics and fractal dimension, site 4.

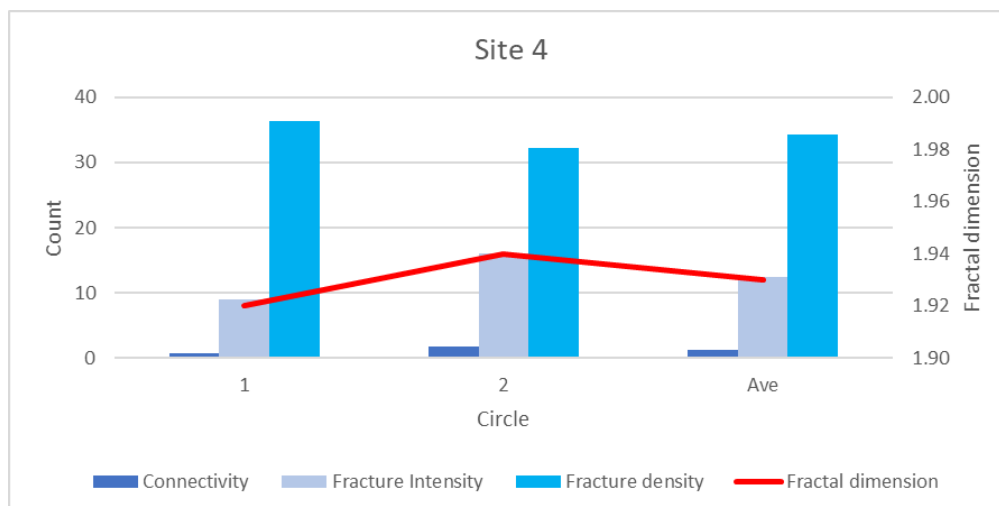


Figure 4.28: Fracture characteristics and fractal dimension, site 4.

4.2.1.5 Site 5

Site 5 is sited in the east-west valley near the intersection of the Margalla Hills and Kot Jandaan roads (Figure 4.29) in the northern portion of the Losar Baoli region (Figure 4.6).

It is positioned on a southward dipping back-thrust in the light grey packstone of the Lockhart Formation. The thrust surface has prominent calcite veining developed across the exposure surface, including matching conjugate shears with an acute bisector parallel to the thrust direction (S1 and S2)

and fractures perpendicular to the thrust direction (J1). These dominant calcite-filled fractures are on the forelimb of the thrust and are caused by the bending of the beds during thrusting. In between these dominant fractures are fragments of limestone with discontinuous calcite filled hairline fractures in a variety of different orientations. They appear to form part of a larger fracture network that predates the folding and thrusting.

Two measurement circles were placed on the highly fractured thrust plane (Figure 4.29 c). Although the hairline calcite fractures are common in the measurement circles, the larger S1 and S2 fractures dominate the measurement circles (Figure 4.30).

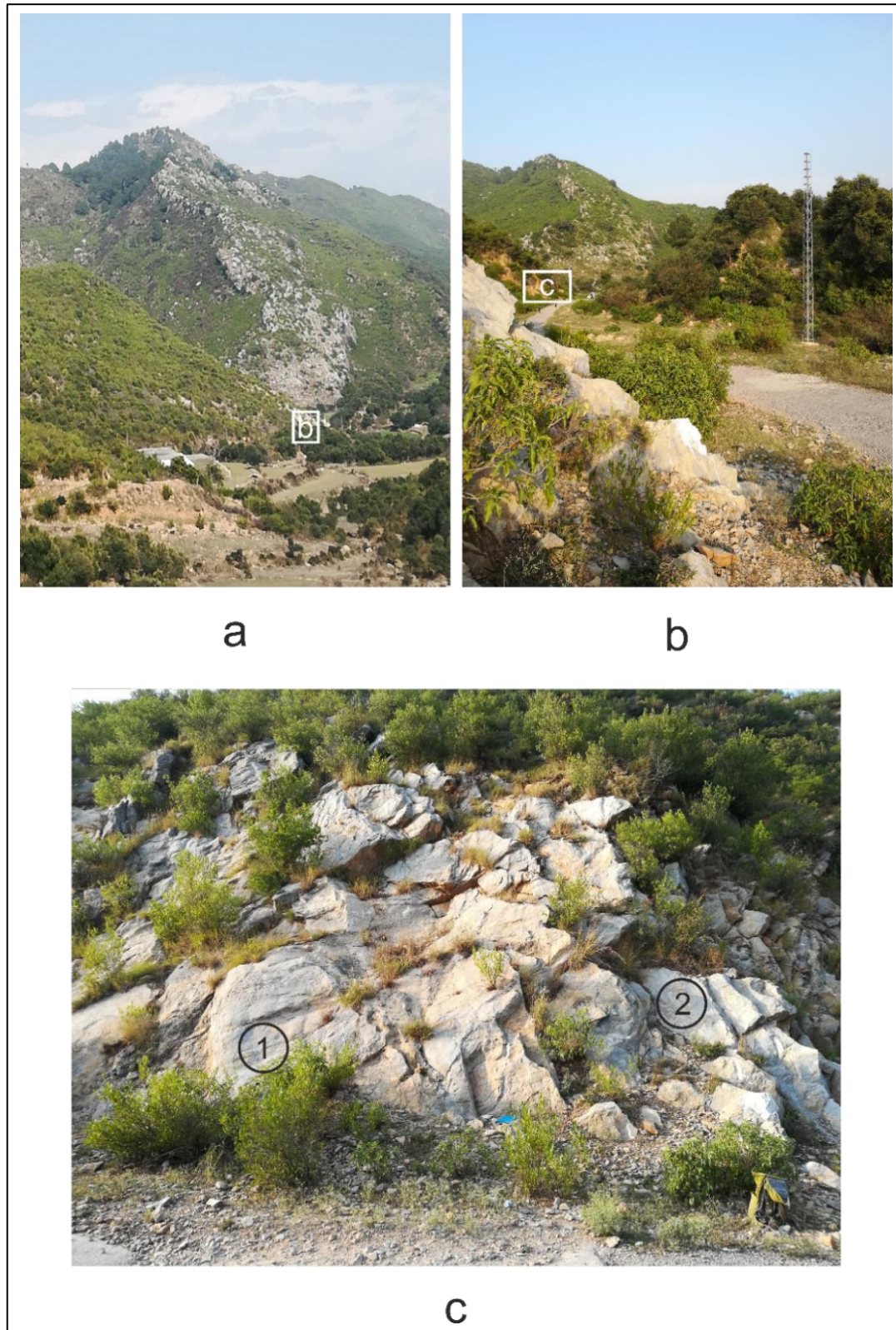


Figure 4.29: View eastward along the Kot Jandaan road (Figure 4.6) showing progressively zoomed in views of site 5 with circles 1 and 2 shown.

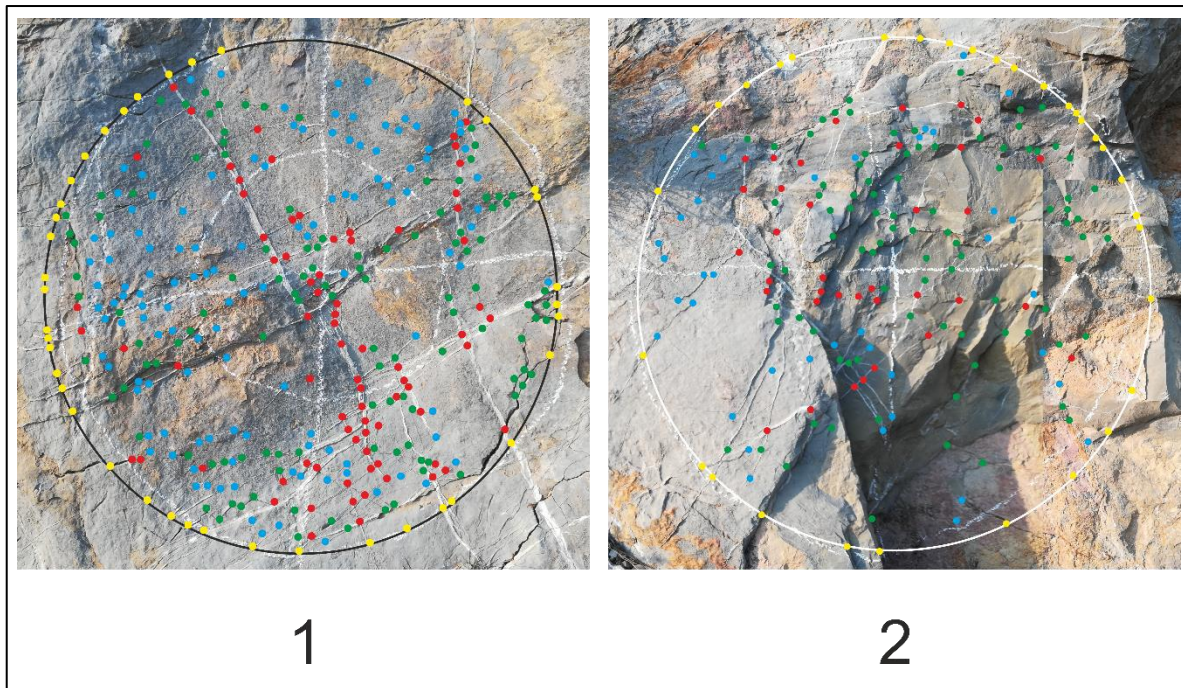


Figure 4.30: Measurement circles, site 5. See Figure 4.29 for location of circles.

Circle 1 has more cross-cutting S1-S2 fractures creating more nodes. In addition to cross-cutting each other, many of these fractures terminate within the circle creating more nodes (Figure 4.31).

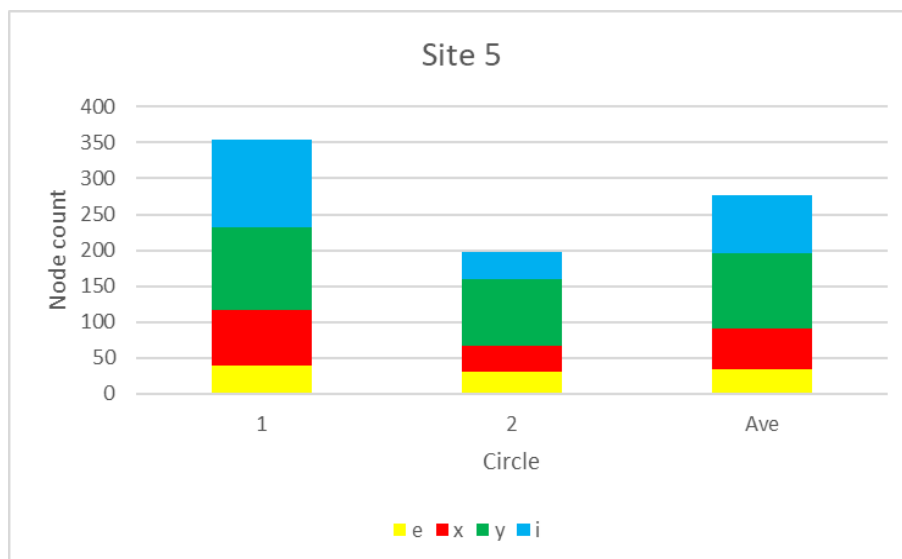


Figure 4.31: Node count, site 5.

Circle 1 has twice as many lines and nodes than circle 2, and nearly double the number of tips (Figure 4.32). The MTL of circle 2 is 50% greater than that of circle 1 (28 cm vs. 12 cm). The fracture density of circle 1 is twice that of circle 2 (Figure 4.33). These quantified fracture characteristics correspond with the abundance of cross-cutting S1 and S2 fractures in circle 1.

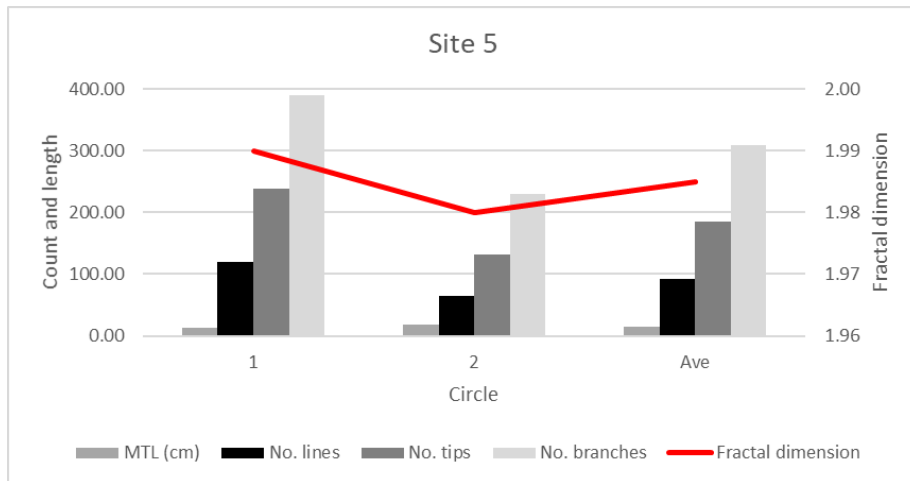


Figure 4.32: Fracture characteristics and fractal dimension, site 5.

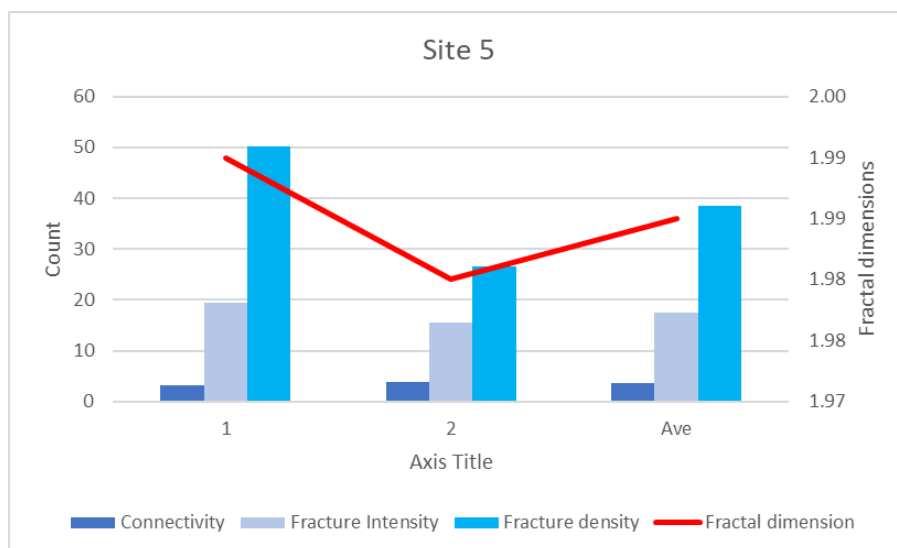


Figure 4.33: Fracture characteristics and fractal dimension, site 5.

To better characterise the closely spaced fractures, three measurement lines were created parallel to the thrust direction (Figure 3.24). Lines 1 and 2 cross-cut the S1-S2 conjugate shears and Line 3 the J1 fractures (Figure 3.24). On average, the fractures are 15 mm apart (Figure 4.34).

The fractures on Lines 1 and 2 are more widely spaced (as they are the prominent S1-S2 conjugate shears), with Line 3 (J1 fractures) being more closely spaced. It is however noted that the J1 fractures occur in clusters separated by portions of less fractured ground.

Table 4.3: Characteristics of the measurement lines at site 5.

Line	Spacing (mm)		
	Average	Maximum	Minimum
1	15	64	1
2	15	37	2
3	10	39	2

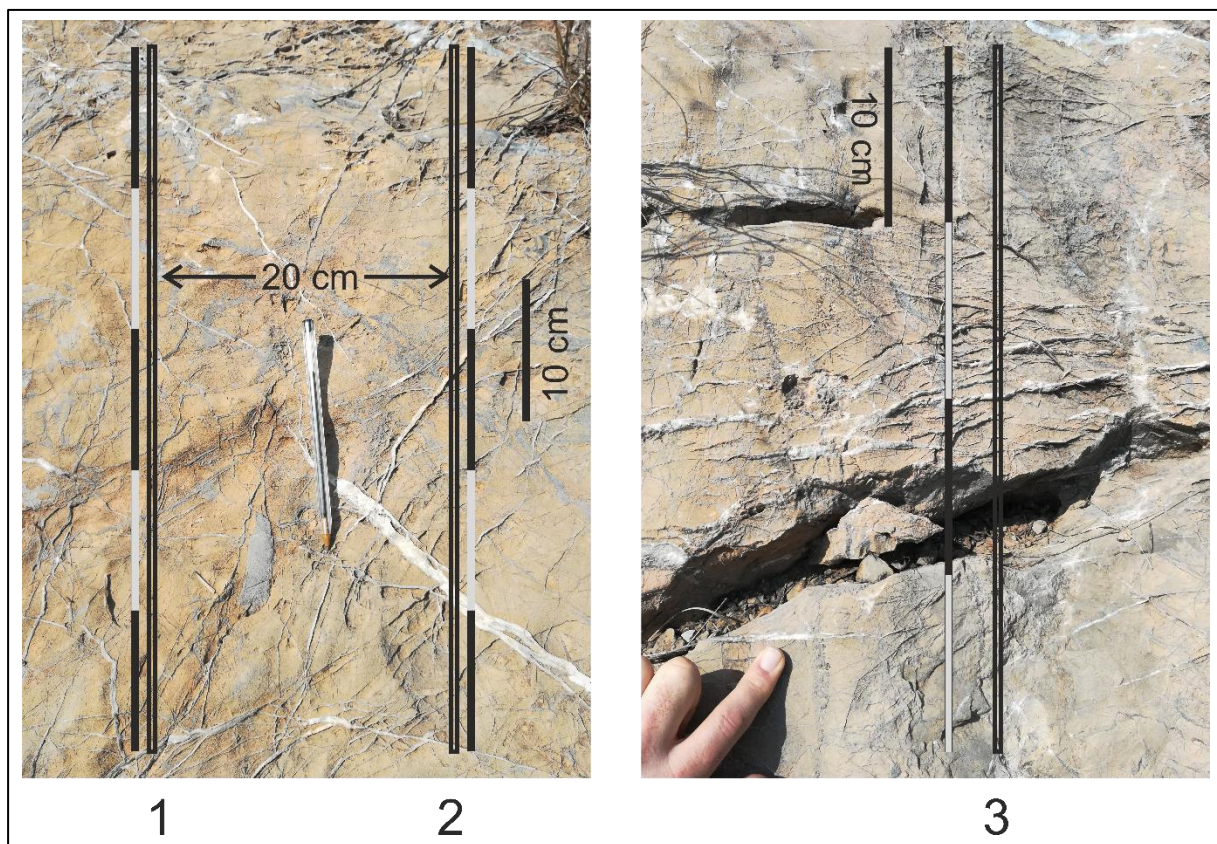


Figure 4.34: Measurement lines, site 5. Lines 1 and 2 are 5 cm long and line 3 is 4 cm long. The short lines are sufficient to characterise the spacing of the fractures.

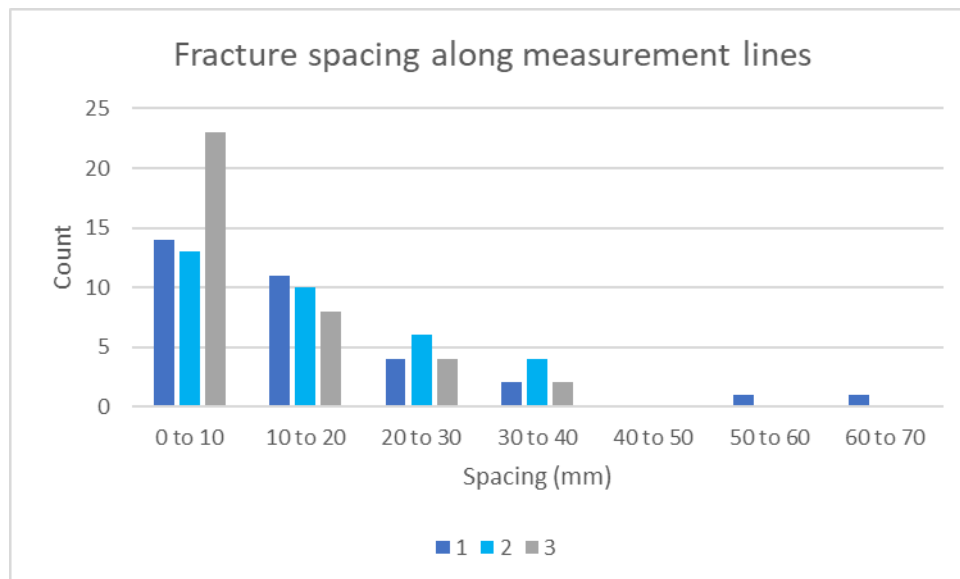


Figure 4.35: Distribution of fracture spacings on measurement lines 1, 2, and 3 at site 5.

Site 5 was actually mapped at the end of a long day after site 6. The kind locals from a farm adjacent to site 5 invited us for tea which was extremely refreshing and gratefully received (Figure 4.36).



Figure 4.36: Local farmer who provided us with a refreshing cup of tea.

4.2.1.6 Site 6

Site 6 is the most northerly of the study sites in the Losar Baoli region (Figure 4.36). It consists of a well exposed southerly dipping back-thrust. The various components of the thrust are visible including the thrust foot-wall, the thrust plane, the fault propagation fold in the hanging-wall, a hanging-wall flat and a triangle zone within the hanging-wall (Figure 4.37).

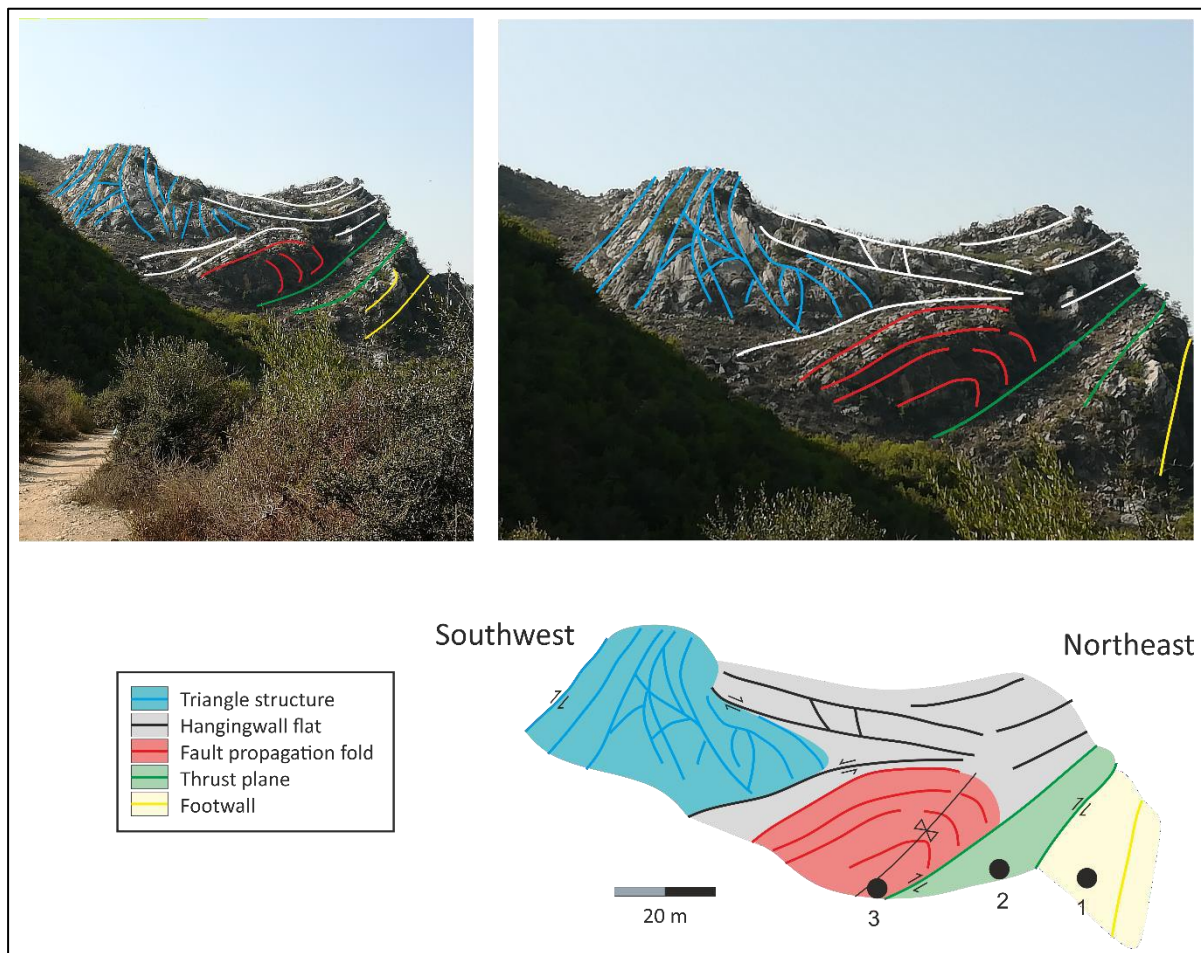


Figure 4.37: View towards site 6 showing the various components of the thrust. Circle positions are labelled 1, 2, and 3. The fault propagation fold above circle 1 is shown in detail in Figure 4.39 and Figure 4.40.

The footwall of the back-thrust at site 6, like site 5, comprises a light grey foraminiferal packstone typical of the upper stratigraphy of the Lockhart Formation. It is only weakly deformed (circle 1, Figure 4.38) with discontinuous, randomly oriented, thin (less than or equal to 1 mm) calcite-filled fractures.

The thrust (circle 2) is characterised by abundant “y” fractures (Figure 4.38 and Figure 4.41). The rock mass within the fault propagation fold (Figure 4.37) is highly fractured by older, iron oxide-rich bedding plane parallel thrust surfaces and steeply dipping fault propagation fold fracture planes. The limestone fragments between these fractures contain abundant small, millimetre-wide, calcite-filled fractures that formed before the folding and thrusting (Figure 4.39 and Figure 4.40).

Although the footwall has the greatest number of nodes (144), the majority of these are “i” type nodes associated with pre-thrusting hairline calcite fractures. These fine fractures are disguised by the strongly developed later fractures (Figure 4.38 and Figure 4.39). The fracture characteristics vary within the different parts of the thrust system, with the most noteworthy being the larger number of tips (Figure 4.42) and lower connectivity of circle 1 (Figure 4.43). Circle 1 also has a significantly lower fractal dimension (1.88) than both of the other circles (1.99).

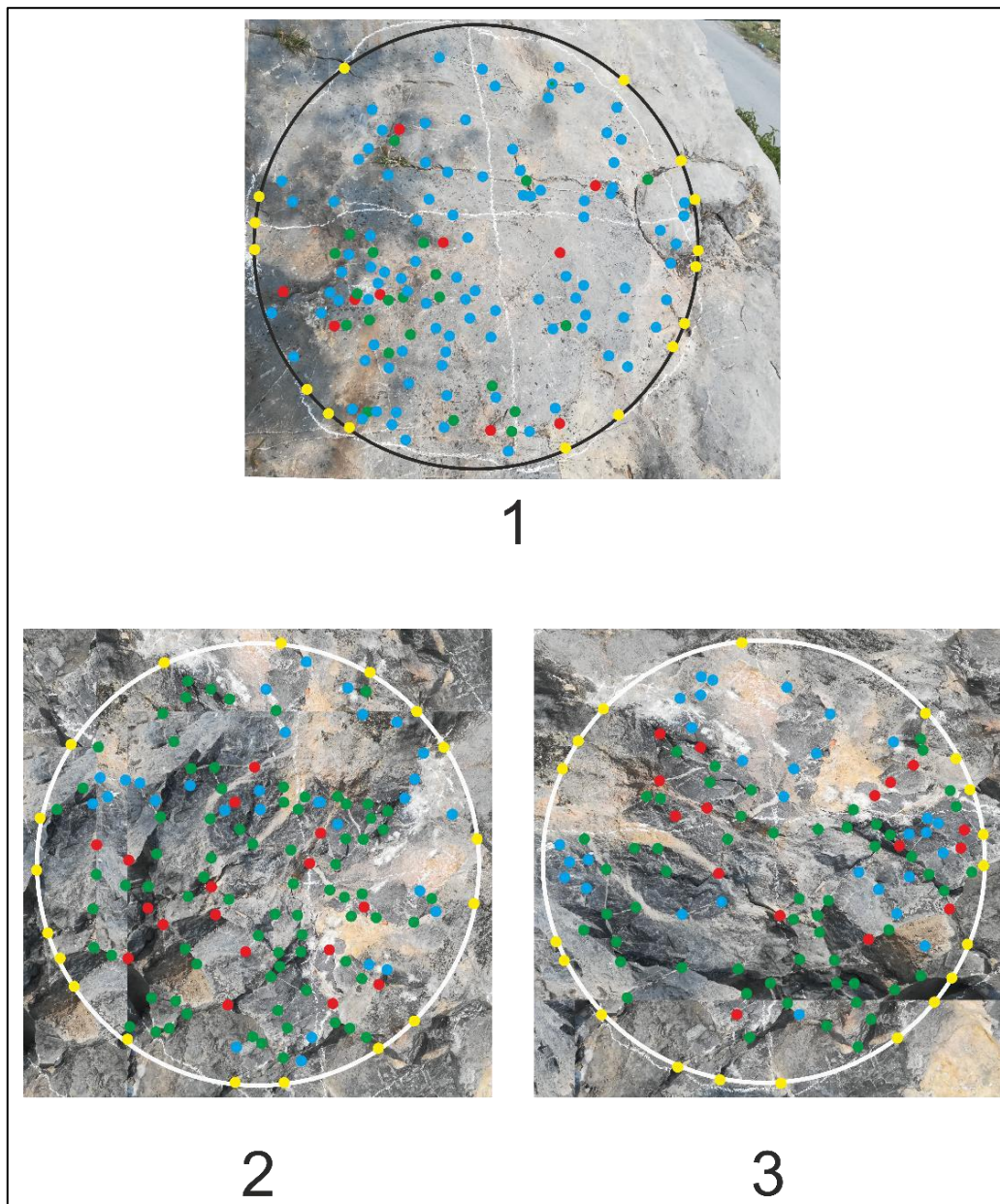


Figure 4.38: Measurement circles at site 3. Figure 4.37 shows the positions of the circles. The ammonite on the right-hand side is not deformed indicating that the footwall is relatively undisturbed by the thrusting.

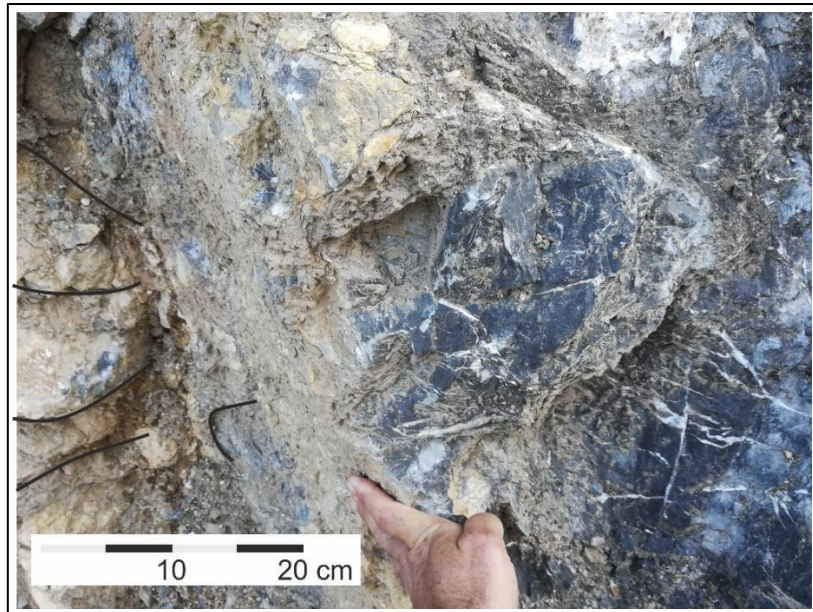


Figure 4.39: Fault propagation fold located just above Measurement circle 1. Steeply dipping fault planes bend portions of the clay-coated bedding upwards through other fragments of bedding. The planes in the fold are both mineralised and unmineralised. Large calcite fractures cross-cut the fold at various angles.

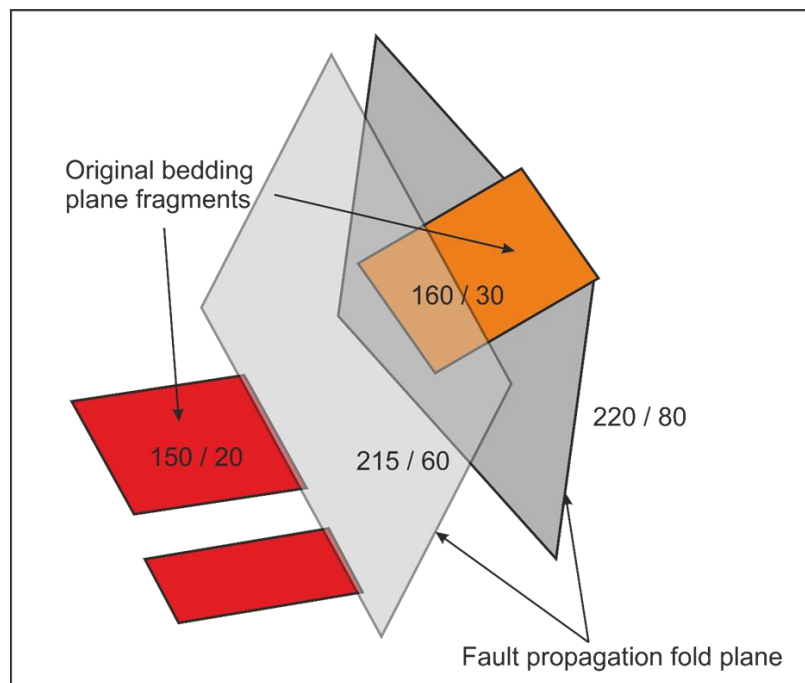


Figure 4.40: Block diagram of the main components of the fault propagation fold shown in Figure 4.39.

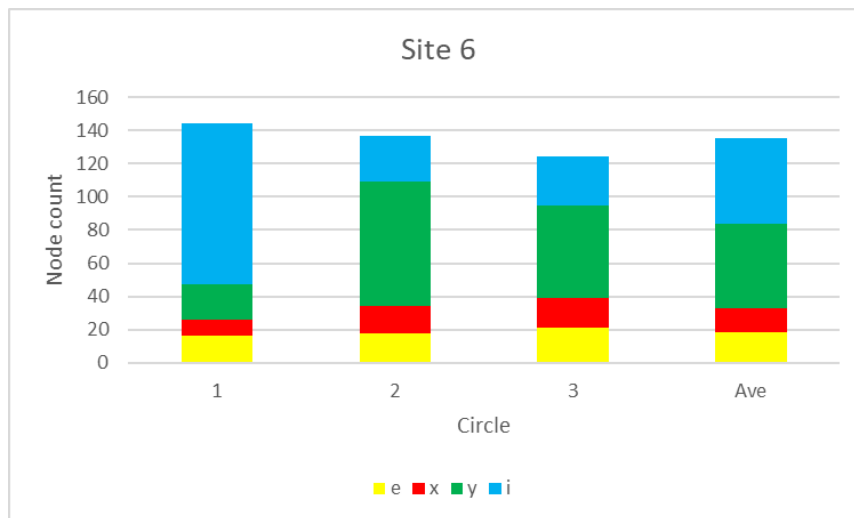


Figure 4.41: Node count, site 6.

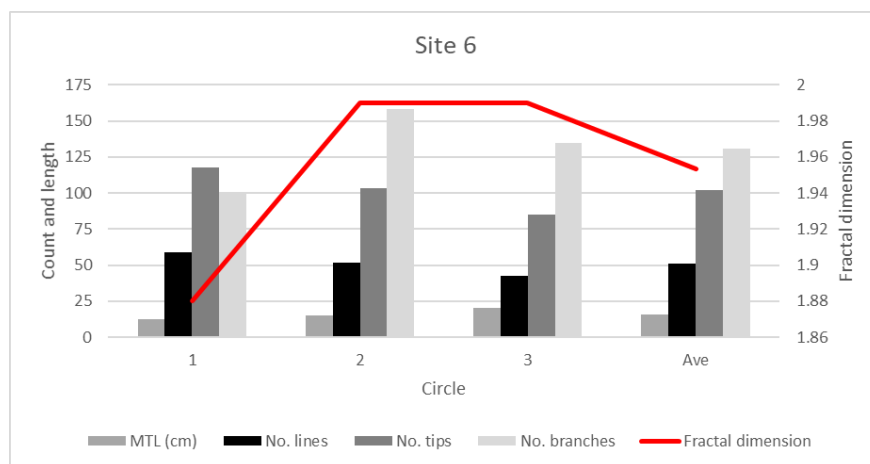


Figure 4.42: Fracture characteristics and fractal dimension, site 6.

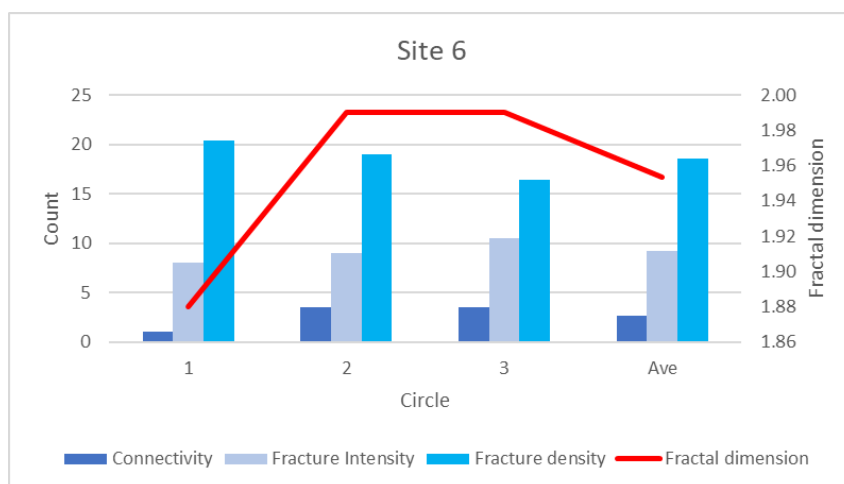


Figure 4.43: Fracture characteristics and fractal dimension, site 6.

4.2.1.7 Summary

Six sites were mapped in the Losar Baoli region (Figure 4.44). The sites were located on the following geological structures:

- 1) Fore-thrust with trailing anticline
- 2) Fore-thrust with trailing anticline
- 3) Fore-thrust with trailing syncline
- 4) Pop-up syncline
- 5) Back-thrust
- 6) Back-thrust

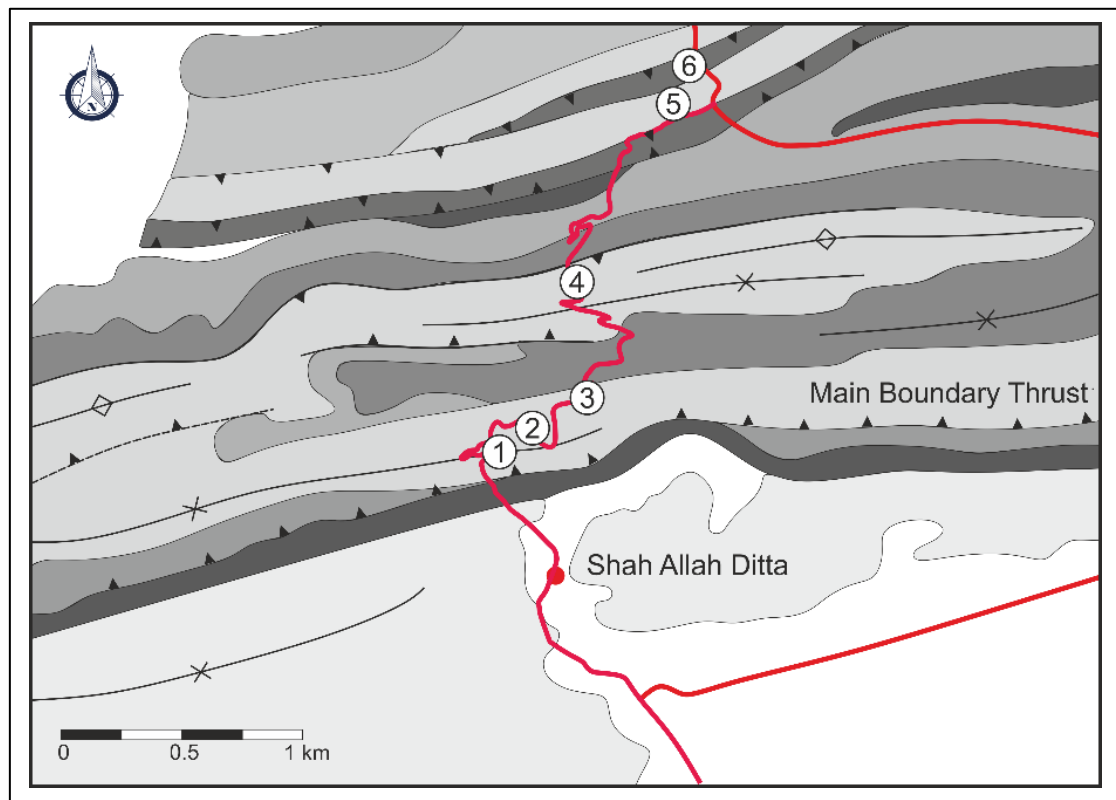


Figure 4.44: Position of the sites in the Losar Baoli region.

A systematic trend in the number of nodes and resultant fracture characteristics, and especially the fractal dimension is evident moving from south to north (i.e., site 1 to site 6). The number of nodes lowest at site 1 and increases progressively towards the centre (Figure 4.45). There is a slight decrease

in the number of nodes at site 4, but this is compensated for by the large number of "i" nodes at this site. The overall number of nodes decreases at the northernmost site 6. The fracture characteristics mimic this node distribution with the number of branches being highest at sites 3 and 5. The mean trace length of site 1 (fore-thrust) is 37 cm, compared to 15 cm and 16 cm for sites 5 and 6 on the back thrust (Figure 4.46).

The two highest fractal dimensions (1.99) are found adjacent to the lowest fractal dimension (1.93) at site 4 (Figure 4.47). This may be related to the higher stresses in the thrusts adjacent to the pop-up structure (site 4) where the confining stresses have been released and the area of rock fractured is less.

Two individual measurements, which is topological and fractal characterisation show the same characteristics; that is an increase in fracturing in both the fore-thrust and back-thrust towards each other and a decrease in the fracturing in the pop-up zone in between.

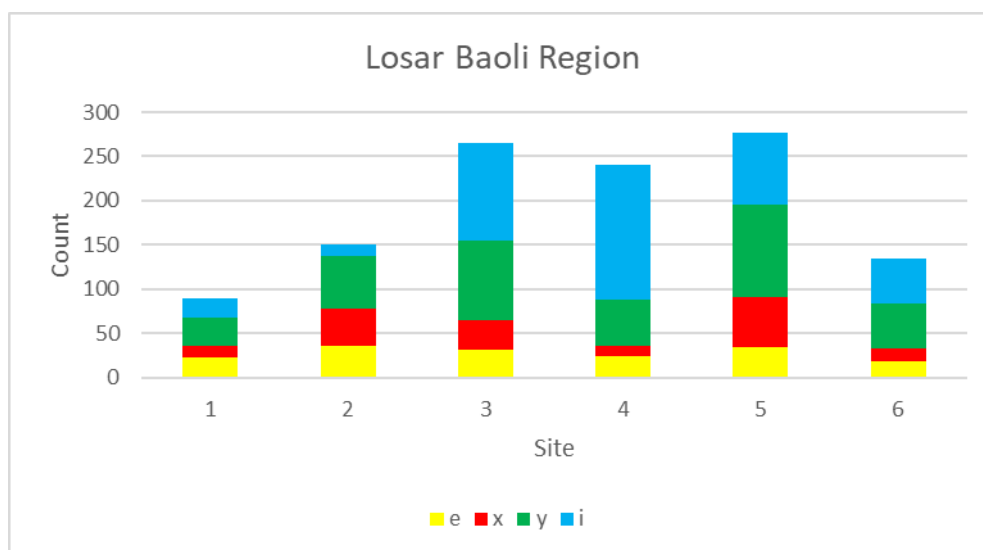


Figure 4.45: Node counts at sites across the Losar Baoli region.

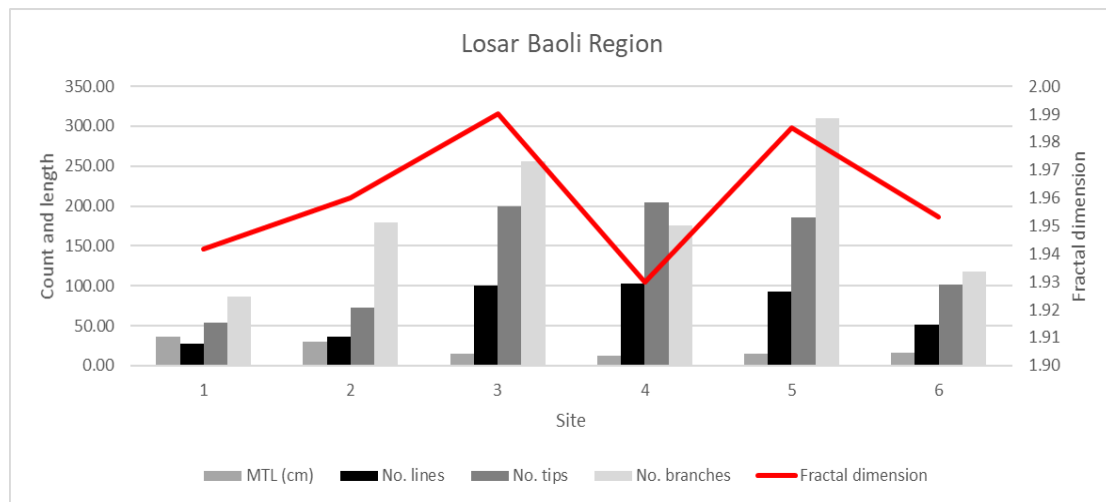


Figure 4.46: Fracture characteristics and fractal dimensions across the Losar Baoli region.

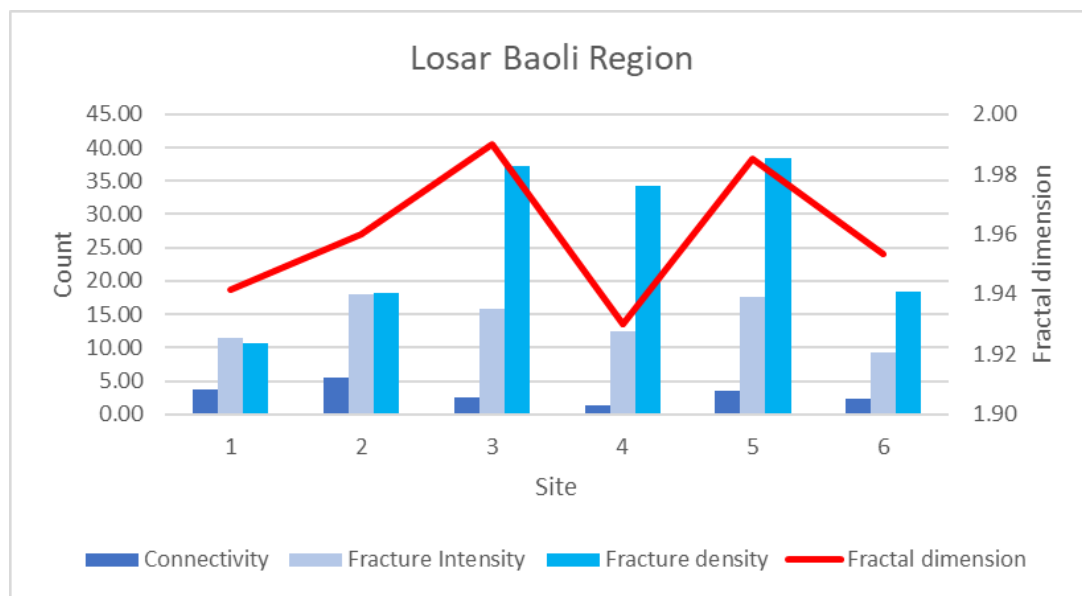


Figure 4.47: Fracture characteristics and fractal dimensions across the Losar Baoli region.

4.2.2. Makhniyal region

This region is located between two and five kilometres north-east of the Islamabad Capital Territories and the Khyber Pakhtunkhwa border, along the Pir Sohawa Road. The village of Makhniyal (33° 49.3' N, 79° 7.3' E) is sited on a hilltop developed on an overturned anticline in fine-grained Kawagarh Formation mudstone (Figure 4.48). The strata, including the axis of large-scale overturned anticline have a strike and dip parallel to the large regional scale thrust fault encountered across the area (Figure.4.49). The thrust fault has been termed the “Whispering Pines Fault” as the fault and adjacent rocks were mapped at four different sites on the road to the Whispering Pines Resort (Figure 4.50).



Figure 4.48: Road to the hilltop village of Makhniyal.

The mapping sites are in rocks ranging in age from the Upper Cretaceous Kawagarh Formation to the Early Eocene Nammal Formation (Table 4.4 and Figure.4.49). Half of the mapping sites are in the Nammal Formation as it has good exposure of the Whispering Pines Fault (Figure 4.50 and Figure 4.51). The

difference in the rock types of the other formations and associated deformation styles is compared with the those of the Nammal Formation in this area.

Table 4.4: Location and stratigraphy of study sites.

Site	Latitude (N)	Longitude (E)	Formation	Age	Structure
1	33.807°	73.127°	Patala	Late Palaeocene	Fold
2	33.807°	73.126°	Nammal	Early Eocene	Fore-thrust
3	33.807°	73.127°	Nammal	Early Eocene	Fore-thrust
4	33.807°	73.128°	Nammal	Early Eocene	Fore-thrust
5	33.812°	73.134°	Nammal	Early Eocene	None
6	33.815°	73.134°	Patala	Late Palaeocene	Normal fault
7	33.820°	73.133°	Kawagarh	Upper Cretaceous	Overtured anticline
8	33.826°	73.129°	Lockhart	Late Palaeocene	None

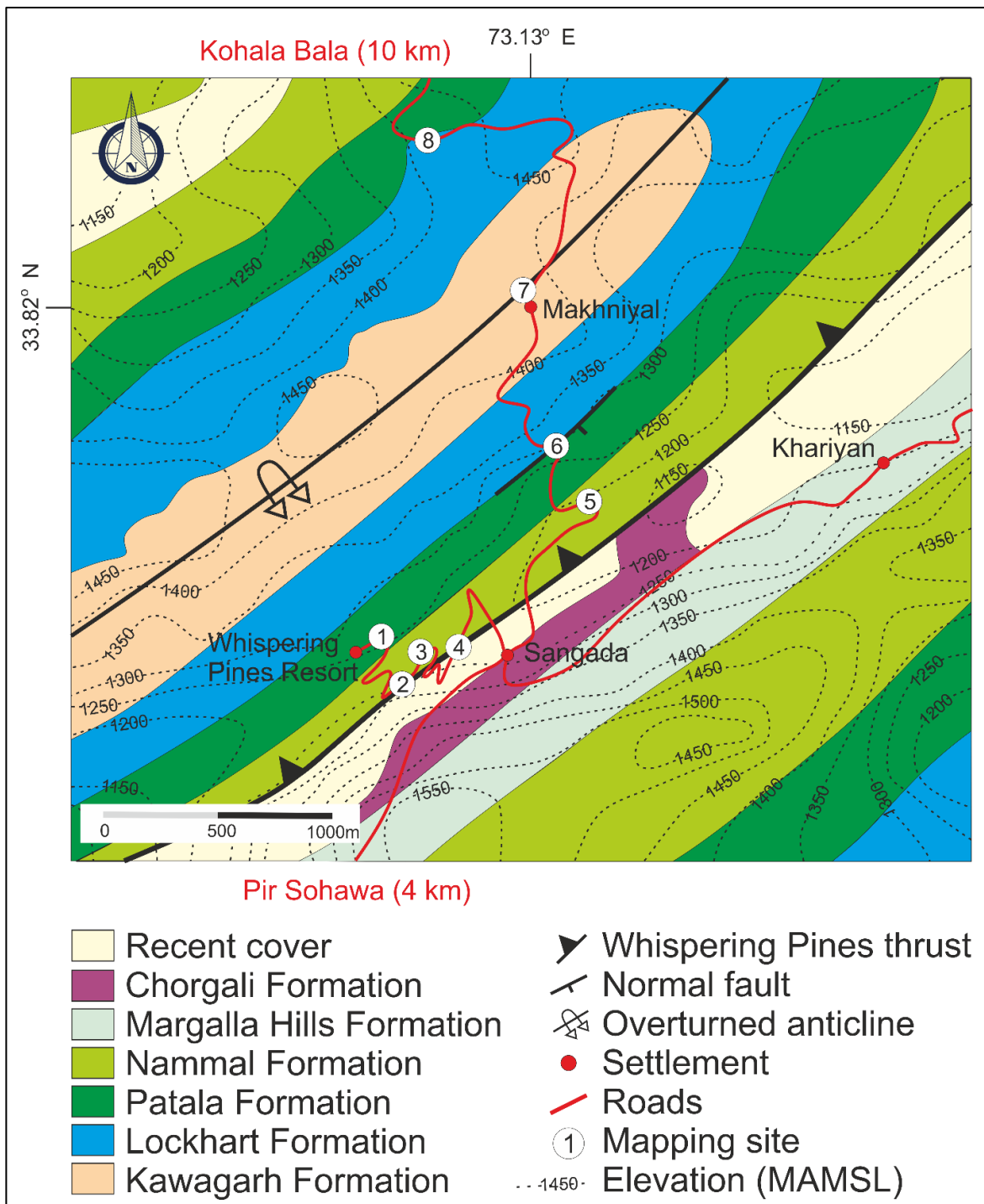


Figure.4.49: Geological map of the Makhniyal region. The dominant NE-SW striking thrust, and overturned anticline control the orientation of the stratigraphy. Figure 4.50 provides a more detailed view of the distribution of sites 1 to 4. Modified after Ali (2014).

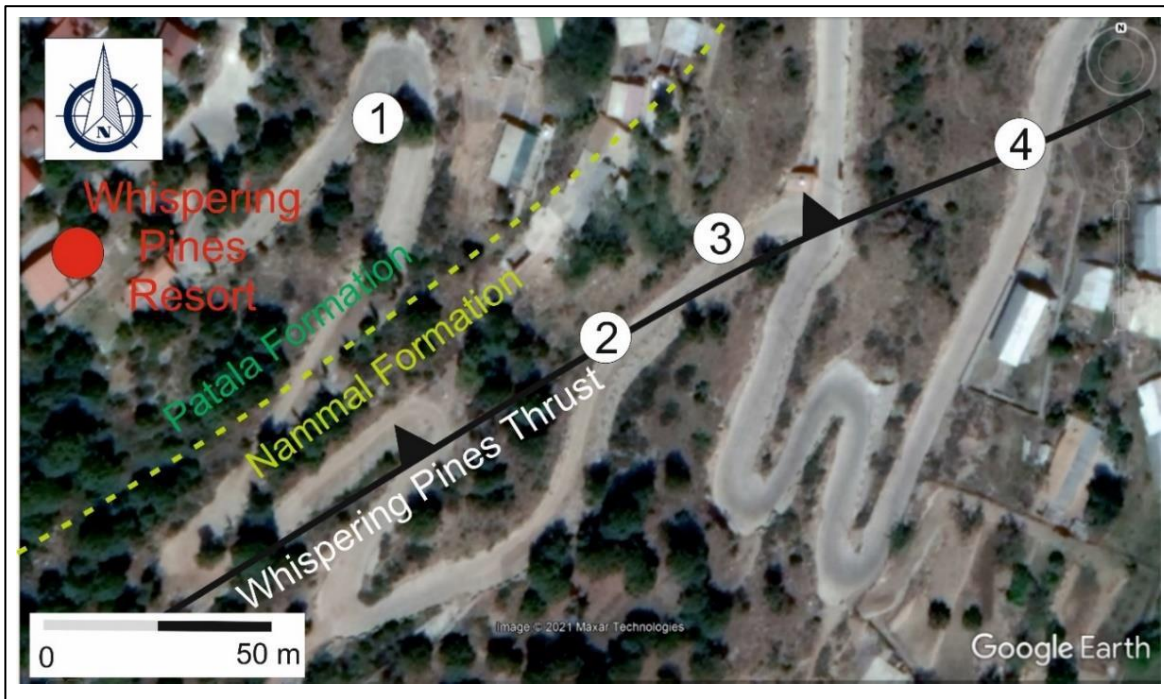


Figure 4.50: Google Earth image showing the geology and the position of sites 1 to 4 relative to the thrust on the road to the Whispering Pines Resort. Figure 4.49 is a geological map of the entire region.

4.2.2.1 Site 1

The Patala Formation is exposed at site 1 at the top of the hill. The rocks are dominated by grey-brown coloured mudstone beds interbedded with 10 to 20 cm thick grey limestone beds grouped together forming units of approximately 1 m thickness. The limestones are highly fragmented into centimetre to decimetre sized pieces and are stained orange-brown with iron oxides such as goethite and limonite, but when it is fresh it is a dark grey colour. The strata have an overall orientation like that of the Whispering Pines Thrust (320/60). Smaller scale folds are also apparent in the strata of the Patala Formation – it is suggested that these are caused by small amounts of differential movement on bedding surfaces parallel to the thrust that cause small-scale folding and faulting and intense fracturing (Figure 4.51 and Figure 4.52).

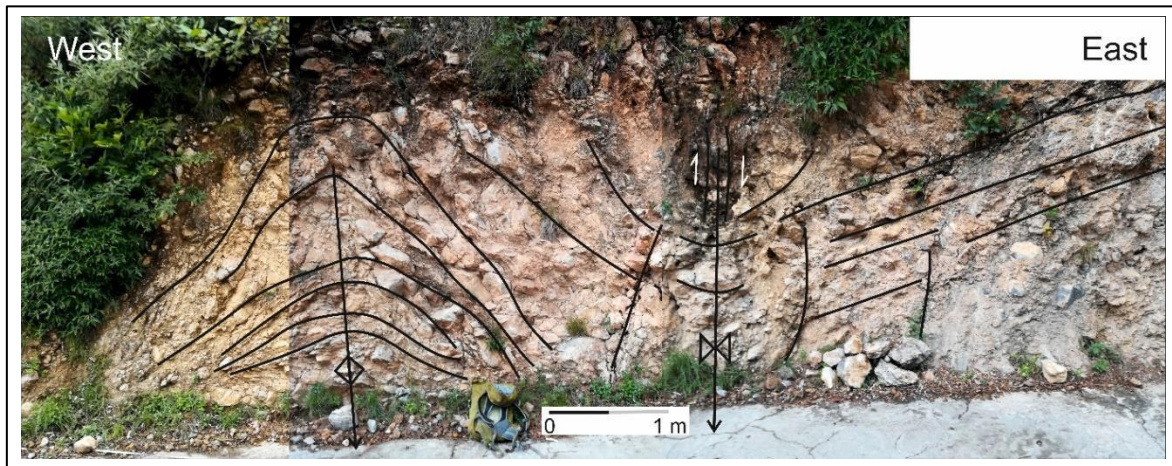


Figure 4.51: Photo-mosaic of site 1 showing highly fractured rock mass and iron oxide staining. View towards Whispering Pines Thrust (approximately 75 m ahead).

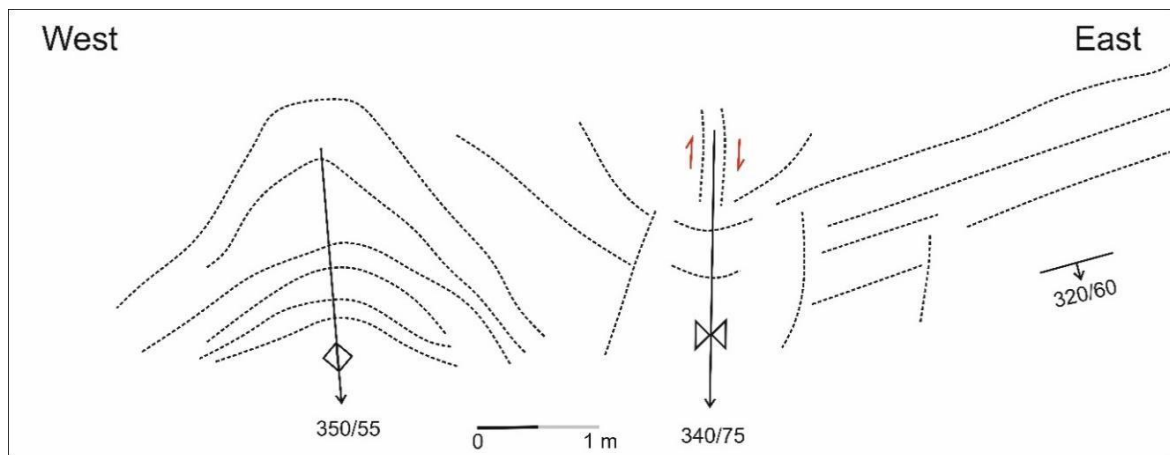


Figure 4.52: Line drawing of site 1 showing the general orientation of the strata (320/60) and plunging anticline (350/55) and syncline (340/75) pair caused by slight differential movement related to the Whispering Pines Thrust.

4.2.2.2 Site 2

Site 2 is a 45 m long section that cuts across the Whispering Pines Fault with the thrust foot-wall exposed up to 12 m along the section, the thrust between 12 and 42 m and the hanging-wall up to 45 m (Figure 4.53). Both the hanging-wall and foot-wall are composed of Nammal Formation. The foot-wall rocks consist of decimetre-thick beds of tightly cemented packstone interbedded with centimetre-thin grey mudstone. These rocks are strongly sheared, but the orientation and spacing of bedding is still visible. In contrast to this, the Nammal Formation in the immediate hanging-wall of the

thrust is highly crushed as it is folded into a fault tip fold. Within the thrust, distinct faults and zones of secondary folds are present. The fault zones appear to dip steeply towards the west as shown in Figure 4.54 through to Figure 4.53, but this is due to the orientation of the road-cutting, with the fault zones actually dipping steeply to the north-east. An exposure consisting of fragments of calcite-coated fault blocks is visible between 14 and 24 m because the road-section is at an acute angle to the thrust allowing a large exposure of these fractures.

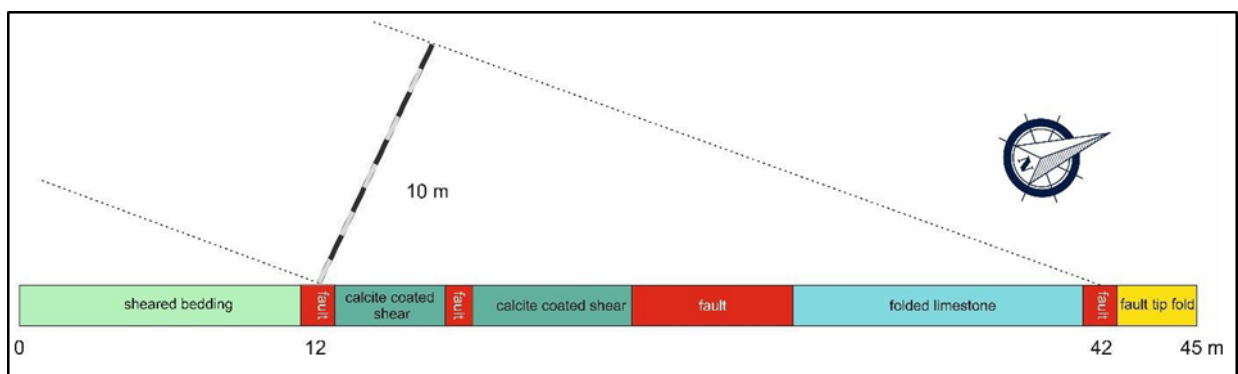


Figure 4.53: Diagram showing the orientation of the Whispering Pines Thrust. The rock sequence is drawn parallel to the road edge for easy comparison with Figure 4.54 and Figure 4.55.

1 m wide measurement circles were placed in the hanging- and foot-walls of the thrust as well as the thrust itself (Figure 4.54), circles 1, and 2 were located in the foot-wall, circles 3 to 8 in the thrust and circles 9, and 10 in the hanging-wall. Photographs of the measurement circles with their fracture node types indicated are shown in Figure 4.57 and Figure 4.58. The fractal dimensions of the fracture distribution within the circles was determined by placing a measurement grid with square box sizes between 1 m and 5 cm over the measurement circle and counting the number of boxes containing fractures. Utilising the box-counting method, it was possible to determine the fractal dimension of each circle.

Analysis of the number of nodes (fracture intersections), both in the individual categories (“e”, “x”, “y”, and “i”) and as a total for each circle does not show a clear discrimination between the various structural elements (hanging-wall, thrust and foot-wall) exposed at this site (Figure 4.59).

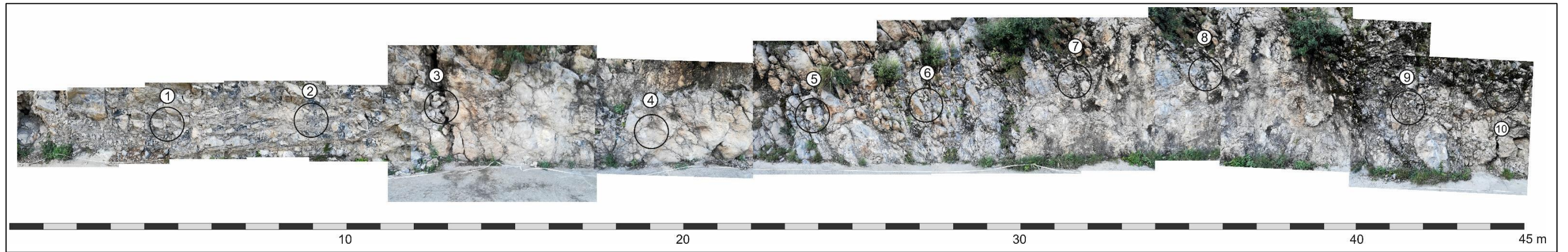


Figure 4.54: Photo-mosaic of the Whispering Pines Thrust outcropping at site 2 - view northward. Positions of the measurement circles shown.

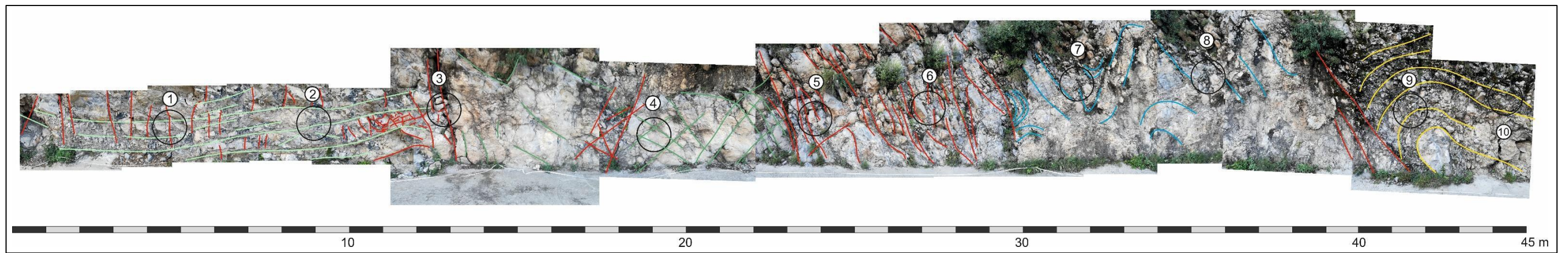


Figure 4.55: Photo-mosaic of the Whispering Pines Thrust outcropping at site 2 with major fracture trends drawn on. The thrust extends from 12 m to 42 m in this view but it is only 10 m wide and at an acute angle to the section Figure 4.53).

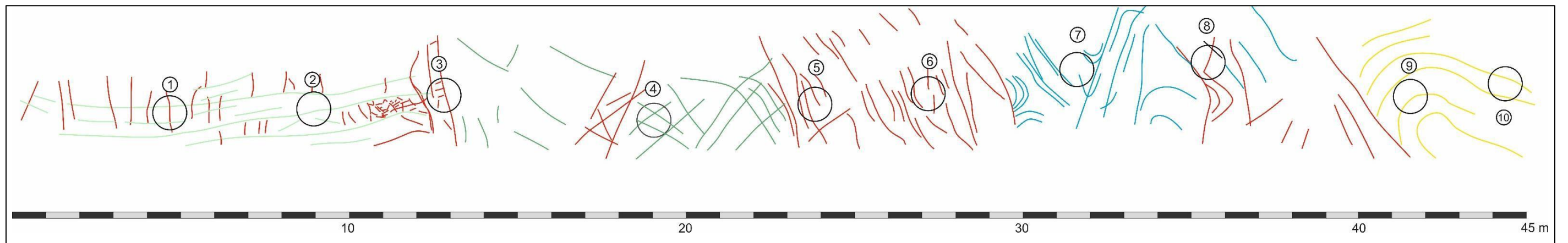


Figure 4.56: Line drawing of major fracture trends of the Whispering Pines Thrust at site 2. The thrust extends from 12 m to 42 m in this view but it is only 10 m wide and at an acute angle to the section (see Figure 4.53).

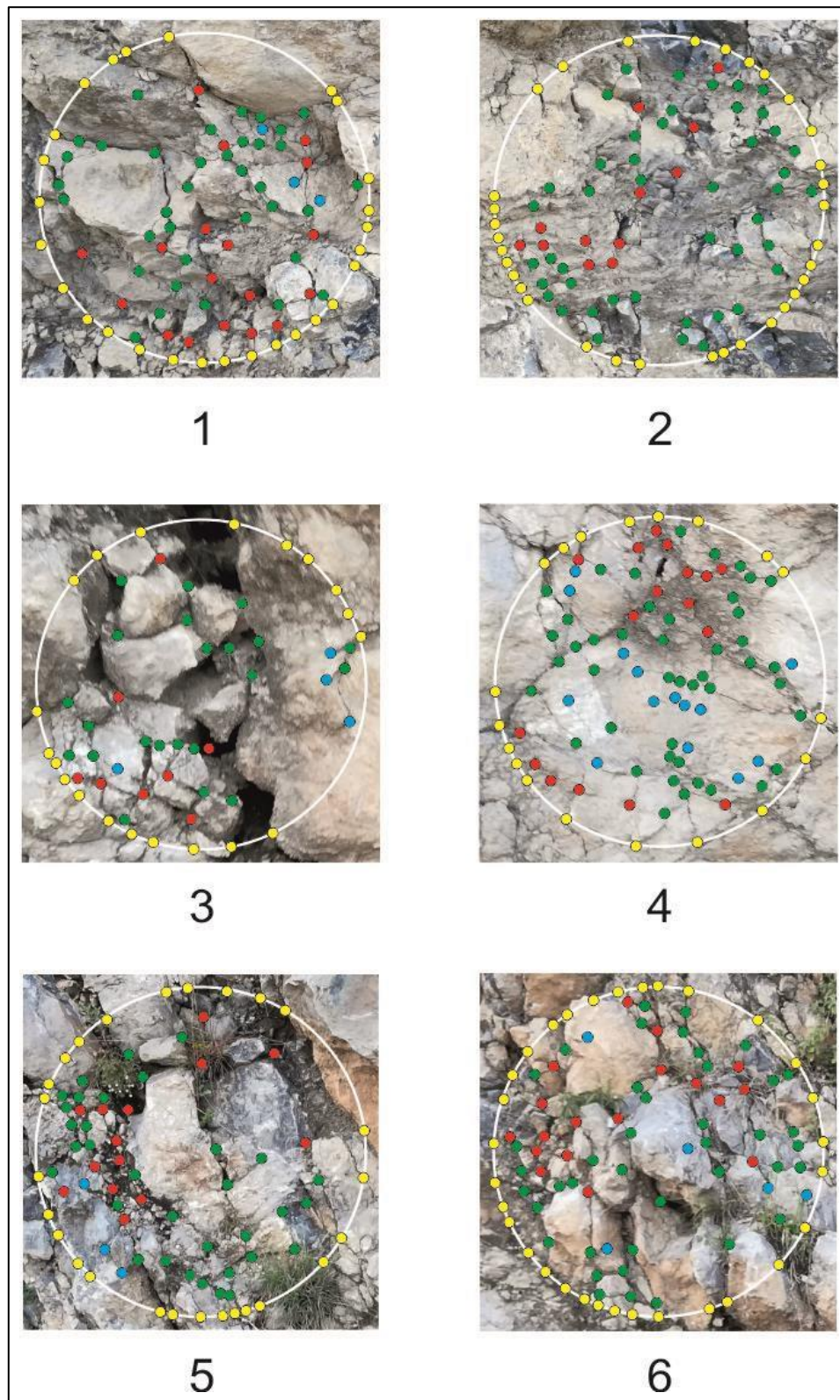


Figure 4.57: Measurement circles 1 to 6 at site 2. See Figure 4.56 for position of circles. Circles 7 to 10 are shown in Figure 4.58 Standard colours are used throughout to show the various node types, that is yellow for “e”, red for “x”, green for “y” and blue for “i”.

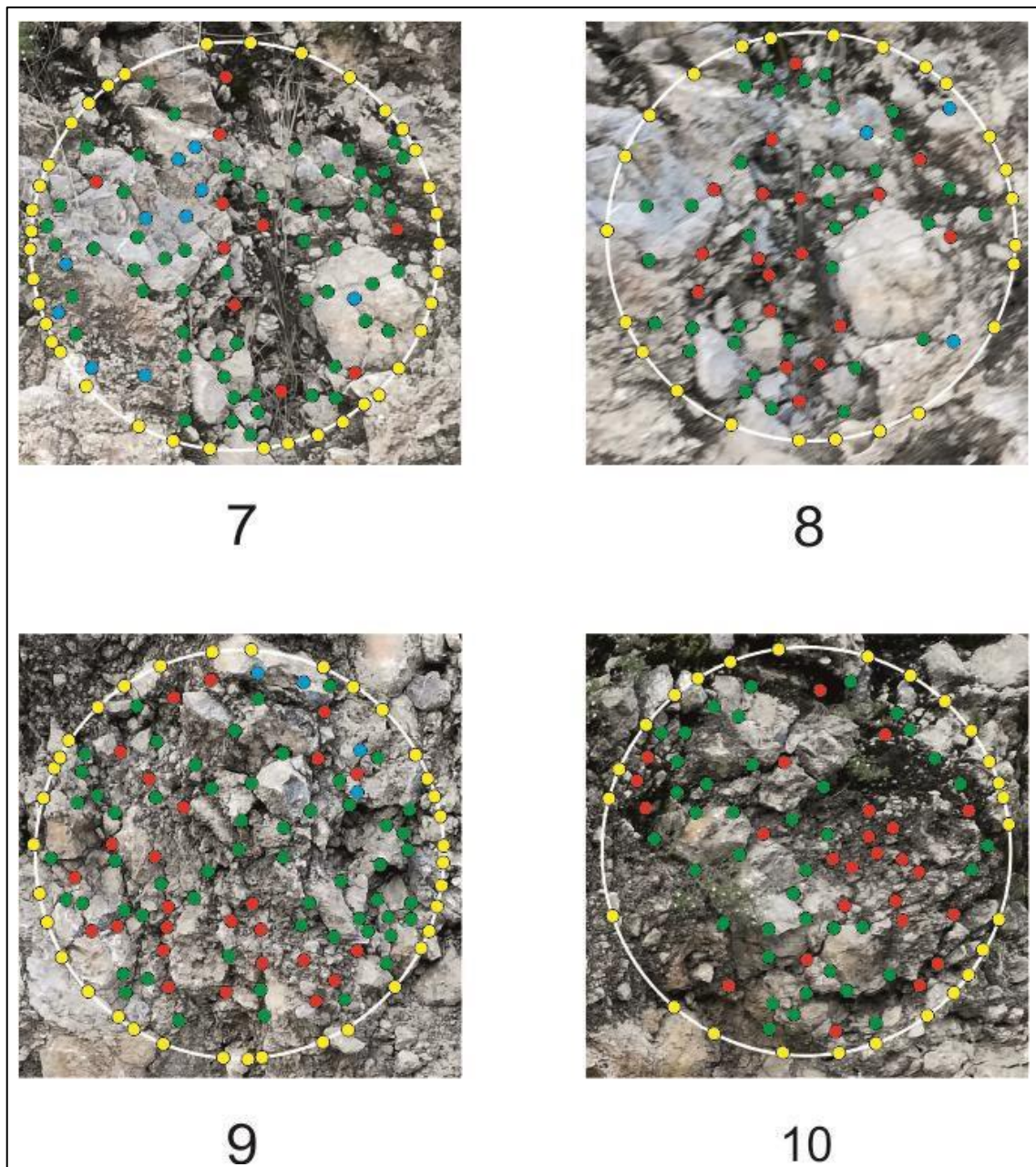


Figure 4.58: Measurement circles 7 to 10 at site 2. See Figure 4.57 for position of circles 1 to 6.

The “i” nodes are rare throughout site 2, making up only 5% of the total number of nodes. There are more than three times as many “y” (terminating) as “x” (cross-cutting) nodes at site 2 (Figure 4.59).

Number of nodes at site 2 – derived from the measurement circles shown in Figure 4.57 and Figure 4.58.

The topological analysis of the data does show some differences in the various domains. In general, the mean trace length of the fractures is longer (50 cm) within the thrust, apart from circle 4, where the mean trace length is 25 cm (Figure 4.60). Figure 4.60 shows that the number of tips and branches are

slightly higher within the thrust. The fracture connectivity is higher in both the foot-wall (6.09) and hanging-wall (5.31) than the thrust (4.84) as shown in Figure 4.61. This may be because the hanging-wall and foot-wall are highly crushed whereas the thrust itself consists of larger fragments of entrained rock. Circle 4 has the greatest number of “i” nodes and lowest fractal dimension. This relationship is not consistent as the circle with the second-highest number of “i” node (circle 7) has the highest fractal dimension of the site.

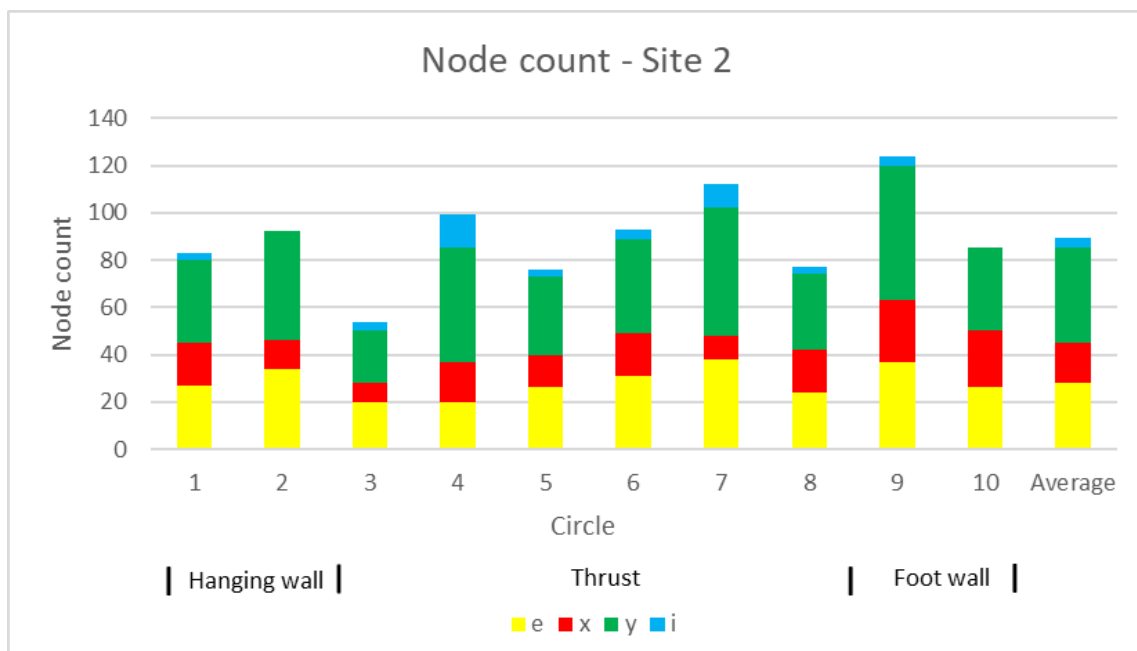


Figure 4.59: Number of nodes at site 2 – derived from the measurement circles shown in Figure 4.57 and Figure 4.58.

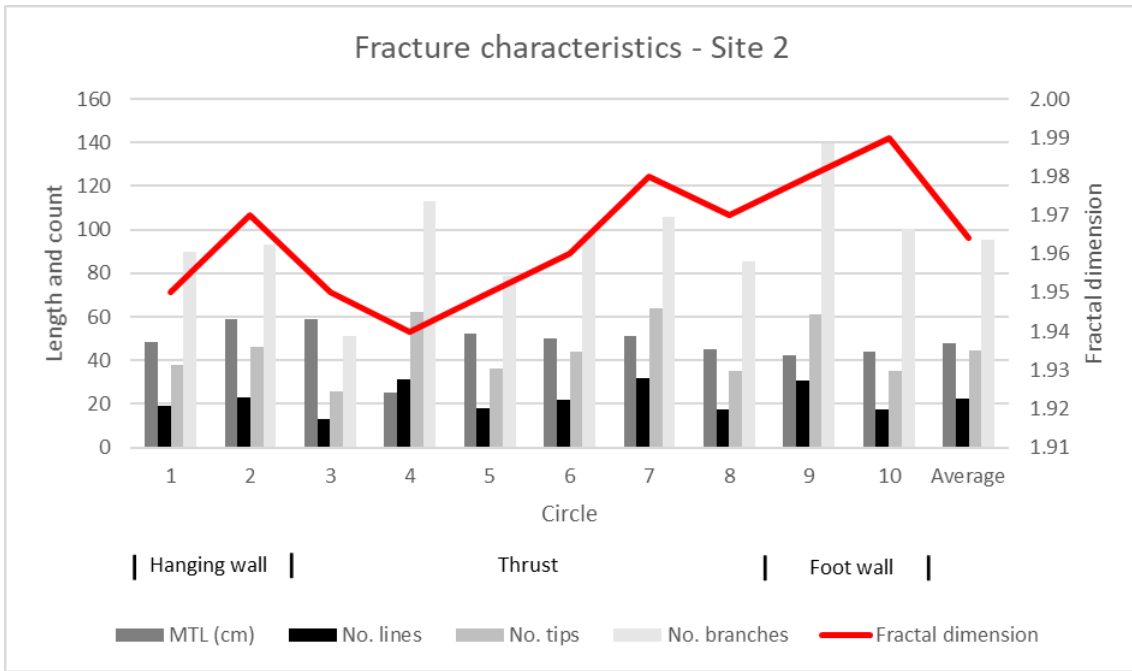


Figure 4.60: Mean trace length (MTL) in centimetres, number of lines, nodes, and branches and fractal dimension at site 2.

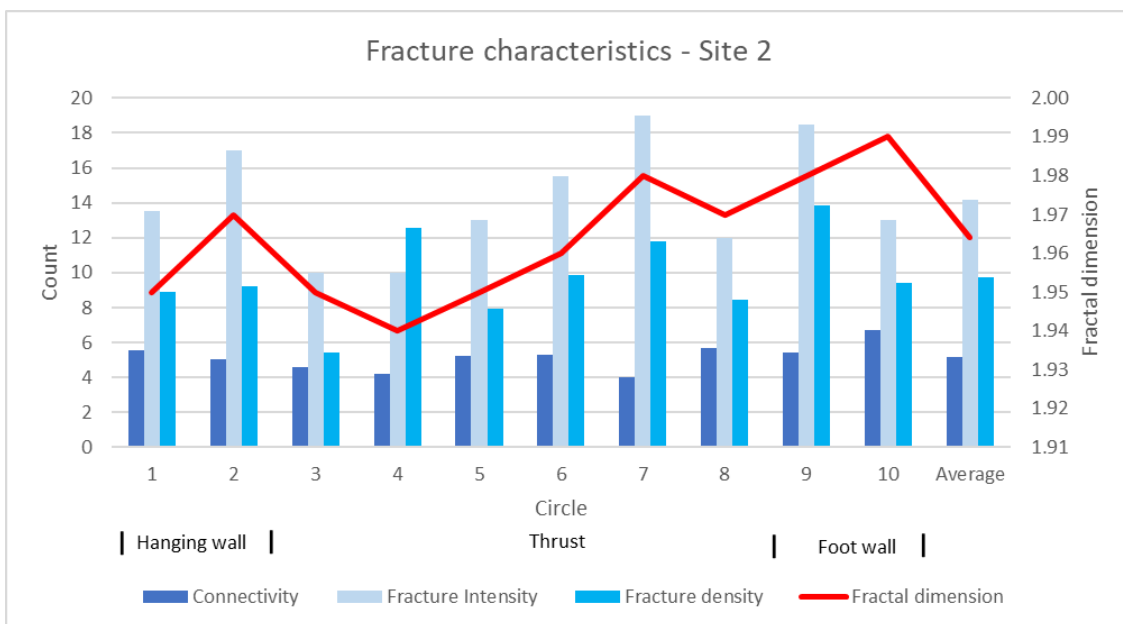


Figure 4.61: Connectivity, fracture intensity, fracture density and fractal dimension at site 2. The fracture intensity is highest in the thrust zone, increasing towards the thrust surface.

4.2.2.3 Site 3

The Whispering Pines Thrust is a laterally extensive structure (Figure.4.49) with intense fracturing of the rock mass in the immediate hanging-wall and foot-wall (Figure 4.51 and Figure 4.54). However, the damage zone of this thrust is of limited width, due to the straight orientation of the thrust surface in this area. Site 3 is approximately 50 m east of site 2 and 10 m into the hanging-wall of the Whispering Pines Thrust, but the fracture pattern at this site does not show any influence of the thrust (Figure 4.62). Rather, the fracture spacing, and orientation is controlled by the thickness and orientation of the bedding of the Nammal Formation. Five sedimentary layers are clearly recognisable at this site (Figure 4.62 and Figure 4.63) consisting of alternating thick (approximately 1 m) and thin (approximately 15 cm) beds. The thick beds consist of nodular limestone and the thin of alternating layers of limestone and shale. The fractures in the thicker beds (labelled a, c, and e in Figure 4.63) are mainly vertical where-as in the thinner beds (labelled b, and d, in Figure 4.63) are sub-horizontal, possibly related to bedding parallel shear. Various fracture sets are restricted to a single bed.

Four measurement circles (Figure 4.64) were employed at site 3 to characterise the fracture pattern. As beds b, and d are only 15 cm thick, it was not possible to place a measurement circle on these beds alone. Rather, two sets of circles were utilised. Circles 1 and 2 were located on thicker bed whilst circles 3 and 4 crossed beds b, c, and d and beds c, d, and e, respectively (Figure 4.63). This was to ensure that data regarding the thinner beds would be obtained.

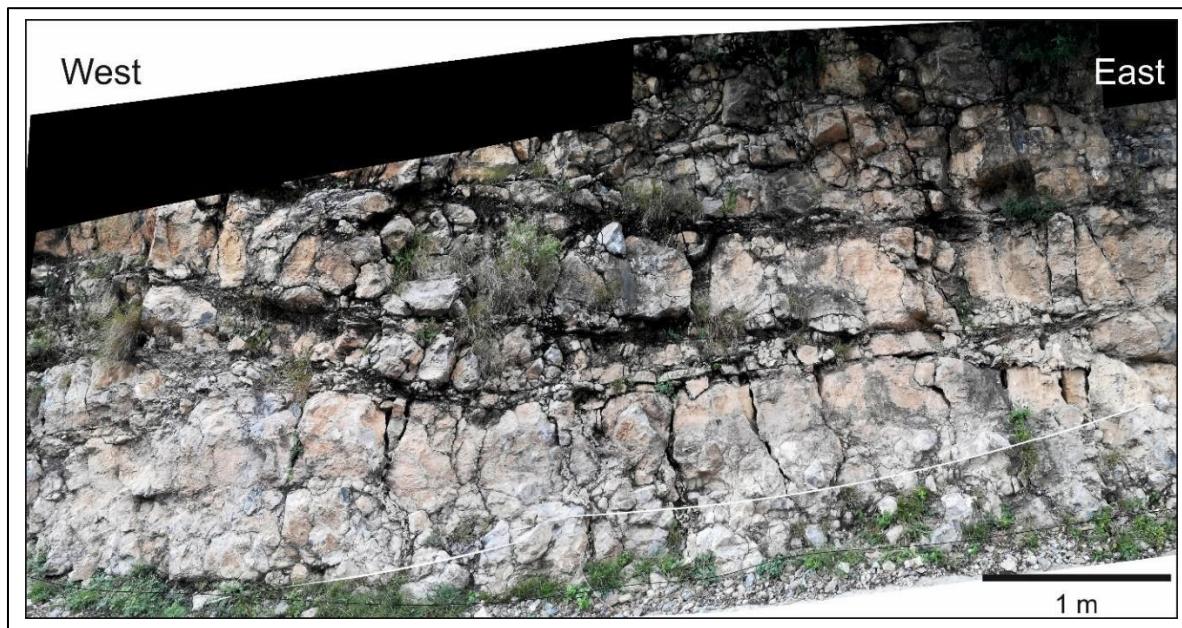


Figure 4.62: Composite, orthorectified image of the Nammal Formation outcrop at site 3. Although this is only 50 m east of the outcrop of the Whispering Pines Thrust and, in the hanging-wall, 10 m north of the thrust plane (see Figure 4.53), no damage specifically related to the thrust can be seen.



Figure 4.63: Line drawing of the fracture patterns at site 3 derived from Figure 4.62 . Five layers are recognised with the thicker layers (a, c, and e) being dominated by near-vertical fractures (shown in black). In contrast, the thinner layers (b, and d) contain mainly horizontal fractures (shown in red). The positions of measurement circles are also indicated in blue.

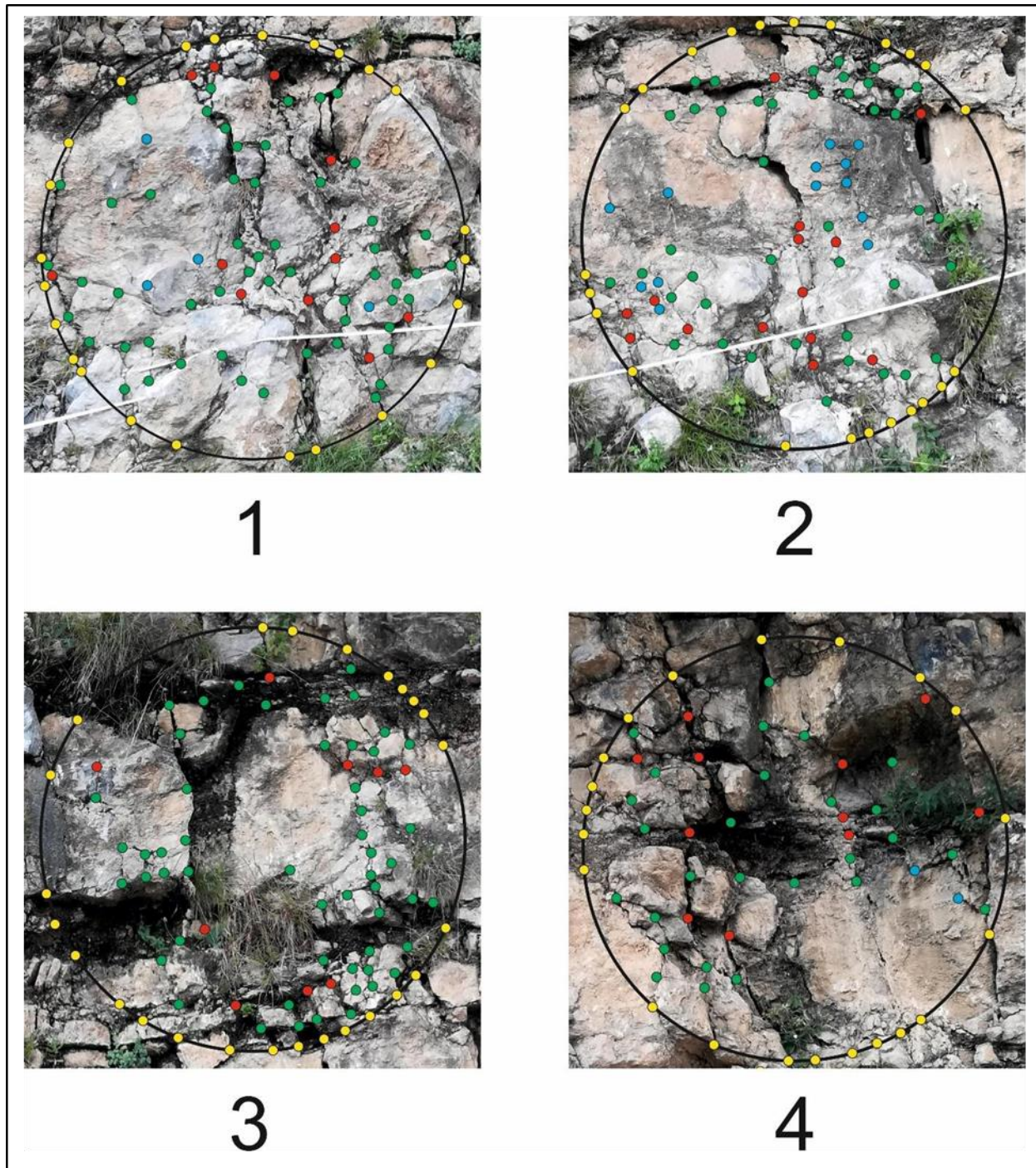


Figure 4.64: Measurement circles at site 3. See Figure 4.63 for positions.

The circles in the thicker layer (1 and 2 in Figure 4.63) have very similar numbers of all fracture types whereas the circles that incorporate the thinner layers (3 and 4 in Figure 4.63) have greater differences in number of nodes, especially “y” nodes (Figure 4.64). This is due to the strongly developed bedding parallel shear in the lower third of measurement circle 3 (Figure 4.63).

Circles 1 and 2 each have 88 and 89 nodes in total, but ten more of the nodes are “y” and eight fewer are “i” in circle 1 resulting in circle 1 having a higher fractal dimension. This is correlated with the higher fractal dimension of circles 3 and 4, which also have more “y” nodes and fewer “i” nodes like circle 1, (Figure 4.65 and Figure 4.66). Circle 3 has the greatest number of nodes and hence the number of lines, tips and branches is highest in this circle (Figure 4.66). Interestingly, circle 3 has the lowest mean trace length.

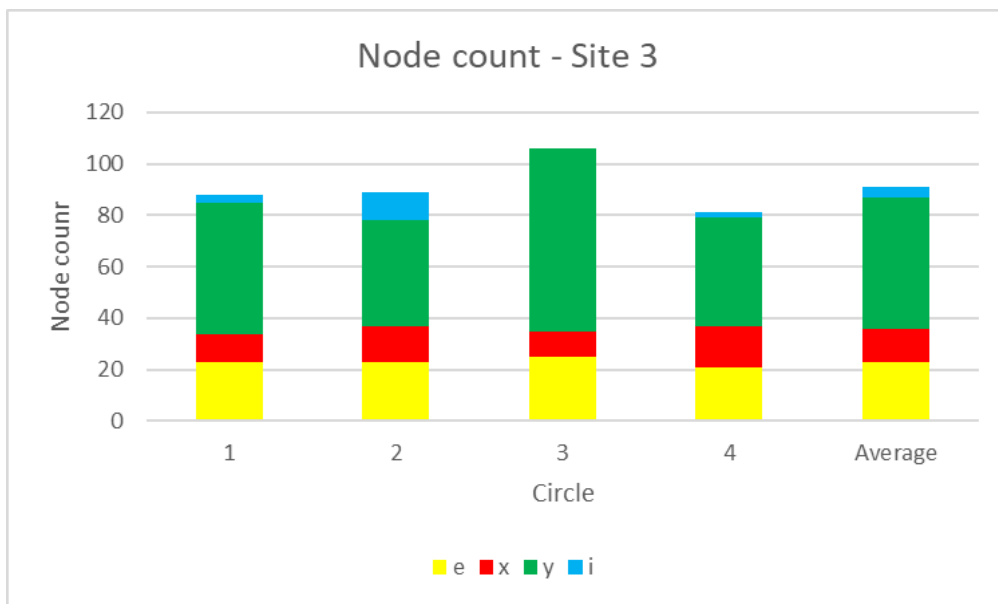


Figure 4.65: Number of nodes at site 3 – derived from measurement circles show in Figure 4.64.

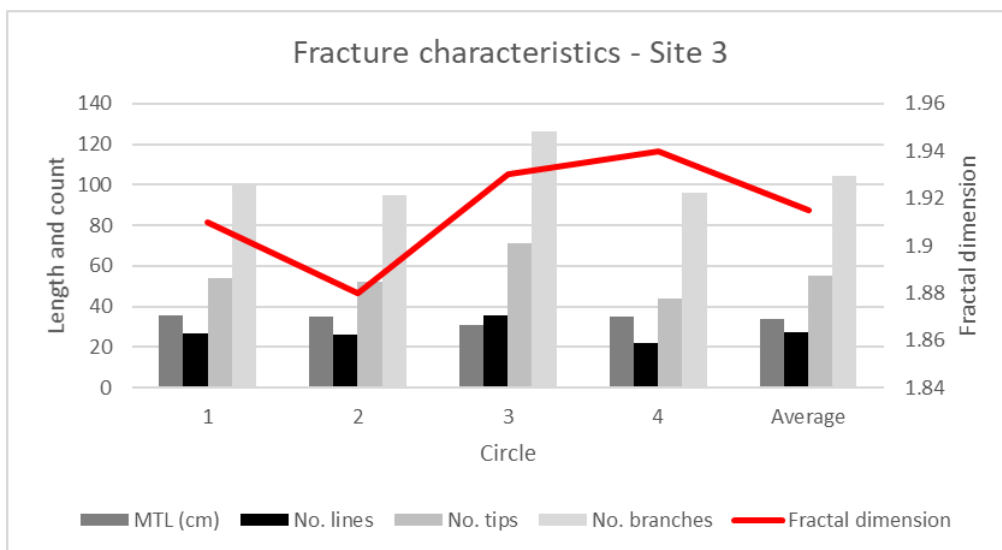


Figure 4.66: Mean trace length (MTL) in centimetres, number of lines, nodes, and branches and fractal dimension at site 3.

With the higher number of nodes, circle 3 has greater fracture connectivity, density, and intensity than the other circles (Figure 4.67).

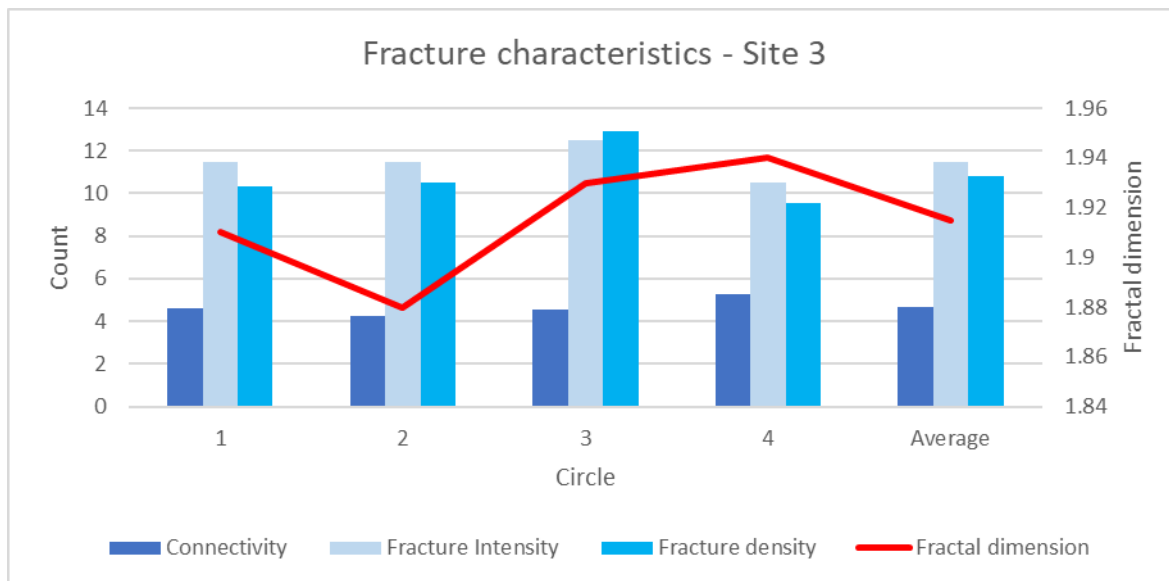


Figure 4.67: Connectivity, fracture intensity, fracture density and fractal dimension at site 3.

4.2.2.4 Site 4

Site 4 is an exposure of the Whispering Pines Thrust, approximately 70 m to the east in the valley below Site 2. The various portions of the thrust are clearly visible, but the rock mass within the thrust is highly fractured and it was decided that the normal 1-metre-wide measurement circles would be overwhelmed with fracture node data. As such, six measurement areas were selected within the thrust (Figure 4.68), on which 5 cm wide measurement squares were drawn (Figure 4.69). All the measurement squares were 5 cm by 5 cm, although different numbers of squares were analysed at each area to see whether zooming in (and hence resolution) had a significant effect on the node ratios.

The density of the nodes within the measurement squares (i.e., the “x”, “y” and “i” nodes) was calculated by calculating the total area of the total numbers of nodes and dividing these by the area of each set of measurement squares. For example, in area 1, there are 15 squares resulting in a total area of 375 cm² and in area 3 there are four squares resulting in a total area of 100 cm². This transformation normalised the node distribution. The number of edge (“e”) nodes were counted

around each square and although this results in the double counting of nodes where squares share a boundary, the average spacing of the “e” nodes was determined by taking the total length of the perimeter of the square, thereby giving a true reflection of the spacing of the “e” fractures around the square edge. With a three-fold increase in resolution, no differences in the node density or average spacing is discernible (Figure 4.70).

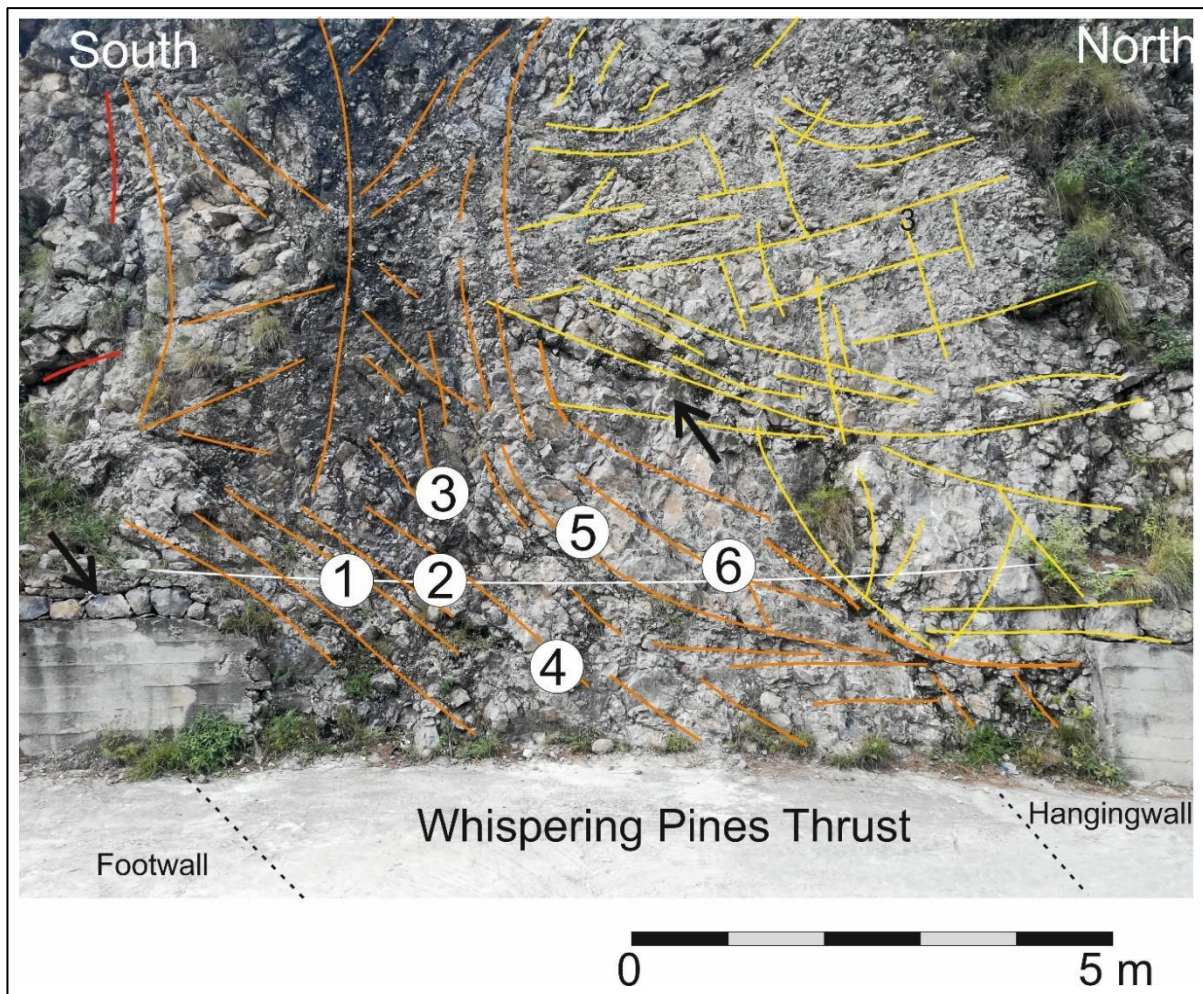


Figure 4.68: Image showing the intensely brecciated fault rock of the Whispering Pines Thrust, well exposed at site 4. Measurement squares were evaluated at the sites labelled 1 to 6 as shown in Figure 4.69. This method of data gathering was utilised to characterise the fracture pattern as the fracturing at this site is too intense to use the conventional 1 m measurement circles.

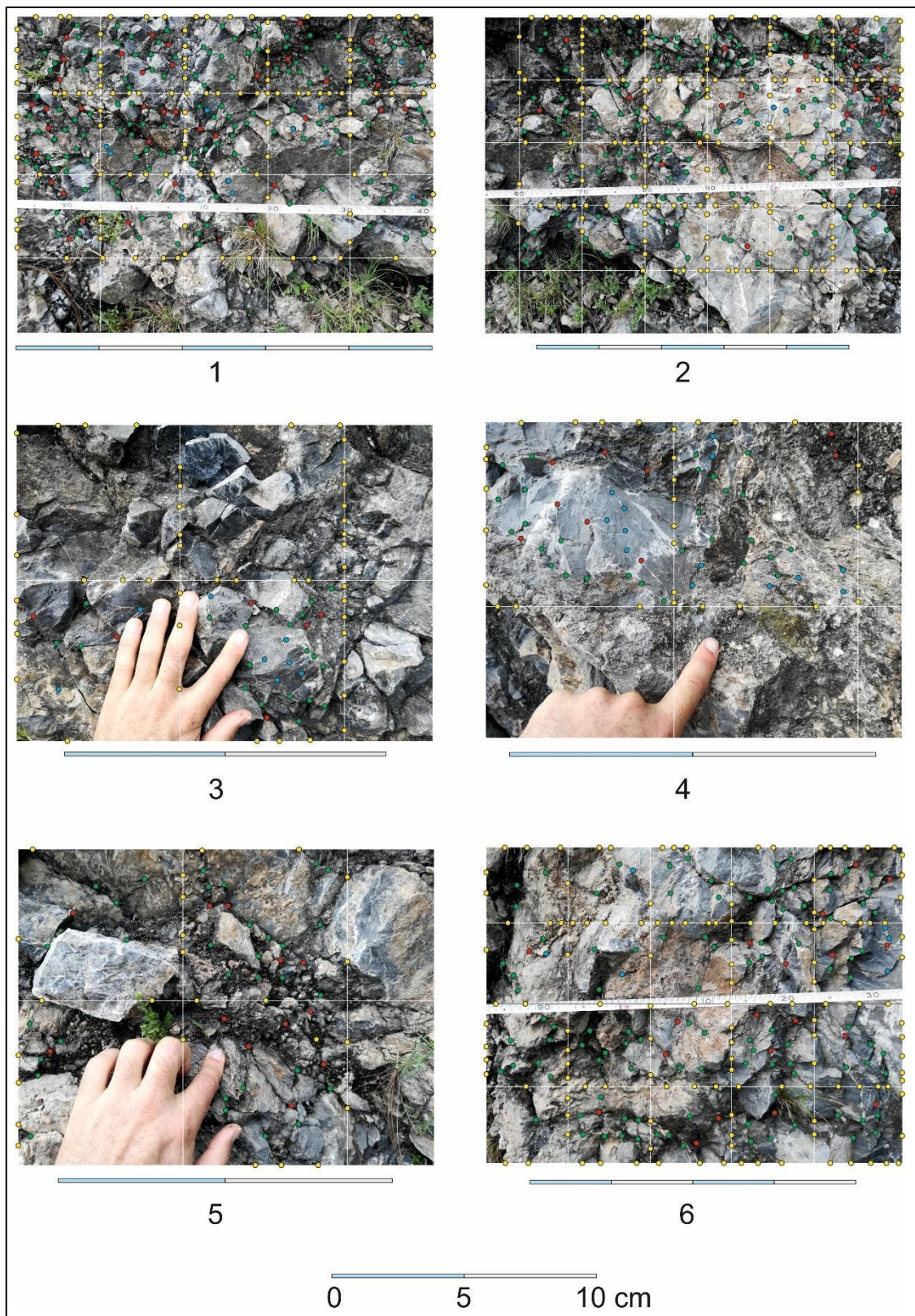


Figure 4.69: Detailed view of the measurement blocks indicated in Figure 4.68 which illustrates the steeply dipping 5 m width of the brecciated Whispering Pines Thrust. Node distribution in the different measurement squares within the rectangles. Scale bar is 10 cm but note that it is of different lengths in

each photograph. The measurement squares are all 5 cm by 5 cm.

Importantly, even though counts of the same four node types were made in the measurement squares as the conventional measurement circles, it is not possible to determine the topological characteristics as these require circles to calculate the values. Even the number of nodes cannot be realistically evaluated as the area of the high resolution fracture patterns in a 5 cm by 5 cm square, as a 1 m measurement circle would be more than 300 times bigger and potentially contain a large number of fractures at too high a resolution.

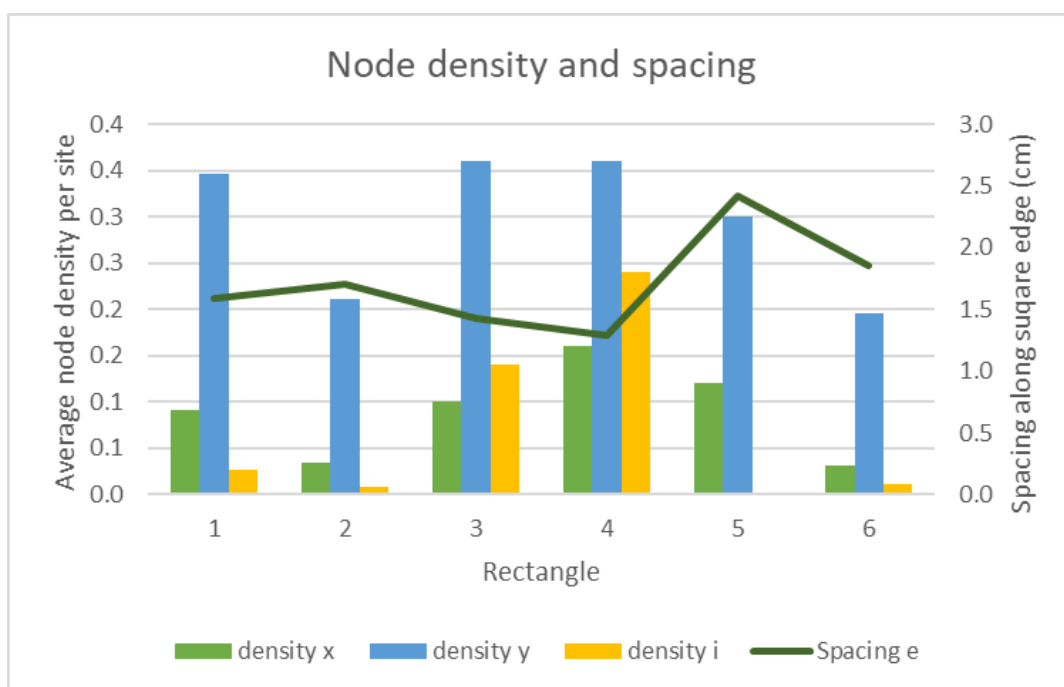


Figure 4.70: Average density of x , y , and e fractures in measurement squares and spacing of e fractures along square edges in each rectangle. The double counting of “ e ” nodes on adjacent squares is accounted for by dividing by the total length around each box, however the “ e ” count and node ratios cannot be compared with circles.

4.2.2.5 Site 5

Site 5 is located in the Nammal Formation away from any major geological structures (Figure.4.49), The rock mass at this site consists of light grey limey northwards dipping mudstone beds approximately 1 m thick, which are bounded by thin centimetre wide sheared mudstone layers .East-

west striking, steeply dipping shear fractures cross-cut the beds forming large 1 m by 1 m blocks. Around the edges of these blocks there is further fracturing.

Although the strata have been tilted to the north at approximately 30 degrees and there are at least two sets of fractures, this site is relatively undisturbed relative to sites 1, 2 and 4 on the Whispering Pines Thrusts, site 6 on the sheared contact between the Patala and Lockhart formations and site 8 sited in a large-scale anticline axis. The topological and fractal characteristics of this site therefore represent the minimum fracturing of the Makhniyal region. Interestingly, site 8, which is located on the northern flank of the anticline running through the village of Makhniyal, and approximately 1 km away from the axis has similar numbers of nodes to this site which is approximately 1 km south of the anticline. The composition and dip of the rocks at site 8 is quite different to those at site 5. Figure 4.71 is a series of merged photographs of the northward dipping Nammal formation exposed in the road-cut at site 5. The upper image has three rectangles labelled a, b, and c which correlate with the lower three images labelled a, b, and c. Within each of these lower images, the positions of the measurements circles 1 to 6 is indicated. Figure 4.72 shows the measurement circles and nodes within each circle.

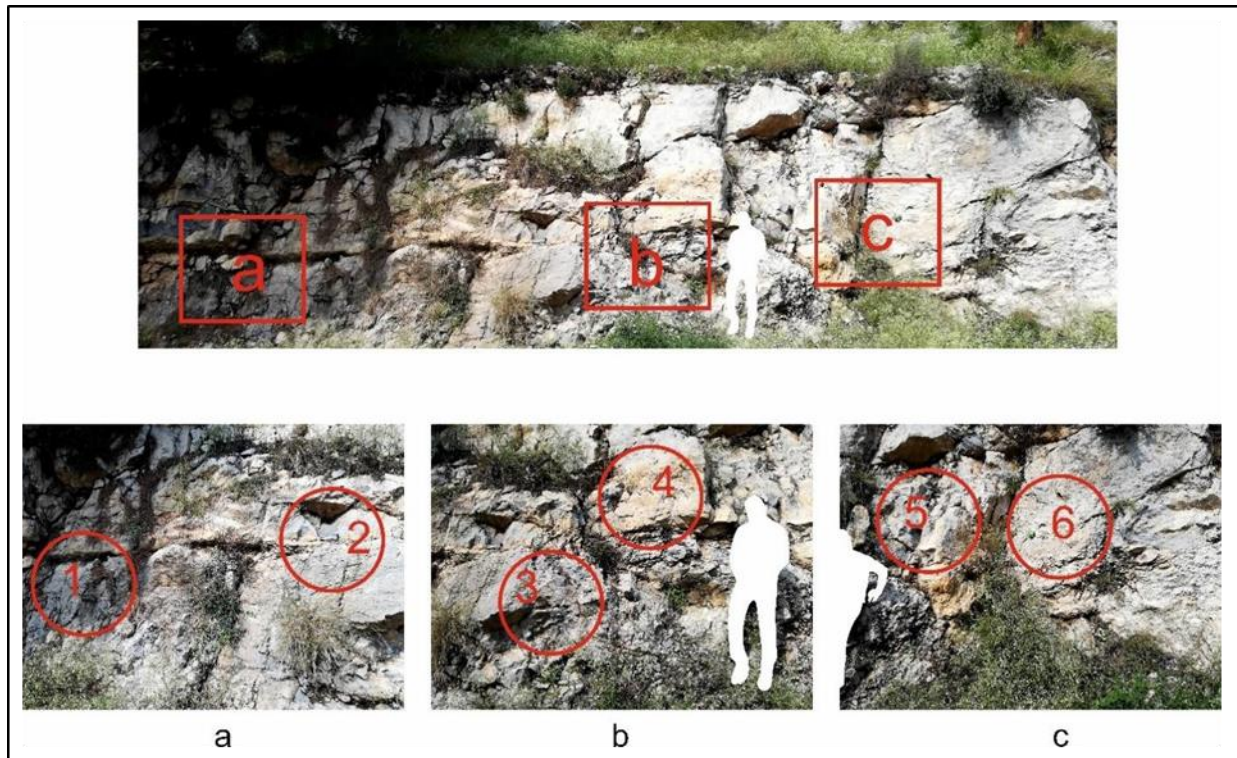


Figure 4.71: Site 5 – bedding dips in the direction of view (north) at 30 degrees, with steep east-west cross-cutting fractures. Squares a, b, and c in the upper part of the image indicate the position of the zoomed in views shown in the lower part. In turn, the position of the 1 m wide measurement circles illustrated in Figure 4.72 below is indicated in the zoomed in views. Geologist in white.

The total number of nodes in each of the measurement circles is similar, varying between 65 and 74 (average = 69). The greater numbers of “i” nodes (circles 2 and 6) are associated with lower fractal dimensions (Figure 4.73). The average mean trace length of circles 2 and 6 (Figure 4.74) is shorter – 29 cm compared to the average of 42 cm for the other four circles because the fractures terminate on “i” nodes and do not cross-cut or intersect other fractures. As more of the fractures have “i” nodes at both ends in circles 2 and 6, the number of tips is higher (Figure 4.74). As these nodes make up a larger proportion of the total number of nodes, there is lower connectivity (Figure 4.75).

The greater proportion of “i” nodes at site 5 compared to the other sites on the faults may be due to shorter fractures being extended by shearing and linking up with other fractures with “x” and “y” nodes.

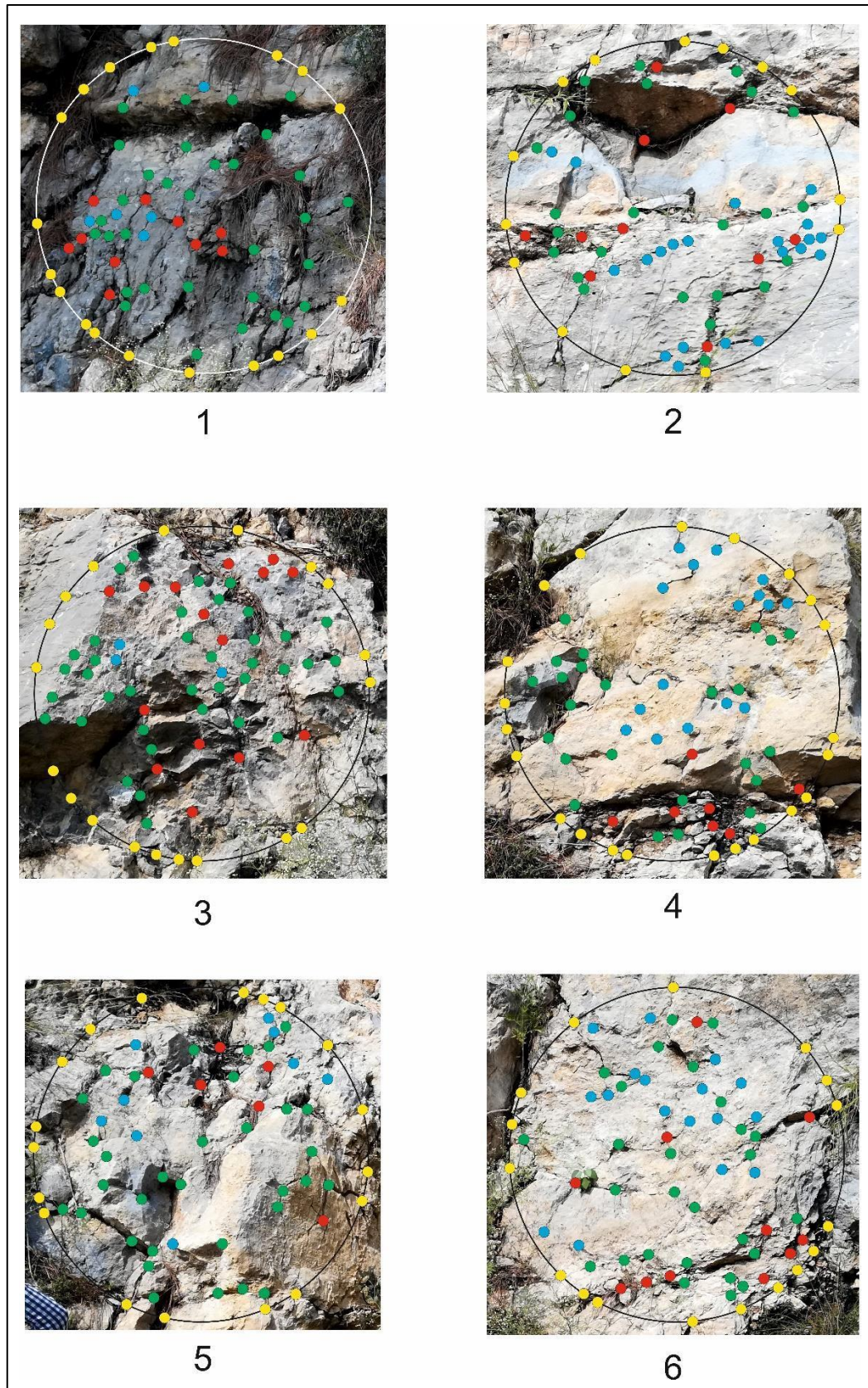


Figure 4.72: Fracture node measurement circles at site 5.

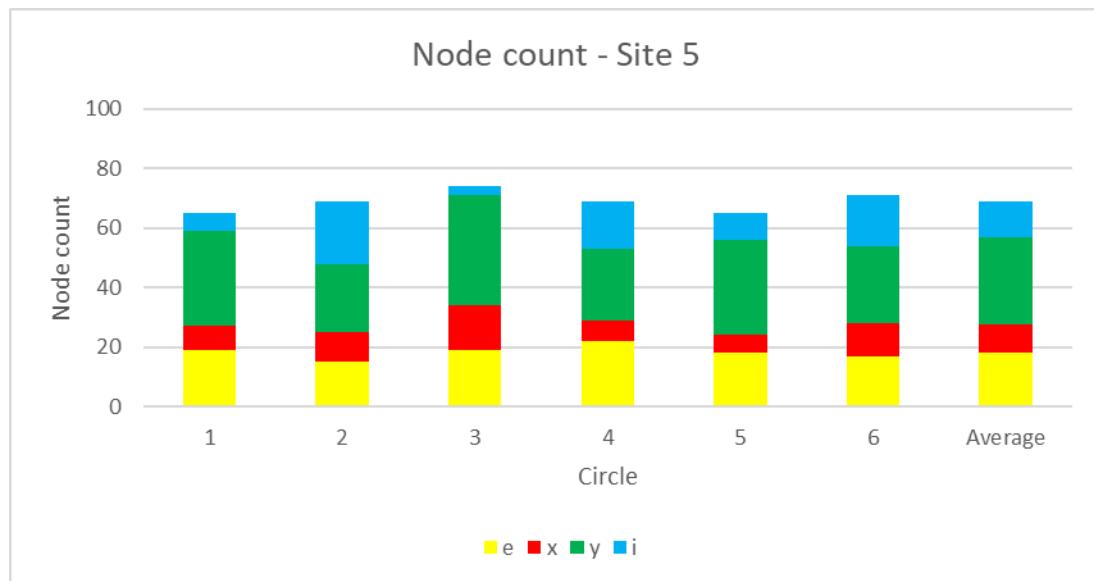


Figure 4.73: Number of nodes at site 5 – derived from the measurement circles shown in Figure 4.72.

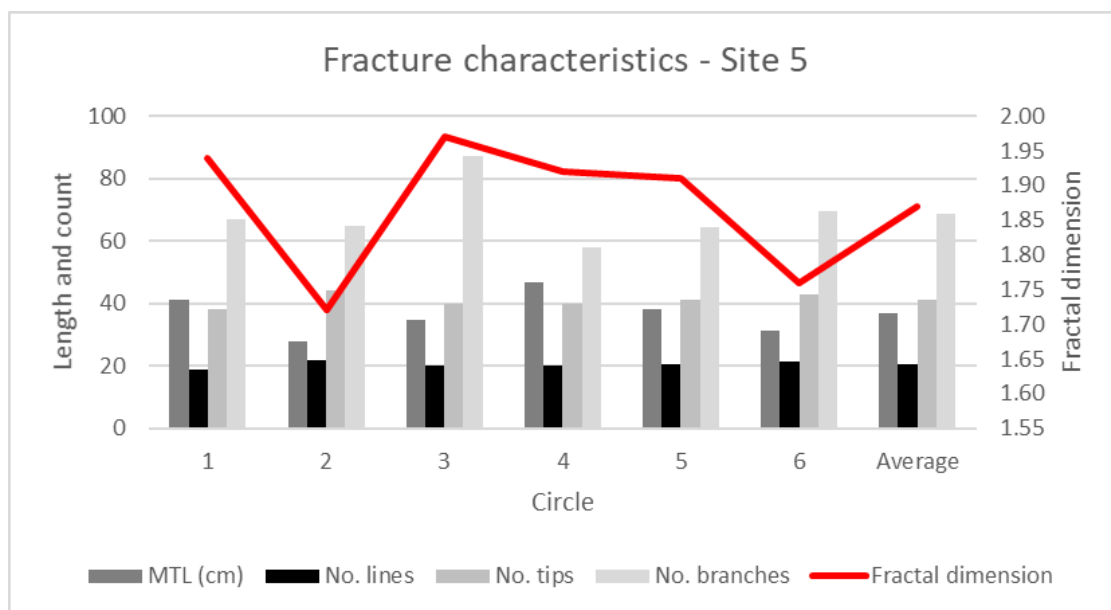


Figure 4.74: Mean trace length (MTL) in centimetres, number of lines, tips, and branches and fractal dimension at site 5.

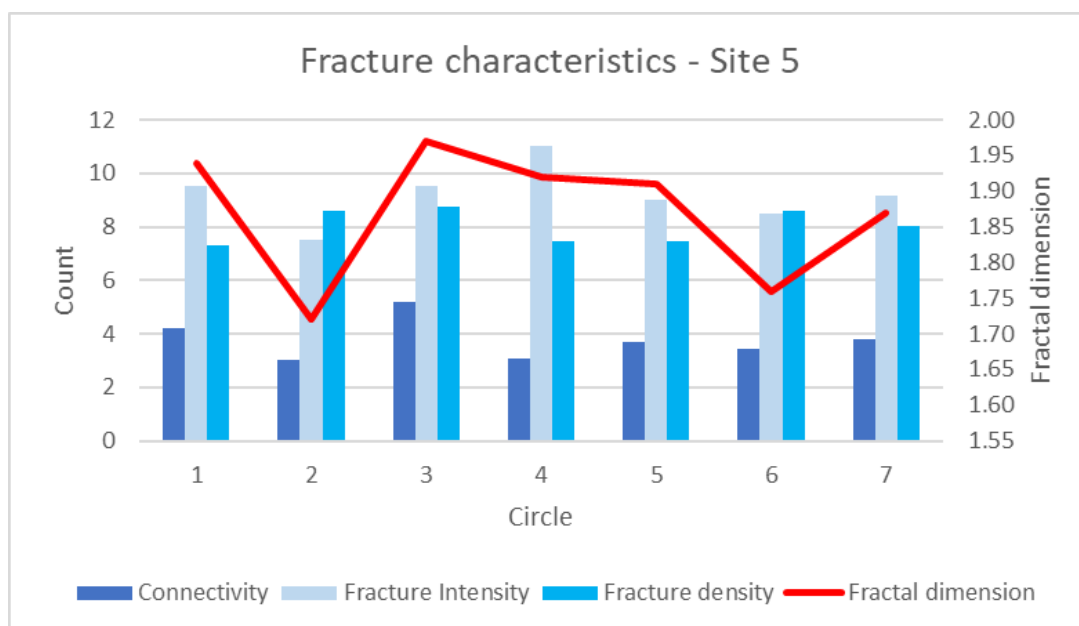


Figure 4.75: Connectivity, fracture intensity, fracture density and fractal dimension at site 5.

4.2.2.6 Site 6

A large steeply dipping reverse fault zone consisting of at least 10 m of highly fractured, grey-coloured limestone and several metres of highly laminated (sheared) brown shale, is developed at site 6 (Figure 4.75). As the rocks on the north-western side of the fault only consist of limestone, they are considered to be of the Lockhart Formation. The highly laminated shale on the south-eastern edge of the fault zone is of the Patala Formation (Figure 4.76). Stratigraphically, there is a gradual transition between shale-dominated and limestone-dominated strata of the Patala to the Lockhart formations, but where thrusting is developed, this contact becomes abrupt. The appearance of the thinly-bedded, brown-coloured shale of the Patala Formation matches closely with the mapped contact of Ali (2014) and is consistent with the rocks on the north-western side of the fault being the Lockhart Formation. This prominent 10 m wide reverse fault is not apparent on the map of Ali (2014), which only indicates thrust and folds.

Five measurement circles were placed on the Lockhart Formation limestone from the faulted contact with the Patala Formation. The first circle is positioned on the foot-wall contact of the fault and the

subsequent circles at 4 m, 6 m, 8 m, and 11 m northwards (Figure 4.76). Circles 1 and 2 are located within the fault zone, circle 3 on the hanging-wall contact and circles 4, and 5 deeper into the north-western hanging-wall block.

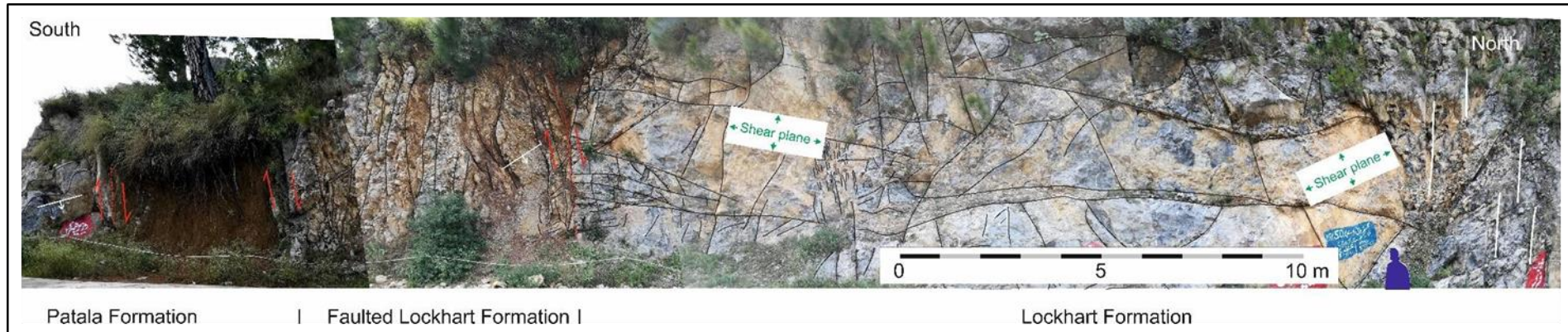


Figure 4.76: Faulted contact between the Patala and Lockhart formations (site 6). This is a large steeply dipping reverse fault, at least 10 m wide and highly faulted (as shown in detail in Figure 4.77) is located approximately 500 m north of the Whispering Pines Thrust. Note that because this is a composite image of photographs around a bend in the road, it gives the incorrect impression that the fault is dipping to the northwest. Figure 4.50 illustrates that the fault actually dips southeast as do the hanging-wall strata shown in Figure 4.77.

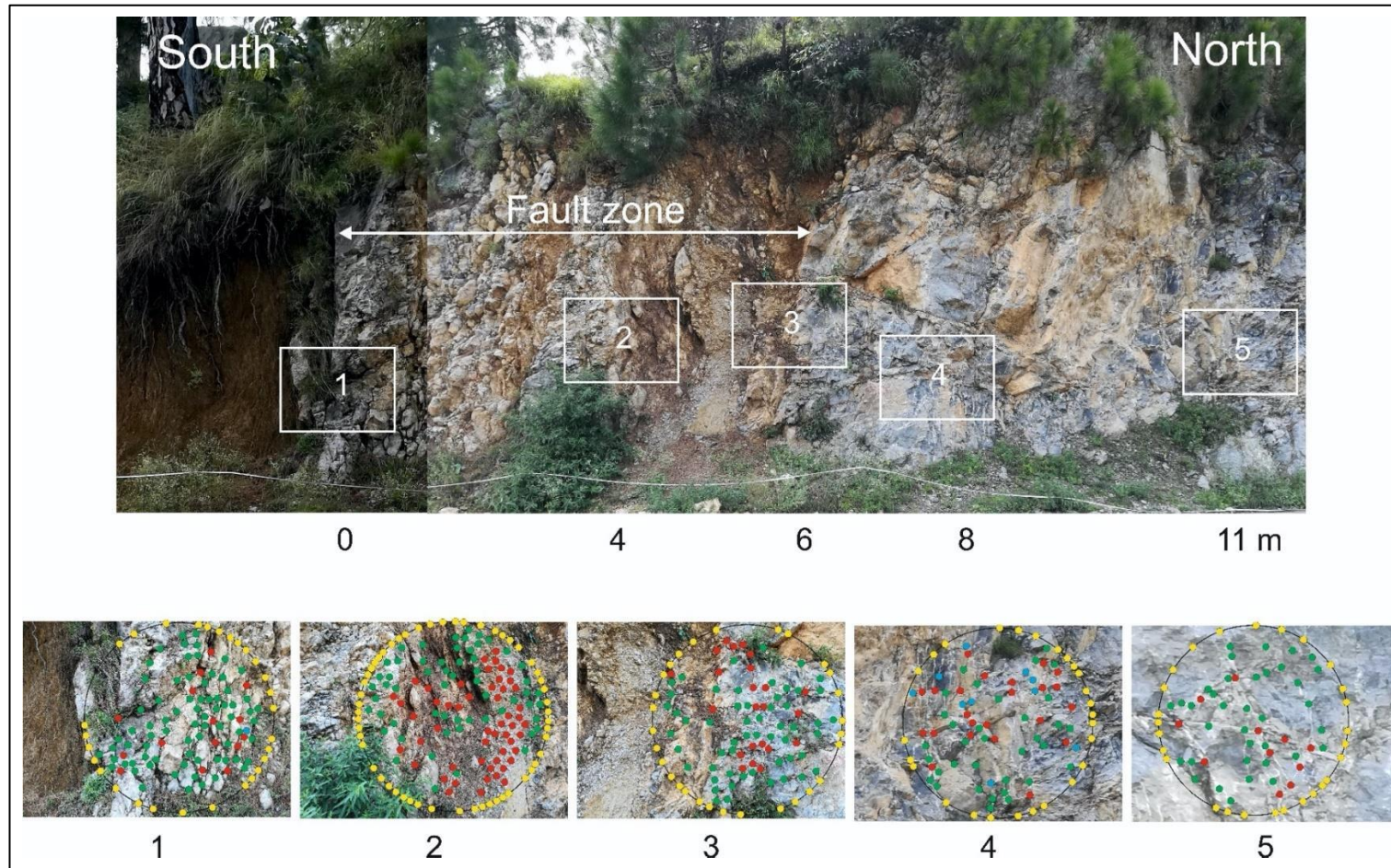


Figure 4.77: 1 m diameter measurement circles in the fractured Lockhart Formation at site 6. The fault contact between the Nammal and Lockhart formations is at 0 m and measurement circles progress northwards further consisting of greater fragments of Lockhart Formation limestone (from Circle 1) into the foot-wall of the normal fault zone. The long mean trace length of the faults are shown by the large number of yellow "e" nodes in the measurement circles.

Circles 1 and 2 have an average of 137 nodes in each circle. There are fewer "e" nodes in circle 1 as part of the circle edge is obscured by vegetation (Figure 4.76). The high degree of fracturing close to the contact with the Patala Formation is highlighted by the large number of "y" fractures (68). Circle 2 is more representative of the faulted Lockhart Formation with 53, 54, and 53 "e", "x", and "y" nodes respectively and no "i" nodes (Figure 4.77) due to fault movement extending fractures until they intersect or cross-cut. Circle 3 is sited across the foot-wall contact of the reverse fault. A large portion of the measurement circle is covered by a steeply dipping major shear-plane oriented parallel to the road-cut surface (Figure 4.77). These shear-planes dominate the immediate foot-wall of the fault (Figure 4.71) and appear to pre-date the fault as they terminate against it and are not visible in the foot-wall. Due to the presence of this shear surface, the total number of nodes is lower (105), also there are still no "i" nodes.

In circles 4 and 5, located in the hanging-wall of the reverse thrust there is an average of 84 nodes, significantly lower than the average number of nodes in the fault (126). Circle 4 is different as "i" nodes compose 10% of the total nodes, versus an overall average of 3% of for this site. Circle 5 has the fewest nodes of all categories of all circles at this site clearly showing the decrease in the number of nodes moving away from the fault (Figure 4.78).

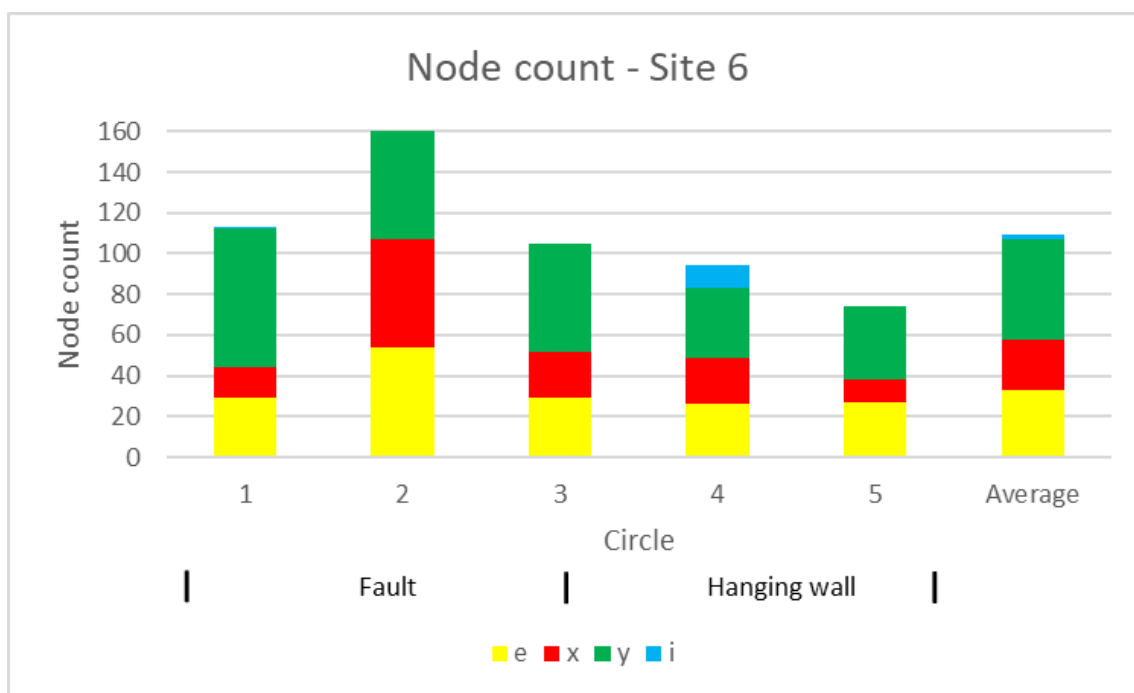


Figure 4.78: Number of nodes at site 6 – derived from the measurement circles shown in Figure 4.77.

There is a clear correlation between the number of nodes and the fractal dimension with the circle with the lowest number of nodes (particularly “y” nodes) having the lowest fractal dimension (compare Figure 4.78 and Figure 4.79). Circles 1 and 2 have a fractal dimension of 2, that is, the entire surface is fractured down to the resolution of the 5 cm measurement box-length.

Topologically, circle 5 is characterised by the longest mean trace length as well as the lowest number of lines, tips, and branches (Figure 4.79) which is consistent with the few (long) fractures visible in the measurement circle (Figure 4.77). Circle 2, with its large number of nodes (the most for the entire region) has the highest fracture connectivity, intensity, density, and number of branches (Figure 4.80). The significant contribution of the fracture characteristics of circle 2 to the generally more fractured ground at site 6 has resulted in this site showing more damage than site 2 located on the Whispering Pines Thrust.

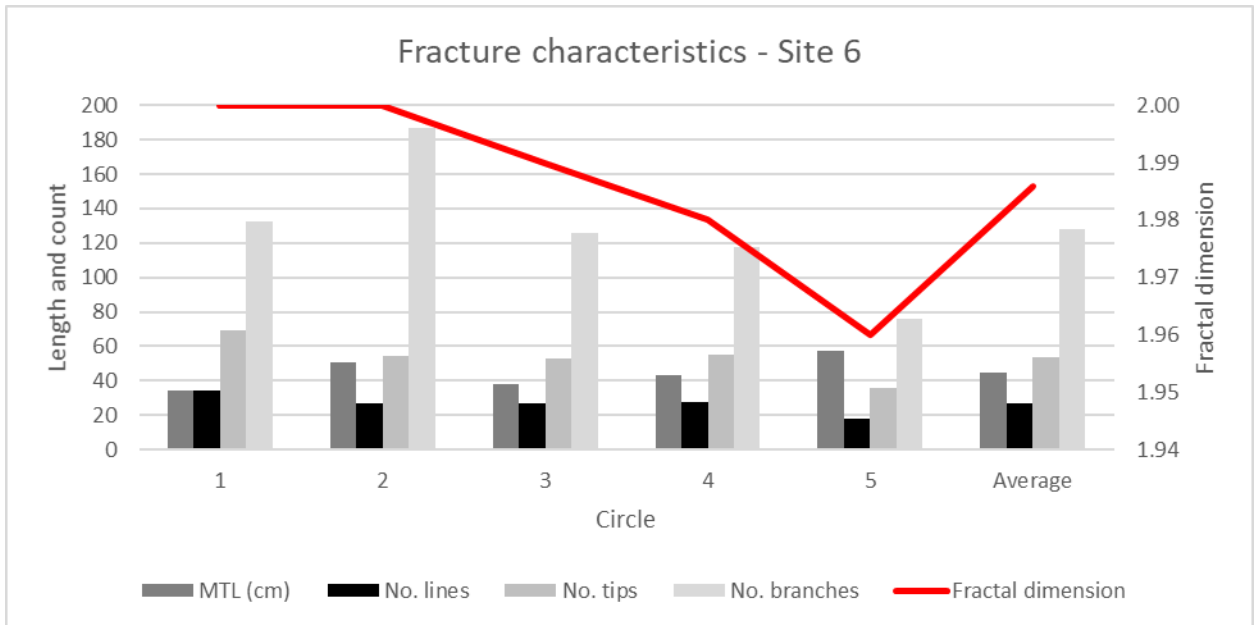


Figure 4.79: Mean trace length (MTL) in centimetres, number of lines, nodes, and branches and fractal dimension at site 6.

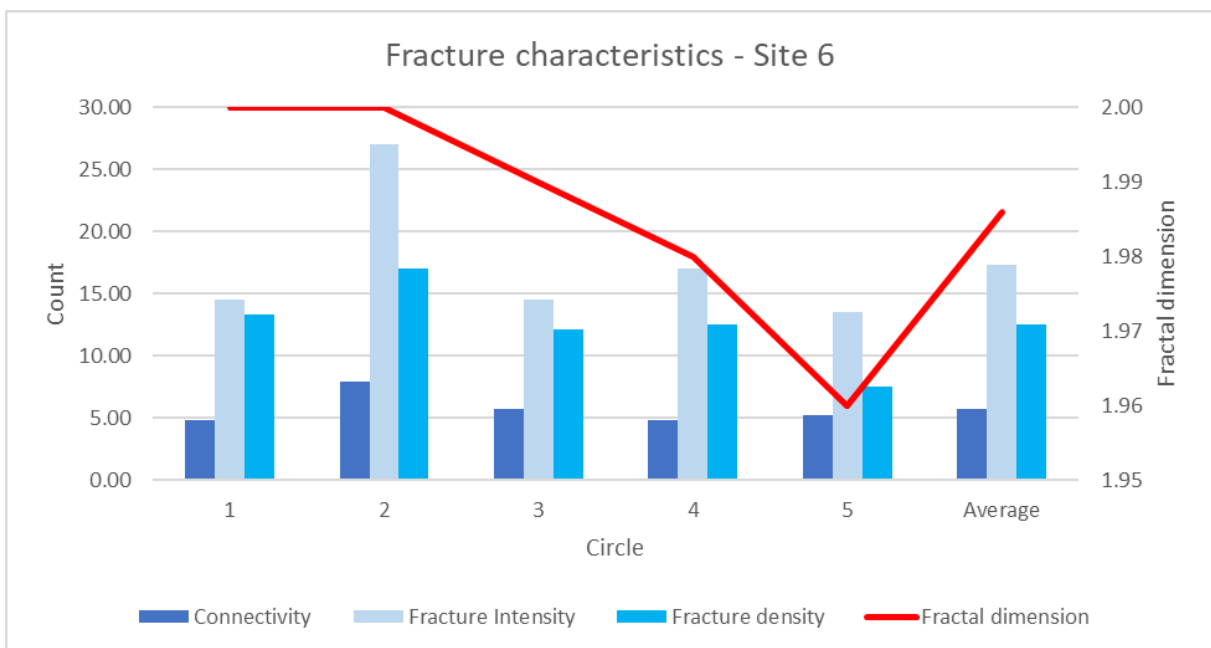


Figure 4. 80: Connectivity, fracture intensity, fracture density and fractal dimension at site 6. Highest intensity in the 'fault zone. But interestingly the connectivity does not show the same relationship.

The alternating thick (1 m) and thin (centimetre-scale) limestones beds exposed in the road-cut approximately 200 m north into the foot-wall of the faulted contact between the Patala and Lockhart formations dip steeply to the south-east (Figure 4.81). The southwest-northeast strike of the beds matches both the dip and strike of the normal fault exposed at this site, and also, the structural characteristics of the overturned anticline at site 7 and the south-eastward dipping strata at site 8.



Figure 4.81: Steeply south-eastward dipping beds of the Lockhart Formation exposed approximately 200 m north of the faulted contact between the Patala and Lockhart formations shown in Figure 4.77. The white squares labelled "SP" indicate the position and orientation of a major shear-plane similar to those shown in Figure 4.76.

4.2.2.7 Site 7

Site 7 is located in the village of Makhniyal on the hinge-line of regional overturned anticline (Figure.4.49). Both the north-eastern and south-western flanks of this anticline dip steeply to the southeast; and the Cretaceous Kawagarh Formation (the oldest rocks in the region) is exposed at this site. The Kawagarh Formation is a medium to dark grey coloured, calcareous shale. The rock mass is highly damaged with six different discontinuity sets being identified. These range in size from metre-wide clay-gouge covered bedding to millimetre sized chaotic breccia (Figure 4.82).

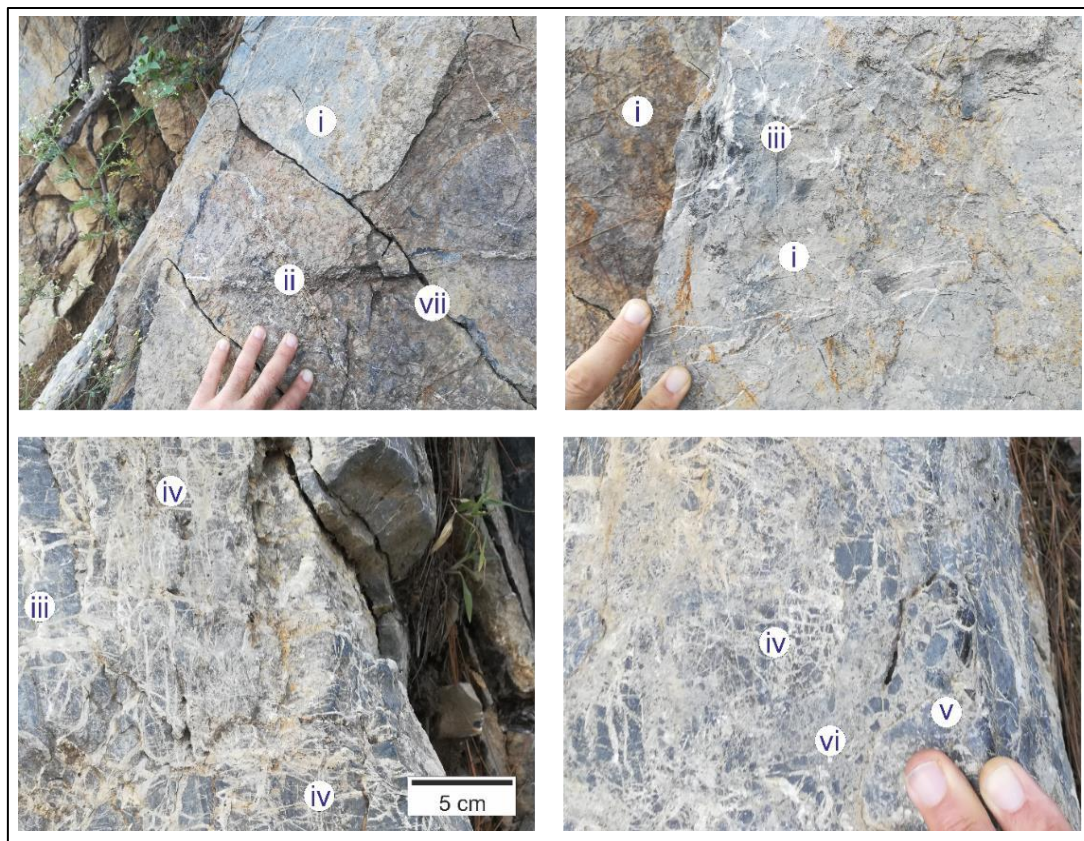


Figure 4.82: Discontinuities at site 7: (i) clay gouge coated sheared and folded bedding; (ii) calcite filled Riedel shears developed across the fold axis; (iii) millimetre thick, decimetre long calcite-filled fractures developed in the limy shale; (iv) intense network of randomly oriented calcite fractures, typically less than 5 mm thick and 5 cm long; (v) chaotic matrix-supported breccia with millimetre sized rotated calcite fragments; (vi) fault gouge with remnant fragments of limestone; (vii) unmineralised late-stage cross-cutting metre-long fractures.

The predominant fracture type is an intense network of small (millimetre-scale) calcite-filled fractures which is present through-out the rock mass at this site (Figure 4.83). These calcite fractures are both cross-cut by, and terminate on, the sheared bedding planes (Figure 4.84). This is clearly due to re-activation of bedding plane movement as the same calcite fracture can be seen off-set on the opposite side of the of bedding plane. The small calcite fractures, breccia and associated fault gouge most likely represent tight anticlinal crush fractures as no shearing or preferential orientation is evident. The abundant small fractures and re-activation of bedding parallel movement can be directly attributed to the tightening of the steeply dipping overturned anticline at site 7. Other small calcite-filled fractures in different areas are not directly related to tight folding and may represent hydraulic or release joints (Engelder, 1985).

Due to the high intensity of fractures (especially type iv), it was decided not to use the conventional 1 m measurement circles to quantify the fracture pattern of site 7. Instead, four 5 cm diameter measurement circles were placed on the unmineralised late stage fracture surface (Figure 4.83), and the characteristics of the fractures within each circle was determined by digitising the calcite fractures in ArcMap (Figure 4.86).



Figure 4.83: Outcrop at site 7 – dark grey Kawagarh Formation limestone with small millimetre-sized calcite fractures throughout. Strongly developed layering related to the folding and overturning of the anticline axis at this site (Figure.4.49) is super-imposed on these fractures. Geologist in blue.

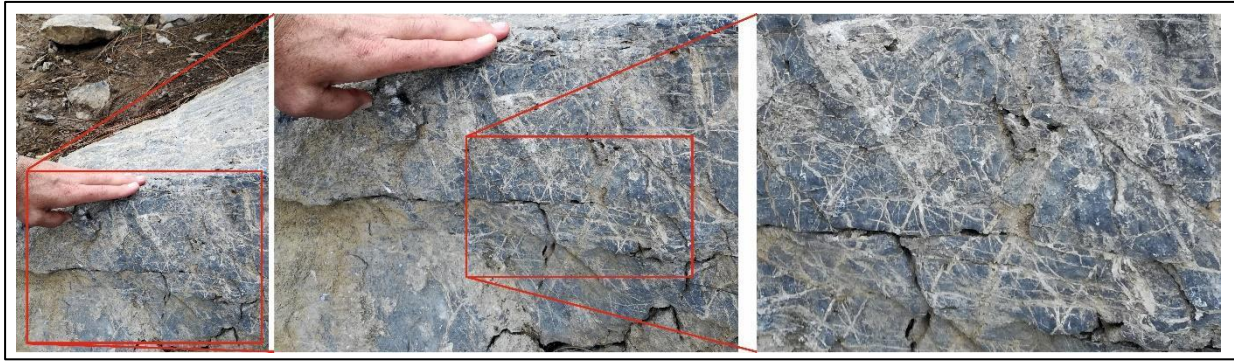


Figure 4.84: Close-up view of fractured rock mass perpendicular to bedding. Rock is not in-situ having fallen off the outcrop shown in Figure 4.85. Red rectangles indicate zoomed in area. Final zoom (left) is 20 cm wide. Randomly oriented calcite fractures are clearly visible.



Figure 4.85: View of earlier generations of fractures exposed on a late-stage fracture surface (see Figure 3.24). The zoomed in view (right) shows the distribution of 5 cm wide measurement circles.

The image was scaled, and fractures traced within each circle to allow the determination of the length and number of fractures within each circle. These results are shown in *Table 4.5* and illustrated in *Figure 4.86*. There are an average 175 fractures in each 5 cm circle. These fractures have an average length of 0.6 cm, but because of the large number, it equates to a total fracture length of 5.4 m. More

importantly, 80% of the fractures have a length of less than 0.75 cm (Figure 4.87) and cross-cut and intersect each other frequently (Figure 4.86).

Table 4.5: Characteristics of the fractures measured in the four 5 cm wide measurement circles illustrated in Figure 4.86.

Circle	1	2	3	4	Ave
Fracture count	150	245	168	147	178
Min length (cm)	0.1	0.1	0.1	0.2	0.1
Max length (cm)	2.6	2.3	2.0	3.6	2.6
Total length (cm)	101.1	130.9	103.7	99.6	108.8
Average length (cm)	0.7	0.5	0.6	0.7	0.6
SD	0.5	0.4	0.4	0.5	0.4

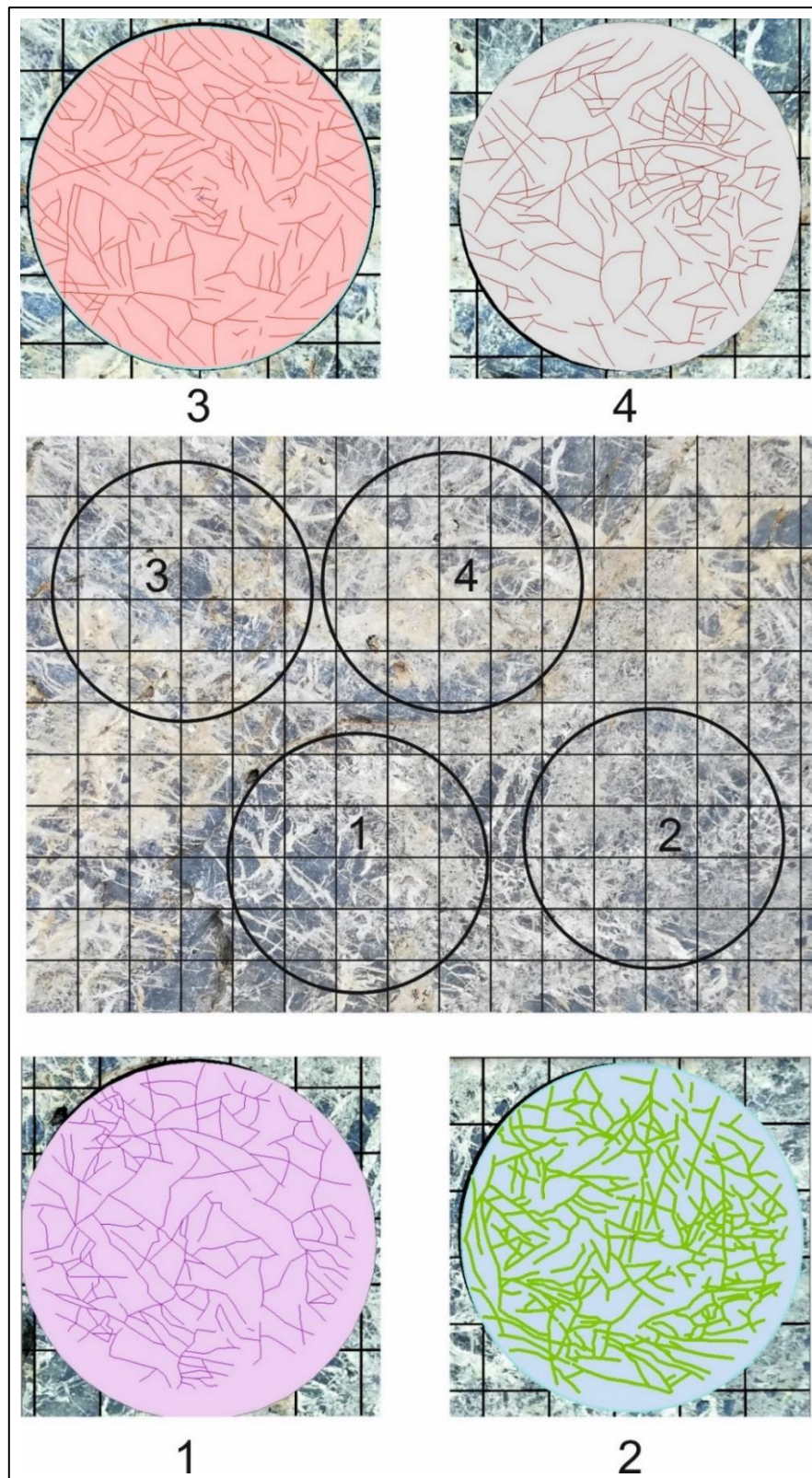


Figure 4.86: Fracture lengths of 5 cm wide measurement circles. Image was imported into ArcMap, calibrated and the fractures traced out in each circle. Table 4.5 summarise the characteristics of the fractures.

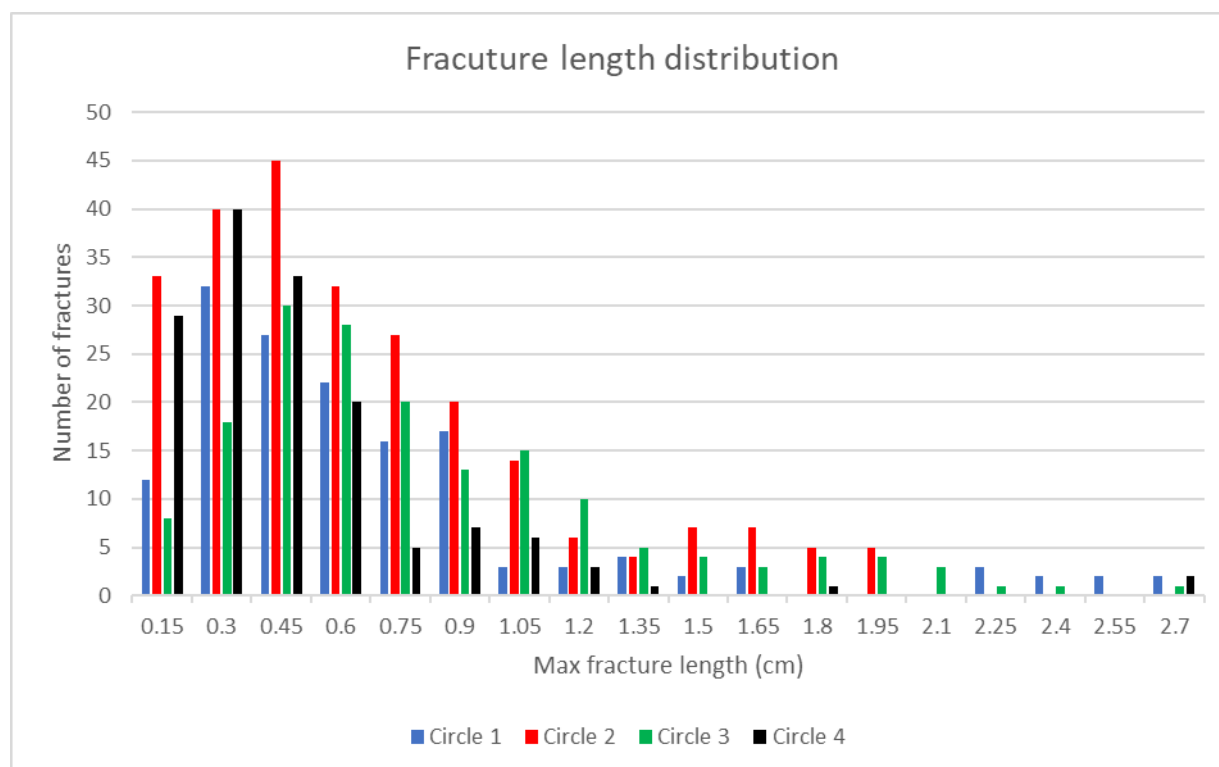


Figure 4.87: Fracture length distribution in the 5 cm wide measurement circles (Figure 4.86). It clearly illustrates the logarithmic distribution in the fracture length with more than 80% of the fractures having a length of less than 0.75 cm.

Figure 4.88 and Table 4.6 show the distribution and number of nodes within the 5 cm wide measurement circles. When the number of nodes is determined for the 5 cm and converted to equivalent numbers in a 1 m circle, interesting fracture characteristics are revealed (Table 4.6). The circumference of a 1 m wide circle is 20 times that of a 5 cm wide circle and the area is 400 times greater. The number of “e” nodes is therefore multiplied by 20 and the number of “x”, “y”, and “i” nodes is each multiplied by 400. In the larger theoretical circle, the connectivity remains the same, the fracture intensity increases twenty-fold, and the mean trace length decreases twenty-fold. The fracture density, the number of lines, tips, and branches all increase 400 times. This shows that the topological values from measurement circles of different sizes cannot be directly compared as they vary by different amounts and can result in anomalously high node counts such as 138 650, obtained from converting the number of nodes in circle 2 (Table 4.6) compared to the average total of 86 nodes per circle for the rest of the area. Interestingly, the connectivity of the fractures in the

measurement circle remains the same, but as fractures are not distributed uniformly, it is also not possible to equate the connectivity of fractures in measurement circles of assorted sizes directly with each other. Having measurement circles of the same diameter at various sites is the only way in which the topological and fractal characteristics can be correctly compared across different areas and structural domains.

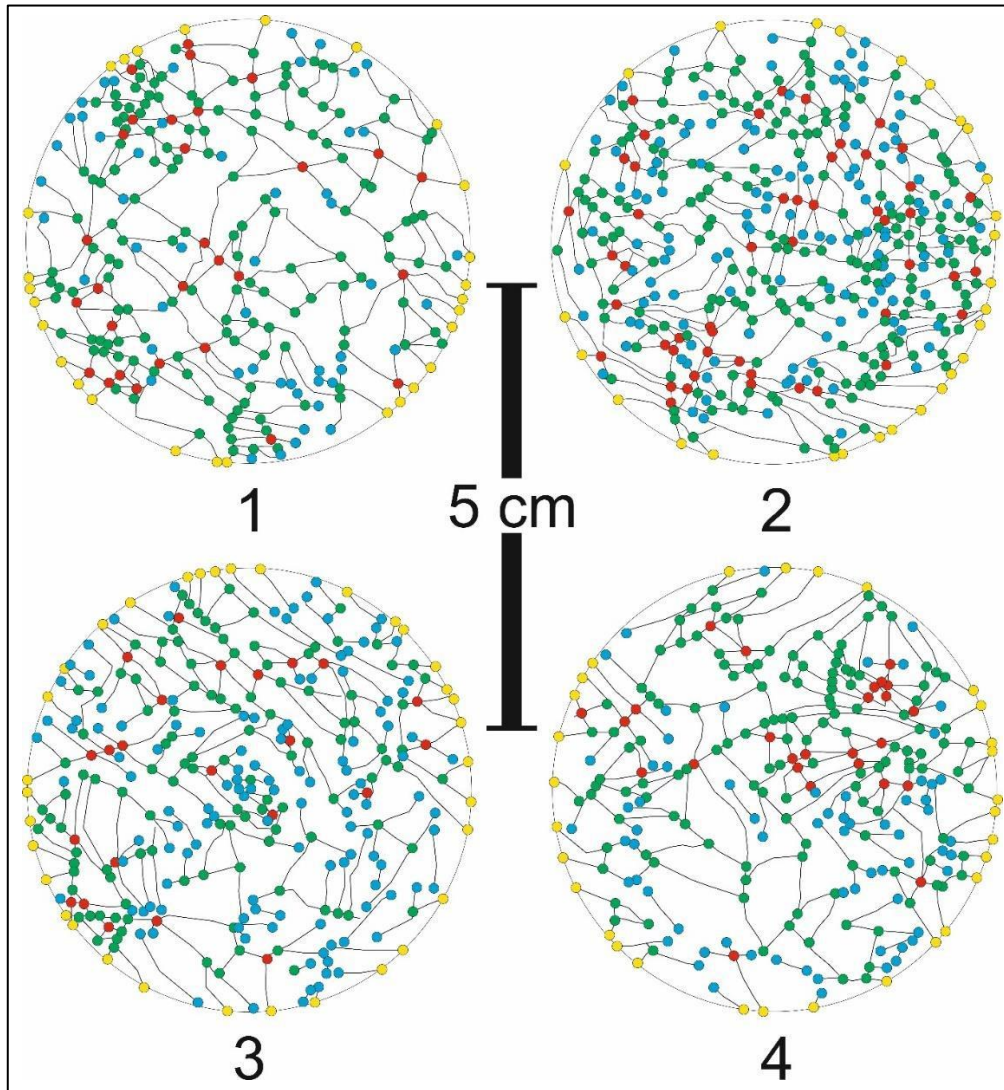


Figure 4.88: Fracture nodes of the measurement circles. Note that these circles are 5 cm in diameter, not the conventional 1 m. Table 4.6 provides the node count for each circle and the associated topological values. It also lists the hypothetical number of nodes and topological characteristics if these circle were converted to the usual 1 m wide measurement circles.

Table 4.6: Node count and topological characteristics of 5 cm diameter measurement circles at site 7 converted to 1 m circle equivalents by multiplying the number of “e” nodes by 20 (increase in circumference) and “x”, “y”, and “l” nodes by 400 (increase in area).

circle		Characteristic	1	2	3	4
cm	Nodes	E	29	28	34	30
		X	28	46	23	26
		Y	124	186	112	132
		I	49	113	122	168
		Total	230	373	291	356
	Topology	Connectivity	4	3	2	2
		Fracture Intensity	15	14	17	15
		Fracture density	32	55	41	52
		Mean trace length (cm)	0.14	0.08	0.13	0.09
		No. lines	87	150	117	150
		No. tips	173	299	234	300
		No. branches	267	428	275	334
	1 m	Nodes	E	580	560	680
X			11 200	18 400	9 200	10 400
Y			49 600	74 400	44 800	52 800
I			19 600	45 200	48 800	67 200
Total			80 980	138 560	103 480	131 000
Topology		Connectivity	4	3	2	2
		Fracture Intensity	290	280	340	300
		Fracture density	12 796	21 963	16 361	20 754
		Mean trace length (m)	0.0072	0.0041	0.0066	0.0046
		No. lines	34 600	59 800	46 800	60 000
		No. tips	69 200	119 600	93 600	120 000
		No. branches	106 600	171 000	110 000	133 600

4.2.2.8 Site 8

Site 8 is characterised by two different types of limestone that dip north-westward forming the overturned limb of the anticline centred at site 7 (Figure.4.49). The rocks consist of a series of younger, underlying dark grey coloured wackestone beds, structurally overlain by older fossiliferous packstone beds (Figure 4.89). The bioclastic foraminiferal packstone contains abundant foraminifera as well as broken gastropod and bivalve shells. Distinctive *Cruziana* and *Thalassonoides* trace fossils (horizontal feeding burrows) are exposed on the bedding surface (Figure 4.90).

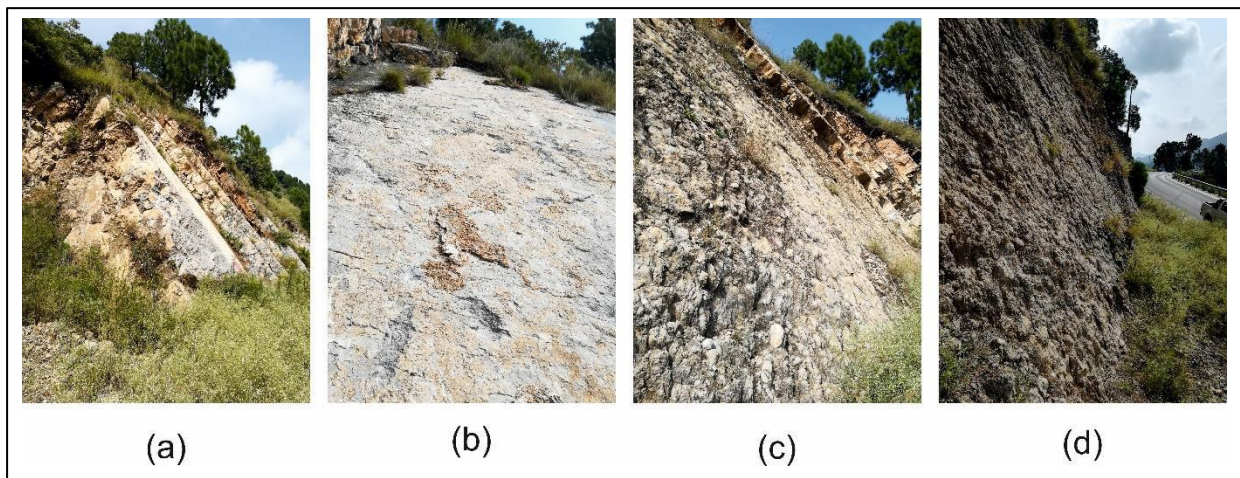


Figure 4.89: Site 8 – view northeast along Kohala Bala Road showing overturned Lockhart Formation limestones units dipping steeply to the northwest (Figure.4.49). Images (a) through to (d) are of progressively older limestone units. Strongly sheared bedding contacts are present between the beds.



Figure 4.90: Contact between the fine-grained dark grey-coloured wackestone (left) and older bioclastic foraminiferal packstone. Both have bedding surfaces that are weathered and sheared, but the older packstone surface is more irregular due to trace fossils.

The bedding surfaces are strongly weathered at this site. The minerals present on the surface have been dissolved, and become muddy, reducing friction among grain interfaces, enlarging gaps among the particles, and weakening cohesion within mineral grains. This leads to reduced strength and mechanical deformation with the beds able to slide past each other (Li *et. al.*, 2018).

Despite this, millimetre thick calcite fractures cross-cutting the bedding surfaces are common at this site, both in the packstone (Figure 4.91) and wackestone (Figure 4.92). These fractures are developed almost perpendicular to the bedding, and both terminate against the weathered bedding surfaces and cross-cut it. This suggests that they post-date bedding plane shear. However, these fractures do not change their orientation relative to bedding even when the strata are more shallowly dipping. As the greater variety and density of fractures at site 7 shows, there have been several phases of movement associated with the anticline. It is suggested that the calcite filled fractures are able to be developed and extended during different phases of movement along the weathered bedding surface.

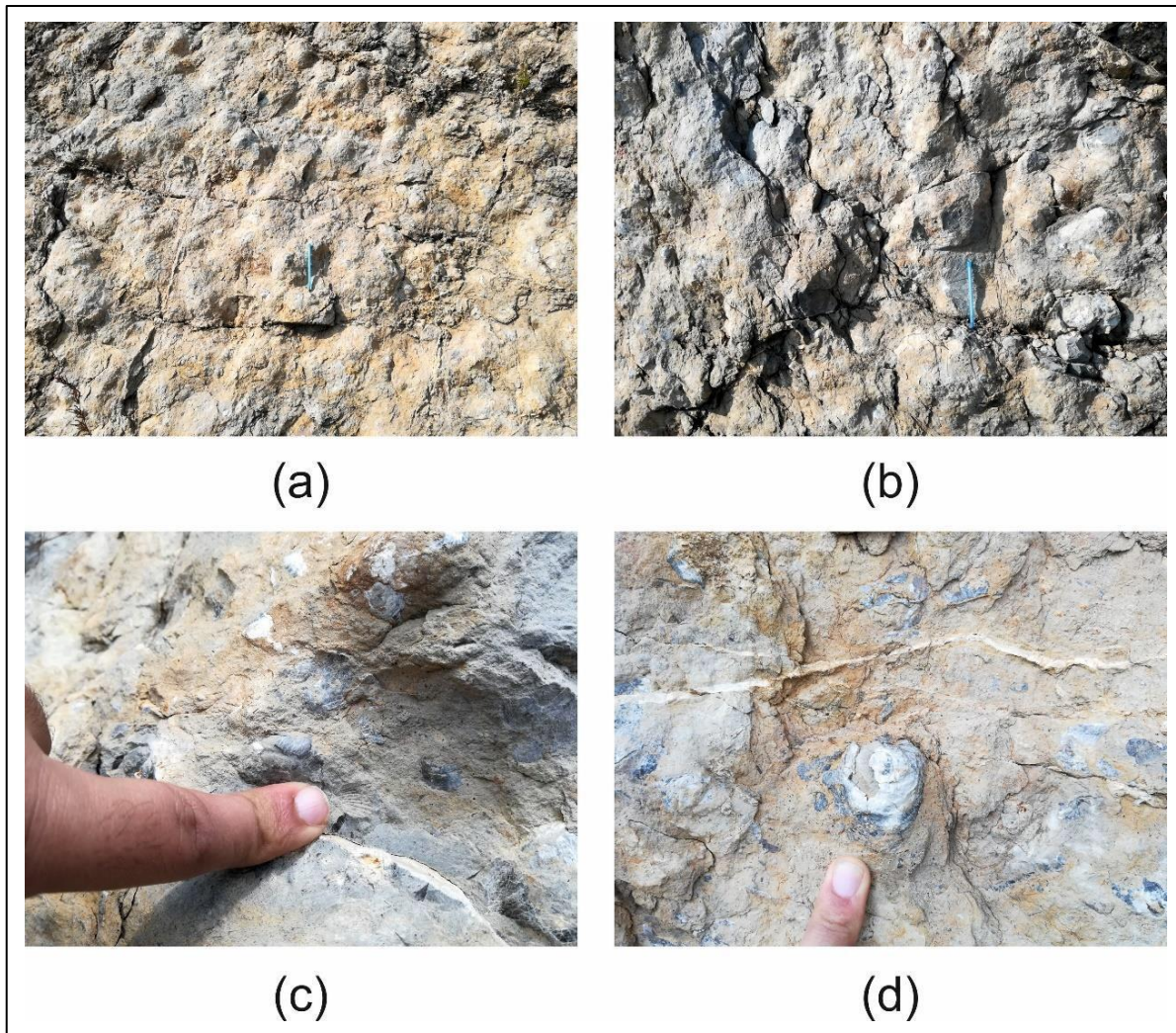


Figure 4.91: Bioclastic foraminiferal packstone. (a) and (b) bedding surface showing a variety of *Thalassonoides* ichnofossils (mostly horizontal feeding burrows); (c) and (d) bivalve and gastropod shells exposed on the bedding surface. Also visible are millimetre thick bedding perpendicular calcite fractures.

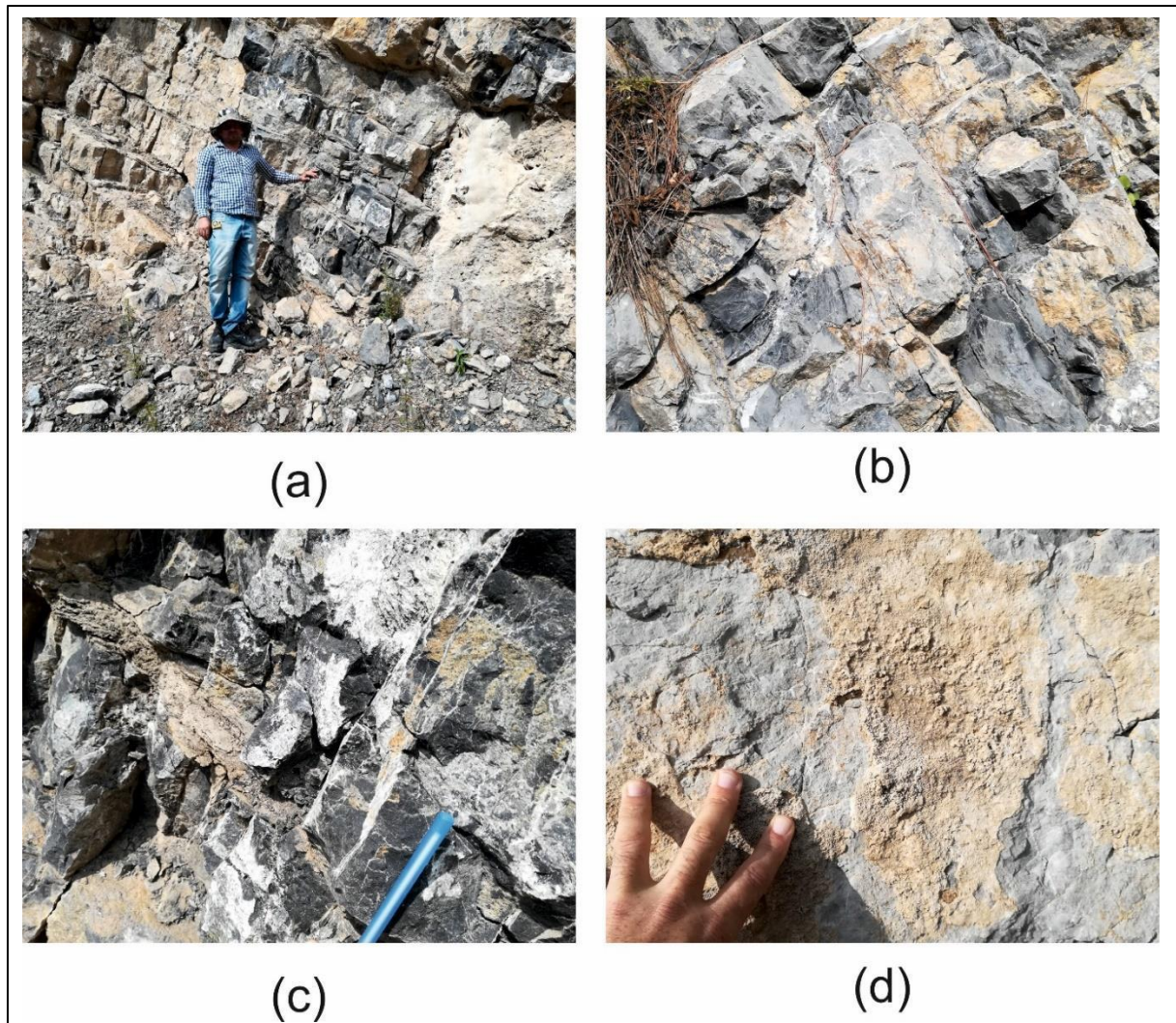


Figure 4.92: Younger, dark grey-coloured wackestone with extensive cross-cutting brittle calcite-filled fractures and bedding parallel shears. (a) approximately 500 m west of the contact between the two different limestone types (Figure.4.49); (b) bedding parallel gouge coated shear fractures and open orthogonal calcite which also have gouge fill; (c) close-up view of bedding parallel gouge-filled fractures and orthogonal calcite fractures which are much longer and more parallel than the abundant small calcite fractures at site 8; (d) bedding plane fracture consisting of sheared weathered calcite and limonite.

The wackestone and packstone appear to have different fracture patterns, with more brittle calcite fractures present in the younger wackestone and the older packstone containing more weathered bedding parallel fractures (Figure 4.93).

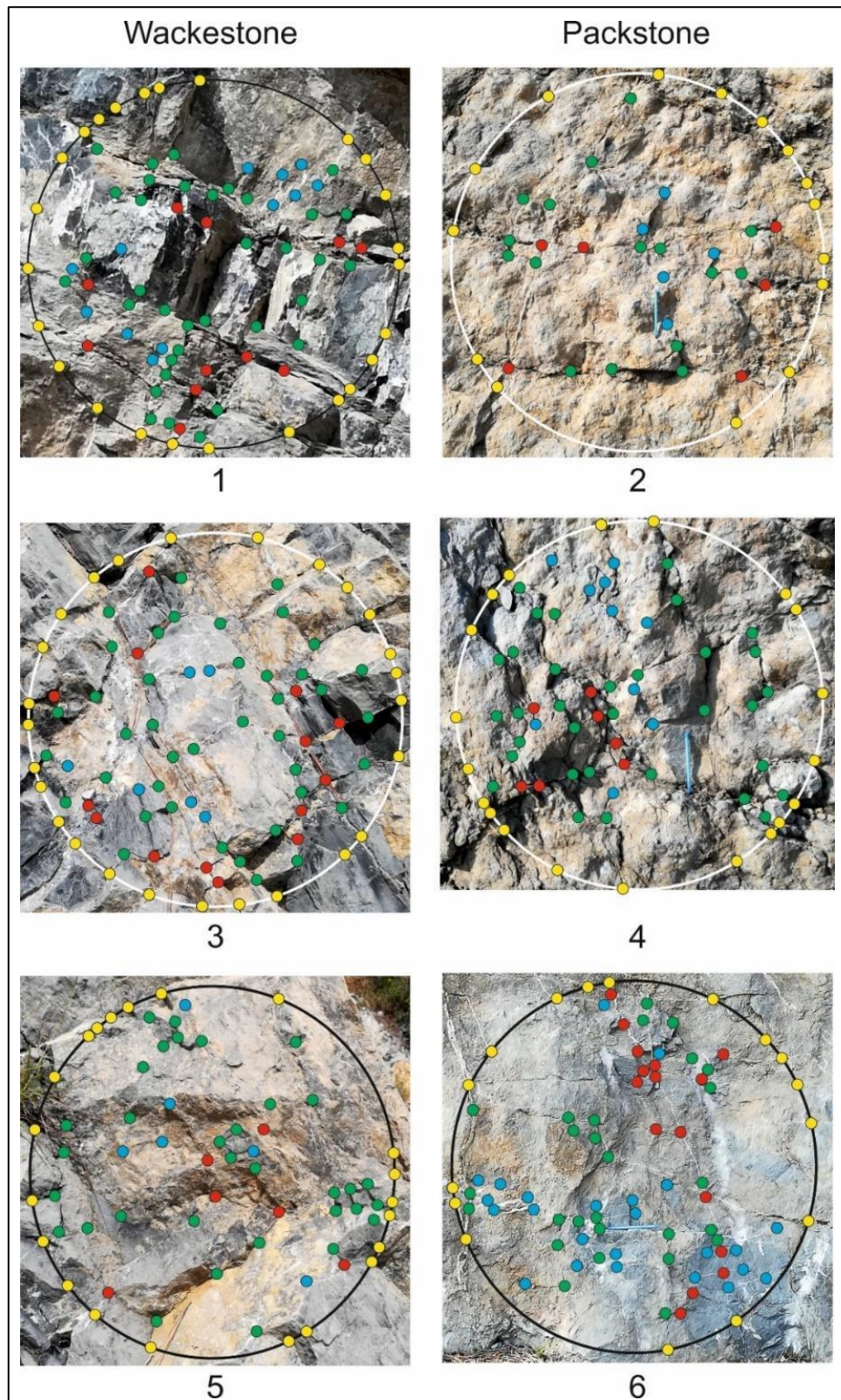


Figure 4.93: Measurement circles placed on the distinctly different wackestone and packstone at site 8. Wackestone circles are shown on the left and packstone circles on the right. This has resulted in the wackestone circle having odd numbers and packstone circles having even numbers.

There are more “e” and “y” nodes in the wackestone, the same number of “x” nodes in the two rock types and more “i” nodes in the packstone (Figure 4.94). On average, there are fewer nodes in packstone which agrees with the empirical observations of the packstone being less fractured.

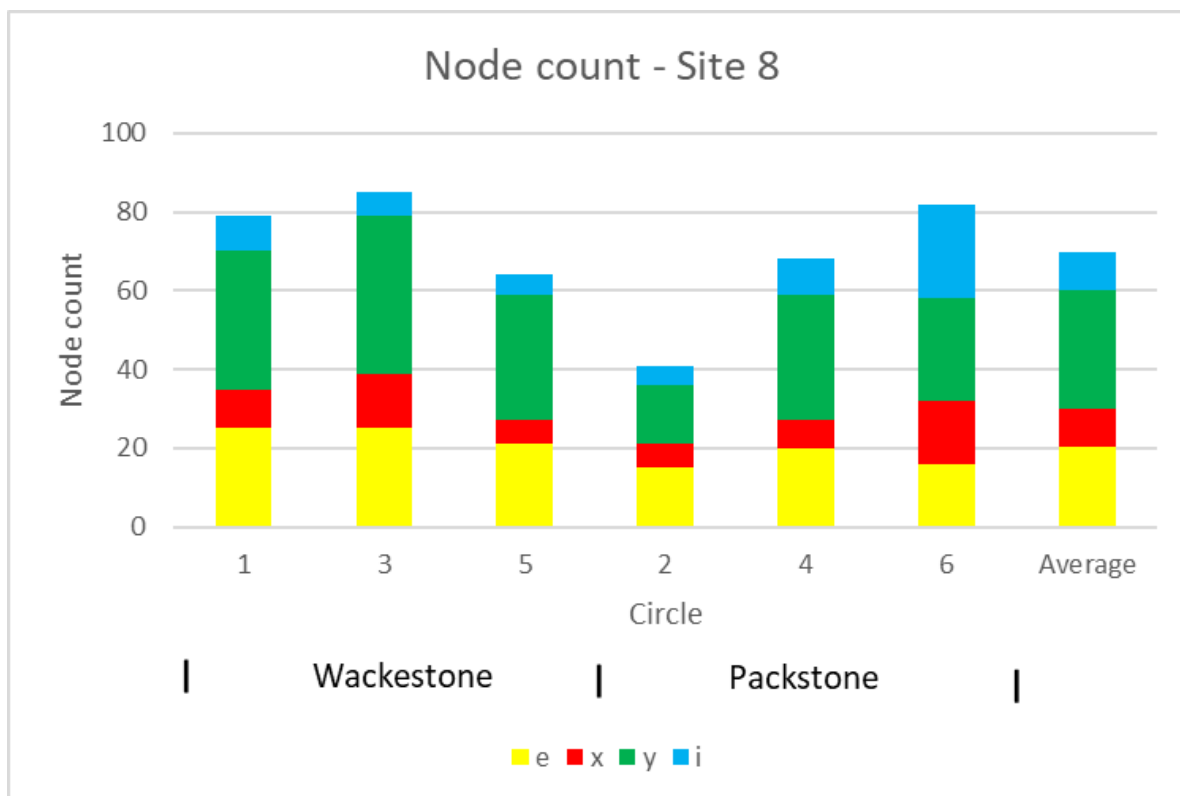


Figure 4.94: Number of nodes at site 8 – derived from the measurement circles shown in Figure 4.93.

The wackestone has a greater (and more consistent) number of tips, lines and especially branches as well as a slightly shorter mean trace length (Figure 4.95). Figure 4.95 also shows that the wackestone has a lower average fractal dimension (1.95) compared that of the packstone (1.97).

The wackestone is also characterised by higher connectivity, fracture intensity, and fracture density than the older fossiliferous packstone (Figure 4.96).

It is suggested that the *Thalassonoides* burrows and surface tracks in the packstone may have impacted its mechanical behaviour. As a result of the bioturbation, the thicker beds are less mud-rich (either because the mud has been filtered for food or disturbed by movement). Thin layers of mud are periodically deposited on the thicker units which has allowed a significant difference in the shear

strength of different units to develop. This contrast in shear strength, especially considering the associated weathering of the mud-rich layers has caused the fracture pattern of the packstone. The wackestone was probably deposited at a greater depth and therefore not inhabited but similar periodic deposits of shale also allow the development of low cohesion layers that can be sheared.

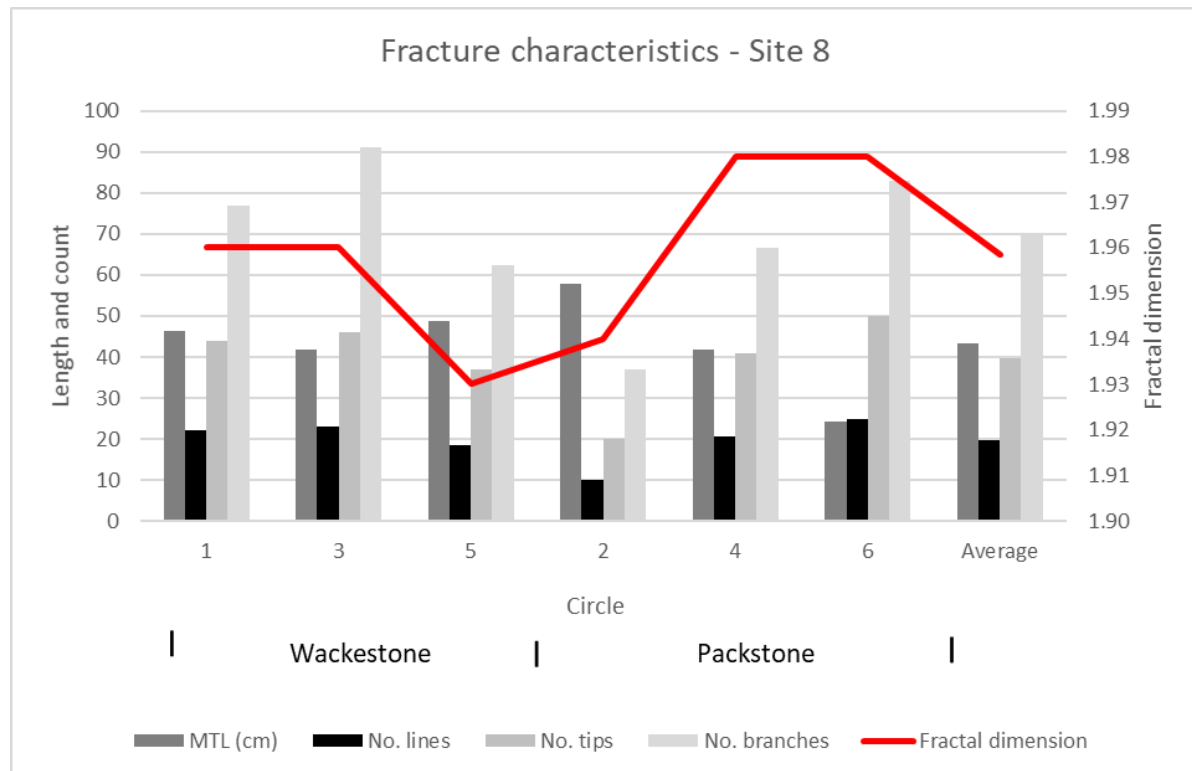


Figure 4.95: Mean trace length (MTL) in centimetres, number of lines, nodes, and branches and fractal dimension at site 8.

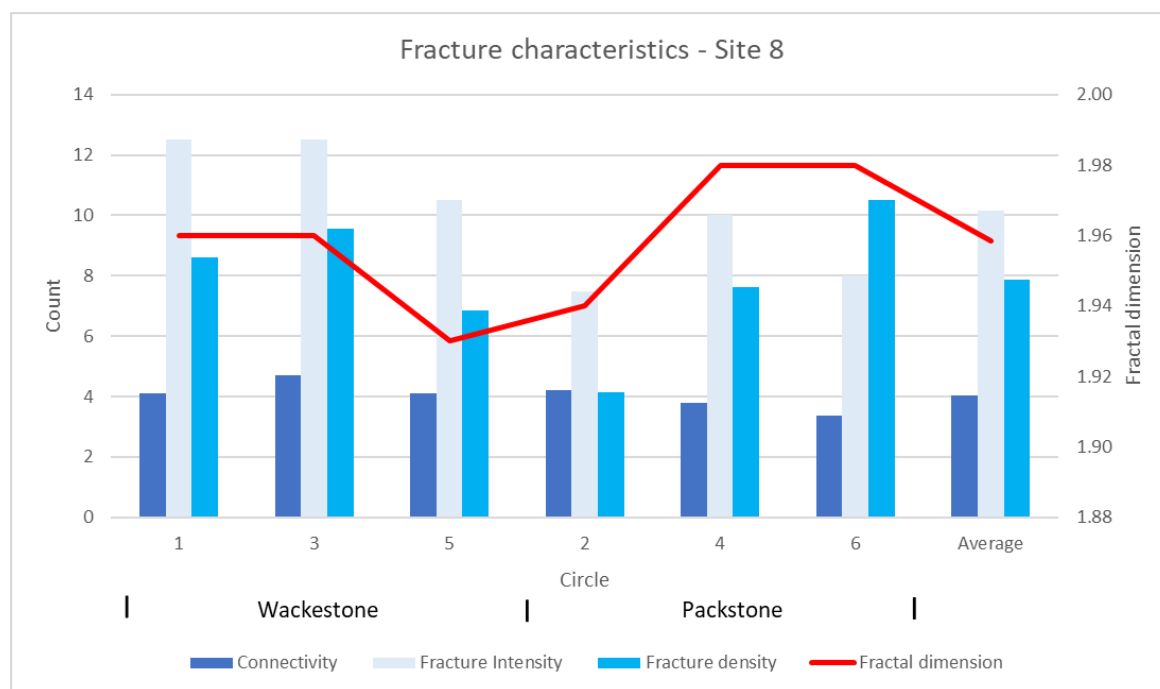


Figure 4.96: Connectivity, fracture intensity, fracture density and fractal dimension at site 8.

4.2.2.9 Summary

Overall, the sites in the Makhniyal area have a high degree of fracturing, being located on a regional thrust (1,2, and 4), a large normal fault (6) and a tightly folded and overturned anticline (7). Different methods were employed to characterise the most highly fractured sites. Topological and fractal fracture characteristics were derived from conventional 1 m wide measurement circles in both highly fractured sites (2, 3, and 6) and less fractured sites (5 and 8). As the rock mass was highly weathered at site 1, it was decided that no meaningful measurements of the fracture characteristics could be made there.

Site 4, located on the Whispering Pines Thrust, was examined using squares to evaluate the density and spacing of fracture node intersection types in grids of 5 cm squares. At site 7, the intensity of the fracturing required the evaluation in 5 cm wide circles to determine the different fracture types, the distribution of different fracture lengths. The graphs in Figure 4.97 through to Figure 4.99 only show data from sites 2, 3, 5, 6, and 8, as site 1 does not have measurement circles and at site 7, the circles are 5 cm in diameter. Site 6, located on a large-scale normal fault (Figure.4.49), has the greatest number of nodes (“e”, “x”, and total) of data-sets of the Makhanyal region (Figure 4.97). The site is characterised by the highest (Figure 4.98). It also has the highest fracture intensity, density, and connectivity (Figure 4.99). These all appropriately characterise the highly fractured rock mass of the fault zone shown in Figure 4.101

The high values of the intensely fractured rock mass quantified above for site 6 are closely followed number

of fracture nodes, the calculated topological characteristics, and the high fractal dimension by the characteristics of site 2 (Whispering Pines Thrust). This site has the second highest “e”, “x”, and total number of nodes. It has the second highest connectivity and fracture intensity as well as the longest MTL. It also has the second highest fractal dimensions. These lower values are because foot-wall and hanging-wall measurements needed to be included to properly characterise the rock mass. Focussing only on the thrust (site 4) generates high values indicative a highly fractured rock mass. However, as the thrust is part of a structural and fracture system (including the immediate foot-wall and hanging-wall), it is appropriate to consider the characteristics in the manner that they have been done (two measurement circles in the foot-wall, six in the thrust and two in the hanging-wall).

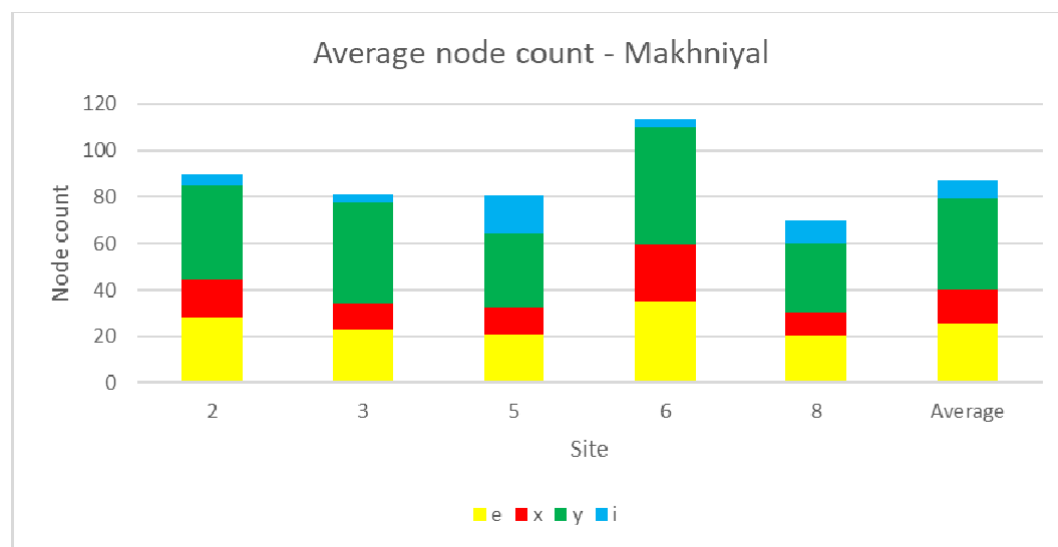


Figure 4.97: Average number of nodes at the measurement sites in the Makhniyal region.

The high values of the intensely fractured rock mass quantified above for site 6 are closely followed by intense fracturing as evidenced by the high number of “e”, “x”, and “y” nodes (Figure 4.97) with resulting higher topological values, especially the number of branches (Figure 4.98). Site 3 has the lowest MTL. The fracture connectivity, density, and intensity as well as the fractal dimension (1.87) is also lowest at this site which has been subjected to the least structural deformation.

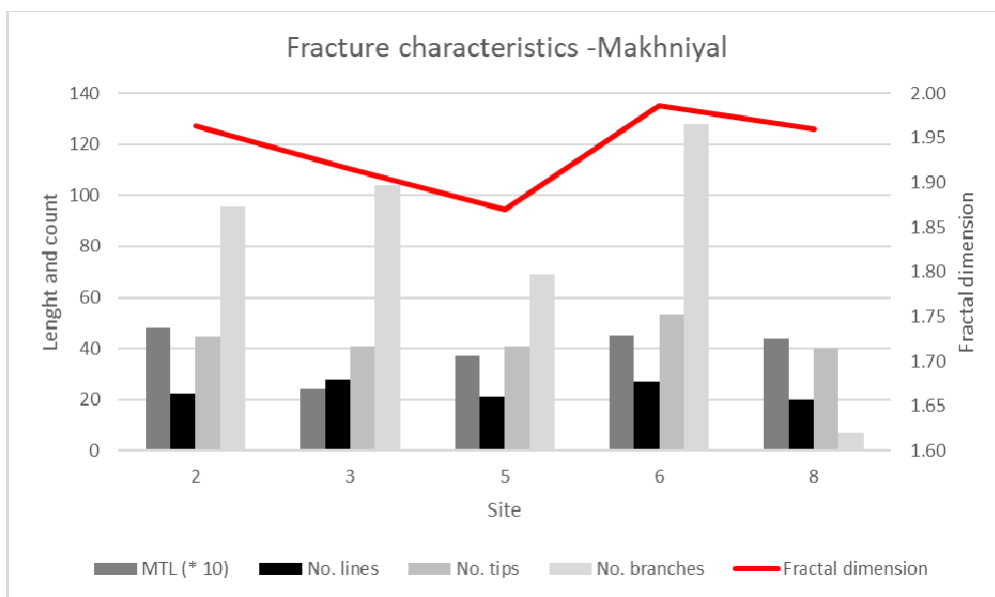


Figure 4.98: Fracture characteristics – mean trace length (MTL), number of lines, tips, and branches as well as fractal dimensions at the various mapping sites in the Makhniyal region.

The overturned limb of the anticline (site 8) is very similar, low numbers in the same relative abundance with “y” nodes being the most abundant followed by “e”, “i” and “x” nodes. As a result of this, the calculated topological values with them either having the lowest or second lowest value for each parameter, apart from MTL which is shortest in the thrust hanging-wall (site 3). A similar distribution occurs when considering the fractal dimension with site 5 having the lowest, followed by site 3 and then only site 8. (Figure 4.99).

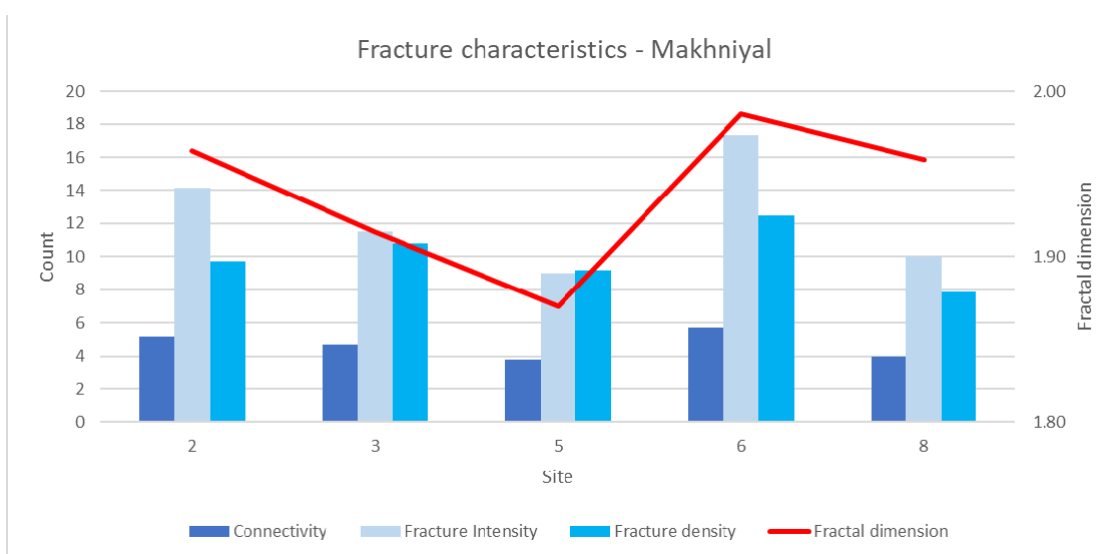


Figure 4.99: Fracture characteristics – connectivity, fracture density, fracture connectivity and fractal dimension at the various mapping sites in the Makhniyal region.

When comparing the number of nodes with the associated fractal dimension for each measurement

circle, several distinctive characteristics are evident:

1. Figure 4.100 shows that the overall number of nodes and fractal dimensions have a limited distribution and form a tight concentration. There is no systematic relationship between the two parameters and the slope of the best-fit line (0.001) suggests that the fractal dimensions will remain similar whatever the number of nodes is.
2. When divided into different sites, distinct clusters are apparent (Figure 4.101). Site 2 has, on average, the second highest number of nodes and a similar fractal dimension to site 8, which has much fewer nodes. Site 3 forms a tight cluster with a lower fractal dimension. The lowest fractal dimension is at site 6, but it also has the greatest variety in fractal dimensions (Figure 4.101). The highest average number of nodes and fractal dimension is found at site 6 and in fact circle 2 of this site has the greatest value (161, 2.00).
3. The most abundant of node types are “y”, followed by “e”, “x” and “y” nodes (values of 39, 25, 14, and 6 respectively). There is large amount of overlap between the number of each type of node (Figure 4.102).

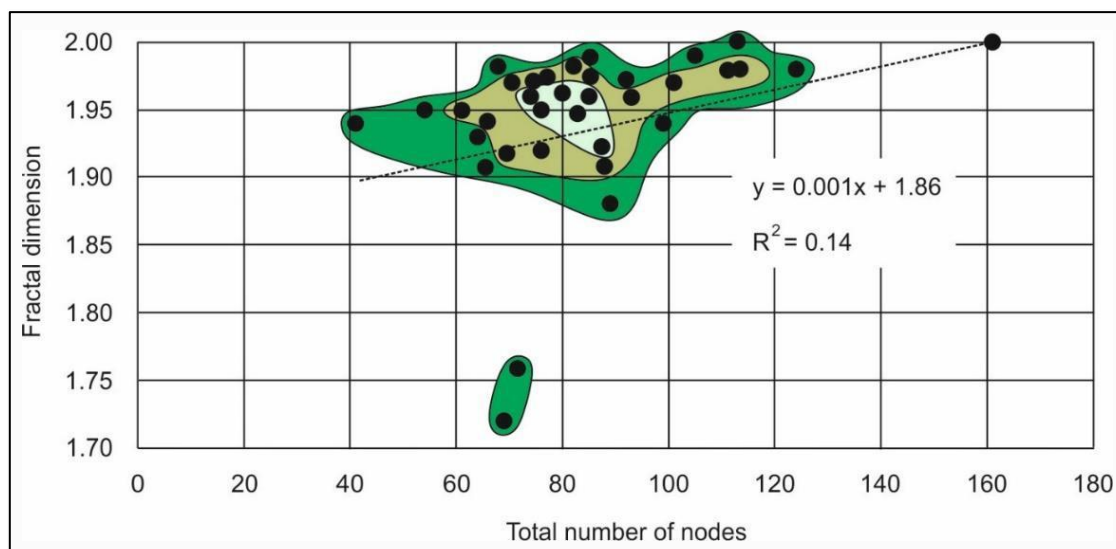


Figure 4.100: Contoured plot of the total number of nodes versus fractal dimensions for all circles in the Makhniyal region.

There is a distinct separation in the number of different of nodes, irrespective of site (black symbols

in Figure 4.102) and the fractal dimensions show separation depending on the site (different coloured symbols in Figure 4.102). This is because there are an increased number of longer cross-cutting “y” nodes that intersect the circle boundary where-as there are few “i” nodes that do not intersect. This suggests a greater shear stress in the region relative to the strength of the strata.

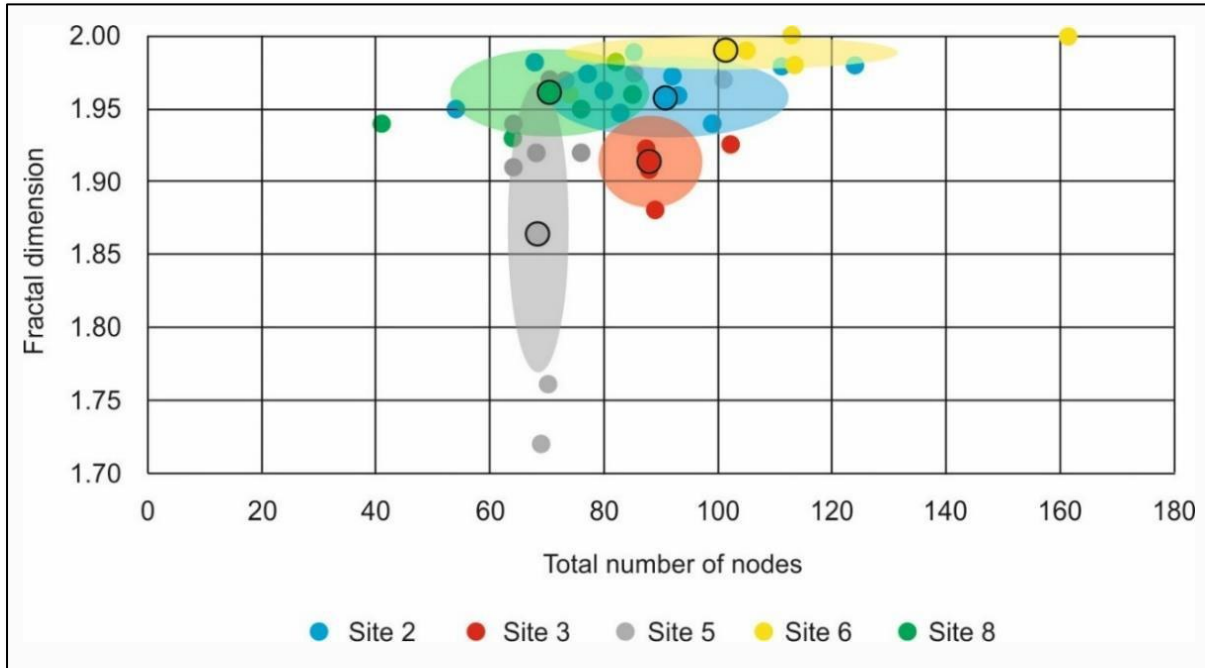


Figure 4.101: Plot of the total number of nodes versus fractal dimension at each site in the Makhniyal region. The average number of nodes and fractal dimension is shown by the larger circle bordered in black. The semi-transparent ovals, the same colour as the site, indicates the area covered by one standard deviation.

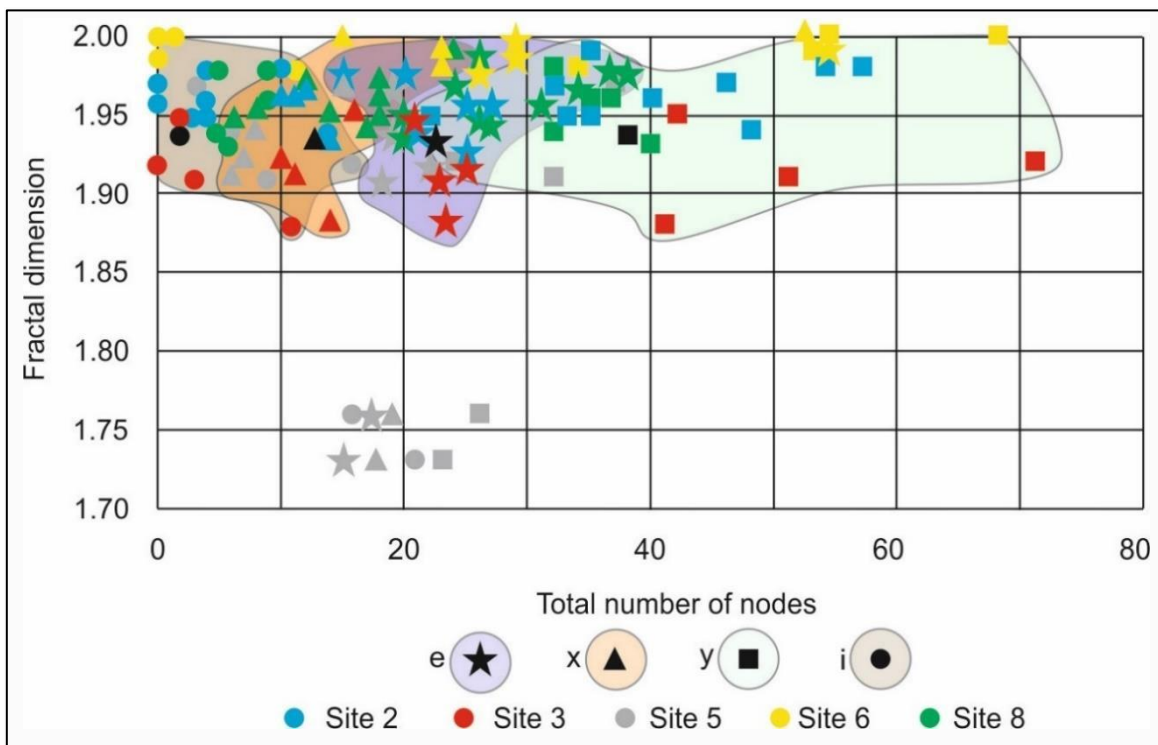


Figure 4.102: The number of nodes of each type at each site (in the Makhniyal region) are plotted against their fractal dimension. The extent of the different node types is highlighted; “y” nodes are generally more numerous, followed by “e” and “x” nodes, with “i” nodes being the least abundant.

4.2.3. Najafpur region

The Najafpur region is located north of the Talhar region (Section 4.2.2) and immediately to the west of the Makhniyal region (Section 4.2.4). The river valley is extensively farmed with fields and scattered farmhouses spread across the alluvium (Figure 4.103), and the only settlement in the area that is demarcated on Google Earth is the village of Najafpur (33° 48.1' N, 72° 59.1' E). The field mapping sites are located along the road between the Kanpur Dam to the west and Pir Sohawa to the east (Figure 4.104 and Table 4.7).



Figure 4.103: View southwards from site 1 across the farms in the river valley towards mountains composed of the Lockhart Formation.

The most geologically significant feature in this area is a large, overturned anticline (which is examined in detail in the description of site 3). The anticline has controlled the flow of the rivers and hence the guided the distribution of the farming and accompanying roads (Figure 4.104).

The rocks in the region range from the Lower Cretaceous Lumshiwal through to the Early Eocene Margala Hills formations. Of all of the rocks, the Early Eocene Nammal Formation had the best exposure, due to the east-north-east striking folds and the cover of recent alluvium (Figure 4.104).

The only good exposure of the Middle Paleocene Lockhart Formation (which usually outcrops well because it is a wackestone, that is resistant to erosion), was in the steep sided valley near site 3.

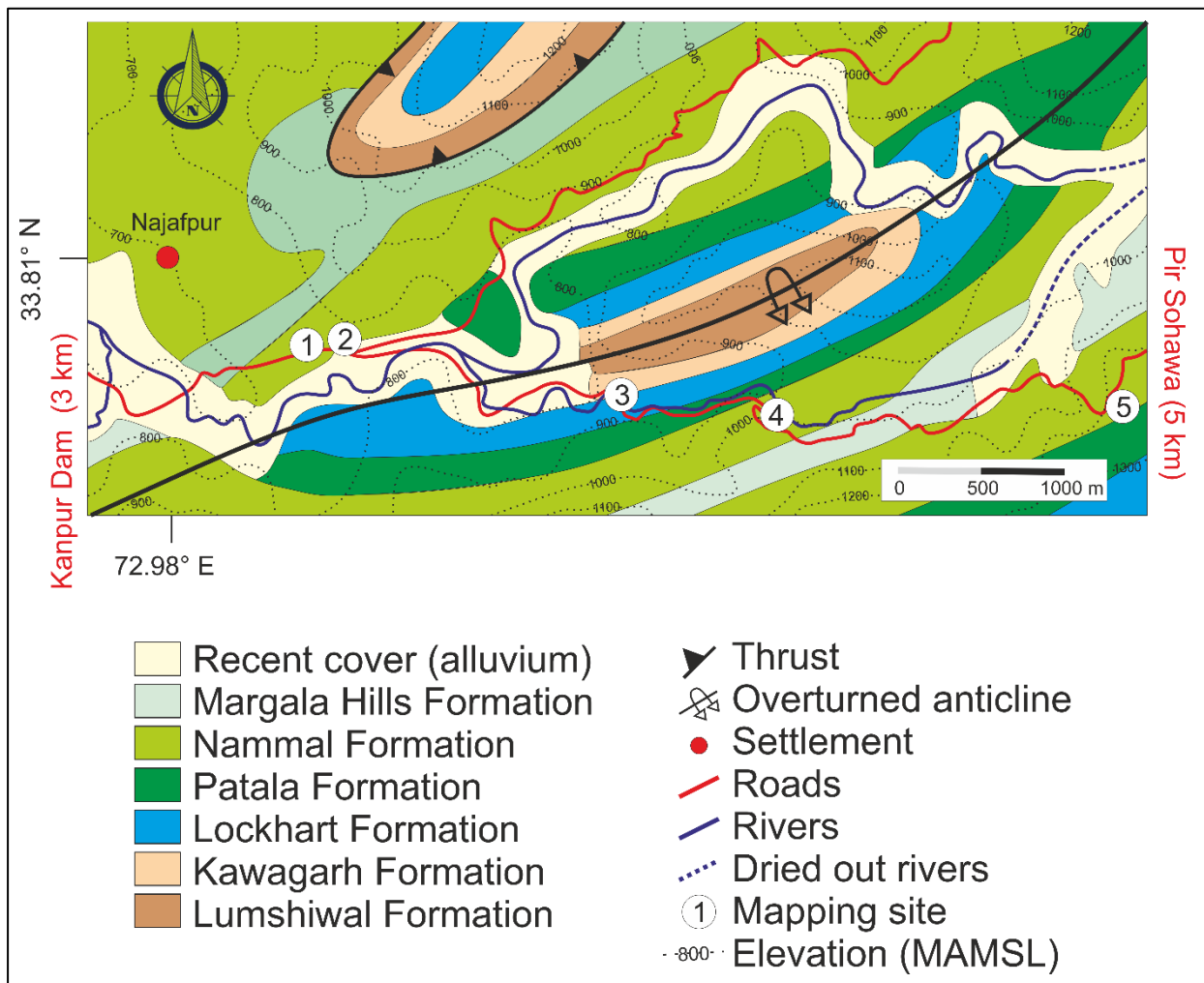


Figure 4.104: Geological map of the Najafpur region. The region is separated from the Talhaar region (Section 5.2.3) directly to the south by a 1 300 m high range of mountains.

Table 4.7: Location of mapping sites relative the major structure and their stratigraphy.

Site	Latitude (N)	Longitude (E)	Stratigraphy	Structure
1	33.796°	72.998°	Nammal	1.5 km from overturned anticline
2	33.796°	73.000°	Nammal	1.5 km from overturned anticline
3	33.792°	73.022°	Lockhart	Overtured anticline
4	33.793°	73.035°	Nammal	1 km from overturned anticline
5	33.793°	73.059°	Nammal	1.5 km from overturned anticline

4.2.3.1 Site 1

The rock exposure is poor at site 1 (Figure 4.105). However, it was possible to determine both rock type and structural features. The rock is a light grey wackestone without any fossils or any internal sedimentary structures visible. Fractures are developed in a variety of orientations, with NNE-SSW striking, unmineralised and calcite filled fractures dominating the assemblage. This is sub-parallel to the regional strike and is a similar strike to the shears encountered at site 2. As the strata have a steep regional dip, the 30 cm width of the exposures may indicate bedding thickness.

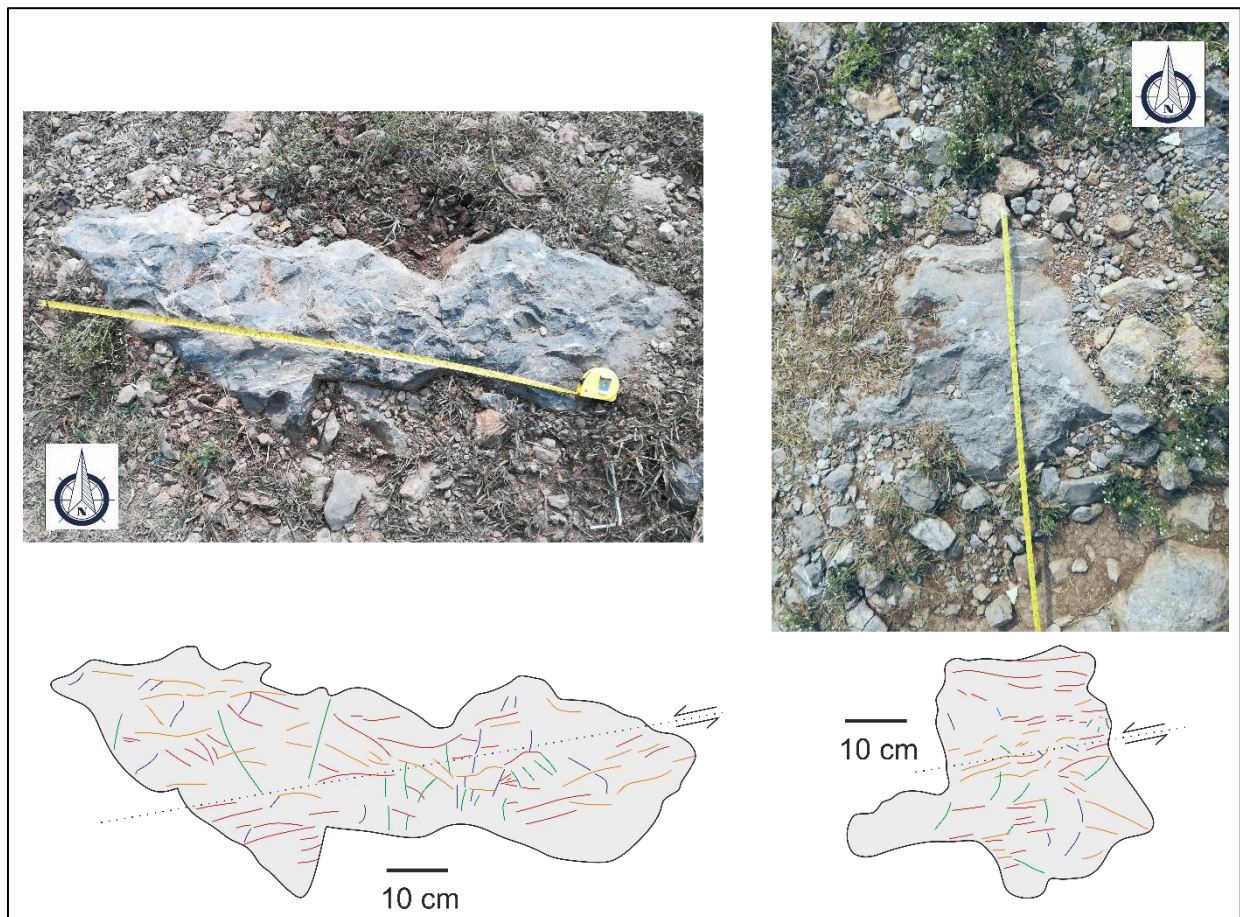


Figure 4.105: Plan-view of light grey wackestone at site 1. Although fractures are developed in many different orientations, the predominant direction is ESE-WNW (shown in red and orange). The rocks are steeply dipping with the upper and lower contacts possibly representing bedding surfaces. Ruler in photographs = 1 m.

4.2.3.2 Site 2

Approximately 200 m east of site 1, a multi-faceted group of rocks is present at site 2. This variety is due both to the original sedimentary characteristics and how the rock has subsequently deformed and weathered. The rocks consist of a sheared dark grey shale and limestone layer bound by fragmented wackestone and underlain by a section of flowstone covered limestone fragments (Figure 4.106). As the strata are steeply dipping and may have been overturned, it is not possible to determine the relative stratigraphic age. The assemblages are therefore described in terms of the structural deformation with the addition of flowstone defining a third rock-type, which is re-cemented limestone

fragments. The uppermost portion of the exposure consists of decimetre-sized fragments of light grey wackestone.

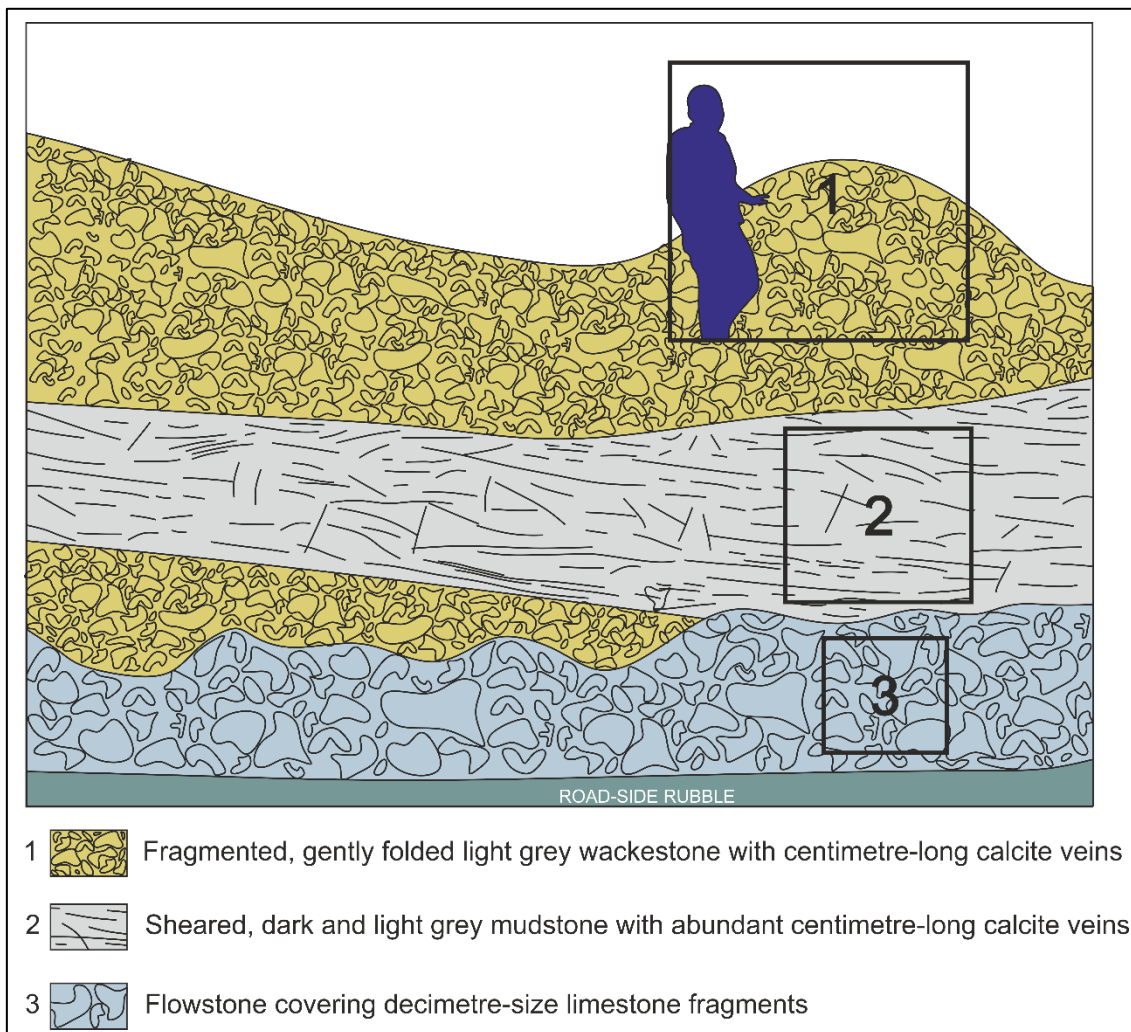


Figure 4.106: Cross-sectional sketch of the rock types exposed at site 2. The rocks are categorised according to their primary sedimentary character, deformation characteristics and subsequent weathering into three types. Geologist in blue.

These rocks are folded both north-south and east-west to form a small dome structure that dips to the north at approximately 50 degrees (Figure 4.107). It is not known if this dome is the right way up or overturned. The central portion of the exposure at site 2 is similar in character to the rocks at site 1, being a strongly sheared shale. At site 2, there is much better exposure and the strongly developed steeply dipping sheared bedding with decimetre-long calcite veins are well developed (Figure 4.107).

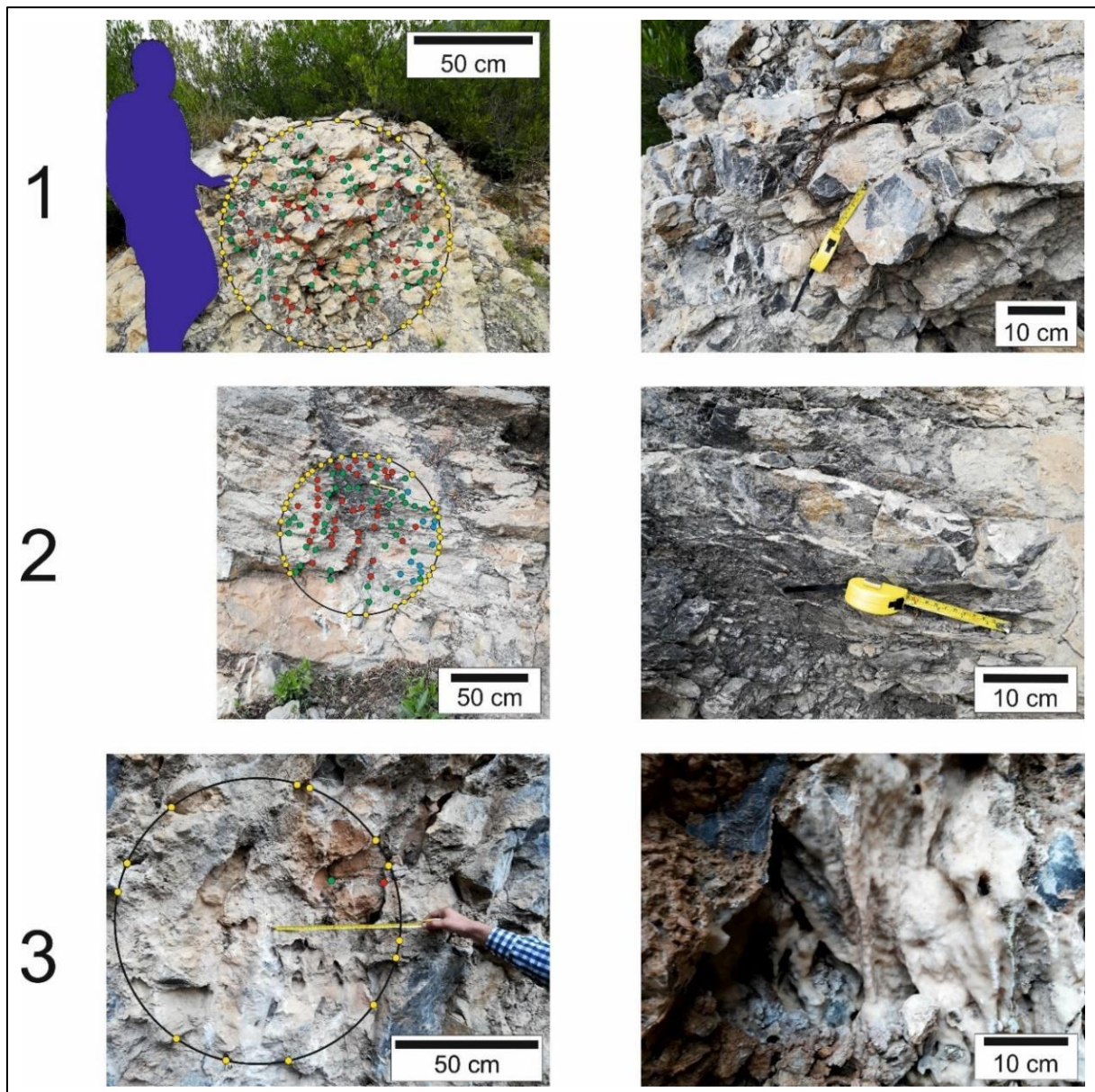


Figure 4.107: Metre- and decimetre-scale images of the three rock types exposed at site 2. (1) sectional view of fragmented and gently folded light grey wackestone, (2) plan view of sheared dark and light grey shale, (3) sectional view of flowstone coated limestone fragments. Coloured dots on metre-wide measurement circles indicate positions of fracture nodes used in topological analyses. See Figure 4.106 for position of images.

The bedding (and shearing) is sub-parallel to the regional WNW-ESE strike of the strata (Figure 4.104). The lower portion of site 3 consists of fragmented limestone covered with flowstone (Figure 4.107) indicating that the fractures in this portion of the rock have been open for some time. The fragmented

rock of circle 1 (Figure 4.107) has the highest number of nodes (Figure 4.108). Circle 3 was mapped in the flowstone coated portion of the exposure. The flowstone obscured many of the nodes and fractures, and as a result the total number of nodes at each site varies between 25 and 154 (Figure 4.108), with an average of 100 and standard deviation of 55. With this sort of variability, it is unlikely that the average topological characteristics, such as porosity and permeability derived from these measurements would be widely applicable to the rock mass as flowstone tend to precipitate at the edge of a void rather than throughout the rock mass.

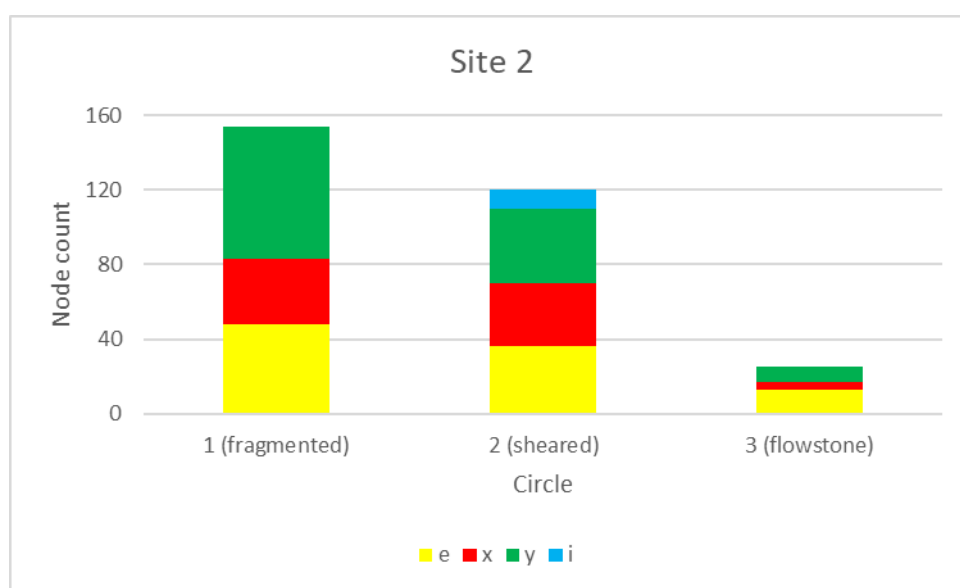


Figure 4.108: Node counts for circles at site 2. The fragmented rock of circle 1 has the greatest number of nodes. Although circle 3 may have the same underlying rock type as circle 1, most of the nodes and fractures have been covered by flowstone.

The average topological and fractal values of site 2, with and without the flowstone measurements were calculated (Figure 4.109). Without the data from the flowstone measurements (circle 3), the fracture connectivity, intensity and density increase the mean trace length is reduced (more individual fractures), and the number of lines, tips and branches increases. It was therefore decided to use the average of circles 1 and 2 alone, to characterise the rock mass at site 2.

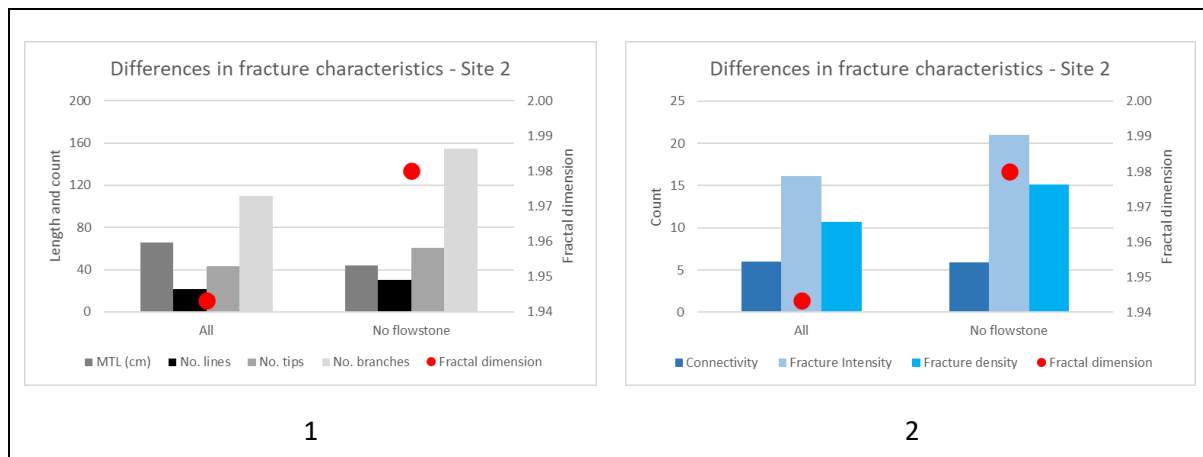


Figure 4.109: Average topological values of site 2, with and without data from the flowstone coated circle 3. (1) The average mean trace length (MTL) decreases in value as more individual fractures are considered. The average number of lines, tips, and branches all increase. (2) The average connectivity, fracture intensity and density are higher when data from circle 3 is removed. The fractal dimension increases from 1.94 to 1.98.

4.2.3.3 Site 3

The Najafpur region is dominated by an overturned anticline (Figure 4.104) which is clearly visible on Google Earth (Figure 4.110). The overturned anticline extends down to site 3 where the steep dipping Lockhart Formation is folded into a smaller 4 m wide parasitic fold on the main 200 m wide fold.



Figure 4.110: Eastward looking Google Earth image showing the dip and strike of the large, overturned anticline and their relationship to the smaller parasitic fold exposed at site 3. “R” indicates the reference point for the position of the anticline ($33^{\circ} 47.9' N$, $73^{\circ} 01.4' E$). The lighter brown rocks in the centre are of the Lumshiwai Formation, whilst the steep, light grey ridge extending eastwards from site 3 is the Lockhart Formation.

Measurement circles 1, 2, 3, 4, and 5 are located from the gently northward dipping strata of the tight parasitic fold, through the tight fold-axis (circle 6) to steeply southward dipping strata in circles 7 and 8 (Figure 4.111). The dip of the strata in these last two circles is the same as the steep regional dip to the north (Figure 4.110). The locations of the fractures were digitised into ArcMap 10.2.2, from which the box density, linear density and fracture length were determined for the fractures (Figure 4.112). Figure 4.113 and Figure 4.114 show the characteristics of individual fracture sets.

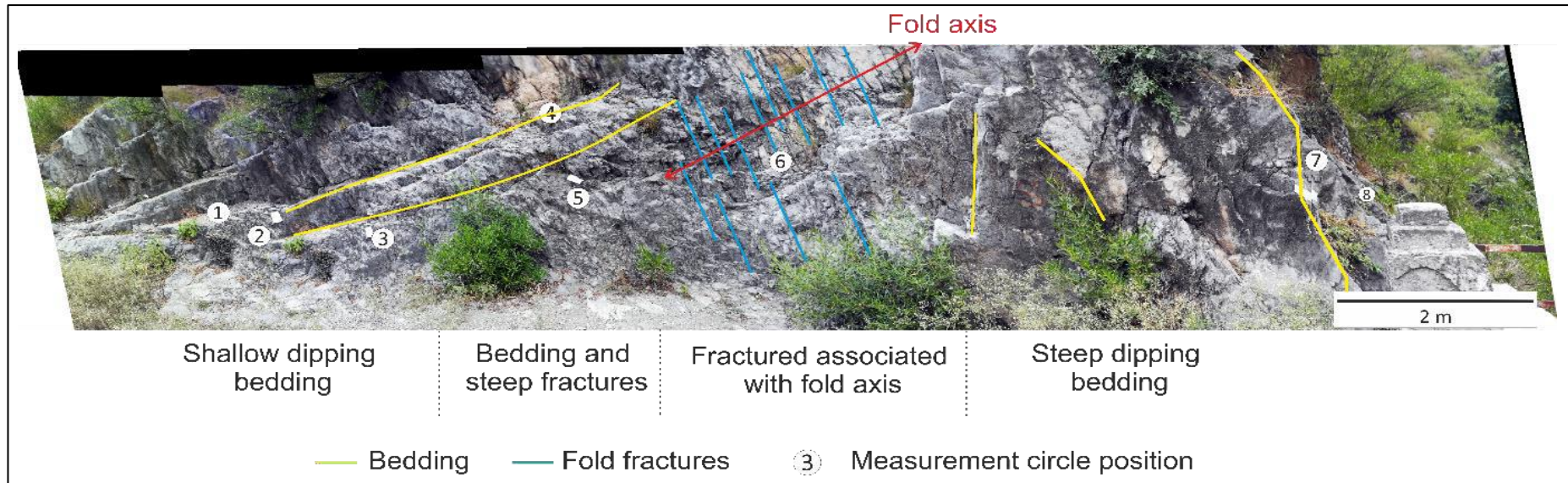


Figure 4.111: View eastwards of the outcrop of the Lockhart Formation at site 3. Fold axis may be assumed to be more to the right, but this is due to fractures being parallel to the line of section. The true position of the fold axis can be identified by the more intense fracturing. The site is located in a deep narrow gorge affording view of the strata on both sides (see Figure 4.110). The western side is however not accessible due to the deep, steeply sided river.

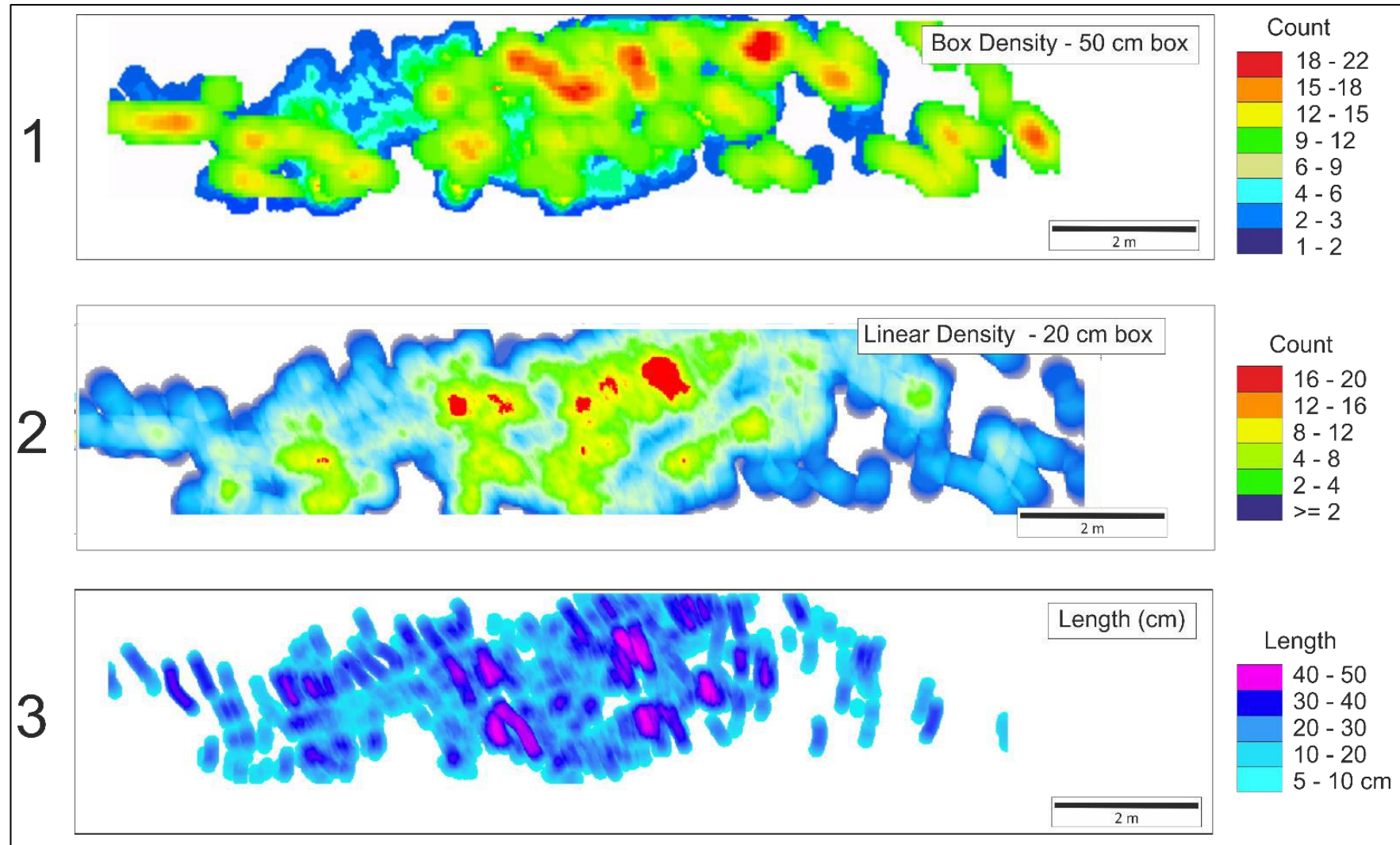


Figure 4.112: Fractures characteristics at site 3 determined by digitising individual fractures. Conventional ArcMap geostatistical tools are used to calculate box

density, linear density, and length of features. Typically, in ArcMap, these tools would be used to evaluate for example road characteristics, but as these are relative measurements the fact that the scale of the combined photographs is probably a 100 times smaller doesn't matter. (1) Fracture density – average number of fractures in a 50 cm box on the photograph. This box is moved stepwise to define changes in the fracture density. The highest density of fractures is along a gently northward dipping bed with abundant internal fractures related to the folding. (2) Linear density of fractures on a stepwise box-count across the surface. The small section in the centre of the image with the highest linear density corresponds to the fold axis. (3) moving average fracture length. The fractures are longest around the fold axis. Interestingly the fractures appear to radiate outwards from the fold axis. This is due to the combined lengths of the smaller fractures restricted to particular beds. When average across the beds, the overall orientation becomes apparent.

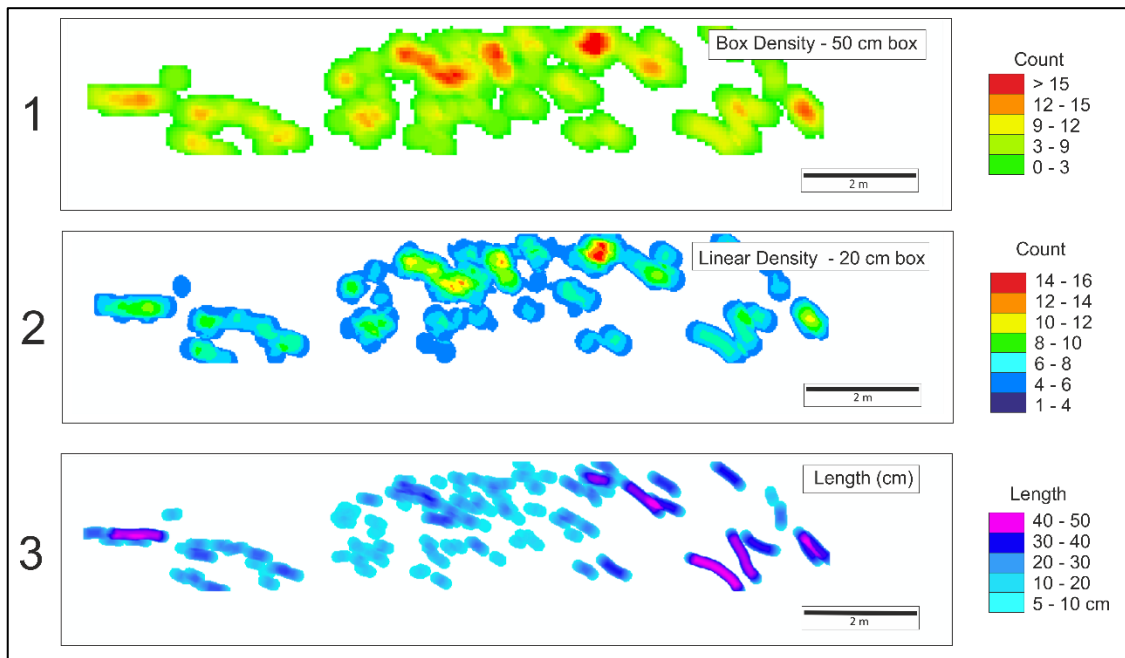


Figure 4.113: Characteristics of bedding surfaces and fractures contained within a single bed. Conventional ArcMap geostatistical tools are used to generate the images.

When the individual fracture sets are considered, a different picture, both of density and length emerges. The fracture densities are lower and show different distributions. More interesting is the variation in the estimated fracture length. When the fractures from a single set are considered, they are not broken up by intersections with other fractures and therefore appear longer (compare Figure 4.112 and Figure 4.113). Similarly, closely spaced fractures are combined to form a more continuous fracture (compare Figure 4.112 and Figure 4.114).

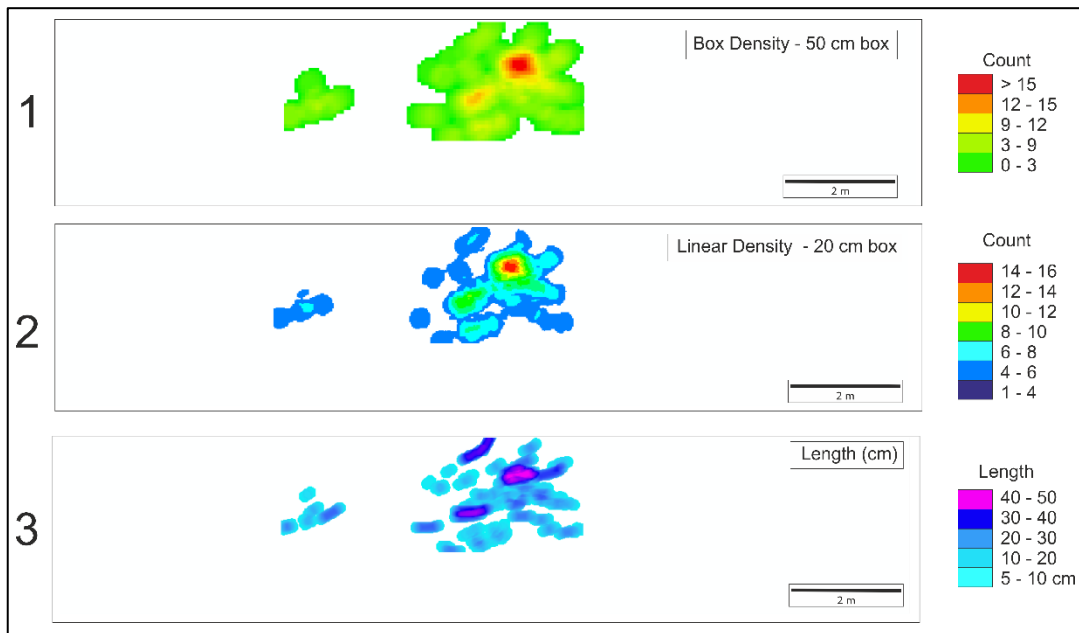


Figure 4.114: Characteristics of cross-cutting fractures of the fold axis. Conventional ArcMap geostatistical tools are used to generate the images.

The length of the bedding plane fractures (n = 137), and the bedding plane bound fractures (n = 560) show a similar exponential distribution between 0.1 m and 1.0 m with a mean length of 0.19 m and 0.17 m, respectively (Figure 4.115). In contrast to this, the length of the fractures associated with the fold axis (n = 58) varies irregularly between 0.15 m and 1.65 m with a mean length of 0.60 m (Figure 4.116). These differences are summarised in Figure 4.117.

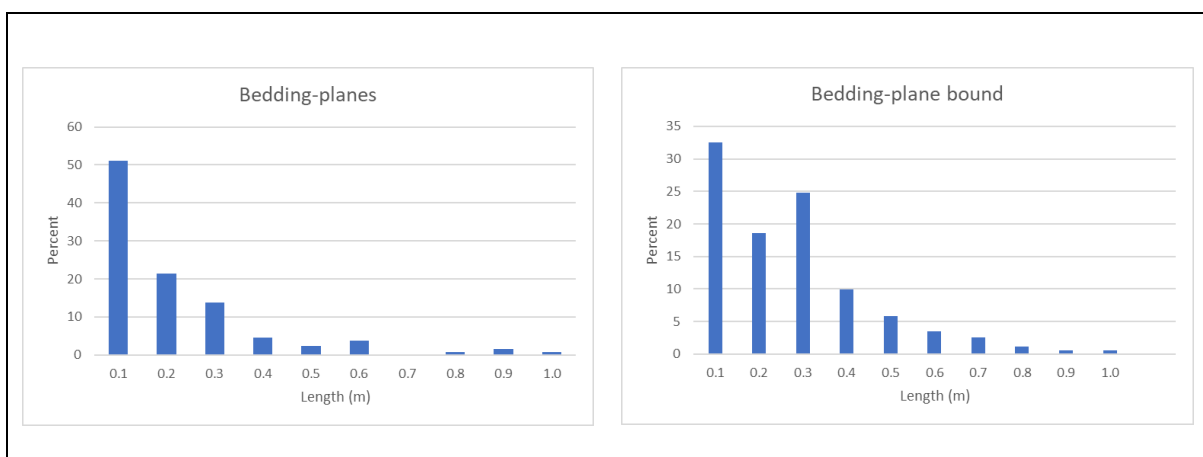


Figure 4.115: Length distribution of bedding plane fractures and fractures within bedding plane.

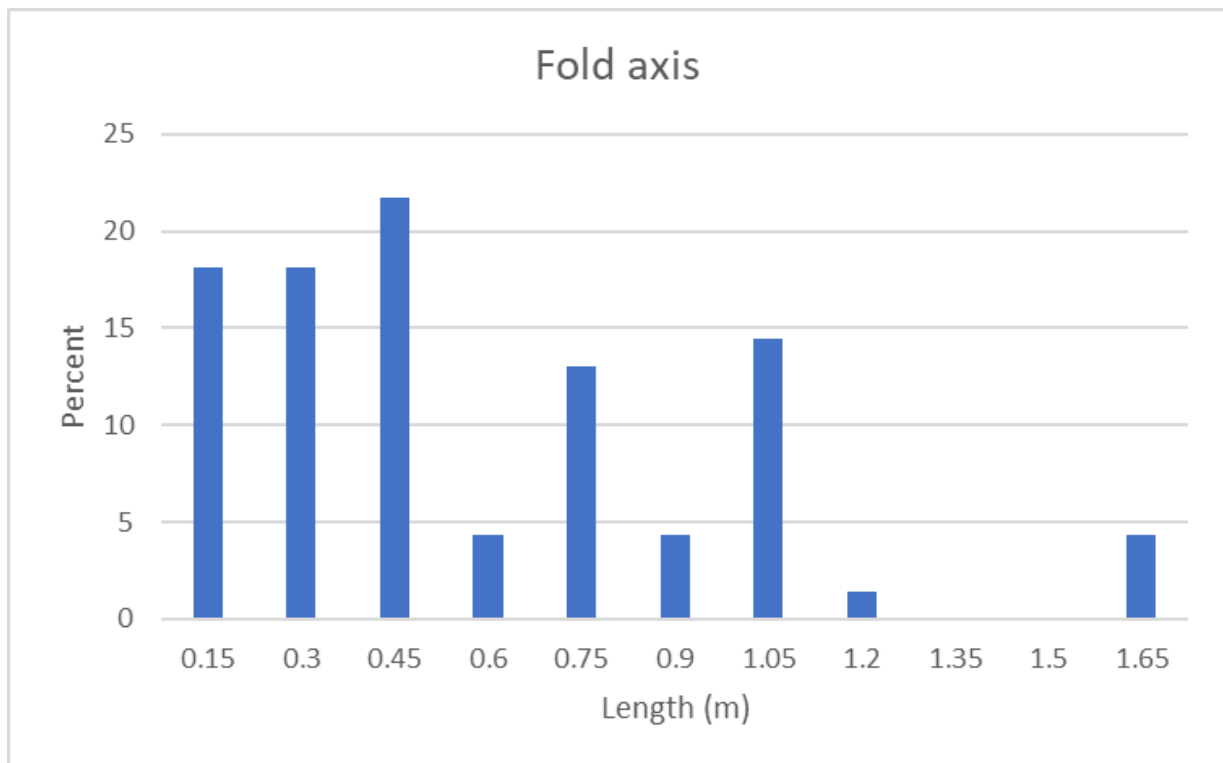


Figure 4.116: Length distribution of fractures associated with the fold axis at site 3.

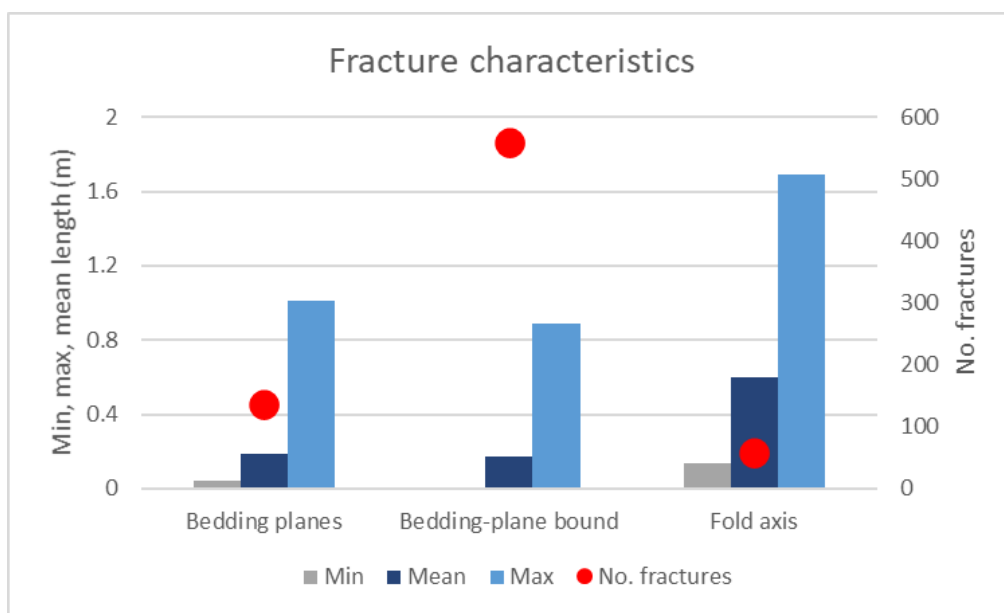


Figure 4.117: Number of fractures and length characteristics. Due to their similar characteristics bedding plane fractures and bedding plane bound fractures are considered together in the spatial analysis (Figure 4.113).

Eight measurement circles were inscribed (in chalk) on the outcrop, with circles 1 to 5 being on the northward, flatter dipping beds, 6 on the fold axis and 7 and 8 on the steep dipping strata. Circles 1 and 4 were located on the bedding plane, whilst circles 2, 3, and 5 were orthogonal to the bedding and between bedding planes. Circles 7 was orthogonal to and bound by the steeply dipping bedding planes and circle 8 on a bedding surface.

The higher number of nodes on the measurement circles orthogonal to the bedding planes is clearly visible in Figure 4.118 and Figure 4.119. Circle 6 (in the fold axis) has the highest number of nodes followed by circles 2, 3, 4, 7, and 5.

The variation of fracture numbers affects the ratio of nodes in the circles at different positions and orientations has had a clear impact on the across the sites.

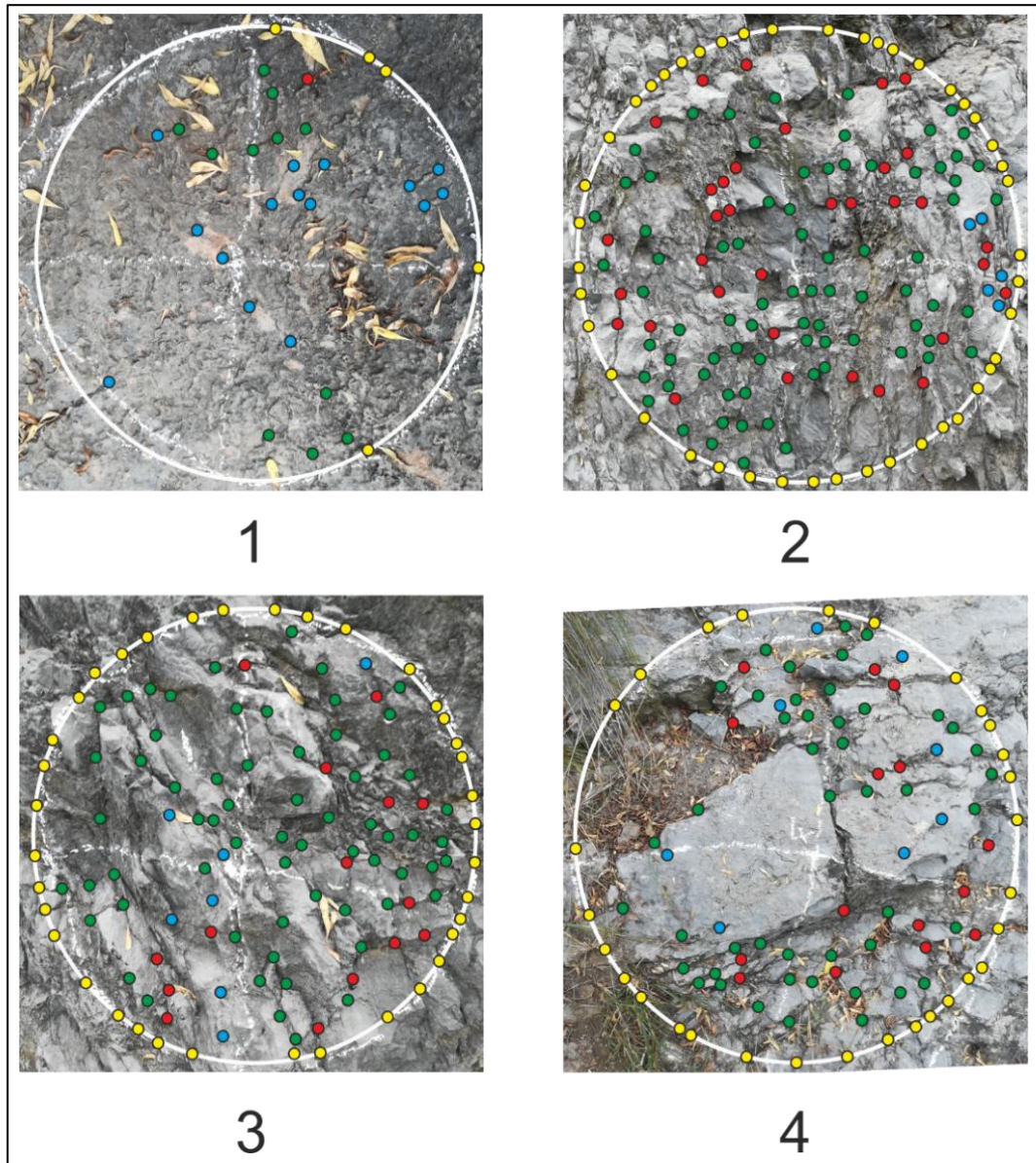


Figure 4.118: Site 3 measurement circles 1 to 4. See Figure 4.111 for location of circles on the outcrop.

Circles 5 to 8 are shown in Figure 4.119.

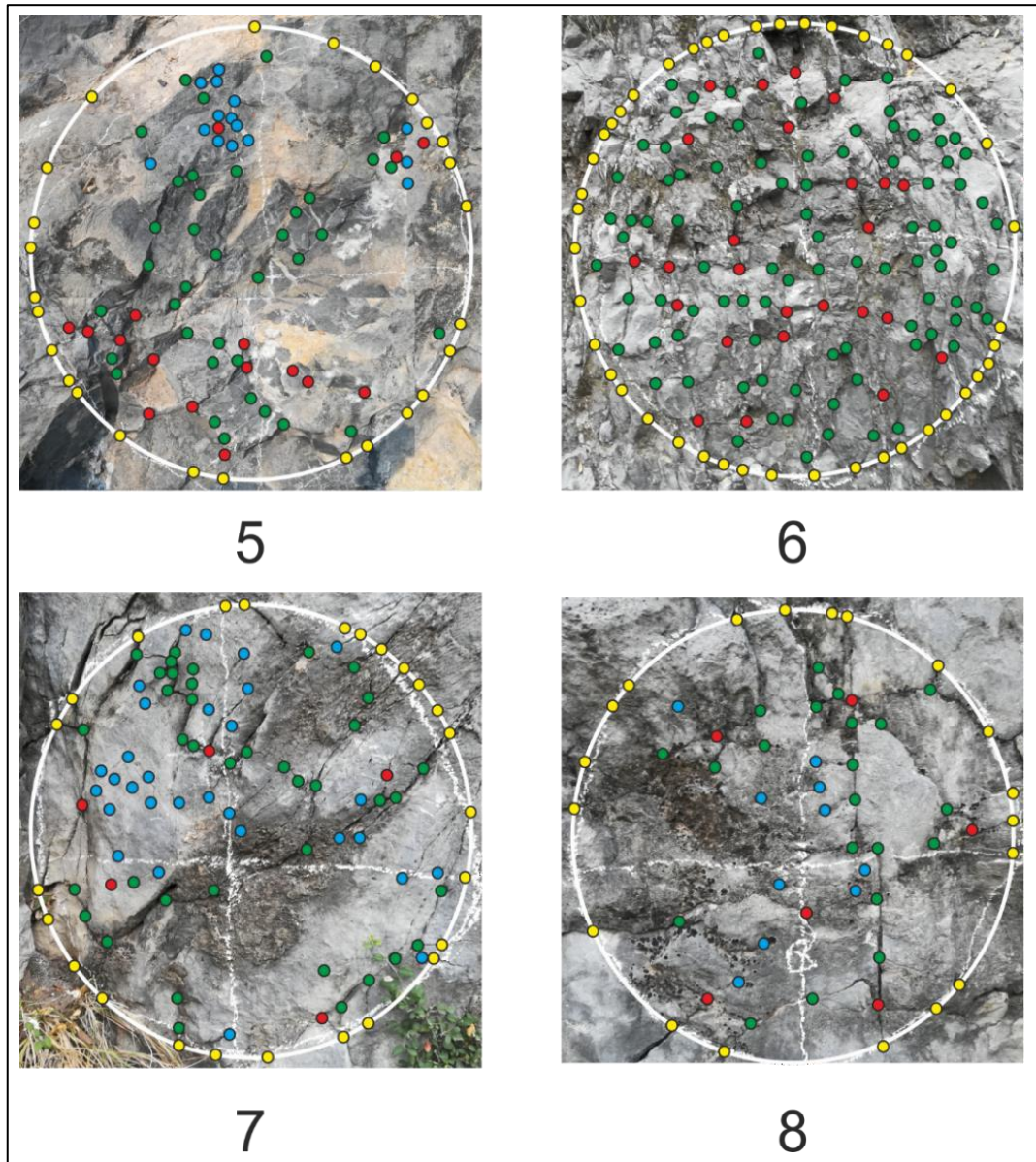


Figure 4.119: Site 3 measurement circles 5 to 8. See Figure 4.111 for location of circles on the outcrop.

Circles 1 to 4 are shown in Figure 4.118.

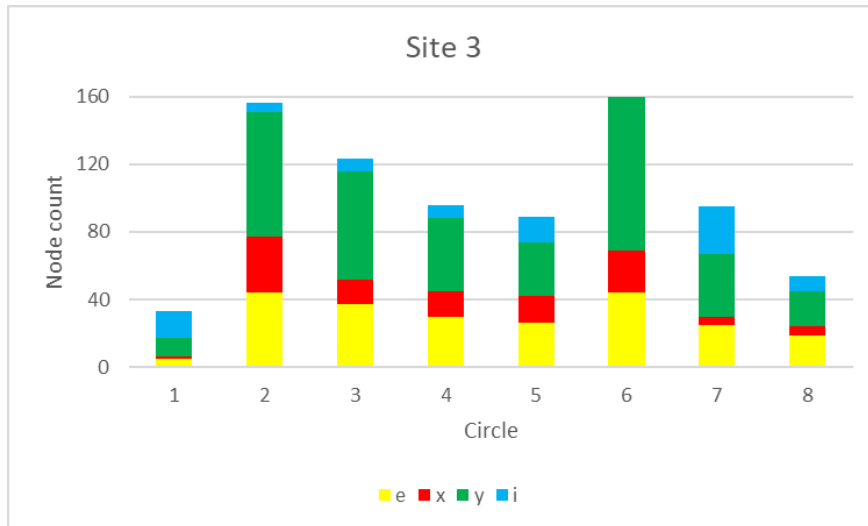


Figure 4.120: Node counts for circles at site 3. The highest number of nodes is in circle 6 in the fold axis.

With the highest number of nodes, circle 6 has the highest connectivity, fracture intensity, fracture density, and the greatest number of lines, tips, and nodes. It also has the highest fractal dimension (Figure 4.121 and Figure 4.122). The cross-cutting fractures of the shallow dipping beds (circles 2, 3, and 5) are the second highest in all the categories. These are followed by the steep dipping cross-cutting fractures, and the bedding parallel circles have the lowest topological values and fractal dimension.

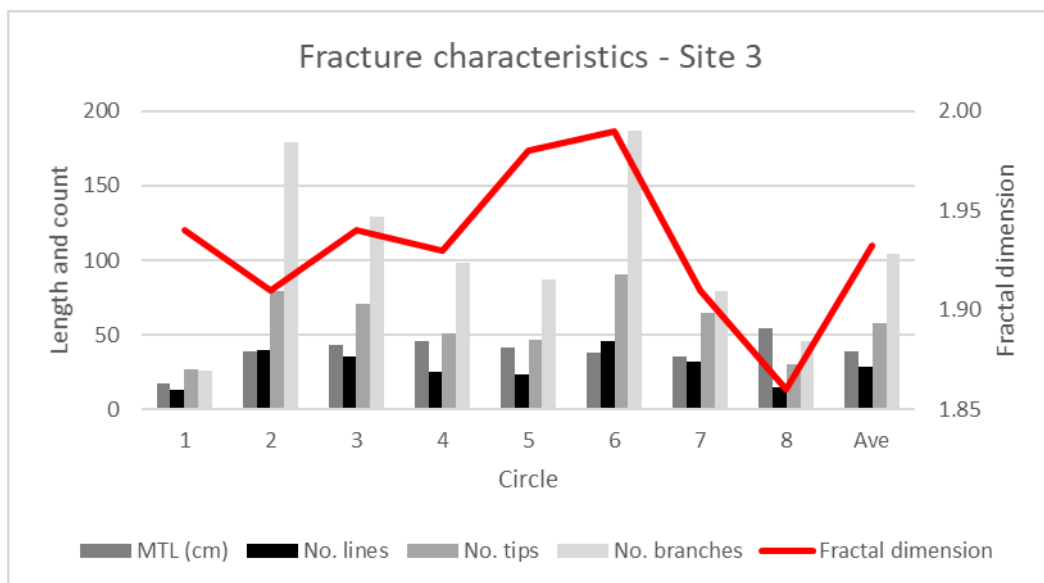


Figure 4.121: Fracture characteristics and fractal dimension, site 3.

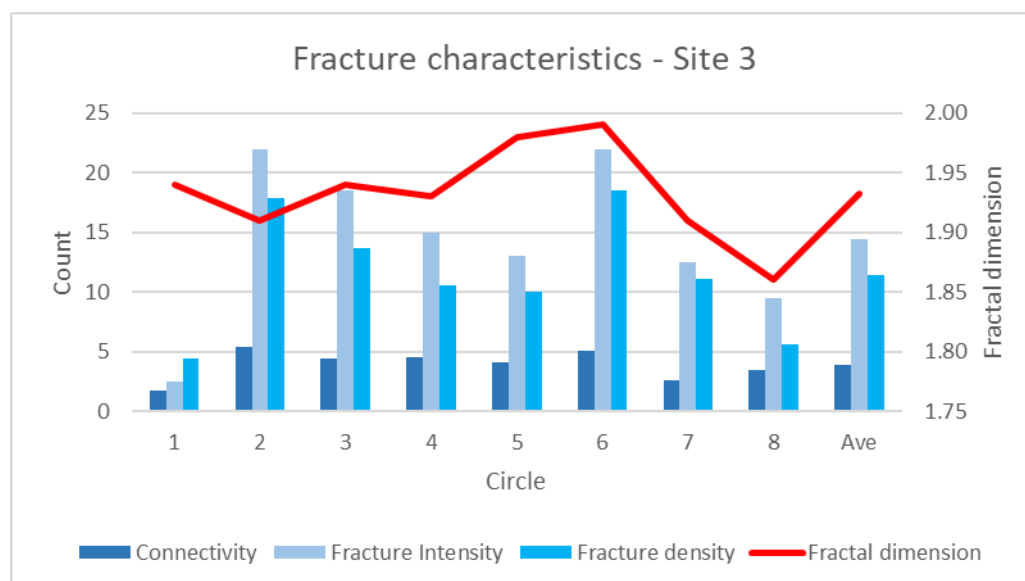


Figure 4.122: Fracture characteristics and fractal dimension, site 3.

This allows the separation into fracture groups into those centred around the fold axis, those orthogonal to and bound by bedding and those parallel to bedding. The length distribution of the latter two categories is very similar (Figure 4.115), it is likely the large number of bedding plane bound fractures ($n = 560$), compared to the number of bedding plane fractures ($n = 137$) that have resulted in different topological characteristics, resulting in them being separated into two different sets. The fracture set around the fold axis contains fractures of both other sets and that the orientation and frequency of these sets influence each other.

4.2.3.4 Site 4

No mappable exposures of the fissile dark brown Patala Formation marine shales were present along the road (Figure 4.104). Site 4 is a steeply dipping exposure of the Nammal Formation (Figure 4.104). The interbedded layers of more erodible sheared shale and more resistant wackestone are visible in Figure 4.123. Figure 4.124 illustrates the location of the measurement circles on a 5 m wide accumulation of 50 cm thick packstone beds. The nodes mapped in these measurement circles are shown in Figure 4.125.



Figure 4.123: Steeply dipping strata of the Nammal Formation. View northeast, across the river valley along strike in opposite direction of Figure 4.124.



Figure 4.124: Distribution of measurement circles on the western sidewall of the road cutting at site 4. Geologist in blue.

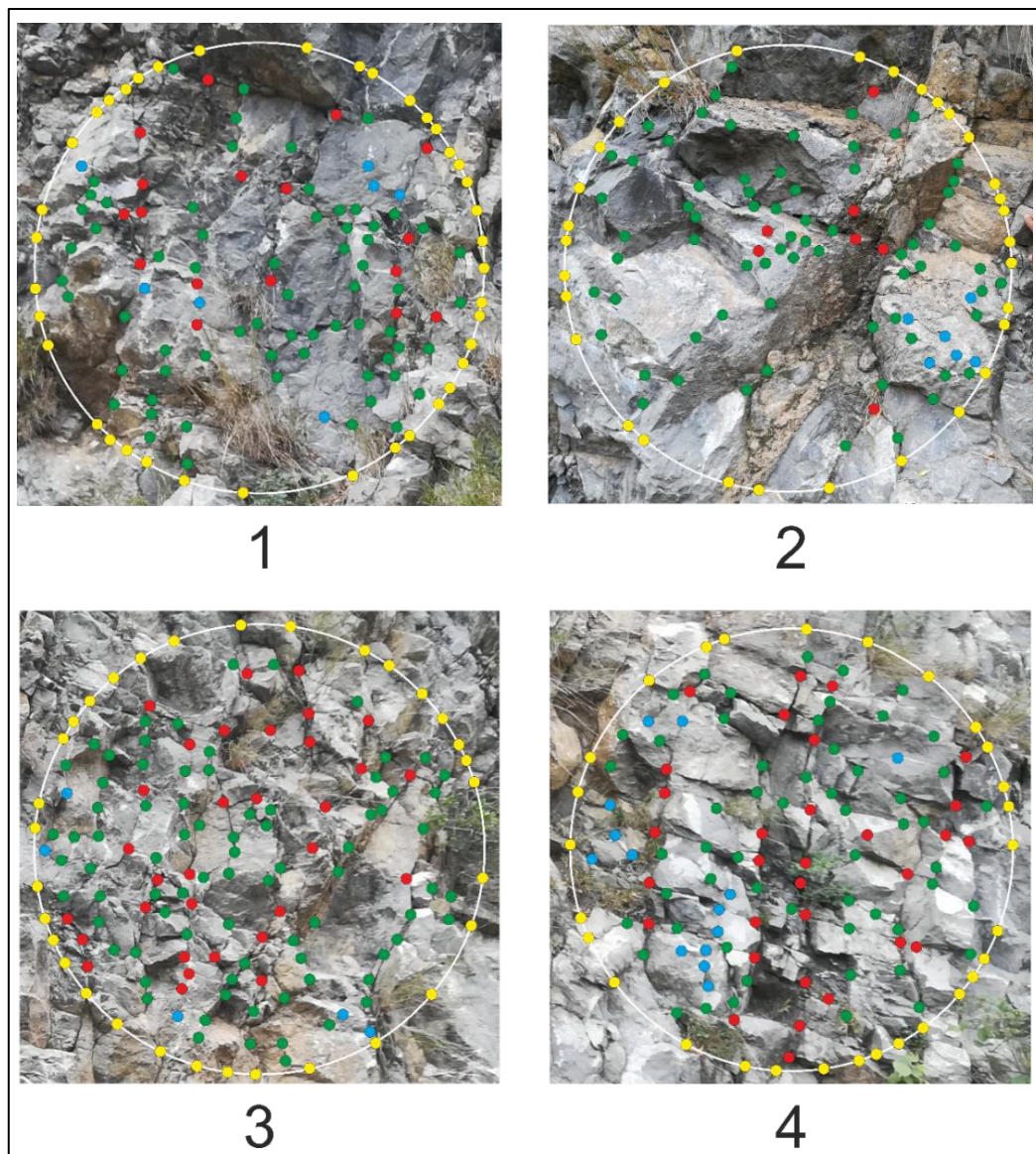


Figure 4.125: Measurement circles at site 4.

The total number of nodes in the different measurement circles does not vary significantly (average = 130 and SD = 13). The node ratios are the same for the various circles being dominated by “y”, followed by “e”, then “x” and few “i” nodes (Figure 4.126).

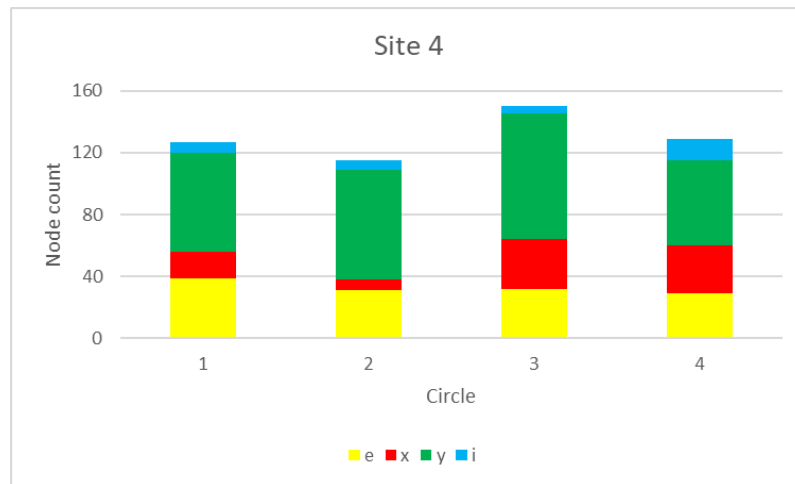


Figure 4.126: Node counts for circles at site 4.

Figure 4.127 shows that different fracture nodes could be related to bedding and specific fracture sets. Nearly half the nodes of the measurement circle are not included in this grouping of fractures. These nodes may be related both to fractures that are bound by and cross-cut the sets identified or be independent of them. The true interaction of the fractures can only be defined if all the nodes are considered together.

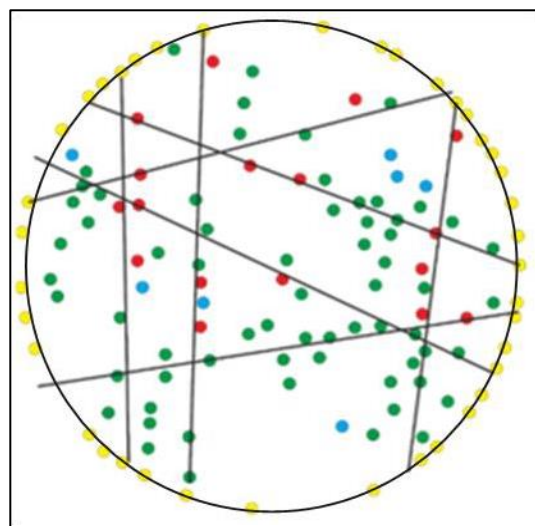


Figure 4.127: Bedding and two possible fracture sets defined by the distribution of nodes in circle 1. More than half the nodes are not included in these two fracture sets. These nodes may be bound by, or cross-cut the fracture sets indicated. Many of the nodes on the two fracture sets are defined by their intersection with the other set.

As there is limited variation in the number and ratio of nodes in the circles the topological characteristics of the fractures are similar (Figure 4.128 and Figure 4.129). Circle 2 has a lower fractal dimension (1.93) whilst the fractal dimensions of the other circles are almost identical (1.97, 1.98, and 1.97). The similarity of the topological and fractal characteristics show that it is appropriate to use the average values to characterise this mapping site.

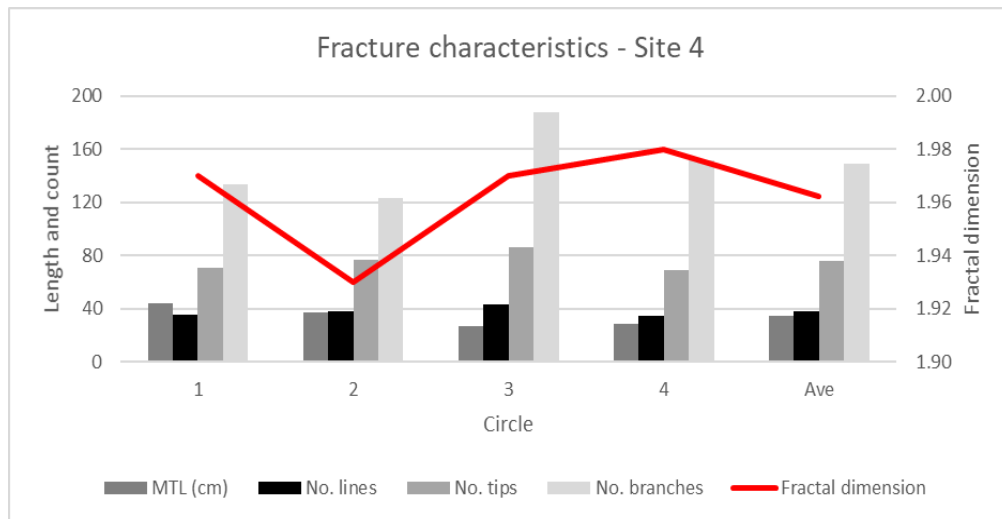


Figure 4.128: Fracture characteristics and fractal dimension, site 4.

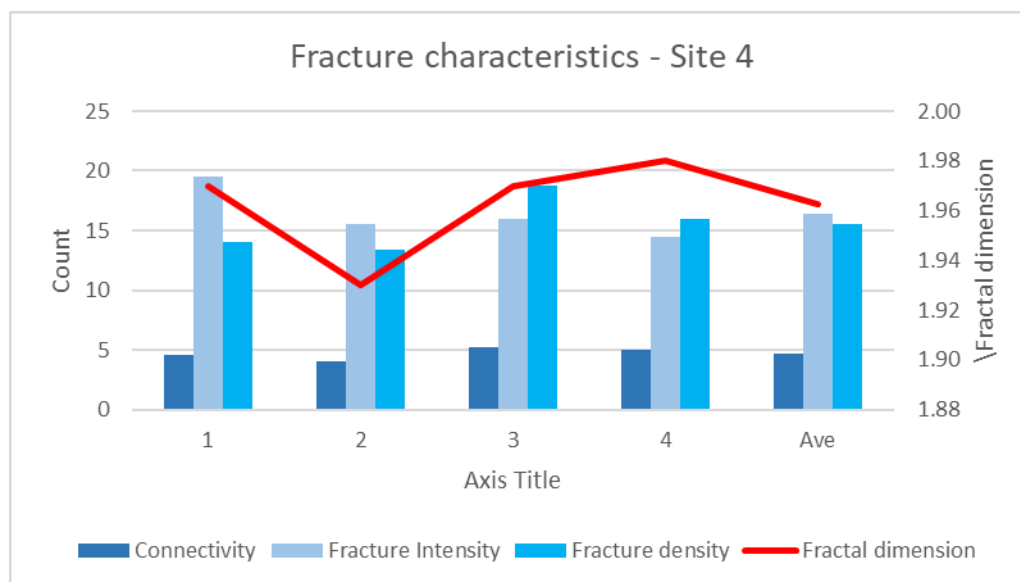


Figure 4.129: Fracture characteristics and fractal dimension, site 4.

4.2.3.5 Site 5

Site 5 (Figure 4.104) is located on a stub of road that has recently been excavated to provide access to a private residence. It is evident that during the excavation of this road that a large amount of material had to be removed to stabilise both the loose rocks and gravel, and portions of the underlying fresh rock (Figure 4.130). The bedding dips at approximately 50° to the south and consists of fine-grained, dark grey wackestone separated by calcite and/or clay coated bedding planes. The low cohesion bedding planes have allowed the rocks to slide into the excavation, and it is likely that portions of beds could continue to do so. This may be the reason for this road being abandoned.

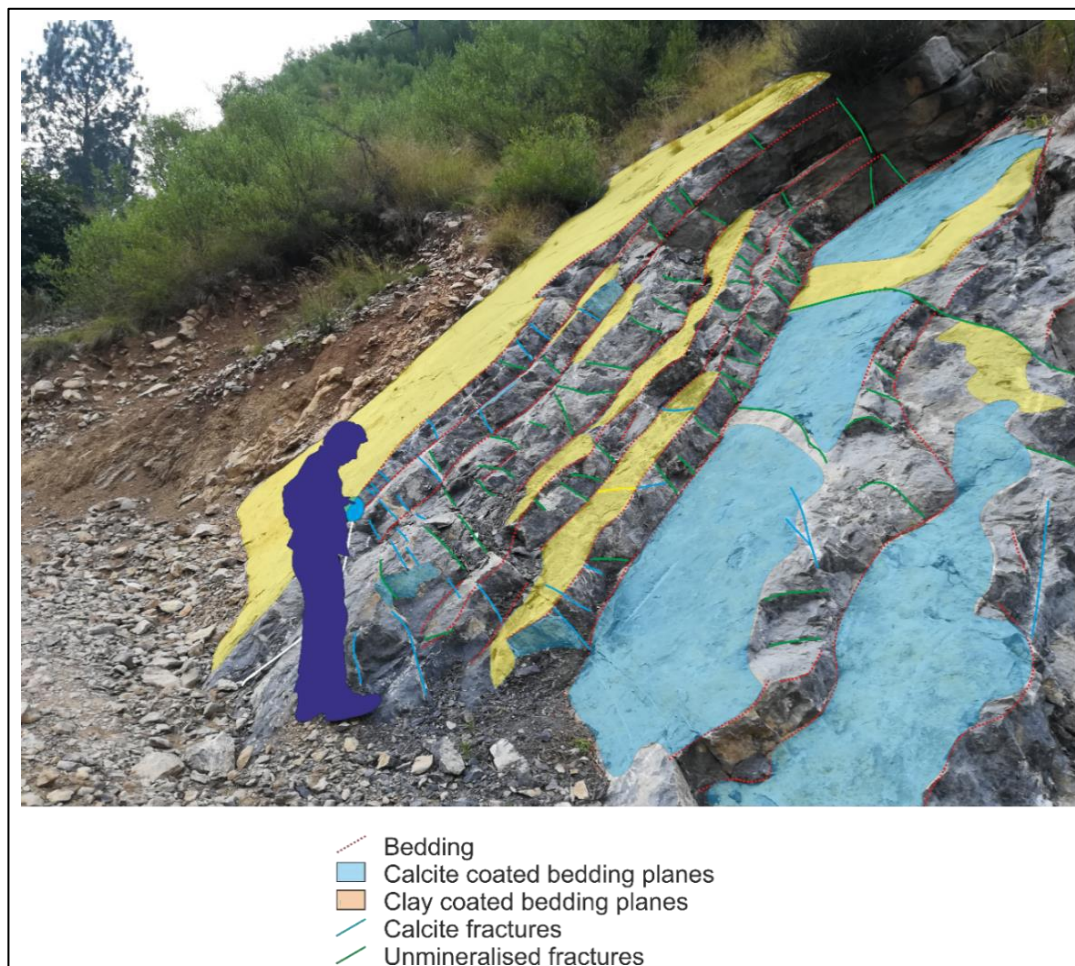


Figure 4.130: View westward at site 5 of 0.5 m thick wackestone beds coated by millimetre thick calcite and clay partings. Also visible are abundant bedding perpendicular calcite filled and unmineralised fractures. These fractures are generally restricted to a single bed with the low cohesion of the calcite and clay partings preventing their propagation through to adjacent beds. Geologist in blue.

In addition to the low cohesion clay and calcite coated bedding planes there are also abundant bedding perpendicular calcite and unmineralised fractures. The calcite fractures are present either as longer fractures (approximately 2 m) that cross-cut bedding (Figure 4.130) or sets of short (up to 10 cm long) *en echelon* sets (Figure 4.131). The unmineralised fractures are restricted to individual beds (Figure 4.131). It is clear that the smooth surface of the low cohesion shale beds are what caused the formation of the antithetic calcite fractures. This mechanism of fracturing is common in areas such as fore-thrusts where the rock types are similar and the rocks are strongly sheared by thrusting.

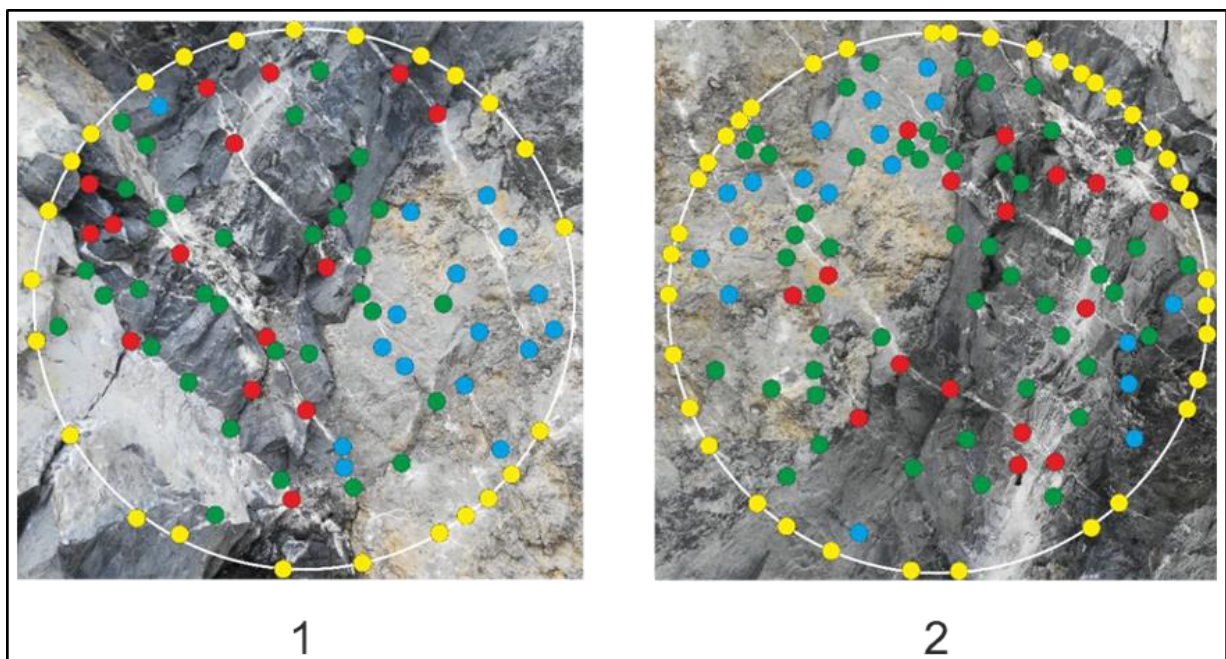


Figure 4.131: Measurement circles at site 5 showing bedding shears and antithetic calcite fractures.

Figure 4.132 shows that there are twice as many “y” nodes and 20% more “e” nodes in circle 2 compared to circle 1. Circle 1 has 80 nodes in total and circle 2 has 122. Despite these differences the only significant effect on the topological characteristics is a greater number of branches (Figure 4.133) and higher fracture intensity (Figure 4.134) in circle 2. The fractal dimension (1.96) is the same in both circles.

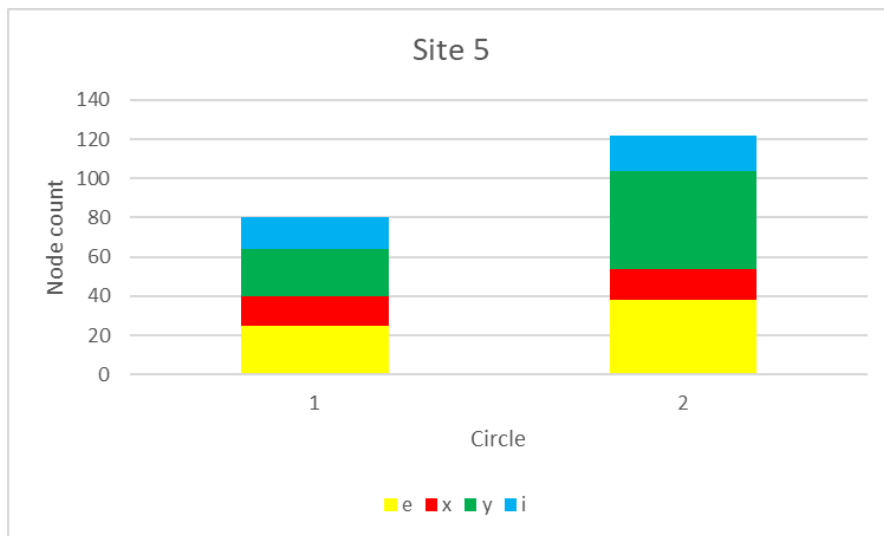


Figure 4.132: Node counts for circles at site 5.

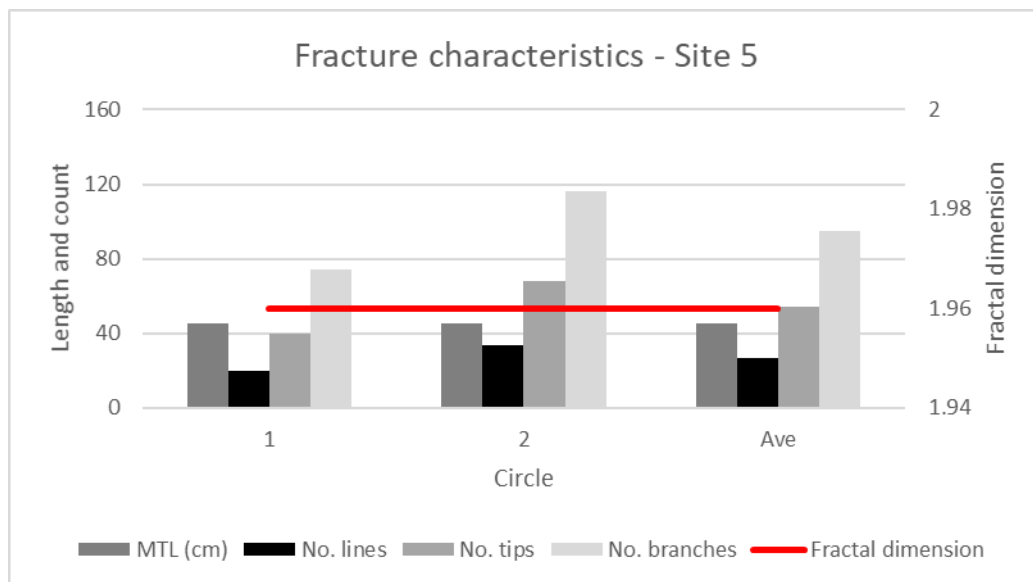


Figure 4.133: Fracture characteristics and fractal dimension, site 5.

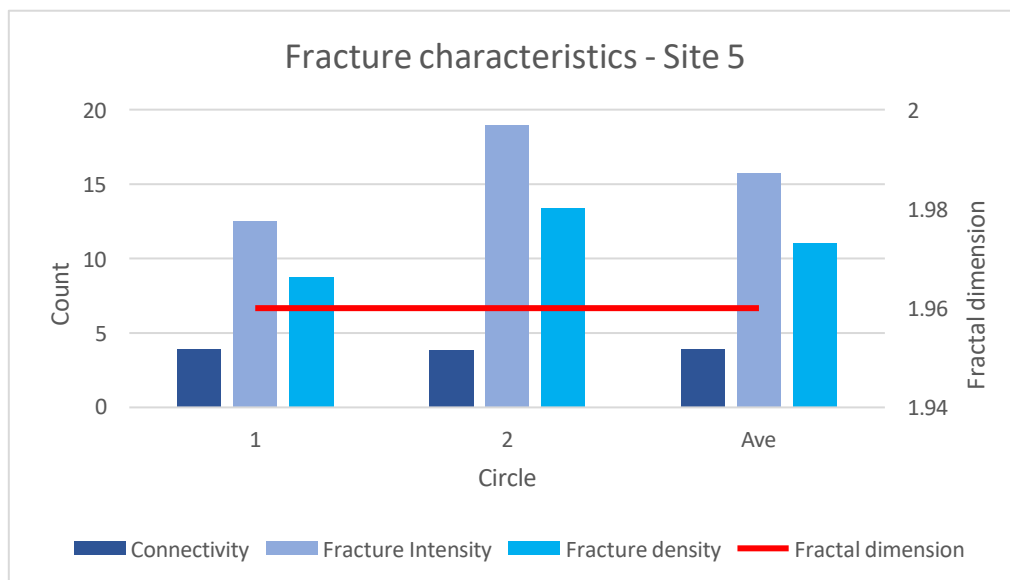


Figure 4.134: Fracture characteristics and fractal dimension, site 5.

4.2.3.5 Summary

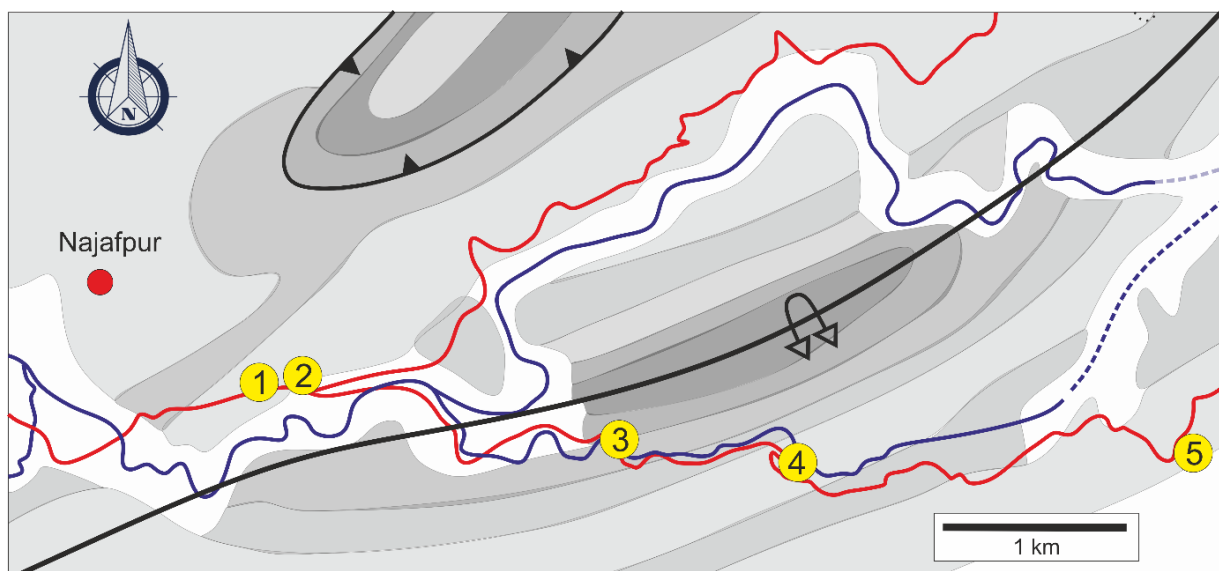


Figure 4.135: Sketch map showing location of sites relative to major geological features, rivers, and roads. Variations in stratigraphy are shaded grey – see Figure 4.104 for details.

Due to the limited outcrop at site 1, it was not possible to draw a measurement circle and collect data. Hence all the topological and fractal analyses presented do not contain information from site 1. Site 1 and site 2 are only 200 m apart and the being a strongly sheared shale at site 2 is very similar in composition and structural deformation. The average characteristics of site 2 ignore the

measurements taken in the flowstone coated circle 3 at the site. The flowstone has obscured many of the nodes and fractures on the exposed surface, but this does not represent the general rock mass conditions. The highest average number nodes (137) were measured at site 2, but the circle with the greatest number of nodes is circle 2 at site 3 (Figure 4.136). This difference is likely due to the fact that there are two circles at site 2 and eight at site 3. “y” nodes are the most abundant type, making up between 37% and 52% of the nodes at each site. The next most abundant are “e” comprising 25% to 31% of the nodes at each site (Figure 4.136).

No systematic variation is evident in the number of nodes, or the percent of the different node types at each site. This may be due to the fact that the transect is subparallel to the regional strike (Figure 4.135) and that three of the four sites analysed were located in the Nammal Formation (Figure 4.104).

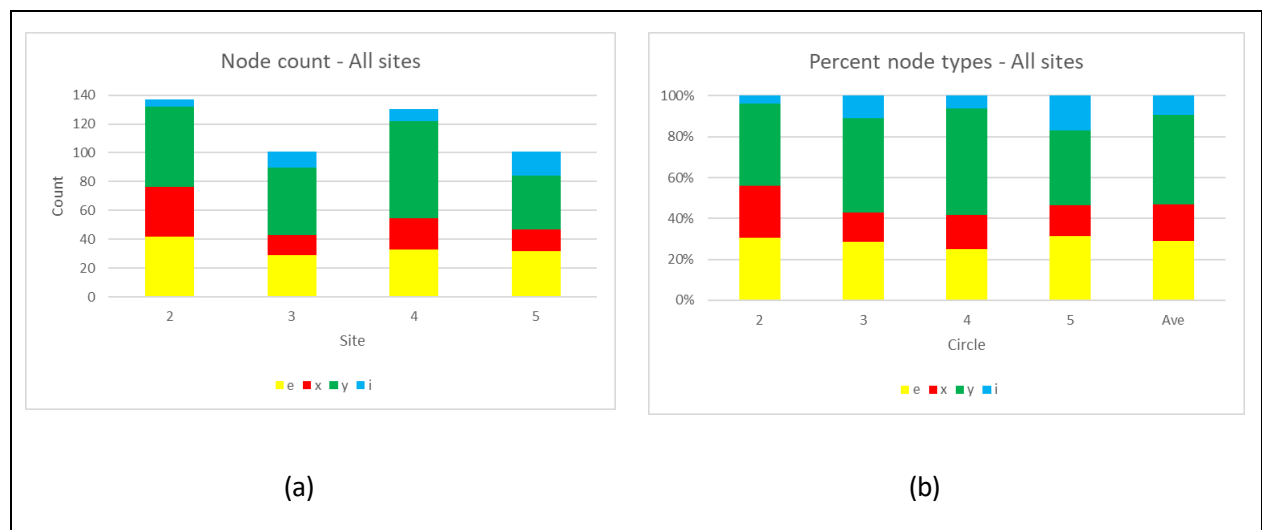


Figure 4.136: (a) Node count of all sites in the Najafpur region, and (b) percent distribution of the different node types across the sites. Sites run from west to east as shown on the sketch map (Figure 4.135).

Overall, the fractal dimension (D) varies between 1.94 and 1.96 with an average of 1.96, which is the same value as sites 4 and 5 (Figure 4.137). Although site 3 has the lowest average fractal dimension (1.94), the values at this site vary between 1.91 and 1.99.

The mean trace length is greatest further away from the overturned anticline, that is at sites 2 and 5. Sites 2 and 4, approximately 1 km to the west and east of the overturned anticline (Figure 4.135) have similar numbers of lines, tips, and branches when compared to site 3, on the overturned anticline, and site 5, 3 km to the east of the overturned anticline (Figure 4.137). Connectivity and fracture density are lowest at site 5, furthest away from the overturned anticline (Figure 4.139).

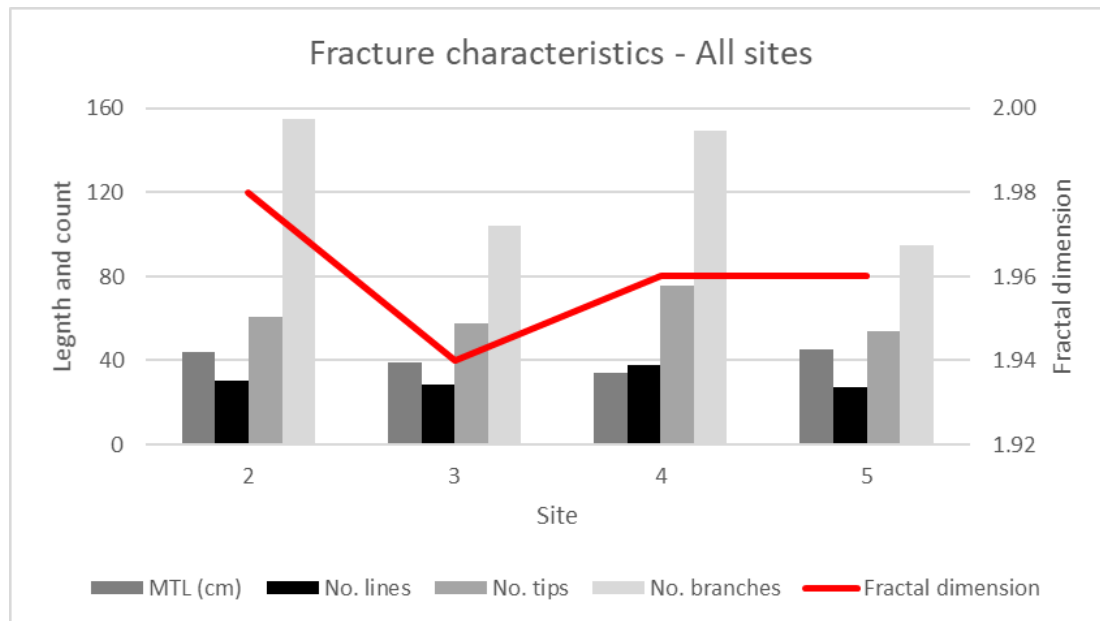


Figure 4.137: Variations in fracture characteristics across the sites in the Najafpur region. Sites run from west to east as shown on the sketch map (Figure 4.135).

There is a good correlation between the average number of nodes and the average fractal dimension of each site (Figure 4.138). The relationship of this trend with the geological features is less clear. Sites 2 and 4, located 1 km to the west and east of the major overturned anticline axis have the highest average number of nodes and fractal dimension. Site 5 (3 km east of the anticline axis) has as expected, a much lower number of nodes. The overturned anticline itself (site 3), despite having zones of intense fracturing (Figure 4.138) also has portions that are less fractured. As a result, the average number of nodes and fractal dimension is lower. This emphasises the fact that it is necessary to consider the whole rock mass.

Unfortunately, when the number of nodes and fractal dimensions of each of the circles in the study area is considered, no trend is apparent (Figure 4.139). This may however indicate a more uniform rock mass with similar characteristics across the region.

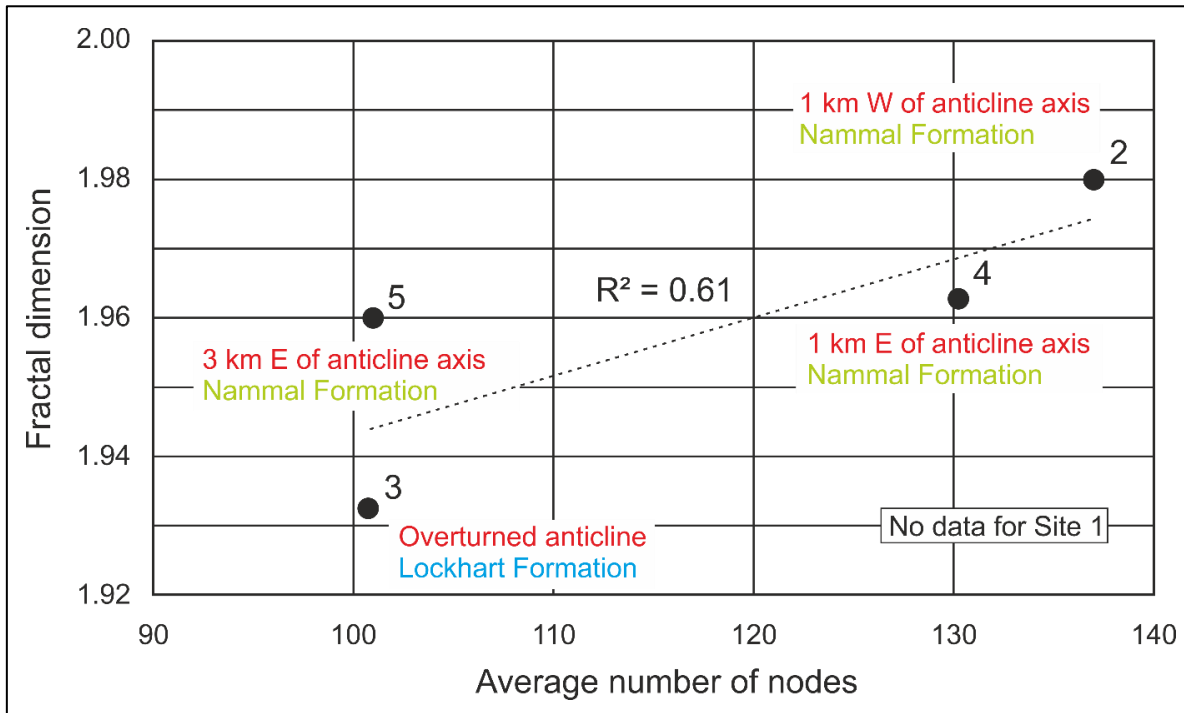


Figure 4.138: Average total number of nodes vs. fractal dimension at all the circles at each site.

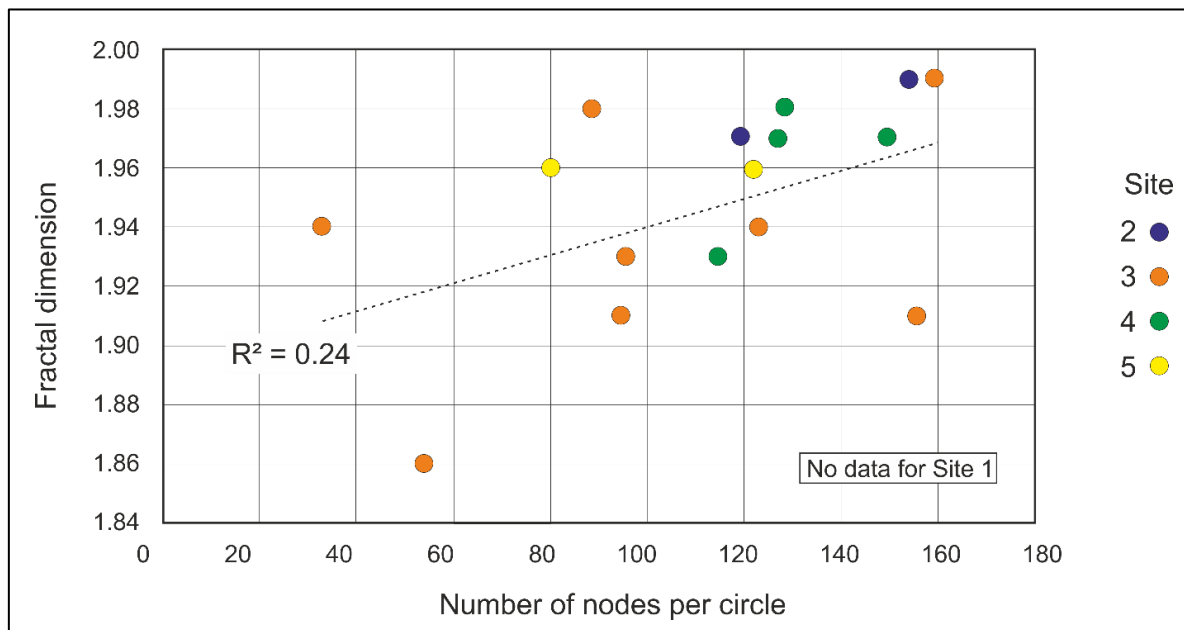


Figure 4.139: Total number of nodes vs. fractal dimension for all the circles at each site.

4.2.4. Talhaar region

The Talhaar region is located approximately 6 km north of Islamabad, via the Pir Sohawa Road. It is 1 km south of the Najafpur region (Section 4.2.3). It is possible to look down into the Najafpur region valley from site 6. Regionally, the strata strike northeast -southwest (Figure 4.140). The dip varies with proximity to the thrust with values between 15 and 30 degrees at sites 1, 2, 4, 5, and 6. In contrast to this sites 3, 7, 8, and 9 have steep dips of greater than 70 degrees.

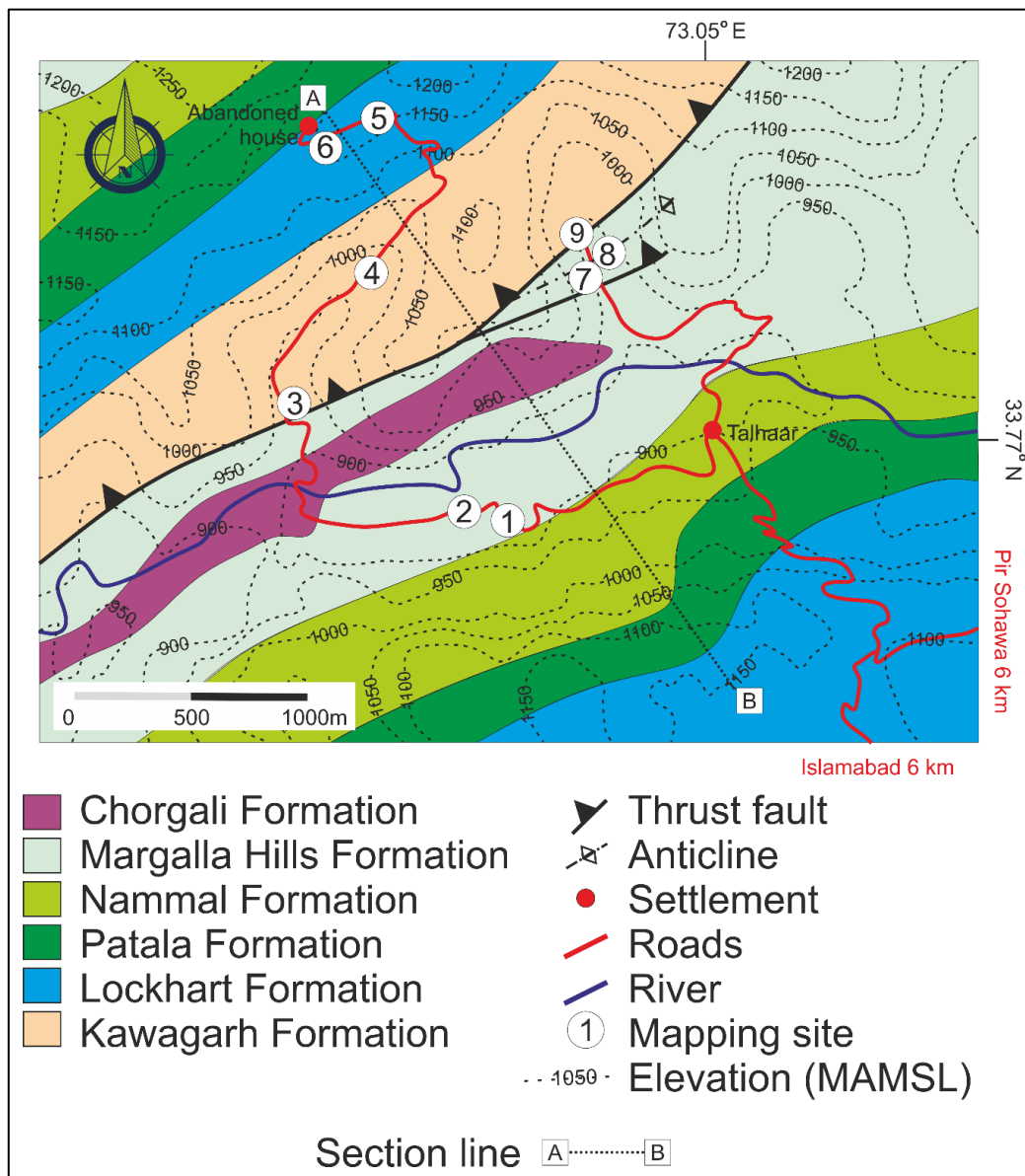


Figure 4.140: Geological map of the Talhaar region. It lies directly to the south of the Najafpur region (Section 4.2.3) which can be seen from the mountain top at site 6.

In the southerly portion of the region (Point B in Figure 4.140 and Figure 4.141), the strata dip southeast due to a steeply dipping fold (Figure 4.142). Traveling northwards towards the town of Talhaar and onwards into the valley (Point A in the cross section) the strata form an overturned fold that was later thrust into by the Kawagarh Formation (Point B in Figure 4.140 and Figure 4.141).

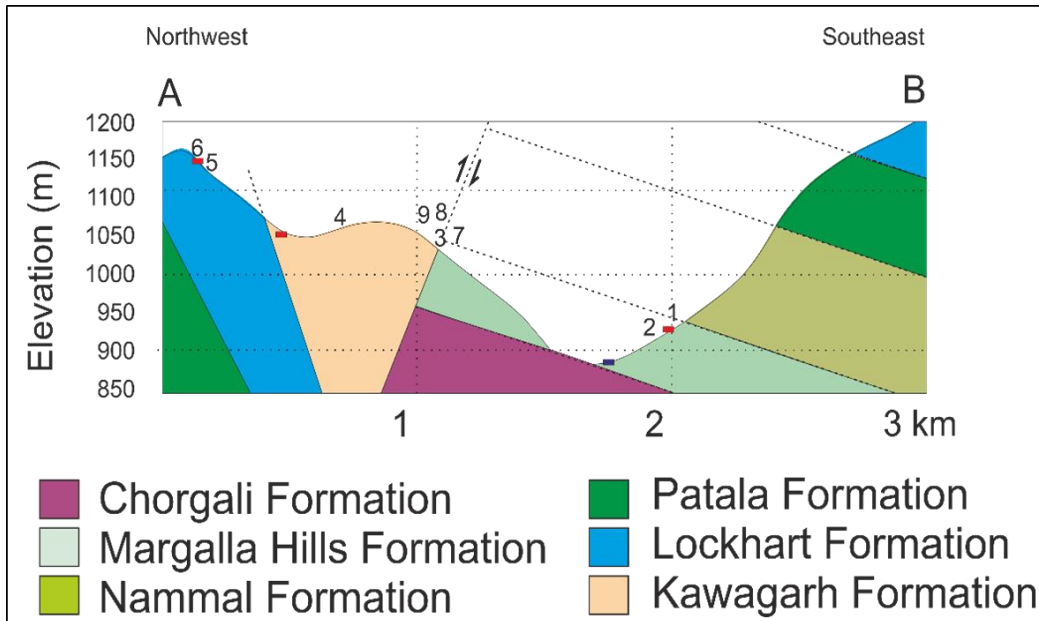


Figure 4.141: Cross-section through the Talhaar field region, view eastward. See Figure 4.140 for position of section-line.



Figure 4.142: View westward along strike from the Talhaar road towards site 1 showing the erosion of the Nammal Formation (N) to expose the overturned south-easterly dipping Margalla Hills Formation (M).

Nine sites were mapped – sites 1 and 2 are within 100 m of each other, sites 3 to 6 were measured up a road to the mountains that overlook the Najafpur region to the north and the cluster of sites 7,8, and 9 are located in a relatively narrow valley trending northwards (Figure 4.140). The geographical co-ordinates of the sites are listed in *Table 4.8*

Table 4.8: Location of mapping sites.

site	Latitude (N)	Longitude (E)
1	33.766°	73.039°
2	33.766°	73.037°
3	33.771°	73.031°
4	33.776°	73.036°
5	33.781°	73.037°
6	33.781°	73.036°'
7	33.773°	73.046°
8	33.774°	73.046°
9	33.777°	73.045°

Sites 1 and 2 are located in the uppermost strata of the Margalla Hills Formation directly beneath the contact with the Nammal Formation. As the silty shales of the Nammal Formation are easily erodible, there is good exposure of the Margalla Hills. Formation at site 1 (Figure 4.143).

4.2.4.1 Site 1

The exposed bedding surface is inscribed with three sets of fractures (Figure 4.144). The fracture sets are oriented parallel to strike (Set 1), parallel to dip (Set 2) and cross-cutting (Set 3). The relative ages of the sets are difficult to determine as both Set 1 and Set 2 terminate against each other. The terminations of Set 1 appear to be by displacement along Set 2, making Set 1 (strike-parallel fractures) the oldest. Set 3 fractures terminate against both of the other fracture sets. Set 1 fractures are typically spaced between 50 and 75 cm apart but can occur in closely spaced groups only a few centimetres

apart. Set 2 fractures occur at 1 m intervals, whilst Set 3 fractures do not show a regular spacing (Figure 4.144).



Figure 4.143: View eastwards at site 1 across the Margalla Hills Formation (M) into the dark brown shaley siltstone of the Nammal Formation (N). Strata dip gently towards camera, with the slope of the contact representing erosion and scree of the weak Nammal Formation. Circled vehicle for scale.

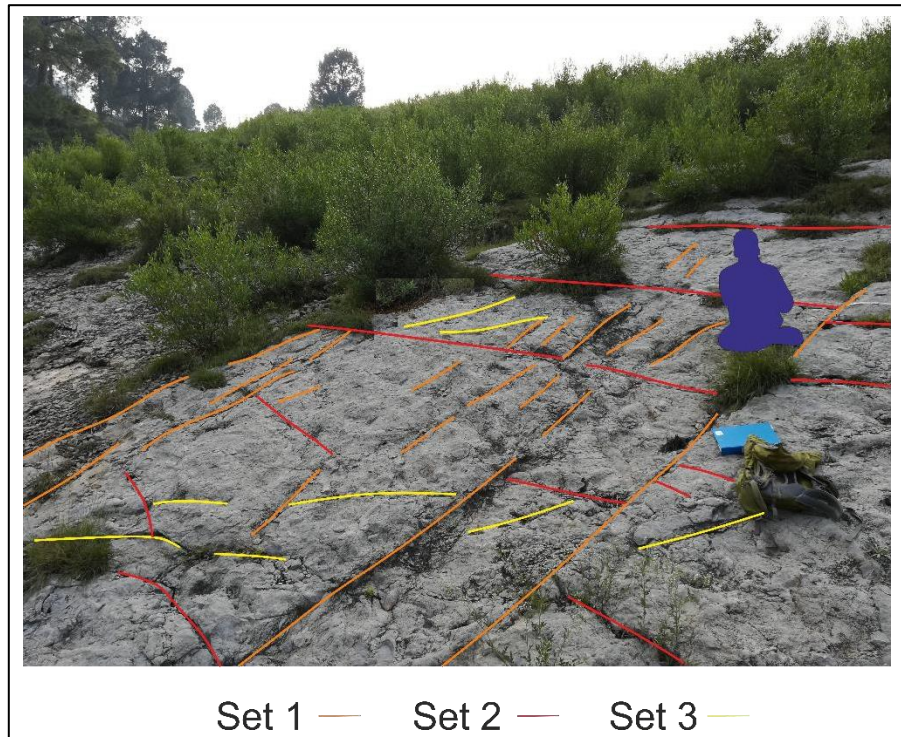


Figure 4.144: Fracture sets visible on a limestone bedding surface of the Margalla Hills Formation. Set 1 is oriented parallel to strike, Set 2 along dip and Set 3 cross-cuts these two. Geologist in blue.

Robust *Thalassinoides* trace fossils (several centimetres wide and up to a metre long) are common at site 1 (Figure 4.145).



Figure 4.145: *Thalassinoides* trace fossils at site 1. GPS is 10 cm long.

The relatively wide spacing of the major fracture sets resulted in few cross-cutting “x” nodes. Numerous shorter “y” and “i” nodes are present. There are no “x” nodes in circle 1 (Figure 4.148 and Figure 4.146) and the total number per circle varies between 56 and 65 with an average of 61 nodes per circle (Figure 4.146). These lower numbers of nodes have reduced the values of the topological characteristics of the circles, and hence those of the site overall. The number of lines, tips and branches is the lowest of the Talhaar region (Figure 4.147). Likewise of the region has the lowest connectivity, fracture intensity and fracture density (Figure 4.149). The mean trace length (43 cm) is the second highest in the region due to lower number of nodes in the circles at this measurement site. The average fractal dimension of 1.87 (Figure 4.147). The topological node and fractal characteristics of four 1 m wide measurement circles on the bedding surface were determined (Figure 4.148).

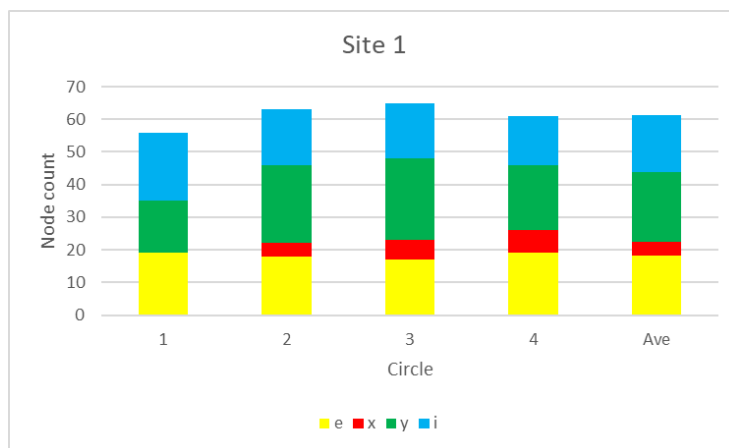


Figure 4.146: Number of nodes per circle at site 1. Colours match node type colours in circles.

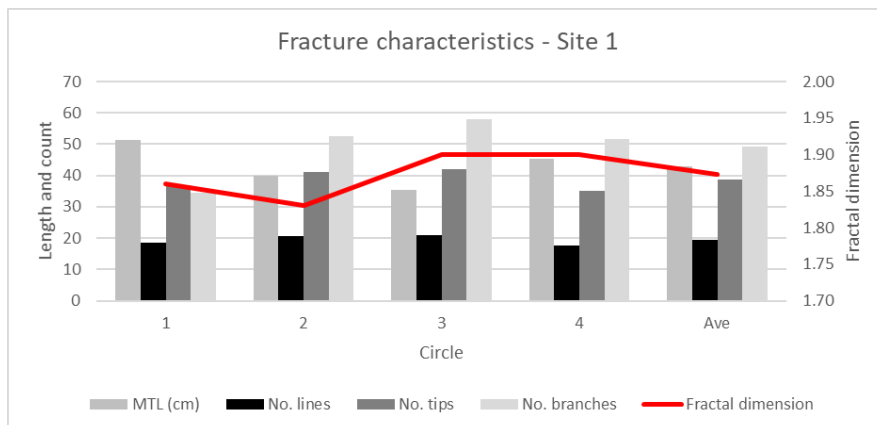


Figure 4.147: Fracture characteristics of site 1

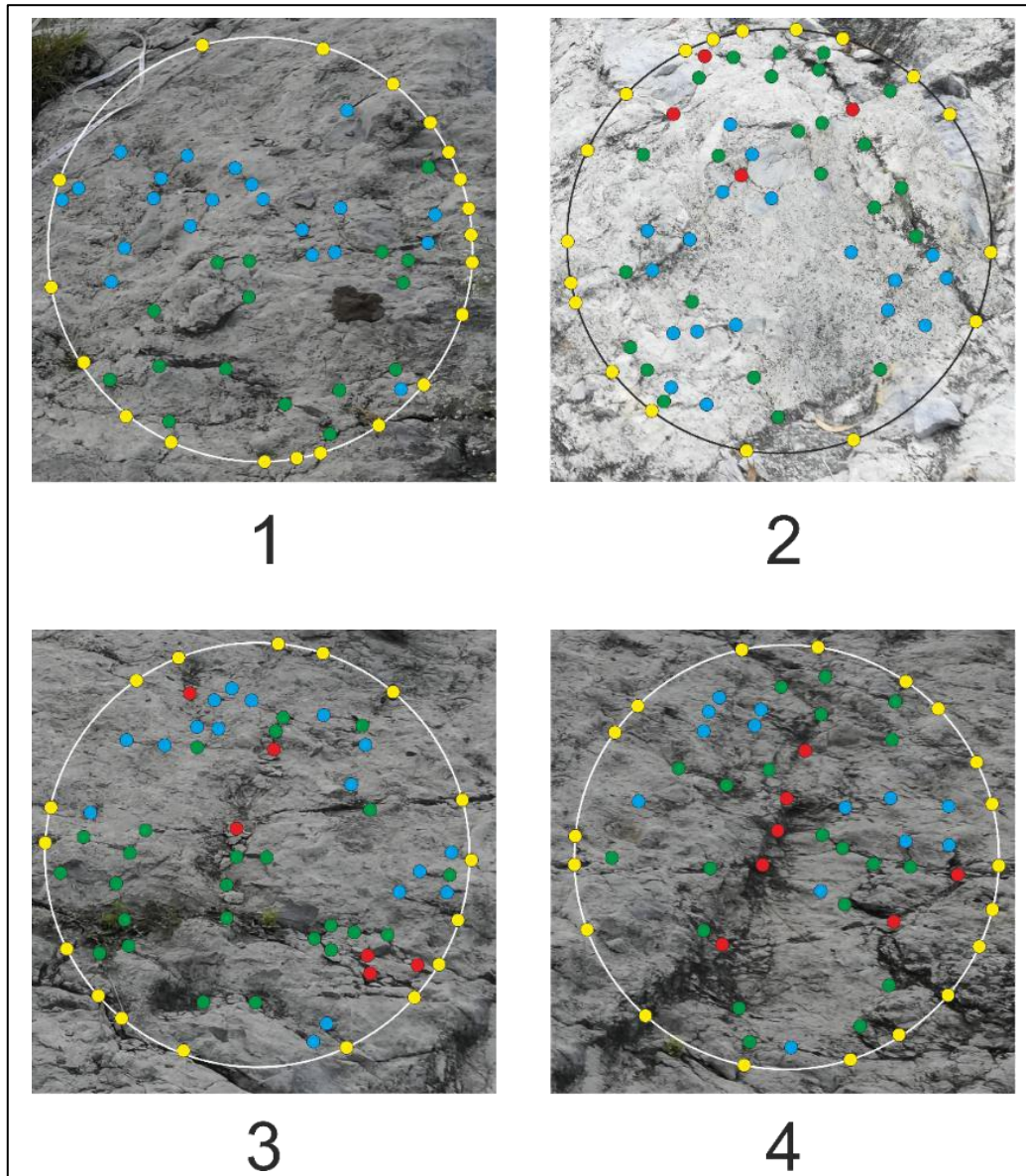


Figure 4.148: Measurement circles at site 1. As with all images of circles, “e” nodes are shown in yellow, “x” in red, “y” in green, and “i” in blue.

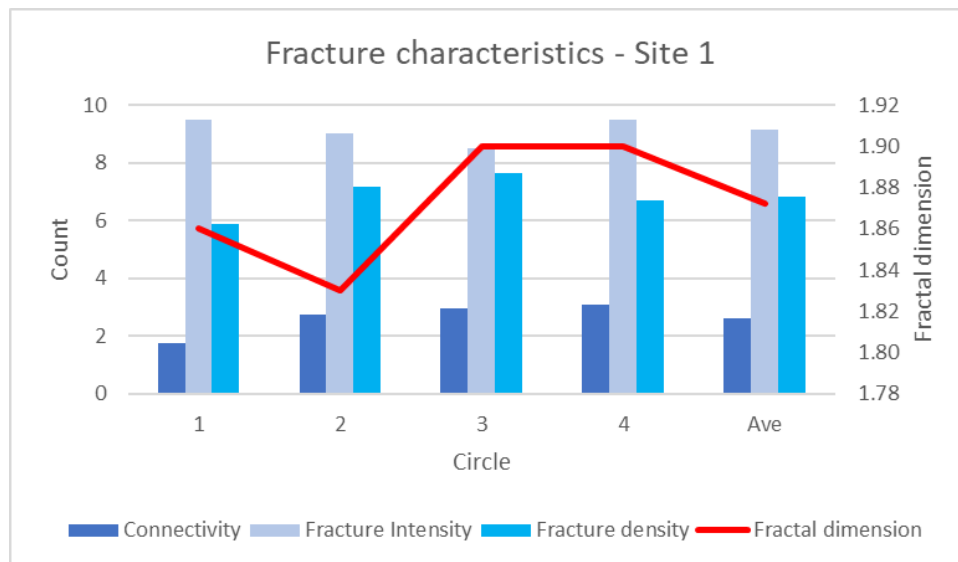


Figure 4.149: Fracture characteristics of site 1.

4.2.4.2 Site 2

Site 2 is a cross-section of the beds exposed at site 1. The rocks at the site consist of a light grey limestone that weathers to a creamy colour. These occur as 20 cm thick beds in clusters of approximately 1 m thick. Dark grey shaley siltstone beds, up to 2 cm thick separate the light grey limestone clusters. Data from four circles and two measurement lines (one horizontal and one vertical) was collected from this site (Figure 4.150).

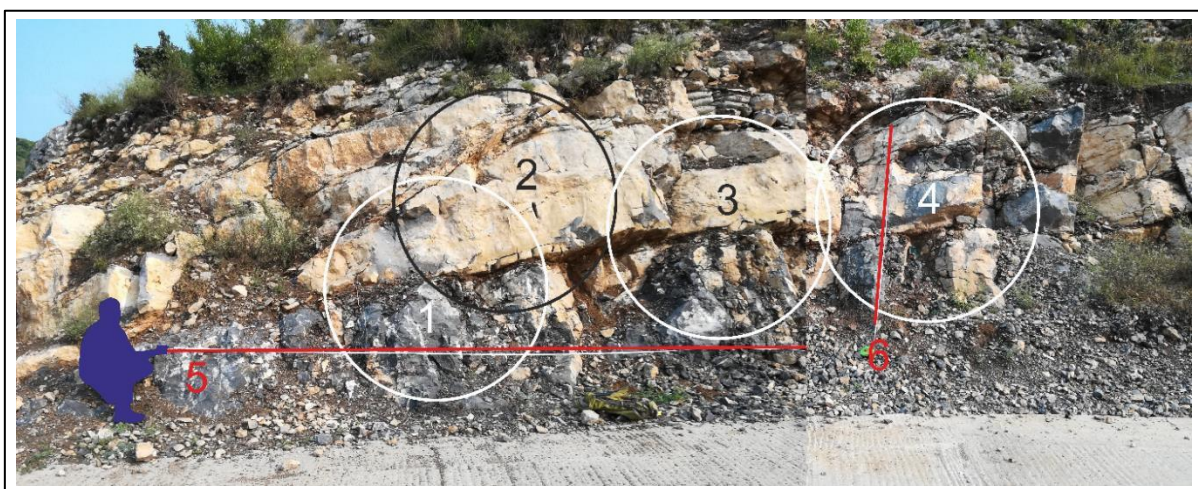


Figure 4.150: Circle and measurement line positions at site 2. Circles are labelled 1 to 4 and measurement lines 5 and 6. Geologist is shaded dark blue.

The fracture characteristics are different between the two rock types. On the fresh surfaces of the light grey limestone, abundant near-vertical calcite fractures are visible. In the uppermost, weathered layer, these fractures were seldom visible indicating that water has dissolved the calcite. The thin shale band acts as a barrier against further downward movement of water and the rock beneath it remain fresh (Figure 4.150). The shale band is highly fractured and sheared, broken into fragments only a few centimetres long and a few millimetres wide. The appearance of the strong bedding parallel alinement of these fragments is why these units are often referred to as shaley.

The measurement circles were placed across the shaley beds to see if nodes (especially “x” nodes) could be detected along the bedding contact. The effect of this bed can be clearly seen with a line of nodes present along the contact; it also forms a clear separation between the upper portion with few nodes and the lower with more nodes (Figure 4.151).

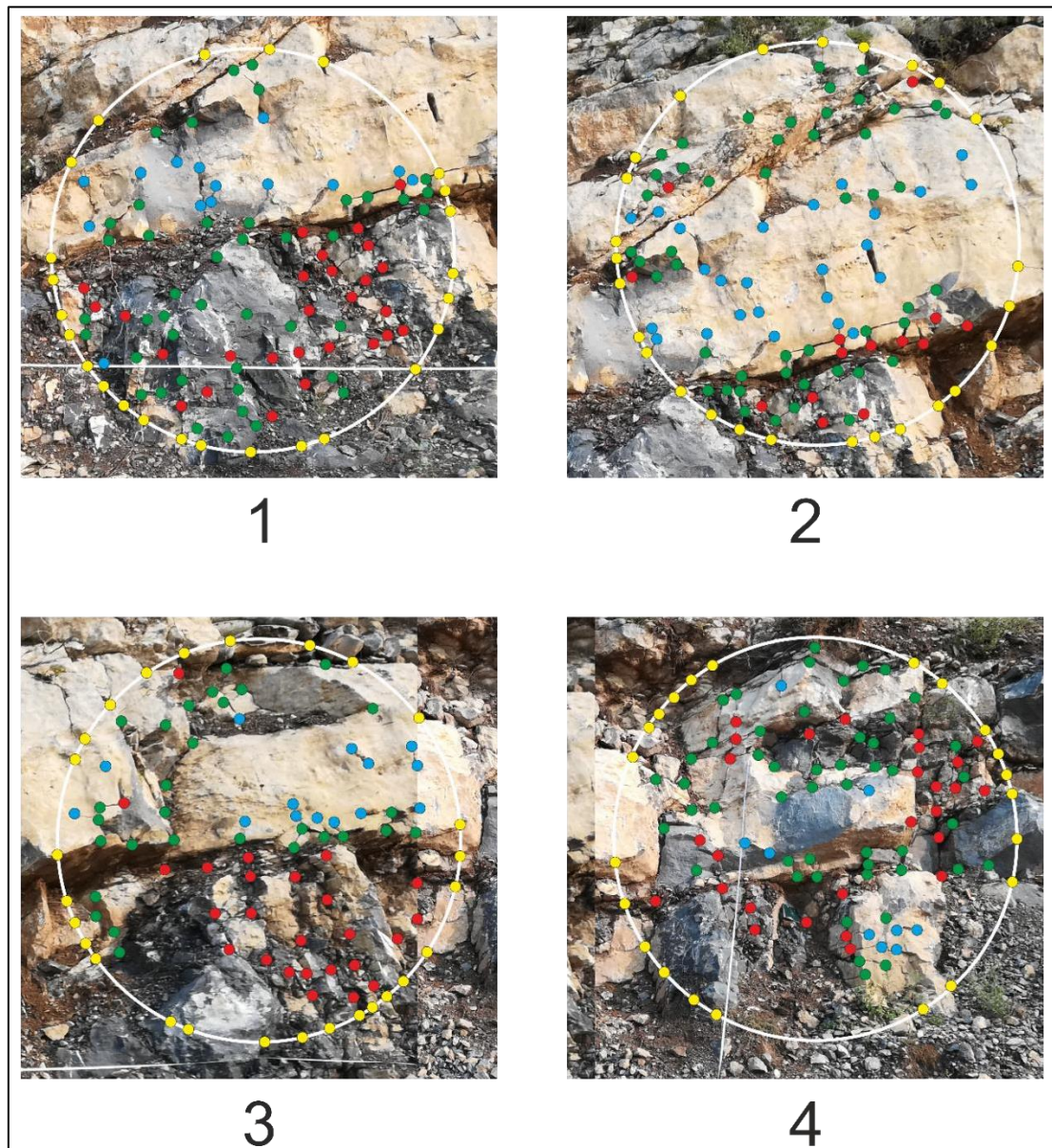


Figure 4.151: Measurement circles at site 2. Figure 4.150 shows distribution of circles at the site.

On average there are 106 nodes per measurement circle, with a standard deviation (SD) of 7. The most abundant node-type are the “y” nodes, having nearly twice as many as both the “e” and “x” type and three times as many as the “i” type (Figure 4.152). These distributions suggest that the fractures terminating against the shaley layer are a significant contribution to the fracture population.

At site 2, fractures are generally restricted to within the measurement circle, resulting in a shorter mean trace length. There is inverse correlation between the topological characteristics of the number of lines and the mean trace length – the fewer the lines, the longer they are. Those circles with a longer mean trace length also have a greater fracture intensity. The circles with more branches more have more tips, and when considered together have the highest connectivity. As can be expected, the circles with the greatest number of tips have the highest fracture density.

The fractal dimension of the cross-section of the strata, that is, site 2 is significantly higher (1.95) than that of site 1, the bedding surface of the same strata (viz. 1.86).

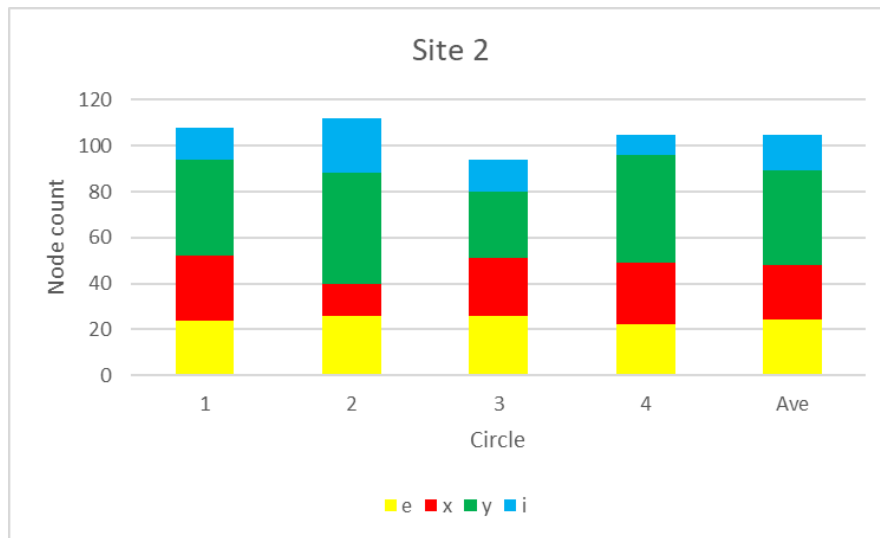


Figure 4.152: Node counts at site 2.

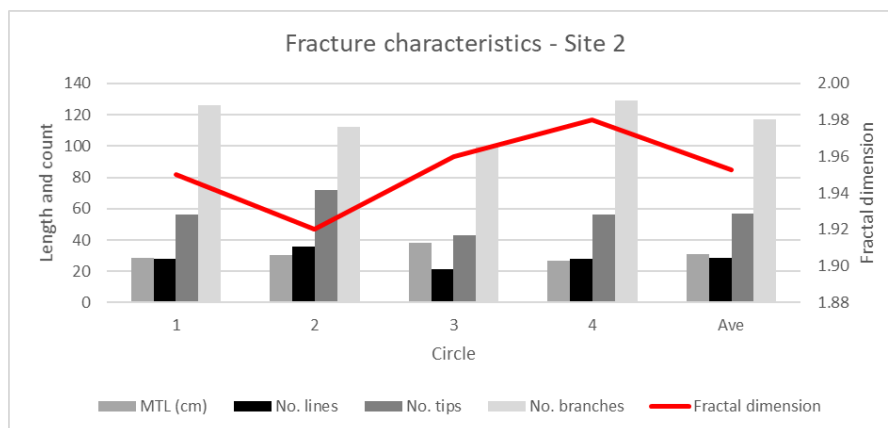


Figure 4.153: Fracture characteristics, site 2.

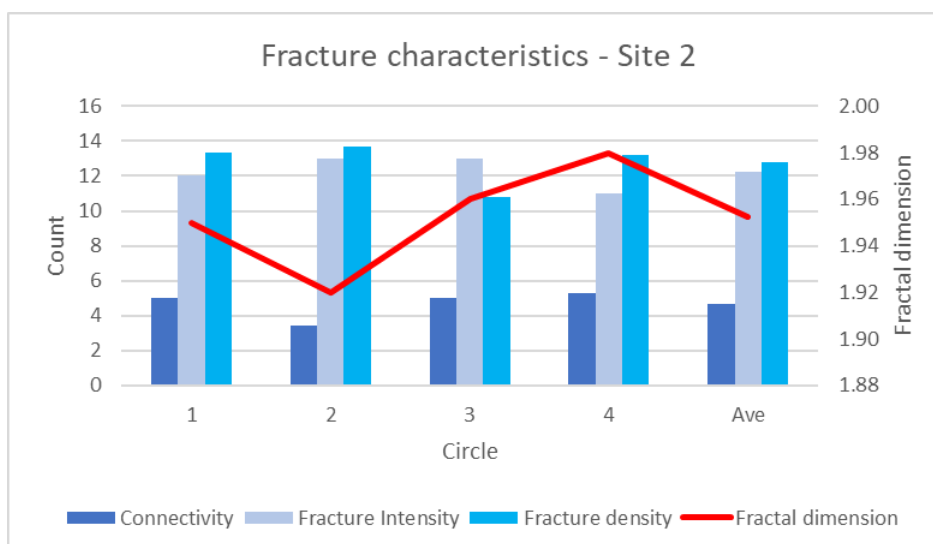


Figure 4.154: Fracture characteristics, site 2.

The horizontal and vertical distributions of fractures were measured in lines 5 and 6 respectively. Line 5 (Figure 4.155) lies entirely within the fresh, light grey limestone and Line 6 (Figure 4.156) cross-cuts vertically from the fresh into the weathered limestone (Figure 4.150). The characteristics of the two fracture lines is summarised in Table 4.9.

Table 4.9: Characteristics of the measurement lines at site 2

Parameter	Line 5	Line 6
Orientation	Horizontal	Vertical
Length (m)	6	1
Number of fractures	60	15
Average spacing (m)	0.10	0.06
Maximum spacing (m)	0.99	0.12
Minimum spacing (m)	0.01	0.02
Percent less than 10 cm apart	90	60

Figure 4.157 and Figure 4.158 show the distribution of fracture spacings and clearly illustrate that the majority of fractures are less than 19 cm (0.10 m) apart along these two measurement lines.

Table 4.10: Fracture characteristics of Lines 5 and 6. This is also shown graphically in Figure 3.26

	Combined 5	Calcite 5	Unmineralised 5	Combined 6	Calcite 6	Unmineralised 6	Overall
Ave	0.10	0.14	0.35	0.06	0.20	0.09	0.08
Max	0.99	1.03	1.32	0.12	0.58	0.24	0.56
Min	0.01	0.01	0.03	0.02	0.02	0.02	0.02
SD	0.13	0.19	0.38	0.03	0.20	0.06	0.08
Count	60	44	16	15	4	11	75
Frequency	10	7	3	15	4	11	13

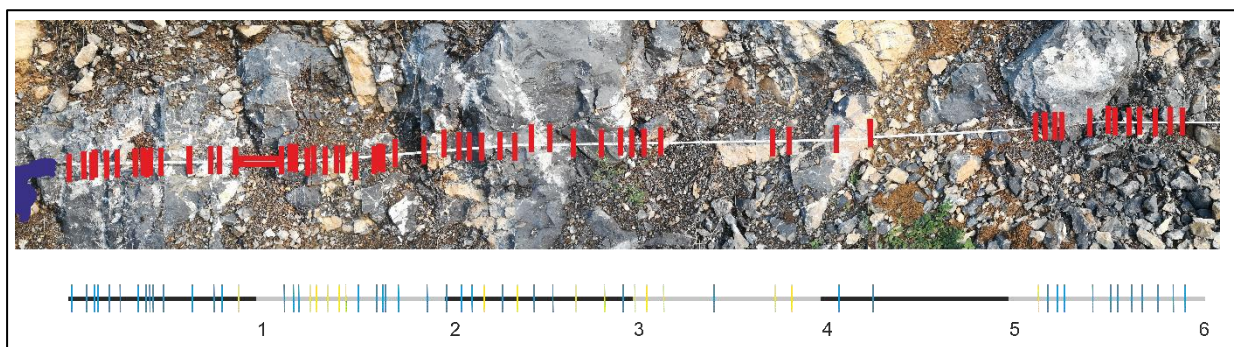


Figure 4.155: Horizontal Measurement Line 5 at site 2. Actual fracture positions are shown in the photo-mosaic at the top of the image, whilst the lower portion of the image shows these fractures along a straight line. Calcite fractures are shown in blue and unmineralised fractures in yellow. Line length is 6 m. Figure 4.150 shows position of line.

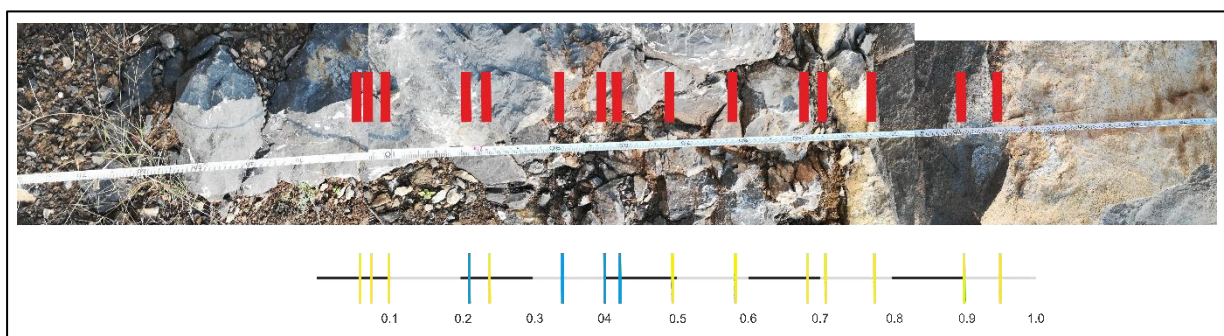


Figure 4.156: Vertical Measurement Line 6 at site 2 (see Figure 4.150 for position). The measurement line runs upward from the fresh light grey limestone on the left into the weathered creamy coloured limestone on the right. The shale layer occurs between the fractures at 0.71 and 0.78 cm.

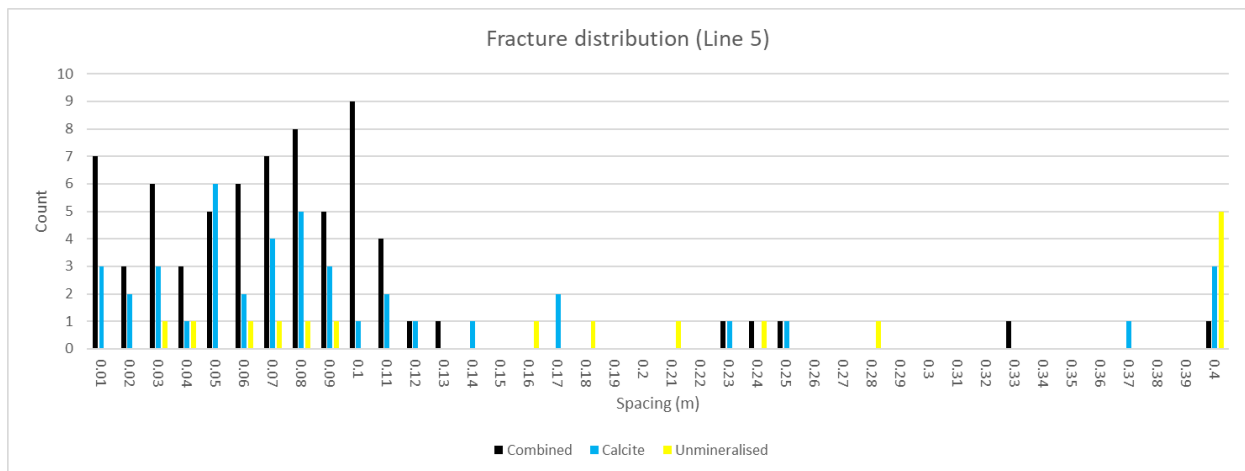


Figure 4.157: The number of fractures at different spacings along Measurement Line 5 at site 2. 90% of the fractures are less than 10 cm apart. 65 fractures were measured along the 6 m line.

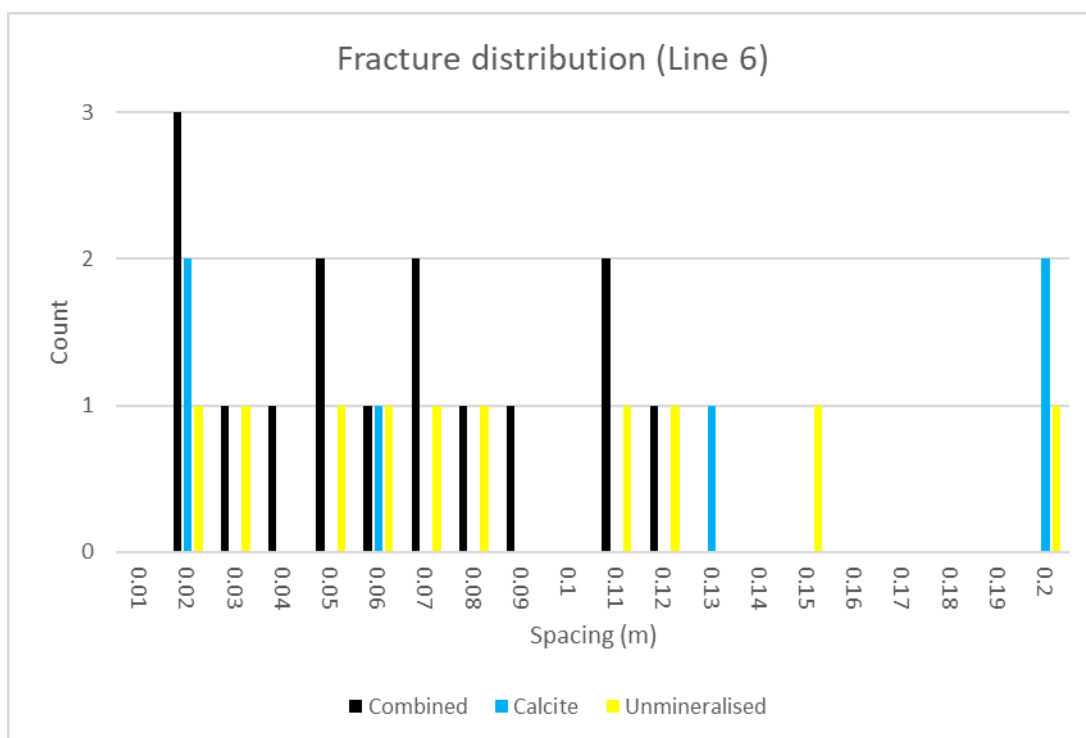


Figure 4.158: The number of fractures at different spacings along Measurement Line 6 at site 2. 60% of the fractures are less than 10 cm apart. 20 fractures were measured along the 1 m line.

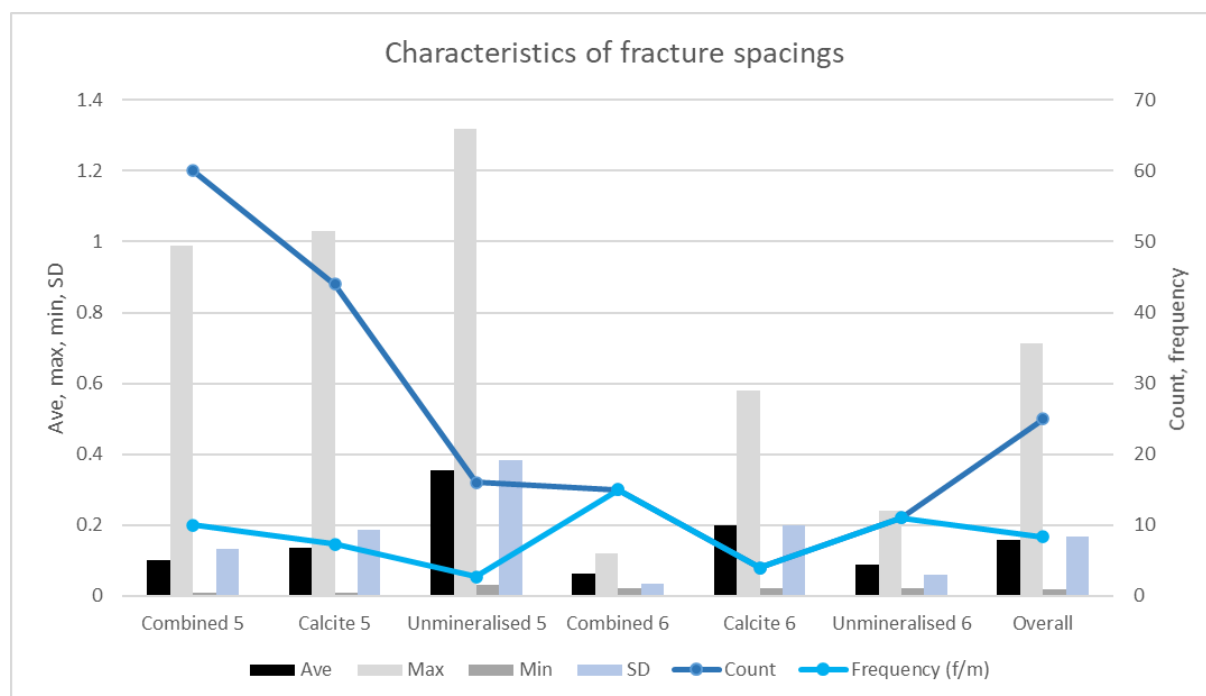


Figure 4.159: Fracture spacing characteristics of measurement lines 5 (horizontal) and 6 (vertical) as well as the overall spacing of all fractures combined at site 2. See Table 4.10 for details.

4.2.4.3 Site 3

Site 3 is the westernmost exposure of a large southwards directed thrust that cross-cuts the field region (Figure 4.140). This thrust and associated geological structures have been characterised in detail at site 7, 8, and 9. The change in orientation across the valley into the steeply dipping bedding of the thrust zone relative to the strike planes of the south-easterly dipping footwall strata to the south are clearly visible at the site (Figure 4.160). Moving northwards, deeper into the hanging-wall, no sudden change in dip is apparent, varying from steep north-westerly to steep south-easterly. The fractures on the thrust plane consist mainly of open, unmineralised bedding perpendicular spaced 10 cm apart. The bedding planes are strongly developed and, like the other fractures are typically unmineralised, apart from insignificant amounts of iron oxide probably introduced into the dolomitisation of strata from other areas (Figure 4.161). The rock fragments at site 3 are composed of light grey Margalla Hills limestone (Figure 4.162, circle 2). Three measurement circles (Figure 4.162)

were mapped on the exposure of the thrust, with circle 1 oriented vertically and circles 2 and 3 horizontally (Figure 4.161).

As expected from the general rock-mass characteristics (i.e., fractures cross-cutting and trapped within other fractures and bedding planes) there are more “x” nodes than all the others combined (Figure 4.163). This greater number of “x” nodes results in a higher overall connectivity, and fracture density (Figure 4.164). There are more lines, tips, and branches in the vertical circle 1. Other topological parameters do not show a clear relationship with circle orientation (Figure 4.165).

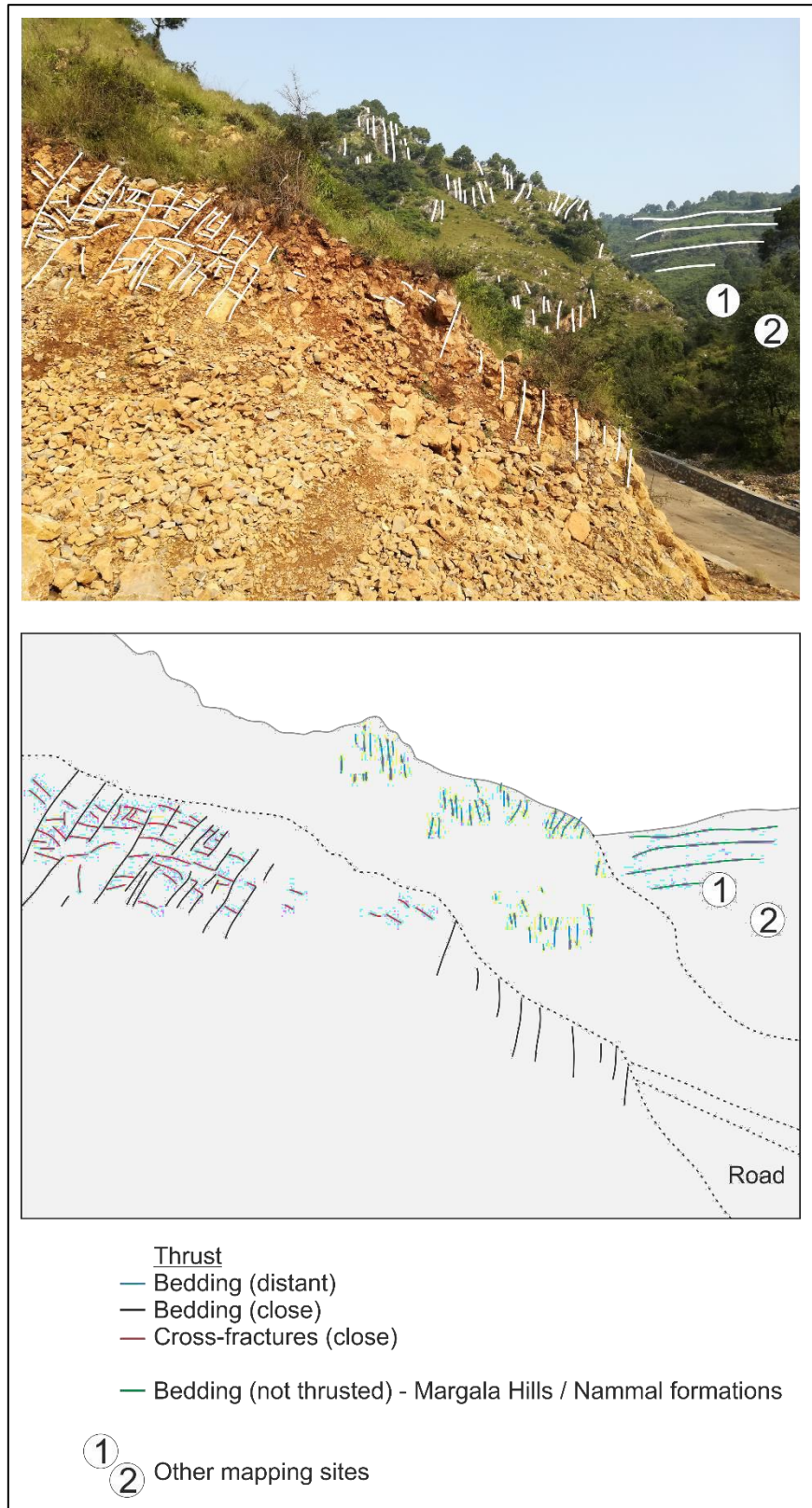


Figure 4.160: View northeast from site 2 along the strike of the thrust fault. The steep dip of the bedding within the fault relative to the shallow dip at sites 1 and 2.

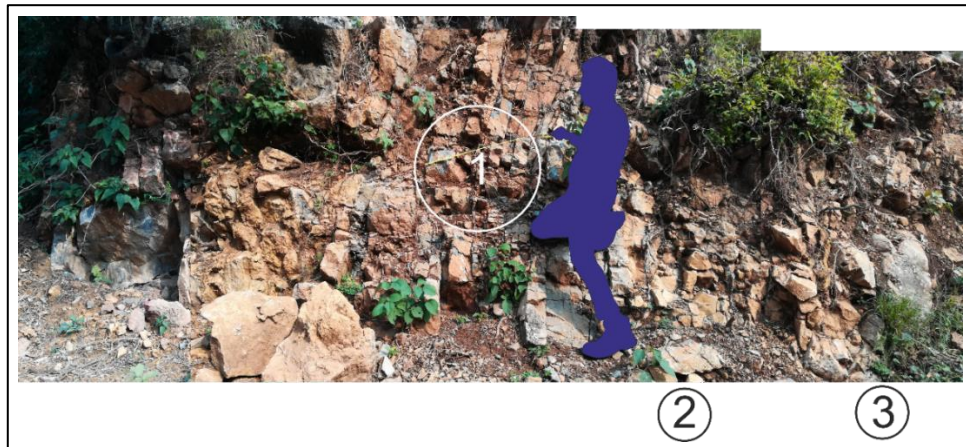


Figure 4.161: View northeast of the road sidewall at site 3 showing the general disposition of the fractures and bedding planes. The location of measurement circles is also indicated; circles 2 and 3 are measured on the flat horizontal surface exposed during road excavation. Geologist in blue.

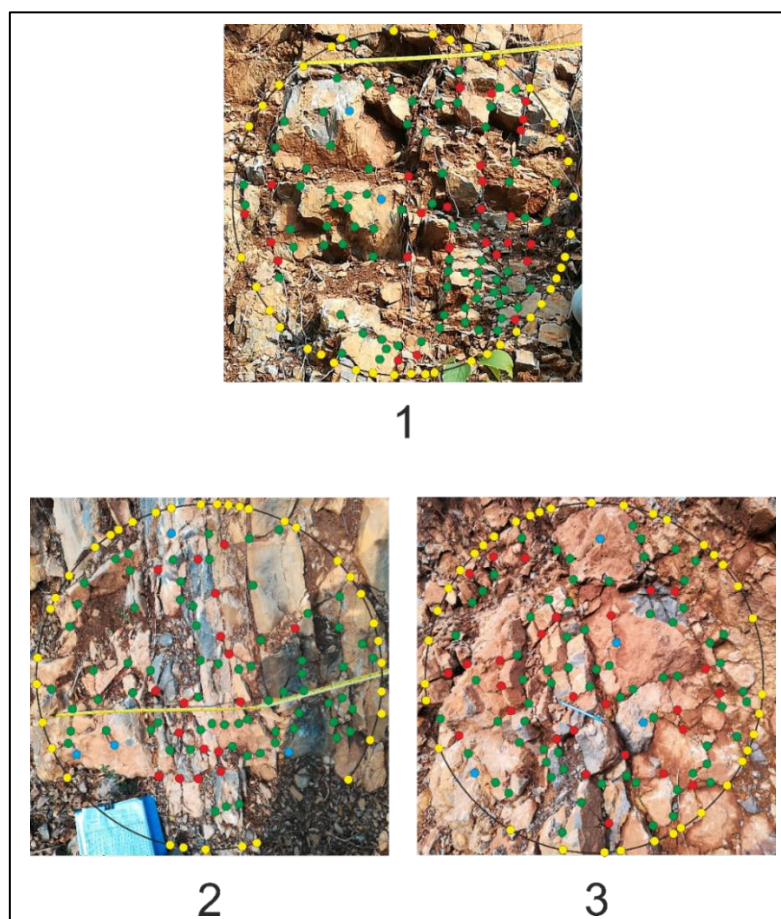


Figure 4.162: Measurement circles at site 3. Circle 1 is oriented vertically and circles 2 and 3 are oriented horizontally. See Figure 4.161 for locations.

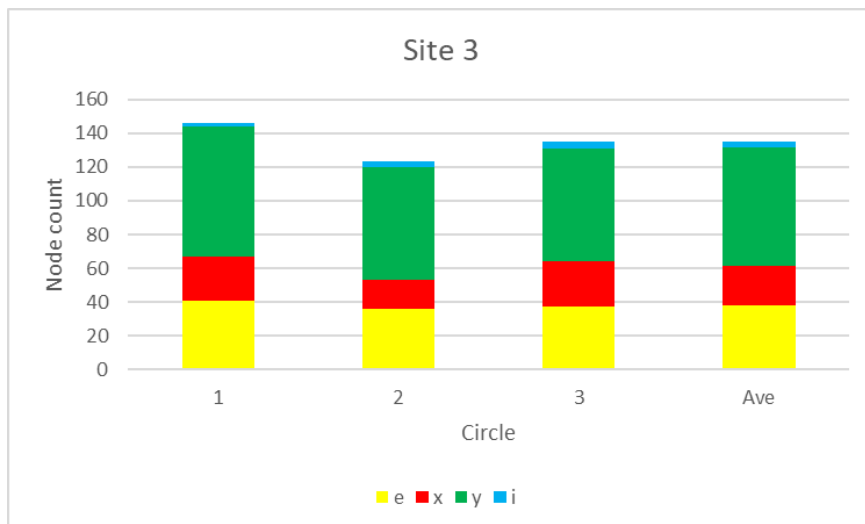


Figure 4.163: Node count, site 3

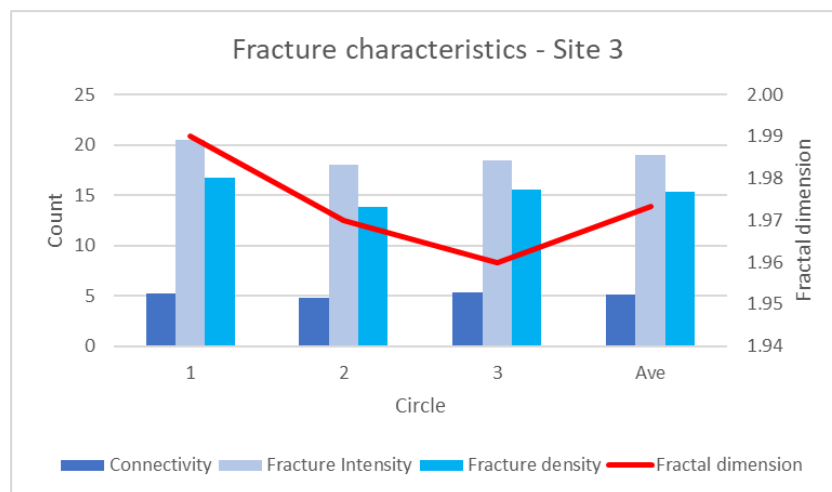


Figure 4.164: Fracture characteristics, site 3

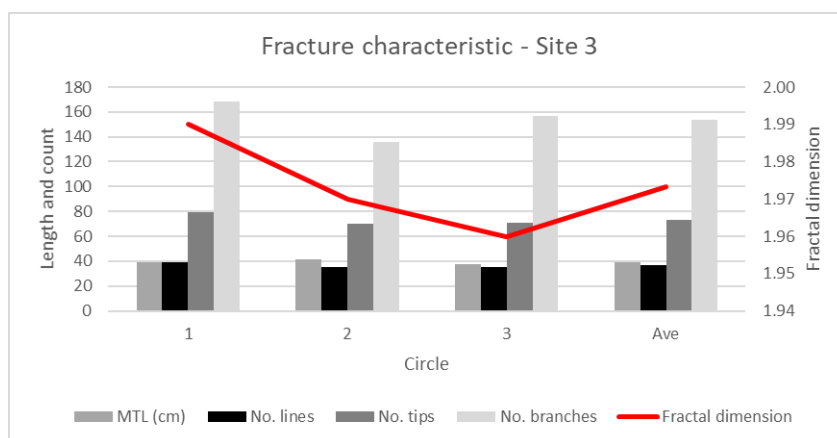


Figure 4.165: Fracture characteristics, site 3.

4.2.4.4 Site 4

Site 4 is located in the middle of the Kawagarh Formation, which in this area consists of 50 cm thick marlstone interbedded with 50 cm thick dark grey carbonaceous shale that is typically strongly sheared into the marlstone (Figure 4.166 and Figure 4.167).



Figure 4.166: View down road at site 4 (Figure 4.140). Note the steep dip of the strata towards the thrust fault in the southeast.

The node and fractal data from four circles along strike was collected and analysed. The circles were located along a 10 m section of the road sidewall (Figure 4.167) each contain both marlstone and shale. There are more nodes in the fractured (sheared) shale (see especially circle 1 in Figure 4.169). As this site is away from any major geological structures or lithological contacts, it has a lower average number of nodes in the circles (104) similar to site 2, despite being in a different stratigraphic unit.

Here the “y” nodes are the most abundant (Figure 4.168) followed by “e” nodes, most likely representing the bedding parallel shear fractures in the shale. There are few “i” nodes at site 4 (Figure 4.168). The standard deviation of the number of nodes in the different circles is low, apart from the “i” nodes, where the average and the standard deviation are the same (4). But on average, “i” nodes are less than 4% of the total number of nodes in a circle. Hence the topological fracture characteristics are similar for the various circles at site 4 (Figure 4.164 and Figure 4.165).



Figure 4.167: Positions of measurement circles on the south-eastern sidewall of the road at site 4. Pens and notebooks are circled in red for scale. View is along strike.

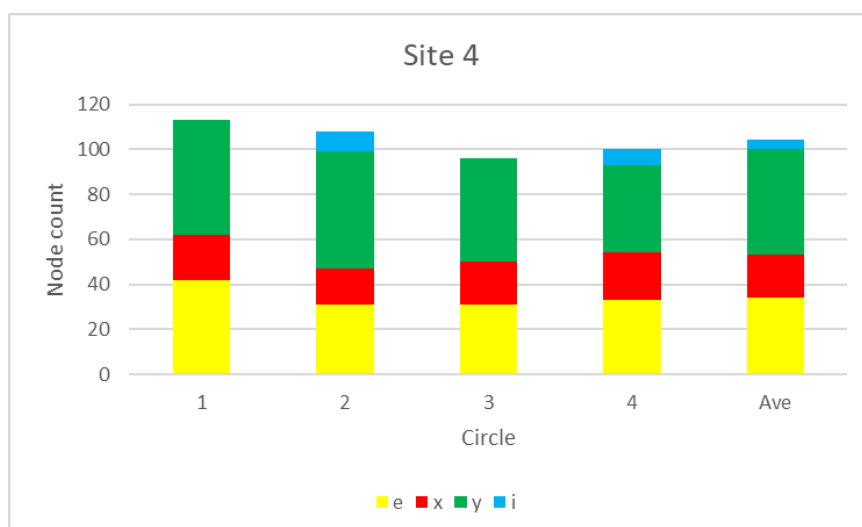


Figure 4.168: Node count, site 4.

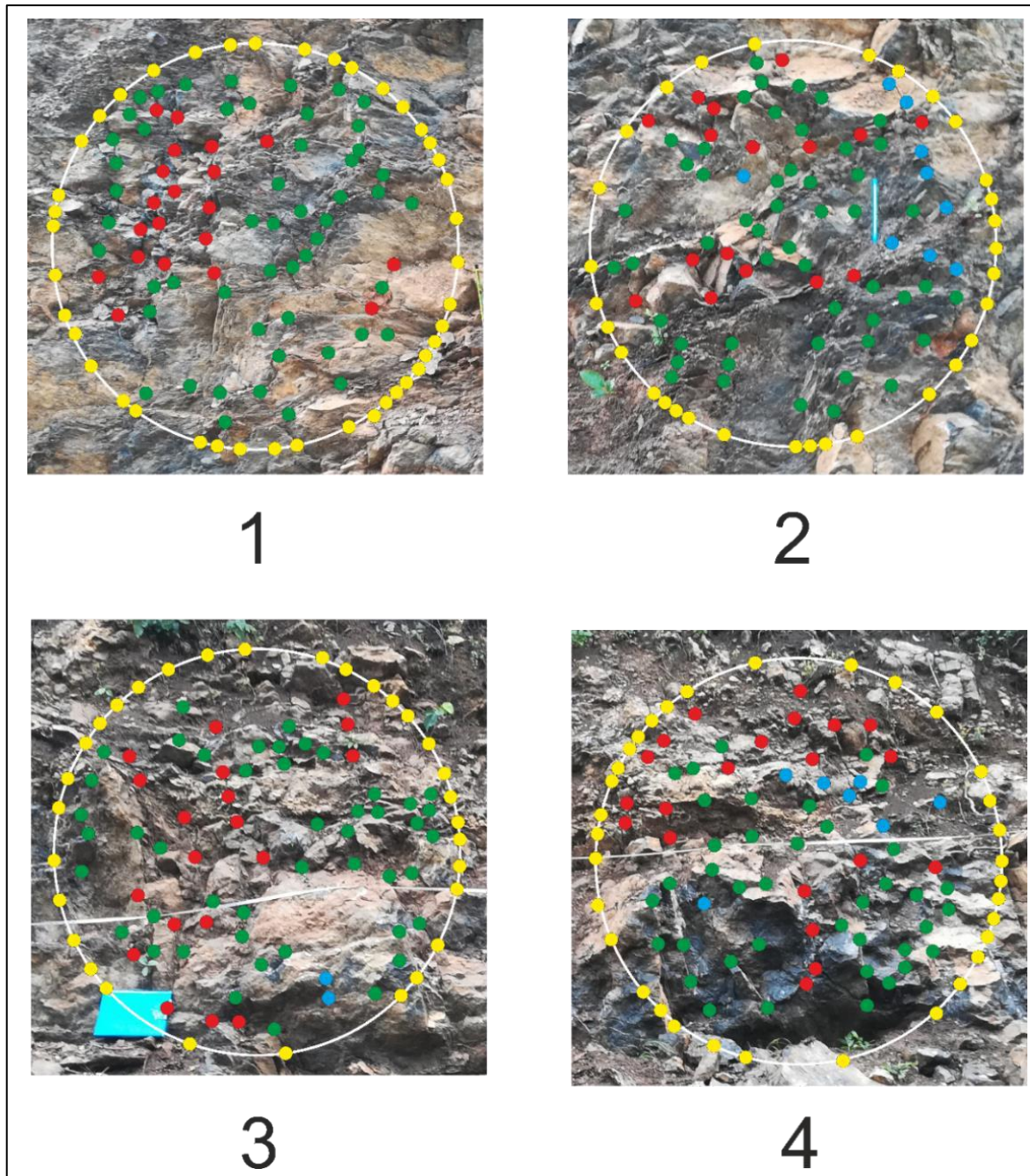


Figure 4.169: Measurement circles, site 4.

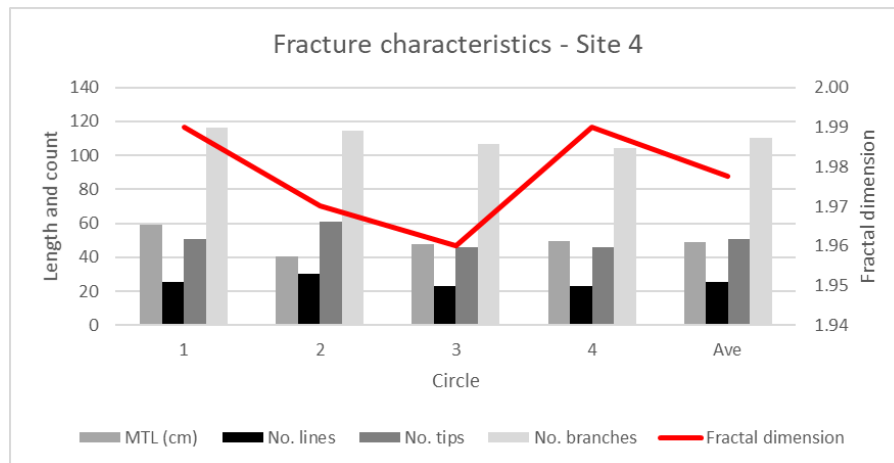


Figure 4.170: Fracture characteristics, site 4.

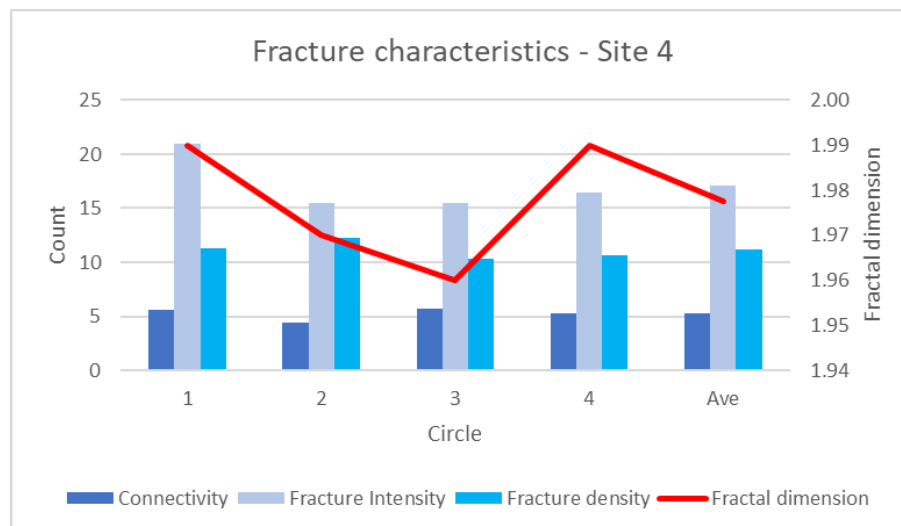


Figure 4.171: Fracture characteristics, site 4.

4.2.4.5 Site 5

Site 5 is located 500 m further north (Figure 4.140) and 200 m higher (Figure 4.172) than site 4. At this location, intensely fractured Lockhart Formation with abundant calcite fractures separated by only a few centimetres is exposed. The road-cuts are over 10 m deep but access to the steep limestone cliffs is not possible due to the extensive debris (Figure 4.178) and hence only limited mapping was possible.



Figure 4.172: View from site 5, southwards down the hill towards site 4, approximately 200 m below.

Two measurement circles were characterised at site 5 (Figure 4.173). Circle 1 has significantly more nodes than the average number of nodes at a site in the region, with half of the nodes being “y” nodes, and a quarter of the nodes being “x” (Figure 4.175). Circle 2 has an extremely high number of nodes. It has 629 nodes, which is six times as many as the regional average and it has 383 more nodes than the circle with the next highest number of nodes (318). This is in circle 2 at the nearby site 6. Despite the large volume of data in circle 2 (site 5), no preferred distribution of the nodes, indicating a preferred orientation of fracturing is apparent (Figure 4.174).

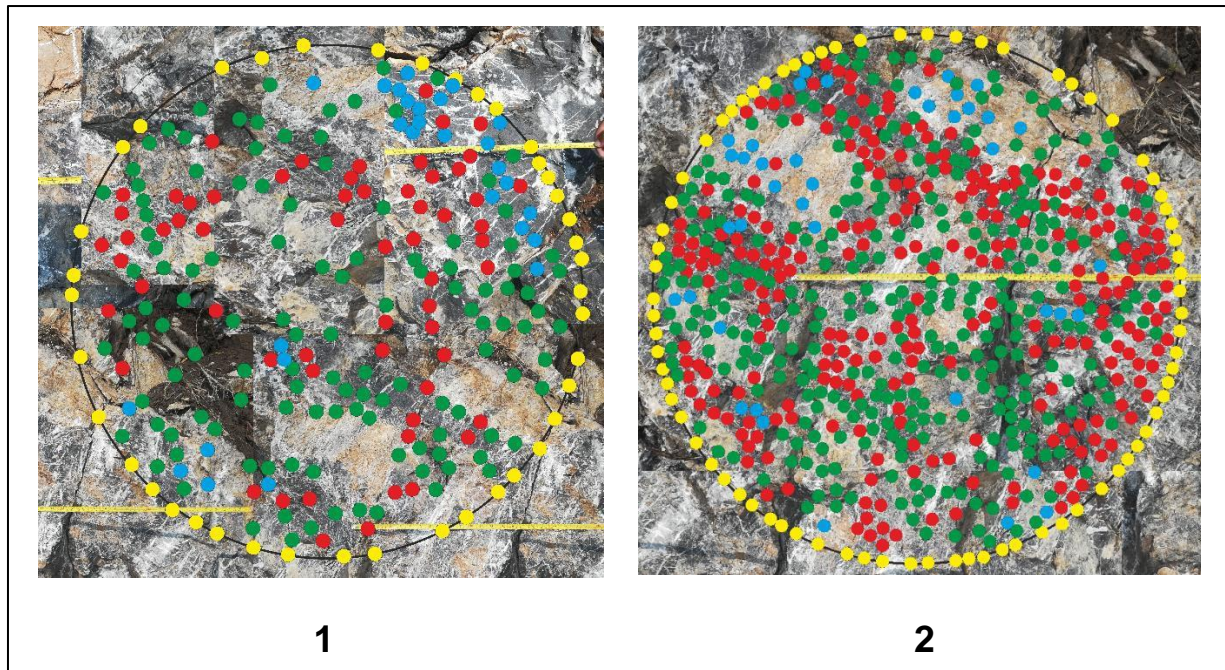


Figure 4.173: Measurement circles, site 5. The high number of nodes is due to the intense calcite fracturing.

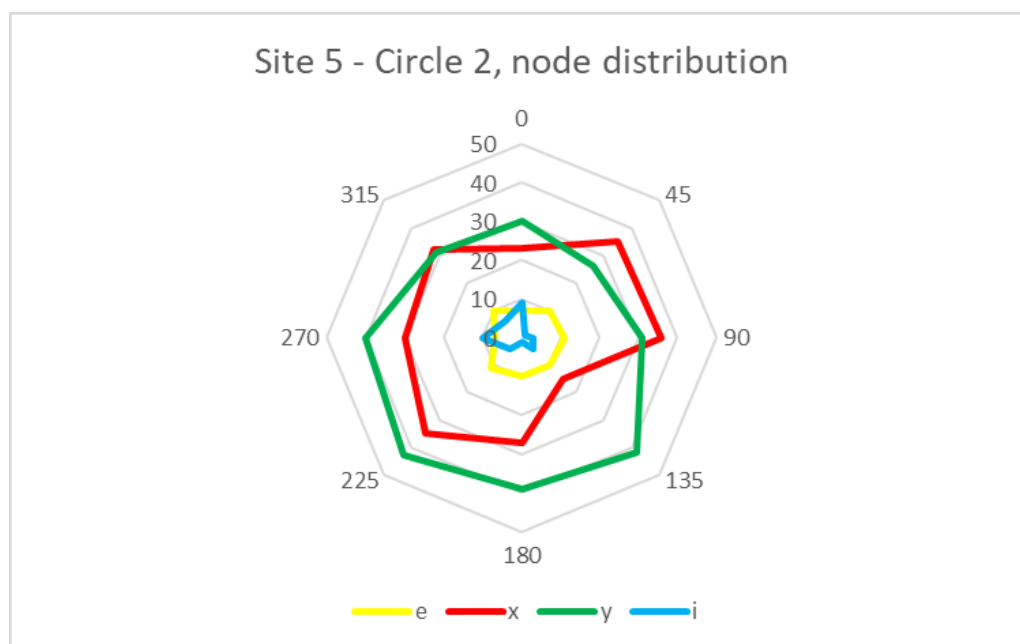


Figure 4.174: Distribution of nodes in circle 2. This is not in true geographical space, but merely represents the different portions of the circle where the different node types are clustered.

The fracture characteristics of site 5 are shown in Figure 4.176 and Figure 4.177. The high values of number of branches and fracture density in circle 2 are evident. The values of the different fracture characteristics at sites 5 were compared with the rest of the Talhaar region (Table 4.11). Significant differences include nine times as many “x” nodes, five times the fracture density, and number of branches. The total number of nodes, tips and lines increased four-fold. The fractal dimension is the same (1.99) and the mean trace length surprisingly only showed a very small decrease.

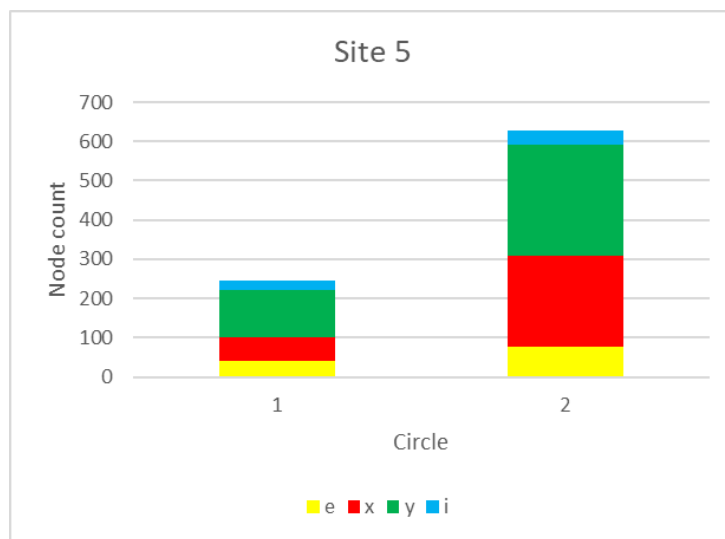


Figure 4.175: Node count of the single measurement circle at site 5.

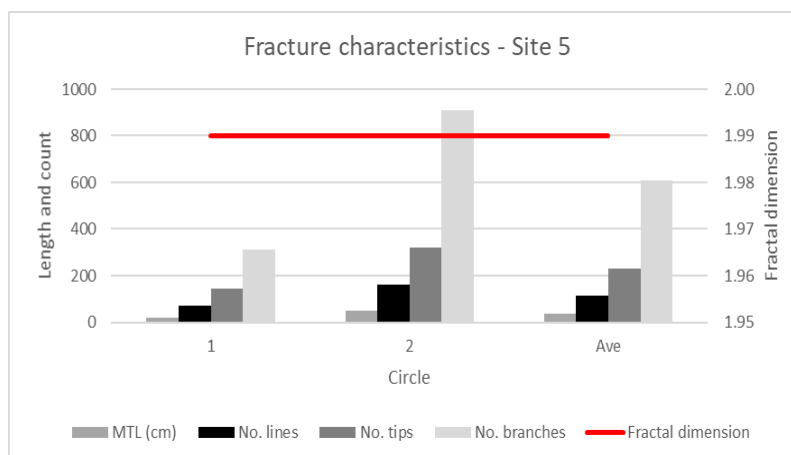


Figure 4.176: Fracture characteristics, site 5.

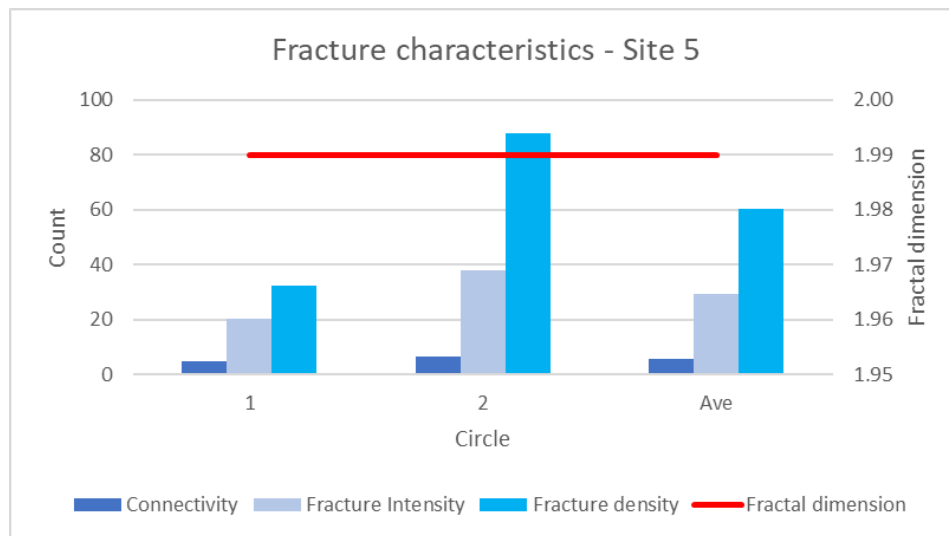


Figure 4.177: Fracture characteristics, site 5.

Table 4.11: Ratios of nodes and fracture characteristics at site 5 compared to the rest of the Talhaar region. Numbers of x, and y nodes are a lot greater and hence fracture density is higher and mean trace length is slightly shorter,

e	X	Y	i	Total nodes	Connectivity	Fracture Intensity	Fracture density	MTL (cm)	No. lines	No. tips	No. branches	D
2	9	4	2	4	1	2	5	0.9	4	4	5	1

Other techniques were used to characterise the rock mass. A series of 5 cm squares were placed on the exposed rock (Figure 4.178) and the characteristics of the fractures within these squares was examined in detail (Figure 4.179).

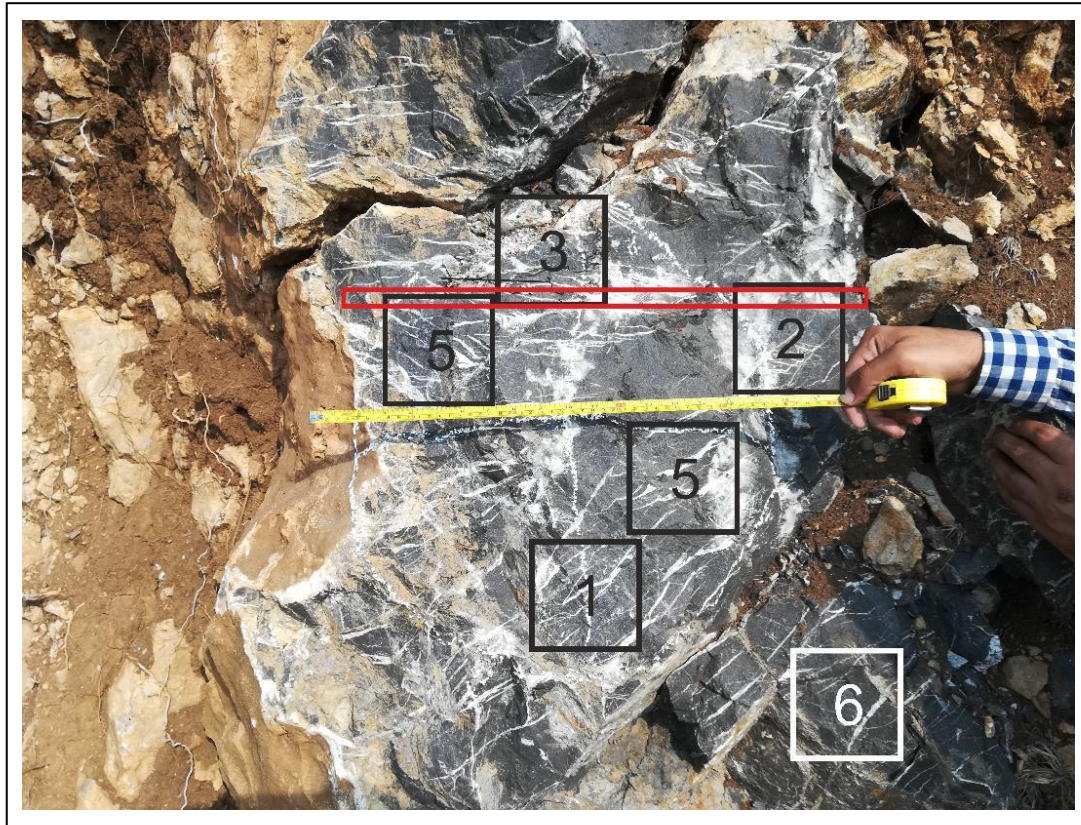


Figure 4.178: Fresh, in-situ, Lockhart Formation exposed within the debris at site 5. The positions of the detailed images in and the measurement line (red box) are shown.

Several generations of fractures are visible within the detailed image, especially an image surface set parallel and at least one set of image surface perpendicular fractures. Millimetre to centimetre thick fractures are visible from the top right to the bottom left of the images. These appear to have undergone sinistral shear as evidenced by the orientation of the second-order fractures in squares 2, 3, and 4, and the overstep of the fractures in square 5 (Figure 4.179). It is not known if these second-order fractures were formed contemporaneously with the top right to the bottom left, both sets cut through the image surface parallel fractures (Figure 4.179, square 2 and 3).

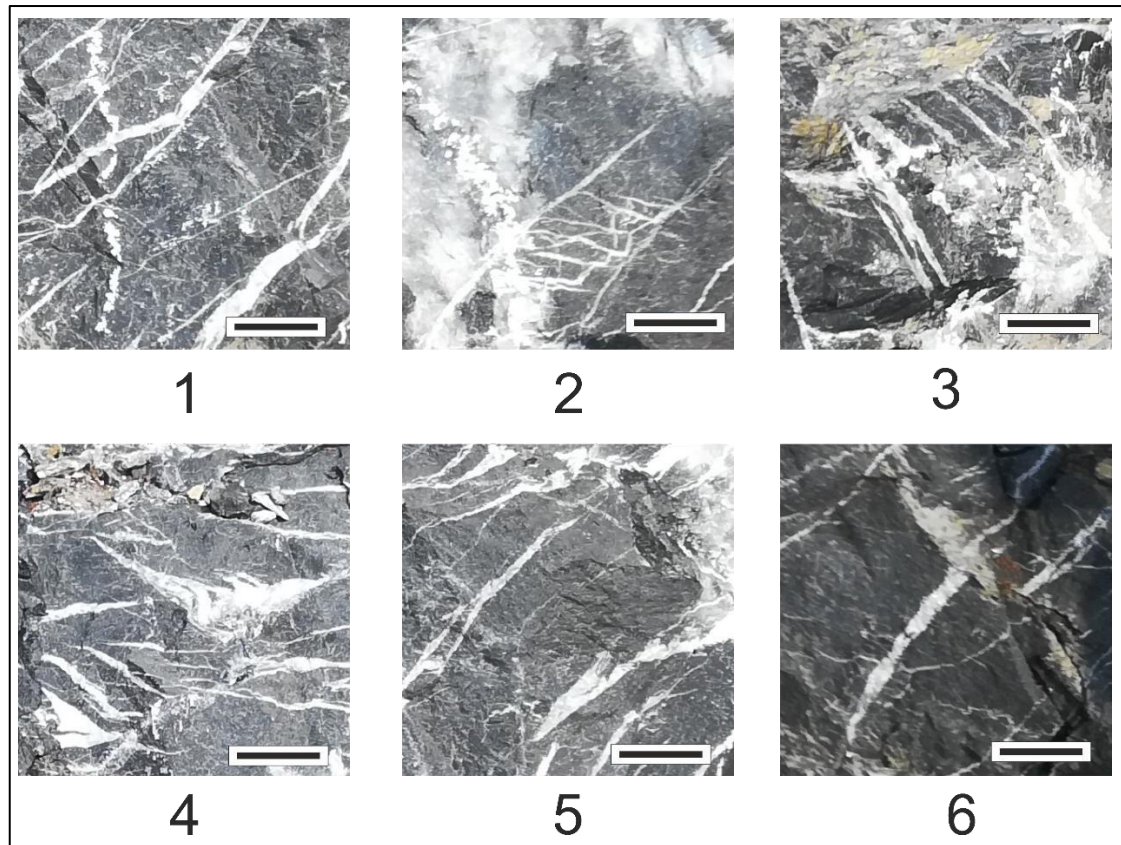


Figure 4.179: 5 cm * 5 cm detailed images of the fracture patterns at site 5 (see for distribution). Scale-bar is 1 cm.

To determine the linear density of the calcite fractures, 50 cm (Figure 4.180) and 1 m (Figure 4.181) measurement lines were drawn on the limited fresh Lockhart Formation.

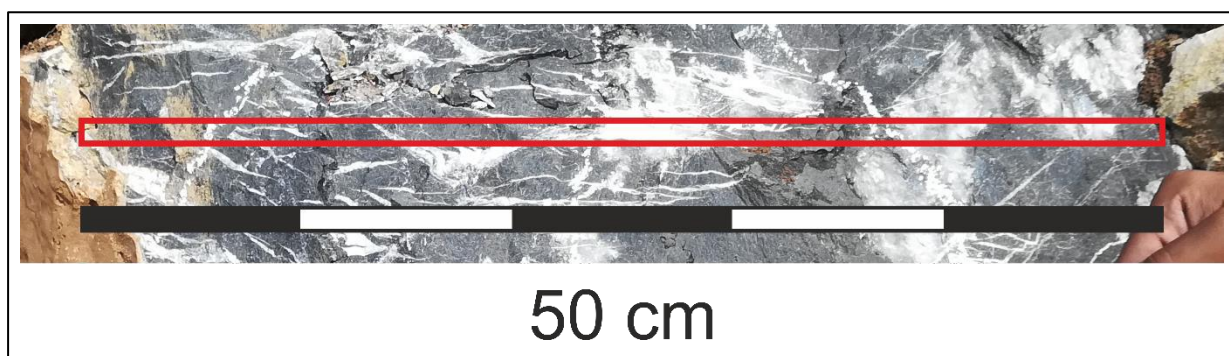


Figure 4.180: 50 cm measurement line at site 5. Figure 4.178 shows the position of this line relative to the detailed images in Figure 4.179.

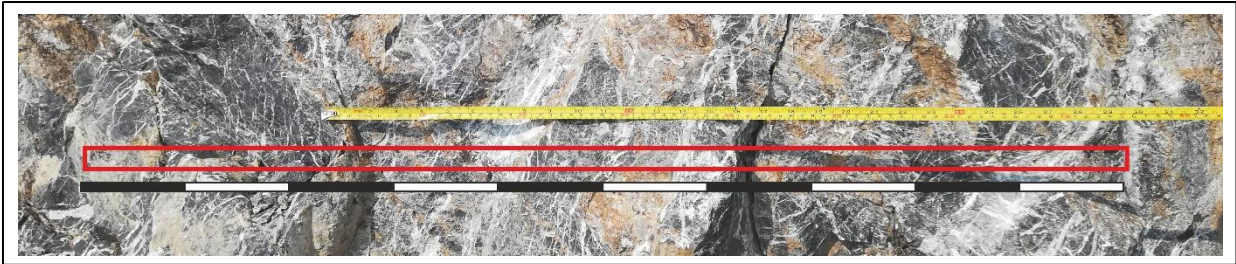


Figure 4.181: 1 m measurement line on a different fragment of Lockhart Formation at site 5.

Utilising the measurements from these lines, the centimetre scale distribution of the fractures at was calculated. The fractures are less than 5 cm apart with the majority being less than 1 cm apart (Figure 4.182a, and Figure 4.182b). Average fracture spacing is 1.1 and 0.8 cm for lines 1 and 2 respectively. Although the sorted spacing data shows that the spacing increases in a regular manner (Figure 4.182c, and Figure 4.182d), the actual distribution of separation is not regular (Figure 4.182c Figure 4.182d).

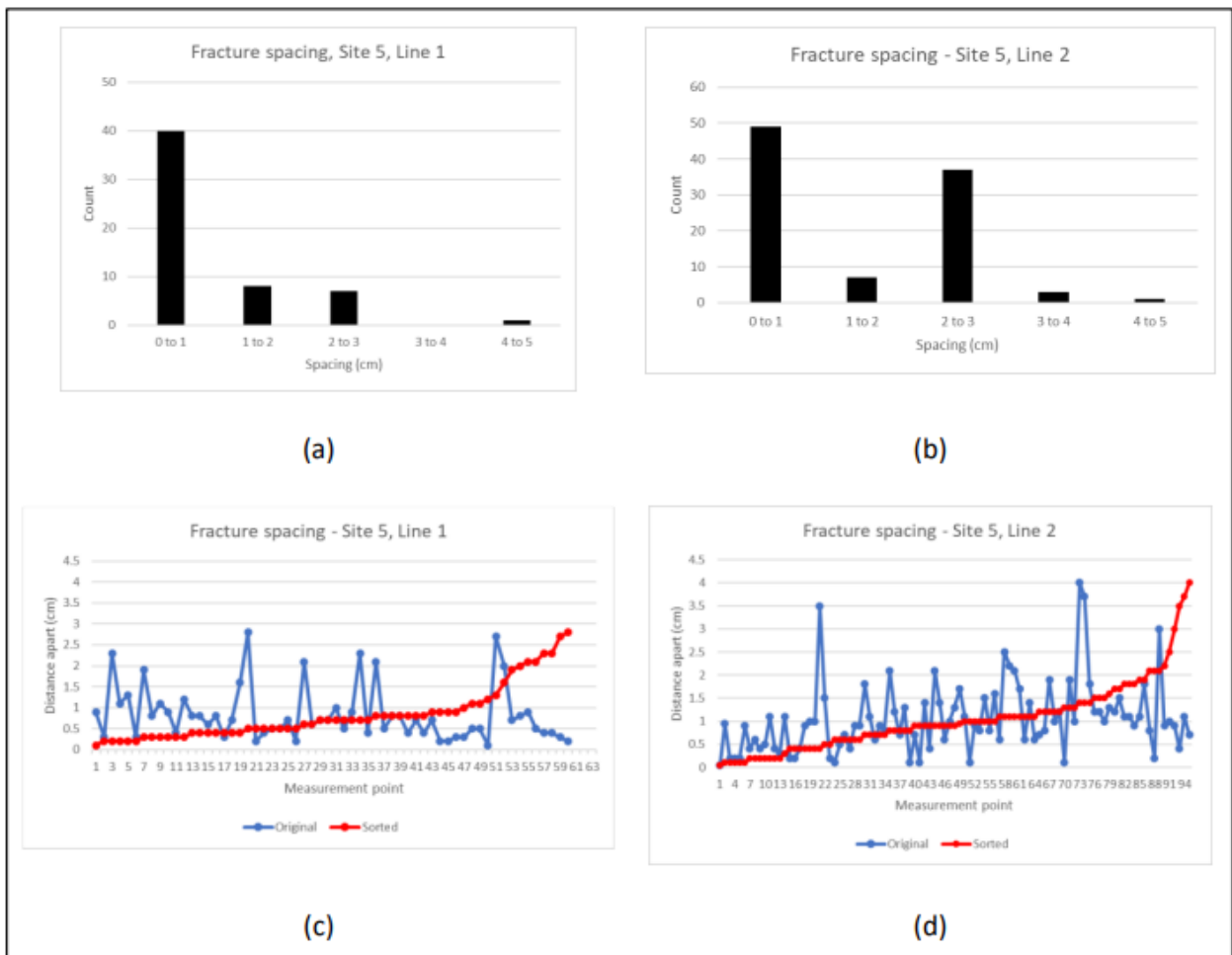


Figure 4.182: The number of fractures at different spacings along the measurement line at site 5.

4.2.4.6 Site 6

Site 6 is located at the crest of the mountains (Figure 4.183) forming the northern edge of the Talhaar region (Figure 4.140) which is immediately adjacent to the Najafpur region (Section 4.2.3). The Lockhart Formation dips to the south at approximately 50 degrees and the fragments of outcrop are separated by soil and dense vegetation (Figure 4.184).



Figure 4.183: View northwards from the mountain-top at site 6 down into the Najafpur region.



Figure 4.184: View northwest at site 6, along strike showing the poor outcrop of the Lockhart Formation.

Although sites 5 and 6 are within 250 m of each other, there are fewer fractures evident at site 6. This

is mainly because the thin calcite fractures have been obscured by surface weathering, compared to the fresh road-cut exposures at site 5. The weathering has also changed the colour of the limestone from dark to light grey making it difficult to see thinner fractures (Figure 4.185).

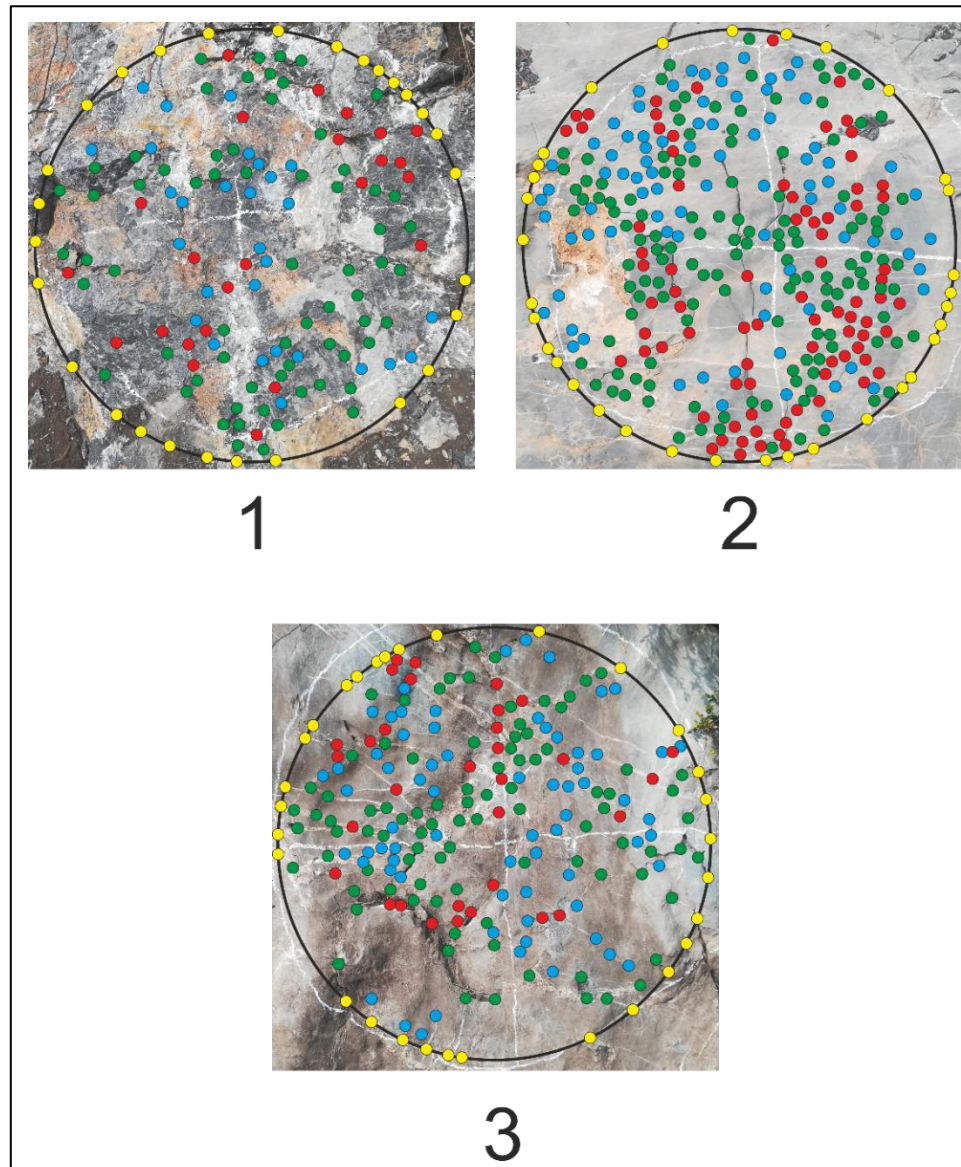


Figure 4.185: Measurement circles, site 6. The circles were drawn on widely separated fragments of Lockhart Formation.

The different node types are not spread evenly around measurement circle (Figure 4.186). As the measurement circle is not oriented in geographical space, these measurements only show relative

distribution. The number of “x” nodes is highest (20) towards 135 degrees and the number of “i” nodes is highest towards 270 and 315 degree (20 and 17 respectively). The clusters of these two node types are directly opposite to each other (Figure 4.186). Circle 2 has 318 nodes, compared to circles 1 and 3 with 144 and 221 nodes each – this results in an average number of nodes of 228 (Figure 4.187). In circle 2, with its high number of nodes, the connectivity not significantly higher when compared with the fracture characteristics of the rest of the region (Figure 4.188). As expected, the mean trace length is shorter, and the fracture density is greater (Figure 4.188). Circle 2 has more lines, tips, and branches (Figure 4.189).

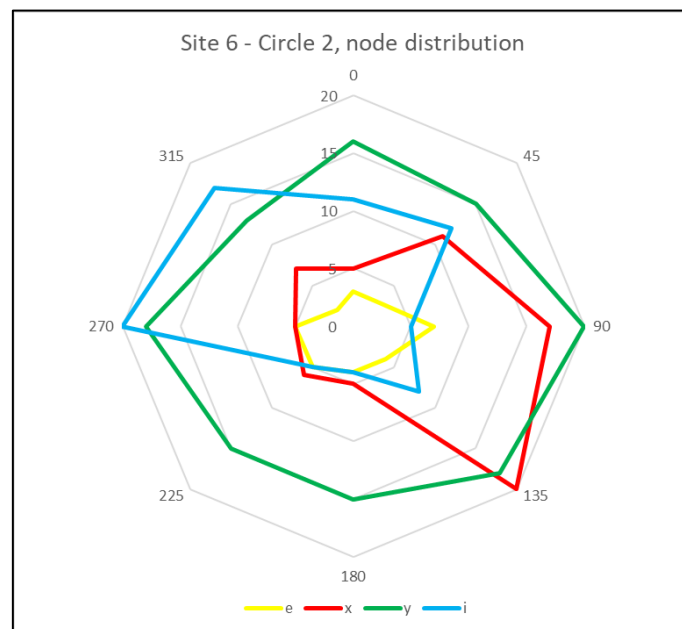


Figure 4.186: Node distribution, in circle 2 at site 6.

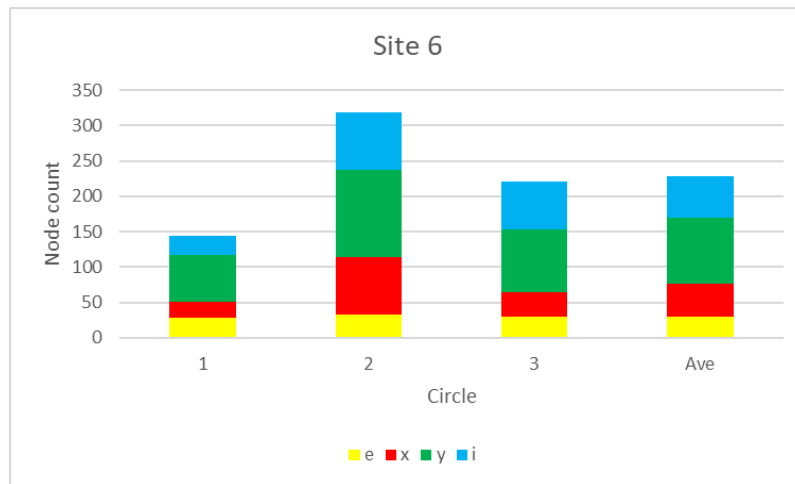


Figure 4.187: Node count, site 6.

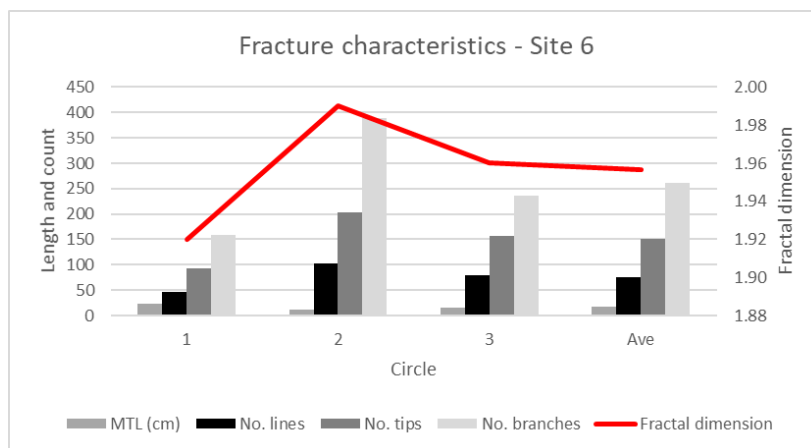


Figure 4.188: Fracture characteristics, site 6.

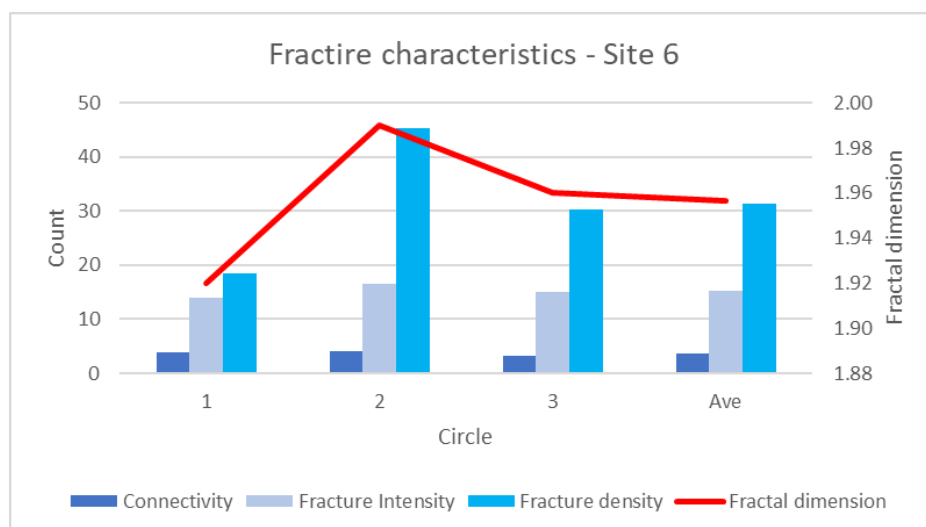


Figure 4.189: Fracture characteristics, site 6.

4.2.4.7 Site 7

Sites 7,8 and 9 should be considered together as they form parts of the same fold and thrust structure (Figure 4.140). The sites are located on a road that travels northward up a steep sided valley, with 7 being on the west, 9 on the east and 8 within a gravel pit on the edge of the road (Figure 4.190).

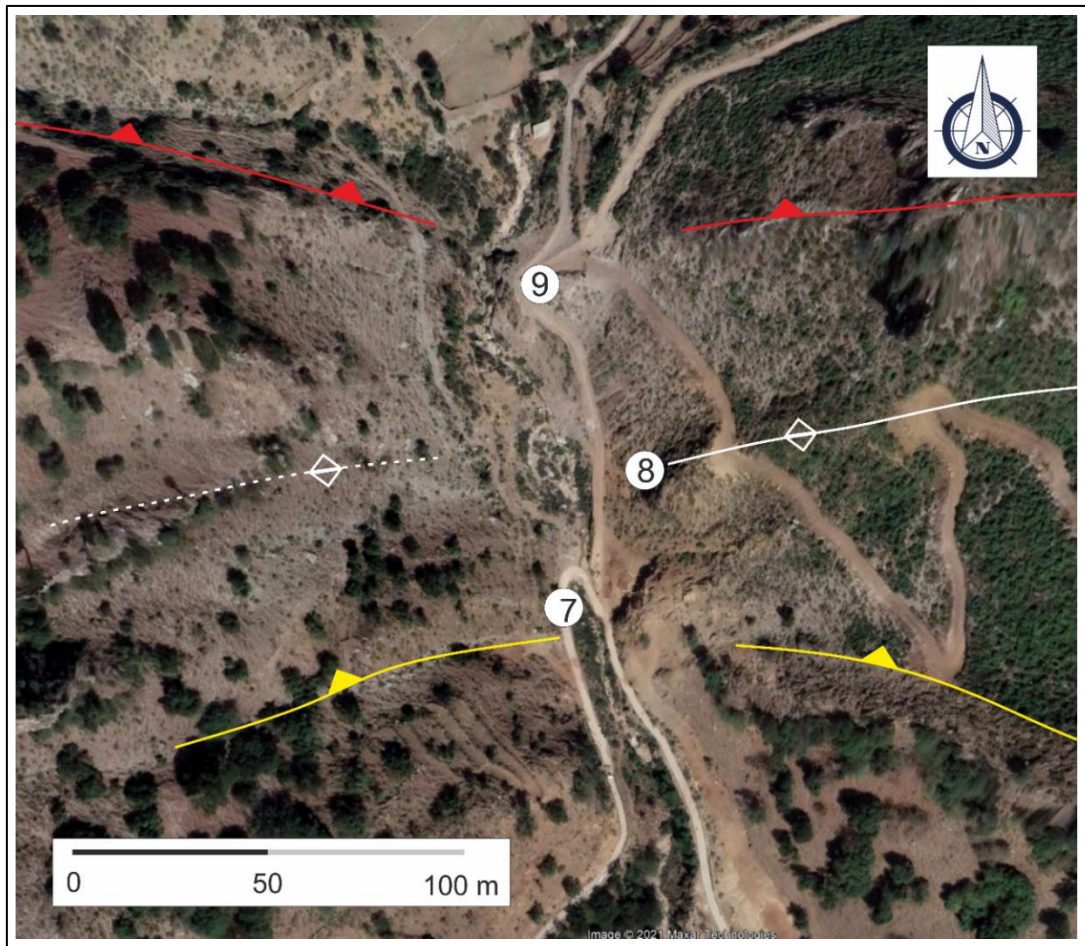


Figure 4.190: Google earth image showing the positions of site 7, 8, and 9 and the associated geological structures.

At site 7, an ortho-rectified 20 m long image of the Margalla Hills Formation was generated from 12 different photographs of the western sidewall of the road, using ICE (Image Composite Editor from Microsoft Corporation). This was then cropped into an 18 m long by 2 m high image, which was imported into ArcMap for further data capture and image processing.

The relative fracture and bedding lengths was determined in ArcMap using the Kernel Density method,

which for lines involves placing a smoothed curve along the line and determining the value in a circle around each line point. The raster is then coloured based on the sum of all the values for that point. Separate images are shown for bedding parallel fractures (Figure 4.191.3) and bedding orthogonal fractures (Figure 4.191.4). In both images red indicates longer lengths and blue shorter, but the absolute values are not the same.

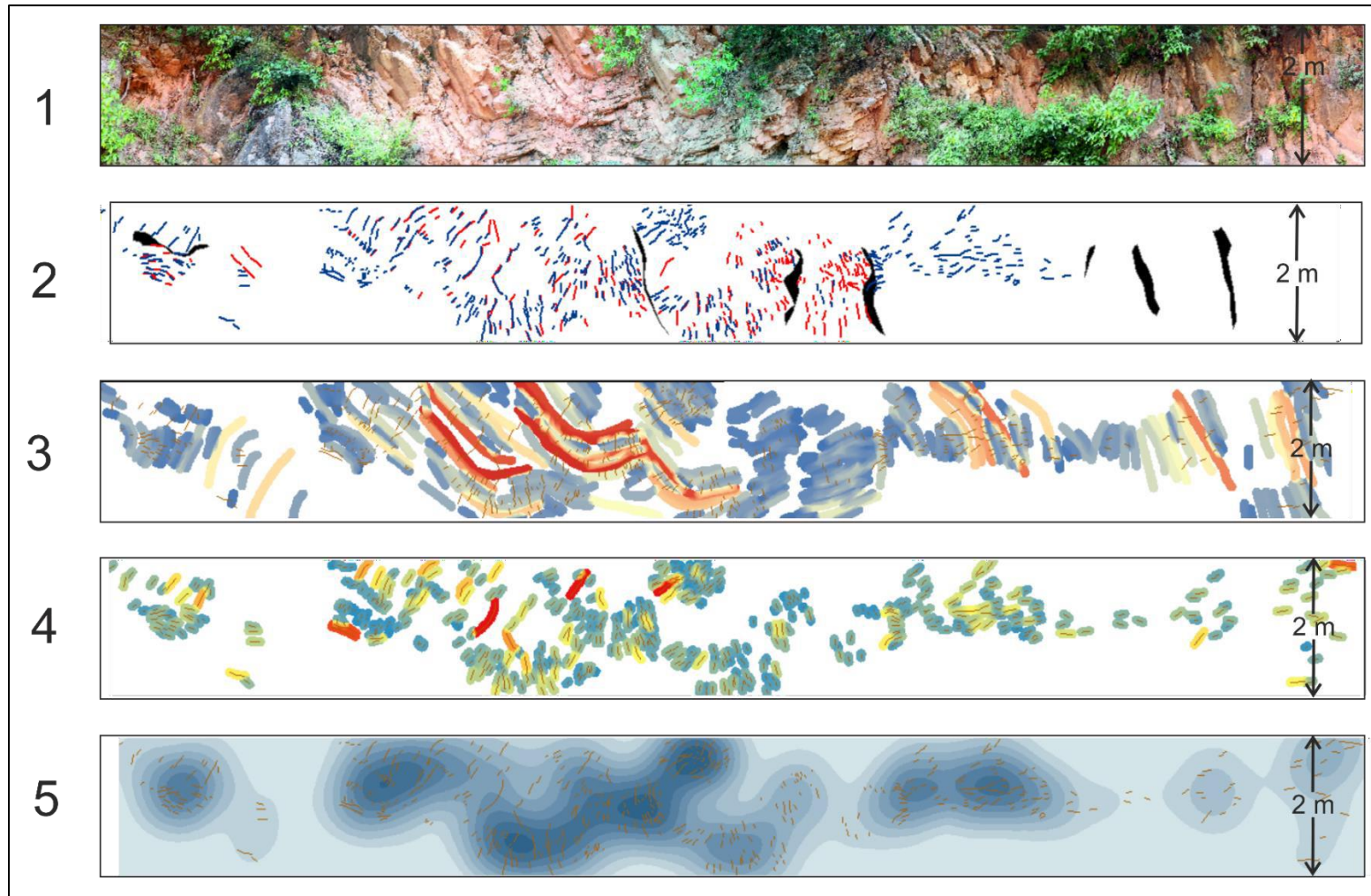


Figure 4.191: (1) composite image of the western sidewall of the road at site 7; (2) traces of fractures (blue), bedding (red) and faults (black) from image; (3) bedding parallel fracture length; (4) bedding orthogonal fracture length;(5) fracture and bedding density combined. As before conventional ArcMap tools are used to quantify the fracture characteristics.

The density of the bedding parallel and bedding perpendicular fracture traces was also calculated using the Kernel Density method, but with a wider search radius of 50 cm to increase the range of influence. This allowed regions of higher fracture density to be defined (Figure 4.191.5), rather than the restricted 5 cm search radius, which ensured that the values were determined for individual fractures.

The number of bedding parallel and bedding orthogonal fractures was determined. In total, 502 bedding perpendicular fractures and 450 bedding parallel fractures were measured. Figure 4.193 shows the distribution of both of these fracture types, with the majority occurring between 6 and 12 m.

The length characteristics of were also determined. Bedding parallel fractures are the longest, with an average length of 1.29 m. The bedding parallel are longer between 4 and 8 m, and also at 12 to 14 m and 16 to 18 m the section (Figure 4.191). Bedding orthogonal fractures do not show a preferred distribution (Figure 4.194) and have a maximum average length of 0.28 m and an overall average length of 0.12 m.

Fracture density (the product of the number of fractures and their lengths) is highest between 4 and 12 m, where the highest fracture counts (Figure 4.193) and lengths (Figure 4.194). This is confirmed by Figure 4.191.

A series of measurement circles were placed on the sidewall exposure at site 7 (Figure 4.192). The correspondence of these circles with the blocks used in Arc for the systematic analysis of fracture distribution and lengths is presented in Figure 4.192: Western sidewall at site 7 (the same 18 m long section as Figure 4.191). The photographs are offset to show the true position of the measurement circles. Compare with Figure 4.191, where uniform 2 m high section is shown.

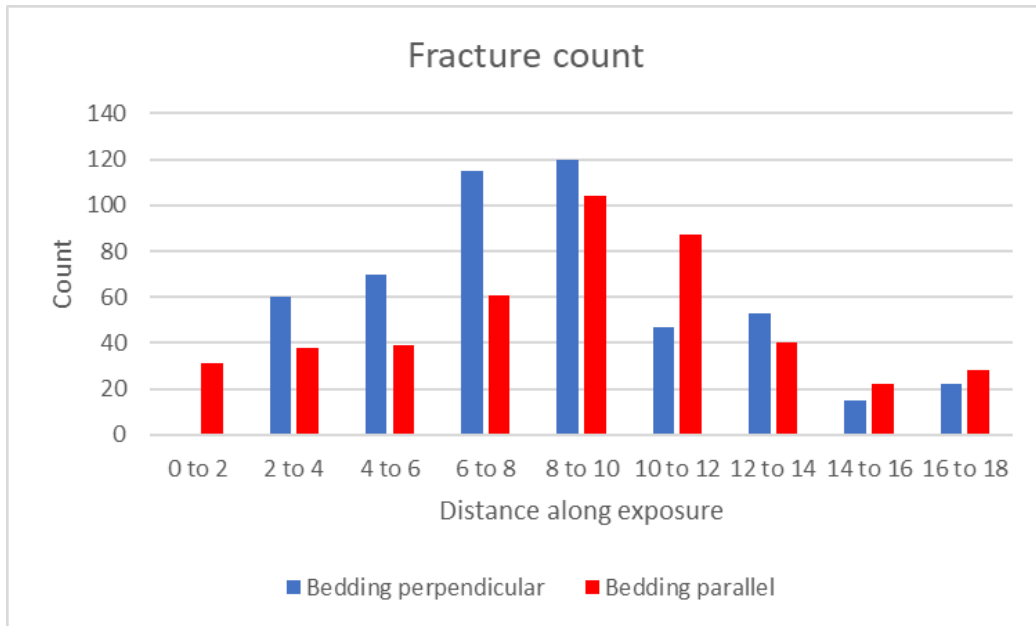


Figure 4.193: Fracture counts from ArcMap counting boxes placed along the sidewall at site 7.

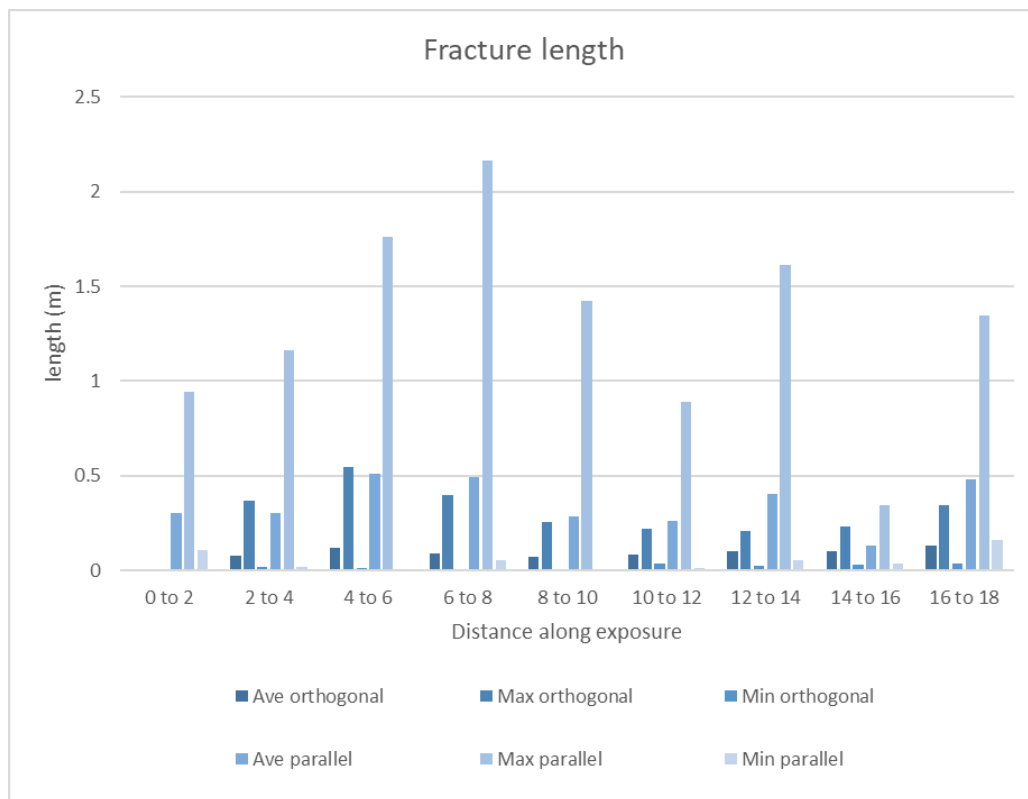


Figure 4.194: Fracture characteristics for 2 m sections along the exposure at site 7. Compare with fracture characteristics derived from circle measurements along the same section.

Table 4.12: Location of measurement circles relative to distances along the section at site analysed for fracture density and lengths.

Distance (m)	Circle number
0 to 2	None
2 to 4	1
4 to 6	2, 4
6 to 8	3, 5
8 to 10	6, 7
10 to 12	8
12 to 14	None
14 to 16	9
16 to 18	10

On average 100 nodes were identified in each measurement circle with 50 of them being “y” nodes (Figure 4.197). The “y” nodes are formed by the termination of the bedding orthogonal fractures against the longer bedding parallel fractures (Figure 4.195 and Figure 4.196).

Circle 5, which has the highest number of nodes (Figure 4.197), and greatest number of lines, tips, and branches (Figure 4.198). It also has the high fracture intensity and fracture density (Figure 4.199).

Circle 9 has the longest trace length, but the lowest fracture intensity and fracture density. This is because the long fractures are fewest in number at the site and also have the least tips and branches.

The fractal dimension is also remarkably low at in this circle (1.62). Examination of Figure 4.196 shows the long, widely spaced fractures of circle 9.

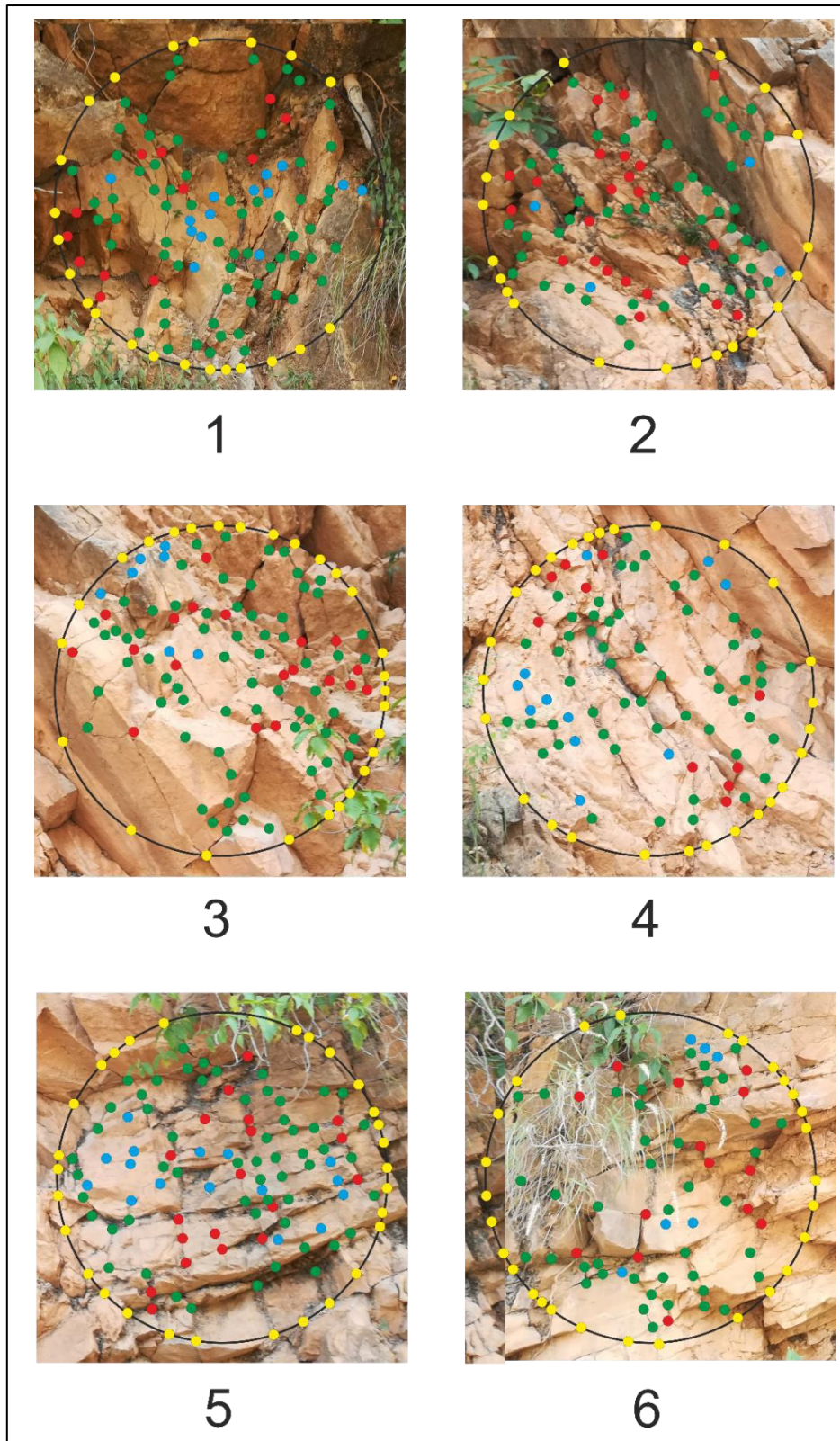


Figure 4.195: Measurement circles 1 to 6, site 7. Figure 4.196 shows circles 7 to 10. The location of measurement circles at the site is indicated in Figure 4.192.

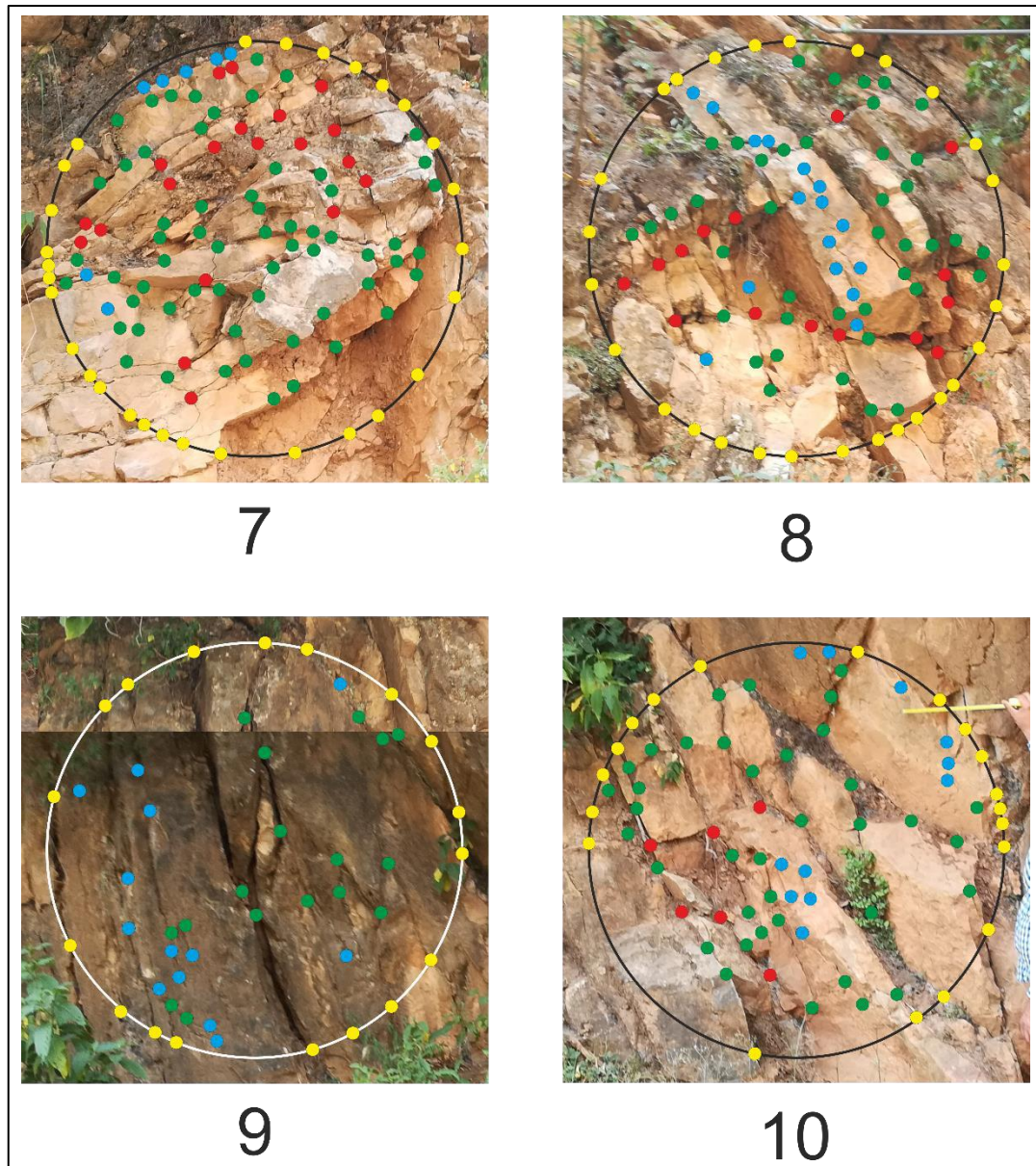


Figure 4.196: Measurement circles 6 to 10, site 7. Figure 4.195 shows circles 1 to 6. The location of measurement circles at the site is indicated in Figure 4.192.

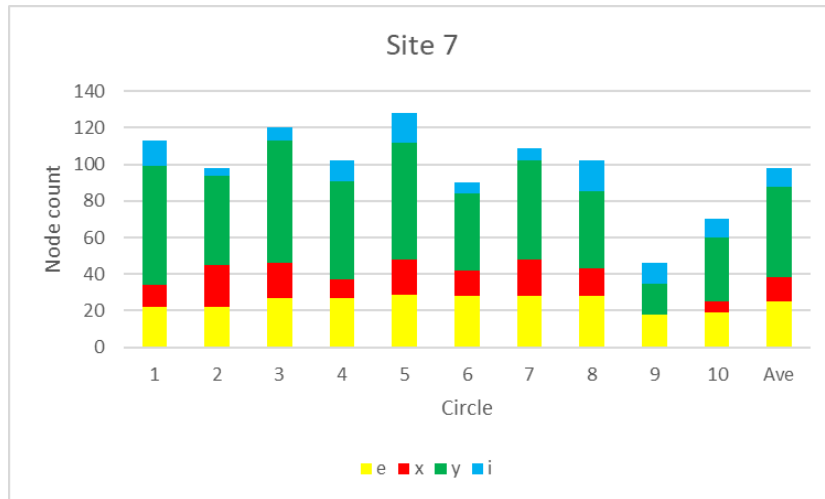


Figure 4.197: Node count, site 7.

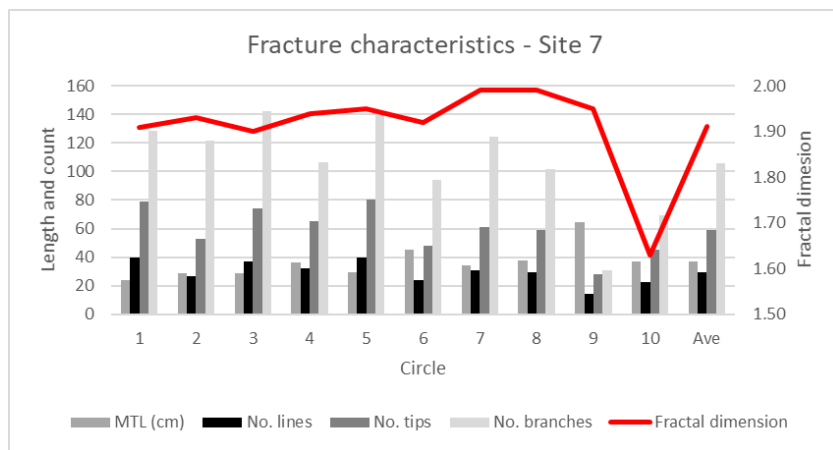


Figure 4.198: Fracture characteristics, site 7.

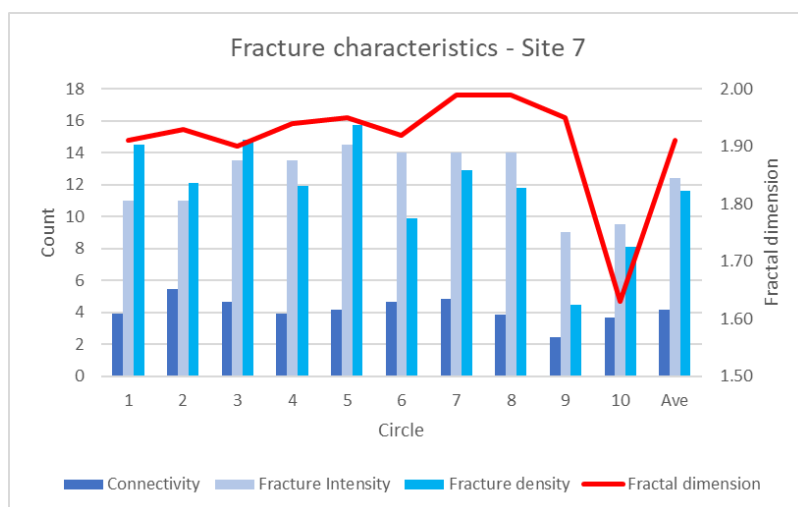


Figure 4.199: Fracture characteristics, site 7.

The relationship between the topological and fractal parameters (derived from ArcMap) were compared utilising the distribution of the measurement circles defined in Table 4.12. The relative values of each parameter were determined in Excel using the Conditional Formatting tool. These values were then converted into rankings of one to ten (ten circles, with "1" representing the highest ranking) and then summed to determine the highest amount of fracture damage (Table 4.13). It was found that circle 5, located in the tightest part of the syncline above the thrust has the greatest amount of fracturing. It is followed by circles 3 and 7 which are located higher in the fold-plane and further from the thrust. Interestingly, circles 4 and 6, which lie closer to circle 5 (centre of the hanging- wall syncline), have lower values. This is due to the reduced of nodes (and hence topological values), which is because the stress is being relieved more by shearing along the bedding parallel fractures rather than the development of additional orthogonal fractures.

Table 4.13: Compound ranking of different circles at site 7.

Circle	Mean γ and fractal dimension ranking
1	6
2	5
3	2
4	8
5	1
6	9
7	3
8	4
9	10
10	7

4.2.4.8 Site 8

Site 8 is located in within a gravel pit adjacent to the road, to the east of site 7 (Figure 4.200). The sidewall of the gravel-pit provides exposure to a shallow, gently folded anticline developed in the between the thrusts at site 7 and site 9. The dip of the beds in the anticline flattens out to almost horizontal at the base of the gravel pit. In general, the rock mass at site 8 is highly fragmented, but the

most noteworthy features are bedding parallel clay filled partings, up to 20 cm thick, consisting of a muddy, undeformed red-brown iron-oxide clay (Figure 4.201).

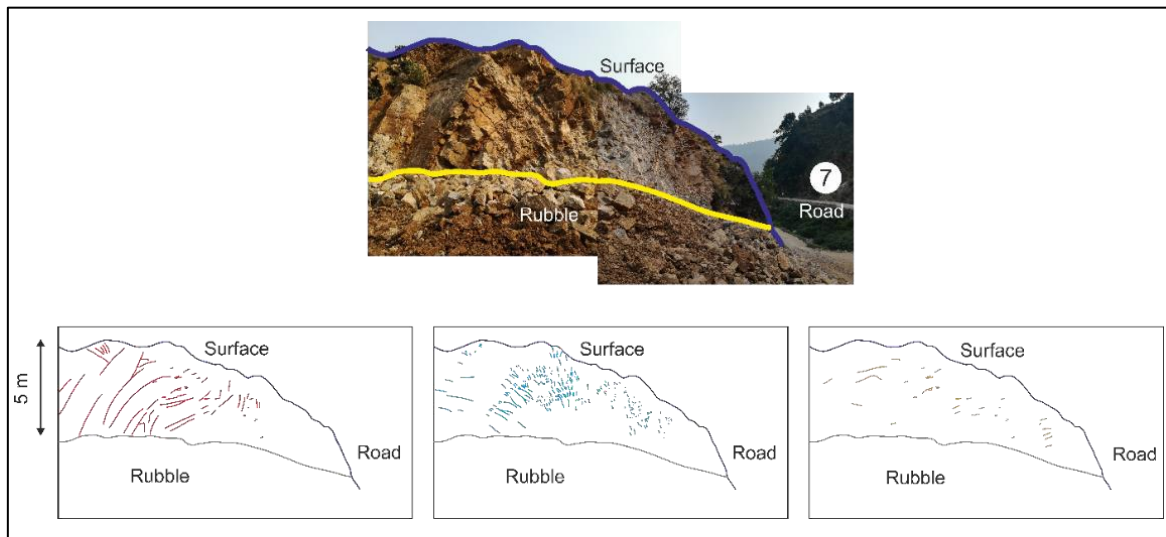


Figure 4.200: View southwest towards site 7. The beds in the upper portion of the anticline dip northwards at 50 degrees.

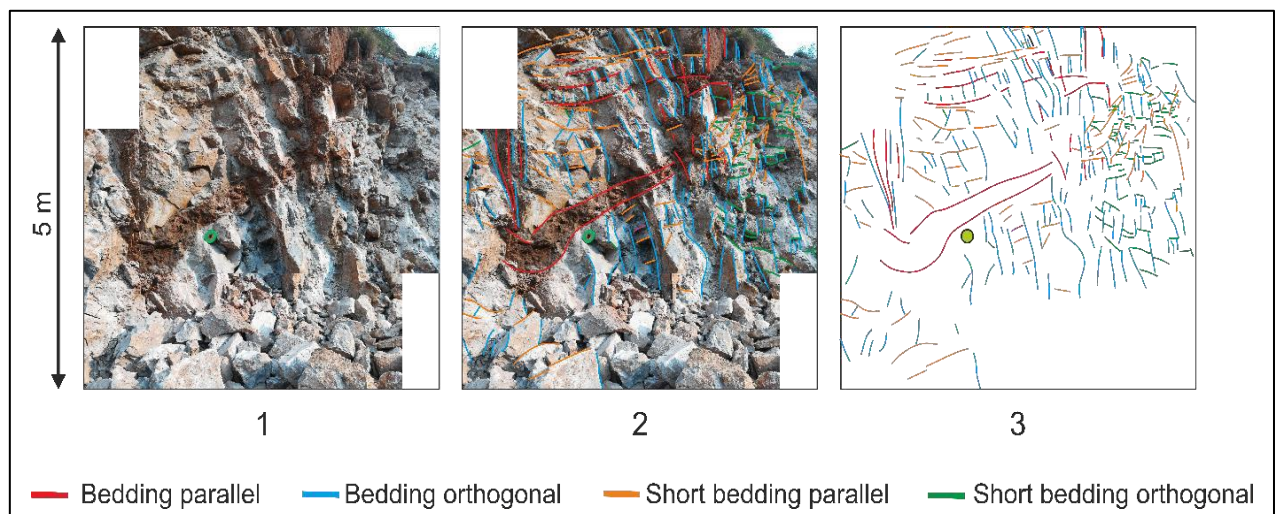


Figure 4.201: Fractured rock mass at site 8, including 20 cm thick partings of red-brown clay.

These parting are generally separated by about 1 m, and only a few centimetres thick, apart from the prominent shear in the middle of the outcrop (Figure 4.201). The lack of shear on this very soft material suggests that it is a recent fill of voids created by the differential buckling of adjacent beds. Instead of sliding past either of the thrust layers, the various beds in this central anticline folded upward to different degrees creating the voids that could later be filled. The steep fractures have a variety of coatings from

unmineralised light grey limestone, through orange iron oxide to red-brown clay coated fractures that lead down to the bedding parallel fractures of the same composition. Six measurement circles were placed on the fresh exposure of the quarry sidewall (Figure 4.202). The red-brown clay partings are visible in all of the measurement circles, especially circle 4 (Figure 4.203).

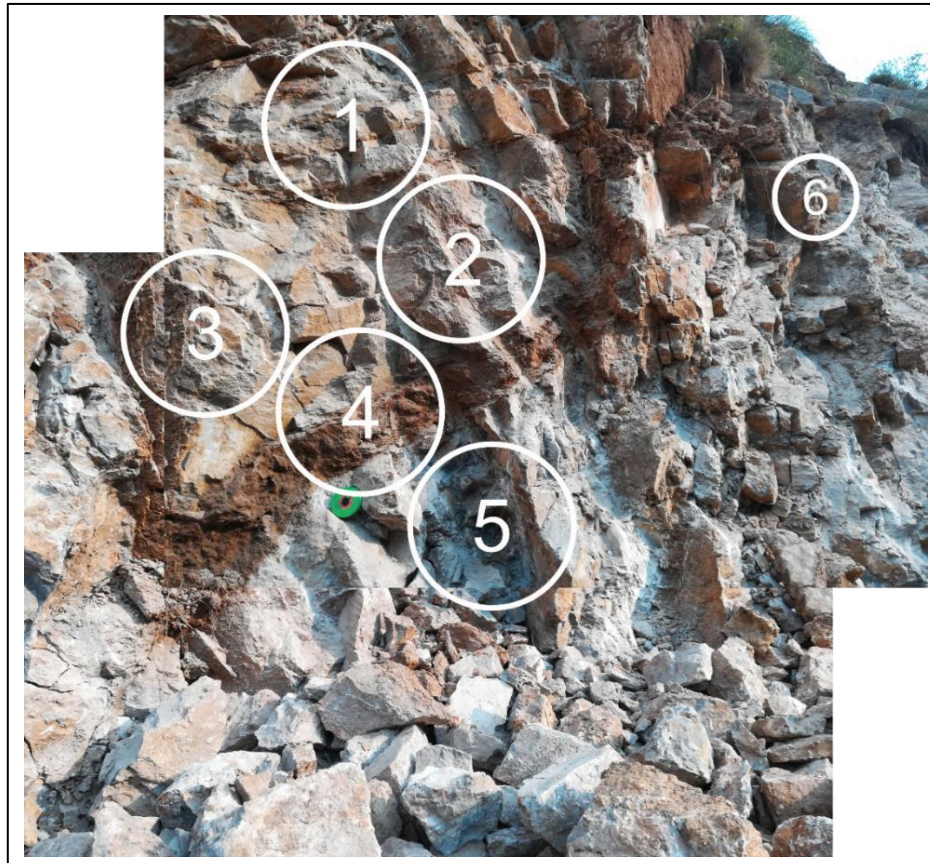


Figure 4.202: Location of 1-metre-wide measurement circles at site 8. Circle 6 is not of a smaller diameter, but at a greater distance from the camera, making it look smaller.

An average of only 78 nodes are present in each circle, with the majority being “y” and “e” nodes (Figure 4.204). The limited number of “x” and “i” node fractures suggests that the limestone beds between the clay parting have been subjected to less buckling. Thus, even though the exposure contains abundant fractures, most of these cross-cut each other (especially in the limestone). There are fewer lines, tips, and nodes and hence lower topological values at site 8 (Figure 4.205), compared

to other sites. Fracture density and intensity is low, particularly in circle 3 (Figure 4.206). The relative rankings of the circles at site 8 is shown in Table 4.14 which includes the node counts, fracture characteristics and fractal dimension as shown in Figure 4.204 to Figure 4.207

Table 4.14: *Compound ranking of different circles at site 8.*

Circle	Node and fractal dimension ranking
1	2
2	6
3	3
4	4
5	1
6	5

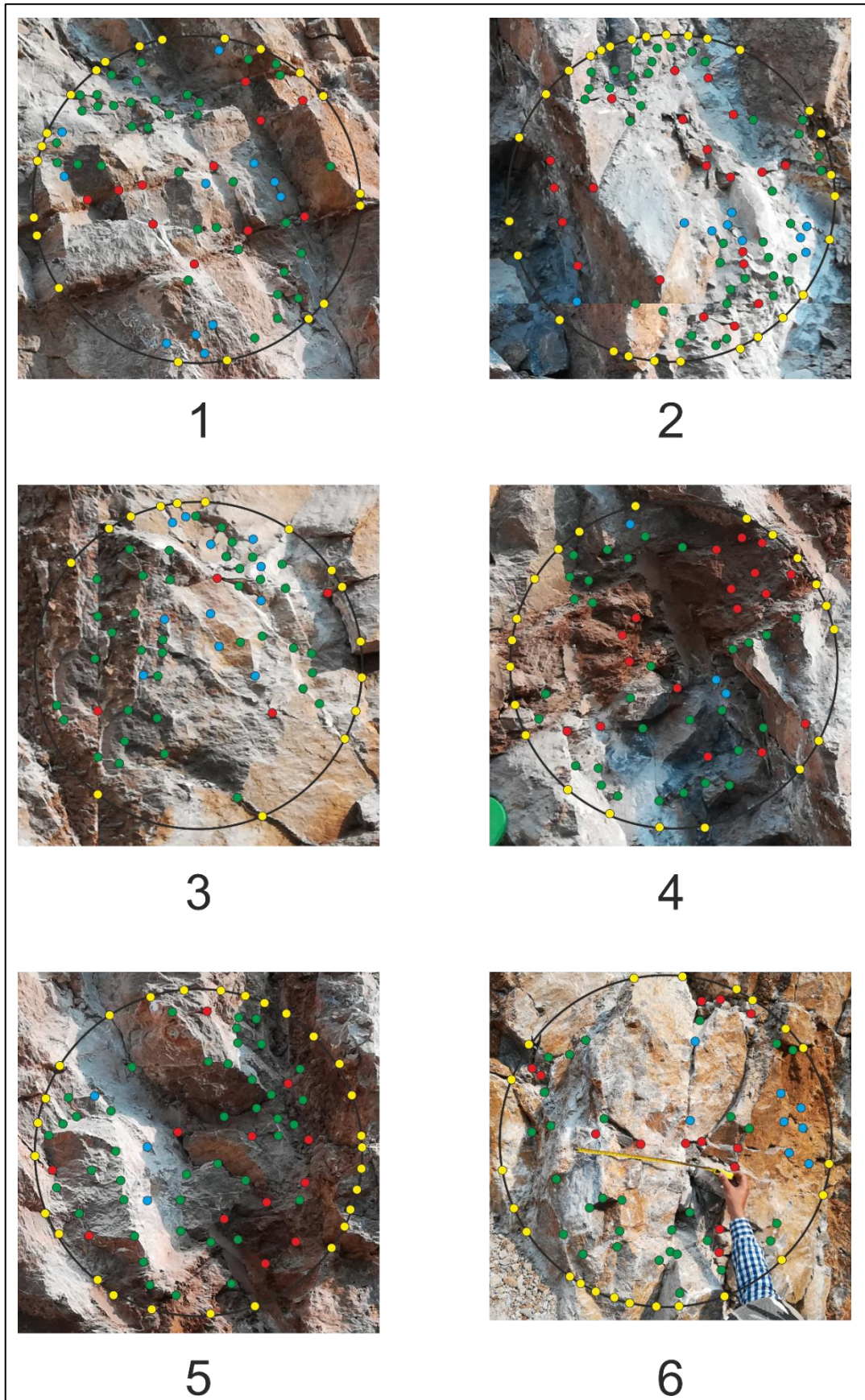


Figure 4.203: Circles 1 to 6 at site 8.

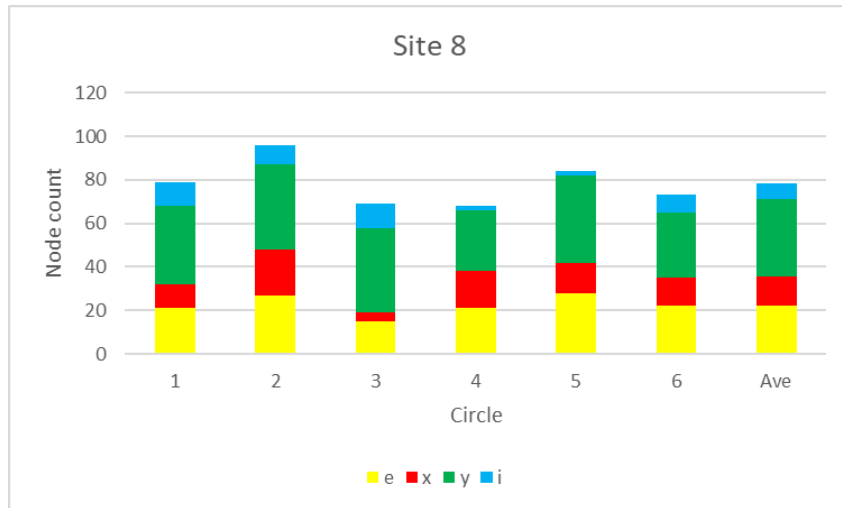


Figure 4.204: Node count, site 8.

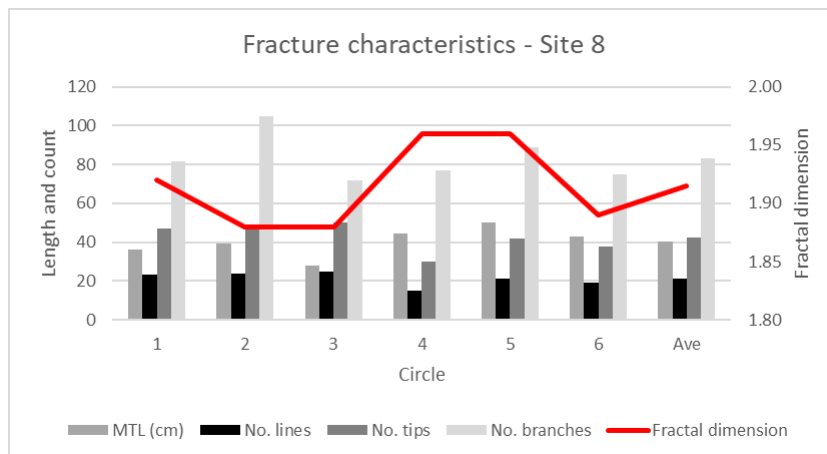


Figure 4.205: Fracture characteristics, site 8.

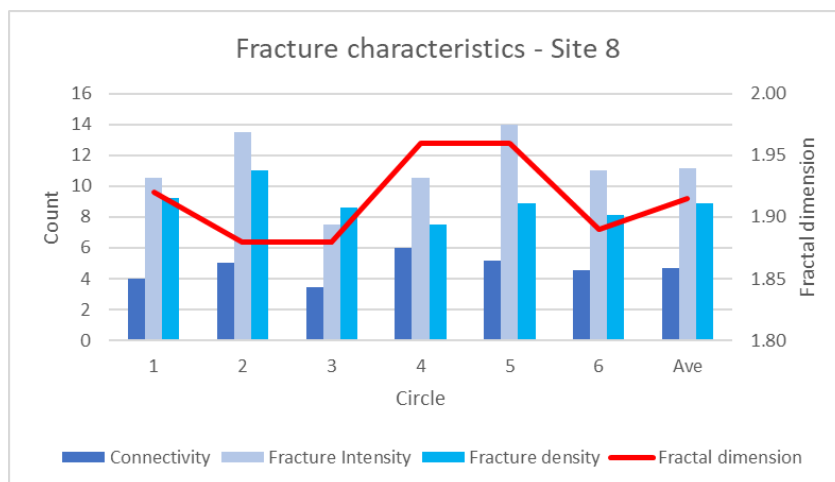


Figure 4.206: Fracture characteristics, site 8.

4.4.9 Site 9

Site 9 is the northern-most of this cluster of three sites (7, 8, and 9) and hence furthest up the valley (Figure 4.207). It was attempted to travel further up the valley, but within 200 m, the road became impassable.



Figure 4.207: View southwards down the valley from site 9 towards site 8 and site 7.

Due to gravel and bush-cover, there is limited exposure of the thrust on the road at site 9. It is however clearly visible to the east of the road. On the western side of the road, the steeply dipping beds can be seen, but it is difficult to determine the position of the thrust (Figure 4.208) and access was not possible due to a deep river valley.

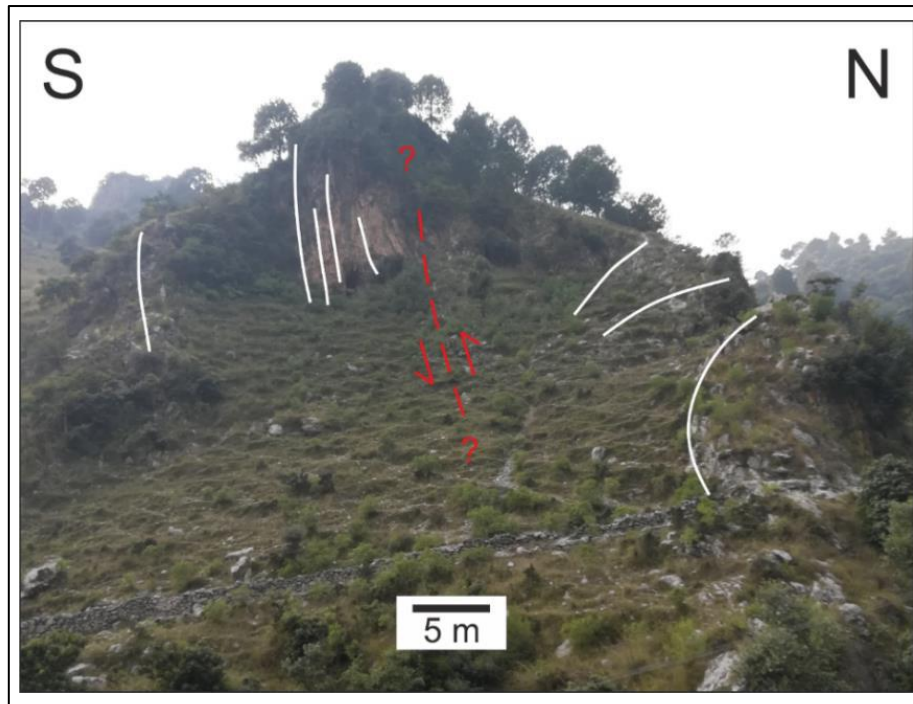


Figure 4.208: View westward at site 9. An estimate position of the thrust is shown by the dashed red line.

The view of the thrust to the east is much clearer. As it is possible to determine the change in dip of individual beds, the position and shape of the thrust could be defined (Figure 4.209). Loose boulders and extensive vegetation prevented access to the outcrop. Fortunately, several exposures of the thrust were present closer to the road.

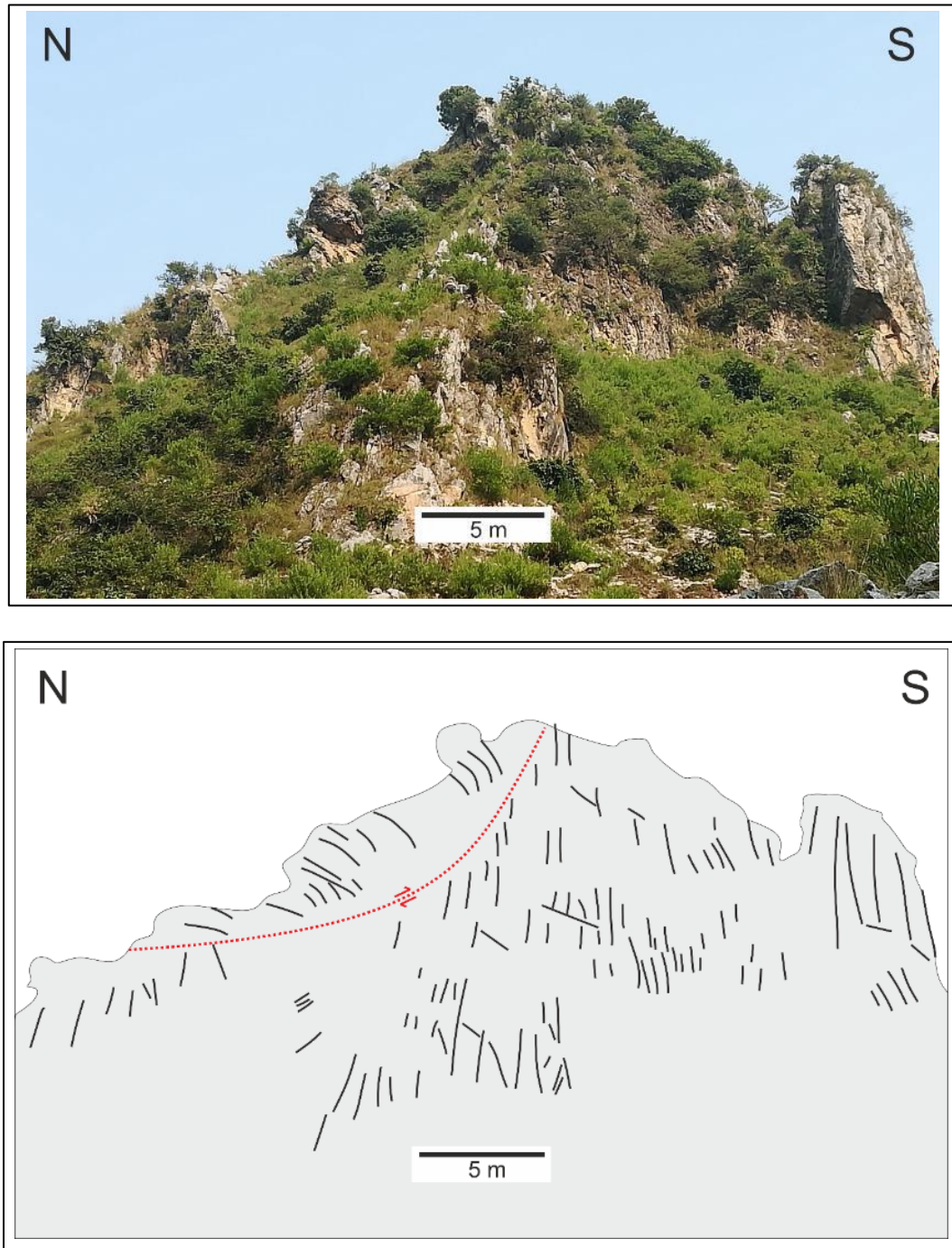


Figure 4.209: Photograph and sketch of thrust at site 9. View eastward.

The Margalla Hills Formation limestone has been sheared into decimetre wide layers. On a larger scale, these bands appear to have been weathered smooth, with only centimetre thick layers of fragmented and more deeply weathered rock separating these smooth layers (Figure 4.210). When exposures of the limestone were examined in more detail, it is apparent that there are several types of fractures (Figure 4.211).

These fractures include:

- Unmineralised, straight, approximately east-west striking
- Calcite filled, showing northwards displacement with smaller calcite fractures (same direction as bedding)
- Flat dipping, fractures coated with sheared calcite gouge.

Measurement circles were drawn on horizontal exposures on the road surface (Figure 4.212). As the number of nodes in the two circles is very similar (157 and 150, with an average of 154), the topological characteristics of the fractures in the circles are also similar. The mean trace length is longer in circle 2. The number of lines, tips, and branches is only just greater in circle 2, with values higher by 2, 4, and 5 respectively (Figure 4.214). Even though there are more lines, tips, and branches in circle 2, the fracture intensity is significantly lower (Figure 4.215). The fractal dimensions are 1.96 (circle 1) and 1.97 (circle 2).

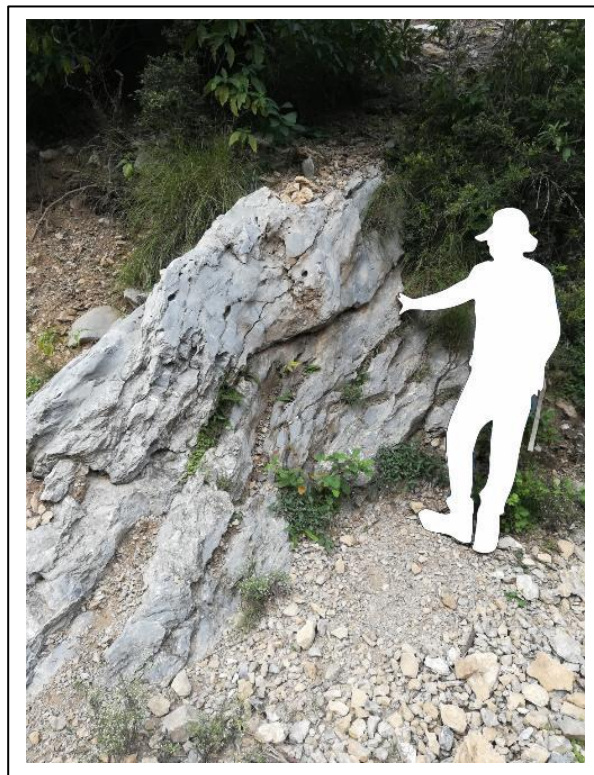


Figure 4.210: Eastern side of road with an exposure of the Margalla Hills Formation in the footwall of the thrust. Geologist in white.

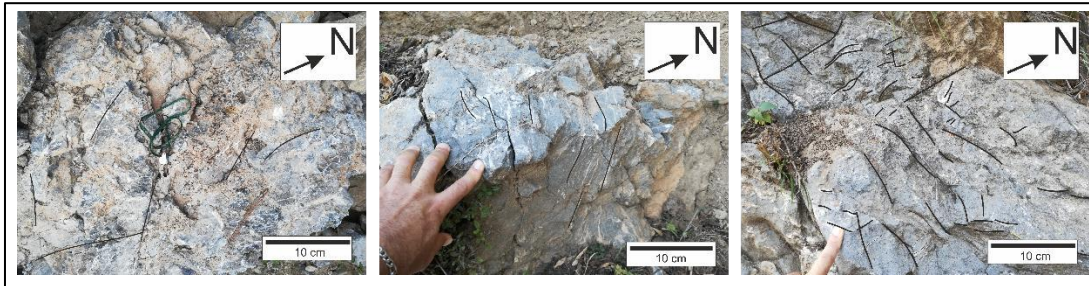


Figure 4.211: Exposures of fractures in the Margalla Hills Formation (footwall) of the thrust.

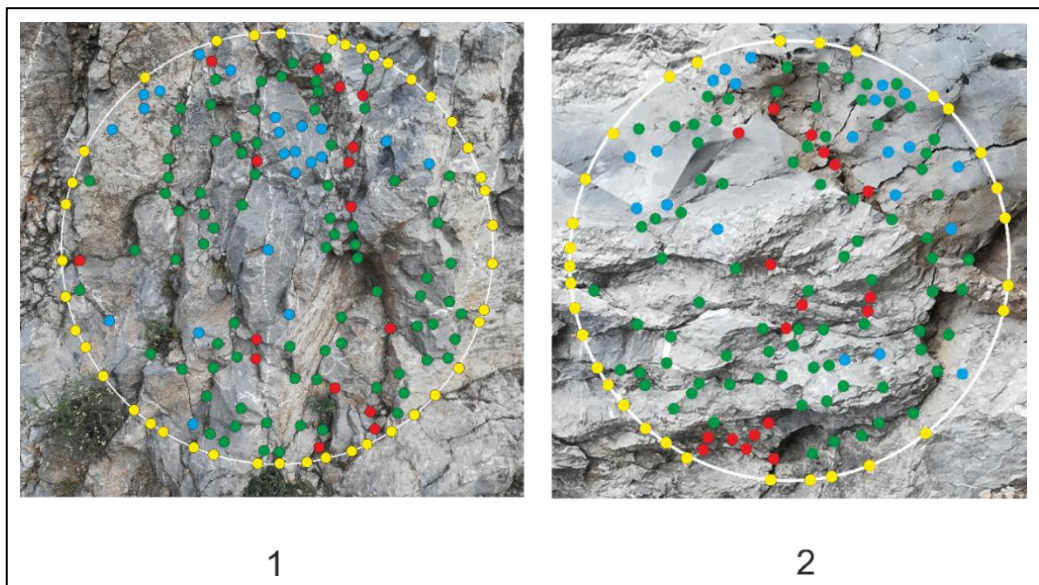


Figure 4.212: Measurement circles at site 9.

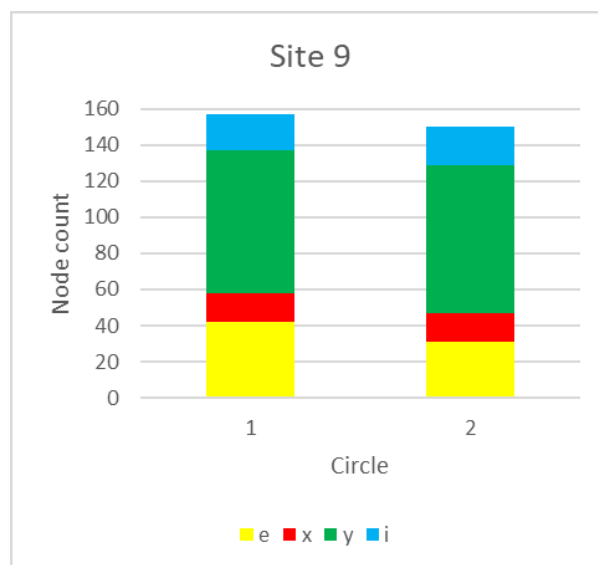


Figure 4.213: Node count, site 9.

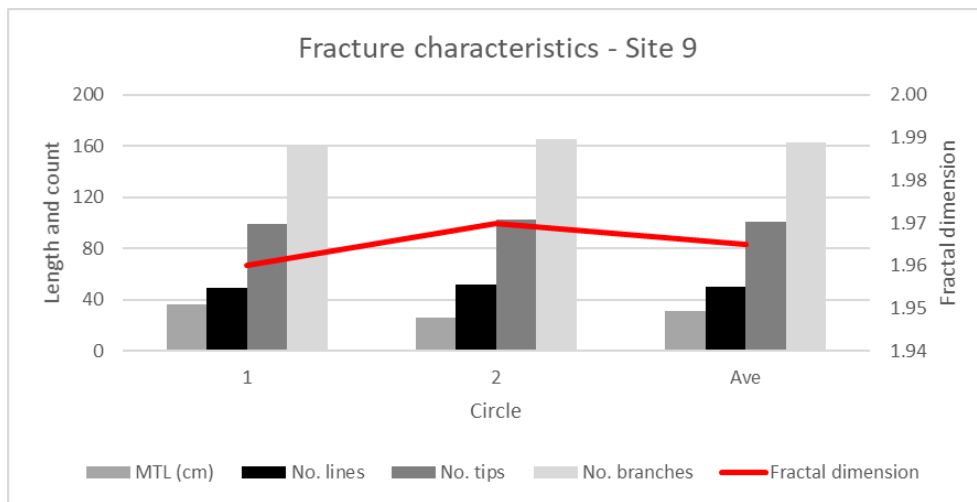


Figure 4.214: Fracture characteristics, site 9.

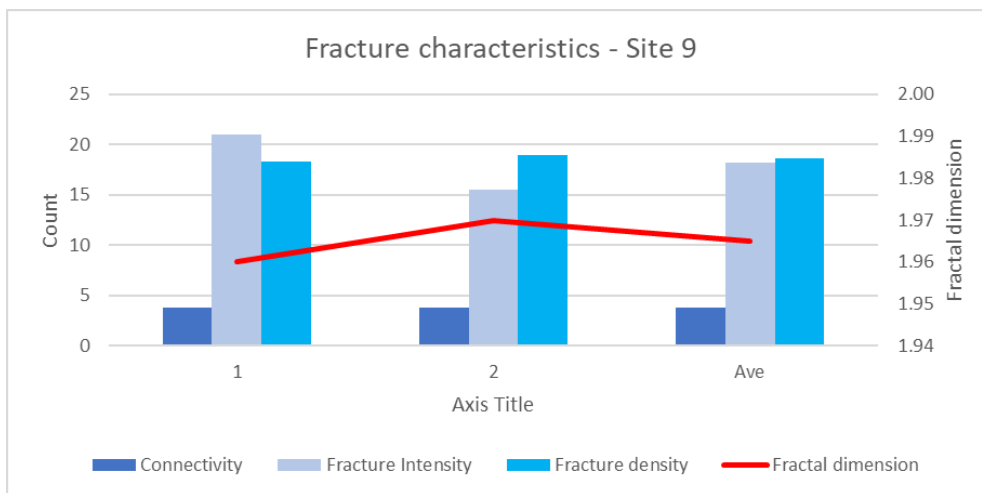


Figure 4.215: Fracture characteristics, site 9.

4.4.4.10 Summary

The average number of nodes at each site was evaluated in a north-south direction (see Figure 4.216 for location of sites).

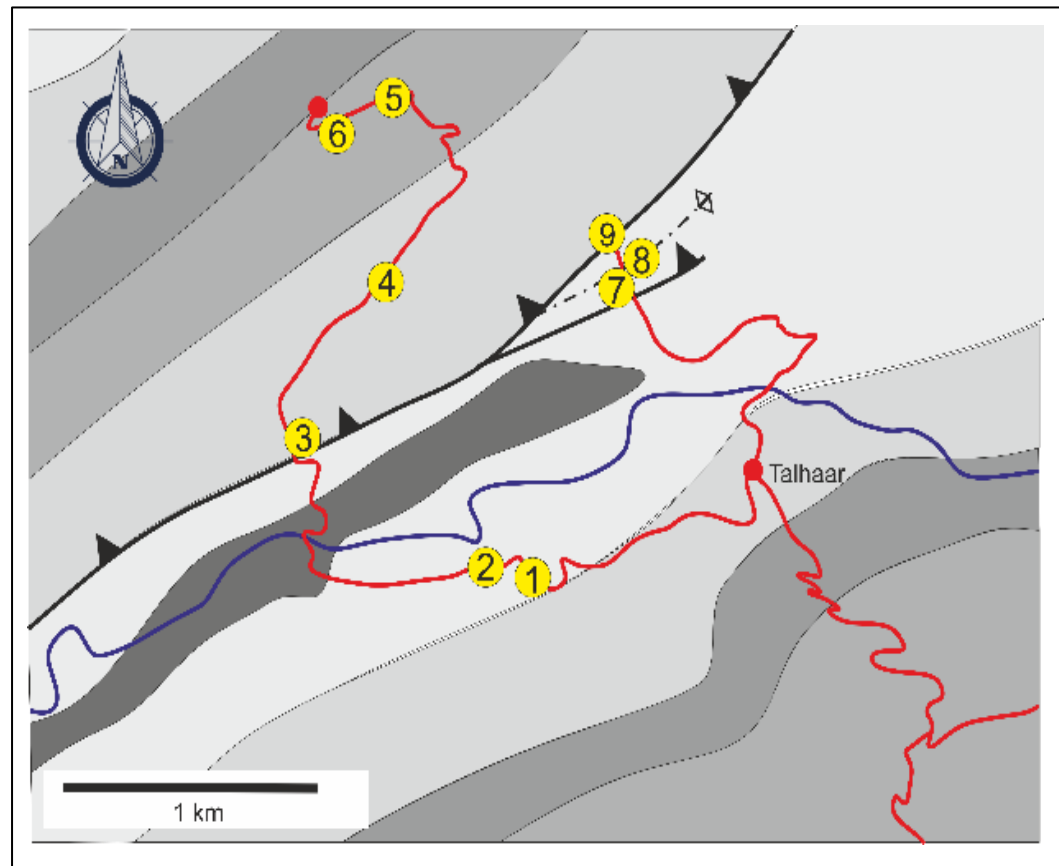


Figure 4.216: Sketch-map of location of measurement sites. Geology of the region is shown in Figure 4.140.

The number of nodes is dominated by the northernmost site, site 5 (Figure 4.217) with an average of 438 nodes (including the highest number of nodes in a circle, 629). The adjacent site 6 has the second-highest number of nodes, but the values of site 5 are removed from the stacked column plot of the different nodes at each site to allow these to be better resolved (Figure 4.218).

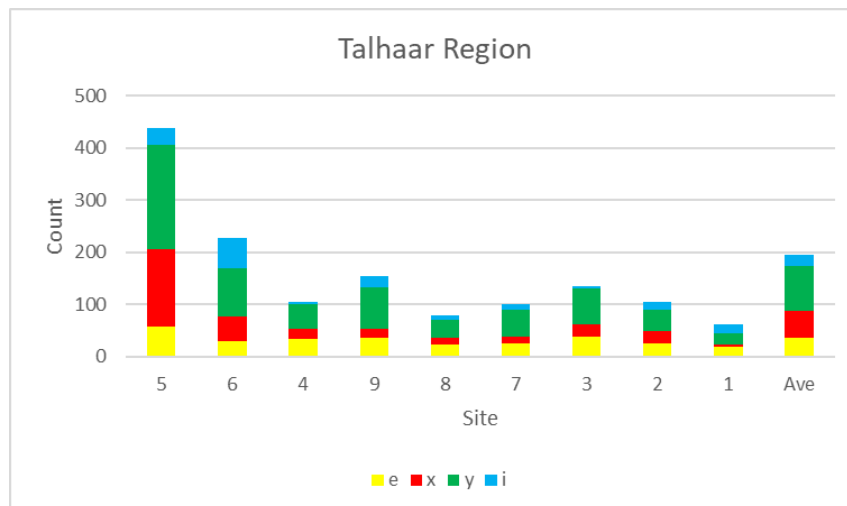


Figure 4.217: Node distribution across the measurement sites in the Talhaar region. Sites are arranged from north to south (see Figure 4.216).

In addition to the high number of nodes in the northern portion of the Talhaar region, there is a peak in the number of nodes at site 9 and site 3, located on the thrust plane (Figure 4.218). Sites 7 and 8 are also on this thrust structure but each have a low total number of nodes. This may indicate that the stresses along the thrust and hence the fractures (as quantified by the number of nodes) has been sub-divided at sites 7 and 8 to form the smaller thrust and anticline developed at these sites.

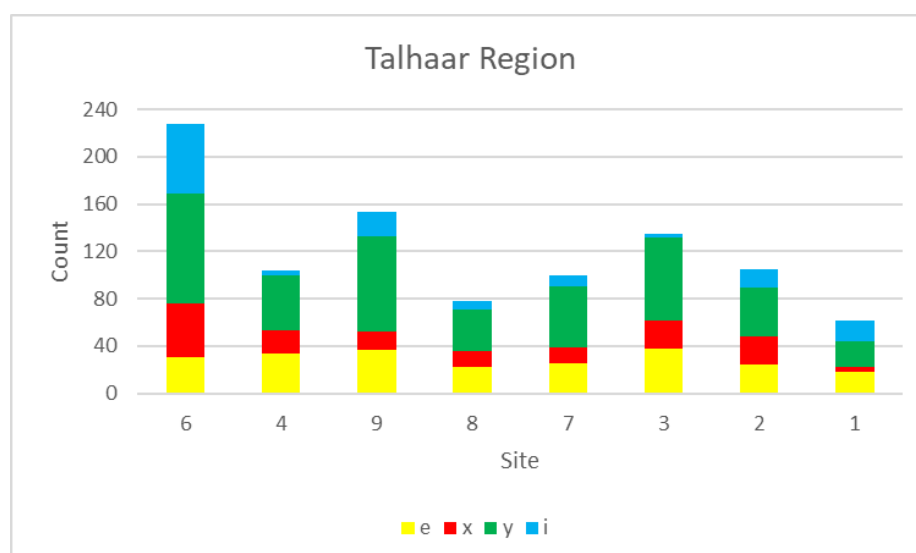


Figure 4.218: Node distribution across the Talhaar region. The northern-most site, site 5, is not shown in this plot as it has twice as many nodes and hence obscures the differences between the other sites.

The lowest fractal dimension (1.87) is located at site 1 (Figure 4.219). This low value is likely due to the relatively smooth bedding surface that was measured at this site. Site 5 has the highest fractal dimension (1.99) due to the high intensity of small-scale calcite fractures across the mapping circles. Sites 3 and 4 have the next highest fractal dimension. Site 3 is located on a thrust which accounts for the high fractal dimension, but site 4 is not near any major structures and is in the Kawagrah Formation which consists of marls and shales. The number of lines and tips decrease gradually towards the south, apart from site 4, which is significantly lower than the neighbouring sites.

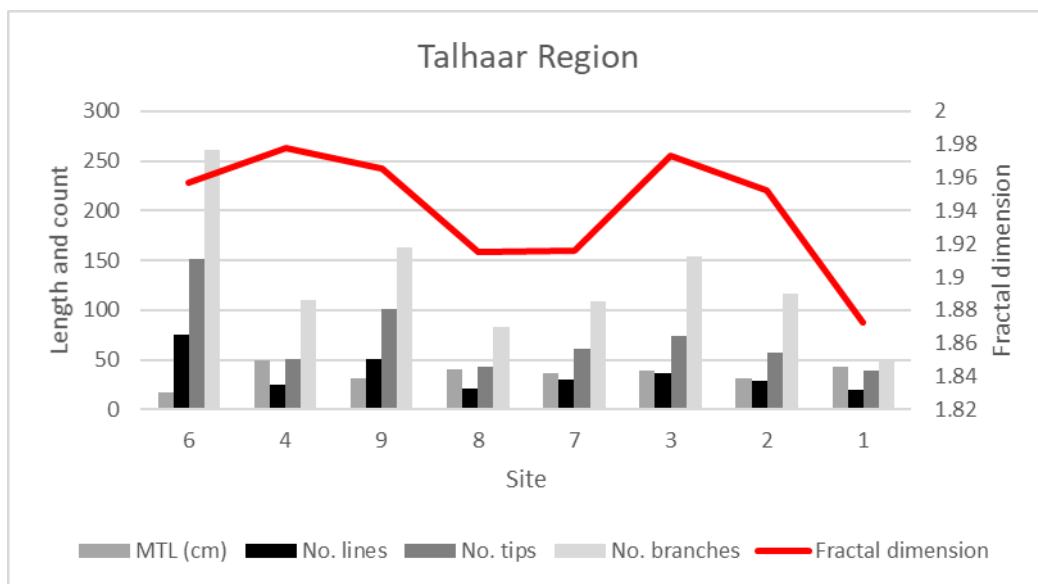


Figure 4.219: Fracture characteristics across the measurement sites in the Talhaar region.

Fracture density decreases gently towards the south. As with the other node counts and resultant topological characteristics, apart from the very high values at sites 5 and 6 in the north, there are also increases in fracture density at the two sites located on the thrust, namely sites 9 and 3 (Figure 4.220). The connectivity is highest at site 5, followed unusually by site 4 and site 3.

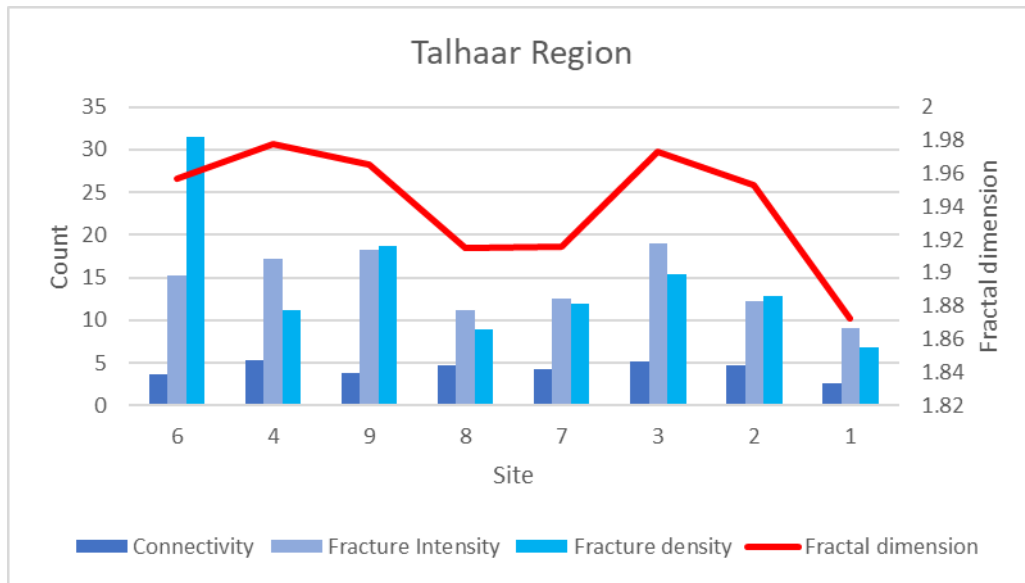


Figure 4.220: Fracture characteristics across the measurement sites in the Talhaar region.

With the large number of nodes and high fractal dimension at site 5 and the low fractal dimension at site 1, a power-curve can be fitted to a plot of the average number of nodes vs. the fractal dimension of each site (Figure 4.221). The different sites are better characterised than simply placing them on this curve.

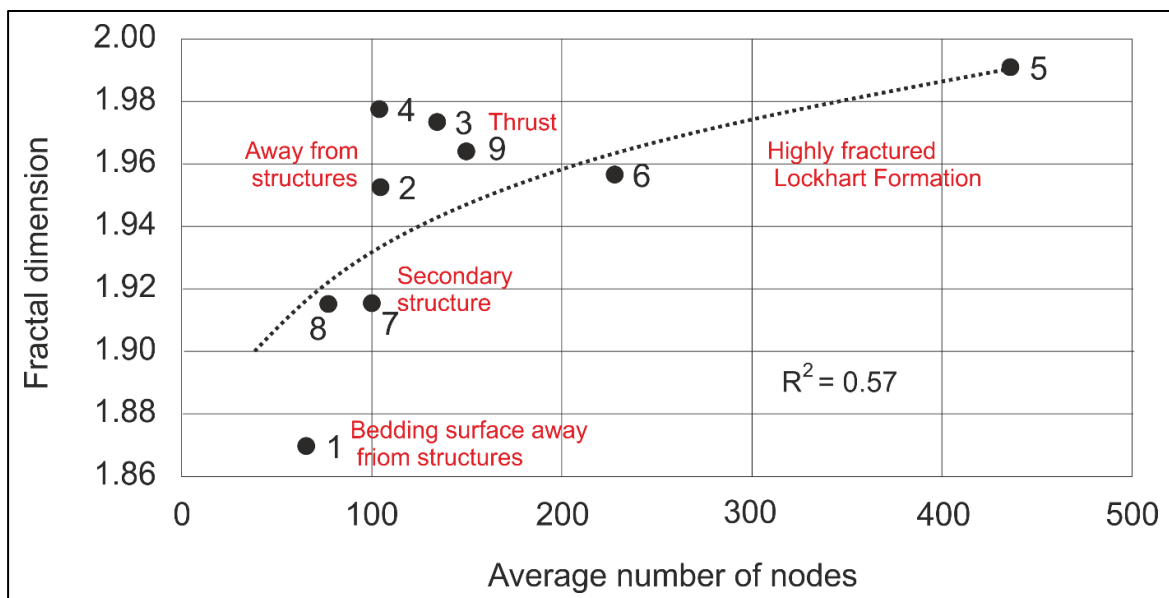


Figure 4.221: Total number of nodes vs. fractal dimension at all the circles at each site

Site 1 is located on its own with a low number of nodes and a low fractal dimension as it is located on the overturned contact between the Margalla Hills Formation limestone and the Nammal Formation shales. This low cohesion contact absorbed most of the stresses, reducing the development of fractures. Sites 7 and 8 contain extensive amounts of bedding parallel fractures. Although these fractures are long, they do not interlock to form a fracture network.

The lower fractal dimension and number of nodes is unusual for this site as mapping of the fold and thrust structures indicated that there is significant movement (both as folding and thrusting). In contrast to these two sites, the other two measurement sites on the thrust, sites 3 and 9 have the higher fractal dimensions and number of nodes expected of a thrust. The points plot close to each other confirming that they are the same forethrust (Figure 4.221). Although site 4 is away from major structures it has a higher fractal dimension, but the number of nodes is low. This indicates a densely fractured rock mass with limited intersections ("x" and "y" nodes) of these fractures such as what may form in the shales of the Kawagrah Formation at site 4.

The highly fractured Lockhart Formation at sites 5 is different to the other sites due to the high number of nodes and a fractal dimension of 1.99, which indicates that the measurement circle can essentially be considered as a plane (that is a fractal dimension of 2.00).

This is due to the closely spaced fractures of several generations, both tensile and later shear fractures. These may have formed on an anticline axis along the top of the mountain. No evidence of this structure was found, apart from the flattening of the dip on the limited exposure outside the house at the end of the road (Figure 4.140). The relationship between the nodes and fractal dimensions of all 38 circles measured in the Talhaar region was examined to determine if trends or clusters in the circle characteristics could be defined (Figure 4.222 and Figure 4.223).

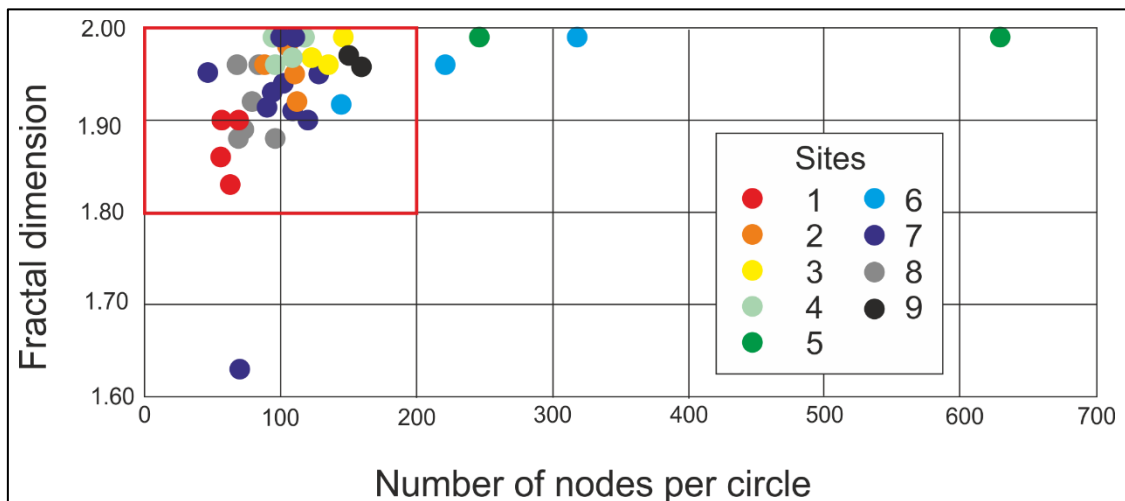


Figure 4.222: Total number of nodes vs. fractal dimension for all the circles at each site. The red rectangle outlines the subset of data shown in Figure 4.223.

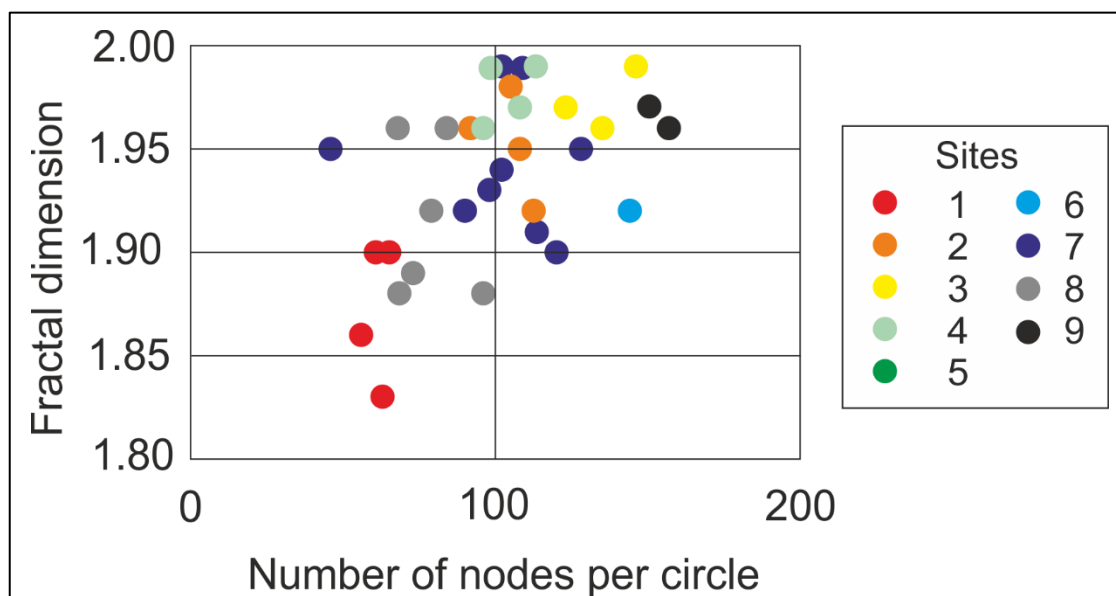


Figure 4.223: Zoomed in view of a subset of the nodes vs. fractal dimensions for the circles in the Talhaar region. The red rectangle in Figure 4.222 shows the location of this subset.

Due to the considerable variability of the number of nodes and fractal dimensions of the different circles at each site, this was not possible. This is in contrast to the evaluation of the average values of the number of nodes and fractal dimension at each site (Figure 4.221). Thus, even though the larger amount of data ensures greater confidence in the assumptions, the fact that it is “noisy” makes it unrealistic to consider the number of nodes and fractal characteristics of each circle individually. Because of the variability, individual circles of different sites could be compared, and incorrect assumptions made.

4.2.5. Shah Dara region

The Shah Dara region is located at the intersection of the Shah Dara Road to Islamabad with a minor gravel road from the east ($33^{\circ} 46.7$ N, $73^{\circ} 10.1$ E), approximately 18 km northeast of central Islamabad. Four sites were mapped (Table 4.13) between two ranges of hills between 300 and 400 m above the valley floor running parallel to the northeast-southwest strike of the strata (Figure 4.224). The north-south oriented valley through which both the Shah Dara Road and a river run, is orthogonal to the strike of the strata and is related to later faulting. Many valleys in this orientation are present immediately north of Islamabad, parallel to the strike-slip Jhelum Fault to the east, although larger-scale geological maps do not show fault traces or displacement of strata. A wonderful picnic site is situated in the river in the valley close to the mapping sites (Figure 4.225).

Table 4.13: Location of mapping sites and other points of interest.

Site	Latitude (N)	Longitude (E)	Formation	Age	Structure
1	33.778°	73.169°	Nammal	Early Eocene	Fore-thrust
2	33.779°	73.171°	Nammal	Early Eocene	Fore-thrust anticline
3	33.776°	73.170°	Nammal	Early Eocene	Syncline
4	33.775°	73.173°	Chorgali	Early Eocene	Anticline & small thrusts
Picnic site	33.777°	73.171°	River gravel	Recent	

The rocks in this region are the youngest that have been evaluated in this study, all being Early Eocene strata of Ypresian (Ilerdian) age (Swati *et al.*, 2013). The oldest of these, the Nammal Formation, consists predominantly of light grey coloured limestone, with olive green to grey siltstone and light grey marl layers present towards the base. It is interpreted as a transgressive system tract (Gill, 2020) consisting of shallow water limestone interbedded with near-shore marine to lagoonal silts. It has a transitional contact from the underlying Patala Formation. The upper contact is also transitional with the Margalla Hill (equivalent to the Sakesar) Formation (Farid *et al.*, 2018).

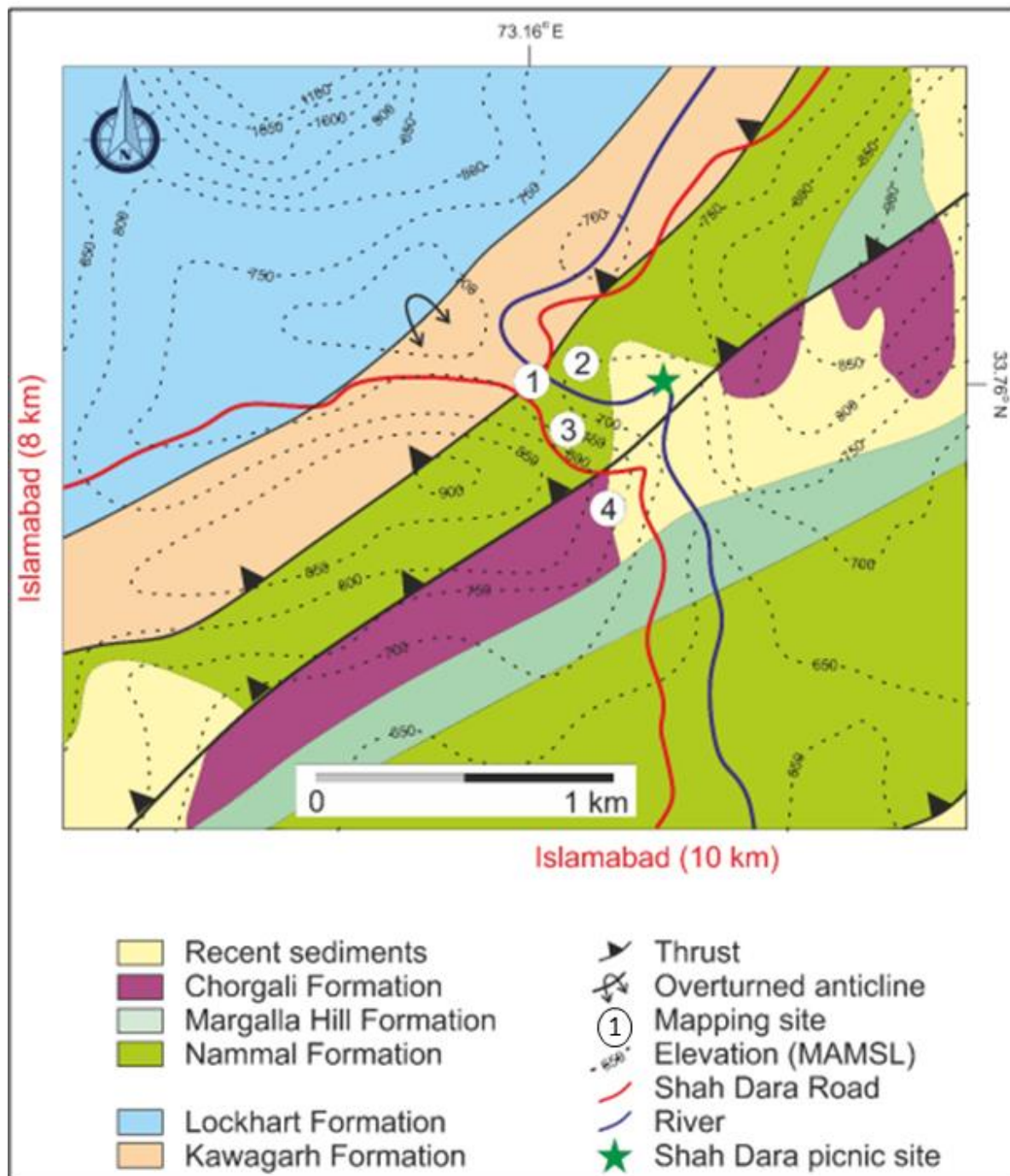


Figure 4.224: Geological map of the Shah Dara site. Table 4.13 lists the co-ordinates of the sites.

The Margalla Hill Formation is thrust out in this area. The overlying Chorgali Formation consists mainly of thin to thick bedded fossiliferous nodular limestone with abundant carbonaceous marl and shale at the base (Swati *et al.*, 2014). This formation is interpreted to have been deposited in an inner shelf lagoon to middle shelf subtidal environments during a falling stand systems tract (Gill, 2020).



Figure 4.225: Shah Dara picnic site. The author cooling off after a hot day's fieldwork.

4.2.5.1 Site 1

Site 1 is situated on the hanging-wall of the northern flank of a near-vertical anticline. The light grey limestone of the Nammal Formation is fractured into blocks approximately 20 cm by 10 cm (Figure 4.226). The fractures on the longer side are parallel to the dip of the bedding and the shorter fractures do not generally cross the bedding. Occasional calcite veins are present, less than 0.2 cm wide (Figure 4.226, circle 4). All other fractures are open (between 0.5 and 1 cm wide) and often contain fragments of sheared limestone or clay.

Due to the relatively large size of the rock fragments (20 cm by 10 cm), there are fewer nodes at this site than any of the others in the area. Unsurprisingly, “y” nodes are the most common (Figure 4.227), as they are formed at the intersection of the shorter fractures within and perpendicular to the beds and the longer, bedding-parallel fractures. This lower fracture density has also resulted in the lowest average fractal dimension of the area (1.91). As the measurement circles at site 1 are in a geologically uniform area, the standard deviations are typically within 10% of the mean value.

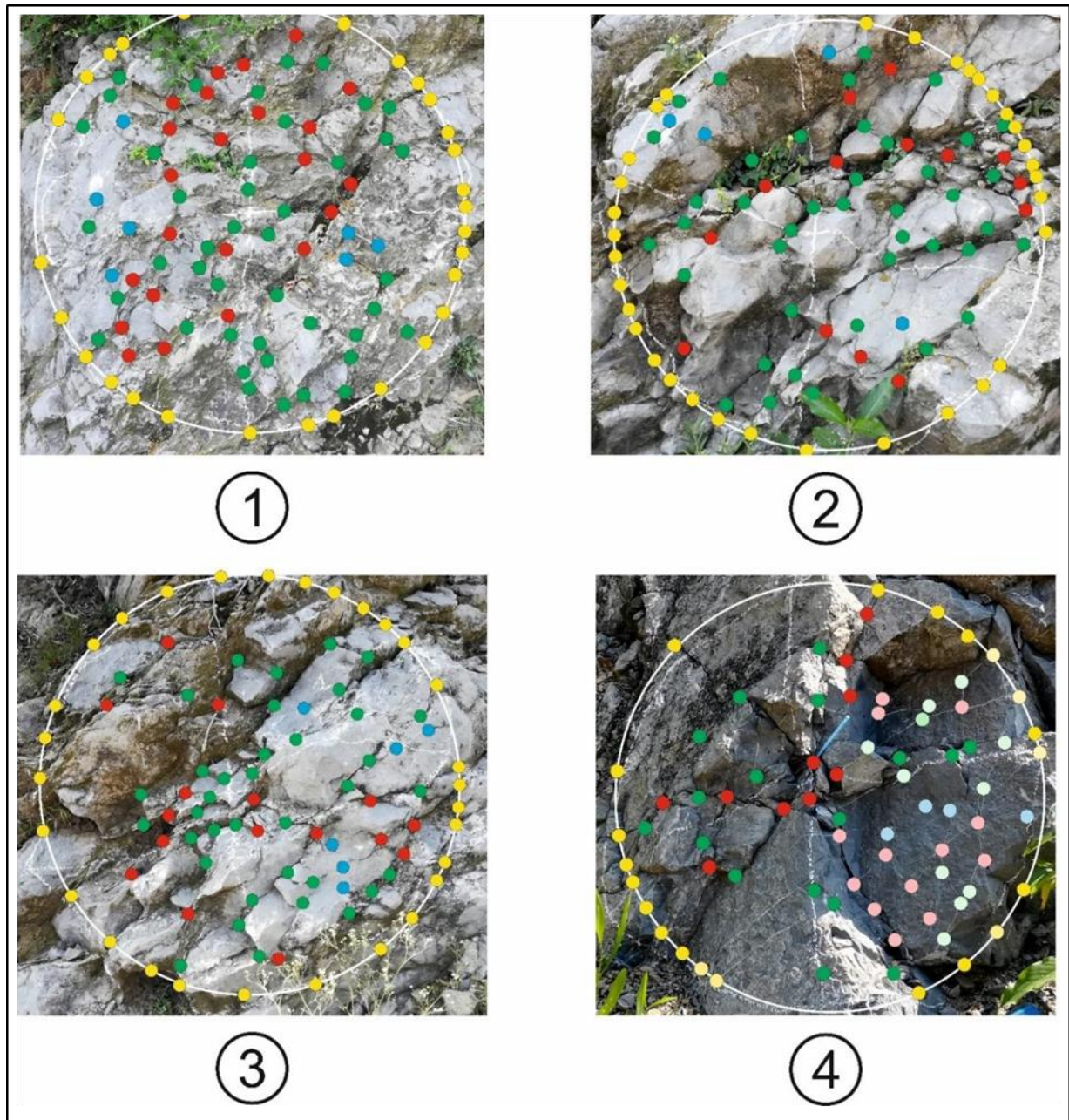


Figure 4.226: Mapping circles at site 1 (see Figure 4.224 for location).

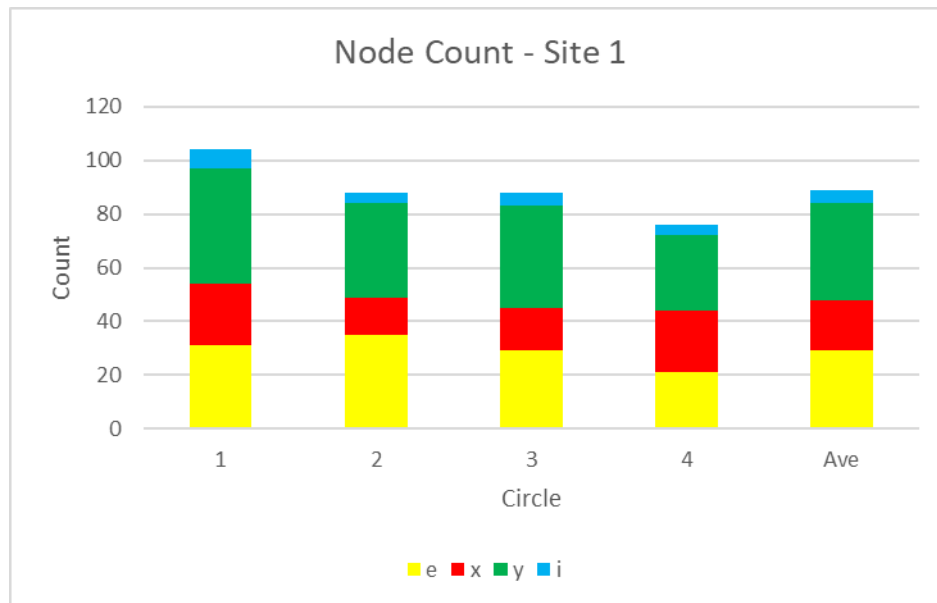


Figure 4.227: Number of nodes at site 1.

Due to the fact that the fractal dimension does not vary significantly between the circles at site 1 ($SD = 0.02$), relationships between the topology and fractal dimension could not be discerned for this site (Figure 4.228). When compared with other measurement sites in the area, it becomes evident that site 1 has the longest mean trace length and the fewest lines tips, branches. The connectivity is high as a result of the long mean trace length, but the fracture intensity and density are low (Figure 4.229). This matches with the physical characteristics of the site, that is, long bedding-parallel fractures.

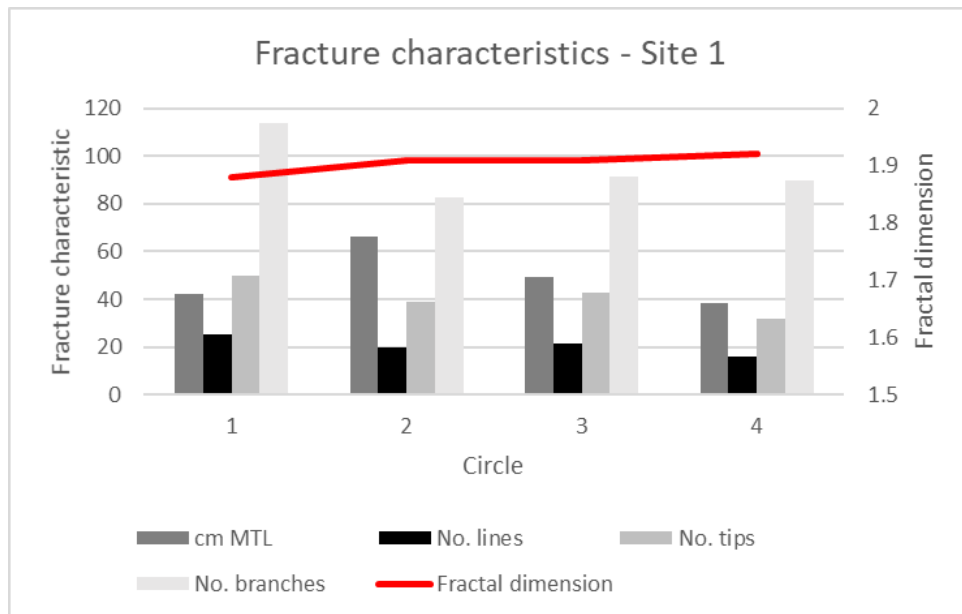


Figure 4.228: Mean trace length, number of lines, tips and branches and fractal dimension at site 1.

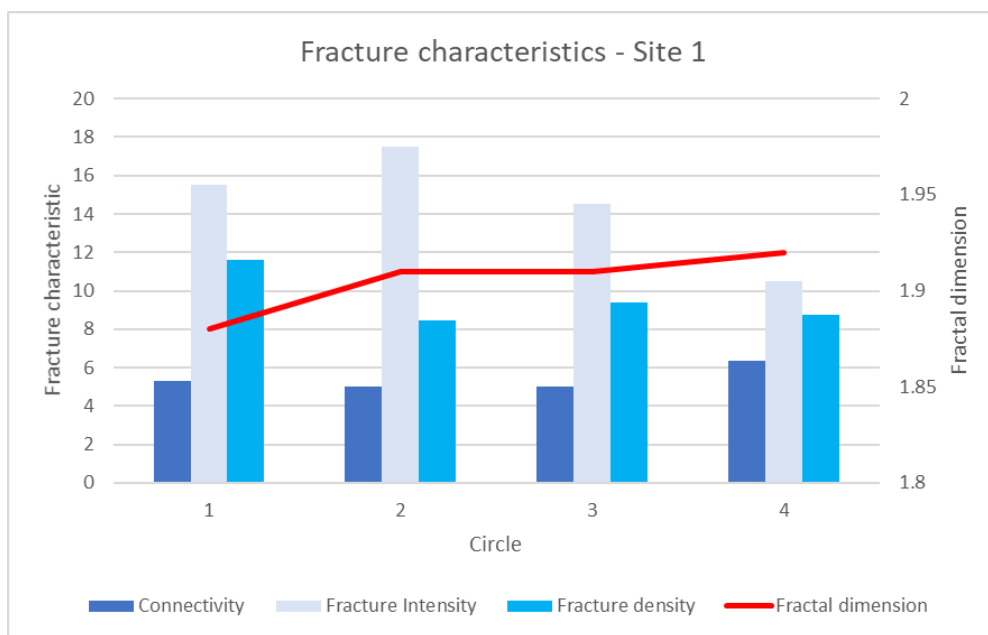


Figure 4.229: Connectivity, fracture intensity and density and fractal dimension at site 1.

4.2.5.2 Site 2

Site 2 is situated on a spectacular foot wall anticline (Figure 4.230). Unfortunately, it was not possible to access the thrust plane itself as the cliff was too steep and covered in dense vegetation. Field observations show that is a near-vertical, overturned thrust fault where the overturned Kawagarh Formation has been pushed over the Nammal Formation. As the Kawagarh Formation consists

predominantly of interbedded shale and wackestones, it has weathered to form a wide, flat valley bounded by the overturned Lockhart Formation approximately 1 km to the north.

The thrust and associated anticline at site 2 is part of a trailing imbricate fan formed from an overlapping array of fault propagation folds. The thrust is the older surface and has experienced greater displacement with its overlying fault propagation fold being eroded.

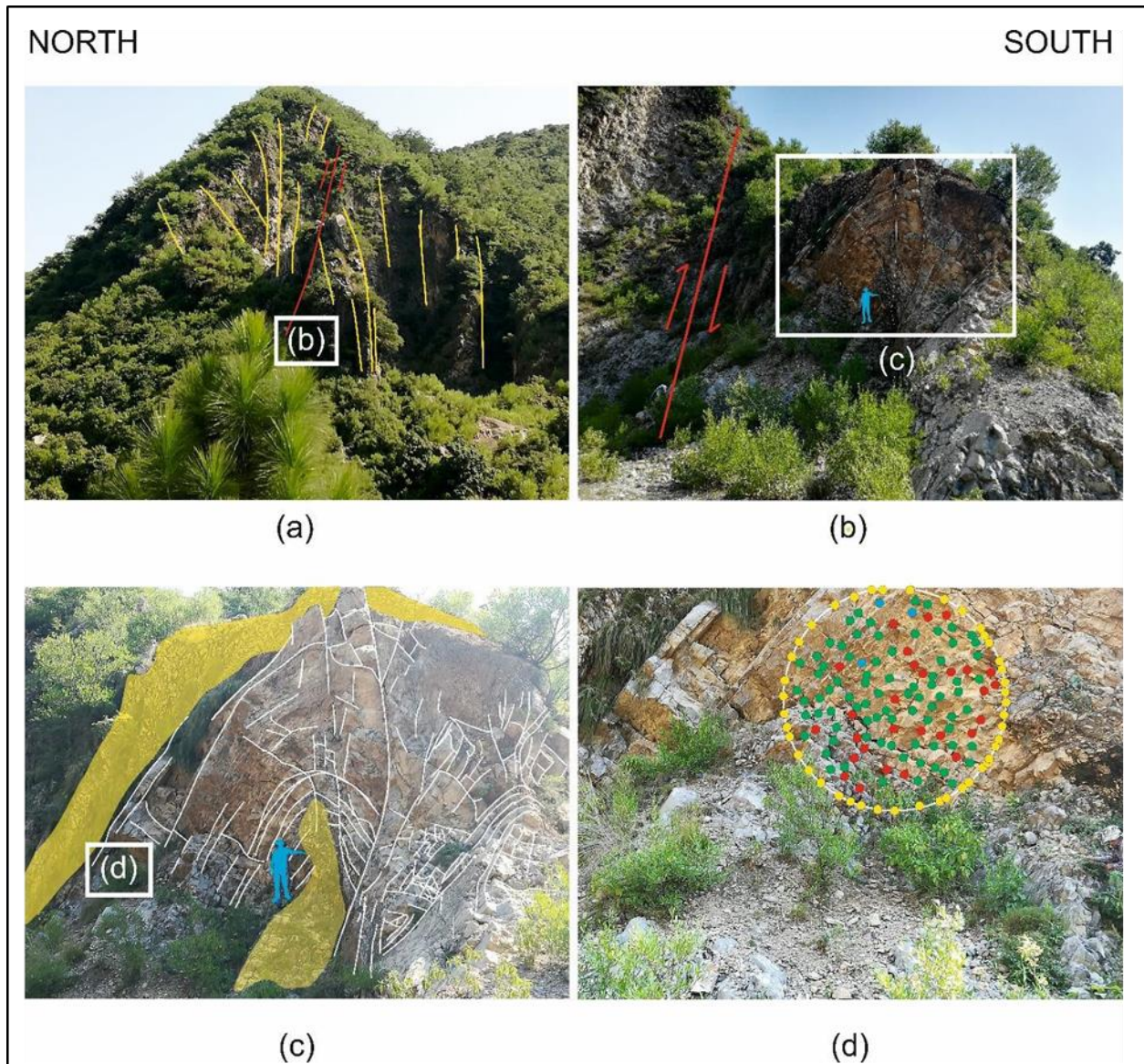


Figure 4.230: Photographs of site 2. Each successive image is a zoomed in view of the previous one, with the location of the zoomed in image shown by a white square.(d) indicates a 1 m measurement circle Geologist in blue.

Re-looking at Figure 4.230 (c) in detail, the exposed thrust and two thrust-tip fold anticlines with associated radial fractures can be seen (Figure 4.231). The order of initiation of structural deformations is:

- Thrusting
- Folding of bedding (New Thrust 1)
- Faulting (New Thrust 1)
- Re-folding of bedding (New Thrust 2)
- Re-faulting (New Thrust 2)

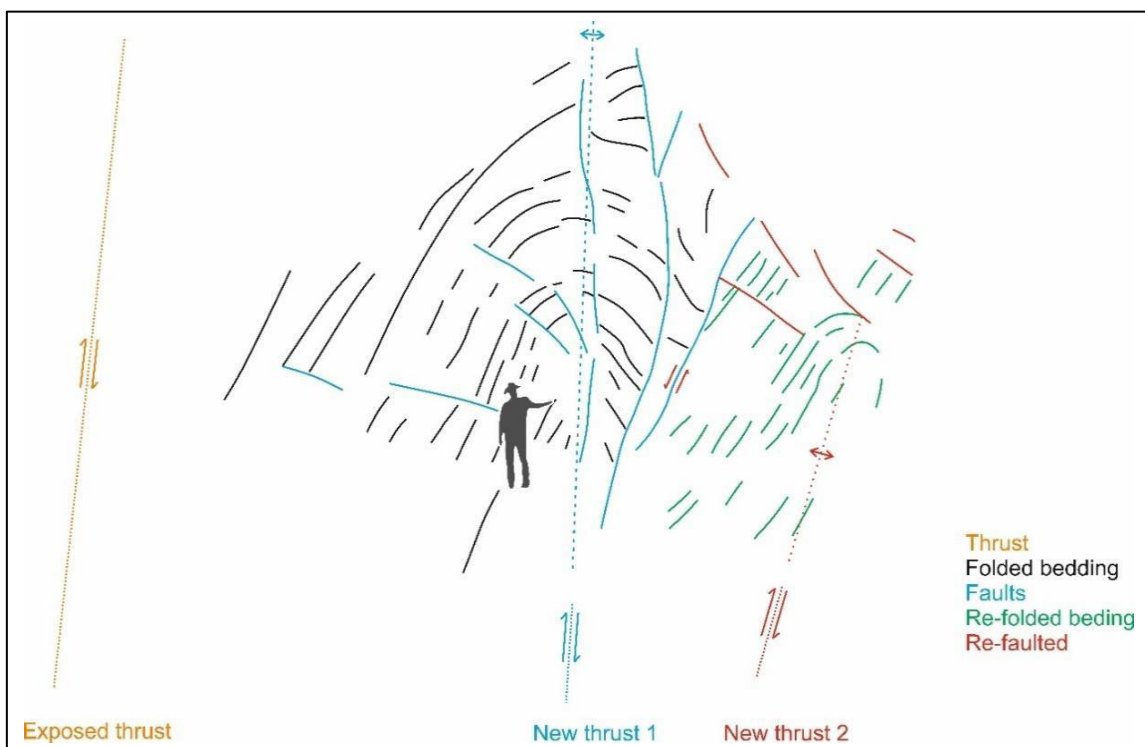


Figure 4.231: Line drawing of the thrusts and folds at site 2- compare with Figure 4.230 (c). The structural deformation occurred in this order:

- 1) Development of initial exposed thrust
- 2) Development of new thrust 1 with associated faulting and folding of the strata into an anticline
- 3) Development of new thrust 3 with associated re-faulting and re-folding of the strata into another anticline
- 4) is listed on the left-hand side. The different phases of deformation continue to develop at the same

time with it being possible for the oldest thrust and faulting associated with the youngest thrust occurring at the same time. Geologist in black.

Folding develops first above the thrust tip and then fold-axis parallel fractures radiate out from the thrust tip for both of the new thrusts. Although the area is covered in gravel, the orientation of the fractures of New Thrust 1 suggests that the thrust tip is just below the geologist in the photograph. The more widely radiating faults of New Thrust 2 suggest that the thrust tip is deeper.

The large cross-cutting faults form structural boundaries and allow the movement of significant amounts of fluid but are not characteristic of the majority of the rock mass. As such, a measurement circle was placed on the anticline limb to allow the characterisation of the folded rock away from the large faults. The fracture intersection nodes are dominated by “y” nodes with more of these than all other node types combined (Figure 4.232). This node distribution has resulted in the measurement circle having a high number of branches and low trace length compared to the other measurement circles in the Shah Dara region (Figure 4.233). Although there are many “y” intersections, suggesting a good connectivity between fractures of different orientations, because these do not cross-cut the connectivity is the lowest in the region (Figure 4.234).

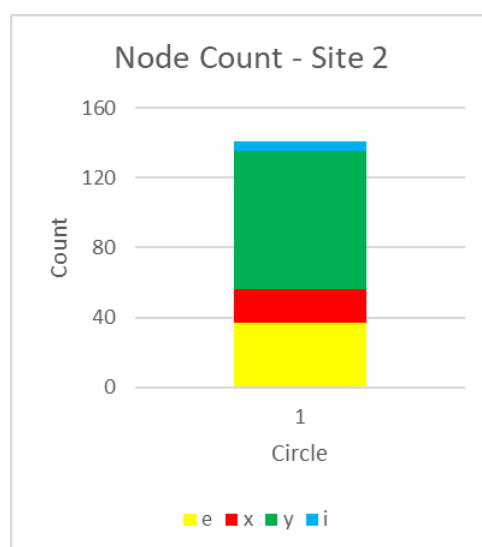


Figure 4.232: Number of nodes at site 2.

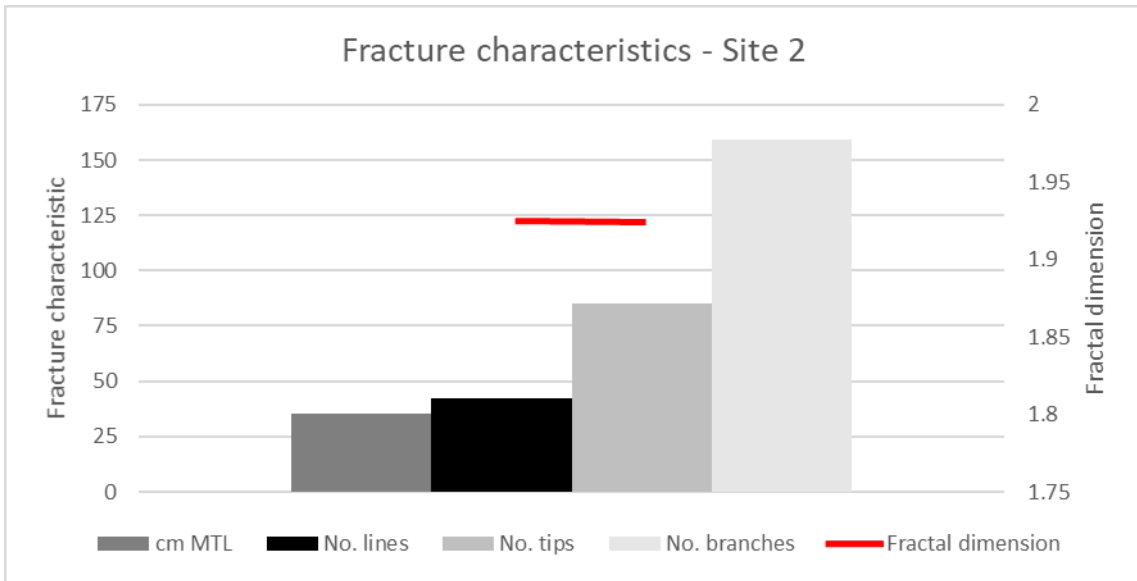


Figure 4.233: Mean trace length, number of lines, tips and branches and fractal dimension, site 2.

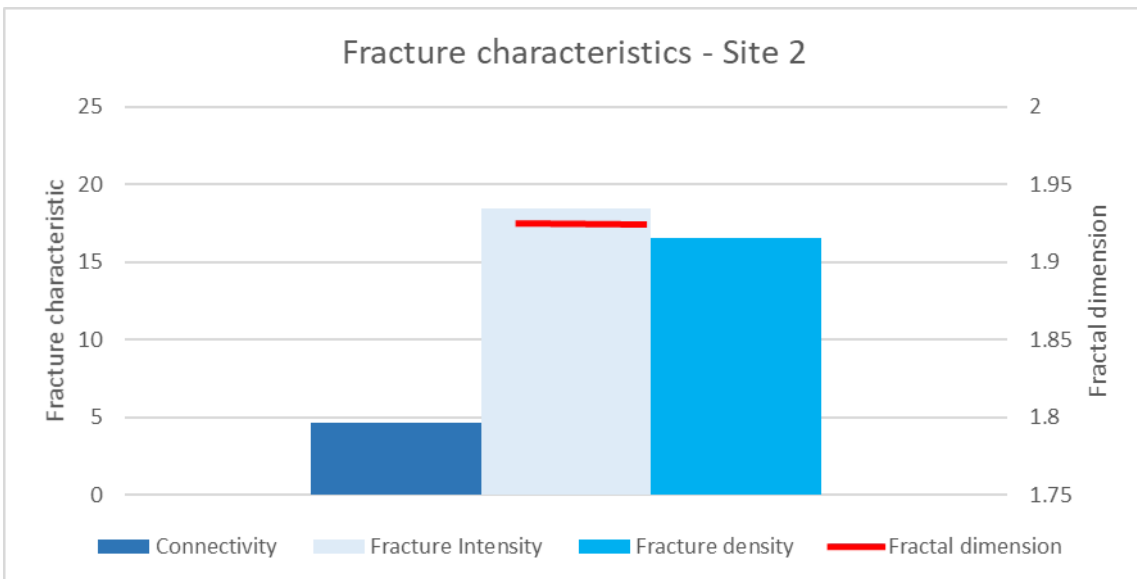


Figure 4.234: Connectivity, fracture intensity and density and fractal dimension at site 2.

4.2.5.3 Site 3

Although no large-scale structural features (such as the thrust at site 1 and the footwall anticlines at site 2), are present at site 3, the rock is still highly fractured. The site is positioned to the south of these features in the dark grey coloured limestones of the Nammal Formation (Figure 4.224). This fresh

exposure devoid of vegetation has allowed the effect of changing the diameter of the measurement circle to be tested (Figure 4.235).

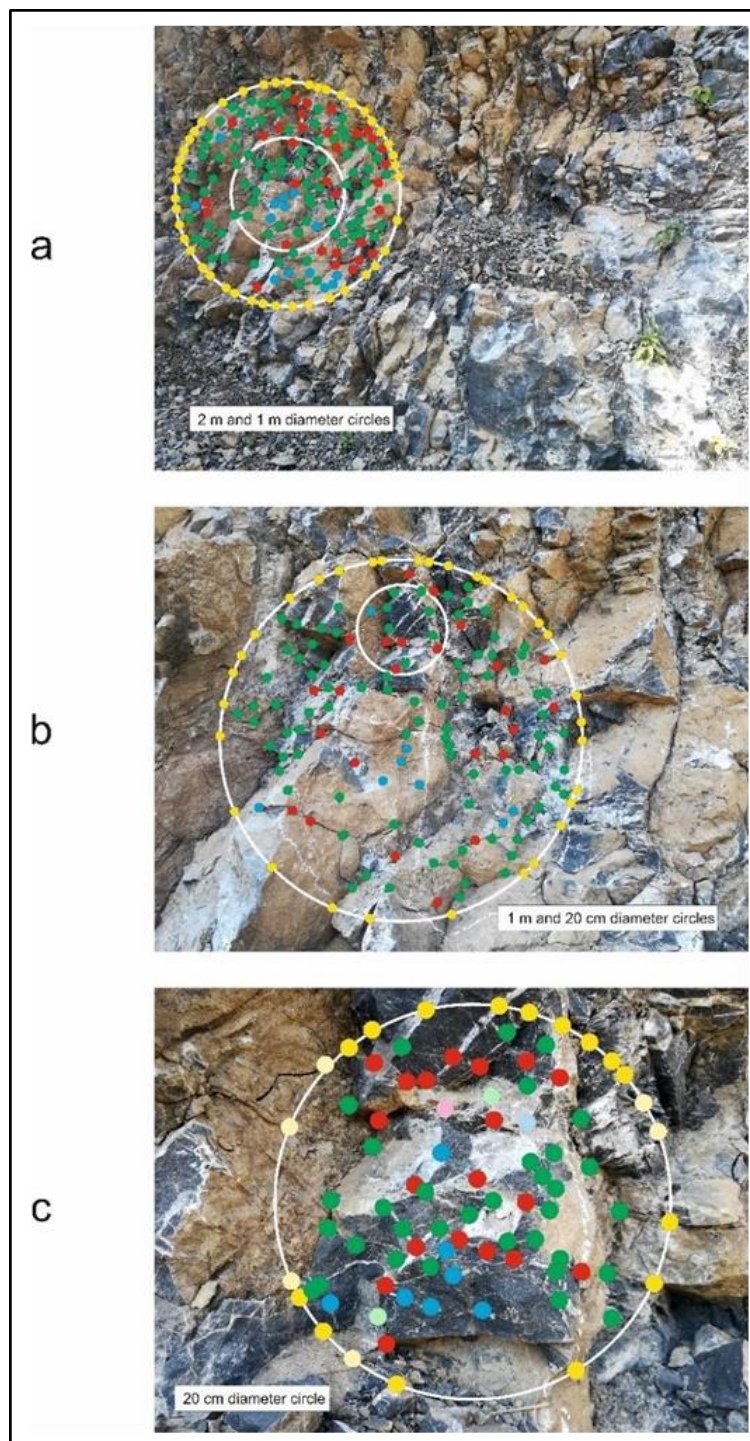


Figure 4.235: Measurement circles of different diameters on the same part of the outcrop at site 3. nodes measured in a 2 m circle with the position of the 1 m measurement circle within it shown, nodes measured in a 1 m circle with the position of the 20 cm circle measurement circle within it, nodes within the 20 cm measurement circle.

Measurement circles of decreasing diameters were placed within each other on the outcrop and the number of nodes within each of these was counted. Importantly, the smaller the circle became, the smaller the size of the fracture that was measured. This progressively higher resolution can be seen in Figure 4.235. A fractal relationship between the various circles and fractures (along with associated nodes) could therefore be expected.

However, the total number of nodes and the number of nodes of each of the circles was very similar (Figure 4.236). This suggests that, for at least this site and its associated fracture pattern, the size of the measurement circle does not affect the node count and hence the topological characteristics.

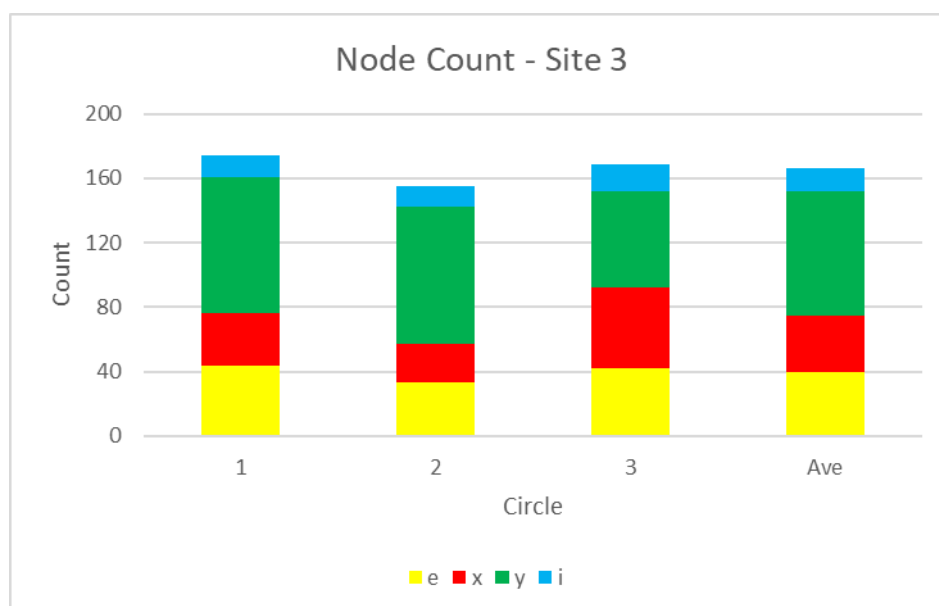


Figure 4.236: Number of nodes at site 3. Circle 1 is 2 m in diameter, circle 2 is 1 m in diameter and circle 3 is 20 cm in diameter, and the circles placed within each other.

None of the topological parameters show significant variation (Figure 4.237 and Figure 4.238). The maximum and minimum values for each are within 10% of the average. In contrast to this, the fractal dimension of the circles increased progressively from 1.61 to 1.94 to 2.00 for circles 1, 2 and 3, respectively. Fractal dimensions were calculated using the box-counting method with boxes of the same ratio being placed over the circles (Table 4.14). This variation in fractal dimension is expected as in a smaller diameter circle, there is greater likelihood of a box having a fracture, especially as the

resolution is higher. The consistency in the number of nodes and resultant topological characteristics shows that the connectivity is independent of the spatial distribution.

Table 4.14: Box-counting sizes for circles at site 3. All values are in metres.

Circle	Diameter	Box 1	Box 2	Box 3	Box 4
1	2	1	0.5	0.2	0.1
2	1	0.5	0.25	0.1	0.5
3	0.2	0.1	0.05	0.02	-

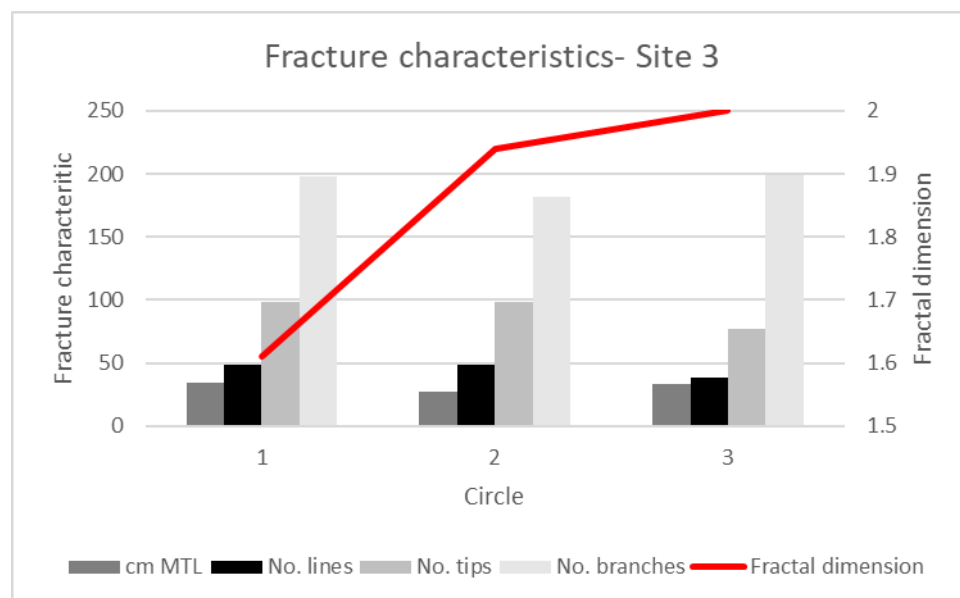


Figure 4.237: Mean trace length, number of lines, tips and branches and fractal dimension, site 3. Circle 1 is 2 m in diameter, circle 2 is 1 m in diameter and circle 3 is 20 cm in diameter, and the circles are placed within each other.

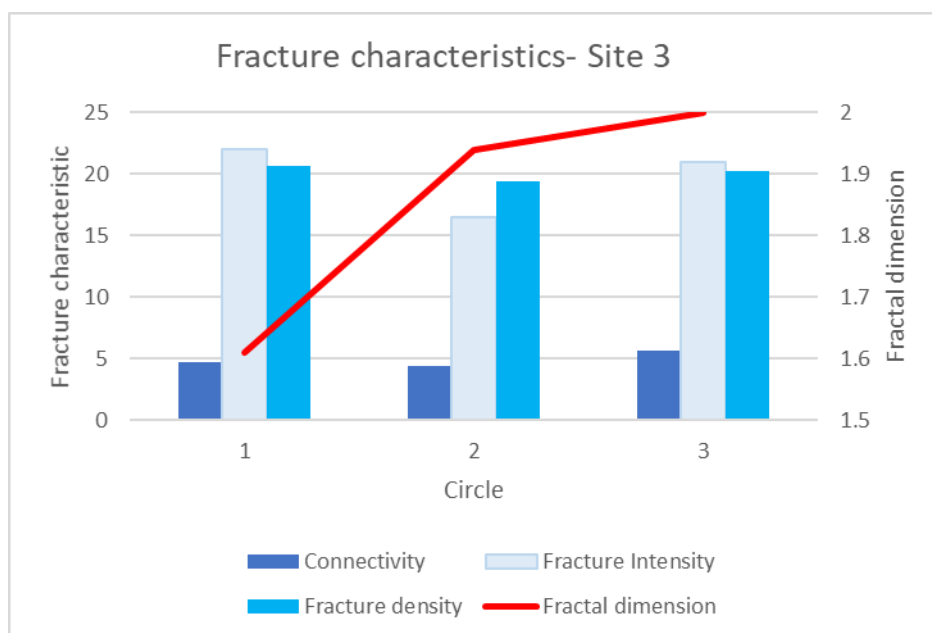


Figure 4.238: Connectivity, fracture intensity and density and fractal dimension at site 3. Circle 1 is 2 m in diameter, circle 2 is 1 m in diameter and circle 3 is 20 cm in diameter, and the circles are placed within each other.

4.2.5.4 Site 4

The Chorgali Formation is a thin- to thick-bedded, fossiliferous nodular limestone with abundant carbonaceous marl and shale at the base (Swati *et al.*, 2014) and is exposed at site 4 (Figure 4.239) which is located on an abandoned, older portion of the Shah Dara Road (Figure 4.224). The sequence of rock types is (from oldest to youngest) is:

1. Thinly-bedded, light grey coloured limestone,
2. Medium-bedded limestone with thin shale interbeds,
3. Grey-brown coloured shale with 20 cm long fragments of fractured limestone beds formed by the tectonism,
4. Thickly-bedded, yellow-brown coloured wackestone, and
5. Fine-grained, medium-bedded grey coloured shale.

The rocks are tightly folded and thrustured (Figure 4.240). The various lithological layers deform differently within these folds (Figure 4.241).

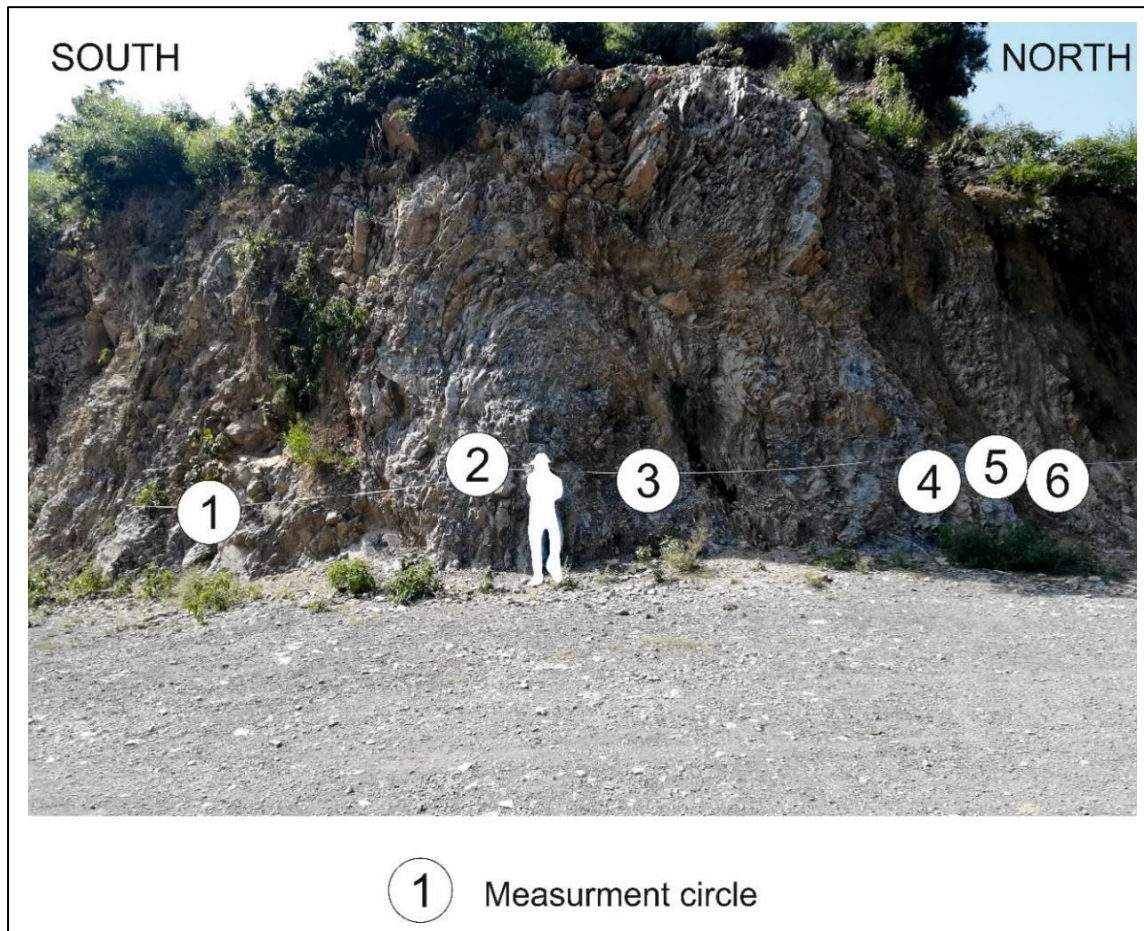


Figure 4.239: Composite photograph of site 4 with numbered circles indicating measurement circle positions. Compare with interpretations shown Figure 4.240 and Figure 4.241 Geologist shown in white.

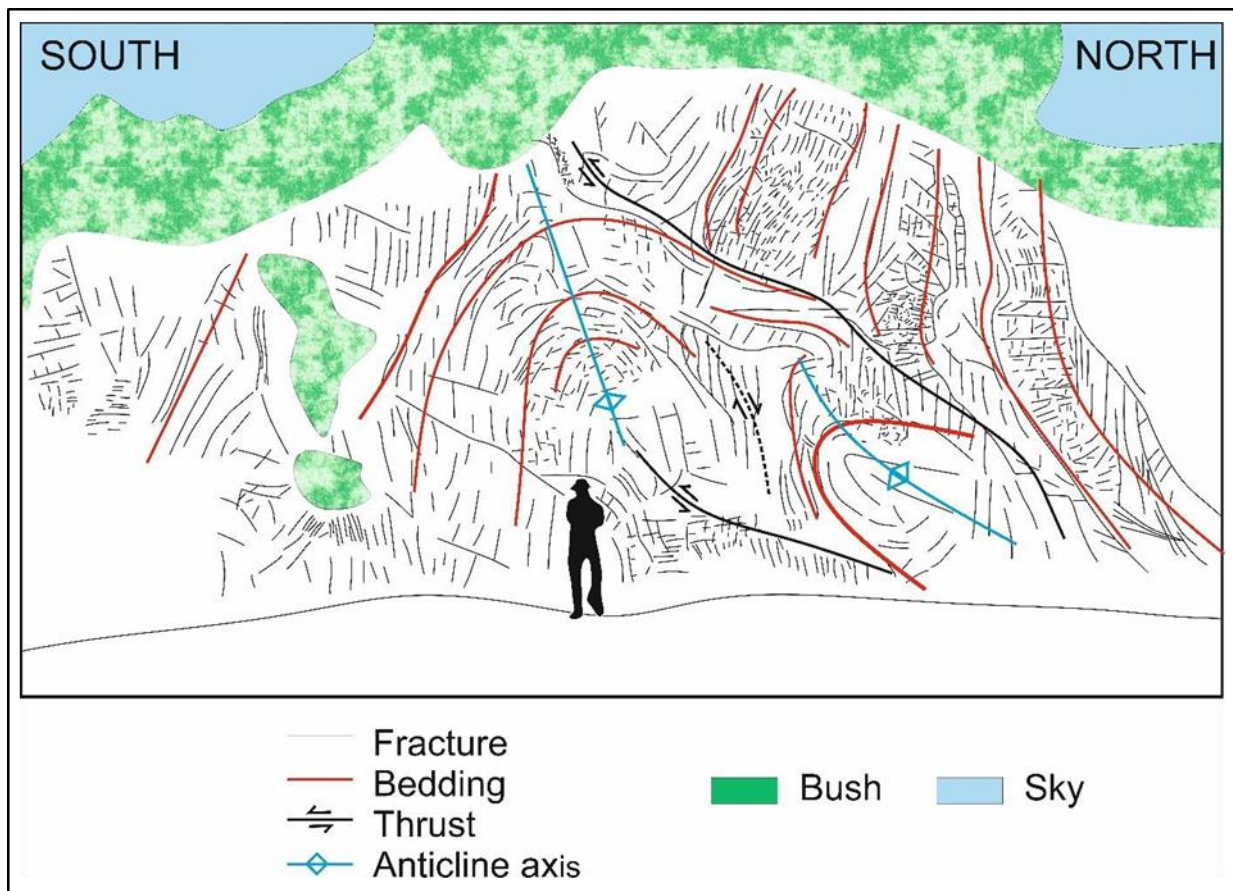


Figure 4.240: Line drawing of fracture patterns at site 4 (Figure 4.239). Major features (bedding, thrusts, and anticlines) are highlighted to show structural complexity. See Figure 4.241 for the various rock types associated with the structural features. Geologist shown in black.

The rocks consist of thinly bedded brown shale interbedded units consisting of grey-brown shale and fragmented limestone beds up to 30 cm long. These rocks are highly fragmented along the thrust surfaces. At the top of the anticline, the 1 m thick strong yellow-brown wackestones is developed, probably being the youngest stratigraphic unit (Figure 4.241).

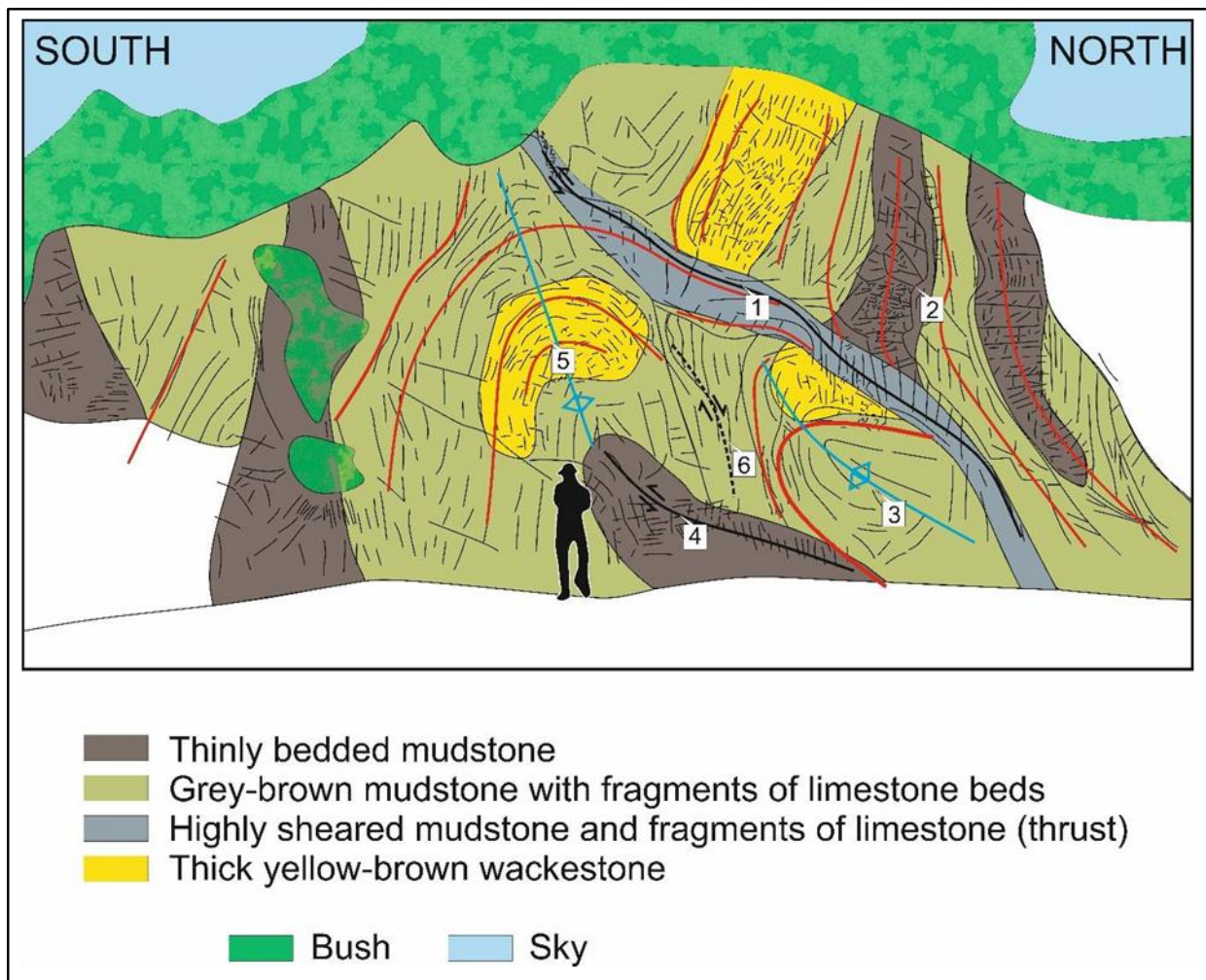


Figure 4.241: Fractures and lithological types at site 4 - compare with Figure 4.239 and Figure 4.240. Geologists shown in black. The deformation sequence shown on the drawing in numbers as follows:

1. Development of first (upper) thrust plane,
2. Southward thrusting of the hanging-wall strata of this thrust,
3. Thrust tip fold develops in the foot wall of the thrust forming a tight anticline restricting movement,
4. Thrust tip emerges through thinly bedded shale in deeper footwall,
5. Thrust tip fold develops in thick yellow-brown wackestones ahead of this thrust-tip, and
6. Fault develops between two footwall anticlines and wackestones is fragmented as thrusting continues.

The earliest deformation at this exposure is the development of first (upper) thrust plane. Thinly bedded shales intercalated with grey-brown fragments of limestone beds broken during the deformation are thrust southward in the hanging-wall strata of this thrust with steepening of dip. The deformation continued in the shales beneath the thrust which became folded into a tight thrust tip fold. The progress of this fold appears to have been restricted by its intersection with the older thrust, causing it to tighten up and reducing the ability of the thrust tip to progress. It is possible that the fragments of the broken limestone also aided in the locking up of this feature. As such a new thrust tip is likely to emerge through thinly bedded shale in deeper footwall. It is preceded by a thrust tip fold developing in thick yellow-brown wackestones ahead of this thrust-tip. This folding continues to develop between the wackestones in the two footwall anticlines, which is broken up into separate pieces.

The lower portion of the Chorgali Formation exposed at site 4 consists of highly sheared shale beds and occasional limestone and shale beds as described above. Unlike the Nammal Formation at sites 1 to 3, there is not a thick, strong, brittle rock present which is necessary for the accumulation of stresses and eventual failure through the development of a thrust. Instead, stress has been accommodated and released incrementally, predominantly by small-scale flexural flow around folded the shaley beds. The interbedded limestones have been fragmented and incorporated into the shaley beds. The thicker, stronger wackestones have also been fragmented but remain as coherent units (Figure 4.241).

The two standard models for strain deformation in a brittle, near surface environment are the tangential longitudinal and flexural flow (Cosgrove, 2015). These develop in isotropic and anisotropic layers respectively, that is in this case, the thicker limestones beds and the finely bedded shales. Layer-parallel buckling and extension tends to occur within the limestone and bedding parallel shear in the shale. The various lithological units at this outcrop are composed of differing amounts of shale and limestone causing them to deform and fracture in different ways. To quantify the variations in the fracture patterns of the different rocks. six measurement circles were placed across the outcrop (Figure 4.241). The number of "e", "x", "y" and "i" nodes (Figure 4.242) was counted in each circle and used to define the topological and thereby fracture characteristics of the different sites. The fractal

dimension was determined using the box-counting method with the box size ranging from 100 cm to 5 cm at the various sites.

The distribution of node types is independent of the total number of nodes with all measurement circles having more “y” and “e” type nodes (Figure 4.243). Circle 3 is sited within the highly crushed anticline axis of the thinly bedded shale in the footwall of the thrust (Figure 4.241) and has the highest total number of nodes and no terminating “i” nodes (Figure 4.243). Circles 2, 4, and 6 are in same rock type (thinly bedded shale) but all have fewer nodes as they are not sited on a fold axis. The measurement circles on the thinly bedded shale have more “i” nodes than those on other rock types.

The fractal dimension is highest in circle 3 (1.99) and lowest in circle 1 (1.88). Circles 2, 4, and 6 have similar dimensions of 1.90, 1.92 and 1.91, respectively. These differences are due both to structural and lithological variations. Circle 3 is located within a fold axis and is fractured throughout with circles 2, 4, and 6 on finely bedded shale that is less fragmented. Physical characteristics of the fractures derived from the analysis of the topological vary between the circles. Due to the high number of “y” nodes at circle 3, it has the highest number of fracture lines, branches, and tips (Figure 4.244). The fracture density and intensity are also highest in circle 3 (Figure 4.245), although the mean trace length is the second shortest at this site, characterising the highly crushed wackestones accurately.

The fracture density and intensity are highest in circle 3 and decreases in both directions away from it (Figure 4.245). The fracture connectivity is similar in all the circles.

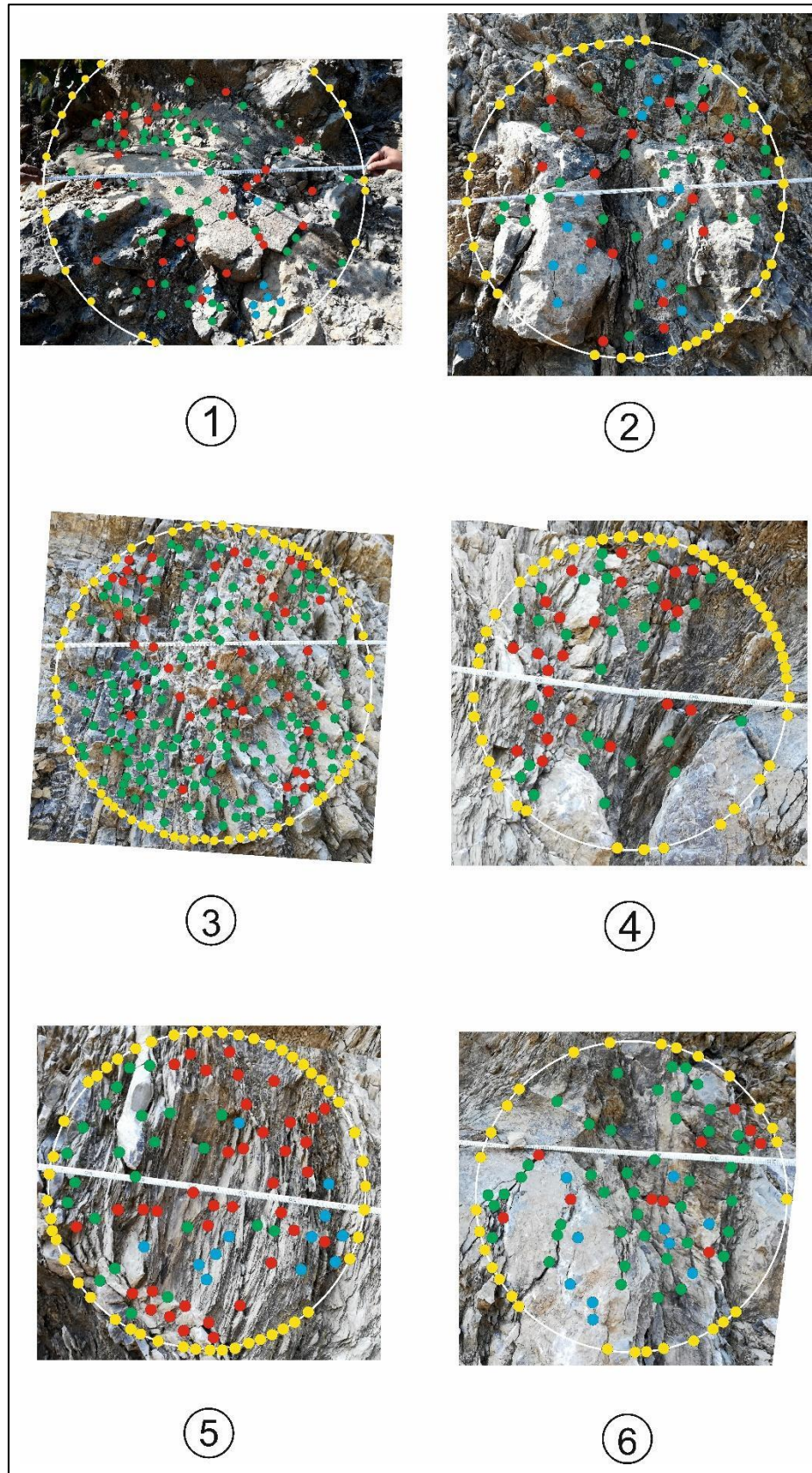


Figure 4.242: Measurement circles at site 4. See Figure 4.239 and Figure 4.241 respectively, for the location of the circles on the outcrop and the different rock units.

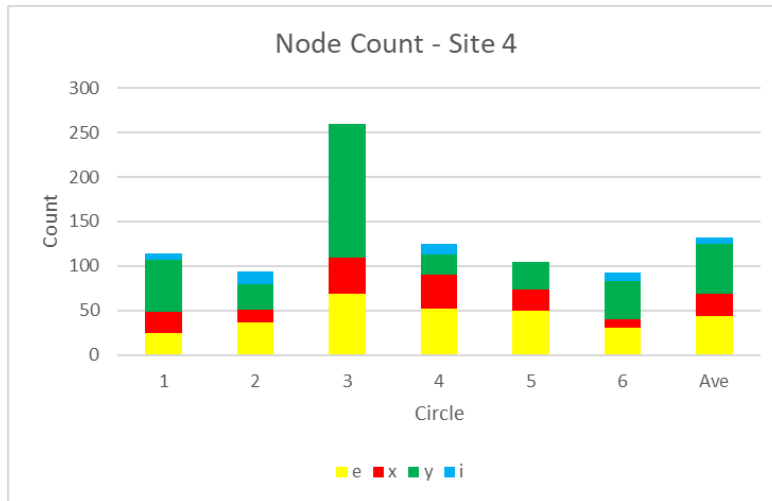


Figure 4.243: Number of nodes in the different measurement circles at site 4.

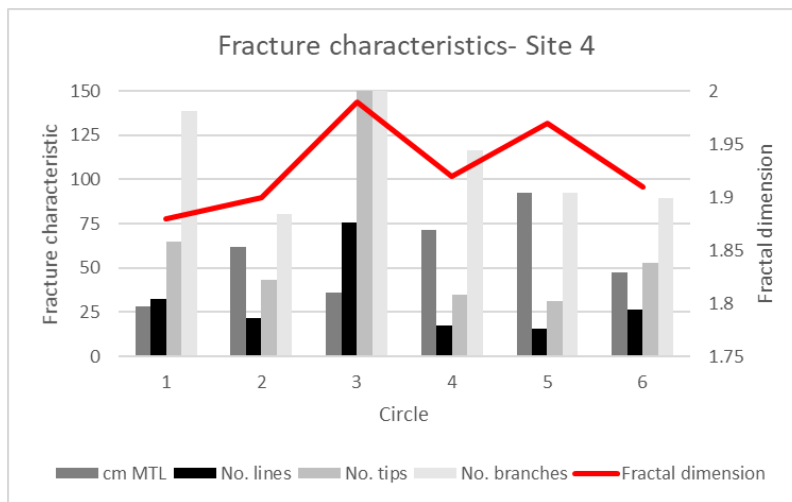


Figure 4.244: Mean trace length, number of lines, tips and branches and fractal dimension, site 4.

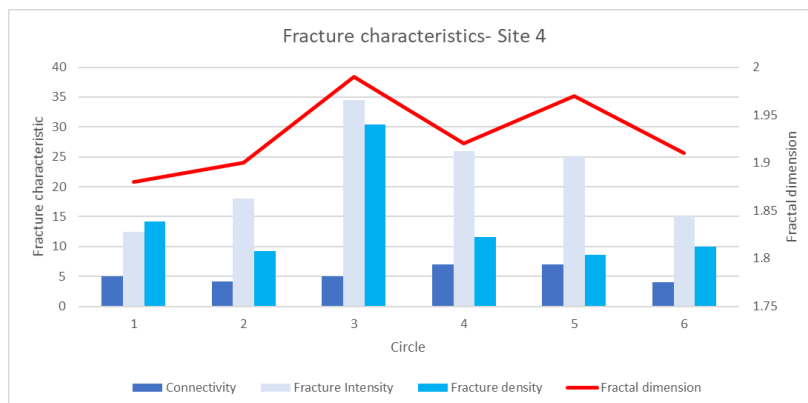


Figure 4.245; Connectivity, fracture intensity and density and fractal dimension at site 4.

4.2.4.5 Summary

The measurement sites of the Shah Dara region are positioned in the:

1. Thrust hanging-wall, Nammal Formation
2. Footwall anticline, Nammal Formation
3. Thrust horse, Nammal Formation
4. Stacked footwall folds, Chorgali Formation

The locations of sites are shown by the map in Figure 4.224 and the cross-section in Figure 4.246. The detailed information of the fractures associated with small-scale folds and thrusts quantify the characteristics of each site. This allows structural features such as back-thrusts to be identified as they have specific sets of these characteristics that are quantified by the topological and fractal features. The trend of these features and the resultant thrust complexes at the front of the Himalayan thrust belt provide insight into the larger regional scale tectonics.

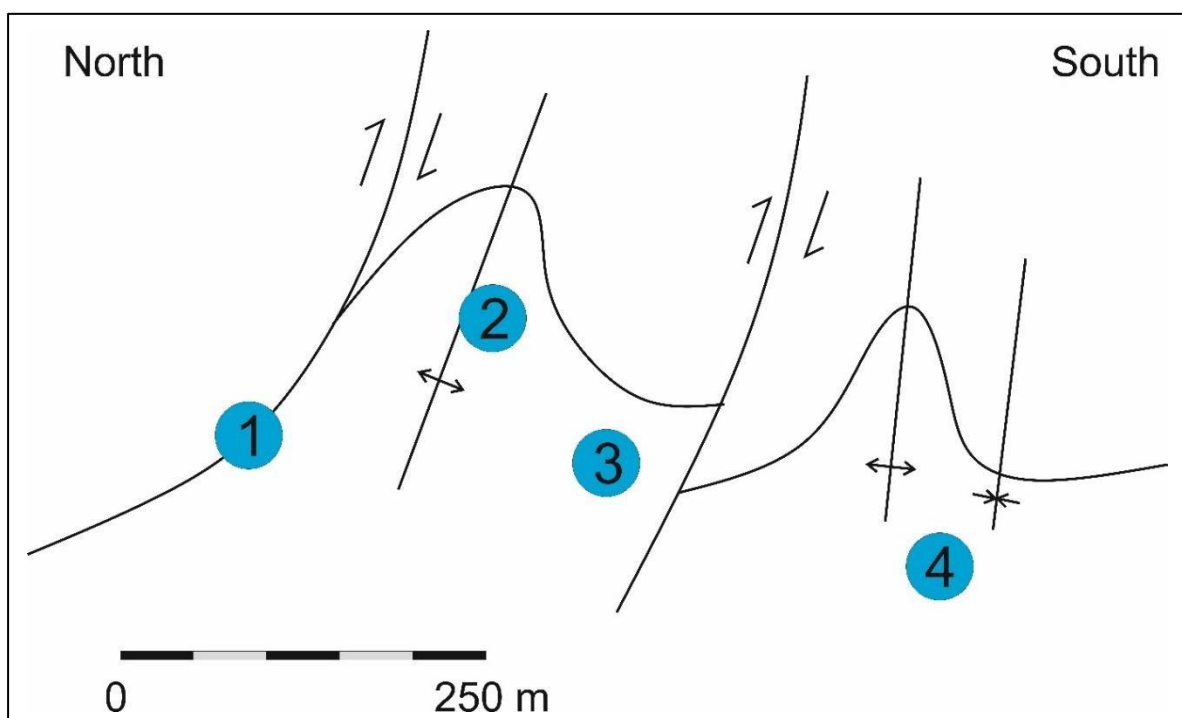


Figure 4.246: Schematic cross-section of the Shah Dara region .Circles show positions of mapping site.

Compare with Figure 4.224, the plan of the region.

Although the different measurement sites are within 500 m of each other, slight variations in the fracture patterns are apparent. The average number of nodes increases southwards from site 1 to site 3 but decreases at site 4 to below the average number of nodes at site 2 (Figure 4.247). The percentage distribution of the different node types is similar across the different sites (Figure 4.247). “y” nodes dominate and make up from 40 to 48% of the number of nodes in the various measurement circles at each site; “e” nodes have a similar percentage throughout of around 30%; “x” nodes also have a restricted range of between 13 and 25%; “i” nodes are uncommon with an average contribution of just 8% in all the circles at the different sites.

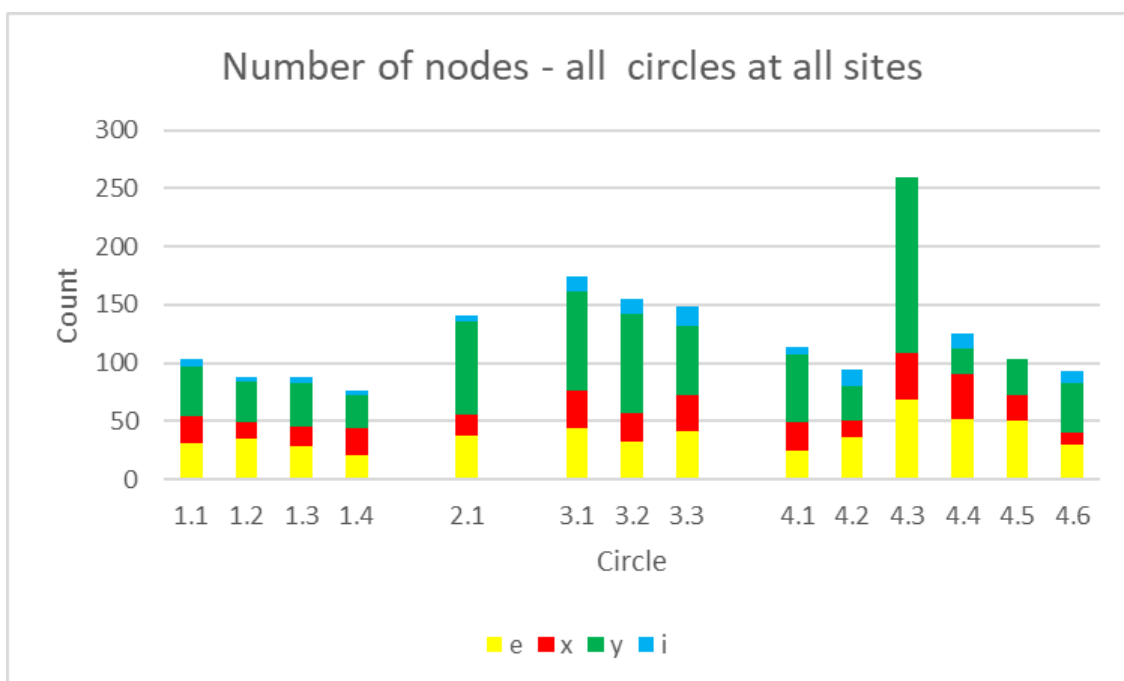


Figure 4.247: Node counts in the different circles at the various sites of the Shah Dara region. Whole numbers indicate the different sites.

The number of fracture nodes, lines, tips, and branches is highest at site 3 (Figure 4.248). It has the lowest fractal dimension. These characteristics describe a rock mass with distinct areas of higher fracturing. The highest fracture connectivity, density and intensity and longest the mean trace length

and highest fractal dimension is present at site 4 (Figure 4.249), defining a more uniformly fractured rock mass.

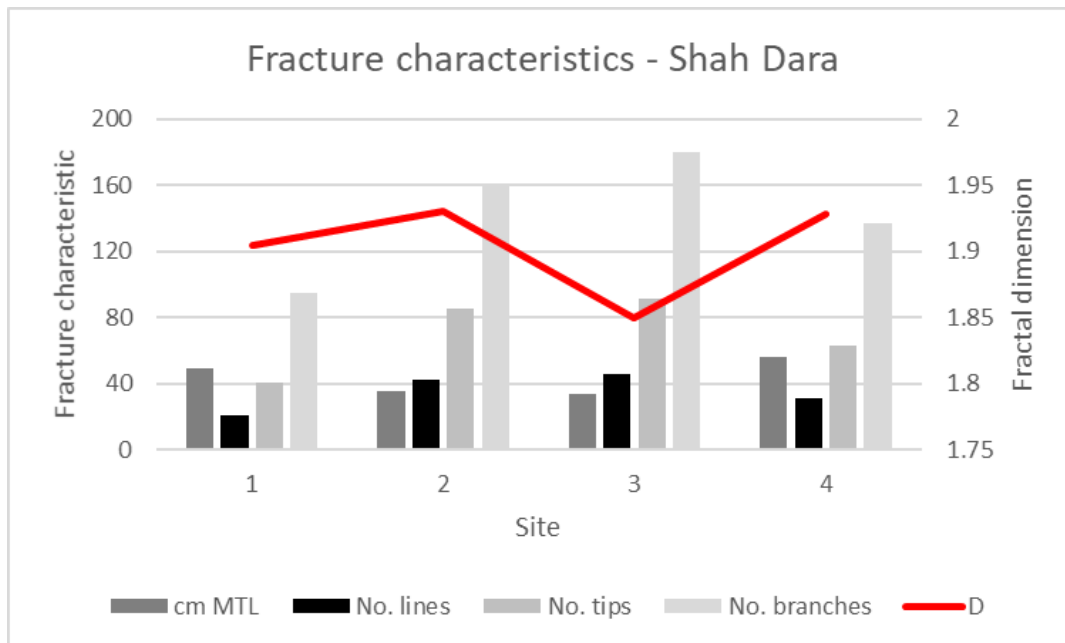


Figure 4.248: Average mean trace length in centimetres, (cm MTL), number of fracture lines, tips, and branches the fractures and fractal dimensions of the various sites of the Shah Dara region.

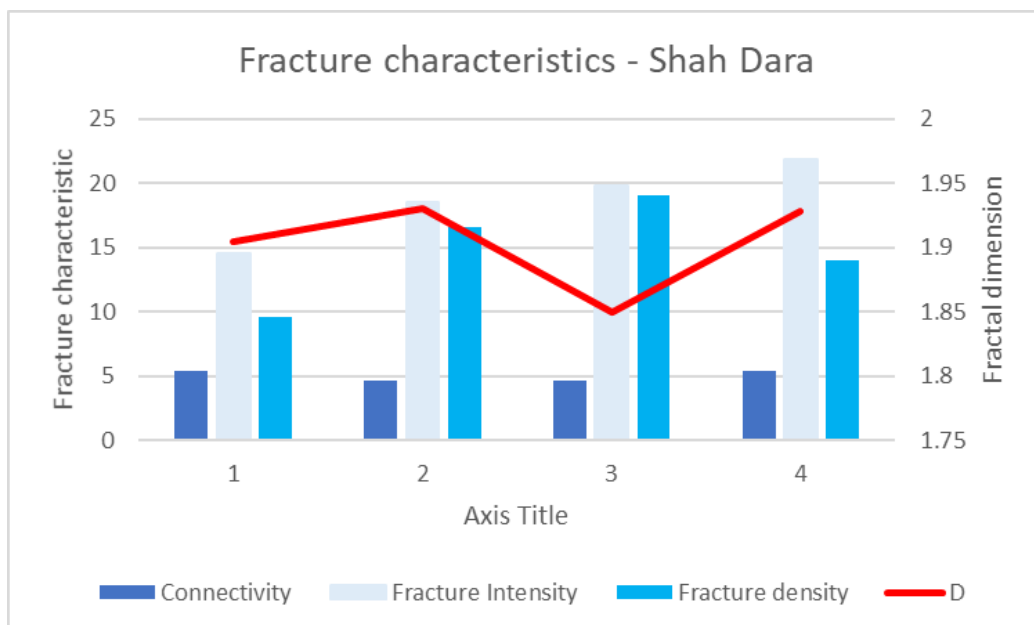


Figure 4.249: Average topology and fractal dimension of the various sites of the Shah Dara region.

Sites 1 and 3 are located on tightly folded anticlinal axes of the Nammal Formation and thus have a limited distribution in number of nodes and fractal dimension. In contrast to this, site 4 is located in thrusted Chorgali Formation with numerous shale layers allowing the development of a variety of structural features. This increases the variability in both the number of nodes and the fractal dimension (Figure 4.250).

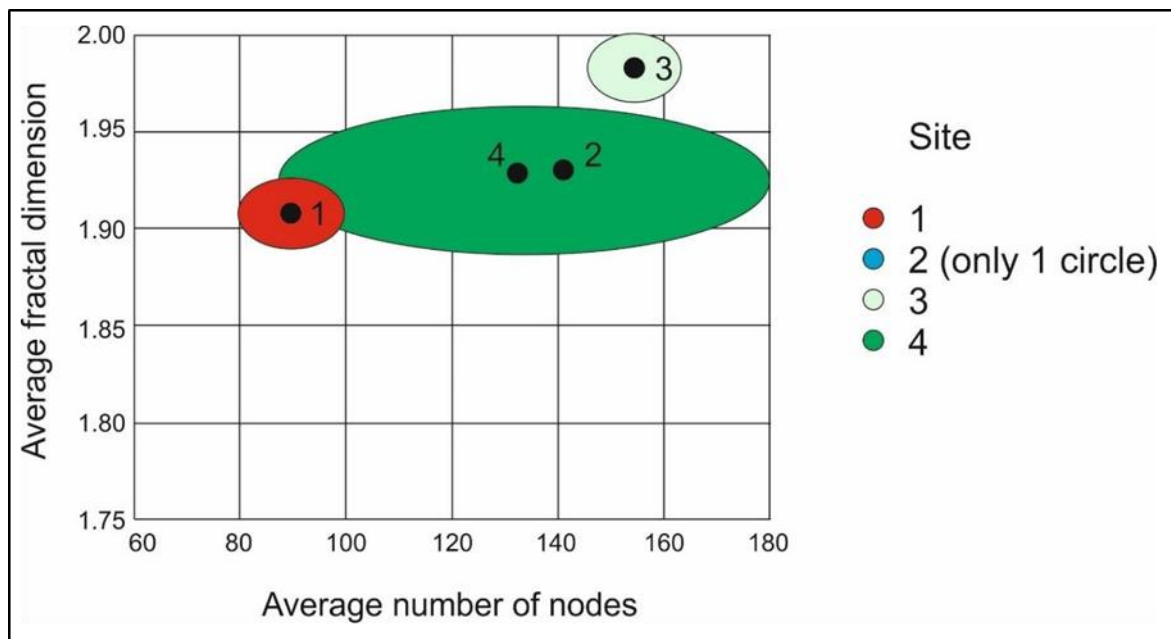


Figure 4.250: Average number of nodes and fractal dimensions at Shah Dara.

4.2.6 Jabbri region

This area, centred around the settlement of Jabbri ($33^{\circ} 54.3' N$, $73^{\circ} 10.4' E$), is characterised by an east-northeast to west-southwest strike of folded and highly thrust strata. As a result, the area has a pronounced topography which parallels the fold and thrust structures, including rivers that flow through the middle of the area broadly along strike (Figure 4.251) and the ridges to the north and south which define this part of the study area.



Figure 4.251: View downstream (westward) of the river next to site 4 that is aligned parallel to the strike of the structural features and stratigraphy (see Figure 4.252).

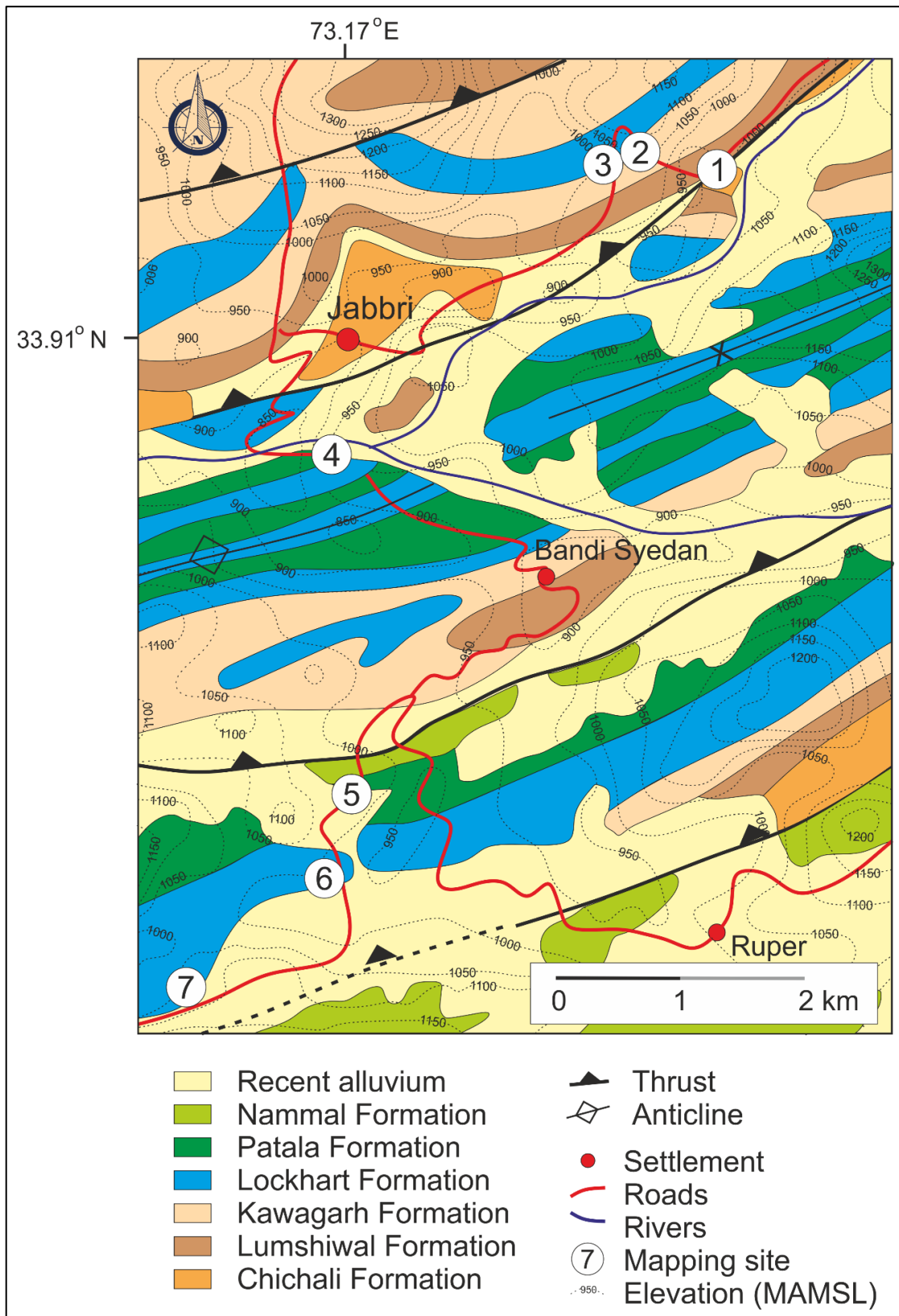


Figure 4.252: Geological map of the Jabbari region. Note the dominant ENE – WSW orientation of structural features and stratigraphy.

Seven sites have been mapped (Figure 4.252). The first three are in the immediate hanging-wall of a large-scale thrust. The fourth site is located close to an anticline axis (possibly a detachment fold) whilst the final three are located between the two oldest back-thrusts (Figure 4.252). The sites are located in strata ranging in age from the Middle Jurassic Samana Suk Formation but are mainly sited in the Upper Palaeocene Lockhart and Patala formations (Figure 4.252). The Chichali Formation was not encountered in the field investigations – the shales of this unit most likely form the decollement surfaces for the large thrusts in this area (Figure 4.252), breaking the up this shale-dominated unit and decreasing its outcrop exposure. Outcrop is poor at the first two sites as road-cuttings have not been dug into the more gently sloping strata. The glauconitic sandstone and the shale of the Lumshiwai Formation (Williams *et al.*, 1995) were not mapped as the fieldwork was focussed on the carbonate rocks of the Lockhart and Patala formations.

Table 4.15: Location, stratigraphy, and major structure of study sites in the Jabbari region.

Site	Latitude (N)	Longitude (E)	Formation	Age	Structure
1	33.919°	73.203°	Samana Suk	Lower Cretaceous	Thrust
2	33.922°	73.197°	Kawagarh	Mid Cretaceous	Southward dipping
3	33.922°	73.192°	Lockhart	Upper Palaeocene	Normal fault
4	33.895°	73.171°	Lockhart	Upper Palaeocene	Shear fault
5	33.872°	73.173°	Patala	Upper Palaeocene	Tight fold
6	33.867°	73.174°	Lockhart	Upper Palaeocene	Steep dipping
7	33.857°	73.161°	Lockhart	Upper Palaeocene	Thrust tip fold

4.2.6.1 Site 1

The Samana Suk Formation consists of thin- to thick-bedded limestone, dolomitic limestones and dolomites alternating with marls and marlstone (Qureshi *et al.*, 2018) and formed in a shallow marine environment (Wadood *et al.*, 2020). At site 1 it is exposed as a thinly bedded (on a 1 cm scale), light

grey coloured, micritic limestone that is highly fractured (Figure 4.253a), with the predominant fracture direction striking parallel to the regional thrust and fold-axes. Oblique joints (oriented in the textbook 60 and 120 degrees to the fold axis) are also present (Figure 4.253b). Together these joints result in a highly fractured rock that is dominated by cross-cutting “x” nodes (Figure 4.253c).

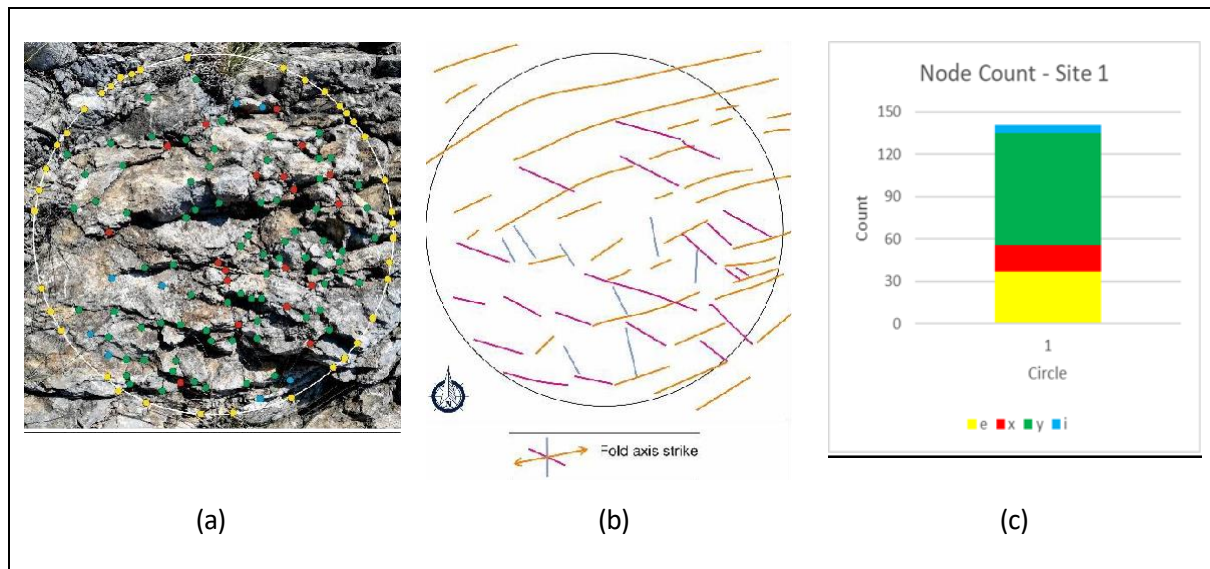


Figure 4.253: Site 1 (a) measurement circle photograph with different nodes indicated; (b) fracture trends - the majority of the fracture are parallel to the strike of the fold axis; (c) node count.

4.2.6.2 Site 2

The grey coloured marl of site 2 has weathered to an orange-brown colour, typical of the Kawagarh Formation. Millimetre-sized foraminifera are visible on the outcrop surface due to weathering. Closely spaced discontinuities between beds of generally less than 30 cm in thickness have allowed movement of water through the rock mass enhancing the weathering on the limestone surfaces. The fractured and weathered nature of the rocks made it unsuitable for conventional circle mapping. A series of vertical sections (each 10 cm wide) were measured at the site to determine if there was a relationship between bedding thickness and fracture. Figure 4.254 shows no such relationship occurs in the four

sections mapped at site 1. Sections were of limited length (between 0.5 and 2.0 m) but did properly sample the thinly bedded strata.

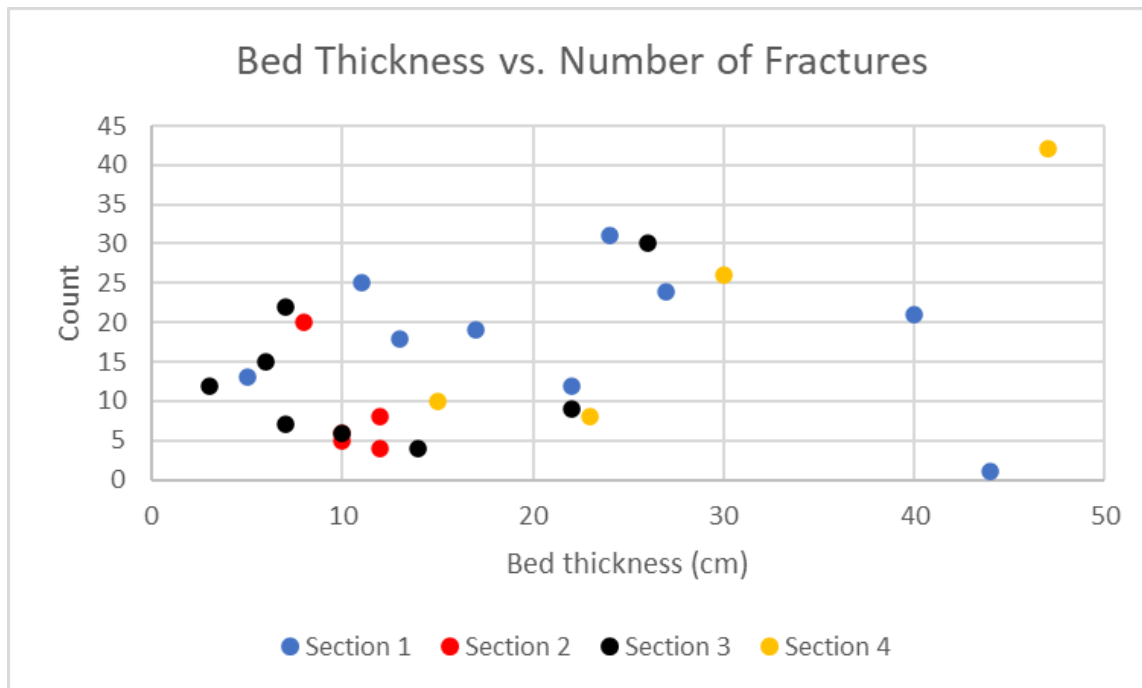


Figure 4.254: Bed thickness vs. number of fractures. A 10 cm wide column was drawn against the outcrop and the number of fractures within each lithological rectangle was counted. No clear trend (or clustering) is apparent.

4.2.6.3 Site 3

The fine-grained, light grey limestones of the Lockhart Formation at site 3 have been folded into a gentle southward plunging syncline-anticline pair with a wavelength of 10 m (Figure 4.255). The limestone beds are approximately 1 m thick and are separated by centimetre-thick layers of sheared lime shale with prominent slickensides (fracture set 1) formed during the formation of the plunging folds. Open fractures partially coated with iron-oxides (fracture set 2), are restricted to individual limestone beds and do not cut across shale interbeds. The folds are likely associated with a fault in the adjacent valley that can be discerned on Google Earth from the change in position of strata (Figure 4.256). These changes indicate that it is oriented north-south and downthrown to the east by approximately 20 m and therefore not directly associated with the NNE-SSW regional structures.

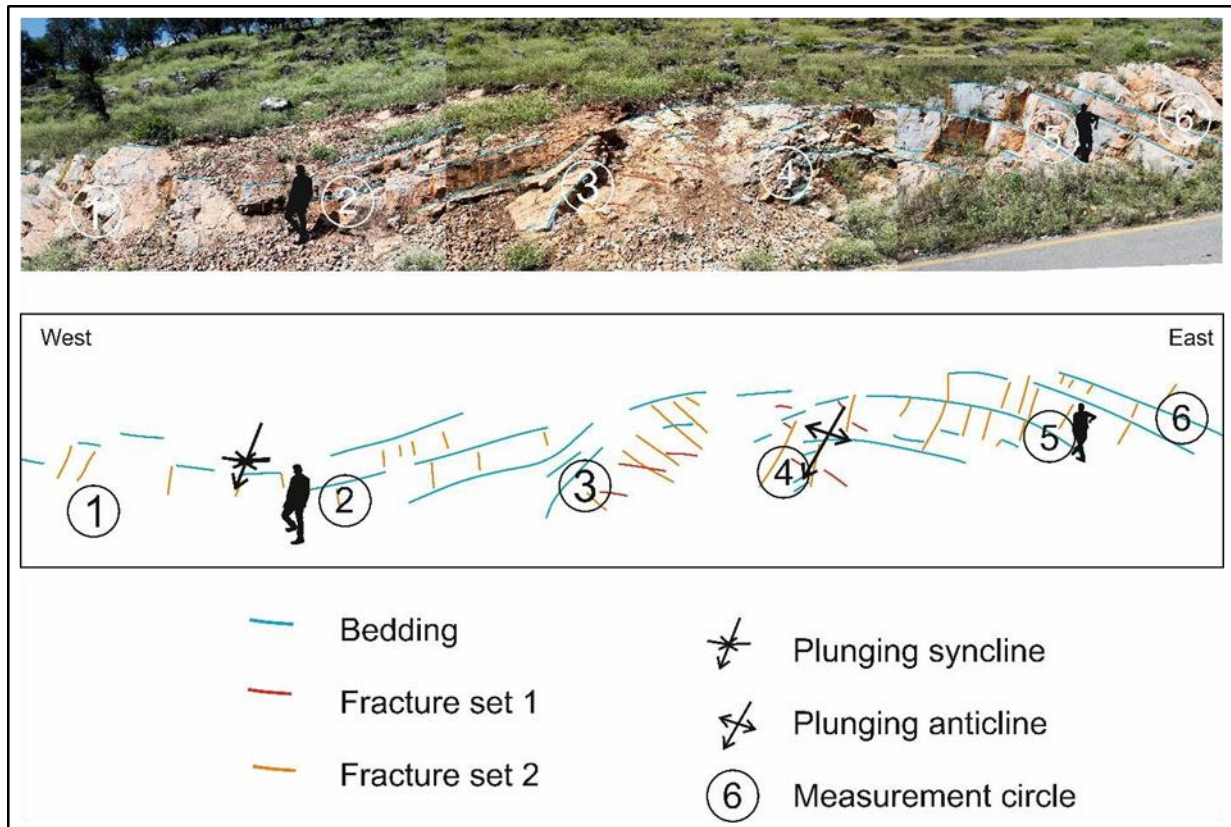


Figure 4.255 Photograph and line-drawing of site 3. The geologist in the image is 1.8 m tall – the apparent change in his height is due to the fact that the eastern portion of the section is further away, around a bend in the road (Figure 4.256).

Circle 1 contains both a bedding surface and cross-section of a limestone bed (Figure 4.257 (1)). There are few cross-cutting fractures. “i” nodes are more common in the limestone bed. Circle 2 is closer to a syncline axis and has more Set 2 fractures. This results in there being more cross-cutting “x” nodes. Circle 3, sited on a sheared shale bedding surface, is dominated by “y” nodes due to the intersection of fissures and slickensides. These do not typically cross-cut suggesting that the movement associated with the slickensides post-dates the tensile fractures and smears the contact between them.

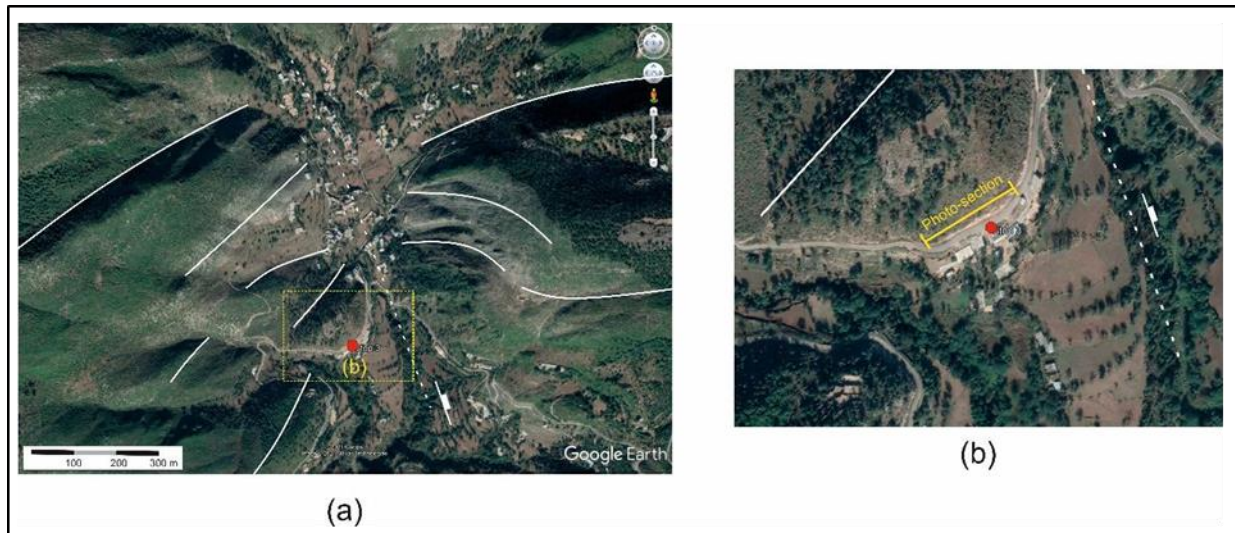


Figure 4.256: Google Earth images of site 3. (a) change in outcrop lineaments due to a fault with a downthrow to the east, (b) zoomed in view showing position of photographic section. Red dot indicates position of site 3.

Circle 4 is sited on an anticline axis (Figure 4.255). The large number of fractures (Figure 4.257 and Figure 4.258) indicate that there has been significant brittle deformation as it is not possible to accommodate the applied stresses by flexural movement as occurs between the layers of highly sheared shale and limestone on the adjacent flanks; but the deformed axial zone is only 2 m wide (Figure 4.255). Circles 5 and 6 are dominated by limestone bedding planes cutting across from the left to right (Figure 4.257). The restriction of fractures to particular limestone beds is clearly seen in these two circles.

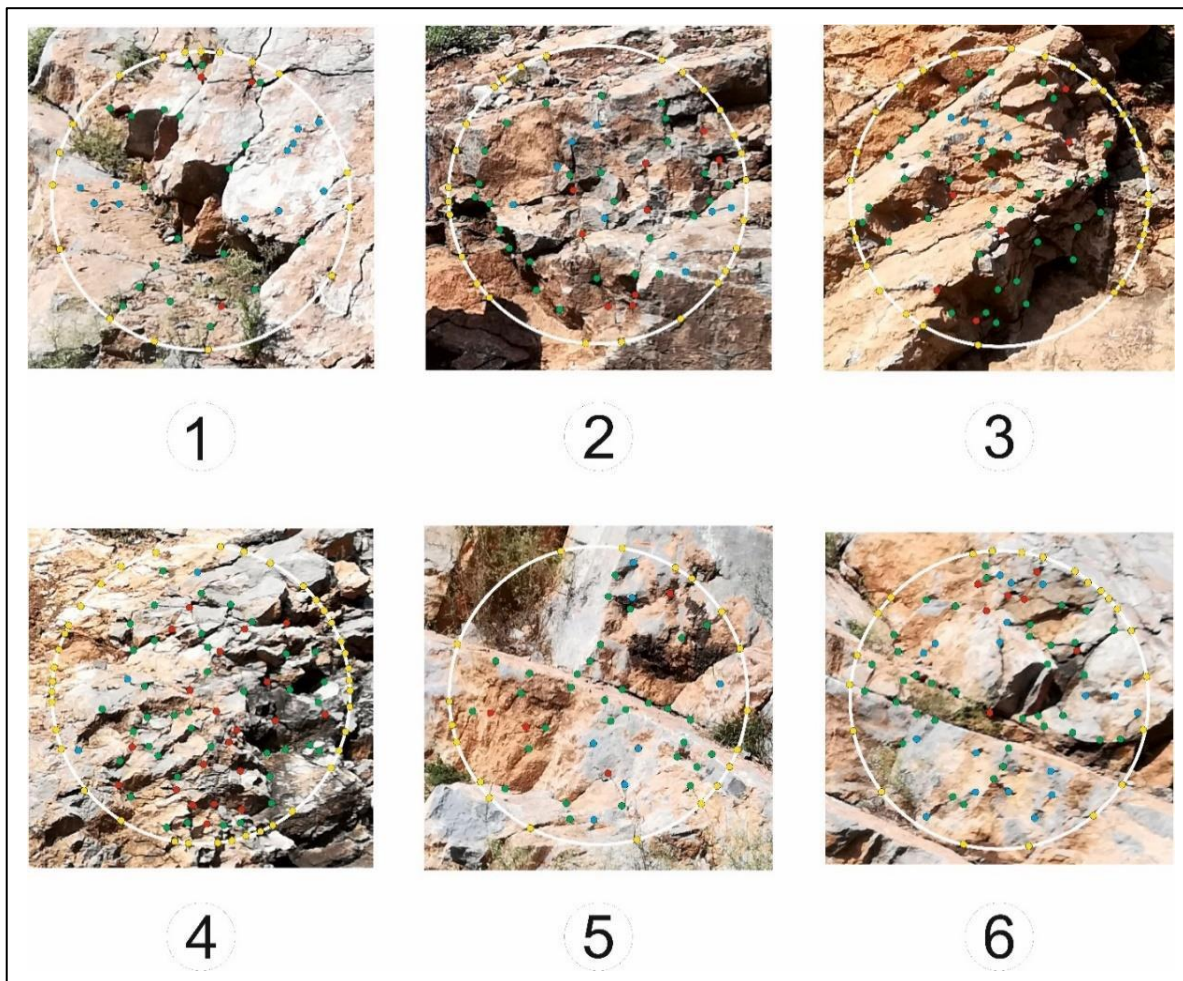


Figure 4.257: Measurement circles at site 3. Various node types are indicated with standard colours (“e” in yellow, “x” in red, “y” in green, and “i” in yellow). See Figure 4.255 for positions of circles.

The large number of fractures in circle 4 on the anticline axis increased the number of “x” nodes with the circle having the greatest number of nodes (101) compared to an average of 67 for the other circles (Figure 4.258). Sites 3 and 4 have a higher number of fracture branches (Figure 4.259), as the fractures are not restricted to a single bed as they are elsewhere on the outcrop. The connectivity, fracture intensity and fracture density are all greater in circle 4, but only by a small amount.

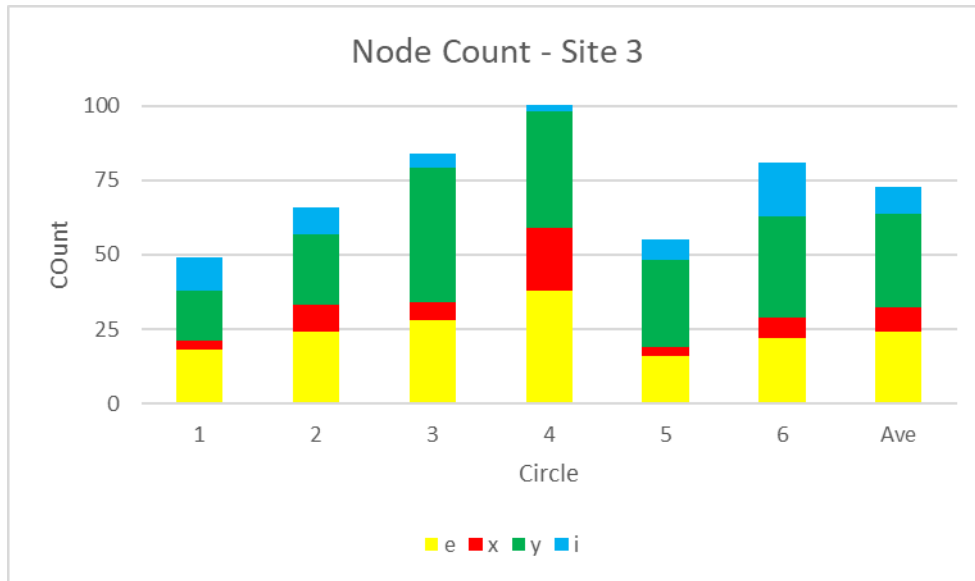


Figure 4.258: Node count at site 3, dominated by “y” type nodes. More “x” nodes are present in circle 4 (on the anticline axis) compared to the other five circles sited on the flanks which have more “i” fractures in the thicker limestone strata.

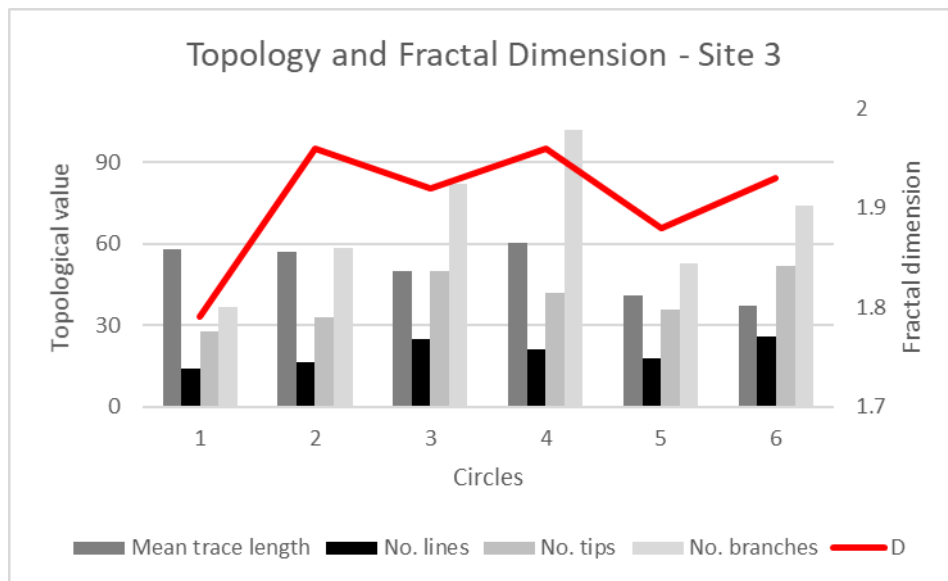


Figure 4.259: Topological values and fractal dimensions of the circles at site 3.

4.2.6.4 Site 4

Site 4 is located in highly faulted Lockhart Formation (Figure 4.252). The fresh dark grey limestone is more argillaceous and is characterised by scattered small (> 5 mm long) calcite fractures with the fracture length and connectivity increasing in lighter coloured, mostly clay-free limestones (Figure 4.260). These smaller fractures do not show a preferred orientation and are cross-cut by larger faults, typically up to 5 cm wide, both un-mineralised and calcite coated that form an eastward verging thrust system (Figure 4.261).

Further large calcite and calcite-iron oxide fractures cross-cut these two earlier fracture sets. These east-west striking fractures are sub-parallel to the regional-scale structures. Their steep dip (80° south) compared to the dip of the bedding (20° south) indicates that they cross-cut and probably connect several of the folded layers.



Figure 4.260: Photo-mosaic image of site 4, view northward. Locations of the different numbered measurement circles are shown. Geologist in yellow.

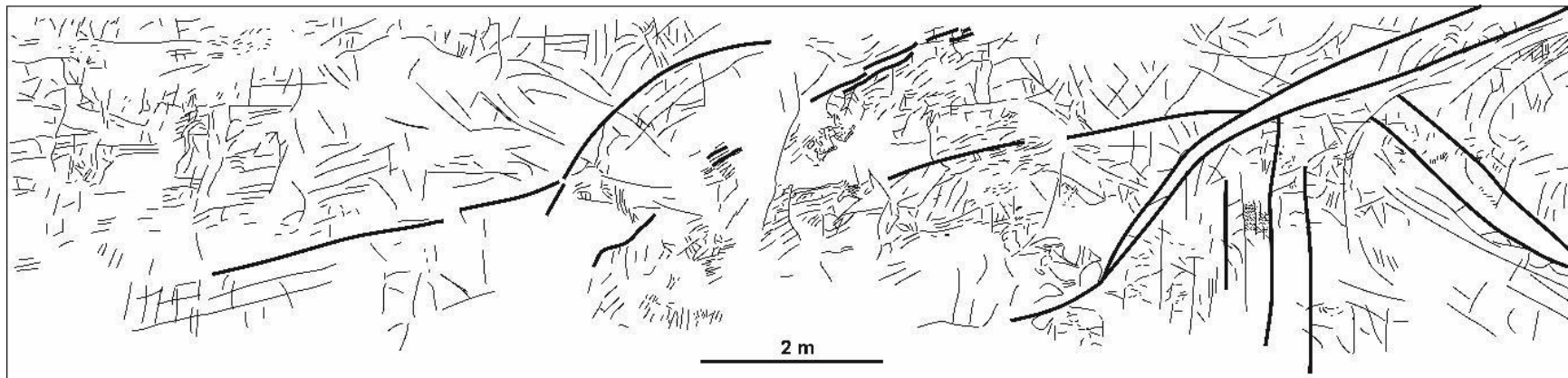


Figure 4.261: Line-drawing of showing the fractures at site 4. The eastward verging thrusts are clearly visible.

Six measurement circles were placed on the outcrop (Figure 4.260) to evaluate the variations in rock type and structural features (Figure 4.262). Measurement circles situated in different rock types (Table 4.18) have similar numbers of nodes, but those on the intermediate age west-east thrusts show the greatest differences from the average values (Figure 4.263). Circle 4, located on a thrust-flat, has significantly more nodes, mainly “y” type. In contrast to this, circle 5, on a thrust ramp, has fewer nodes than average and these are dominated by “i” nodes unlike the other measurement circles (Figure 4.263).

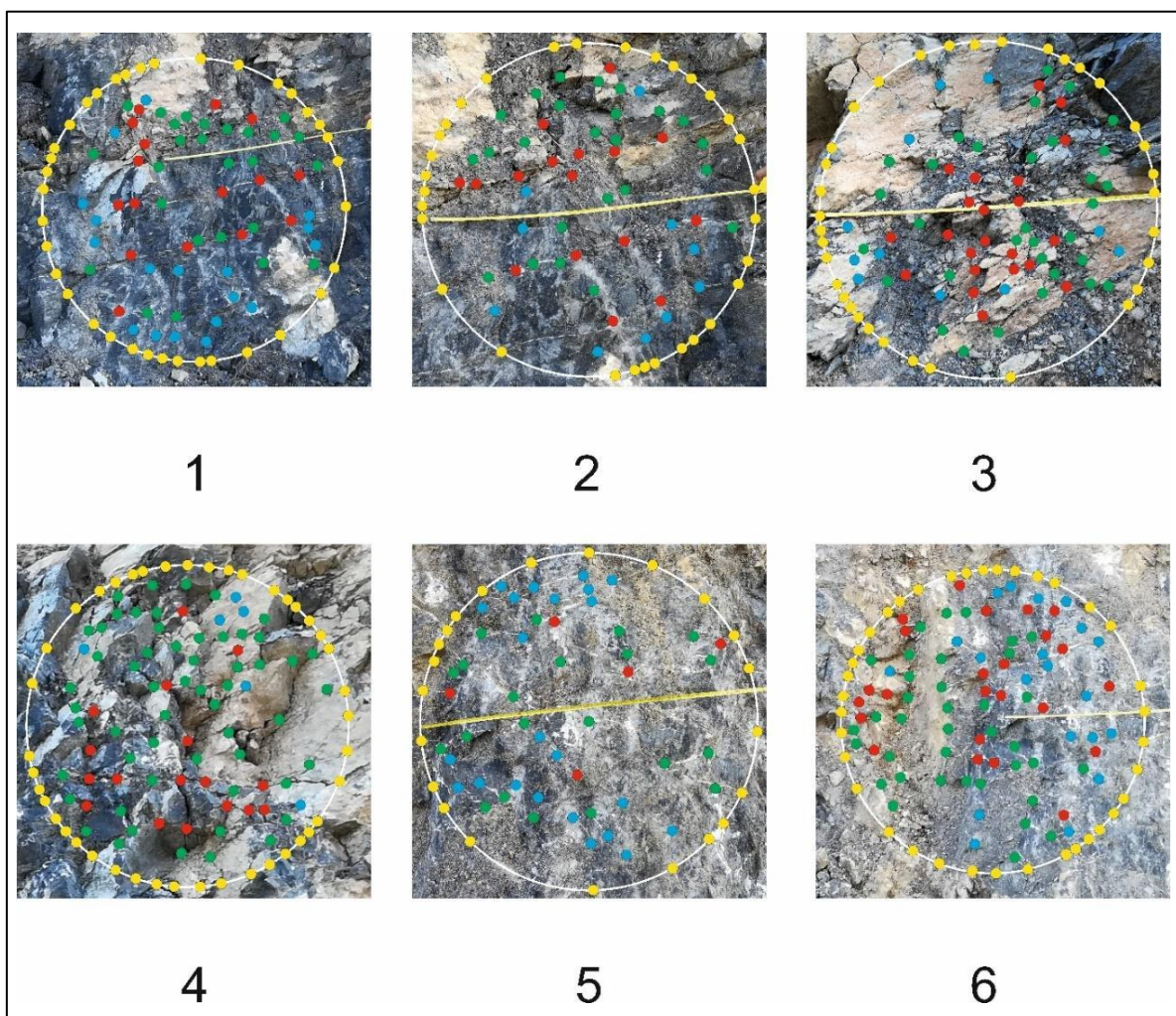


Figure 4.262: Measurement circles at site 4. See Figure 4.260 for positions of circles.

Table 4.16: Measurement circle characteristics, site 4.

Site	Structural position	Rock-type description
1	Foot wall	Dark grey limestone with small calcite fractures
2	Foot wall	Dark grey limestone with small calcite fractures
3	Fault plane (thrust ramp?)	Calcite joint with underlying dark grey limestone
4	Thrust	Calcite joints and dark grey limestone
5	Thrust	Fractured grey limestone
6	Vertical shear	Sheared and fractured light grey limestone

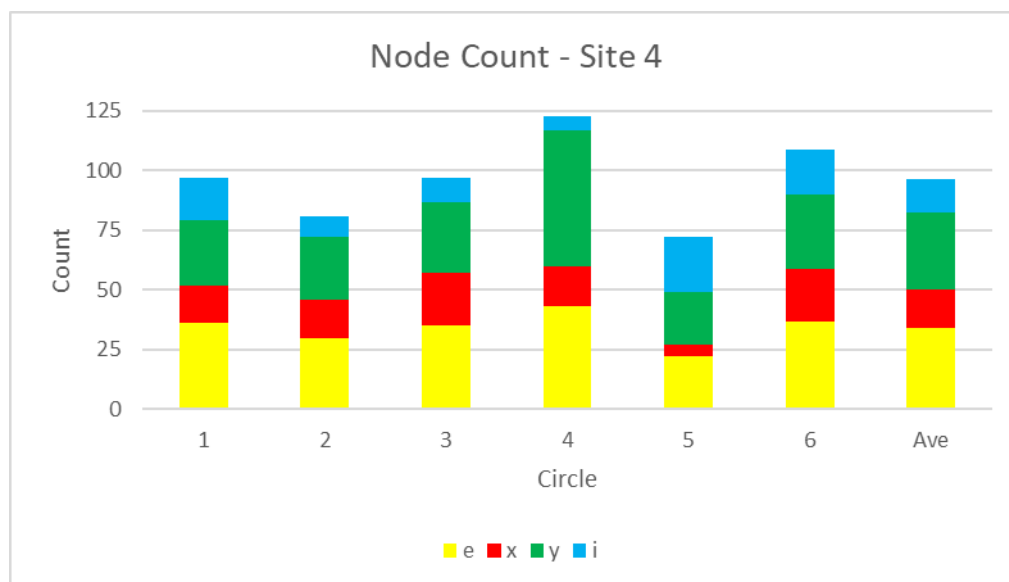


Figure 4.263: Node count of measurement circles at site 4. The highest and lowest number of nodes are on a thrust flat (circle 4) and a thrust ramp (circle 5) respectively.

Only small topological differences were calculated for the measurement circle (Figure 4.264). As expected, has the greatest number of lines, tips, and branches. As the rock is highly fractured in all the measurement circles (Figure 4.262), the fractal dimension is also high in all, making it difficult to discern differences in the fractal dimension despite employing a box-size of 5 cm.

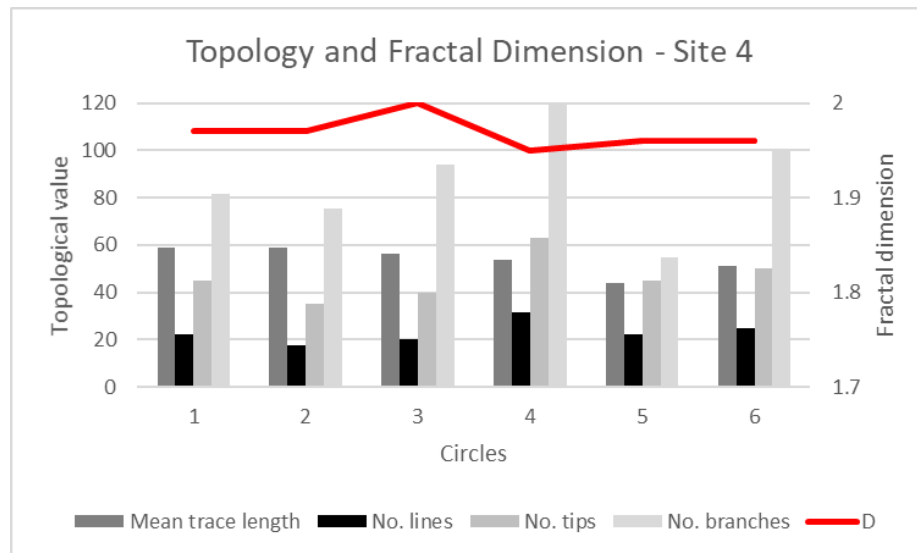


Figure 4.264: Topological characteristics and fractal dimensions of measurement circles at site 4. The greatest number of lines, tips, and branches is in circle 4, located on a thrust flat.

4.2.6.5 Site 5

The Patala Formation is a late Palaeocene to early Eocene limestone and shale- sequence deposited on a carbonate platform which is interpreted as representing a continuation of the transgressive phase of the Lockhart Formation (Hanif, 2011). It also contains less limestone than the Lockhart Formation because of the Palaeocene-Eocene Thermal Maximum (PETM) that killed much of the temperature sensitive corals (Hanif *et al.*, 2013) whilst the shale continued to be derived from benthic algae. This change in composition from limestone dominated to sheared shale dominated strata has resulted in a change in the type of failure of the rock mass. The thinly interbedded shale and limestone layers are able to shear past each other with flexural flow (FF) being the dominant failure mechanism (Cosgrove, 2015). Small tangential longitudinal (TL) fractures are still developed within individual beds, but most of the strain is accommodated by sliding of the different rock types and the transformation into shale. This shear-failure has resulted in the development of tightly folded strata, often with closely spaced recumbent or overturned fold axes (Figure 4.265 and Figure 4.266).

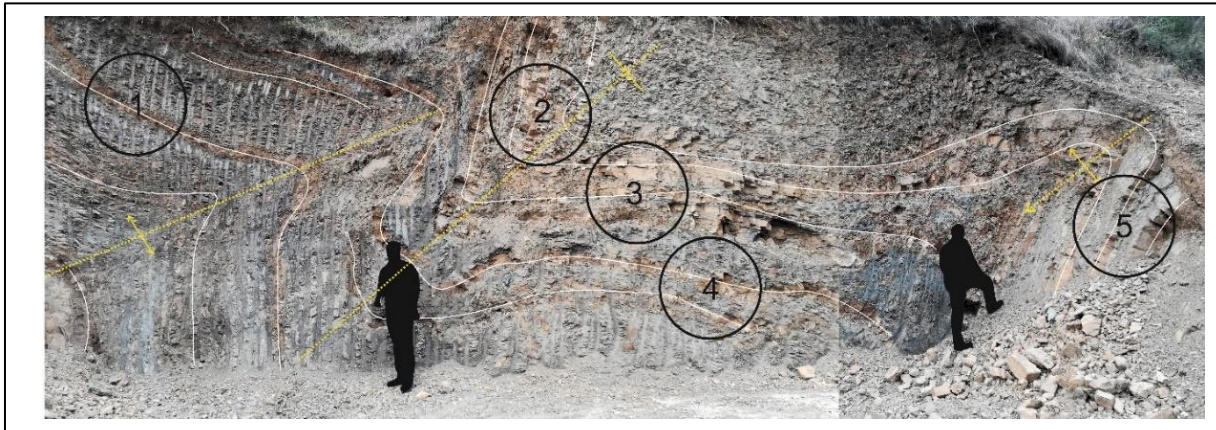


Figure 4.265: Photo-mosaic of the tightly folded Patala Formation at site 5. See Figure 4.266 for a line-diagram of the site. Geologists shown in black.

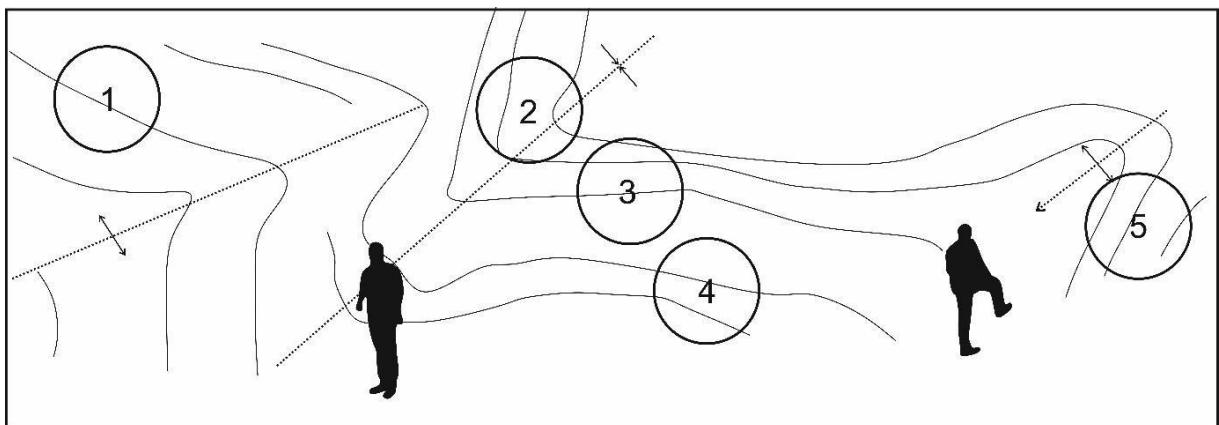


Figure 4.266: Line-diagram of the tightly folded strata of the Patala Formation at site 5. Only general trends and not all the strata have been mapped as beds are typically only centimetres thick. Positions of measurement circles (shown in Figure 4.267) around the fold axis are also shown. Geologists shown in black.

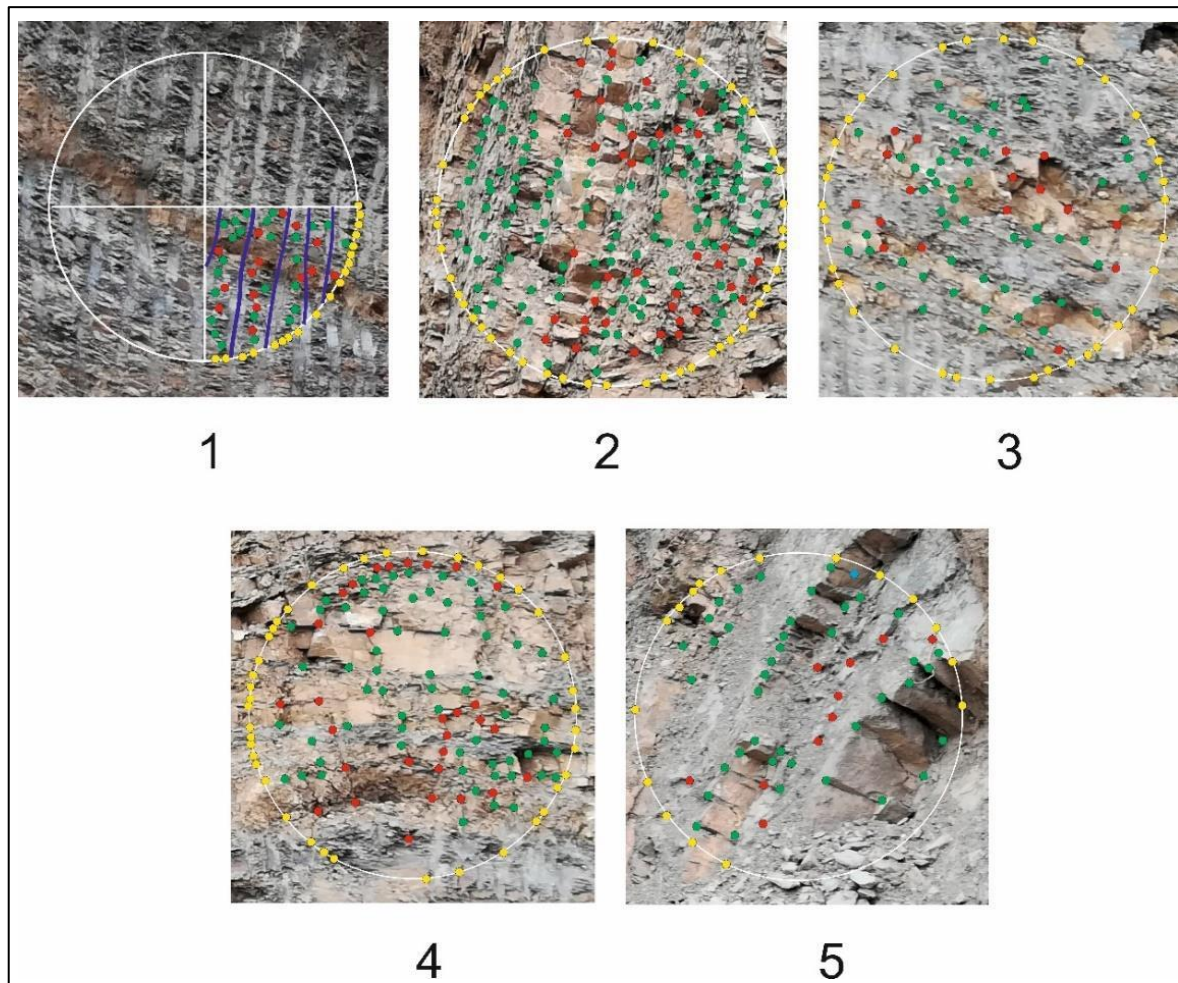


Figure 4.267: Annotated photographs of the measurement circles at site 5. Natural fracture intersections in circle 1 are obscured by excavator tooth marks (shown by blue lines) but it been included to show the soft and plastic nature of the Patala Formation shales. Almost all the other fractures in the measurement circles represent small-scale transitional longitudinal failures in a layer rather than the larger scale flexural flow between them.

Up to two to three times as many nodes are present in the measurement circles at site 5 (Figure 4.268), mainly due to the thin bedding with FF fractures and TL fractures within the beds intersecting as “y” nodes. Only one of the 801 nodes measured at the site is an “i” type and more than half of the nodes (414) are “y” type, the remainder split between “e” (231) and “x” types (155). The high quantity of nodes in circles 1 and 2 has resulted in a large number of branches being calculated for these two circles (Figure 4.269). Importantly, the mean trace length (4 cm) is very similar across all six circles, as

a result of the strong control of the intercalated thin shale and limestone beds on the fracture pattern. The fractal dimensions of the different circles are all high due to the large number of widely spread fractures.

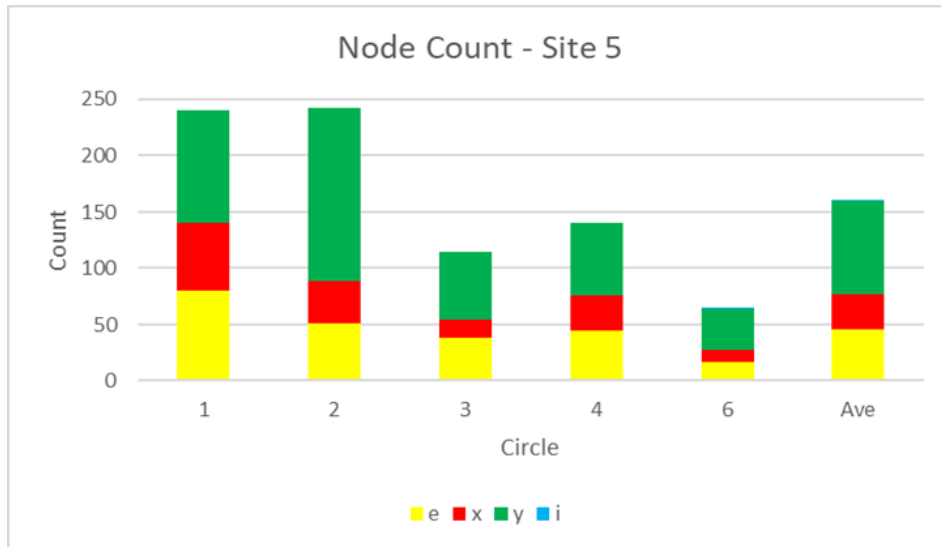


Figure 4.268: Node count at site 5 - “y” type nodes predominate.

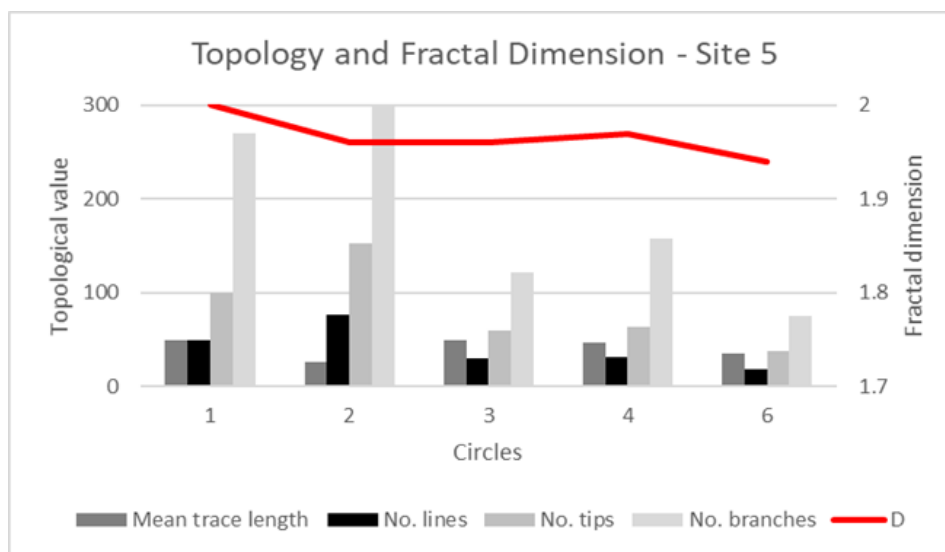


Figure 4.269: Topological and fractal characteristics of the measurement circles at site 5. The large number of branches and dominance in other topological characteristics in circles 1 and 2 is due to the larger number of nodes developed in the more thinly bedded shale. Although circle 6 has lower topological values and the lowest fractal dimension (1.94), the difference in the fractal dimension is not significant due to the high density of fractures.

4.2.6.6 Site 6

At site 6 the steeply dipping Lockhart Formation limestone beds (between 10 and 20 cm thick) are interbedded with thin centimetre thick shale beds (Figure 4.270). This interbedding allows the beds to shear past each other with flexural flow (Cosgrove, 2015). As the limestone beds are thicker and more dominant, tangential longitudinal (TL) stress redistribution has caused the number of layer perpendicular fractures to increase. It is important to note that these abundant layer perpendicular fractures do not cut through shale beds or even across adjacent limestone beds (Figure 4.271).

Interestingly though, because the limestone bed are thicker, cross-cutting “x” nodes are also common making up approximately 30% of the total number of nodes compared to “y” nodes which constitute 46% of the total (Figure 4.272). No “i” nodes are present due to the fact that both the FF between the layers and the TL failure within the layers is extensive in this type of mechanical layering, which is intermediate layers brittle rocks interbedded with thin ductile layers.



Figure 4.270: Photograph of highly fractured, steeply dipping Lockhart Formation at site 6. The site is located approximately halfway between two thrusts, 1 km to north and 1 km to the south (see Figure 4.252). Geologist in white.

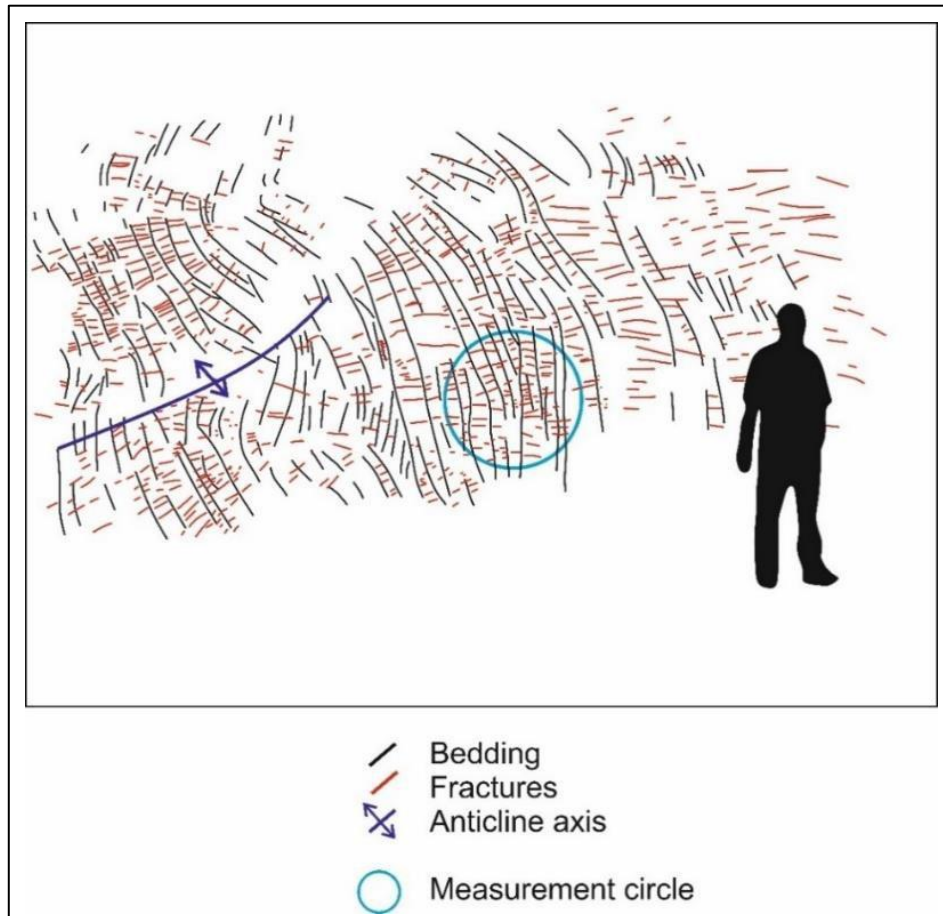


Figure 4.271: Line sketch of Figure 4.270. The large number of fractures within the limestone beds is clearly evident as is the fact that these fractures do not link up to form longer continuous features. Geologist in black.

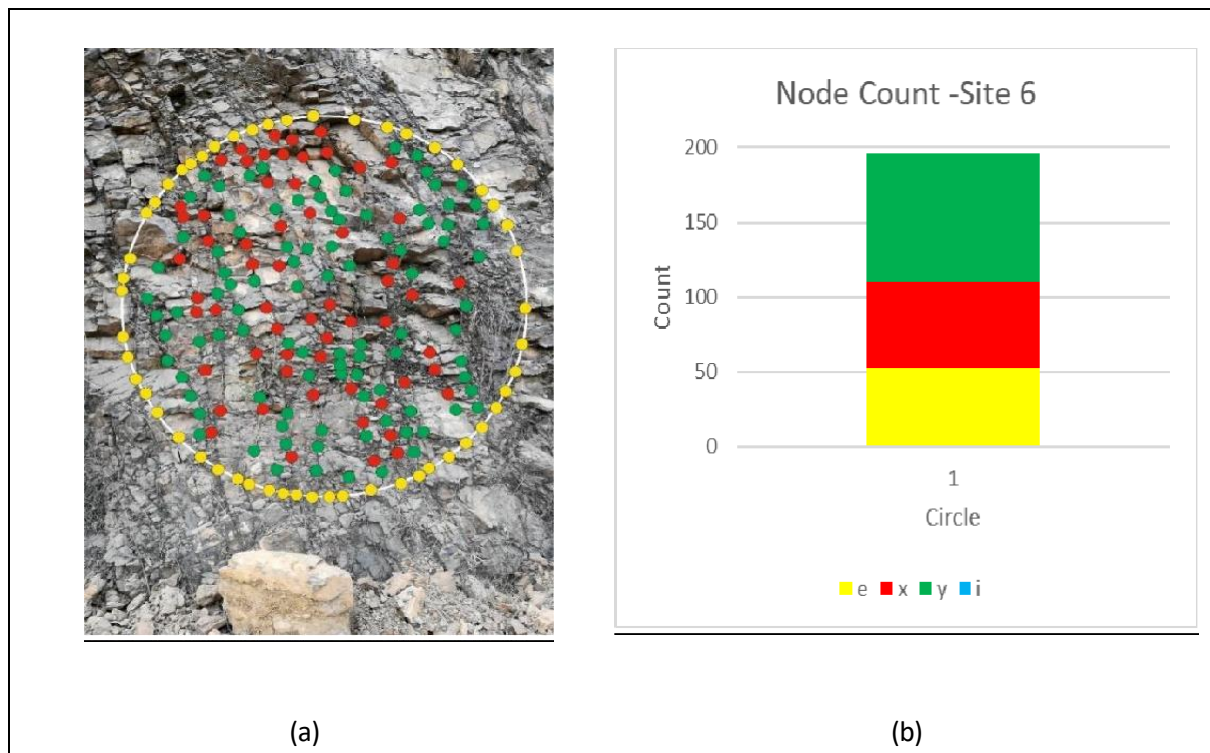


Figure 4.272: Measurement circle at site 6. Note the steeply dipping and closely interbedded strata, (b) node count – no “i” nodes are present.

4.2.6.7 Site 7

Site 7, the most southerly site of this area is also within the Lockhart Formation (Figure 4.252). The rocks here also consist of wackestone and shale, the latter makes up a very small amount of the total (Figure 4.273). Although fractures can terminate at the edge of a wackestone bed, on the shale interlayers, these may be too thin or absent, allowing many fractures cross-cut the bedding (Figure 4.274). This has resulted in the average number of “x” nodes (49) and the number of “y” nodes “(52) per circle being very similar.

The greatest number of nodes was measured in circle 2, sited on the anticline axis (Figure 4.276). The number node-is present in circle 1 – this may be caused by the thicker limestone beds in this circle compared to circle 3. The thicker limestone beds with the associated decrease in the number of fractures has resulted in a lower fractal dimension of 1.67 (Figure 4.277).

A horizontal series of ten 10 * 10 cm squares was drawn on the rock. This strip was measured to see if trends in topological characteristics might be seen across a measurement circle. No clear trends were evident and most significant problem was the fact that the “e” fractures were recounted at each boundary changing leading to incorrect node-counts. These combined with the fact that the topological analysis tools used in this work are designed for a circle and all the measurement sites have 1 m wide measurement circles allowing comparison resulted in this technique being abandoned.

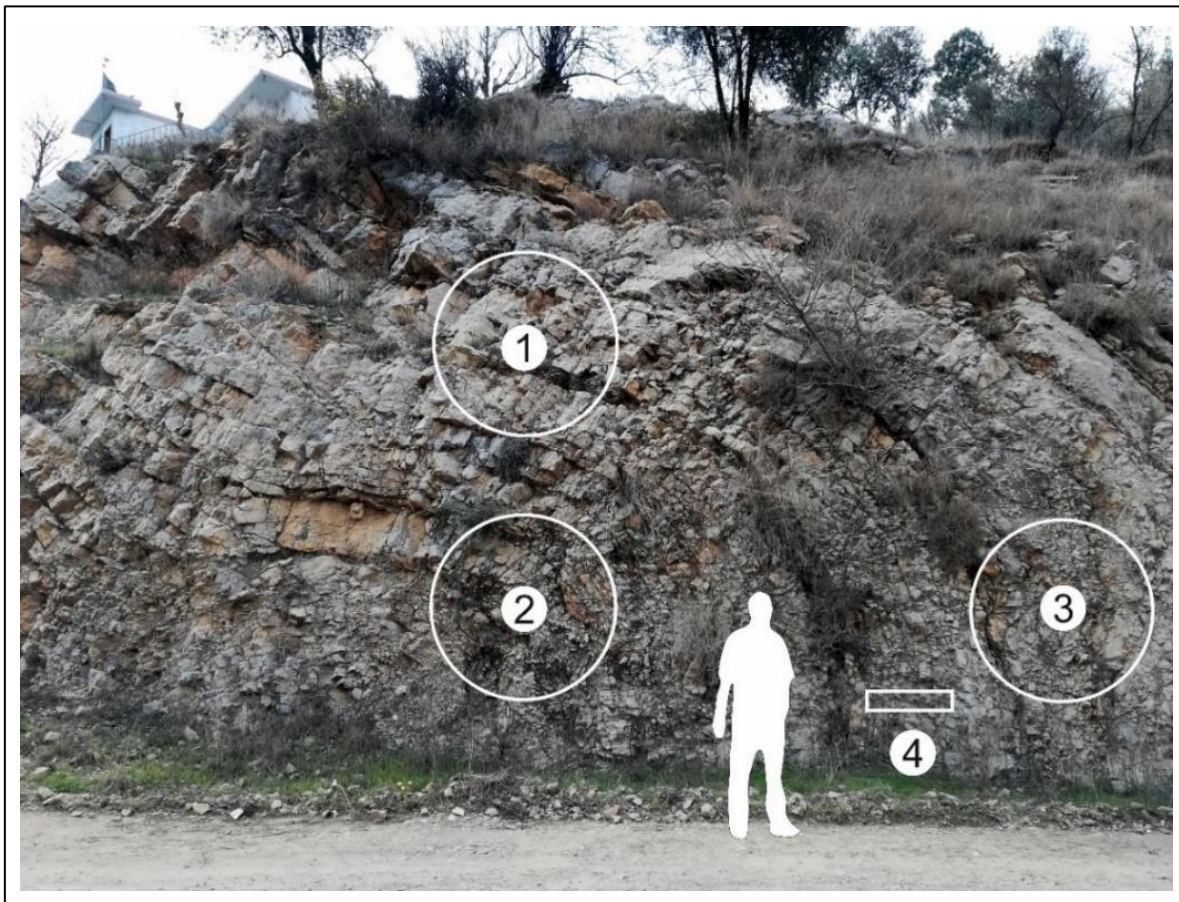


Figure 4.273: Photograph of site 7 showing the gently folded Lockhart Formation limestone and the well-developed typical fold fractures. See Figure 4.252 for location. Figure 4.274 is a line-drawing of the photograph. Geologist in white.

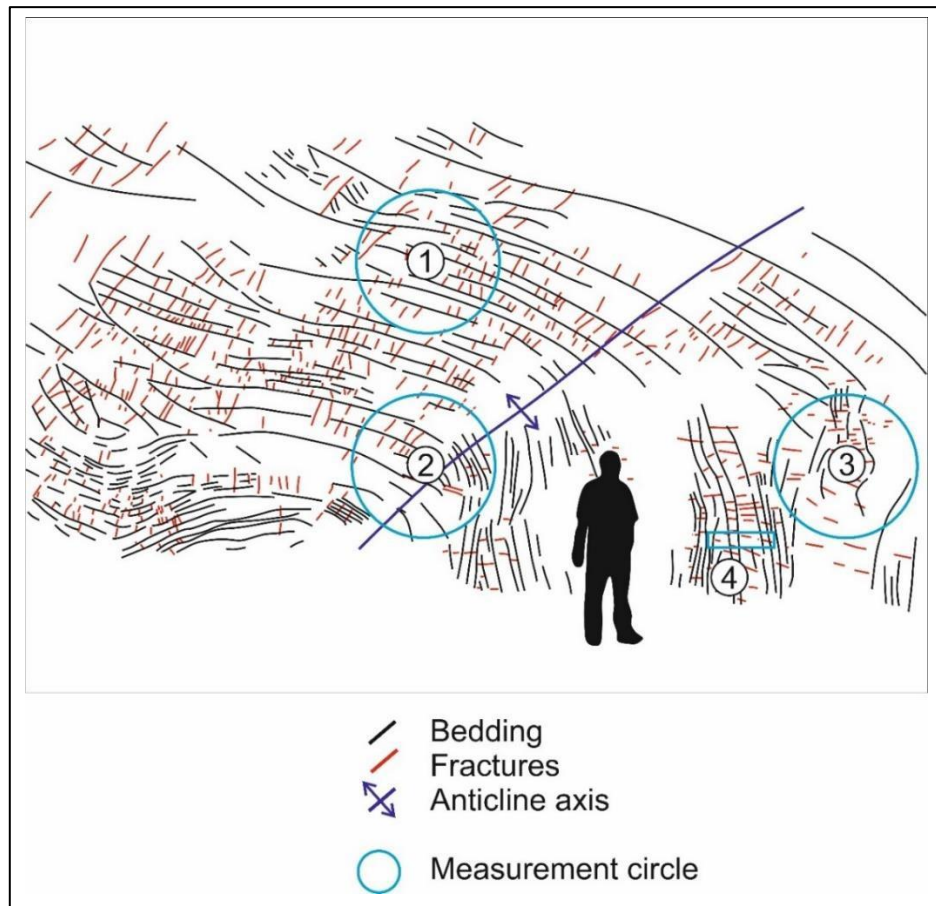


Figure 4.274: Line drawing of Figure 4.273. Bedding (which often has FF) and TL fractures within the beds are highlighted. The anticlinal axis and positions of measurement circles and strip are also shown. Geologist in black.

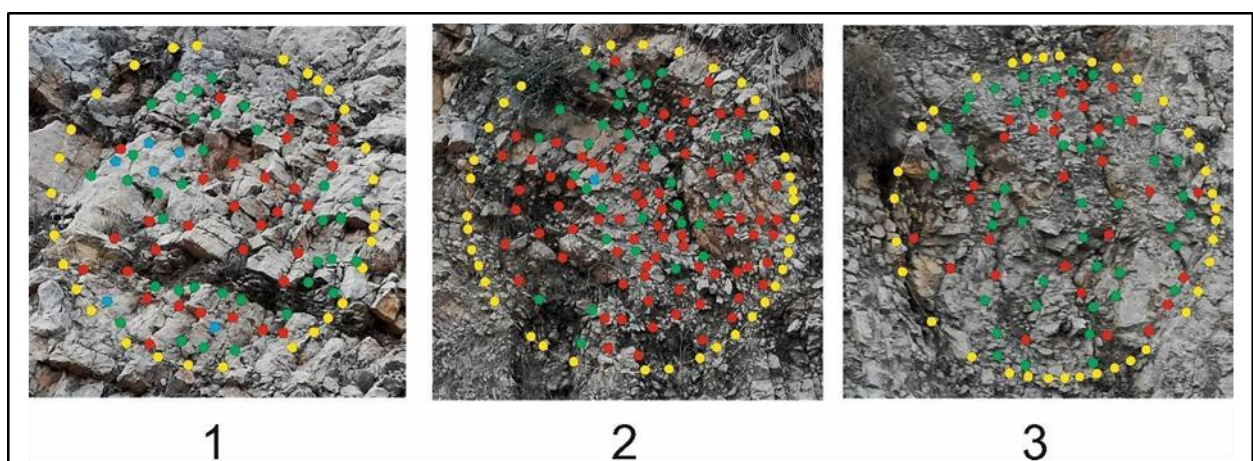


Figure 4.275: Circles at site 7. See Figure 4.274 for locations.

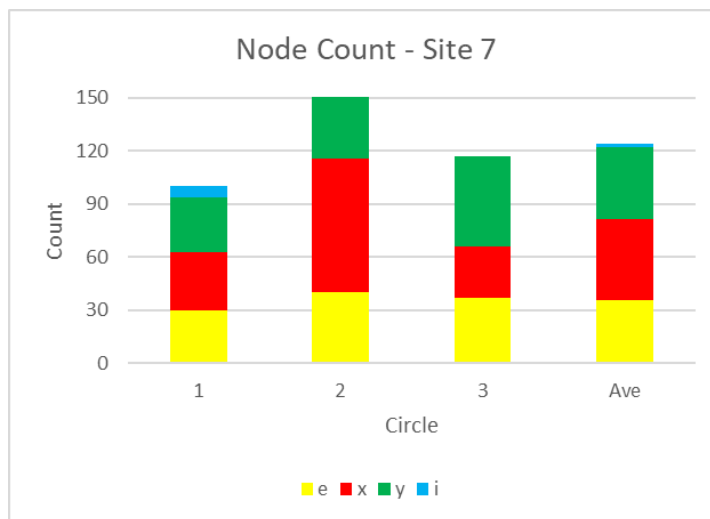


Figure 4.276: Node count, circles at site 7. The highest number of nodes is present in circle 2, on the anticline axis.

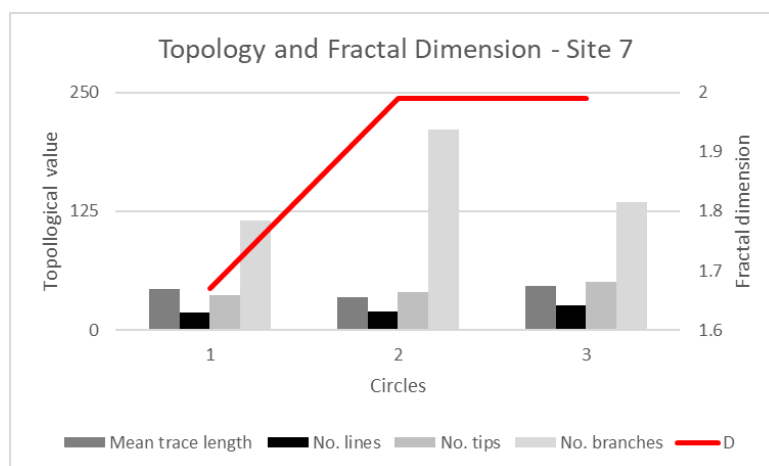


Figure 4.277: Topology and fractal dimension, site 7.

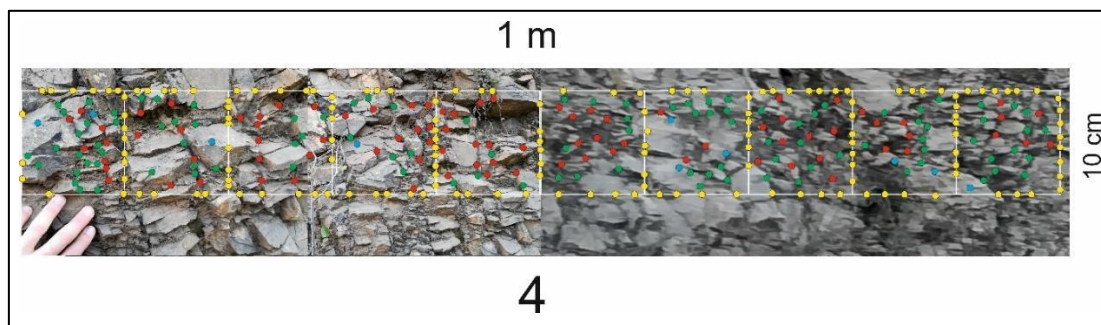


Figure 4.278: 1 m long horizontal measurement strip divided into ten 10 * 10 cm squares. See Figure 4.274 for location.

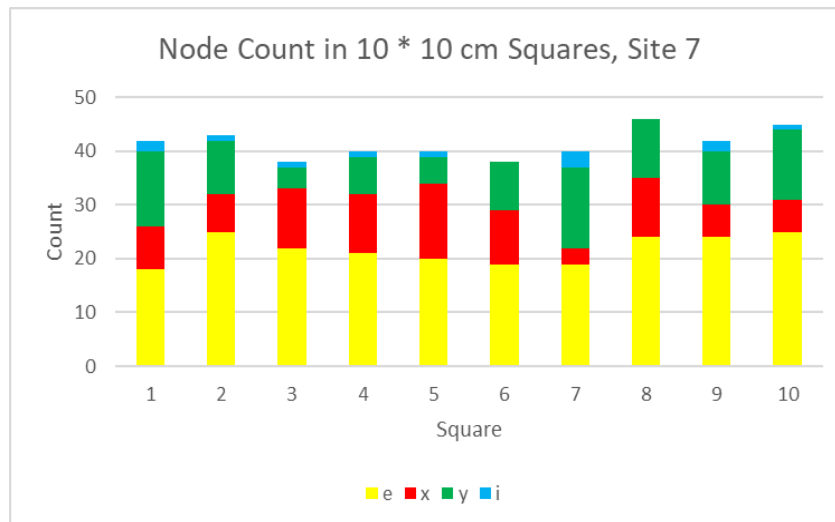


Figure 4.279: Node counts of the ten 10 * 10 cm squares at Position 4 in Figure 4.274.

4.2.6.8 Summary

The average number of nodes decreases towards the centre of the study area (site 4) and then increases again (Figure 4.280). Unusually, there does not seem to be a correlation between the stratigraphic unit and the number of nodes. Sites 4, 6, and 7 are all located within the Lockhart Formation but have quite different average numbers of nodes in their measurement circles (97, 196, and 124 respectively).

The northerly nodes have, on average, ten "i" node per circle and the southerly nodes have on average one "i" node. These patterns in node distribution may be associated with the local hinterland dipping backthrust duplex. The older thrust-blocks to the north may not have been as confined during their initial development. In contrast, the sites in the south are associated with a more restricted backthrust duplex and are hence more fractured.

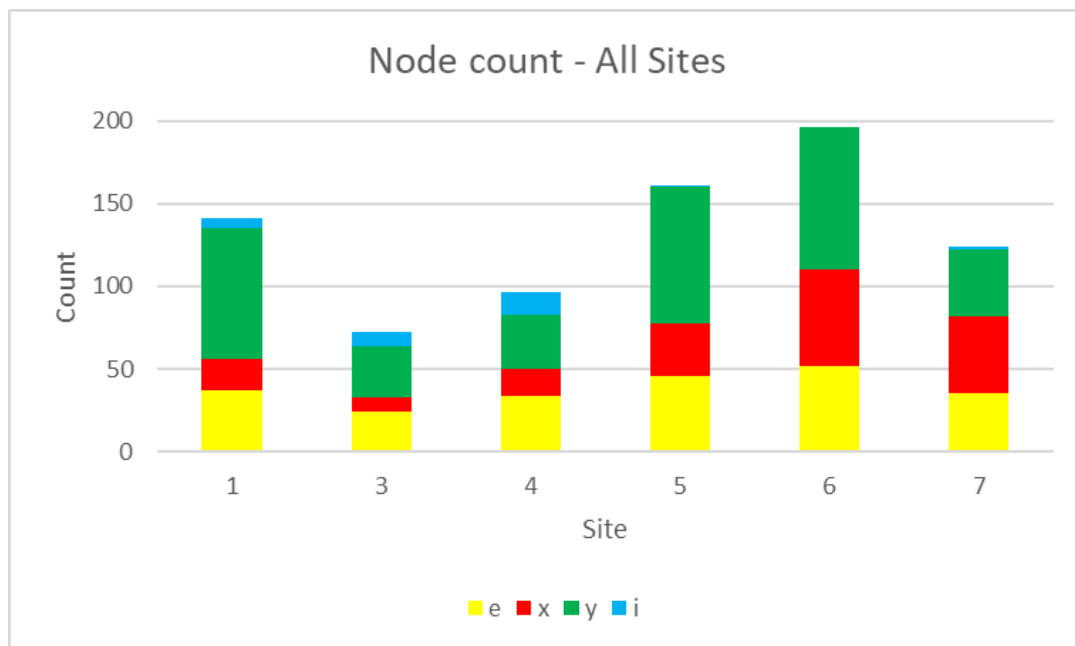


Figure 4.280: Node count of all sites in the Jabbri region. Sites run from north to south as shown on the sketch map on the right. See Figure 4.252 for details of the geology.

As there is very little variation in the fractal dimensions of the different sites and in all cases, it is extremely high (greater than 1.85), any conclusions about trends is not justified by the data. All that can be said from the fractal dimension information is that the rock is highly fractured throughout the area.

Topologically, there are a variety of trends (Figure 4.281):

1. The mean trace length is greatest at sites 3 and 4,
2. The number of lines is lowest at sites 3, 4, and 7,
3. Approximately half the number of tips at sites 3, 4, and 7 compared to the other sites, and
4. Half the number of branches at sites 3 and 4.

This suggests fewer, longer, less interconnected fractures at sites 3 and 4.

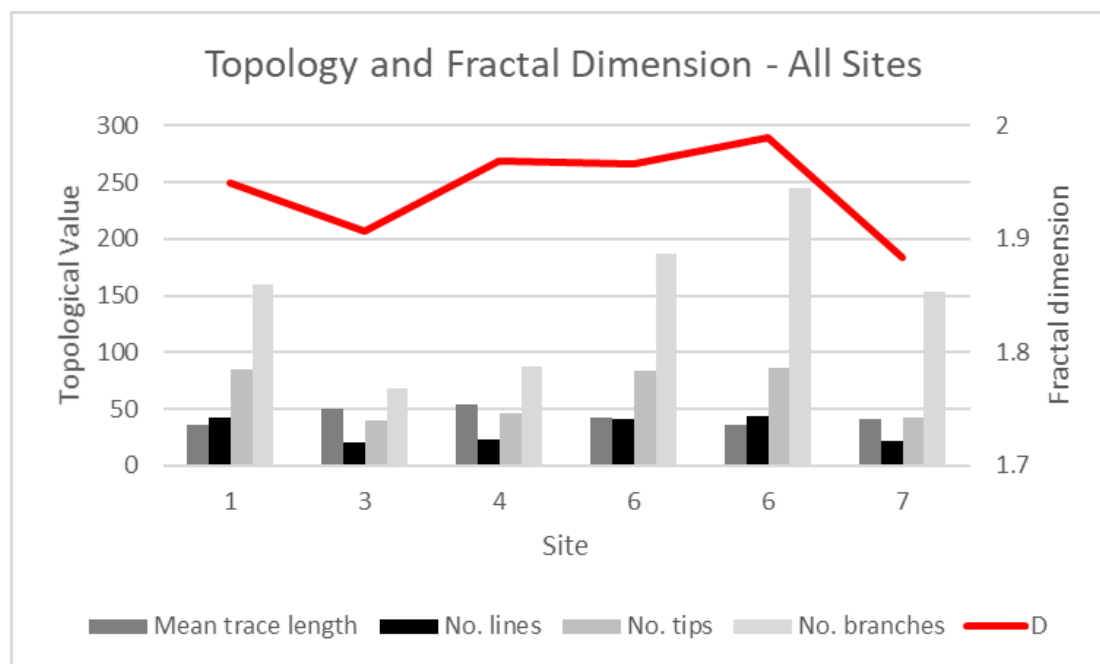


Figure 4.281: Topology and fractal dimension of all sites in the Jabbri region. Site numbers run from north to south.

When the average number of nodes is compared with the average fractal dimension, the large number of interbedded shales in the different sites cause the average fractal values close (all lie between 1.91 and 1.99), it is not possible to define any relationship between the average number of nodes and the fractal dimension of the different sites (Figure 4.282). This may be due both to the high degree of deformation at the measurement sites and the fact that all the sites are in a fore-thrust sequence. The lack of correlation between fractal dimensions and number of nodes is even more apparent when the values for the individual circles are compared (Figure 4.283). The best-fit curve of this data has a coefficient of determination of 0.17.

Unfortunately, because of the lack of correlation between the number of nodes and the fractal dimension, it does not allow meaningful predications of flow and mechanical properties of the rockmass. All that can be noted is that comparison of fractal dimension with the number of nodes has not allowed the recognition of any trends or clusters of fractures within the Jabbri area itself.

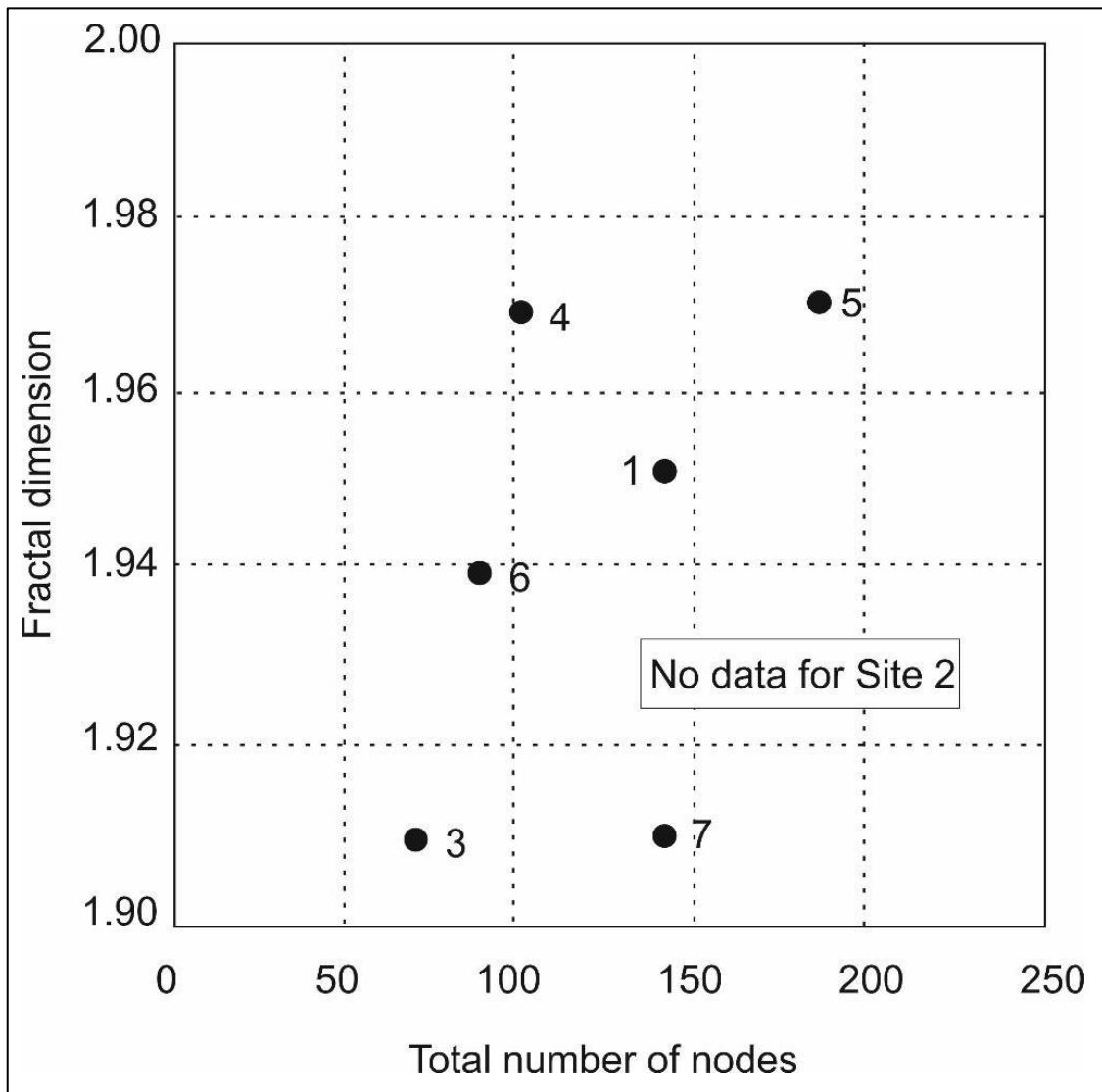


Figure 4.282: Average total number of nodes vs. fractal dimension at each site.

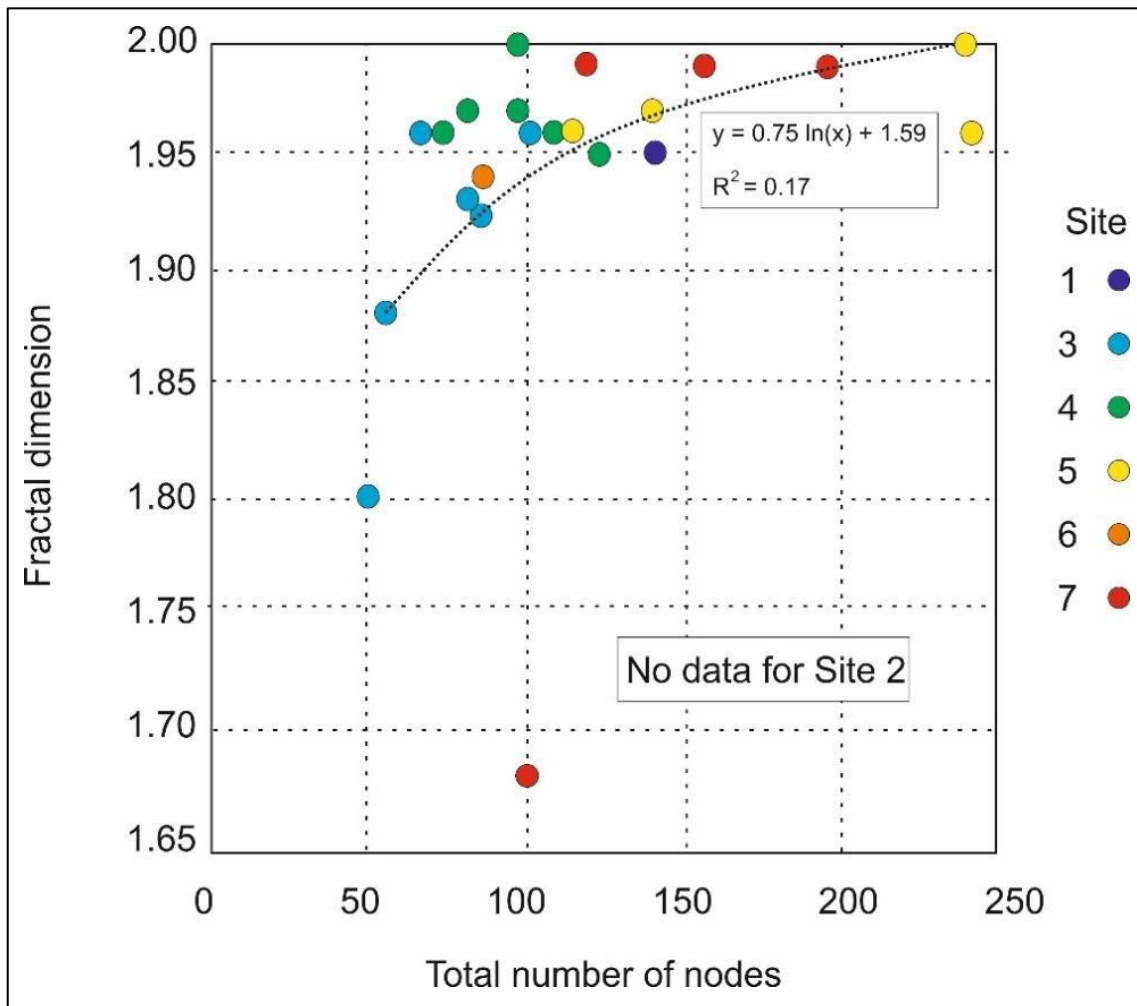


Figure 4.283: Total number of nodes vs. fractal dimension for all the circles at each site.

4.2.7. Changla Gali region

Different fracture sets at Changli Gali are intriguing – any thoughts on their formation?

The Changla Gali region is the most north-easterly portion of the study area and is located approximately 40 km from Islamabad, close to the village of Changla Gali (33° 59.6' N, 73° 23.0 E).

The oldest rocks of the Pakistan study area are reported either side of the measurement sites (Figure 4.284). The rocks include the Chichali Formation (of the Sugar Group) and the Samana Suk Formation (Williams *et al.*, 1999; Ali *et al.*, 2013).

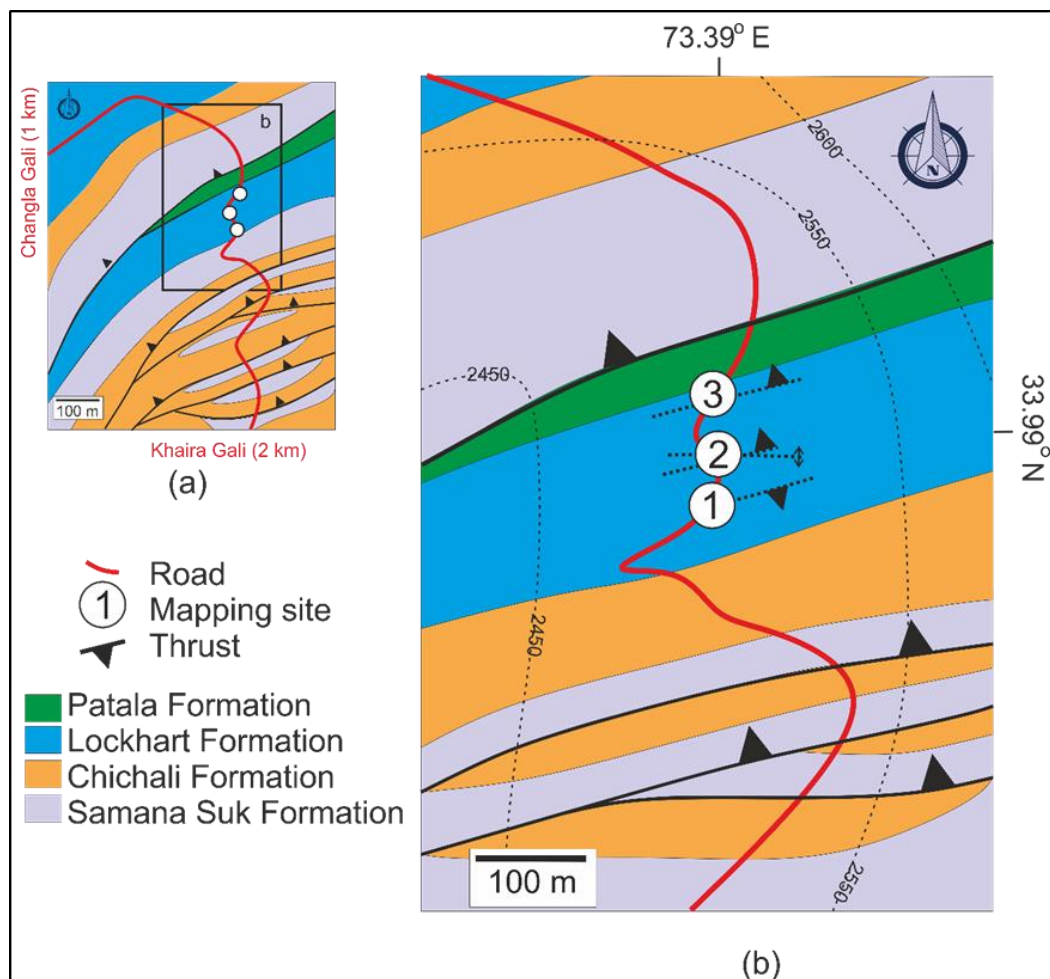


Figure 4.284: Geological map of the Changla Gali outcrop region (modified after Chambers, 1991).

Apparently several large thrusts are developed between the Samana Suk and Chichali as well a large thrust observed in the Lockhart Formation before it terminates against the Patala Formation in a thrust.

The Samana Suk Formation (Middle Jurassic) is a fossiliferous, dark grey limestone interbedded with subordinate greenish-grey marl. The Early Cretaceous (Neocomian) to Late Jurassic (Tithonian) Chichali Formation (Williams et. al., 1999) has been found some 300 m north of site 1 by Khan (2017) who describes the Chichali Formation as consisting of dark bluish-grey to black splintery carbonaceous shales and glauconitic fossiliferous sandstones and investigated the shales as potential hydrocarbon source rocks.

The study sites are positioned within the Lockhart Formation (Figure 4.284) which is the main unit mapped throughout the study area. By doing this, structural relationships on a regional scale can be examined without the variable of switching between stratigraphic units. In this area, the Lockhart Formation is a light grey, foraminiferal wackestone with occasional centimetre thick dark brown shale bands between packages of limestone approximately a metre thick. The overlying Patala Formation represents a gradual transition from shallow marine to lagoonal and subtidal settings. In this region it has a significant shale content and hence its deformational characteristics are different to that of the Lockhart Formation. Large-scale thrusts are present in the area (Chambers, 1991) bringing the Samana Suk and Chichali Formation on top of the Patala and Lockhart Formations (Figure 4.284). The focus of the current investigations is on the intra-formational thrusts within the Lockhart Formation. The fracture characteristics of three sites, approximately 150 m apart (Figure 4.285) are quantified using the standard methodology comprising identification of controlling geological features, identifying fracture sets, and measuring the fractal and topological characteristics of each set at the different sites.

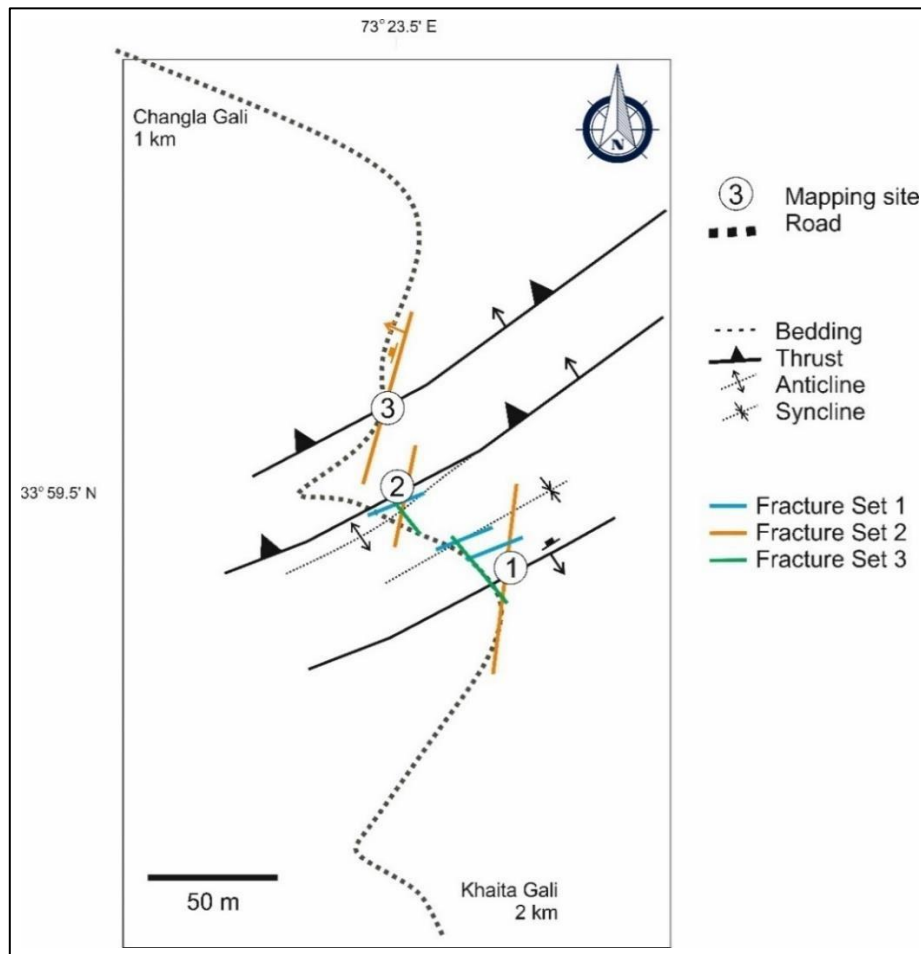


Figure 4.285: Location of study sites and orientation of major geological features at Changla Gali.

At site 1, a reverse fault is visible as well as examples of Fracture Set 1, Set 2, and Set 3 (Figure 4.286). A single circle (Figure 4.286) was mapped at this site. A series of different node and fracture measured at finer and finer scale to account for the significant number of the Set 3 features on the data-set. The large-scale measurements were mapped at the outcrop, followed smaller scale measurements from the measurement circle and finally a series of 10 cm squares analysed within the circle to define the characteristics including those of the Set 3 fracture surface (Figure 4.287).

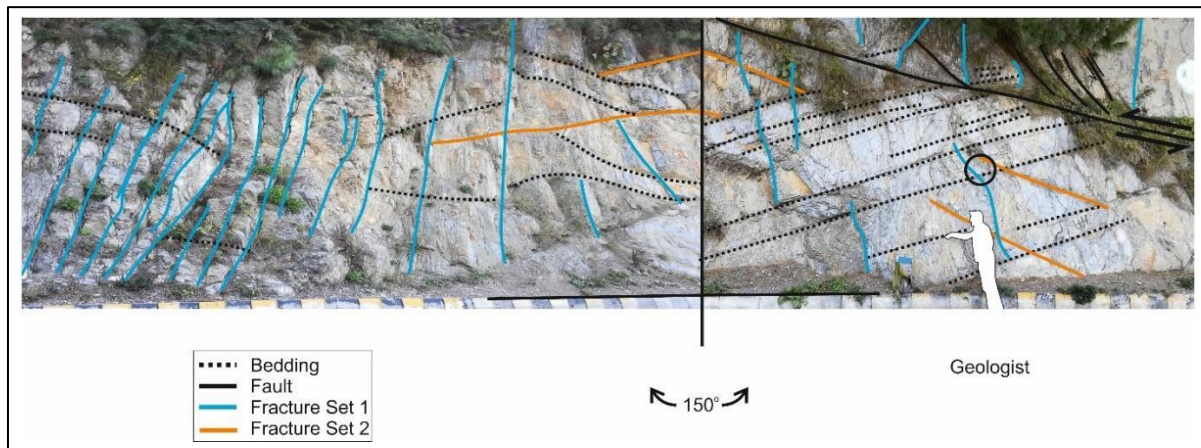


Figure 4.286: Photo-mosaic of site 1, Changla Gali. The majority of the surface visible in this image is the surface of Fracture Set 3. It is not coloured in as it would not be possible to see any other features. Fracture Set 2 surfaces are also sub-parallel to the orientation of the photograph, but terminations of the fracture plane are visible as lines. Note, the reverse fault is southward dipping and hence has the opposite sense of movement to the thrusts at site 2 and 3. The circle above the geologist's head indicates the position of the 1-metre-wide mapping circle.

The smaller squares were used to determine an equivalent area as to that of the normal 1 m wide measurement circle (Figure 4.287).

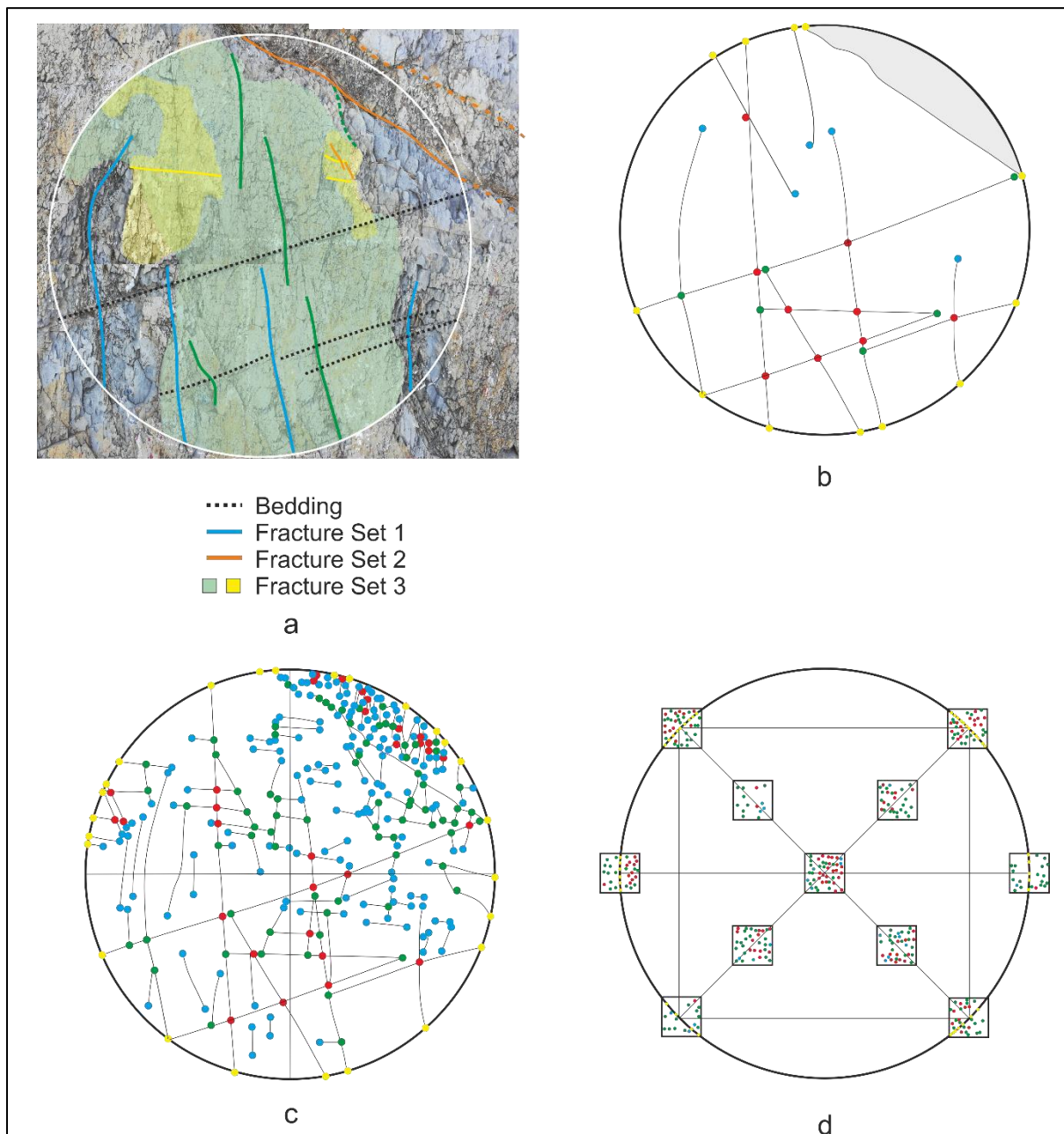


Figure 4.287: Fractal and topological mapping of site 1, Changla Gali, at different scales. (a) Photograph with different fracture sets indicated – note how Fracture Set 3 covers the majority of the circle; (b) large-scale fractures; (c) smaller scale fractures (only visible with later analysis of photographs); (d) detailed analysis of fractures in 10 cm * 10 cm squares to examine the effect of the intense fracturing on the surface of Fracture Set 3. “e” nodes are coloured yellow, “x” red, “y” green and “i” blue as they are throughout the thesis.

Due to the fact that the total number of nodes increases by orders of magnitude as the resolution is increased, the topological characteristics of the number of branches and tips, fracture density, and intensity follow a similar pattern, (Table 4.17). Connectivity at a large scale and at a detailed level is similar, where-as the small-scale analysis shows a much lower degree of connectivity. The detailed evaluation produces a fractal dimension of 2. This is because each of the 10cm by 10 cm squares used to estimate the characteristics of the surface had approximately 30 nodes. Thus, at the smallest box size of 5 cm used in the calculation of the fractal dimension there would always be a fracture. This shows that it is incorrect to include the data from a fracture surface parallel to the measurement circle as this will disguise any other fractal relationship that might be present.

Table 4.17: Topological characteristics of the different measurement scales at site 1.

Mapping circle	Large-scale	Small-scale	Detailed
Connectivity	5.60	1.72	5.54
Fracture Intensity	6	13	99
Fracture density	3.02	41.86	350.14
Mean trace length	0.63	0.10	0.09
No. lines	5	116.5	735.5
No. tips	10	233	1471
No. branches	28	247	3501

At site 2, an anticline is developed over a thrust-tip (Figure 4.288), which indicates that another thrust must be developed within the Lockhart Formation. All three fracture sets are present at this exposure (Figure 4.285), allowing the reason for their orientations to be determined. Fracture Set 1 is developed parallel to the anticline axis (and also the thrust) whilst Fracture Set 2 and 3 are developed at approximately 60 and 120 degrees to the fold-axis, thus representing synthetic and antithetic fracture sets. It is likely that these initial fractures have been re-exploited and further sheared during continued compression. Five measurement circles (Figure 4.289) were analysed at this

site to determine the variation in fracture patterns associated with parts of the anticline and parts of the thrust, including the footwall and the thrust-tip. Figure 4.290 illustrates that the greatest number of nodes is present at the thrust-tip (circle 5) followed by the thrust (circle 4). The topological analysis shows corresponding results (Figure 4.291). The thrust-tip has triple and the thrust has double the fracture intensity of the other measurement circles. The fracture density in the thrust-tip is twice that of circles 1 to 3. In fact, the thrust tip has the highest topological values for all categories, except for connectivity, where the thrust itself has a higher value. The thrust and thrust-tip have fractal dimensions of 1.98 and 1.99 respectively compared to the values of 1.85 and 1.84 of circles 1 and 2 at the edge and centre of the anticline.

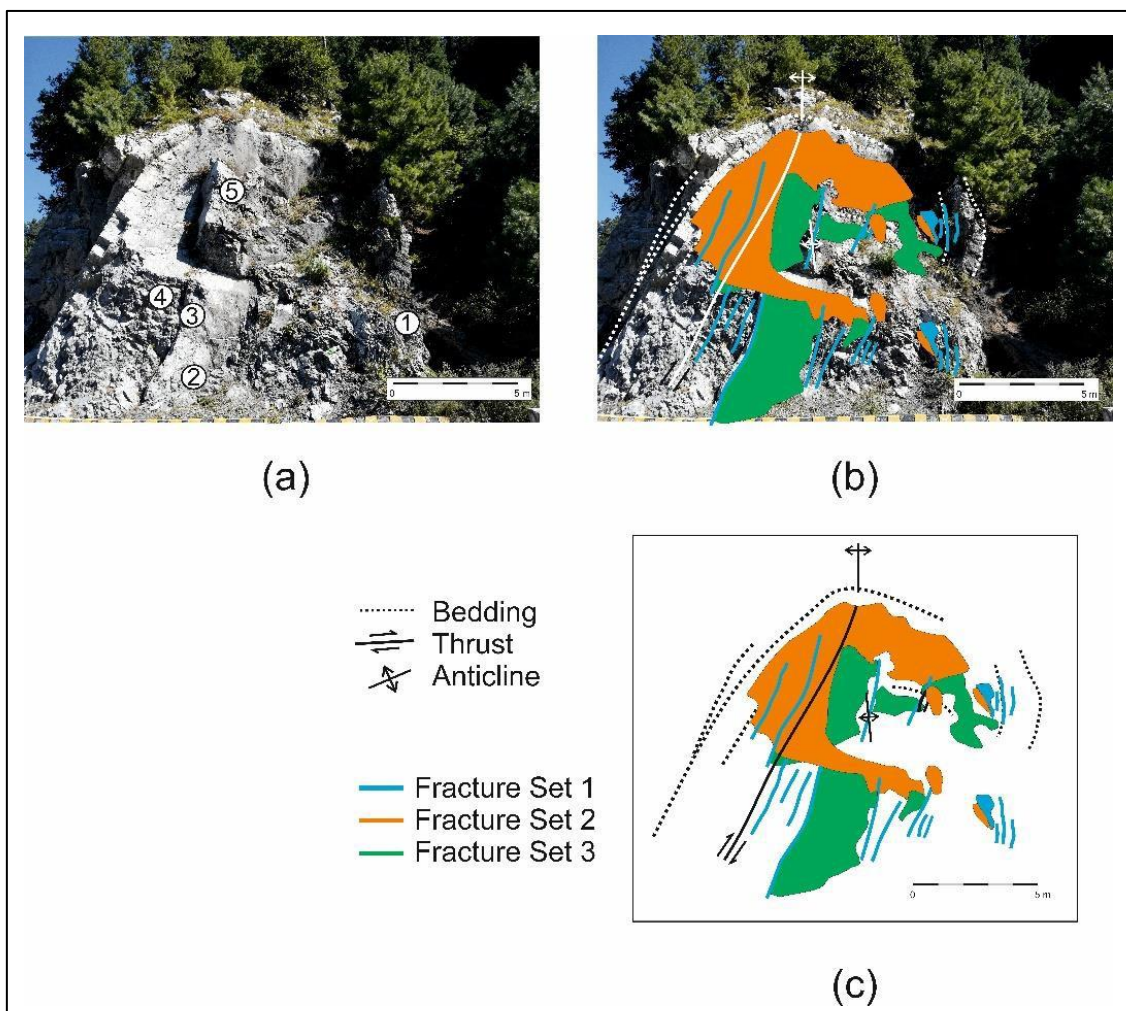


Figure 4.288: (a) Photograph of thrust and anticline at site 2, Changla Gali; (b) interpretation of fracture orientations; (c) line diagram of bedding, thrust, anticline and fracture surfaces.

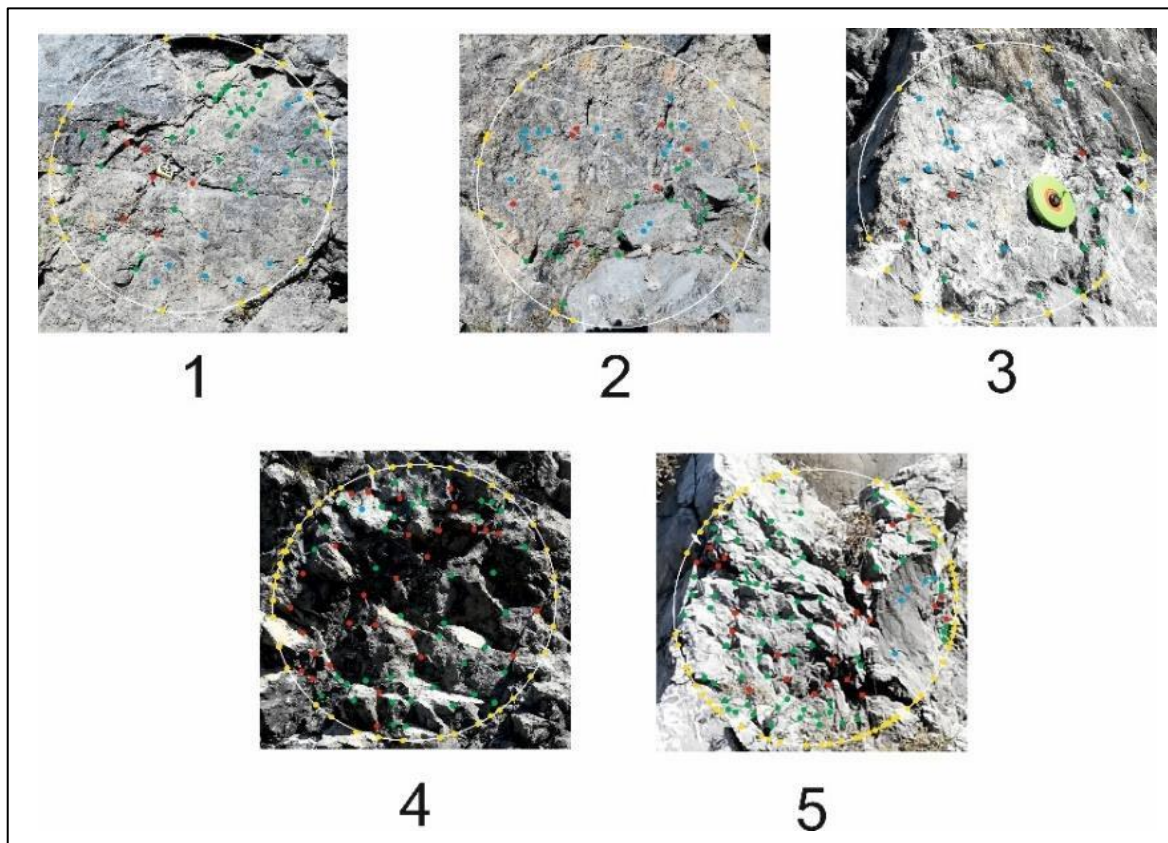


Figure 4.289: Measurement circles at site 2, Changla Gali with nodes indicated. The position of the measurement circles is shown in Figure 4.0.288 (a).

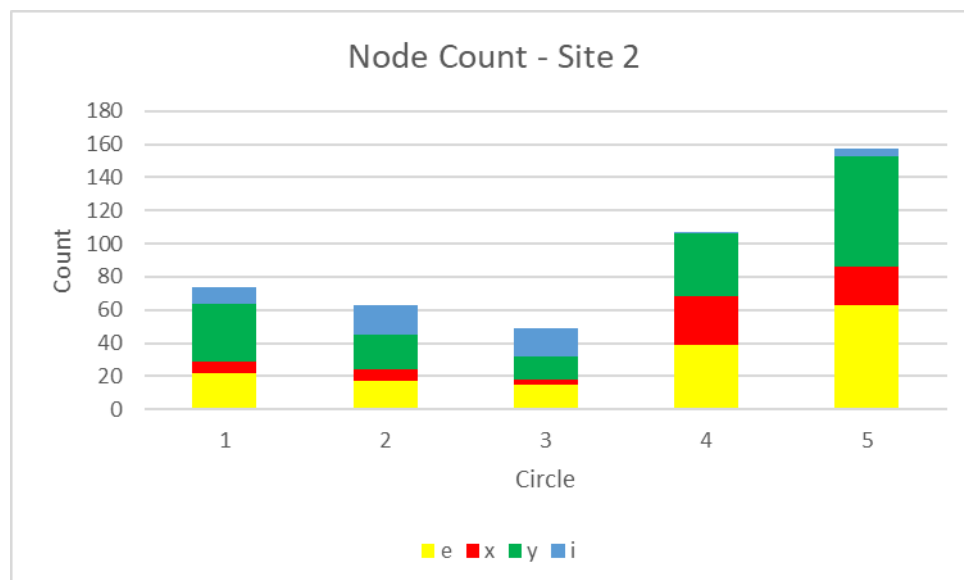


Figure 4.290: Node count at site 2, Changla Gali. The greatest number of nodes is in circle 5 (thrust-tip anticline) followed by circle 4 (thrust).

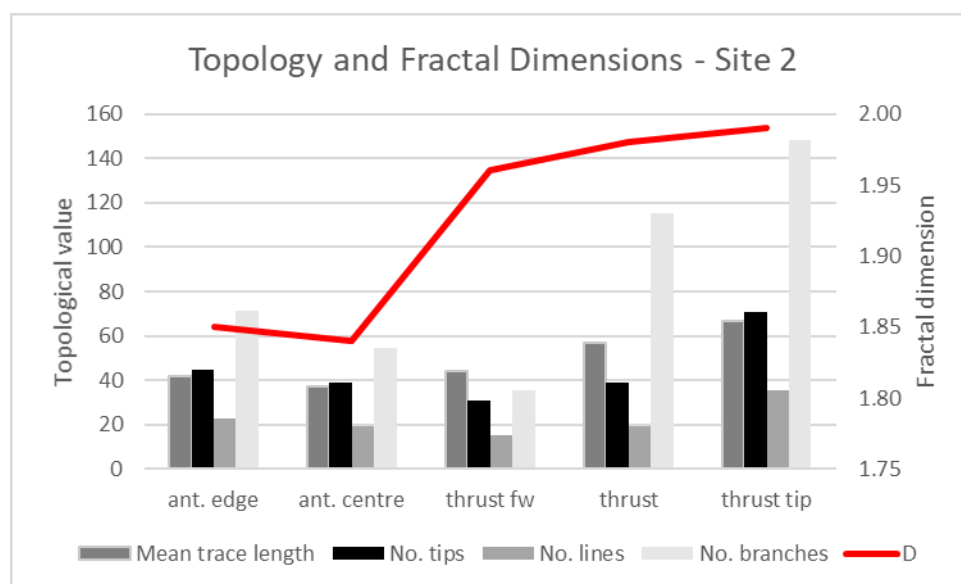


Figure 4.291: Topological and fractal characteristics of the measurement circles at site 2, Changla Gali. "ant." is an abbreviation of anticline. Note separation of data into those circles related to the anticline and those related to the thrust.

At site 3, a large, 6 m wide thrust is present (Figure 4.292). Examination of the limestone either side of the thrust reveals that it is an intra-formational thrust in the Lockhart Formation. The Patala Formation is exposed approximately 5 m to the north in the hanging-wall of the thrust. Elsewhere in the field area, the thrust would have been likely to be sited on the contact between the Lockhart and Patala formations. This suggests that a greater amount of thrusting has occurred in the northern portion of the field-area. This may be due to structural variation with the strike of the strata trending to the north-east and the site being further from the Main Boundary Thrust (Figure 3.16). It may also be due to the different rheological properties of the different rocks that are interacting at Changla Gali.

As at site 3, many of the fractures are obscured by a surface parallel shears - in this case those of Fracture Set 1. These clearly pre-date the thrust which cross-cuts them. If the other two fracture sets formed contemporaneously, perhaps due folding around the thrust-tip they would also pre-date the emergence of the thrust at this higher level.

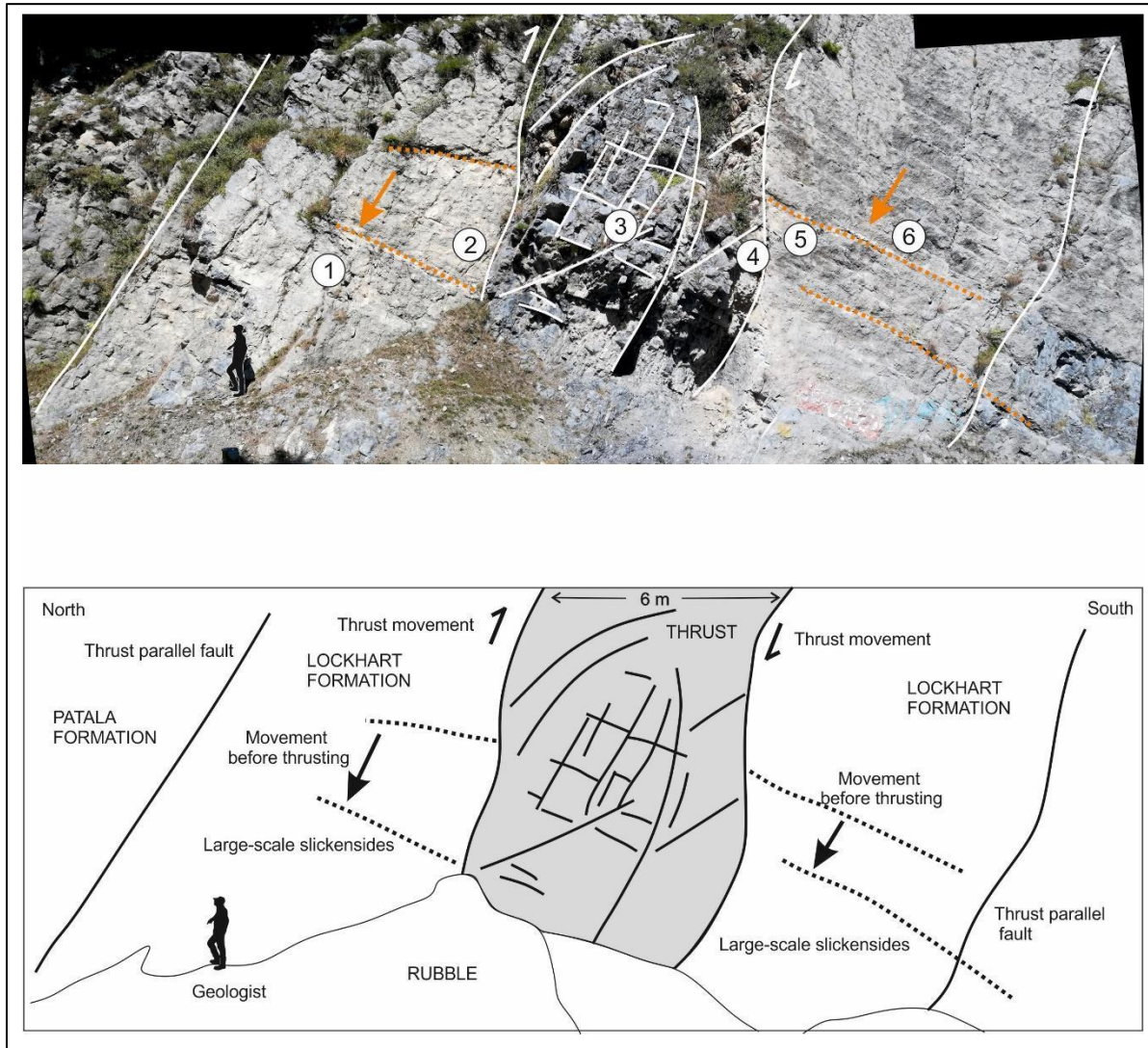


Figure 4.292: Photo-mosaic image and corresponding line drawing of site 3, Changla Gali. The positions of the measurement circles are shown on the photo-mosaic.

Six measurement circles (Figure 4.293) were evaluated in the Lockhart Formation across the hanging-wall of the thrust, the thrust, and the footwall of the thrust to determine if variations relative to the thrust could be discerned. Although the total number of nodes is similar in each circle, the number of “y” nodes is higher closer to the thrust and the number of “i” nodes increases further away from the thrust (Figure 4.294). The thrust (circle 3) has the highest connectivity, fracture intensity and longest mean trace length (Figure 4.295). Away from the thrust, there is a decrease in connectivity, intensity, and mean trace length and an increase in number of lines. The number of tips increase away from the thrust – the greatest difference in the number of tips is however only 9 (between the thrust (36) and

the footwall (45)). Fractal dimensions are range from 1.94 to 1.96. The two lowest dimensions (1.94) are in the footwall of the thrust which is unusual because the fracture density is highest in the footwall. The measured characteristics the various parts structure is similar. The differences of the characteristics of different structures is likely to be greater than that within a single structure.

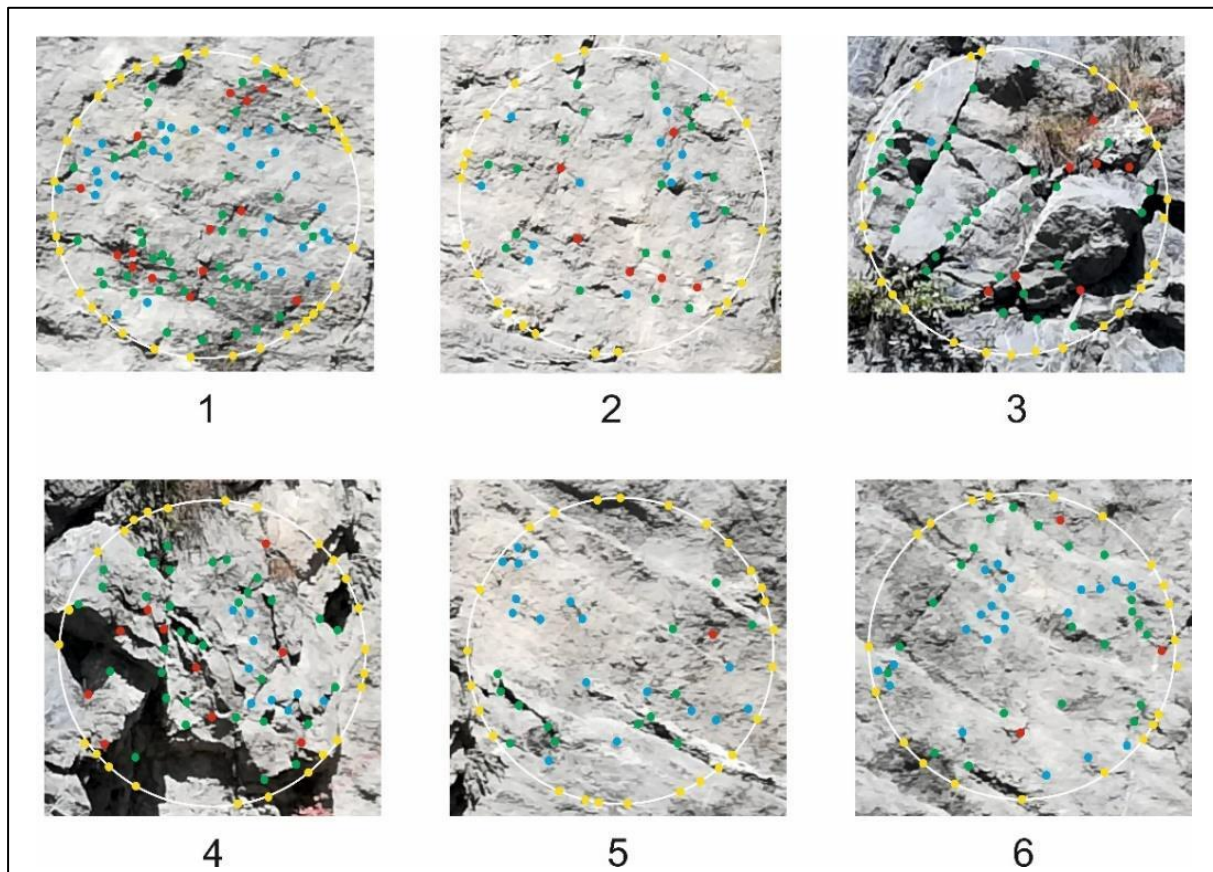


Figure 4.293: Measurement circles from site 3, Changla Gali. See Figure 4.292 for their positions relative to the thrust.

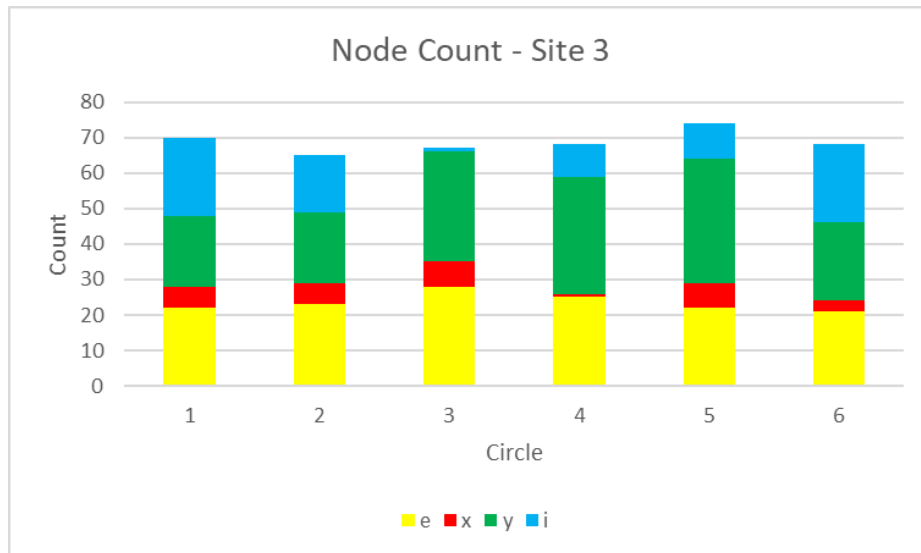


Figure 4.294: Node count at site 3, Changla Gali. The total number of nodes is similar in each circle. The number of “y” nodes is higher closer to the thrust (circle 3) and the number of “i” nodes increases further away from the thrust.

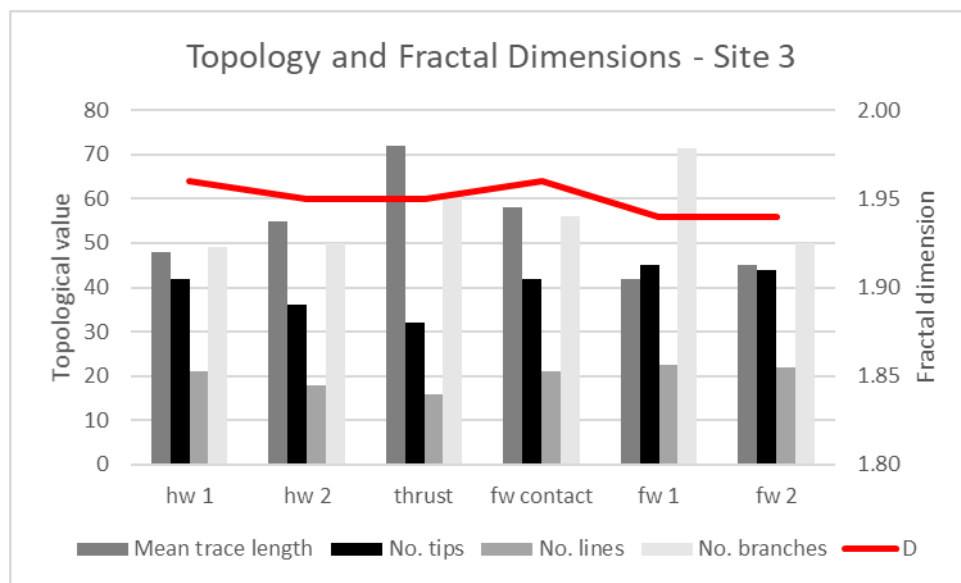


Figure 4.295: Topological and fractal characteristics of the measurement circles at site 3, Changla Gali.

By comparing the number of nodes with the fractal dimension, characteristics of the individual fracture sets and the various sites can be evaluated (Figure 4.296). At site 1, the effect of measuring at higher and higher detail is evident with the exponential increase in the number of nodes producing

a logarithmic curve (Figure 4.296). This curve has an excellent fit ($R^2 = 0.97$), however there are only three data points. The characteristics of five different structural features are evaluated at site 2. As expected, these do show variations with, for example, the thrust-tip having the greatest number of nodes and highest fractal dimension (Figure 4.296). When considered together, the data form a tight cluster, indicative of a single structural regime. The data from site 3 are even more tightly clustered (Figure 4.296 and Figure 4.297). When comparing the topological values and fractal dimensions of the various sites against each other, it is necessary to use the broad-scale values of site 1. The site has a low fractal dimension and long mean trace length; all other topological parameters have lower values than the other two sites. The topological values and the fractal dimensions are very similar for sites 2 and 3. It is only the number of branches that varies much between the sites, and this is due to the high number of branches at the fracture-tip.

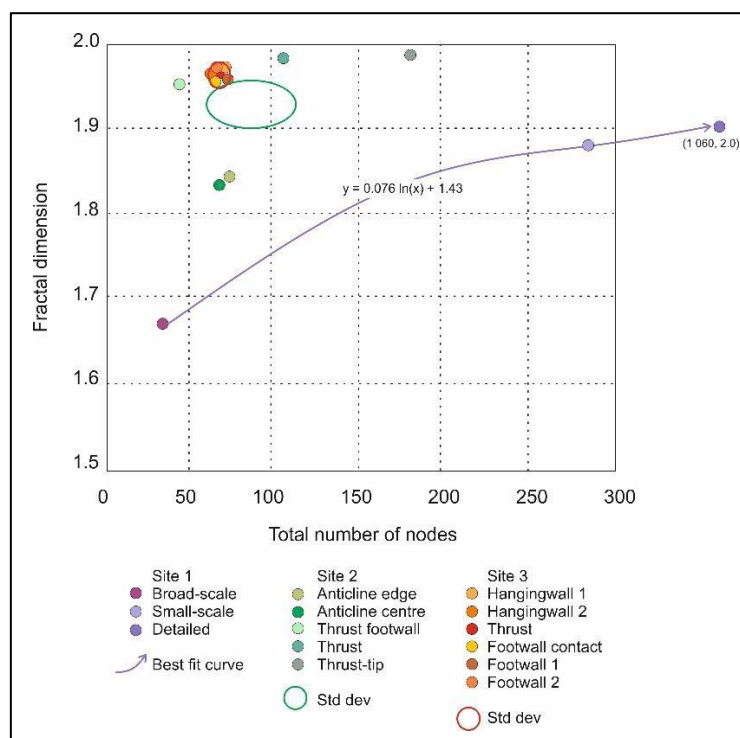


Figure 4.296: Distribution of the total number of nodes versus fractal dimension used to identify groupings. Site 1 does not have any grouping, the “detailed” point is (1 060, 2.0), far to the maximum x of the graph. The data from both sites 2 and 3 show little dispersion and lie close to each other, indicating the similarity in the structural environment.

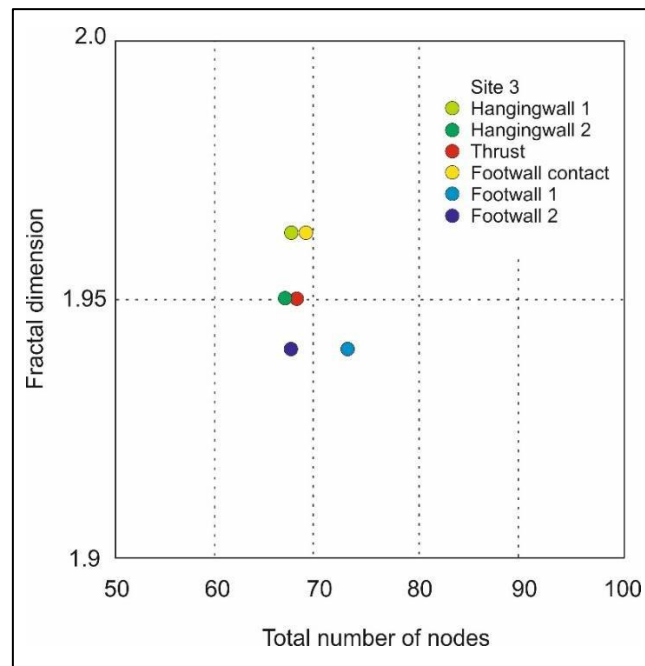


Figure 4.297: Tightly clustered data from site 3, Changla Gali. The standard deviation of the total number of nodes is only 3 and that of the fractal dimension only 0.01.

5. Interpretation of fractures

In this chapter, the fracture data presented in Chapter 4 are interpreted to relate fracture characteristics and their spatial arrangement to the structural domain (back-thrust, fore-thrust, pop-up structures, anticlines, synclines, and overturned anticlines) in the frontal thrust belt north of Himalayan Main Boundary Thrust in the field area. In the interpretation presented, different types or sets of fractures are not separated using composition, orientation, or termination styles, as none of these attributes are considered likely to be unique to a given set of fractures formed in response to a single deformation event. Instead, fractures are considered in terms of their spatial distributions and their topological characteristics. The hypothesis posed at the beginning of the study was that by combining an analysis of the spatial distribution of the fractures in fracture networks as discrete objects, such as fractal dimensions, with topological analysis (to characterises the connectivity of the constitutive fractures) in that network (Sanderson *et al.*, 2019) would provide new and potentially unique insights into the relationships of the fractured rock-mass in various structural domains within a fold and thrust belt. As the fractal dimension and topological characteristics measure different dimensions (space and intersections), the analysis of a fracture network is better defined (Sanderson *et al.*, 2019). These combined approaches have provided a comprehensive, quantified set of data to interpret the characteristics of the different fracture networks and predict fracture patterns in the inaccessible remote of the field study area with the same fractal and topological characteristics. By considering the topological characteristics and the fractal dimensions of all the fractures together, all the discontinuities and intersections are included, and the true complexity of the rock-mass can be determined.

Such an approach is inherently better at unravelling how the cumulative effects of successive tectonic stresses discriminate between different characteristics of the rock-mass. The focus of this interpretation is to understand the spatial and connectivity relationships of the whole fracture population in the context of the wider structural scale. In addition, the field observations have shown

that rock fracture behaviour is highly dependent on the amount of shale, equivalent to the term 'volume of shale' or V_{shale} , that is an estimate of the rock's shale volume from the gamma ray log from a wireline log in a borehole (Miaha, 2014). As the topological and fractal characteristics are different for the different types of rocks, it may be possible to determine the fracture patterns from the V_{shale} of the wireline log. The limestone sequences are typically tightly bound by secondary microspar cement during diagenesis.

Due to the low clastic-mud content of most of the limestones, a result of pervasive microspar precipitation and recrystallisation that tightly cements the limestones, they are mechanically strong and brittle. It is this brittle nature of the limestones that results in the extreme deformation and fracture intensity of the limestone packages. The interbedded discrete clay units (effectively shales) by contrast are characterised by ductile deformation and the presence of calcite cemented veining. Strong lateral shearing is present in areas such as fore-thrusts, which often occur with shale bands.

5.1 Fractures and lithology

The sediments in the study area were deposited within a closely related suite of depositional environmental settings spanning from a coastal-lagoonal setting to the middle ramp (shallow open marine) sedimentological range along a carbonate-dominated shoreline. The detailed characteristics of the limestones in the different rock assemblages from ramp to lagoon facies are very similar (see Figure 5.1) but differ mainly in the proportions of lime mudstone and bioclastic debris (e.g., Khawaj *et al.*, 2018; Rehman *et al.*, 2016). The different formations of these assemblages are described in Chapter 2 (sections 2.3., especially Figure 5.2.4). The various limestones are defined by the presence of specific algae and foraminifera (Khawaj *et al.*, 2018; Swati *et al.*, 2013). There are no reefs recognised in any these ramp limestones (Kendall and Flood, 2011) and corals are rare. Most of the framework bioclasts are foraminifera, dasyclad algae and gastropods. Bioturbation is common with

several trace fossils being recognised, which result in the sediment texture being pervasively homogenised (Khan *et al.*, 2018). The majority of the limestones were deposited on the middle ramp, within the influence of wave action, except for the Patala Formation and the Chorgali Formation sediments, which indicate deposition in increasingly shallow water such as a lagoonal and potentially supratidal environments (Fahaad *et al.*, 2021; Mizra *et al.*, 2022). The detailed characteristics of the different formations of the sedimentary succession are described in Chapter 2 (section 2.3.1).

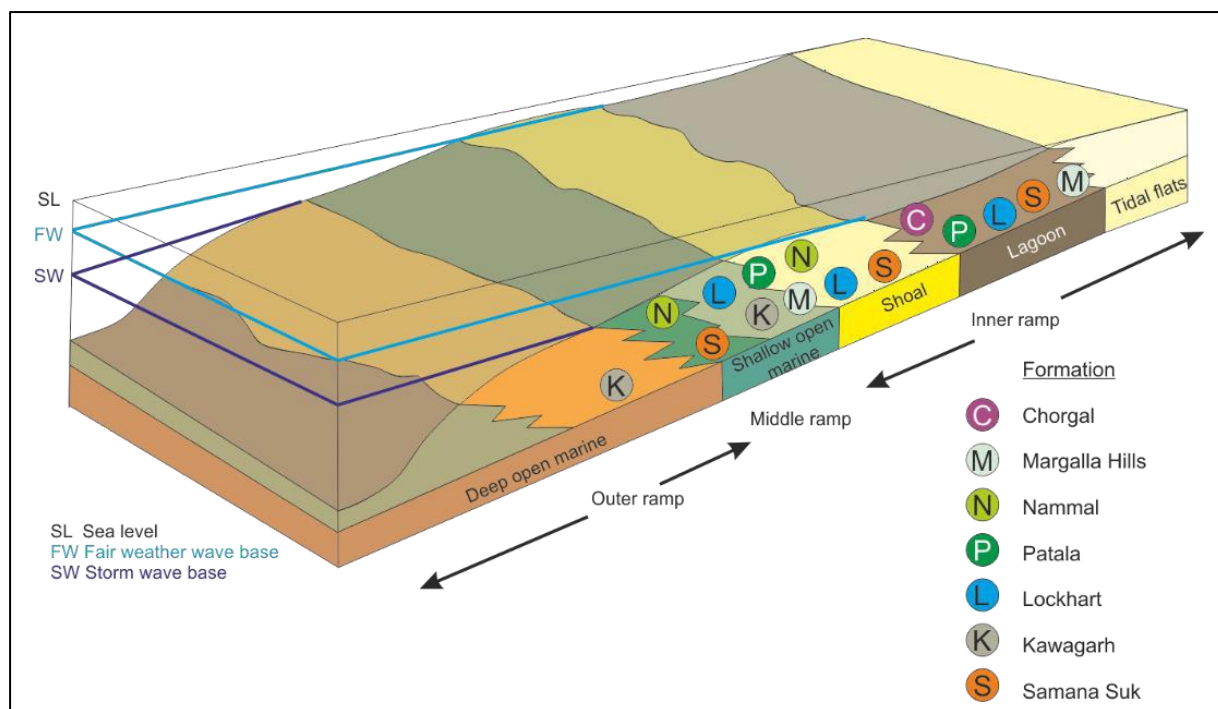


Figure 5.1: Distributions of the closely spaced depositional environments in the study.

Shale is present in the stratigraphy of the Palaeocene limestones ranging from the Kawagarh Formation (Rehman *et al.*, 2021) through to the Chorgali Formation (Awais *et al.*, 2020) as discrete layers of a dark brown coloured, fine-grained clastic mud that is a mixture of clay minerals and silt-sized particles, especially quartz and calcite, (Chapter 2) separating lime mudstones and wackestones in the ramp limestones, especially of the Lockhart and Nammal formations (Figure 5.2).



Figure 5.2: Typical ramp limestone sequence within the Patala Formation showing cleaning-upwards beds of wackestone separated by dark brown, highly deformed shale. The thin interbeds of shale decrease in frequency with thicker limestone beds (site 5, Jabbri region).

The shales are fissile and usually highly deformed, concentrating strain in the form of shear zones and folds. The shales range between 0.5 and 2m in thickness, and they typically split into beds of less than 1 cm thick, which has a significant effect on the fracture patterns (Figure 5.2). The strong bioturbation fabrics (Figure 5.4) further contribute to homogenising the sediment fabric, combining thinly bedded limestone and shale.



Figure 5.3: Light-coloured wackestone displaying transitional longitudinal (TL) fractures, with dark shale layers deformed by flexural flow (FF) to fill the void created by the initial TL fracture of the wackestone. TL fractures do not propagate through the shale, but instead develop as bedding parallel shears such as this outcrop in the Nammal Formation (site 2, Makhniyal region).



Figure 5.4: (a) Bedding parallel Thalassinoides ichnofossils visible as prominent branching tubes protruding above a bedding plane within the Nammal Formation (site 1, Talhaar region); (b) Small chondrites type ichnofossils visible as light grey tubes within a foraminiferal wackestone of the Lockhart Formation (site 8, Najafpur region).

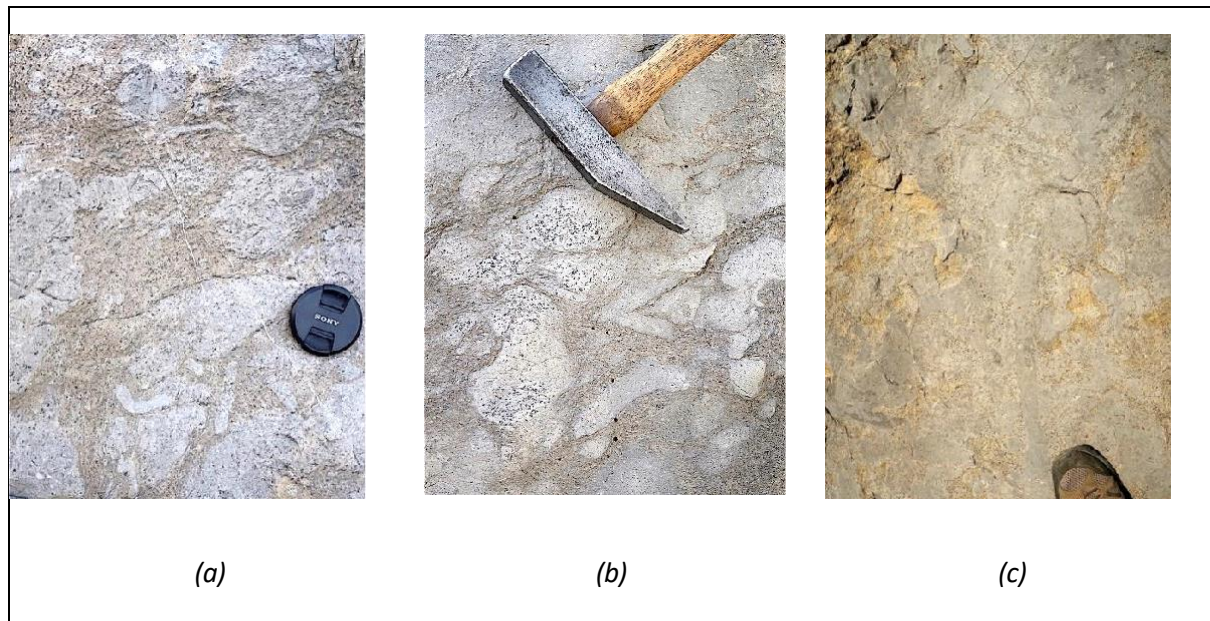


Figure 5.5: (a) Discrete burrows within fine grained argillaceous wackestone of the Margalla Hills Formation (b) nodular appearance of the lower part of the Margalla Hills Formation produced by intense bioturbation. (c) large horizontal burrows resulting in a strongly mixed wackestone texture of the Lockhart Formation. From Burley, 2022.

These observations are the basis for the logic to categorise the rocks based on the proportion of limestone and shale that can be approximated in the field from hand specimen observation (Table 5.18 and Figure 5.7). The different amounts of limestone and shale and other minor constituents (such as vein-quartz) are determined by the areal coverage of the measurement circles which were mapped in a variety of orientations. This enabled the percentage of shale to be estimated in the combined rock assemblages.

Importantly, the limestones in the field area have no significant intergranular porosity, which has been excluded due to both pervasive early diagenesis including recrystallisation (Chapter 4, sections 4.1, 4.2, 4.3, 4.4 and 4.5). During the early diagenesis of lime muds, the calcium carbonate matrix is transformed to micrite and subsequently to microspar cements (Figure 5.6). Microspar is formed by the conversion of high magnesium calcite (micrite) to inequigranular low magnesium calcite, that is microspar (Mosher, 1989; Munneke, 1997; Lucia and Loucks, 2013). In the limestones studied, early

diagenetic micritisation, cementation, neomorphism and recrystallisation followed by compaction during mesogenesis has completely destroyed any remaining primary porosity and permeability, to be replaced by secondary fracture-controlled porosity and permeability (Khan, 2018; Shoaib *et al.*, 2022). Recrystallisation of micrite to microspar with no visible intergranular porosity is now pervasive in all of the studied limestones (Cheema, 2010) such that most of the limestones now have a uniform microspar microfabric (Chapter 4, as illustrated in sections 4.1.3, 4.3.1 and 4.3.6). These diagenetic processes homogenise the texture and strength of the limestones such that their response to stress is also very similar (Chapter 4). Hence from a structural perspective, the limestone lithologies have little variability in the study area so type and character of fracture patterns in each limestone lithology are not significant (Figure 5.6).

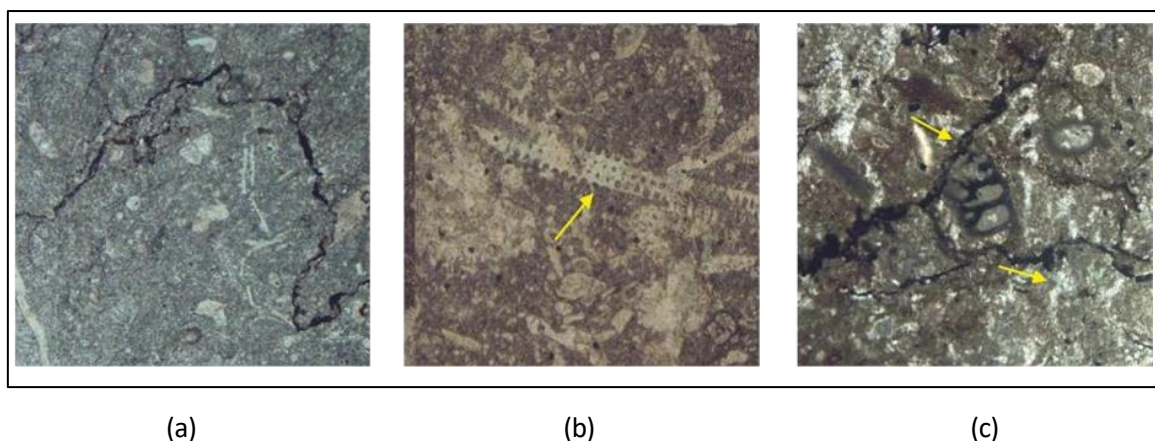


Figure 5.6: Micrographs illustrating the strong effect of microspar content in various microfacies in the field area: (a) with crushed shell fragments, (b) with *Dasyclad* algal fragments, (c) with common foraminifera (images from Ali *et al.*, 2014). Width of each image = 1 mm.

The thickness and distribution of shale between the limestone beds defines the continuity of the fractures within the rock-mass. Although bedding parallel fractures develop parallel to shale beds, and seldom cross-cut the limestone, the length of the cross-cutting fractures (interbed fracture continuity) can be defined for the different groups of rocks (Table 5.18). The most important feature is still the shale partings as these typically cause the different beds to terminate. The shale layers cause differential stresses between limestone and hence the thicker shales or more numerous shale partings reduce the transfer of stresses (Figure 5.7).

Table 5.18: Typical minimum and maximum unit thicknesses and bed thicknesses for the specific rock assemblages (quoted in centimetres). The typical interbed continuity is also shown. The % clastic mud represents the spatial percent of the rock assemblages in the different mapping circles, and "label" refers to the rock assemblages shown in Figure 5.7.

Rock type		Lime mudstone	Wackestone	Wackestone & minor shale	Wackestone & shale	Interbed wackestone & shale	Shale
Shale	Min thick	0	1	5	10	10	20
	Max thick	5	5	5	20	75	120
	Bed thick	1	1	1	1	1	1
Limestone	Min thick	1	20	40	10	10	0
	Max thick	150	200	80	50	75	1
	Bed thick	20	20	10	10	10	1
Interbed continuity		50	50	40	30	50	1
% clastic mud		2	20	15	50	65	100
Label		a	B	c	d	e	f

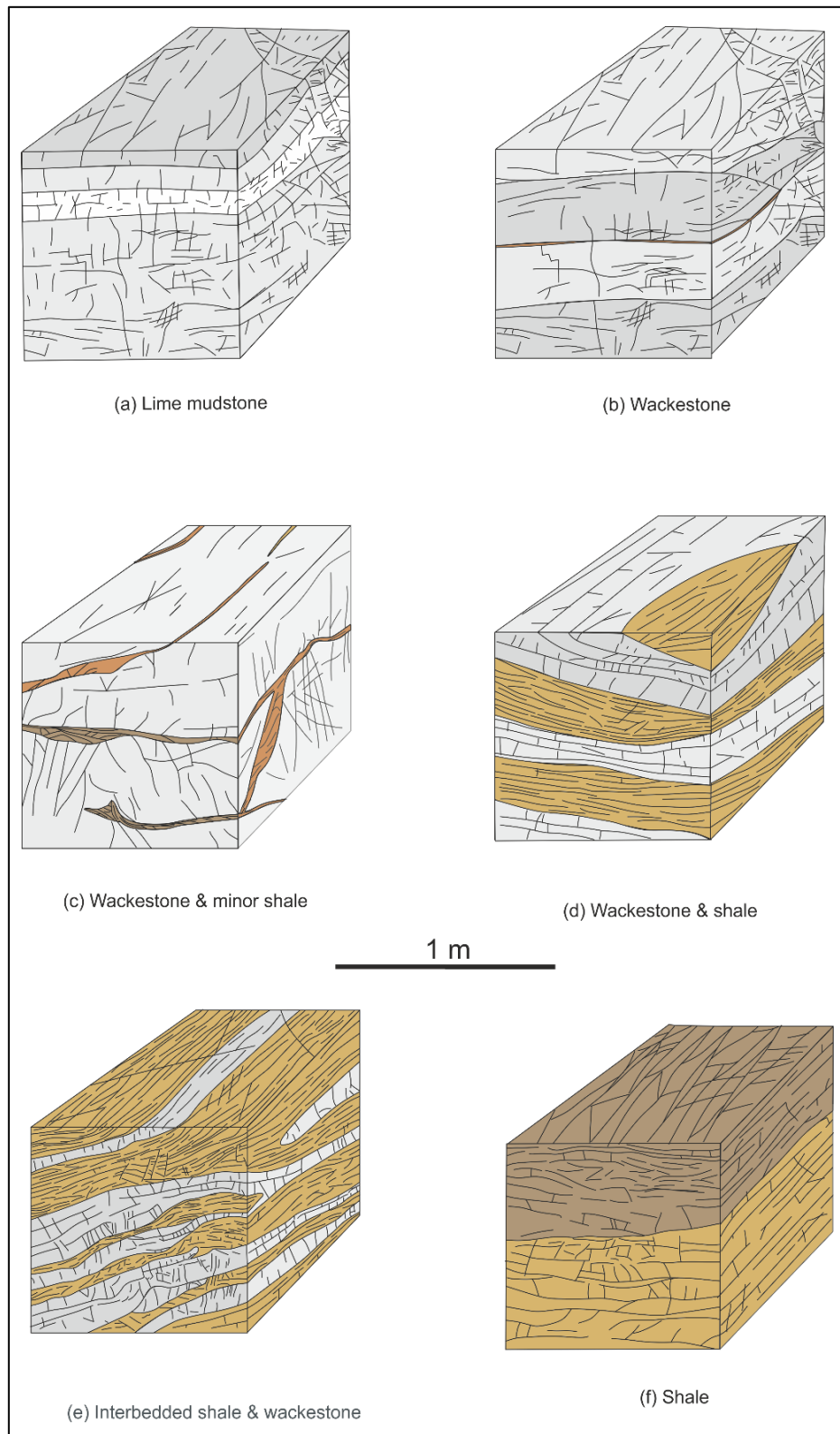


Figure 5.7: Block diagrams showing the idealised fracture patterns in the six variations of rock assemblages considered in this study. Percentage mud and typical number of nodes and fractal dimensions for the different rock assemblages are listed in Table 5.18. Front square = 1 m * 1 m.

Variation in the fracture patterns that develop in the combinations of rock assemblages for the whole study area are shown in Figure 5.8, expressed as the number of nodes and fractal dimension for each rock assemblage. The fractal dimension provides a spatial context of the distribution of the fractures. In this work, the fractal dimensions range between 1 and 2, with 1 being a single dimensional object (i.e., a line or a perfectly straight fracture) and 2 being a perfectly flat surface. The more fractured a rock, the more convoluted the fractures become, increasing its dimensional complexity. Lime mudstone has the highest fractal dimension, a consequence of the more intricate fracture patterns formed in the highly coherent, strongly micritised, uniform matrix. Shale has the lowest fractal dimension, indicating a simpler fracture pattern (Figure 5.8).

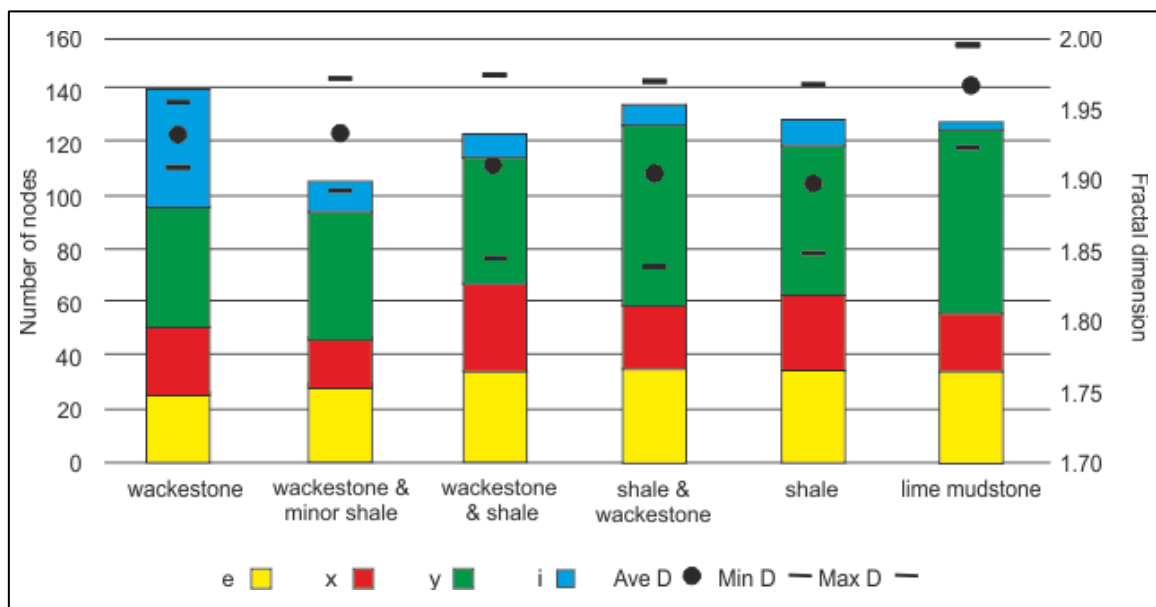


Figure 5.8: Number of nodes of each rock assemblage and the fractal dimension (with one standard deviation). When there are differences between the number of types of nodes specific topological characteristics can be defined for the different rock assemblages.

The number of different types of fracture nodes defines the number of terminations and intersections of fractures. This determines the topological characteristics of the rock including connectivity, fracture intensity, fracture density, and mean trace length (Grodner *et al.*, 2021).

The number of nodes (which determines the connectivity and other topological characteristics) and the fractal dimension (the complexity of the distribution of the fractures) provide two independent measurements of the rock-mass characteristics. The greater the number of nodes, the more of all e, x, y and i nodes are present within a measurement circle. Fractal dimensions are determined by box-counting. These number of nodes and fractal dimension are cross-plotted to determine the differences in the characteristics of the different rock types or geological structures (Grodner *et al.*, 2021). The comparison of the total number of nodes and fractal dimensions (including one standard deviation) are shown in Figure 5.9 which allows the specific characteristics of the spatial distribution of the individual fractures (fractal dimension) and the intensity of fractures (nodes) of the rock assemblages to be determined.

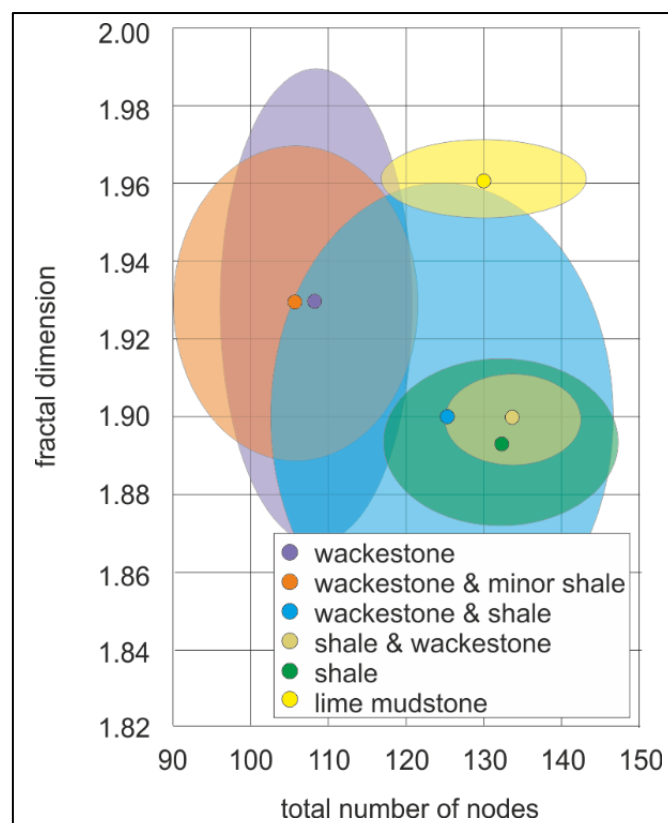


Figure 5.9: Average and standard deviation of the total number of nodes and fractal dimensions of all circles of the different rock type assemblages in the study area. This defines the topology (nodes) and complexity of the fractures (fractal dimension). The average value is indicated by the colour of each rock type and a standard deviation by the semi-transparent ellipse of the same colour.

Wackestone, and wackestone and shale have the greatest range of fractal dimensions indicating that these rock types have a wider variety fractures. The standard deviations of the lime mudstone, the shale, and shale and wackestone lithologies are small, indicating they have a similar set of values (Figure 5.9). In contrast, the wackestones have a limited number of nodes but a wide range of fractal dimensions which shows as wide range of fracture pattern types (Figure 5.9). The fracture patterns of the lime mudstone, and the shale and wackestone also overlap in the two-dimensional node count - versus fractal dimension space (Figure 5.9). This assessment of the two-dimensional total number of nodes versus fractal dimension space of the different rock assemblages do not indicate that distinct fracture patterns can be defined for the assemblages of rock assemblages. However, the topological characteristics are based on the differences between the number of the different nodes which show variations in the fracture pattern and rock mass characteristics.

Fracture densities are higher in wackestones (Table 5.19) as the fractures are able to propagate easily across the pervasive microspar matrix (Kendall and Flood, 2011). Combinations of wackestone and shale have lower fracture densities as the stress build-up in folding and thrusting are relieved by the interbedded shales, forming long fractures (Table 5.19).

Table 5.19: Average topological characteristics of the different combinations of rock types. Topological characteristics are derived from the numbers of different nodes and allow the characteristics of the different fracture patterns in the rocks to be defined. See also Figure 5.10 for the topological characteristics of various geological structures.

Different combinations of rock types	Connectivity	Fracture Intensity	Fracture density	MTL	Fractal dimension
Wackestone	3.47	13.17	19.10	0.25	1.90
Wackestone & minor shale	4.44	15.42	12.77	0.42	1.92
Wackestone & shale	5.60	17.52	14.61	0.40	1.90
Shale & wackestone	4.85	18.10	16.04	0.43	1.94
Shale	5.75	15.52	12.50	0.51	1.94
Lime mudstone	4.65	17.25	17.61	0.37	1.97
Average	4.79	16.16	15.44	0.40	1.94

The geometry of fractures controls both the rock properties, especially between large fractures or fracture sets that have a greater effect on connectivity (Table 5.19 and Figure 5.10). It is especially evident in the shale with through-going fractures parallel to δ_1 (Sanderson and Nixon, 2015). The shale with bedding parallel fractures aligned to the primary stress direction has lower cohesion between bedding which reduces the strength of the rock in this orientation allowing flexural flow (FF) movement. As the similar limestones rock types contain similar distributions of microspar, this part of the rock mass typically does not have preferred uniaxial compressive strength (UCS) and is less likely to fail in a preferred orientation but rather tangential longitudinal (TL) failure and it thus the shale layers that control the fracturing (Cosgrove, 2015).

Shale, and shale and wackestone rock have high fractal dimensions due to the closely spaced alternating The fracture intensities increase as the clastic mud content increases (Table 5.19 and Figure 5.10). wackestone units forming tangential longitudinal (TL) fractures and shale layers generating layer parallel flexural flow (FF) fractures. The high numbers of the shorter discontinuities including calcite

fractures and closely spaced unmineralised fractures in the lime mudstone form more complex fracture patterns and hence higher fractal dimensions.

The Mean Trace Length of the wackestone are the shortest whilst the trace length of the shales and the shales and wackestone are significantly longer due to the thin shale beds allowing flexure flow (FF) and increase in length of the fractures (Table 5.19 and Figure 5.10).

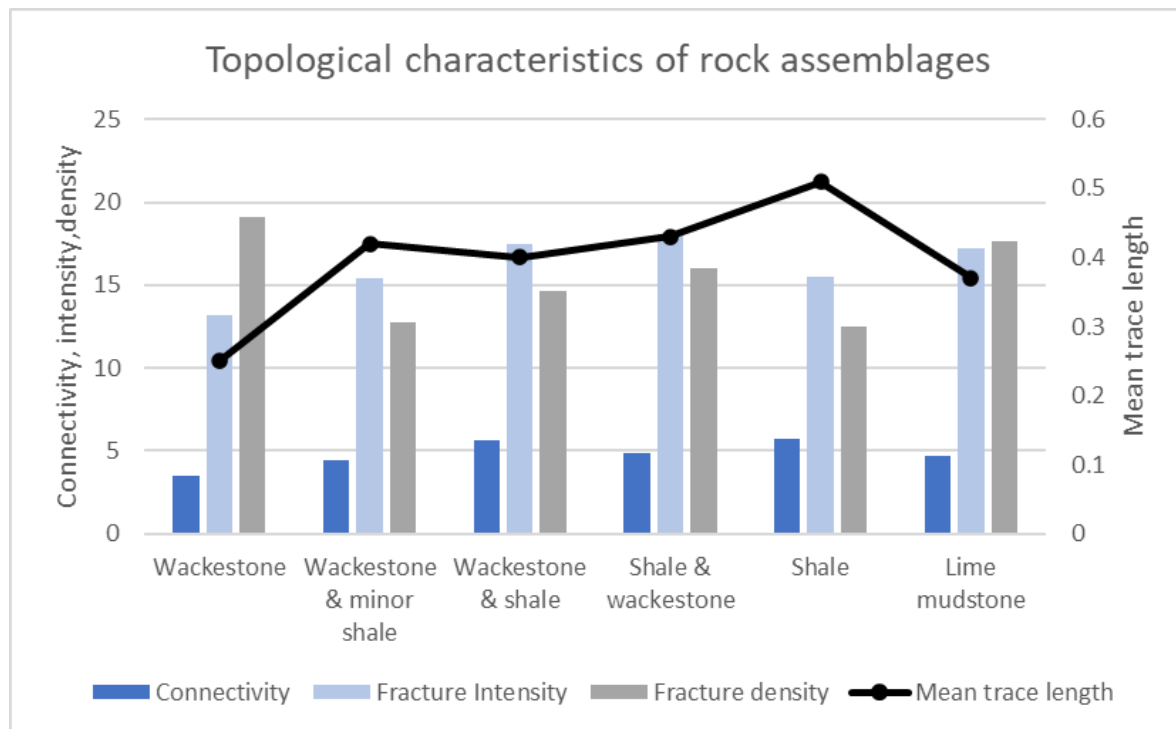


Figure 5.10: Topological characteristics of the different rock assemblages.

The broad-scale lithological variations cause distinctive differences in the rock-mass characteristics. The different rock types are clearly visible in the field, and it is possible to quantify these for each measurement circle or site. The fracture patterns are developed due to the applied stresses on the different combinations of rock types with different strengths. The bioclastic content and bioturbation structures do not have a significant impact on the variation of rock strength and general fracture potential of the rock. The characteristics of the interlayered lime mudstones, shales and wackestones are based on the different mineralogical types that can be approximated in the field from hand specimen observation. In areas where there are lower tectonic stresses, the different rock types in a

rock-mass have few differences in topological or fractal features. When prominent geological structures such as fore-thrusts and back-thrusts occur at a sampling site, the different rock types have more different topological and fractal characteristics. The geometry of fracture patterns thus controls both the rock-mass properties, and the relationships between individual fractures or fracture sets with large fractures or fracture sets having a greater effect on connectivity (Sanderson and Nixon, 2015).

The predominant control on the rock-mass is the relative abundance of shale within the lime mudstone and wackestones as it acts as a decollement surface to allow shear movement of the thrust faults (Figure 5.11). In fact, the areas of strong thrusting typically concentrate in the shale bedding, which allows flexural flow.

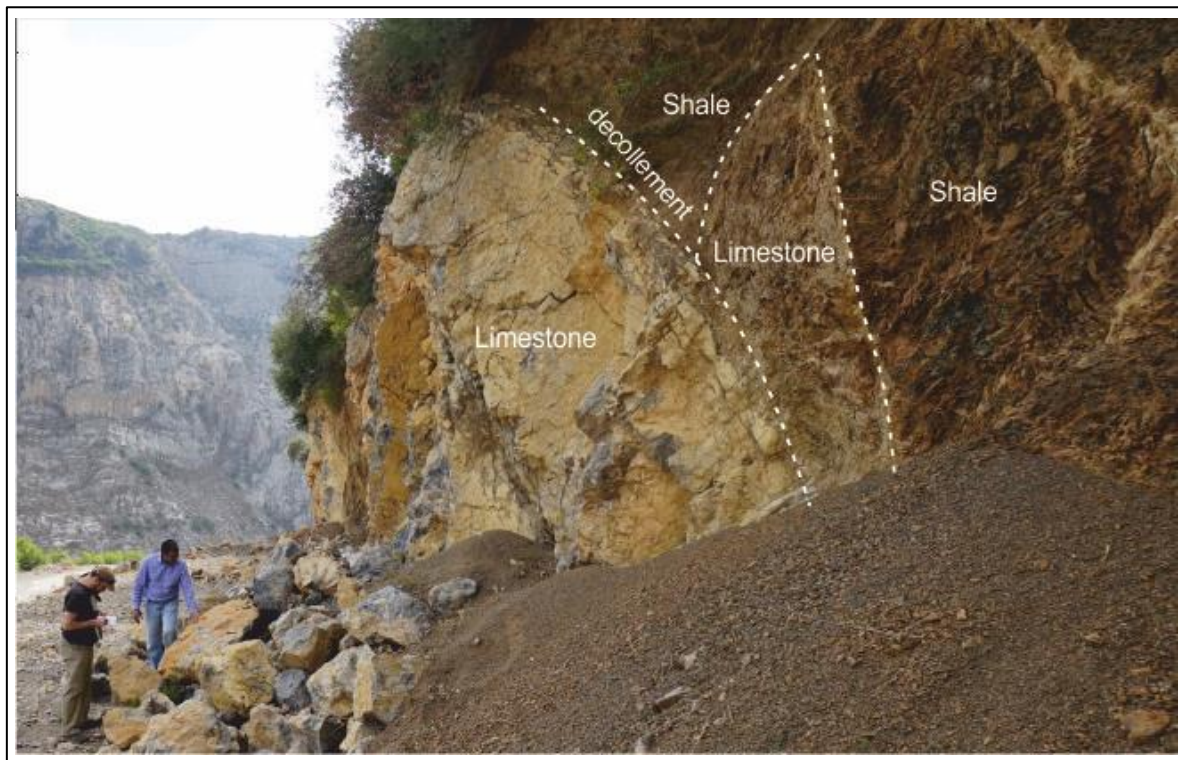


Figure 5.11: Shale beds form a decollement surface around a deformed remnant of limestone that has nearly been thrust into the shale (site 3, Losar Baoli region).

The diagenetic processes including micritisation has resulted in the limestone with no visible intergranular porosity and hence it is deformed by transitional longitudinal (TL) movement, causing the rock-mass to be fractured in a more brittle manner. A larger proportion of shale (and shale and

limestone interbeds) reduces the shear strength of the rock (Maldonado and Dight, 2020). This is due to the preferred orientation of the various clay particles enhancing the development of clay platelets orthogonal to crack alignment at various scales. The anisotropy of clay forms due to a rotational axis normal to the bedding plane forming the clay flakes (Anantharamu and Vernik, 2019). This results in the type and extent fracture patterns around large-scale thrusts and other structures to be predictable in a wide range of rock assemblages ranging from shale to wackestone. Abundant interbedded shales and limestones typically emphasise the shear displacement which is the predominant structural deformation in fold and thrust belts.

5.2 Fracture characteristics in different geological structures

There is no significant variation in fracture characteristics and spatial relations with the lithology of the limestones, except for the presence of shale, relationship between structural position and fracture characteristics.

Figure 5.12 illustrates the type and distribution of the different geological structures related to the formation of the Himalayan Main Boundary Thrust, which is the principal structural feature in the study area. The thrust is manifest at the surface in Mesozoic and lower Tertiary strata forming a series of sub-parallel, gently curving, high level, low angle thrust sheets (McDougall *et al.*, 1993). Individual structural features consist of thrust-related synclinal, anticlinal, and overturned anticlinal folds, back thrusts and compressional pop-ups. The pop-ups are compressional structures formed between fore-thrusts and back-thrusts.

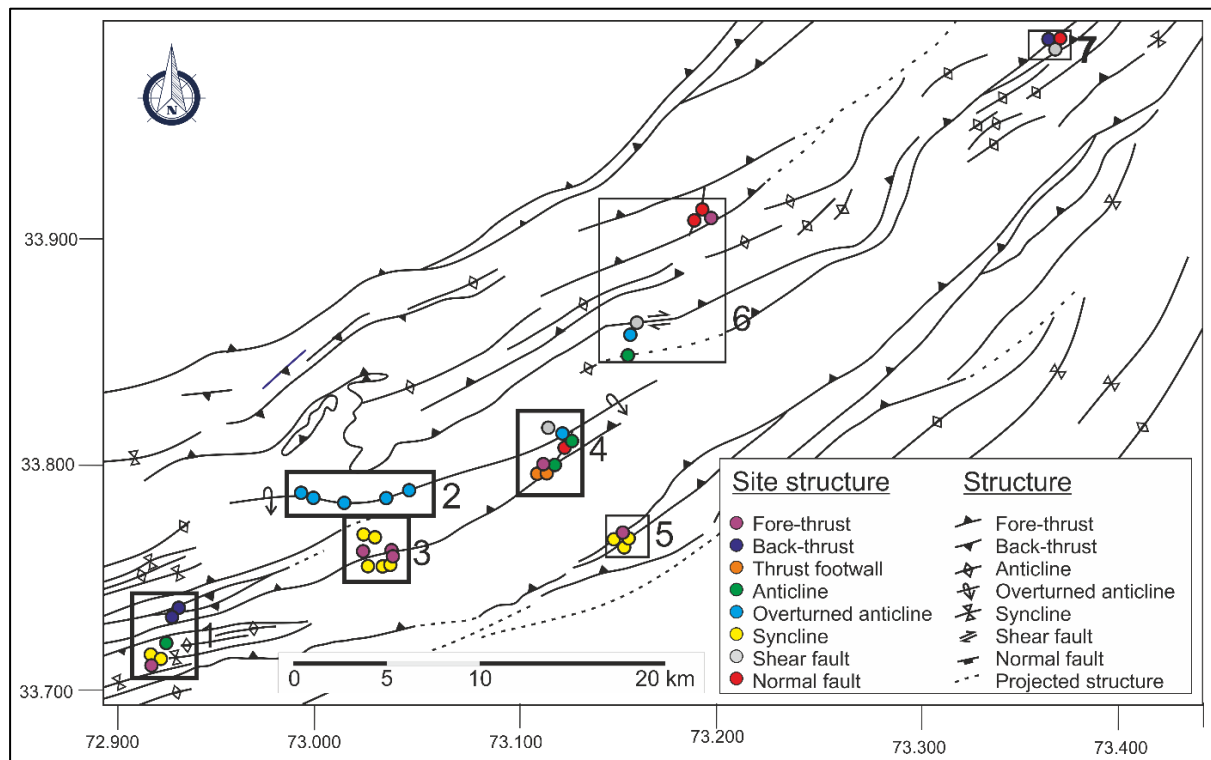


Figure 5.12: Distribution of geological structures in the field area. The hypothetical cross-section in Figure 5.15 is based on the general foreland to hinterland distribution of these structures.

There are variations of the node characteristics and fractal dimensions of between various structures. The most significant structure are the pop-up features located between the fore- and back-thrusts. At the pop-up structures the tectonic stresses are lowest, resulting in the lowest fractal dimension and lowest number of nodes (Figure 5.13). They consist of an uplifted block bounded by a foreland-verging fore-thrust and by a hinterland-verging back-thrust. The identification of pop-up structures are crucial for the assessment of fold-and-thrust belt style at regional scale (Fabbi and Smeraglia, 2019). Pop-up structures commonly occur in fold-and-thrust belts that are characterised by a multi-layered sedimentary sequence such as in the field area, that consists of alternating limestones and shales (Coward *et al.*, 1999). Pop-ups may occur due to the erosional uplift of the crestal extensional faulting associated with the anticline allowing relief of the horizontal stress component (Tavani *et al.*, 2014). Increase in the relative vertical tensile stresses of the rock-mass.

Such conditions allow buckle and/or disharmonic folding and development of weak décollements and fractures before fore-thrusts and back-thrust break through and pop-up generation (Fabbi and Smeraglia, 2019). These discontinuities allow pop-ups to develop before the increased stresses of the rock mass drives through the thrusts. The different stress directions which develop in the pop-up structures cancel out each other resulting in a low number of nodes and a low fractal dimension (Figure 5.13).

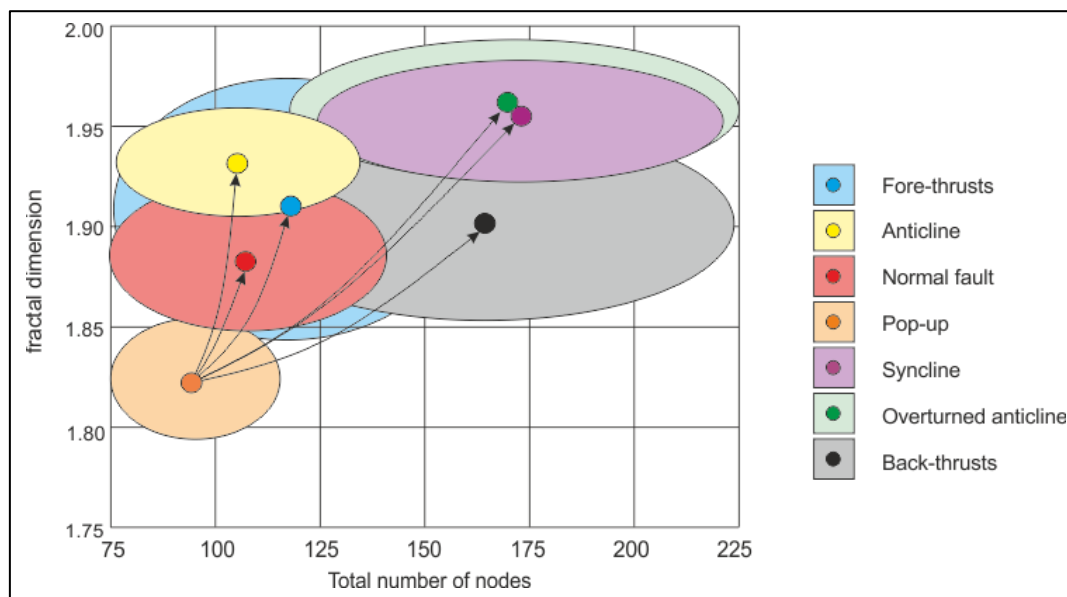


Figure 5.13: Average (solid points) and a single standard deviation (shaded ellipse) of the total number of nodes and fractal dimensions of all circles for each structural feature. The orange point indicates the average value of circles in the pop-up zones. Arrows show the variations from this weakly deformed site relative other structures. The variations in the number of different node types (Figure 5.14) result in different topological characteristics. The figure illustrates the spatial distribution of fractures (fractal dimension) and the fracture intersections (number of nodes) allowing different fracture patterns to be defined (Grodner et al., 2021). See Figure 5.15 for separate images of structures.

All the geological structures increase in fractal dimension relative to the pop-up structure. Anticlines have a greater fractal dimension when compared to the pop-up structures and synclines and overturned anticlines have an even greater number of nodes caused by the greater confining pressure of these folds (Figure 5.13). Fractured limestone rocks adjacent to normal faults have a similar of nodes

as pop-up structures but have a slightly higher fractal dimension.

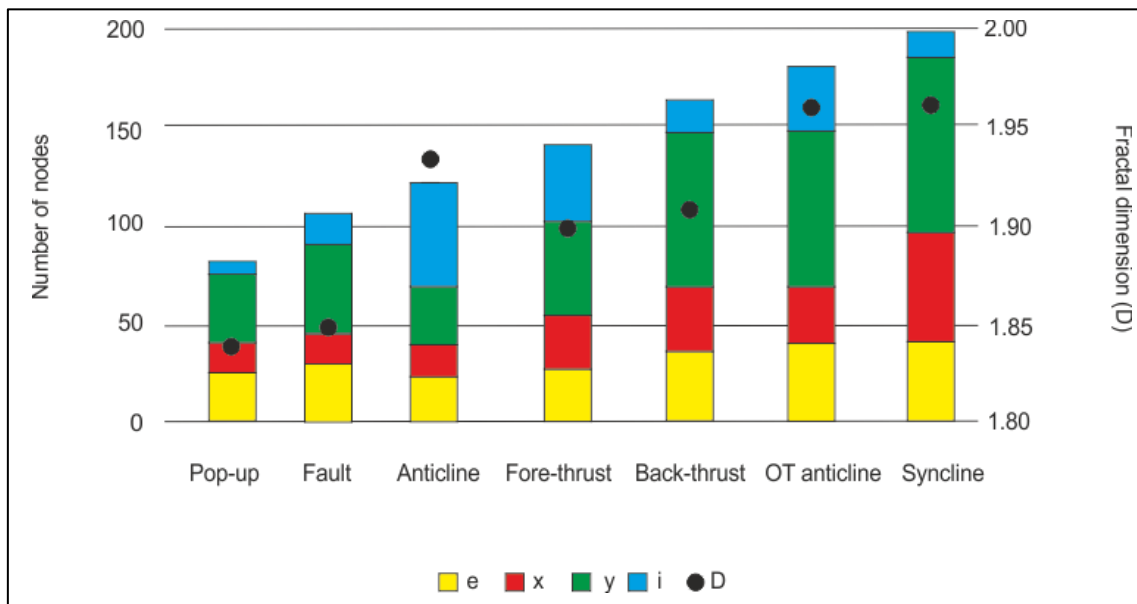


Figure 5.14: Number of nodes of the geological structures and the fractal dimension (D) with one standard deviation. A lower fractal dimension represents less deformed structures with a pop-up structure clearly having this position. The other geological structures have a fractal dimension of greater than 1.90 (close to two-dimensional, resulting in strong connectivity and greater mean trace length (Table 5.20)). The type of nodes present defines the topology of the fracture network. Chapter 3 (Methodology) describes how the topological and fractal characteristics are determined.

Compared to the back-thrusts, the fore-thrusts have a more restricted number of nodes (Figure 5.14) which results in different topological characteristics and rock-mass characteristics that are dominated by fewer but longer fracture planes that are a product of flexural flow in the fore-thrusts. Back-thrusts have a wider range of node-counts, which indicates that the fractures have different length, but all of the back-thrusts fractures have a higher fractal dimension.

The topology defines the type and intensity of deformation the geological structures have been subjected to. For example, back-thrusts typically have higher fracture density than the associated fore-thrusts (Table 5.20). This because the back-thrusts are confined by the hinterland and therefore are subjected to more crushing whereas the fore-land thrusts can be thrust over the large parts of the fold

belt. This helps to identify the structure type and the applied stresses.

Higher fracture intensity and fracture density and are dominated by tangential longitudinal failure. The back-thrusts, overturned anticlines and synclines have higher fracture intensity concentrated especially in the hinge zone thereby causing buckle-folding and the highest number of nodes which creates a greater connectivity (Table 5.20).

Table 5.20: Summary of average topological characteristics of each of the structural features. Compare with Table 5.19 for the topological characteristics of the different rock types in the study area.

Structure	Connectivity	Fracture intensity	Fracture density	Mean trace length	D
Anticline	4.66	14.37	17.40	0.43	1.95
Pop-up	1.25	12.50	14.22	0.52	1.93
Fault	3.72	14.16	15.55	0.43	1.94
OT anticline	4.79	18.12	14.26	0.41	1.96
Back-thrust	4.59	15.64	19.36	0.32	1.95
Fore-thrust	3.93	14.36	12.90	0.40	1.95
Syncline	4.43	17.58	23.44	0.25	1.93

The distribution of the various geological structures across a schematic cross-section of the frontal Himalayan thrust and fold belt and displays the topological characteristics, fracture types and fracture patterns associated with the different geological structures is shown in Figure 5.15. Although the cross-section is schematic, it is drawn in a north-south orientation to represent the general orientation of the main structural elements encountered in the traverses studied and are organised in a sequence that approximates to their actual occurrence. The structural features in the field area have an overall distribution from fore-thrusts in the hinterland to the south and back-thrusts in the hinterland to the north. Pop-up structures are located at an even distribution between the fore-thrusts and back-thrusts. The compressed nature of the overturned anticlines results in these forming in the hinterland. Each of these geological structures are illustrated and described in more detail in Figure 5.16 to Figure 5.22.

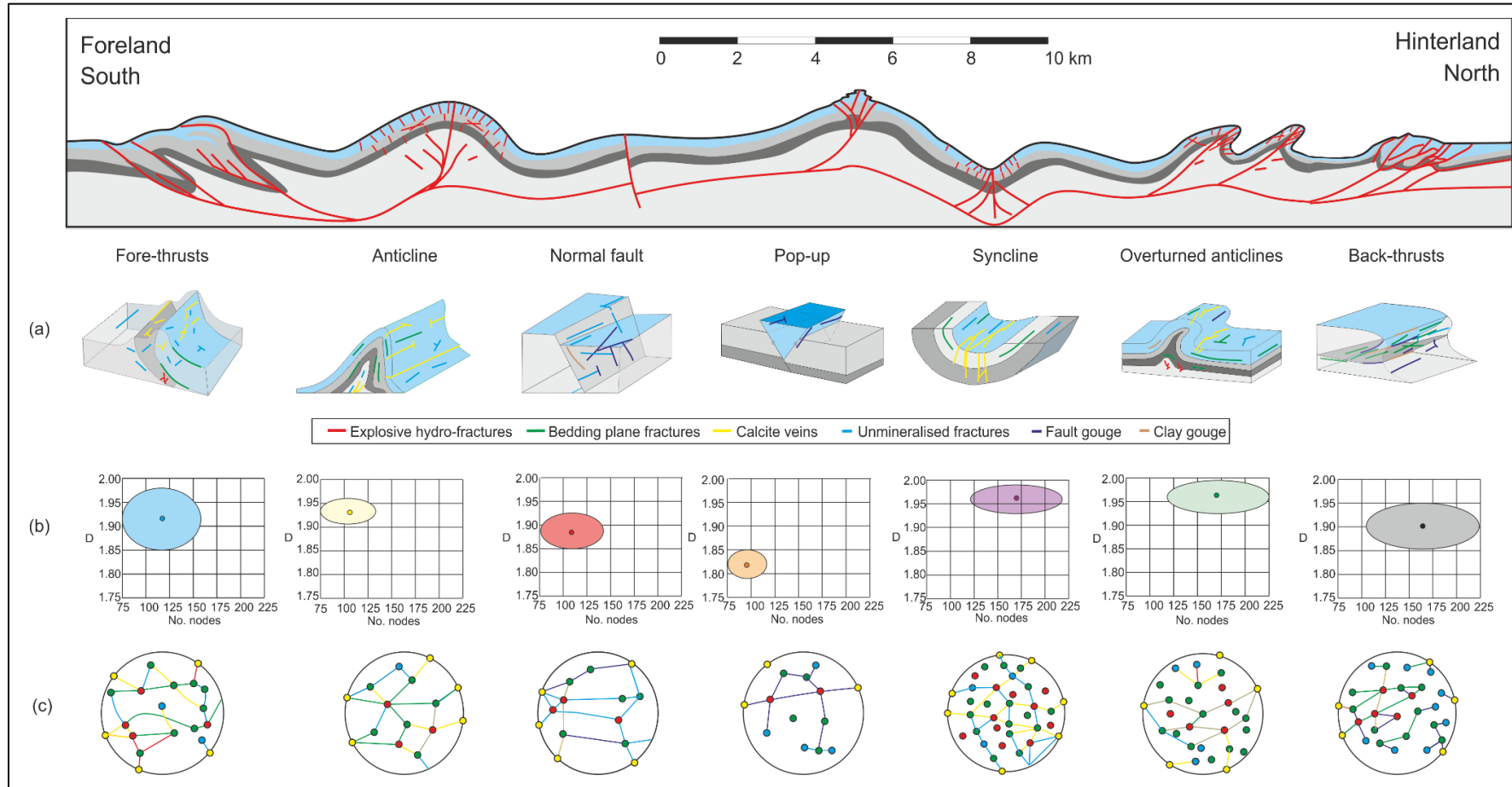


Figure 5.15: Schematic cross-section across the study area of the Himalayan Frontal fold and thrust belt illustrating the theoretical distribution of structural features (shown in red with the different greys representing the strata). The diagrams below the schematic cross-section show: (a) individual cartoons of each of the structural types with their associated fracture patterns shown in different colours (b) cross-plots of the number of nodes and fractal dimension of each structure, colours matched with Figure 5.13 (c) fractures and nodes of each structure as it would appear in a representative measurement circle. Nodes are same colours as all figures, i.e., yellow, red, green and blue represent e, x, y and i nodes respectively. Number of nodes is divided by 5 to unclutter the diagram. The geological structures are described and illustrated in detail below.

The pop-up structures are thrust-bounded but have a low fracture intensity and the lowest fractal dimension in these geological structures (Figure 5.13). This is because the principal compressive forces are accommodated by upthrown fore- and back-thrusts and the upthrown block has a free Earth surface with no significant vertical stress (Figure 5.16). As a result, pop-up structures are not subjected to significant tensile forces compared to anticlines or other structures. Pop-up structures display the lowest fracture connectivity, fracture intensity and mean trace length (Table 5.20) indicating that they are the least disturbed geological structures.

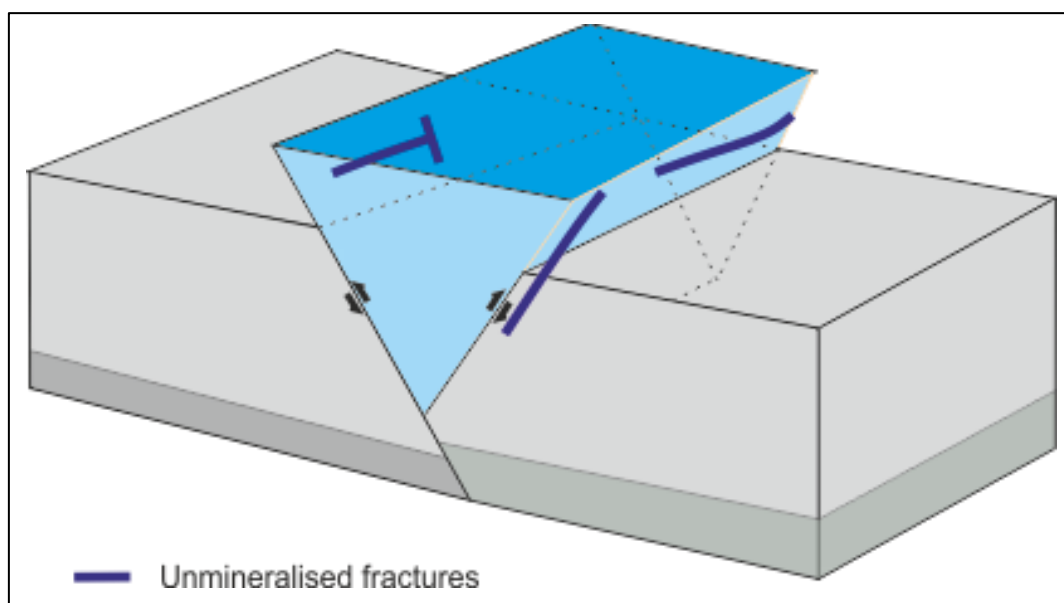


Figure 5.16: Pop-up structure – lowest fractal dimension and only unmineralised fractures.

In the thrust-related anticlines tensional stresses develop in the same orientation as the regional compression, leading to opening mode fractures developing. However, as tensile forces dominate in anticlines these structures develop the fewest nodes (Table 5.20). The low confining stress in these structures also increases the fractal dimension as the fractures are more widely spread. Anticlines have higher fractal dimensions than faults, fore-thrusts, and back-thrusts as well as pop-up structures, but due to their reduced number of nodes, the fracture density, connectivity, fracture density and mean trace length are low (Table 5.20).

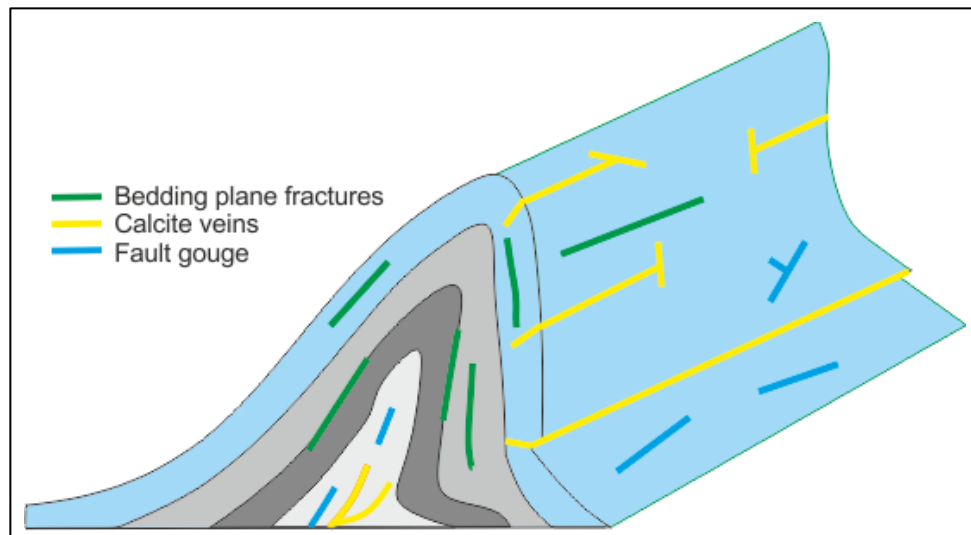


Figure 5.17: Anticline with central thrust, indicated with calcite and fault gouge. It is characterised by fewer nodes but a greater fractal distribution which results in fewer intersections but wider distributions of fractures.

Normal faults (Figure 5.18) are characterised by a similar number of nodes as the pop-up structures and but a lower fractal dimension than thrusts (Figure 5.14). The standard deviations of the various topological parameters associated with normal faults overlaps to a large degree with that of the thrusts. This due to the numerous fracture types including especially unmineralised fractures and clay and fault gouge and orientations creating a wide range of fracture styles in these faults (Mitra, 2002).

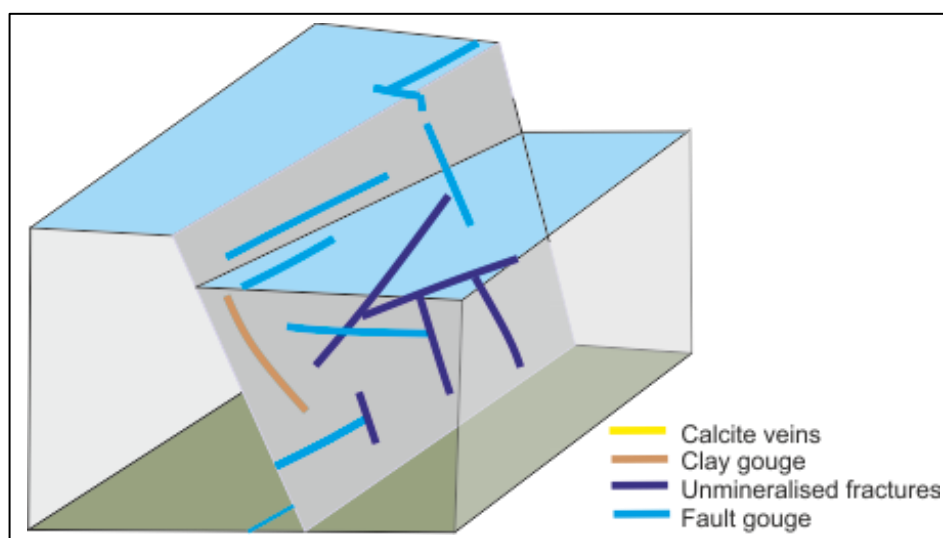


Figure 5.18: Normal fault – consists of unmineralised fractures and fault gouge with limited clay gouge.

Synclines and overturned anticlines have the highest fractal dimensions and the greatest number of

fracture intersections.(Figure 5.19). For example, in the Jababri region, a plunging syncline-consists of thicker wackestone that is separated by centimetre-thick layers of sheared lime mudstone with prominent slickensides formed during the formation of the plunging folds. Unmineralised fractures have formed in the individual wackestone beds and do not cut across mudstone interbeds. The central axis of syncline has even more cross-cutting nodes and the greatest amount of fracturing (Figure 5.19).

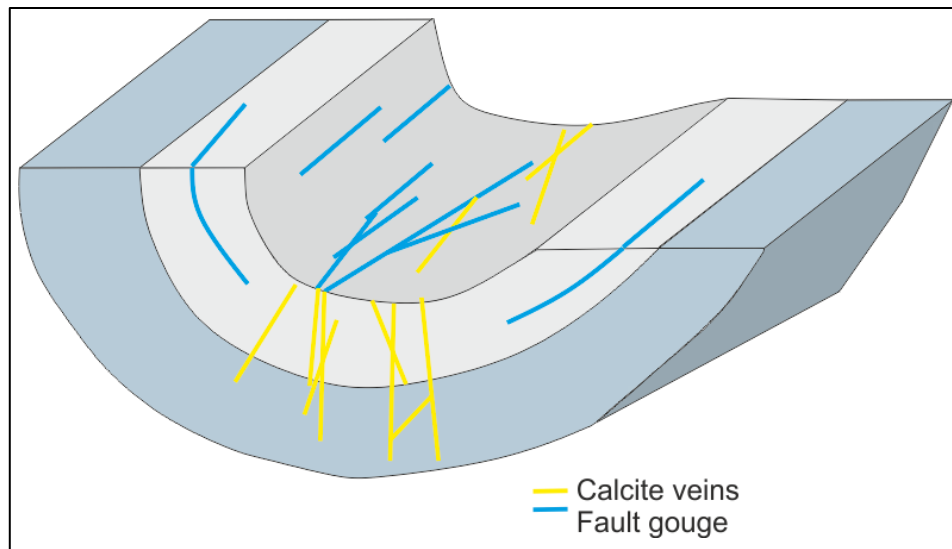


Figure 5.19: Syncline – upper surface is in compression causing a significant number of fracture intersections and high fractal dimension.

The overturned anticline in the Makhniyal field region consists of dark grey calcareous mudstone with calcite fractures that both cross-cut, and terminate on, the sheared bedding planes. The abundant small fractures and re-activation of bedding parallel movement can be directly attributed to the increase in intensity of the fracture pattern particularly in the steeply dipping overturned limb (Figure 5.20).

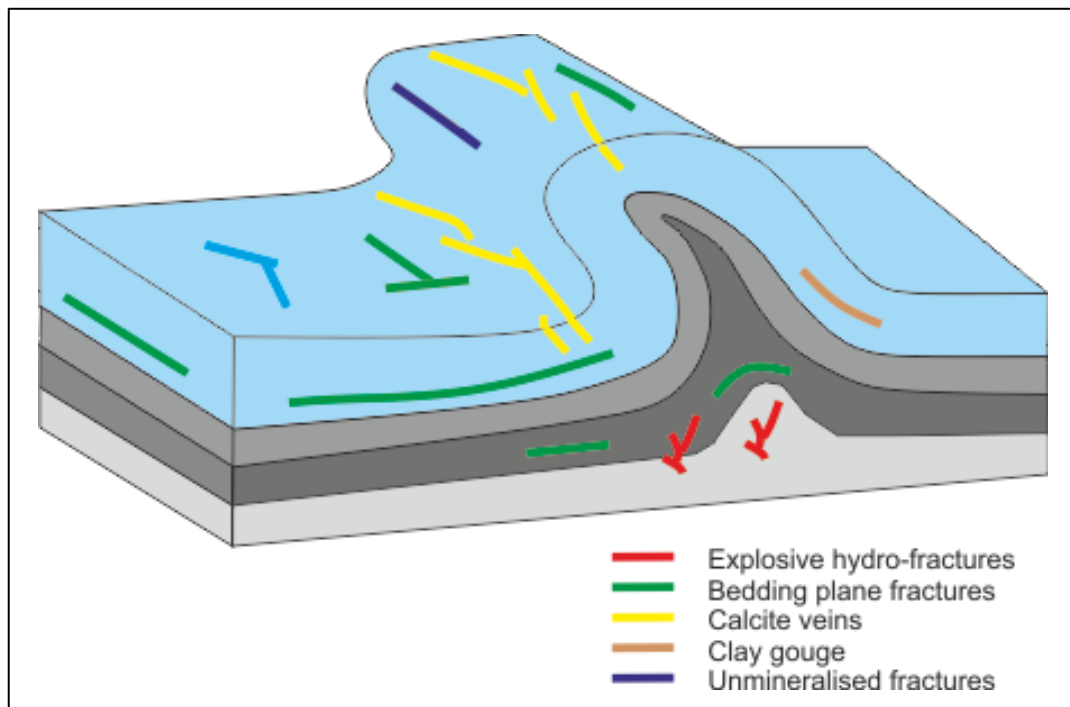


Figure 5.20: Overturned anticline. There are several different fracture sets formed due to the tight compressive forces in the structure.

Back-thrusts have a vergence opposite the dominant trend of a thrust system and can accommodate hanging-wall rocks as out-of-syncline folds if they occur within a competent unit (Mitra, 2002). Back-thrusts, overturned anticline and synclines have the greatest number of total number of nodes due to abundant strike-parallel as well as secondary oblique fractures (Figure 5.21). A strong relationship is observed between fracture spacing and mechanical layer thickness in cases where there has been one single phase of extension and when interbed contacts are weak, such as interbedded competent limestones and incompetent shales of back-thrusts which results in a high number of clay-gouge filled fractures and a high density of unmineralised fractures (Wennberg *et al.*, 2006). Unlike the shales in the fore-thrusts, the shales are rotated and crushed due to the opposite sense of dip in the back-thrust. The rock-mass within the anticline fault propagation fold area of the back-thrusts is highly fractured, due to the dominant compressive forces. It consists of iron oxide-rich bedding-parallel thrust surfaces and steeply dipping fault propagation fold fracture planes. Calcite-filled veins are dominantly strike parallel to the synclinal fold axis of the back-thrust, have a high angle to bedding

and are strata-bound (Wennberg *et al.*, 2006). Back-thrusts consist mostly of lime mud and with abundant small calcite fractures and small unmineralised fractures. The structures therefore have a high number of nodes and fractal dimension causing higher fracture densities and intensities (Figure 5.21). The greater connectivity, lower mean trace length of the back-thrust is due to the higher fracture intensities (Table 5.22).

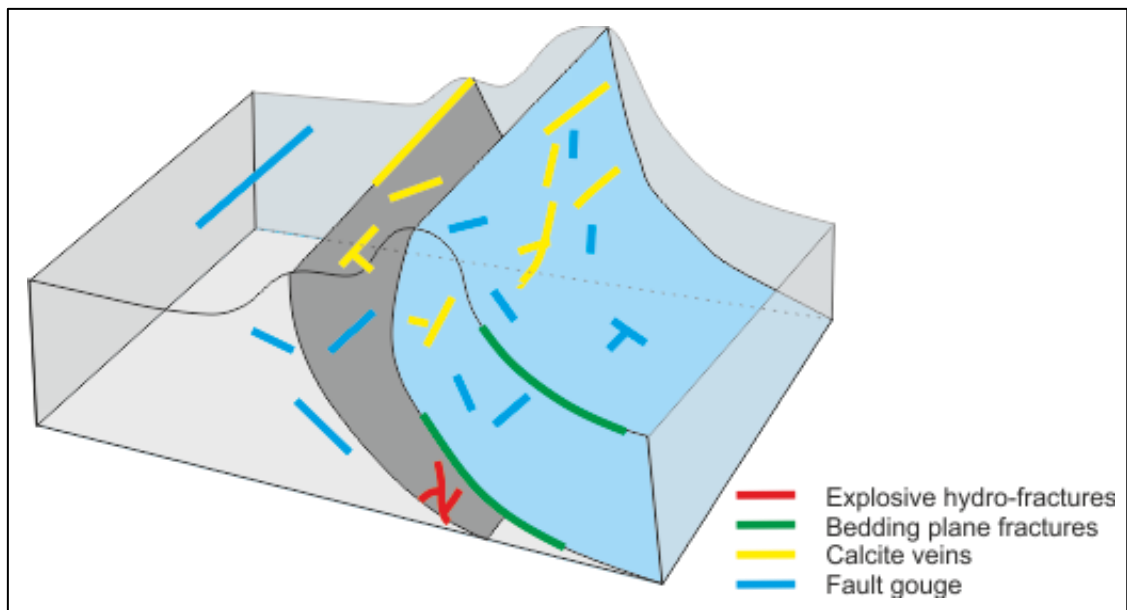


Figure 5.21: Back-thrust –high fracture intensity result in greater connectivity and lower mean trace length.

Topologically, the fracture networks in the fore-thrust setting are the product of flexural flow characterised by fewer nodes and a longer mean trace length, hence a lower density, but higher connectivity of fractures. Extended clay gouge and fault gouge fractures are present in the fore-thrust, as well as long bedding plane fractures (2 to 5 m), as well as unmineralised fractures. This is due to extended periods of movement on the thrust sheets compared to back-thrust settings, where fracture networks are more irregular with higher fracture density and varying mean trace lengths, because of late-stage layer-parallel shortening (Figure 5.22).

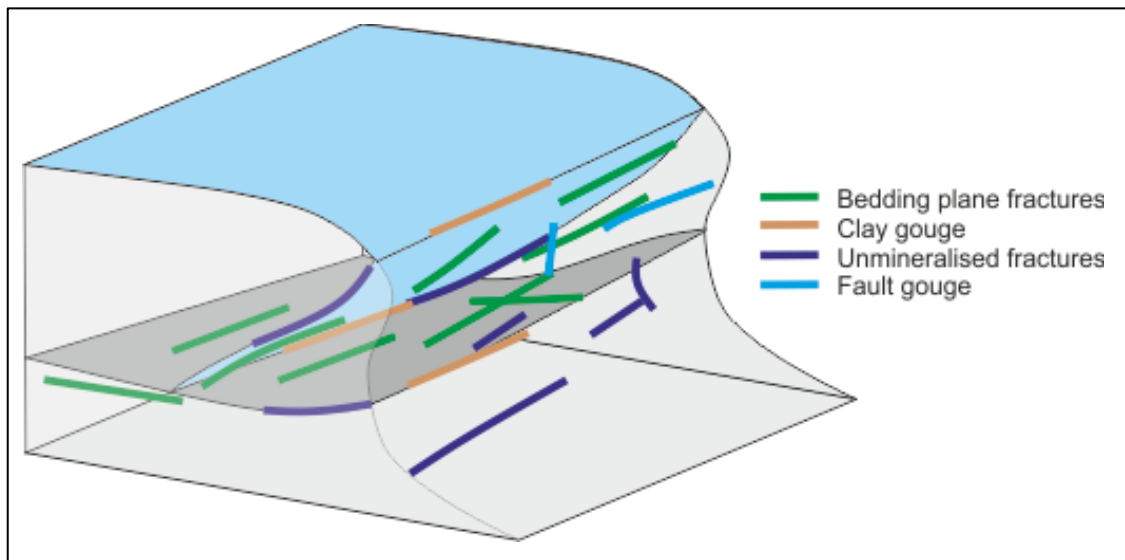


Figure 5.22: Fore-thrust – elongated bedding plane and other fractures due to extended periods of movement on the thrust sheets within the field area.

5.3 Summary of fracture characteristics

The spatial distribution of the fracture networks as discrete objects such as fractal dimensions of the fracture spacing provide valuable insights into the relationships of the fractured rock-mass. The topological analysis of a fracture network characterises the connectivity of the constitutive fractures in that network. This dual approach permits the understanding the spatial and connectivity relationships of the whole fracture population in the context of the wider structural scale.

The recrystallisation of lime mudstone and wackestone to micrite and to microspar with no visible intergranular porosity is pervasive in all of the studied limestones has resulted in the character of fracture patterns in each limestone lithologies being very similar. Shale occurs as discrete layers of a dark brown coloured, fine-grained clastic fissile mud and is usually highly deformed, concentrating strain in the form of shear zones and folds. The thickness and distribution of shale in the limestones defines the continuity of the fractures within the rock-mass as the two rock types have different shear strengths which reduces stress-fracture transfer between the shale and limestone.

Individual structural features consist of thrust-related synclinal, anticlinal and overturned anticlinal folds, back thrusts and compressional pop-ups. In this active fold and thrust belt the complex interaction all of the fracture types that is not easily resolved from fracture cross-cutting relationships. The distinction of the fracture patterns in the different structural features are a result of the cumulative effects of multiple fracturing events which are defined when all the constituent fracture sets of the rock-mass are considered together. However, it is possible to determine different fractal and topological characteristics that are specific to various structural types.

6. Discussion

The geometry and distribution of fold and-thrust (FAT) belt related fractures in the limestone rocks of the study area are extremely complex and variable. Field observations of fractured rocks and their structures represent the most direct and important source of information on how these brittle rocks deform. Conventional fracture mapping techniques of these fractures are laborious and time-consuming. The characteristics of fractures within the rock-mass of different stratigraphic and structural domains and the combined tectonic environment requires the determination of the orientation and spacing of the various fracture patterns. Acquiring this data can utilise linear or grid pattern laid across the rock-mass and mapped to collect these characteristics as shown was shown for example in Chapter 4 (Field Mapping) in Section 4.1 - Makhniyal field region, where fracture intersections in grids were measured and Section 4.3 - Talhaar field region, which examined line measurements. These mapping techniques took a long time or could not be spaced closely enough. This is because the data collected only consisted of the intersection points of fractures on lines or grids but do not represent the true complexity of the fracture pattern. The focus of this research is to determine the true spatial and connectivity relationships of the whole fracture population.

6.1 Topology and fractal dimensions of rock types

A new method for characterising fractures, is presented in this thesis, that has been developed in the FAT belt of the Himalayas in the field area. It investigates the topological and fractal characteristics of the fractures of different rock types and geological structures. Data from a series of measurement circles at various mapping sites has allowed a large amount of this type of fracture information to be acquired. Individual fracture types within the fracture system are not separated, rather a complete analysis of how the cumulative effects of how successive tectonic stresses affect the these complexly fractured rocks is determined (Section 3.3 - Geological data capture methods).

The topological (spatial) and the fractal (complexity) of the fractures provide two independent measurement types. By determining the location of these measurement types on cross-plots, including spread of the data, the fracture pattern various parts of a FAT belt can be identified. It is anticipated that this will allow details of the fracture patterns to be identified within the rock-mass at large distances or depths.

6.1.1 Topology and fractal dimensions of rock types in the study area

The northerly Lesser Himalayan Zone within the field area includes upper Proterozoic to lower Palaeozoic rocks bounded to the north by the Main Central Thrust and to the south by the Main Boundary Thrust (MBT). The southerly Sub-Himalayan Zone in the field area, is bounded by the MBT to the north and the Main Frontal Thrust to the south and consists of Tertiary rocks deposited in front of the rising mountain front. Both of these zones make up the foreland FAT belt of the Himalayas.

The composition of the sedimentary rocks in the FAT belt of the study area are very similar. They were deposited within a closely related suite of depositional environmental settings from the middle ramp (Khawaj *et al.*, 2018; Rehman *et al.*, 2016) to a coastal-lagoonal setting (Khawaj *et al.*, 2018; Swati *et al.*, 2013). These sort of rock sequences are typical of the fore-land FAT belt particularly the Patala Formation and the Chorgali Formation, which indicate deposition in increasingly shallow water such as a lagoonal and potentially supratidal environments (Fahaad *et al.*, 2021; Mizra *et al.*, 2022).

Importantly, in the area investigated, the bioclastic content and bioturbation structures of the limestones do not have a significant impact on the variation of rock strength and general fracture potential of the rock. Rather, the limestones in the field area have no significant intergranular porosity due to both pervasive diagenesis and recrystallisation. During the early diagenesis of the lime muds, calcium carbonate matrix is transformed to micrite and subsequently to microspar cements (Mosher, 1989; Munneke, 1997; Lucia and Loucks, 2013). In the limestones examined, early diagenetic micritisation, cementation by microspar, neomorphism and recrystallisation has completely destroyed any remaining primary porosity and permeability (Khan, 2018; Shoaib *et al.*, 2022). The recrystallisation of lime mudstone and wackestone to micrite and microspar with no visible intergranular porosity makes the character of fracture patterns in the lithologies similar.

From a rock-engineering perspective the most important feature are the shale partings as these typically cause the different beds to terminate. The shale layers result in differential stresses between limestone and hence the thicker shales or more numerous shale partings reduces the transfer of

stresses resulting in shearing. The shale layers have a lower shear strength causing significant shearing in the rock-mass. The characteristics of the interlayered lime mudstones, shales and wackestones can be measured by the topological and fractal features. The predominant control on the rock-mass is the relative abundance of clastic shale as it acts as a decollement surface with the wackestone rock causing high fractal dimensions due to the alternating units. Although there are many thick bands of shale, these do not form a single layer like the Cambrian salt band further to the south. This results in many scales of thrusts, with various fracture patterns due to the surrounding rocks and tectonism.

Lime mudstone has the highest fractal dimension, as a consequence of the more intricate fracture patterns formed in the highly coherent, strongly micritised, uniform matrix. Shale has the lowest fractal dimension, indicating a simpler fracture pattern that is more linear (bedding parallel) on the 2D outcrop exposures of the measurement circles.

Fracture densities are high in wackestones as the stresses cause fractures to develop in the pervasive brittle microspar matrix (Kendall and Flood, 2011). Combinations of wackestone and shale have lower fracture densities as the stress build-up are relieved by the folding and thrusting in the interbedded shales, forming long fractures, particularly in the fore-thrusts.

The Mean Trace Length of lime mudstone and wackestone are the shortest whilst the trace length of the shales and the shales interlayered with wackestone are significantly longer due to the thin shale beds allowing flexure flow and increase in length of the fractures.

In areas of lower tectonic stresses, the different rock types have few differences in topological or fractal features as both the tensile and compressive strengths of the rocks are not variable enough to cause different patterns. However, the higher applied stress in the Lesser Himalayas is why the different rock in the field areas exhibit different patterns.

The shear strength of geological structures, such as faults (particularly large thrusts) is often lower than the compressive strength of the various rock-types, especially lime-mud, so it requires lower stresses for the geological structures to deform. This deformation acts as stress-relief on the rock-mass and the stresses do not reach high enough values to cause extensive brittle fracturing of the

different rock-types. This is why the structural fracture patterns are more common and have strongly developed features reflected by higher fractal dimensions. The statement may appear to be incorrect as interbedded shales and wackestones have extensive fractures. However, the fractures of these layers deform parallel to the low shear-strength bedding caused by folding and shearing of the layers due to flexural flow. They do not break across the rock units as is required by transitional longitudinal fracturing to deform where they presented with the high uniaxial compressive strengths, particularly of the limestones. For this reason, it is more difficult to assign specific fracture patterns to different rock compositions.

The broad-scale rock variations cause distinctive differences in the rock-mass characteristics. The fracture patterns are developed due to the applied stresses on the different combinations of rock types with different strengths. The bioclastic content and bioturbation of the limestone do not vary the rock strength and hence fracture potential of the rock. The geometry of fracture patterns thus controls both the rock-mass properties, and the relationships between individual fractures or fracture sets with large fractures or fracture sets having a greater effect on connectivity (Sanderson and Nixon, 2015).

6.1.2 Topology and fractal dimensions of other FAT belt rock types

Unlike the limestones in the field area, various limestone-strengths exist. The Dunham classification scheme describes the characteristics of the limestones. If the grains of a limestone are touching one another and the sediment contains no mud, then the sediment is a grainstone. If the carbonate is grain supported but contains a small percentage of mud, then it is known as a packstone. Packstones and grainstones are seldom found in the field area. It is expected that these rocks will be less brittle and affected by more fractures, as they have lower UCS strength (Table 6.1).

Table 6.1: Combined percentage carbonate matrix and calcite compared to the of UCS of various limestones (after Abd Ed-Aal et al., 2021).

Rock type	% limestone	UCS
Lime mudstone	93	55
Wackestone	93	52
Packstone	85	35
Grainstone	83	46

Variations in the effects of different strengths of limestones are not discussed in this thesis, as the limestones in the field area are considered to have a uniform strength due to micritisation and microspar cementation. In limestones with less intense diagenetic micritisation and cementation, other facts need to be considered including variations in composition and thus strength (Rehman *et al.*, 2019), causing differences in cleavage (Marshak and Engelder, 1985), and along-strike alterations in the fracture patterns due to the varying strengths of the weaker limestones (Burmeister and Marshak, 2006).

Shale as a detachment lithology is intrinsically weaker as it deforms through shearing rather than building up stress to the point of brittle failure with rocks like limestone and sandstone. This results in local variations in meso-structural suites produced through the fold-thrust belt stress cycle sequences (Ferrill *et al.*, 2021). There are variations in the thickness, and deformation style within shale-prone

major thrusts. Limestone units within a shale-zone can also significantly affect fault zone architecture. Considerable work remains to be done with shale detachments, including overlying structural styles, and the controls of mechanisms and rates of deformation within the shale thrust zones (Morley *et al.*, 2017). It is considered that the evaluation of the fractal dimensions and topology would provide significant insights into these variations.

The composition of sandstone in foreland basins has a wide range of provenance signatures, from older foreland basin infilling marked by quartz-rich sandstones, with a cratonic or continental-block origin. Later, fold-and-thrust belt grains start to be the main producer of lithic fragment-rich and feldspar-rich particles, reflecting the space/time dependent progressive unroofing of the orogenic fold-and-thrust belt (Critelli and Criniti, 2021). Facies variations may result in different rocks developing between sequences of sandstone. The various types of sandstones can also form multilayer stacks when displaced across thrusts. Most of the fracture patterns in brittle sandstones are related to local stresses created by numerous, small intersecting fractures and typically have little relationship to the regional tectonic stresses. These are complex settings that are beyond the scope of this thesis and require continued investigation. The evaluation of the fractal dimensions and topology within the sandstones could provide information on the fracture patterns considering both variations of the sandstone and the structural forces which they have been subjected to.

6.2 Topology and fractal dimensions of structures

Foreland FAT belts are characterised by continent-continent collision forming fore-thrusts and antithetic back-thrusts. In a-foreland FAT belt like the field area, deformation becomes younger towards the foreland with thrusts developing in a break-forward or piggy-back sequence defining a regional foreland-directed tectonic transport direction (Poblet and Lisle, 2011).

Topologically, back-thrusts have higher densities of connected fractures (Grodner *et al.*, 2021). This is because back-thrusts have a vergence opposite the dominant trend of a thrust system and accommodate stresses by fracturing within a competent unit (Mitra, 2002). Back-thrusts, overturned anticline and synclines have the greatest number of total number of nodes and hence interconnected fractures due to abundant strike-parallel as well as secondary oblique fractures. A strong relationship is observed between fracture spacing and mechanical layer thickness of these folds with more fracturing forming in closely spaced limestone and shale layers (Wennberg *et al.*, 2006). Back-thrusts form ideal markers that are also clearly offset and cut by overlying younger fore-thrusts (Alsop *et al.*, 2018). Due to continued and extended periods of movement on the fore-thrusts, the topological data shows that they are dominated by fewer, well-connected fractures and longer fractures that are the product of flexural flow (Grodner *et al.*, 2021). Fore-thrusts and back-thrusts have lower fractal dimensions than pop-up structures but the highest fractal dimensions of both types of thrusts occur immediately adjacent to the pop-up structures and decrease away from them, indicating the tectonic stresses are highest at the intersection of the two types of thrusts. The upper layer adopts its own style of deformation, with pop-up structures independent from thrusts in the lower brittle layer. These are unaffected by later structural movement in this study and therefore represent the initial strains on the rock-mass with the lowest fractal dimension and number of nodes (Grodner *et al.*, 2021) The central Apennines FAT belt has layered carbonates similar to the study area and have rocks above a strong décollement of dolostones (strong limestones). Pop-up structures form above these décollements (Fabbi and Smeragli, 2019). The strain accommodation is attributed primarily to discrete fault surfaces and does not penetrate into the pop-up structure.

6.2.1 Topology and fractal dimensions of structures in the study area

The studies of how rocks deform in response to the stresses consists of descriptive and geometric analysis where geological structures are identified, characterised, and measured to determine the kinematic and dynamic analysis of the geological structures from field measurements. The topology and fractal data provide more information for the kinematic and dynamic analysis of the rock-mass measured.

With applied stress, depending on Young's Modulus, the shear modulus can increase, causing discontinuities to be displaced. An excellent example of this is the shearing of shale layers on fore-thrusts of the field-area. The low cohesion of shale allows the thrust discontinuity to be easily thrusts of the field-area. The low cohesion of shale allows the thrust discontinuity to be easily displaced. This type of thrust environment is identified by lower fractal dimensions and fewer cross- displaced. This type of thrust environment is identified by lower fractal dimensions and fewer cross- cutting nodes which indicates longer fracture lengths and lower fracture intensity. Fore-thrusts are characterised by fewer intersecting (y) nodes and a lower total number of nodes compared to back- thrusts. As a result, these structures are characterised by longer mean trace lengths of the planes that are a product of flexural flow in the fractures. The lower total number of nodes is due to the upward fore-thrusting and release of stresses on the décollement (shale) fault surfaces without causing excessive fracturing.

In contrast to this, in the back-thrust environment of the research area, the rock-mass is confined by the convergent stresses and hence the stress has to be relieved by fracturing. This type of environment is characterised by higher fractal dimensions and greater number of nodes. Back-thrusts consist mostly of lime mud with abundant small fractures have a high number of nodes and thus topologically a greater fracture density and closer fracture spacing which is enhanced because the back-thrusts

have a vergence opposite the dominant trend of a thrust system and can only accommodate hanging-wall rocks as out-of-syncline folds if they occur within a competent unit. Unlike the shales in the fore-thrusts, the shales are rotated and crushed due to the opposite sense of dip in the back-thrust and associated synclines. The rock-mass within the overturned anticline fold area of the back-thrusts is also highly fractured, due to the dominant compressive forces.

Hence, structural characteristics of these different thrusts, rather than the strength of the rock types present that is more important. Portions of the structural features can lock up and prevent shear movement on the faults and then, especially where the stratigraphy is weak, the intact rock will fracture. Where the applied stresses are higher than the strength of the rock, such as back-thrusts, further discontinuities develop in the rock-mass.

Overtuned anticlines and synclines have the greatest total number of nodes of the structures examined in the field, due to abundant strike-parallel as well as secondary oblique fractures as a result of highly compressive forces in the hinterland. The fractures have the highest fractal dimensions and the greatest number of fracture intersections. Anticlines cause opening mode fractures to develop. However, as tensile forces dominate in these anticlines, these structures develop the fewest nodes because the rock is not confined, compressed, and crushed. Due to the reduced number of nodes, the fracture density, connectivity, fracture density and mean trace length are low in the anticlines mapped in the field area.

Pop-ups have the lowest fractal dimension of the geological structures in the study area. This is because the principal compressive forces are accommodated by combined upthrown fore- and back-thrusts and the related upthrown block has a free Earth surface with no significant vertical stress causing a low number of lines and branches. The strain does not penetrate into the pop-up structure resulting in a low fracture intensity. The fractal dimension is lower as the fracture pattern is less convoluted and more linear.

The shear strength of geological structures, such as faults are often lower than the compressive strength of various limestones especially with thicker bedding. Lower shear-stresses that geological structures to deform (including the creation of fragments that form in large-scale thrusts.

This deformation acts as stress-relief on the rock-mass and the stresses do not reach high enough values to cause extensive brittle fracturing of the different rock-types. Hence, the structural fracture patterns are more common and have strongly developed features. Relative influence of rock types and structures.

In areas where there are lower tectonic stresses, the different rock types have few differences in shale, where there is possibly a shear-stress on the discontinuity. Hence, it is the structural characteristics of these different thrusts, rather than the strength of the rock type that is more important. Portions of the structural features can lock up and not allow movement on the faults and then, especially where the stratigraphy is weak, the intact rock will fracture. Only where the applied stresses are higher than the strength of the rock and it is confined, such as back- thrusts, will further discontinuities develop in the rock-mass.

Fracturing and folding provides a clear insight into the mechanics operating in an active fold and thrust belt. The topological and fractal characteristics can be used to determine the relative stresses and strengths in the various parts of a FAT belt. Importantly, these measurements of the rock-mass can also provide information on geometry and distribution of thrust-fold related fractures in buried or older limestone.

6.3 Topology and fractal dimensions of different FAT belt types

In this thesis it is shown that the topological and fractal characteristics can identify the various parts of a limestone dominated foreland FAT belt. These characteristics of the rock types and structural information provide better information on the distribution of the fracture patterns within the rock-mass at distance or depth. Although fold and thrust belts are described as typically occurring on the outer parts of collision mountain belts, there are several types of FAT belts. The techniques presented in this thesis can be used to determine the fracture patterns of the different fold and thrust belts (Figure 6.1 and Table 6.2)

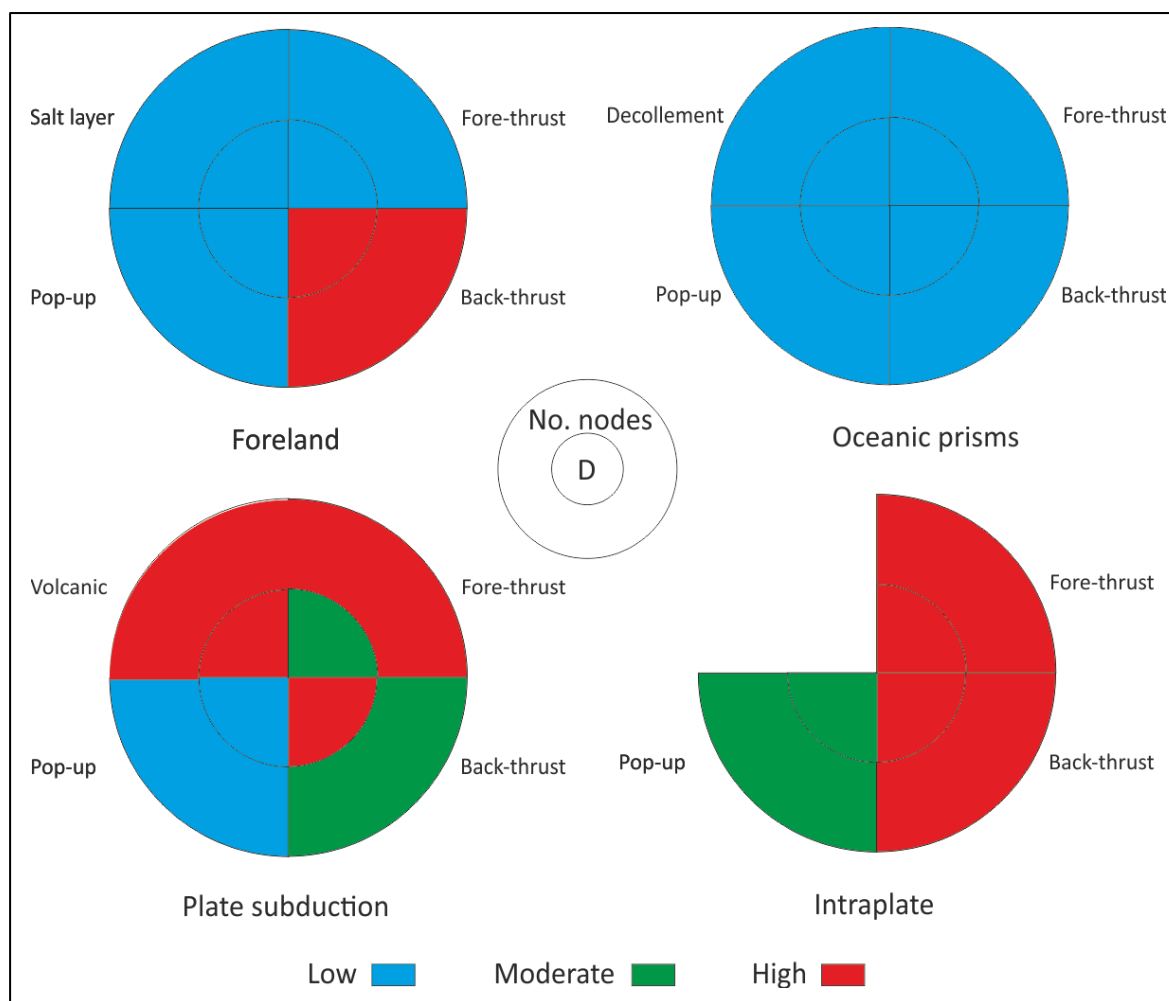


Figure 6.1: Preliminary characteristics of different FAT belts using fractal dimensions (D) and topological characteristics (number of nodes). Compare with Table 6.2.

Table 6.2: Preliminary characterisation of different FAT belts using fractal dimensions and topological characteristics (number of nodes). Compare with Figure 6.1.

FAT belt types	Structure	Fractal dimension	No. nodes
Foreland	Fore-thrust	Low	Low
	Back-thrust	High	High
	Pop-up	Low	Low
	Salt layer	Low	Low
Oceanic accretionary prisms	Fore-thrust	Low	Low
	Back-thrust	Low	Low
	Pop-up	Low	Low
	Décollement	Low	Low
Plate subduction	Fore-thrust	Moderate	High
	Back-thrust	High	Moderate
	Pop-up	Low	Low
	Volcanic	High	High
Intraplate	Fore-thrust	High	High
	Back-thrust	High	High
	Pop-up	Moderate	Moderate

There are many variables that determine the fractal dimensions and topology. These include the strength of the rock types relative to the applied stresses. Different rock type sequences will respond differently, with for example forelands and accretionary prisms being likely to contain shale layers or décollements in the fore-thrusts reducing the fractal dimension and number of nodes. The applied stresses create structural features which can result in compression in areas such as back-thrusts and the volcanic portions of plate subduction. which also determines the fractal dimensions and topology.

7. Conclusions

The objective of this thesis is to understand the distribution of fractures in platform carbonates of a frontal thrust sheet of the Himalayan Fold and Thrust Belt in northern Pakistan. A new method for characterising fractures has been developed in the field area, that analyses the topological and fractal characteristics of the fractures of different rock types and geological structures.

7.1 Fractal dimensions and topological analysis

Quantifying fractal dimensions provides insights into the relationships of the spatial distribution of non-Euclidean shapes. This allows the definition of a broad array of geometrical characteristics, especially the distribution of fractures in different geological structural features. Topological analysis of a fracture network characterises the connectivity of the constitutive fractures in that network, rather than the inherent properties of the individual fractures of a fracture system (Sanderson et al., 2019). By combining these analytical approaches, it has provided an improved understanding of the overall behaviour of the physical properties of the rock mass under consideration.

As a fracture system is not simply the sum of the sets of fractures, but also the interactions between them, it was necessary to develop a methodology that rapidly established the attributes of the overall rock mass. From a geomechanical perspective, the behaviour of the rock mass is the sum of all its constituent inhomogeneities, including both lithological variation and all fracture sets. In each structural domain there is a general brittle failure pattern due to the stress-path that the rock-mass has undergone (Everall and Sanislav, 2018). One cannot simply add together the number of nodes of the different fracture populations as there are intersections between fractures of the different populations which will increase the number and/or type of nodes and hence vary the topology. By combining the topological and fractal characteristics of the fractures into a single group, the cumulative characteristics of all the fractures in a single set of measurements, various combined

stratigraphic and structural domains have been defined within each sampling circle. Because the circles are all 1 m in diameter, the topological and fractal characteristics could be directly compared.

7.2 Key results

By examining the topological characteristics and fractal dimension of all the fractures together it is possible to distinguish and quantify the fracture system of an area based on empirical evidence and use this to define rock assemblages and especially structural domains.

The different limestones in the field area do not have a significant variation in strength. This is due to the diagenesis of lime muds to micrite and microspar cement. The oldest Samana Suk Formation has undergone significant diagenesis converting lime muds to microspar (Nizami, 2019). The Kawagarh Formation is a dolomitised sequence of shales and wackestone. The Lockhart Formation consists of bioclastic limestone converted to micrite with shale partings. The Patala Formation is a shale dominated unit with micritised foraminiferal wackestone. The Nammal Formation consists of nodular limestone with microspar, and minor shale (Ghazi *et al.*, 2020). The Margalla Hills Formation consists of limestone units recrystallised to micrite to microspar. The micrite and microspar layers typically terminate against the shale partings which have low shear strengths. Due to the high compressive strengths of the diagenetically altered limestones, variations in fracture patterns of different rock types are more visible when shale horizons form decollement surfaces, especially in fore-thrusts that allow tectonic stress relief.

It was found that the that fracture type, characteristics and abundance could be related to the main structures, particularly thrusts and folds, and hence a predictive relationship of the topological characteristics and fractal dimensions was established.

The important structural pop-up features are located between the thrusts and become tectonically isolated with greatly reduced stresses in the rock-mass, resulting in the lowest fractal dimension and

lowest number of nodes. These topological and fractal values can therefore be used to determine the trajectory of the topological and fractal characteristics when different structures evolve.

The fracture systems developed adjacent to the pop-up structures, in both fore-thrusts and back-thrust settings have higher fractal dimensions that decreases away from the central pop-up zone.

In general, the fracture patterns developed in the fore-thrusts have lower fractal dimensions than those developed adjacent to back-thrusts. Topologically, the fracture networks in the fore-thrust setting have on average, fewer nodes and a longer mean trace length and hence a lower density, but higher connectivity. Back-thrusts are dominated by more nodes producing topological characteristics of higher fracture density, higher intensity, and lower mean trace length (shorter fractures) which reflects the high compressive forces present. This helps to identify the structure type and the applied stresses from the fractal dimensions and topology of different thrusts that may have been displaced or altered during subsequent tectonism.

In the thrust-related anticlines, that can develop as a fault-propagation folds, the tensional stresses develop in the same orientation as the regional compression, leading to opening mode fractures developing with higher fractal dimensions. As tensile forces dominate in the anticlines these structures develop the fewest nodes, resulting in lower topological values, especially fracture density and intensity.

Synclines and overturned anticlines have the highest fractal dimensions and the greatest number of fracture intersections. This is because there are many different fractures that both cross-cut, and terminate on, the sheared bedding planes creating a complex rock mass.

7.3 Comparisons with previous studies

Previous studies of rock fracture patterns have not been able to determine a uniform way of characterising by expressing it as pair of variables.

Detailed mapping has indicated that rock type is a significant contributor to fracture patterns (Butler, 2018; Watkins *et al.*, 2019). Previous studies have shown that fracture density depends on distance from faults (Vermilye and Scholz, 1999) as well as fault zone architecture (Caine *et al.*, 1996). Other studies have found a stronger relationship between fracture spacing and the thicknesses of geomechanical units, (Pei, 2019; McGinnis *et al.*, 2017; Ortega *et al.*, 2010) forming groups of rock with homogeneous fracture patterns due to the characteristics of the rock-mass (Laubach *et al.*, 2009; Boro *et al.*, 2013).

All of these features can be defined by specific examples of the topological and fractal analysis of the rock-mass behaviour in the field area.

- 1) A greater difference in the rock type results in a higher variability of the fractal and topological characteristics. If, for example, a weak shear strength shale layer interacts with a high uniaxial compressive strength wackestone it results in different fracture node patterns and different topological and fractal features,
- 2) Fracture density decreases away from faults due to the high compressive strength of the micritised limestone and low shear strength of shale partings, and
- 3) The same uniform geotechnical behaviour of the different rock types caused by micrite and microspar cement has resulted in a stronger relationship between fracture spacing and the thicknesses of geomechanical units.

This thesis only considers similar rock assemblages, stress conditions, and structural domains. It would be possible to quantify and compare the fractal and topological values to determine a wider range of rock assemblages, stress conditions, and structural features. It is only by combining and comparing both spatial and topological data types that the characterisation of structural styles become apparent.

Notwithstanding the facts that fracture fill and aperture can contribute greatly to the fracture network, the results indicate that, in a qualitative sense, the permeability and porosity of fracture networks developed adjacent to different structures can be determined from the methodology described in this thesis. The technique requires further development in order for it to provide a truly predictive approach, and the precise nature of these relationships to the structural and physical characteristics of the rock mass requires further analysis.

7.4 Further research

The lithological effects and structural impacts are very interesting, with the latter considered in Grodner *et al.* (2021). There is the potential for the former being investigated in a new paper. It is likely that this will investigate the different rock-engineering characteristics of the strata, such as bedding parallel slip in shales. The relative proportion of the different rock-types will be investigated.

Fold and thrust belts have been widely recognised as the most common mechanism to accommodate shortening in the crust through an enormous heterogeneity of structural characteristics. Fold kinematics play a primary role in determining the type, frequency, and attitude of folding-related deformation structures in fault-related folds. In high strain regions fracturing is influenced by structural controls, such as the area investigated by this thesis. Compared to this, in low strain regions lithology becomes more important in influencing fracturing. It is necessary to confirm the validity of the topological and fractal analytical tool in different types of fold and thrust terrains. Several different field areas have been considered during this thesis but were not possible to visit due to the Covid epidemic. Preliminary investigations have been undertaken at other sites. Suitable projects for investigating the validity of topological and fractal dimensions to define the fracture characteristics include:

- 1) The Pyrenees are an asymmetrical, double-wedge continental fold and thrust mountain belt that formed because of the collision between the Iberian and European plates and are thus different to the area examined in the thesis. The southern, and most significant, thrust system

is developed on top of the subducted Iberian Plate. The northern thrust system occurs on top of the European Plate. The work should consider the stratigraphy and structural geology of the South Pyrenean Zone, especially in the Central Pyrenees as it has a similar mechano-

stratigraphic character to the field area investigated in Pakistan. The Alpine Orogeny deformed the Upper Cretaceous to Paleogene rocks of the South and Central Pyrenean Zone and the Palaeozoic rocks Variscan metamorphic evolution in the Axial Zone (Cochelin *et al.*, 2017, Muñoz *et al.*, 1986). Both the structural differences between these two FAT belts and the validity of the analytical technique would be evaluated.

- 2) Early debates about the Alpine FAT belt considered that folding was a necessary precursor to thrusting (Westermann, 2009). Since that time there has been a tendency to classify structures as fault bend folds, fault propagation folds, and detachment folds using seismics and tomography. However, incremental evolution of the structures imply that folds do not conform to these models. Characterising this by evaluating the topology and fractal dimensions of the fractures and hence determining the appropriate mechanical models will allow the understanding of more detailed features and relate this to the high density of seismic and tomographic research within the Alps.
- 3) The Dorset coast consists of extensive near vertical to overturned bedding with the Lewes to Portsdown chalk formations subjected to intense brittle deformation as the extensional Purbeck Fault was reactivated as the Durdle Dore Thrust. Specific structural features can be mapped in detail including the intensely folded and crumpled anticline Stair Hole, adjacent to Lulworth Cove (West, 2017). Preliminary investigations by the author has showed that it is possible to use the same circle measurements as in this thesis. It is suggested that drone-mapping is also used and compared to variations in the number of nodes and fractal dimension. The strata of the Dorset coast consist mainly of chalk with marls and flint scattered throughout, making these strata a lot weaker than the micritised limestone of the field area. The differences in topological and fractal characteristics and can be quantified.
- 4) In other FAT belts and even in different portions of the same FAT belt, there will be variations of the topology and fractal characteristics. If the rock-mass (both the rock types, and the fractures), has more similar fractal and topological characteristics it can be considered similar to other portions of a FAT belt or different belts. This would be achieved generating a database

of key information on the various rock types present, the styles of geological structures and different scales of topological and fractal information. As more data is accumulated, it will be possible to evaluate FAT belt styles. With this additional data it will be possible to determine topological and fractal characteristics of FAT belt characteristics at a range of scales and hence quantify the fractures associated with specific structural features. This will improve the understanding of the fracture distributions in these rocks.

Further fractal and topologic research projects considering fractures have been examined. Fractals may share the topological properties of “small-world” networks, which is a Graph Theory term for close efficient systems (Valentini *et al.*, 2007). This has important geological implications for a variety of geological processes from fracture mechanics to fluid flow. The fractal and topological properties of fractures defines the structural heterogeneity and anisotropy in a rock volume, and impacts the understanding of how fractures initiate, propagate, and interact during the formation of fracture patterns (Laubach, 2022). It is therefore necessary to understand the details of these processes which can be assessed using topology.

As this this thesis has shown, it is possible to observe the interaction between the topological and fractal characteristics of rocks, especially in FAT belts. The characteristics of microscopic rock fragments are being investigated using these techniques. For example, in tests, the rock-burst tendency has been found to be dependent on the fractal dimension of fractures and shape of the sample (Zhang, 2015). Topological and fractal characterizations of pore systems in low-permeability reservoirs have been undertaken using SEM, MICP, NMR, and X-ray CT. It was found that topological, fractal and transport properties of pore space can be obtained (Wu *et al.*, 2019). It has also been possible to define the topological parameters of a random fractal surfaces and hence provide a statistical description of the various rough surfaces (Borri and Paggi, 2015).

It has been demonstrated that the stresses applied to the rock-mass determine the topological and fractal characteristics. Rock engineering evaluates the increased and reduced stresses caused by excavations and these have been evaluated by fractal analysis (Grodner *et al.*, 2021). If the rock-mass characteristics are better quantified by utilising the fractal and topological characteristics with the well-established rock-engineering scheme, such as the Rock Mass Rating scheme (Bieniawski, 1973), or the Q-System (Barton *et al.*, 1974) it will provide a more accurate description of how the rock may fail, and hence allow better rock-support to be selected.

8. References

Abir I.A., Khan, S.D., Aziz G.M., Tariq, D. 2017. Bannu Basin, fold-and-thrust belt of northern Pakistan: Subsurface imaging and its implications for hydrocarbon exploration. *Marine and Petroleum Geology* 85, 242-258

Acharyya, S. K., Saha, P. 2018. Himalayan Paleogene Foreland Basin, its collision induced early volcanic history and failed rift initiation. *Journal of Asian Earth Sciences* 162, 3-12.
<https://doi.org/10.1016/j.jseas.2018.04.031>

Agard, P., Omrani, J., Jolivet, L., Whitechurch, H. 2011. Zagros orogeny: A subduction-dominated process. *Geological Magazine* 148(5-6). DOI:10.1017/S001675681100046X

Ahmed, M. 2019. Sedimentology of Marl and Marly Limestone Sequence of Upper Cretaceous Kawagarh Formation from Northern Kalachitta Range, Attock Hazara Fold and Thrust Belt, Pakistan. *Open Journal of Geology* (9), 1 – 14

Akhtar, M., Butt, A.A. 1999. Microfacies and foraminiferal assemblages from the Early Tertiary rocks of the Kala Chitta Range (northern Pakistan). *Géologie Méditerranéenne* 26-3-4, 185-201.

Alam, I., Azhar, A.M., Khan, M.W. 2014. Frontal structural style of the Khisor Range, northwest of Bilot: Implications for hydrocarbon potential of the north-western Punjab fore deep. Pakistan. *Journal of Himalayan Earth Sciences* 47(1), 87-98

Al-Kindi, M.H.N. 2020. Understanding the Relationship between Large-Scale Fold Structures and Small-Scale Fracture Patterns: A Case Study from the Oman Mountains. *Geosciences* 10, 490
doi:10.3390/geosciences10120490

Ali, F. 2014. Tectonic evolution of the Margalla Hills and part of the south-eastern Hazara Ranges, Pakistan. Unpublished PhD dissertation, University of Peshawar, Pakistan

- Ali, F., Haneef, M., Anjum, M.A., Hanif, M. and Khan, S. 2013. Microfacies analysis and sequence stratigraphic modelling of the Samana Suk Formation, Chichali Nala, Trans Indus Ranges, Punjab, Pakistan. *Journal of Himalayan Earth Sciences*, 46, 41-53.
- Ali, T.H., Ali, F., Ali, F, Haneef, M., Hanif, M., Ahmad, S., Rehman, G., Fida, S. 2014. Microfacies analysis and diagenetic fabric of Lockhart Limestone exposed along Nathiagali-Murree Road, District Abbottabad, Pakistan. *Journal of Himalayan Earth Sciences* 47 (2),99-114.
- Ali F., Haneef, M., Anjum, M.N., Hanif, M., Khan, S. 2013. Microfacies analysis and sequence stratigraphic modelling of the Samana Suk Formation, Chichali Nala, Trans Indus Ranges, Punjab, Pakistan. *Journal of Himalayan Earth Sciences* 46(1) 41-53.
- Anantharamu, V., Vernik, L. 2019. Linking preferred orientation of shale minerals to their elasticity . SEG International Exposition and 89th Annual Meeting, 3573 – 3577. <https://doi.org/10.1190/segam2019-3213946.1>
- Awais; M., Hanif, M.; Ishaq, M., Jan, I. U. 2020. An integrated approach to evaluate dolomite in the Eocene Chorgali Formation, Khair-e-Murat Range, Pakistan: Implications for reservoir geology. *Journal of Himalayan Earth Sciences; Peshawar* 53 (1)
- Awais, M., Hanif, M, Irfan, J., Ishaq, M., Khan, M. 2020. Eocene carbonate microfacies distribution of the Chorgali Formation, Gali Jagir, Khair-e-Murat Range, Potwar Plateau, Pakistan: approach of reservoir potential using outcrop analogue. *Arabian Journal of Geosciences*. 13(14)
- Azhar, M., Swati, F. Haneef, M., Ahmad, S., Latif, K., Naveed, Y., Zeb, W., Akhtar, N., Owais., M. 2014. Diagenetic analysis of the Early Eocene Margalla Hill limestone, Pakistan: A synthesis for thin section porosity. *Journal of Himalayan Earth Sciences Volume* 47 (2) 49-6.
- Barton, N., Lien, R., Lunde, J. 1974. Engineering classification of rock masses for the design of tunnel support. *Rock Mechanics* 6, 189 – 236. <https://doi.org/10.1007/BF01239496>

- Barbier, M., Hamon, Y., Callot, J-P, Floquet, M., Daniel, J-M. 2012. Sedimentary and diagenetic controls on the multiscale fracturing pattern of a carbonate reservoir: The Madison Formation (Sheep Mountain, Wyoming, USA). *Marine and Petroleum Geology* 29, 50 - 67
- Belayneh, M., Cosgrove, J.W. 2004. Fracture-pattern variations around a major fold and their implications regarding fracture prediction using limited data: an example from the Bristol Channel Basin. *Geological Society, London, Special Publications*, 231, 89 – 102
<https://doi.org/10.1144/GSL.SP.2004.231.01.06>
- Benchilla, L., Swennen, R., Akhtar, K., Roure, F. 2002. Sedimentology and diagenesis of the Chorgali Formation in the Potwar Plateau and Salt Range, Himalayan foothills (N-Pakistan). AAPG Hedberg Conference, Deformation History, Fluid Flow Reconstruction and Reservoir Appraisal in Foreland Fold and Thrust Belts. May 14 – 19, 2002, Palermo – Mondello, Sicily, Italy.
- Berntson, G., Stoll P., 1997. Correcting for finite spatial scales of self-similarity when calculating the fractal dimensions of real-world structures. *Proc. R. Soc. B Biol. Sci.* 264, 1531–1537.
<https://doi.org/10.1098/rspb.1997.0212>.
- Bieniawski, Z.T. 1973. Engineering Classification of Jointed Rock Masses. *Transactions of the South African Civil Engineers*, 15, pp. 335-344
- Bieniawski, Z.T. 1979. The Geomechanics classification in rock engineering applications. *Proceeding of the 4th International Congress of Rock Mechanics*. ISRM, Montreux, 41-48
- Boadu, F.K., Long, L.T. 1996. Effects of fractures on seismic-wave velocity and attenuation *Geophysical Journal International*, 127 (1) 86–110, <https://doi.org/10.1111/j.1365-246X.1996.tb01537.x>
- Bouda, M., Caplan, J.S., Saiers, J.E. 2016. Box-Counting Dimension Revisited: Presenting an Efficient Method of Minimizing Quantization Error and an Assessment of the Self-Similarity of Structural Root Systems. *Frontiers in Plant Science* (7). <https://doi.org/10.3389/fpls.2016.00149>

Bratton, T., Canh, D.V., Cu, N.V.Q., Duc, N.V., Gillespie, P., Hunt, D., Ahmadi, Marcinew, R, Ray, S., Montaron, B., Nelson, R., Schoderbek, D., Sonneland, L. 2006. The Nature of Naturally Fractured Reservoirs. Oilfield Review: <https://www.researchgate.net/publication/220010431>

Burberry, C.M., Cannon, D.L. Cosgrove, J.W., Engelder, T. First published online 31 January 2019. Fracture patterns associated with the evolution of the Teton anticline, Sawtooth Range, Montana, USA. In Bond, C.E., Lebit, H.D. (Eds.), 2019. Folding and Fracturing of Rocks: 50 Years of Research since the Seminal Textbook of J. G. Ramsay, 487, Geological Society, London, Special Publications, <https://doi.org/10.1144/SP487.12>

Buczowski, S., Hildgen, P. Cartilier, L. 1998. Measurements of fractal dimension by box-counting: a critical analysis of data scatter. Physics A: Statistical Mechanics and its Applications 252 (1–2), 23-34. [https://doi.org/10.1016/S0378-4371\(97\)00581-5](https://doi.org/10.1016/S0378-4371(97)00581-5)

Burchette, T. 2012 Carbonate rocks and petroleum reservoirs: A geological perspective from the industry. Geological Society of London Special Publication 370 (1), 17-37

Cahn, R., 1989. Fractal dimension and fracture. Nature 338, 201 – 202.

<https://doi.org/10.1038/338201a0>

Cardona, A., Finkbeiner, T., Santamarina, J.C. 2021. Natural Rock Fractures: From Aperture to Fluid Flow. Rock Mech Rock Eng 54, 5827–5844. <https://doi.org/10.1007/s00603-021-02565->

Carter, B. R., Toggweiler, J. R., Key, R. M., Sarmiento, J. L. 2014, Processes determining the marine alkalinity and calcium carbonate saturation state distributions, Biogeosciences, 11, 7349–7362, <https://doi.org/10.5194/bg-11-7349-2014>

Chambers, A.F. 1991. Kinematics of the Frontal Himalayan Thrust Belt, Pakistan, and the External Western Alps, France. Unpublished DPhil Thesis, Department of Geology, Imperial College of Science, Technology and Medicine, University of London, London

- Cheema, A.H. 2010. Microfacies, Diagenesis and Depositional Environments of Samana Suk Formation (Middle Jurassic) Carbonates Exposed in Southeast Hazara and Samana Range. Unpublished Ph.D. thesis. University of the Punjab. <http://173.208.131.244:9060/xmlui/handle/123456789/2462>
- Chen, L., Khan, S.D. 2009. Geomorphometric features and tectonic activities in sub-Himalayan thrust belt, Pakistan, from satellite data. *Computers & Geosciences* 35, 2011–2019
- Cochelin, B., Lemirre, B., Denèle, Y., de Saint Blanquat, M., Lahfid, A., Duchêne, S. 2017. Structural inheritance in the Central Pyrenees: the Variscan to Alpine tectonometamorphic evolution of the Axial Zone. *Journal of the Geological Society* (2018) 175 (2): 336–351. <https://doi.org/10.1144/jgs2017-066>
- Cooke, M.L., Simo, J.A., Underwood, C.A., Rijkene, P. 2006. Mechanical stratigraphic controls on fracture patterns within carbonates and implications for groundwater flow. *Sedimentary Geology* 184 (3–4), 225-239.
- Corradetti, A., Girundo, M., Tavani, S., Iannace, A., Parente, M., Mazzol, S. Strauss, C., Torrieri, S., Pirmez, C., Giorgioni, M. 2015. Analysis of Reservoir Scale Fracture Sets in Southern Italy's Carbonate Reservoir Analogues, Monte Faito, Sorrento Peninsula (Southern Italy). International Petroleum Technology Conference, 10.2523/IPTC-18433-MSDoha, Qatar, paper Number: IPTC-18433-MS
- Cosgrove, J.W. 2015. The association of folds and fractures and the link between folding, fracturing and fluid flow during the evolution of a fold-thrust belt: a brief review. In Richards, F.L., Richardson, N.J., Rippington, S.J., Wilson, R.W., Bond, C.E. (Eds.). 2015. *Industrial Structural Geology: Principles, Techniques, and Integration*, Geological Society, London, Special Publication 421, 41-68 <https://doi.org/10.1144/SP421.11>
- Dahlstrom, C. D. A. 1970. Structural geology in the eastern margin of the Canadian Rocky Mountains. *Bull of Canadian Petroleum Geology*. 18 (3): 332–406. <https://doi.org/10.35767/gscpgbull.18.3.332>
- Dawers, N.H., Anders, M.H. 1995. Displacement-length scaling and fault linkage. *Journal of Structural Geology* 17(5), 607-614.

- Dunham, R. J. 1962. Classification of carbonate rocks according to depositional texture. In: Ham, W. E. (ed.), Classification of carbonate rocks. American Association of Petroleum Geologists Memoir, pp. 108-121
- Engelder, T. 1985. Loading paths to joint propagation during a tectonic cycle: an example from the Appalachian Plateau, USA. *Journal of Structural Geology* 7(3/4), 459-476
- Everall, T.J., Sanislav, I.O. 2018. The influence of pre-existing deformation and alteration textures on rock strength, failure modes and shear strength parameters. *Geosciences*, 8 1 - 23, [10.3390/geosciences804024](https://doi.org/10.3390/geosciences804024)
- Fabbi, S., Smeraglia, L. 2019. Pop-up structure in massive carbonate-hosted fold-and-thrust belt: Insight from field mapping and 2D kinematic model in the central Apennines. *Journal of Structural Geology* 126, 258-271. <https://doi.org/10.1016/j.jsg.2019.06.011>
- Fahad, M., Khan, M.A., Hussain, J., Ahmed, A., Yar, M. 2021. Microfacies analysis, depositional settings and reservoir investigation of Early Eocene Chorgali Formation exposed at Eastern Salt Range, Upper Indus Basin, Pakistan. *Carbonates & Evaporites* 36 (41) <https://doi.org/10.1007/s13146-021-00708-7>
- Farid, A. Khalid, P., Ali, M.Y., Iqbal, M.A., Jadoon, K.Z. 2018. Seismic stratigraphy of the Mianwali and Bannu depressions, north-west Indus foreland basin. *International Journal of Earth Sciences* 107, 1557-1578
- Fernández-Martínez, M., Sánchez-Granero, M. 2014. Fractal dimension for fractal structures. *Topology and its Applications*, 163, 93-111. <https://doi.org/10.1016/j.topol.2013.10.010>
- Ferreira, M.A.C.M. 2019. Effects of initial rift inversion over fold-and-thrust development in a cratonic far-foreland setting. *Tectonophysics* (757), 88-107. <https://doi.org/10.1016/j.tecto.2019.03.009>
- Ferrill, D.A., Morris, A.P., Wigginton, S.S., Smart, K.J., McGinnis, R.N., Lehrmann, D. 2016. Deciphering thrust fault nucleation and propagation and the importance of footwall synclines. *Journal of Structural Geology* 85 1-11 <http://dx.doi.org/10.1016/j.jsg.2016.01.009>

- Ferrill, D.A., Morris, A.P., Wigginton, S.S., Smart, K.J., McGinnis, R.N., Lehrmann, D. 2016. Deciphering thrust fault nucleation and propagation and the importance of footwall synclines. *J. Struct. Geol.*, 85 1-16. <https://doi.org/10.1016/j.jsg.2016.01.009>
- Ferrill, D.A., Smart, K.J., Cawood, A.J., Morris, A.P. 2021. The fold-thrust belt stress cycle: Superposition of normal, strike-slip, and thrust faulting deformation regimes. *Journal of Structural Geology* 148, 104362. <https://doi.org/10.1016/j.jsg.2021.104362>
- Florez-Nino, J.-M., Aydin, A., Mavko, G., Antonellini, M., Ayaviri, A. 2005. Fault and fracture systems in a fold and thrust belt: an example from Bolivia. *AAPG Bulletin*, 89 (4), 471 – 493. <https://doi.org/10.1306/11120404032>
- Folk, R.L. 1959. Practical Petrographic Classification of Limestones. *AAPG Bulletin* 43 (1) 1 – 8.
- Folk, R.L. 1974. *Petrology of Sedimentary Rocks*. Hemphill Publishing Co., Austin, 170 pp.
- Flügel, E. 2013. *Microfacies of Carbonate Rocks: Analysis, Interpretation and Application*. Germany: Springer Berlin Heidelberg. 976 pp.
- Gee, E. R., Gee, D.G. 1989. Overview of the geology and structure of the Salt Range, with observations on related areas of northern Pakistan. *Geological Society of America. Special Paper* 232
- Ghazi, S., Ali, S.H., Sahraeyan, M. 2014. An overview of tectonosedimentary framework of the Salt Range, north-western Himalayan fold and thrust belt, Pakistan. *Arabian Journal of Geosciences* 8 (3), 1 – 15. <https://doi.org/10.1007/s12517-014-1284-3>
- Ghazi, S., Sharif, S., Zafar, T. 2020. Sedimentology and Stratigraphic Evolution of the Early Eocene Nammal Formation, Salt Range, Pakistan. *Stratigr. Geol. Correl.* 28, 745–764. <https://doi.org/10.1134/S0869593820070047>

Gill, M.M. 2020. Diagenesis, Depositional Model and Stratigraphic Evolution of the Margalla Hill Limestone, Southeast Hazara. Conference Proceedings, 82nd EAGE Annual Conference & Exhibition, Jul 2020, p.1 – 5. European Association of Geoscientists & Engineers. <https://doi.org/10.3997/2214-4609.202010215>

Gillespie, P.A., Walsh, J.J., Watterson, J. 1993. Measurement and characterisation of spatial distribution of fractures. *Tectonophysics* 226, 114-141

Grelaud, S., Sassi, W., De Lamotte, D.F., Jaswal, T., Roure, F. 2002. Kinematics of eastern Salt Range and South Potwar Basin (Pakistan): A new scenario, *Marine and Petroleum Geology*, 19, 1127–1139

Grodner, M.W., Clarke, S.M, Burley, S.D., Leslie, A.G., Haslam, R. 2021. Combining topology and fractal dimension of fracture networks to characterise structural domains in thrust limestones. *Journal of Structural Geology* 153, 104468. <https://doi.org/10.1016/j.jsg.2021.104468>

Groves, D.I., Goldfarb, R.J., Santosh, M. 2016. The conjunction of factors that lead to formation of giant gold provinces and deposits in non-arc settings. *Geoscience Frontiers*, 7 (3), 303-314. <https://doi.org/10.1016/j.gsf.2015.07.001>

Guerrero V, Iannace, A, Mazzoli, S., Parente, M., Vitale, S., Giorgioni, M., 2010. Quantifying uncertainties in multi-scale studies of fractured reservoir analogues: Implemented statistical analysis of scan line data from carbonate rocks. *Journal of Structural Geology* 32, 1271-1278.

Ham, W.E., Pray, LC. 1962. Modern Concepts and Classifications of Carbonate Rocks. In *Classification of Carbonate Rocks--A Symposium*. AAPG Special Volume Reservoirs—Carbonates, 2-19 <http://archives.datapages.com/data/specpubs/carbona2/data/a038/a038/0001/0000/0002.htm>

Hanif, M. 2011. Stratigraphy and Palaeoenvironment of the Palaeocene/Eocene boundary interval in the Indus Basin, Pakistan. Unpublished PhD Thesis, University of Plymouth (UK). <http://hdl.handle.net/10026.1/865>

Hancock, P. L., 1985. Brittle microtectonics: principles and practice. *Journal of Structural Geology*, 7 (3 - 4), 437-457.

Hanif, M., Ali, F., Afridi, B.Z, 2013. Depositional environment of the Patala Formation in biostratigraphic and sequence stratigraphic context from Kali Dilli Section, Kala Chitta Range, Pakistan. *Journal of Himalayan Earth Sciences*, 46 (1), 55-65.

Hanif, M., Imraz, M., Ali, F. Haneef, M. Saboor, A. Iqbal, S., Ahmad, S. 2014. The inner ramp facies of the Thanetian Lockhart Formation, western Salt Range, Indus Basin, Pakistan. *Arabian Journal of Geoscience* 7, 4911–4926. <https://doi.org/10.1007/s12517-013-1099-7>

Hafver, A., Jettestuen, E., Kobchenko, M., Dysthe, D.K., Meakin, P., Sørensen, A.M. 2014. Classification of fracture patterns by heterogeneity and topology. *EPL*, 105 56004 1-6. <https://doi.org/10.1209/0295-5075/105/56004>

Hammerstein, J.A., Di Cuia, R., Cottam, M.A., Zamor, G., Butler, R.W.H. 2020. Fold and thrust belts: structural style, evolution and exploration – an introduction. Geological Society, London, Special Publications 490 1 – 8. <https://doi.org/10.1144/SP490-2020-81>

Hussain, J., Khan, T., Shami, B.A., Zafar, M., Hayat, T. 2021. Microfacies analysis and reservoir evaluation based on diagenetic features and log analysis of the Nammal Formation, Western and Central Salt Range, Upper Indus Basin, Pakistan. *Arab Journal of Geoscience* 14, Article 976 (electronic). <https://doi.org/10.1007/s12517-021-07387-7>

Iqbal, M., Bannert, D. 1998 Structural Observations of the Margala Hills, Pakistan and the Nature of the Main Boundary Thrust. *Pakistan Journal of Hydrocarbon Research* 10, 41-53

- Izquierdo-Llavall, E., Roca, E., Xie, H., Pla, O., Muñoz, J. A., Rowan, M. G. 2018. Influence of overlapping décollements, syntectonic sedimentation, and structural inheritance in the evolution of a contractional system: The central Kuqafold-and-thrust belt (Tian Shan Mountains, NW China). *Tectonics*, 37, 2608–2632. <https://doi.org/10.1029/>
- Jadoon, M. S. K., Jadoon I.A.K., Bhatti, A.H. Ali, A. 2006. Fracture Characterization and Their Impact on the Field Development. *Pakistan Journal of Hydrocarbon Research* 16 11-21
- Jadoon, I.A.K., Hinderer, M., Wazir, B. Yousaf, R., Bahadar, S., Hassan, M., Abbas, Z, Jadoon, S. 2007. Structural styles, hydrocarbon prospects, and potential in the Salt Range and Potwar Plateau, north Pakistan. *Arab J Geosci* 8(5), 111 – 125. <https://doi:10.1007/s12517-014-1566-9>
- Jamil, S., Rabia, S., Hajra, I., Haneef, S.M., Naz, H. 2012. Biostratigraphy of the Patala Formation, Makarwal Area, Sughar Range, Northern Pakistan. *Earth Sciences Pakistan 2012*, Baragali Campus University of Peshawar, Hazara. Retrieved May 25, 2022, from <https://www.thefreelibrary.com/BIOSTRATIGRAPHY+OF+THE+PATALA+FORMATION+MAKARWAL+A+REA+SURGHAR+RANGE...-a0380092689>
- Jolley, S.J., Henderson, I. H. C., Barnicoat, A. C., Fox, N. P. C. 1999. Thrust-fracture network and hydrothermal gold mineralization: Witwatersrand Basin, South Africa. *Geological Society, London, Special Publications* 155, 153 – 165. <https://doi.org/10.1144/GSL.SP.1999.155.01.12>
- Kagan, Y. Y., 1991. Fractal dimension of brittle fracture. *Journal of Non-linear Science* 1, 1–16.
- Kendall C.G.S.C., Flood P., 2011. Classification of Carbonates. In: Hopley D. (eds) *Encyclopaedia of Modern Coral Reefs. Encyclopaedia of Earth Sciences Series*. Springer, Dordrecht. https://doi.org/10.1007/978-90-481-2639-2_269
- Khan, M.Z., Rahman Z.U., Khattak Z., Ishfaque, M. 2004. Microfacies and Diagenetic Analysis of Chorgali Carbonates, Chorgali Pass, Khair-E-Murat Range: Implications for Hydrocarbon Reservoir

Characterization Pakistan Journal of Geology 1(1), 18-23 <https://doi.org/10.26480/pjg.01.2017.18.23>

Khan, S. 2007. Evaluation of Chichali Formation as a Source Rock for Hydrocarbon Generation in the Southern Hazara, NWFP, Pakistan. Unpublished MPhil Thesis, National Centre of Excellence in Geology, University of Peshawar, Peshawar

Khan, A., Hersi, O, S, Ahmed, S. 2018. Lithofacies properties, biostratigraphy and depositional setting of the Palaeocene Lockhart Limestone, Hazara and Potwar Subbasins, Northeast Pakistan. Geoconvention, Calgary, May 7 -11, 2018.

Khan, M., Khan, M.A., Shami, B.A. 2018. Microfacies analysis and diagenetic fabric of the Lockhart Limestone exposed near Taxila, Margalla Hill Range, Punjab, Pakistan. Arab J Geosci 11(29), 1-15. <https://doi.org/10.1007/s12517-017-3367-4>

Khan, S, Ur Rashid, M. 2022. Dolomitization mechanism in the Chorgali formation, Pakistan: Evidence from field observations, Petrography, Mineralogical, and SEM analysis. Turkish Journal of Geosciences; 3 (1), 12 - 21, <https://doi:10.48053/turkgeo.1028669>

Khattak, S.A., Rehman G., Ahmad, S., Jan, M.F., Khurshid, S., Ghani, A. 2017 Deformational style and hydrocarbons trapping mechanism of the sub-Himalayan frontal ranges near Fateh Jhang, Punjab, Pakistan. Journal of Himalayan Earth Sciences 50 (2) 1-13

Khattak, Z., Khan, M., Rahman, Z.U., Khan, M.Y., Ishfaq, M. 2017. Microfacies and Diagenetic Analysis of Lockhart Limestone, Shah Alla Ditta Area Islamabad, Pakistan. Pakistan Journal of Geology 1(1) 24-26. DOI: 10.26480/pjg.01.2017.24.26

Khawaj, M.S., Faisal, M., Ur Rehman Q., Ahmad, T., Khattak S.A., Saeed A., Adnan M.T., Irfan, Ur Rehman S., Ahmed I., Ishfaq, M. 2018. Benthic foraminiferal biostratigraphy, microfacies analysis and depositional environment of Chorgali Formation Yaadgar Section, Muzaffarabad, Pakistan. Journal: Pakistan Journal of Geology. <https://doi.org/10.26480/pjg.01.2018.21.29>

Kidwell, S.M., Holland, S.M. 1991. Field Descriptions of Coarse Bioclastic Fabrics. *Palaios* 6 (4), 426 – 434.

Lacombe, O., Bellahsen, N., Mouthereau, F. 2011. Fracture patterns in the Zagros Simply Folded Belt (Fars, Iran): constraints on early collisional tectonic history and role of basement faults *Geological Magazine* 148 (5-6), 940–963. <https://doi.org/10.1017/S001675681100029X>

Laubach, S. E. 2003. Practical approaches to identifying sealed and open fractures. *American Association of Petroleum Geologists Bulletin* 87 561–579.

Laubach, S. E., Lander, R. H., Criscenti, L. J., Anovitz, L. M., Urai, J. L., Pollyea, R. M., Hooker, J. N., Narr, W., Evans, M. A., Kerisit, S. N., Olson, J. E., Dewers, T., Fisher, D., Bodnar, R., Evans, B., Dove, P., Libicki, E. Ben-Zion, Y., 2005. Stochastic Branching Models of Fault Surfaces and Estimated Fractal Dimensions. *Pure and Applied Geophysics* 162 1077–1111

Laubach; S.E., Olson, J.E., Gross, M.R. 2009. Mechanical and fracture stratigraphy. *AAPG Bulletin* 93 (11) 1413 - 1426. <https://doi.org/10.1306/07270909094>

Ladeira, F. L., Price, N. J., 1981. Relationship between fracture spacing and bed thickness. *Journal of Structural Geology* 13, 179–83

Lamarche, J.E, Lavenue, A.P.C., Gauthier, B.D.M., Guglielmi, Y., Jayet, O. 2012. Relationship between fracture patterns, geodynamics, and mechanical stratigraphy in Carbonates (South-East Basin, France). *Tectonophysics* 581, 231-245

Larsson, C. 2018. Chapter 4 - Self-Similarity, Fractality, and Chaos, 5G Networks, editor: C. Larsson, pp 67 – 102. Academic Press. <https://doi.org/10.1016/B978-0-12-812707-0.00009-7>.

Lasemi, Z., Sandberg, P. 1993. Microfabric and Compositional Clues to Dominant Mud Mineralogy of Micrite Precursors. In: Rezak, R., Lavoie, D.L. (eds) *Carbonate Microfabrics. Frontiers in Sedimentary Geology*. Springer, New York, NY. https://doi.org/10.1007/978-1-4684-9421-1_13

- Li, W, An, X. 2018. Limestone mechanical deformation behaviour and failure mechanisms: a review. *Acta Geochem* 37(2) 153–170 <https://doi.org/10.1007/s11631-017-0259-y>
- Lokier, S.W., Junaibi, M.A. 2016. The petrographic description of carbonate facies: are we all speaking the same language? *Sedimentology*(2016)63, 1843–188. <https://doi.org/10.1111/sed.1229311>
- Lonergan, L., Wilkinson, J. J., McCaffrey, K. J. W. 1999. Fractures, fluid flow and mineralization: an introduction. In, McCaffrey, K. J. W., Lonergan, L., Wilkinson, J. J. (eds). *Fractures, Fluid Flow and Mineralization*. Geological Society, London, Special Publications, 155, 1 - 6.
- Longman, M. 1977. Factors controlling the formation of microspar in the bromide formation. Factors controlling the formation of microspar in the bromide formation. *Journal of Sedimentary Petrology* 47(1), 347 – 350.
- Long, J.C.S., Aydin, A., Brown, S.R., Einstein, H.H., Hestir, K., Hsieh, P.A., Myer, L.R., Kenneth G. Nolte, D.L., Olsson, O.L., Paillet, F.L., Smith, J.L., Thomsen, L., 1996. *Rock Fractures and Fluid Flow: Contemporary Understanding and Applications*. The National Academies Press, Washington, DC. <https://doi.org/10.17226/2309>.
- Lucia, F.J., Loucks, R.G. 2013. Micropores in carbonate mud: early development and petrogenesis. *Gulf Coast Association of Geological Societies* 2, 1- 10
- Majeeda, Y., Abu Bakar, M. Z. 2018. Water Saturation Influences on Engineering Properties of Selected Sedimentary Rocks of Pakistan. *Journal of Mining Science*, 54 (6) 914–930
- Maldonado, A ., Dight, P.M. 2020. The shear strength of bedding partings in shales of the Pilbara: the similarity of non-dilatational angles, mineralogy relationships, and nominal roughness', in Dight, P.M. (ed.), *Slope Stability 2020: Proceedings of the 2020 International Symposium on Slope Stability in Open Pit Mining and Civil Engineering*, Australian Centre for Geomechanics, Perth, pp. 551- 564, https://doi.org/10.36487/ACG_repo/2025_33

- Malik, A.M, Ahmed, N. 2014. Palaeocene Carbonate of Kohat-Potwar Sub-Basin of Upper Indus Basin, Pakistan. *Science International (Lahore)*, 26(5), 2337-2350.
- Mandelbrot B., 1967. How long is coast of Britain - statistical self-similarity and fractional dimension. *Science* 156, 636–638.
- Mandelbrot, B.B. 1983. *The Fractal Geometry of Nature*. Henry Holt and Company, 468 pp
- Mauldon, M., Dunne, W.M., Rohrbaugh M.B. Jr. 2001 Circular scanlines and circular windows: new tools for characterizing the geometry of fracture traces. *Journal of Structural Geology* 23, 247 – 258
- Marshak, S., Engelder, T. 1985. Development of cleavage in limestones of a fold-thrust belt in eastern New York. *Journal of Structural Geology*, 7 (3/4), 345 - 359
- McDougall, J.W., Hussain, A., Yeats, R.S. 1993. The Main Boundary Thrust and propagation of deformation into the foreland fold-and-thrust belt in northern Pakistan near the Indus River. Geological Society, London, Special Publications, 74, 581 - 588.
<https://doi.org/10.1144/GSL.SP.1993.074.01.38>
- Miaha, M.L. 2014. Porosity assessment of gas reservoir using wireline log data: a case study of the Bokabil Formation, Bangladesh. 10th International Conference on Mechanical Engineering, ICME 2013. *Procedia Engineering* 90 (2014) 663 – 668. <http://creativecommons.org/licenses/by-nc-nd/3.0/>
- Mirko, F, Pace, P., Vitulli, M., Sciarra, N., Calamita, F. 2019. Distribution of joints in the hinge-line culmination of foreland-verging overturned anticlines: an example from the Montagna dei Fiori structure in the Central Apennines of Italy. *Geological Magazine; Cambridge*, 156 (8) 1445-1454.
<https://doi.org/10.1017/S0016756819000050>
- Mitra, S. 2002. Fold-accommodation faults. *AAPG Bulletin* 86 (4), 671–693.
- Mirza, K., Akhter, N., Ejaz, A., Fakiha, S., Zaidi, A. 2022. Biostratigraphy, microfacies and sequence stratigraphic analysis of the Chorgali Formation, Central Salt Range, northern Pakistan. *Solid Earth Sciences* 7 (2), 104-125. <https://doi.org/10.1016/j.sesci.2021.11.003>

- Mogensen, K., Masalmeh, S. 2020. A review of EOR techniques for carbonate reservoirs in challenging geological settings. *Journal of Petroleum Science and Engineering*. (195), 107889. <https://doi.org/10.1016/j.petrol.2020.107889>
- Moore, C.H. 1989. Chapter 7 Meteoric Diagenetic Environments. Editor: Clyde H. Moore, *Developments in Sedimentology*, Volume 46, 177 – 217. Elsevier. [https://doi.org/10.1016/S0070-4571\(08\)71061-6](https://doi.org/10.1016/S0070-4571(08)71061-6).
- Moore, C.H., Wade, W.J. 2013. Carbonate Reservoirs. Porosity and Diagenesis in a Sequence Stratigraphic Framework. *Developments in Sedimentology*, Volume 67, 1 - 374. Elsevier B.V.
- Mortimore, R. 2018. The Geology Durdle Door, Dorset Chalk stratigraphy, sedimentology and tectonic structure, new marker beds. Open University Geological Society Wessex Group Field Excursion Sunday 13th May 2018
- Moshier, S.O., 1989. Microporosity in micritic limestones: a review. *Sedimentary Geology* 63 (3–4), 191-213. [https://doi.org/10.1016/0037-0738\(89\)90132-2](https://doi.org/10.1016/0037-0738(89)90132-2)
- Munnecke, A., Westphal, H., Reijmert, J.G.J., Samtlebe, C. 1997. Microspar development during early marine burial diagenesis: a comparison of Pliocene carbonates from the Bahamas with Silurian limestones from Gotland (Sweden). *Sedimentology* 44, 977-990
- Muñoz, J.A., Martinez, A., Verges, J. 1986. Thrust sequences in the eastern Spanish Pyrenees. *Journal of Structural Geology* (8), 3–4, 399-405. [https://doi.org/10.1016/0191-8141\(86\)90058-1](https://doi.org/10.1016/0191-8141(86)90058-1)
- Munneckecke, A., Westphal, H., Reijmer, J.J.G., Samtleben, C. 1997. Microspar development during early marine burial genesis: a comparison of the Pliocene carbonates from the Bahamas with Silurian limestones from Gotland (Sweden). *Sedimentology* 44,977- 990
- Naeem, M. Bin Sadiq, R.A., Anwar, M., Khalid, P. 2014. Mechanical properties and petrographic characteristics of Margalla Hill limestone and Lockhart limestone of Rusli area, Islamabad Pakistan. *Acta Geodaetica et Geophysica* 49(4):441-454. <https://link.springer.com/article/10.1007/s40328-014-0068-2>

- Qayyum, M. Spratt, D.A., Dixon J.M., Lawrence, R.D. 2015. Displacement transfer from fault-bend to fault-propagation fold geometry: An example from the Himalayan thrust front. *Journal of Structural Geology* 77, 260 - 276
- Odling, N.E., 1994. Natural Fracture Profiles, Fractal Dimension and Joint Roughness Coefficient. *Rock Mech. Rock Eng.* 27, 135-153. <https://doi: 10.1007/bf01020307>.
- Ortega, O.J., Gale, J.F.W., Marett, R. 2010. Quantifying diagenetic and stratigraphic controls on fracture intensity in platform carbonates: An example from the Sierra Madre Oriental, northeast Mexico. *Journal of Structural Geology* 32, 1943-1959 <https://doi.org/10.1016/j.jsg.2010.07.004>
- Palmstrom, A., Stille, H. 2007. Ground behaviour and rock engineering tools for underground excavations. *Tunnelling and Underground Space Technology* 22 (4), 363 – 376.
<https://doi.org/10.1016/j.tust.2006.03.006>
- Pan, X., Zhang, D., Zhang, P. 2021. Fracture detection from Azimuth-dependent seismic inversion in joint time–frequency domain. *Science Report* 11, 1269 <https://doi.org/10.1038/s41598-020-80021-w>
- Peacock, D.C.P., Nixon, C.W., Rotevatn, A., Sanderson, D.J., Zuluaga, L.F. 2016. Glossary of fault and other fracture networks. *Journal of Structural Geology* 92, 12-29
<http://dx.doi.org/10.1016/j.jsg.2016.09.008>
- Peacock, D.C.P., Sanderson, D.J. 2018. Structural analyses and fracture network characterisation: Seven pillars of wisdom. *Earth-Science Reviews* 184, 13–28
- Peacock, D.C.P., Sanderson, D.J., Rotevarn, A. 2018. Relationships between fractures. *Journal of Structural Geology*, 106, 41 - 53
- Pfiffner, O.A. 2017. Thick-Skinned and Thin-Skinned Tectonics: A Global Perspective. *Geosciences* 7(3), 71 <https://doi.org/10.3390/geosciences7030071>

- Poblet, J., Lisle, R.J. 2011. Kinematic evolution and structural styles of fold-and-thrust belts. Kinematic Evolution and Structural Styles of Fold-and-Thrust Belts. Geological Society, London, Special Publications, 349, 1 – 24 <https://doi.org/10.1144/SP349.1>
- Procter A., Sanderson, D.J. 2017. Spatial and layer-controlled variability in fracture networks. Journal of Structural Geology 108 52 – 65 <http://dx.doi.org/10.1016/j.jsg.2017.07.008>
- Qayyum, A., Poessé, J.W., Kaymakci, N., Langereis, C.G., Gülyüz, E., Ahsan, N. 2022. Neogene Kinematics of the Potwar Plateau and the Salt Range, NW Himalayan Front: A Paleostress Inversion and AMS study, International Geology Review, 64 (9), 1311 - 1329. <https://doi.org/10.1080/00206814.2021.1929514>
- Qureshi, K.A. Ghazi, S., Butt, A.A. 2018. Shallow shelf sedimentation of the Jurassic Samana Suk Limestone, Kala Chitta Range, Lesser Himalayas, Pakistan. Geol. Bull. Punjab Univ. 43: 1-14
- Rameeni, S. J., Mirza, K., Naz, H. 2007. Planktonic Foraminifera from Upper Cretaceous Kawagarh Formation, Jabri Area, Lora-Maqsood Road, Hazara, Northern Pakistan. Geol. Bull. Punjab Univ. 42, 66 – 68
- Rehman S.U., Mahmood, K., Ahsan, N., Shah, M.M. 2016. Microfacies and depositional environments of upper cretaceous Kawagarh Formation from Chinali and Thoba sections North-eastern Hazara Basin, lesser Himalayas, Pakistan. Journal of Himalayan Earth Sciences Volume 49(1), 1-16.
- Rehman, S. U., Ahsan, N., Shah, M. M., Munawar, M. J., Miraj, M. A. F., Rehman, F., Mahmood, K. 2021. Depositional environments and microfacies of the upper Turonian–Maastrichtian Kawagarh Formation, Kalachitta Range, Lesser Himalayas, Pakistan. Australian Journal of Earth Sciences 68 (7), 1017-1030. <https://doi.org/10.1080/08120099.2021.1889662>
- Rehman, S. U., Ahsan, N., Shah, M. M., Munawar, M. J., Miraj, M. A. F., Rehman, F., Mahmood, K. 2021. Depositional environments and microfacies of the upper Turonian–Maastrichtian Kawagarh Formation, Kalachitta Range, Lesser Himalayas, Pakistan. Australian Journal of Earth Sciences 68 (7), 1017-1030. <https://doi.org/10.1080/08120099.2021.1889662>

Renshaw, C.E., Pollard, D.D., 1994. Numerical simulation of fracture set formation: a fracture mechanics model consistent with experimental observations. *Journal of Geophysical Research* 99(18), 9359-9372.

Revil, A., Ahmed, A.S., Coperey, A., Ravanel, L., Sharma, R. 2020. Induced polarization as a tool to characterize shallow landslides. *Journal of Hydrology*, 589, <https://doi.org/10.1016/j.jhydrol.2020.125369>. [ffhal-03005837f](https://doi.org/10.1016/j.jhydrol.2020.125369)

Robert J. L., Kazmi, A.H. and Jan. M.Q., 1997. *Geology and Tectonics of Pakistan*. Graphic Publisher, Karachi, 554 pp.

Rohrbaugh, J. B., Dunne, W. M., Mauldon, M. 2002. Estimating fracture trace intensity, density, and mean length using circular scan lines and windows, *Am. Assoc. Petr. Geol. B.*, 86 (12), 2089–2104, <https://doi.org/10.1306/61EEDE0E-173E11D7-8645000102C1865D>

Rutty, A.L., Cruden, A.R. 1993. Pop-up structures and the fracture pattern in the Balsam Lake area, Southern Ontario. *Geographie Physique et Quaternaire* 47 (3), 379. <https://doi.org/10.7202/032965ar>

Salvini F., Storti, F. 2001. The distribution of deformation in parallel fault-related folds with migrating axial surfaces: comparison between fault-propagation and fault-bend folding. *J. Struct. Geol.*, 23 (1), 25-32. [https://doi.org/10.1016/s0191-8141\(00\)00081-x](https://doi.org/10.1016/s0191-8141(00)00081-x)

Sanderson D.J., Nixon C.W., 2015. The use of topology in fracture network characterisation. *Journal of Structural Geology* 72, 55-66. <http://dx.doi.org/10.1016/j.jsg.2015.01.005>.

Sanderson, D.J., Nixon, C.W. 2015. The use of topology in fracture network characterisation. *Journal of Structural Geology* 72, 55-66. <https://doi.org/10.1016/j.jsg.2015.01.005>

Sanderson, D.J., Peacock, D.C.P., Nixon, C.W., Rotevatn, A. 2019. Graph theory and the analysis of fracture networks. *J. Struct. Geol.*, 125 155-165. <https://doi.org/10.1016/j.jsg.2018.04.011>

- Sarkarinejad, K., Goftari, F. 2019. Thick-skinned and thin-skinned tectonics of the Zagros orogen, Iran: Constraints from structural, microstructural and kinematics analyses. *Journal of Asian Earth Sciences* 170, 249-273. <https://doi.org/10.1016/j.jseaes.2018.10.021>
- Scholle, P.A., Halley, R.B. 1989. Burial Diagenesis: Out of Sight, Out of Mind! In Scholle, P.A., James, N.P., Read, J. F. *Carbonate Sedimentology and Petrology*, Volume 4. American Geophysical Union. <https://doi.org/10.1029/SC004p0135>
- SEPM STRATA. 2022. Sediments and Rocks > Carbonates. Society for Sedimentary Geology. <http://www.sepmstrata.org/page.aspx?&pageid=88&6>
- Shackleton, J.R., Cooke, M.L., Vergés, J. 2011. Temporal constraints on fracturing associated with fault-related folding at Sant Corneli anticline, Spanish Pyrenees. *Journal of Structural Geology* 33 (1), 5-19. <https://doi.org/10.1016/j.jsg.2010.11.003>
- Shah, S.M.A., Ahmad, N., Ahmad, M.A.N., Ahsan, N., 2013. The mineralogical and petrographical studies of the lithofacies of the Hangu Formation in the Salt Range, Punjab. *Pakistan Journal of Science* 65(1), 142-149
- Shehzad, S., Iqbal, A., Rahim, H., Ahmad, T., Ahmad, W. 2018. Microfacies Analysis and Source Rock Potential of Nammal Formation, Western Salt Range Pakistan. *Int. Journ. Environ. Geol.* 9(1) 8-12. <https://doi.org/10.46660/ijeeg.Vol0.Iss0.0.8>
- Shinawi; A.E., Mésároš, P.; Zelenáková, M. 2020. The Implication of Petrographic Characteristics on the Mechanical Behaviour of Middle Eocene Limestone, 15th May City, Egypt. *Sustainability.* 12 (22) 9710. <https://doi:10.3390/su12229710>
- Shoaib, K, Zafar, Z.A. Raja, Z.A., Burley, S.D. Ratana Field, Potwar Fold Belt, Northern Pakistan: High intensity fracture zones related to major thrust faults as revealed by seismic fracture prediction. *Journal of Petroleum Geology*, 45(3), 253-282. <https://doi.org/10.1111/jpg.12819>

- Sorkhabi, R. 2014. Fracture, Fracture Everywhere - Part I. *GeoExpro*. 11 (3). Accessed 1 October 2022. <https://www.geoexpro.com/>
- Stewart, S.A. 1999. Geometry of thin-skinned tectonic systems in relation to detachment layer thickness in sedimentary basins. *Tectonics* 18 (4), 719 - 732
- Štípská, P., Schulmann, K., Höck, V. 1999. Complex metamorphic zonation of the Thaya dome: result of buckling and gravitational collapse of an imbricated nappe sequence. In *Forced Folds and Fractures*, J.W. Cosgrove; M. Ameen, S., Geological Society of London, 169. <https://doi.org/10.1144/GSL.SP.1999.169>
- Swati, M., Haneef, M., Ahmad, S. Naveed, Y., Zeb, W., Akhtar, N., Owais, M. 2013. Biostratigraphy and depositional environments of the Early Eocene Margalla Hill Limestone, Kohala-Bala area, Haripur, Hazara Fold-Thrust Belt, Pakistan. *Journal of Himalayan Earth Sciences*. (46) 65-77.
- Swennen, R., Ferket, H., Benchilla, L., Roure, F., Ellam, R. 2003. Fluid flow and diagenesis in carbonate dominated Foreland Fold and Thrust Belts: petrographic inferences from field studies of late-diagenetic fabrics from Albania, Belgium, Canada, Mexico, and Pakistan. *Journal of Geochemical Exploration* 78-79, 481-485. [https://doi.org/10/1016/S0375-6742\(03\)00064-5](https://doi.org/10/1016/S0375-6742(03)00064-5)
- Shoaib, K. Zafar, Z.A., Raja, Z.A., Burley, S.D. 2022. Ratana Field, Potwar Fold Belt, Northern Pakistan: high intensity fracture zones related to major thrust faults as revealed by seismic fracture prediction. *Journal of Petroleum Geology* 4 (3) 253 -282. <https://doi.org/10.1111/jpg.12819>
- Swati, M.A.F., Haneef, M., Ahmad, S., Latif, K., Naveed, Y., Zeb, W., Akhtar, N., Owais, M. 2014. Diagenetic analysis of the Early Eocene Margala Hill limestone, Pakistan: A synthesis for thin section porosity. *Journal of Himalayan Earth Sciences* 47(2) 49-61

- Swati, M.A.F, Haneef, M., Ahmad, S., Naveed, Y., Zeb, W., Akhtar, N. Owais, M. 2013. Biostratigraphy and depositional environments of the Early Eocene Margalla Hill Limestone, Kohala-Bala area, Haripur, Hazara Fold-Thrust Belt, Pakistan. *Journal of Himalayan Earth Sciences* 46(2) 65-77.
- Tavani, S., Snidero, M., Muñoz, J.A. 2014. Uplift-induced residual strain release and late-thrusting extension in the Anaran mountain front anticline, Zagros (Iran). *Tectonophysics* 636 257–269
<http://dx.doi.org/10.1016/j.tecto.2014.08.018>
- Tavakoli, V. 2020. Microscopic Heterogeneity. In: Carbonate Reservoir Heterogeneity. Springer Briefs in Petr. Geoscience & Eng. Springer, Cham. https://doi.org/10.1007/978-3-030-34773-4_2
- Torres-Carbonell P. J., Dimieri L. V., Olivero E. B., Poblet J., Lisle R. J. 2011. Progressive deformation of a Coulomb thrust-wedge: the eastern Fuegian Andes Thrust-Fold Belt. *Kinematic Evolution and Structural Styles of Fold-and-Thrust Belt*. Geological Society, London, Special Publications 349, 123 - 147
- Tucker, M.E. 2013. *Sedimentary Petrology: An Introduction to the Origin of Sedimentary Rocks*. 3rdEdition, Blackwell Malden, Massachusetts, USA, 272 pp.
- Unsworth, M. 2010. Magnetotelluric Studies of Active Continent–Continent Collisions. *Surv. Geophys.* 31:137–161. <https://doi.org/10.1007/s10712-009-9086-y>
- Valentini, L., Perugini, D., Poli, G., 2007. The “small-world” topology of rock fracture networks. *Physica Acta* 377, 323–328
- Vandeginste, V., Swennen, R., Allaey, M., Ellamb, R.M., Osadetz, K., Roure, F. 2012. Challenges of structural diagenesis in foreland fold-and-thrust belts: A case study on paleo-fluid flow in the Canadian Rocky Mountains West of Calgary. *Marine and Petroleum Geology* 35 (1), 235-251
- Vermilye J.M., Scholz C.H., 1995. Relation between vein length and aperture. *Journal of Structural Geology* 17(3), 423–34

- Wadood, B., Khan, S., Li, H. Liu, Y., Ahmad, S., Jia, X. 2021. Sequence Stratigraphic Framework of the Jurassic Samana Suk Carbonate Formation, North Pakistan: Implications for Reservoir Potential. *Arabian Journal for Earth Science and Engineering* 46, 525–542. <https://doi.org/10.1007/s13369-020-04654-9>.
- Walsh, J.J., Watterson, J., 1993. Fractal analysis of fracture patterns using the standard box-counting technique: valid and invalid methodologies. *Journal of Structural Geology* 15(12), 1509–1512.
- Wandrey, C.J. Law, B.E., Shah, H.A. 2004. Patala-Nammal Composite Total Petroleum System, Kohat-Potwar Geologic Province, Pakistan. U.S. Geological Survey Bulletin 2208-B. 20 pp. <http://pubs.usgs.gov/bul/b2208-b/>
- Warwick, P.D., Javed, S., Tahir, S., Tariq, M., Asrar, S., Khan, M., Khan, L. 1995. Lithofacies and Palynostratigraphy of Some Cretaceous and Palaeocene Rocks, Surghar and Salt Range Coal Fields, Northern Pakistan. U.S. Government Printing Office, e-book <https://play.google.com/store/books/details?id=9SHg3jC3b9IC&rdid=book-9SHg3jC3b9IC&rdot=1>
- Watkins, H., Bond, C.E., Healy, D., Butler, R.W.H., 2015. Appraisal of fracture sampling methods and a new workflow to characterise heterogeneous fracture networks at outcrop. *Journal of Structural Geology* 72, 67-82
- Watkins ,H., Butler, R.W.H., Bond, C.E., Healy, D. 2015. Influence of structural position on fracture networks in the Torridon Group, Achnashellach fold and thrust belt, NW Scotland. *Journal of Structural Geology* 74, 64-80. <https://doi.org/10.1016/j.jsg.2015.03.001>
- Wennberg, O. P., Svånå, T., Azizzadeh ,M., Aqrawi, A. M. M. 1, Brockbank, P, Lyslo, K. B., Ogilvie, S. 2006. Fracture intensity vs. mechanical stratigraphy in platform top carbonates: the Aquitanian of the Asmari Formation, Khaviz Anticline, Zagros, SW Iran. *Petroleum Geoscience* 12 (3) 235 – 246. <https://doi.org/10.1144/1354-079305-675>
- West, Ian M. 2017. Stair Hole near Lulworth Cove; Geology of the Wessex Coast. <https://wessexcoastgeology.soton.ac.uk/Stair-Hole-Lulworth.htm>. Visited 2023/01/19

Westermann, A. 2009. Inherited Territories: The Glarus Alps, Knowledge Validation, and the Genealogical Organization of Nineteenth-Century Swiss Alpine Geology. *Science in Context*. 22(03):439 – 461. <https://doi.org/10.1017/S0269889709990081>

Williams, V.S., Pasha, M.K., Sheikh, I.M. 1999. Geologic Map of the Islamabad-Rawalpindi area, Punjab, Northern Pakistan. Open-File Report 99-47, U.S. Department of the Interior, U.S. Geological Survey. <https://pubs.usgs.gov/of/1999/0047/report.pdf>

Wu, J., Jin, X., Mi, S., Tang, J. 2020. An effective method to compute the box-counting dimension based on the mathematical definition and intervals. *Results in Engineering* (6), 100106. <https://doi.org/10.1016/j.rineng.2020.100106>

Yeats, R.S., Hussain, A. 1987. Timing of structural events in the Himalayan foothills of north-western Pakistan. *Geological Society of America Bulletin*, 99, 161-176

Zahm, C.K., Zahm, L.C., Bellian, JA. 2010. Integrated fracture prediction using sequence stratigraphy within a carbonate fault damage zone, Texas, USA. *Journal of Structural Geology* 32 (9) 1363-174. <https://doi.org/10.1016/j.jsg.2009.05.012>
